

Peng Yu
Hongxing Xu
Zhiming M. Wang *Editors*

Plasmon-enhanced light-matter interactions

Lecture Notes in Nanoscale Science and Technology

Volume 31

Series Editors

Zhiming M. Wang, Chengdu, China
Greg Salamo, Fayetteville, AR, USA
Stefano Bellucci, Frascati RM, Italy

Lecture Notes in Nanoscale Science and Technology (LNNST) aims to report latest developments in nanoscale science and technology research and teaching – quickly, informally and at a high level. Through publication, LNNST commits to serve the open communication of scientific and technological advances in the creation and use of objects at the nanometer scale, crossing the boundaries of physics, materials science, biology, chemistry, and engineering. Certainly, while historically the mysteries in each of the sciences have been very different, they have all required a relentless step-by-step pursuit to uncover the answer to a challenging scientific question, but recently many of the answers have brought questions that lie at the boundaries between the life sciences and the physical sciences and between what is fundamental and what is application. This is no accident since recent research in the physical and life sciences have each independently cut a path to the edge of their disciplines. As both paths intersect one may ask if transport of material in a cell is biology or is it physics? This intersection of curiosity makes us realize that nanoscience and technology crosses many if not all disciplines. It is this market that the proposed series of lecture notes targets.

More information about this series at <http://www.springer.com/series/7544>

Peng Yu • Hongxing Xu • Zhiming M. Wang
Editors

Plasmon-enhanced light-matter interactions

 Springer

Editors

Peng Yu
College of Optoelectronic Technology
Chengdu University of Information
Technology
Chengdu, China

Hongxing Xu
School of Physics and Technology
Wuhan University
Wuhan, China

Zhiming M. Wang
University of Electronic Science and
Technology of China
Chengdu, China

ISSN 2195-2159

ISSN 2195-2167 (electronic)

Lecture Notes in Nanoscale Science and Technology

ISBN 978-3-030-87543-5

ISBN 978-3-030-87544-2 (eBook)

<https://doi.org/10.1007/978-3-030-87544-2>

© The Editor(s) (if applicable) and The Author(s), under exclusive license to Springer Nature Switzerland AG 2022

This work is subject to copyright. All rights are solely and exclusively licensed by the Publisher, whether the whole or part of the material is concerned, specifically the rights of translation, reprinting, reuse of illustrations, recitation, broadcasting, reproduction on microfilms or in any other physical way, and transmission or information storage and retrieval, electronic adaptation, computer software, or by similar or dissimilar methodology now known or hereafter developed.

The use of general descriptive names, registered names, trademarks, service marks, etc. in this publication does not imply, even in the absence of a specific statement, that such names are exempt from the relevant protective laws and regulations and therefore free for general use.

The publisher, the authors, and the editors are safe to assume that the advice and information in this book are believed to be true and accurate at the date of publication. Neither the publisher nor the authors or the editors give a warranty, expressed or implied, with respect to the material contained herein or for any errors or omissions that may have been made. The publisher remains neutral with regard to jurisdictional claims in published maps and institutional affiliations.

This Springer imprint is published by the registered company Springer Nature Switzerland AG
The registered company address is: Gewerbestrasse 11, 6330 Cham, Switzerland

Preface

With the development of nanoscience and the miniaturization of optical devices, optics has entered the micro-nano scale. Micro-nano structures are subwavelength structures whose study requires new phenomena, new physics, and new technologies that break the diffraction limit of light. Surface plasmon is the collective oscillation of free electrons on the metal surface—with peculiar optical properties and a strong resonance effect. It can confine the light to the nanostructure's surface, thereby overcoming the diffraction limit of light. Besides, it can dramatically enhance various light-matter interactions. Plasmonics has rich physics and broad applications and has rapidly developed into a new discipline—plasmonic photonics [1].

Various light-matter interactions, including fluorescence, single molecular detection, light propagation, photothermal, optical tweezers, photocatalysis artificial metamaterials/metasurfaces, and nonlinear optical conversion, can be significantly enhanced by plasmonics due to the achievable giant electric field enhancement [2–4]. This book is systematically presented to provide an overall understanding and insight into the emerging plasmonic photonics field by discussing the latest development in plasmon-enhanced light-matter interactions. We hope the chapters of this book contribute to the academic exchanges in plasmonic photonics, promote this emerging field to a broader range of readers, and promote the application of some Plasmonic Photonics related technologies.

The main body of the book is comprised of 12 chapters that focus on plasmon-enhanced light-matter interactions. The included chapters do not cover the entire breadth of the field of plasmonics, but we hope it will give the reader an interesting summary of this exciting field. The 12 chapters provide a comprehensive perspective on chiral plasmonics, epsilon-near-zero plasmonics, topological insulator plasmonics, evolutionary algorithms for molding nanostructure geometries, hot electrons, optical tweezers, thermoplasmonics, quantum plasmonics, and plasmonic sensing.

The editors thank all the contributors of this book for their remarkable chapters. We owe special thanks to Dr. David Packer (executive editor) and Ms. Amrita Unnikrishnan (project coordinator) at Springer for supporting this book. Last but not least, we would like to thank Mr. Baoqing Wang, who provided indispensable editorial assistance and support. Peng Yu is funded by Sichuan Science and Tech-

nology Program (No. 2020YJ0041) and the National Natural Science Foundation of China (No. 62005037). The editors acknowledge the support from the National Key Research and Development Program (No. 2019YFB2203400).

References

1. Ozbay, E. (2006). Plasmonics: Merging photonics and electronics at nanoscale dimensions. *Science*, *311*, 189–193.
2. Wei, H., Pan, D., Zhang, S., Li, Z., Li, Q., Liu, N., Wang, W., & Xu, H. (2018). Plasmon waveguiding in nanowires. *Chemical Reviews*, *118*, 2882–2926.
3. Zhu, Y., Xu, H., Yu, P., & Wang, Z. (2021). Engineering plasmonic hot carrier dynamics toward efficient photodetection. *Applied Physics Reviews*, *8*, 021305.
4. Yu, H., Peng, Y., Yang, Y., & Li, Z.-Y. (2019). Plasmon-enhanced light–matter interactions and applications. *npj Computational Materials*, *5*, 45.

Chengdu, China

Peng Yu

Chengdu, China

Zhiming M. Wang

Wuhan, China

Hongxing Xu

Contents

Chiral Plasmonics	1
Zhongyue Zhang	
Epsilon-Near-Zero Plasmonics	27
Hosein Ghobadi, Zeinab Jafari, and Israel De Leon	
Epsilon-Near-Zero Plasmonic Waveguides for Enhanced Coherent Optical Effects	57
Ying Li and Christos Argyropoulos	
Topological Insulator Plasmonics and Enhanced Light-Matter Interactions	89
Hua Lu, Dikun Li, Yangwu Li, Zengji Yue, and Jianlin Zhao	
Advanced Applications of Nonlinear Plasmonics	117
Ming Fang, Qun Ren, Jianwei You, Zhihao Lan, Zhixiang Huang, and Wei E. I. Sha	
Evolutionary Algorithms for Molding with Bezier Curves: A Novel Way to Obtain Optimized Structures at Nanoscale	137
Ramon Diaz de Leon-Zapata, Ivan Alberto Cruz-Garcia, Ariel B. de la Rosa-Zapata, Javier Mendez-Lozoya, Gabriel Gonzalez, and F. Javier Gonzalez	
Plasmon-Induced Hot Electrons in Metallic Nanoparticles	155
Lei Yan, Zhengkun Fu, and Zhenglong Zhang	
Plasmon-Enhanced Optical Forces and Tweezers	177
Domna G. Kotsifaki, Viet Giang Truong, and Síle Nic Chormaic	
Plasmon-Enhanced Optical Tweezing Systems: Fundamental and Applications	207
Mohammad Hazhir Mozaffari	

Plasmon-Enhanced Optothermal Manipulation	233
Zhihan Chen, Jingang Li, and Yuebing Zheng	
Quantum Optomagnetic Plasmonic Nanocircuits	261
Zahraa Al-Baiaty	
Recent Advances and Opportunities of Plasmonic Sensors	297
B. Bhagat, K. Mehta, T. K. Sinha, P. K. Baruah, and K. Mukherjee	
Index	331

Chiral Plasmonics



Zhongyue Zhang

Abstract Chirality is a geometric feature, corresponding to the structures that cannot be brought to coincide with their mirror images. To discriminate the object chirality is critical and significant in many areas such as life science, chemistry and physics. Chiral plasmonic from two aspects including chiral near-fields and chiroptical effects in far-fields of nanostructures will be discussed. Chiral near-fields can be characterized by the optical chirality density. Chiroptical effects in far-fields can be analyzed by the transmission matrix. As for far-field chiroptical effects, circular birefringence (CB), circular dichroism (CD) and asymmetric transmission (AT) are frequently discussed. Additional, chiral biomolecules can change some characteristics of chiral nanostructures and thus can be used for chiral sensing. The sensor is easy to implement and is non-invasive to the analyte. Therefore, chiral plasmons have good application prospects in ultra-sensitive chiral molecular sensing. Plasmonic chirality is still evolving, and many phenomena and challenges remain undiscovered, such as circularly polarized luminescence, nonlinear chiral effects, chiral selective hot electron transfer, ultrafast detection, and chiral quantum optics. The research on plasmonic chirality plays a vital role in the future development of science and technology.

Keywords Chirality · Plasmonic · Chiral near-fields · Chiral far-fields · Circularly polarized light · Sensor

1 Chiral

Chirality splits the material world into left and right, ranging from small metal clusters of atoms to continuous metal surfaces and through the whole range of molecular materials, nanomaterials, hybrid materials, bio-materials and metamaterials. During

Z. Zhang (✉)

School of Physics and Information Technology, Shaanxi Normal University, Xi'an, China
e-mail: zyzhang@snnu.edu.cn

Baltimore lectures on molecular dynamics and the wave theory of light, Lord Kelvin defined chirality as follows: “I call any geometric figure, or group of points, chiral, and say it has chirality if its image in a plane mirror, ideally realized, cannot be brought to coincide with itself” [1]. Chirality is a common natural phenomenon and exists widely in various fields of scientific research such as life chemistry. Chirality refers to the property that a structure and its mirror image cannot be completely overlapped, just as the left and right hands are mirror-symmetric but do not overlap, see Fig. 1. The word “chirality” is derived from a Greek word meaning “hand”; hence, a chiral object must have right or left handedness. These left- and right-handed structures are the mirror images of each other and are termed as enantiomers. In addition to hands, other living organisms have a large number of chiral components [2].

Chirality can be found everywhere in nature, ranging from micro-organisms and biomolecules to spiral galaxies, and plays an important role in the animal world. For example, the coloration of several butterfly wings (e.g., *Parides sesostris* and *Teinopalpus imperialis*) [3] and beetle exoskeletons (*Chrysina gloriosa*) is due to chiral photonic crystals [4]. In plants, the condensed fruit of *Pollia* exhibits iridescent color due to the chiral spiral photonic crystal. One chirality of limonene produces the smell of lemon, and the other chirality generates the smell of orange. The different performances of this smell have important consequences; for instance, in the fruit fly pheromone oil palm, the inertia of one hand attracts females, and the other hand attracts males [5]. In medicine, many drug molecules exhibit chirality. Only one enantiomer is suitable for disease treatment, and the other is non-functional or even toxic to humans [6]. All essential amino acids are chiral and have the same handedness, regardless of the equal energy of both chiral forms and the equal probability of their formation in an achiral environment. However, only one of these two occurs in nature and is the same for humans, animals, plants, and

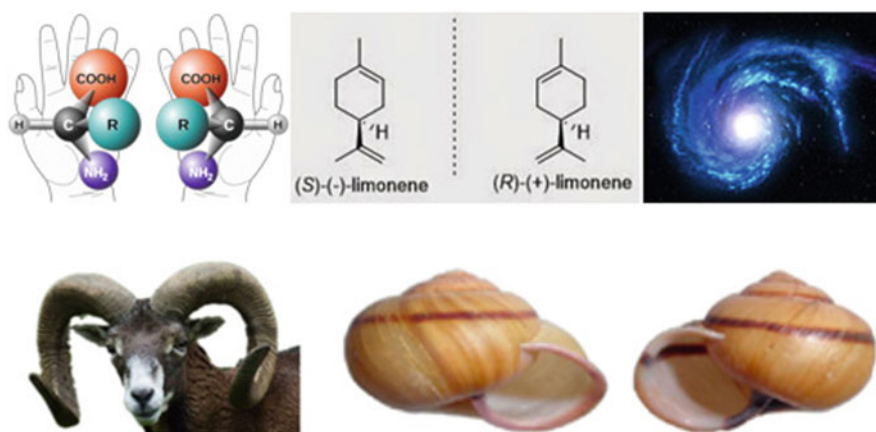


Fig. 1 Chiral objects

microorganisms [7]. Chirality appears to be a basic characteristic of living matter and perhaps even a requirement for life.

In 1848, Pasteur's experiments showed that the enantiomers of chiral molecules produce different results with polarized light. Therefore, polarized light is widely used to detect chirality. For example, the chiral structure can be detected by measuring the different absorption degrees of left circularly polarized (LCP) light and right circularly polarized (RCP) light. However, the chirality of structures in nature is extremely weak, and the interaction between chiral molecules and polarized light is not evident and thus cannot be accurately detected. With the development of nanostructure processing technologies, chiral plasmonic nanostructures or metasurfaces can be artificially manufactured to produce evanescent fields called "superchiral" plasmon near-fields, which have stronger chirality than many natural chiral systems because the artificial nanostructures structures can enhance chiral light-matter interactions [8–10].

The "superchiral" plasmonic near-field generated by the artificial chiral plasma structure can enhance the interaction between chiral light and matter. The chiral plasmonic structure maintains the "superchiral" near-field (also known as the chiral "hot spot"). One of the main research directions of chiral near-field is achiral nanostructures. 2D (planar) achiral nanostructures have attracted research attention because they can enhance local chirality by enhancing the magnetic or electric field and the nano-gap between plasmon and polymer. In general, planar achiral nanostructures can be fabricated by using electron beam lithography (EBL) and focused ion beam technology. 2D (planar) achiral nanostructures and chiral near-fields in 3D achiral nanostructures have also been widely investigated. The local chirality can be enhanced in 3D achiral nanostructures by spatially separating and enhancing magnetic or electric fields. Multiple EBL can be used to prepare 3D achiral nanostructures, the chirality of which is determined by the complex interaction between near-field interaction and phase retardation. Chiral near-fields can be characterized by the optical chirality density. The "superchiral" near-field exhibits different amplitudes and phases in the opposite case and can be used in engineering linear and nonlinear chiral interactions. For example, the "superchiral" near-field exhibits different amplitudes and phases under the excitation of RCP and LCP to manipulate the interaction of CP light materials [11]. In the interaction between quantum emitter and chiral plasmonic structure, the chiral hot spot is favorable for emission and has a specific chirality. The near-field chirality can be reflected in the far-field luminescence of the coupling dimmer, thus benefitting the luminescence of a specific hand.

Far-field chiral effect implies the interaction between polarized lights and artificial chiral plasmonic structures. The main research objects in far-field chirality are circular birefringence (CB), circular dichroism (CD), and asymmetric transmission (AT). CB refers to the optical rotation of polarization of the linearly polarized light transmitted through a chiral medium. Here, the rotation direction (clockwise or counterclockwise) is determined by the handedness of the chiral material. CD points to the differential absorption or transmission of RCP or LCP light. Chiroptical effects in far-fields can be analyzed by the transmission matrix. Assuming that a

given incident plane wave propagates in the $+z$ direction, the Jones matrix T_{circ} of circular polarization [12, 13] is described as follows:

$$T_{\text{circ}}^{+z} = \frac{1}{2} \begin{pmatrix} t_{xx} + t_{yy} + i(t_{xy} - t_{yx}) & t_{xx} - t_{yy} - i(t_{xy} + t_{yx}) \\ t_{xx} - t_{yy} + i(t_{xy} + t_{yx}) & t_{xx} + t_{yy} - i(t_{xy} - t_{yx}) \end{pmatrix} = \begin{pmatrix} t_{++} & t_{+-} \\ t_{-+} & t_{--} \end{pmatrix}, \quad (1)$$

where “ x ”, “ y ”, “ $+$ ” and “ $-$ ” are used to describe the polarized states of linearly x -polarized, linearly y -polarized, RCP light, and LCP light, respectively. $\text{Im}(t_{xx})$ and $\text{Re}(t_{xx})$ represent the real part and imaginary part of t_{xx} , respectively. The CD of the circularly polarized light is usually defined as follows:

$$CD^{+z} = T_{++} - T_{--} = |t_{++}|^2 - |t_{--}|^2 = [\text{Im}(t_{xx}) + \text{Im}(t_{yy})][\text{Re}(t_{xy}) - \text{Re}(t_{yx})] - [\text{Re}(t_{xx}) + \text{Re}(t_{yy})][\text{Im}(t_{xy}) - \text{Im}(t_{yx})] \quad (2)$$

AT is defined as the different RCP light to LCP light or LCP light to RCP light conversion efficiencies. In accordance with the above conditions, AT can also be represented by the transmission matrix.

The AT of the circularly polarized light is defined as follows [14]:

$$\Delta_{\text{circ}}^{+z} = T_{-+} - T_{+-} = |t_{-+}|^2 - |t_{+-}|^2 = [\text{Im}(t_{xx}) - \text{Im}(t_{yy})][\text{Re}(t_{xy}) + \text{Re}(t_{yx})] - [\text{Re}(t_{xx}) + \text{Re}(t_{yy})][\text{Im}(t_{xy}) - \text{Im}(t_{yx})] \quad (3)$$

2 Near-Field Chiral

The enhancement and handedness control of chiral near-fields are also crucial to improve the weak chiral effects of molecules and can be characterized by the optical chirality density, which can be quantified using the so-called optical chirality [15, 16]. In 1964, Lipkin proposed a quantity pseudo vector C [17],

$$C \equiv \frac{\varepsilon_0}{2} \mathbf{E} \cdot \nabla \times \mathbf{E} + \frac{1}{2\mu_0} \mathbf{B} \cdot \nabla \times \mathbf{B}, \quad (4)$$

where \mathbf{E} and \mathbf{B} represent electric field and magnetic field, respectively. ε_0 and μ_0 represent the vacuum dielectric constant and vacuum permeability, respectively. Lipkin’s research also pointed out that C is a quantity stored in arbitrary electromagnetic waves and has no actual physical meaning.

In 2010, Tang and Cohen of Harvard university indicated that C describes the quantity of the chirality of the electromagnetic field and represents the efficiency of exciting the chiral signal of chiral molecules. For simplified calculation and understanding, C can be derived from Eq. (4) [15, 16, 18–22]:

$$C = -\frac{\varepsilon_0\omega}{2} \text{Im}(\mathbf{E}^* \cdot \mathbf{B}), \quad (5)$$

which can be computed for monochromatic electromagnetic field. \mathbf{E} and \mathbf{B} are the complex electric and magnetic fields around the plasmonic nanostructures, respectively, and ω is their angular frequency.

According to the equation, parallel components of electric and magnetic fields can be obtained for fields with non-zero optical chirality. The maximum value of C for a plane wave is calculated from the circularly polarized light as follows:

$$C_{\text{CPL}}^{\pm} = \pm \frac{\varepsilon_0\omega}{2c} |\mathbf{E}|^2, \quad (6)$$

where $+$ and $-$ denote the LCP and RCP light, respectively, and c is the speed of light in a vacuum.

When Tang and Cohen proposed C , they assumed that the chirality of the local electromagnetic field needs be enhanced to improve the chiral signal of chiral molecules. They proposed that a strong C can be achieved at the standing wave node formed by circularly polarized light. In 2011, they experimentally verified a method to enhance chiral molecular signals [15].

To obtain a large optical chirality, researchers studied the influence of electromagnetic wave excitation of different polarization states on the optical chirality and the optical chirality with different metal nanostructures. According to Eq. (5), the magnitude of optical chirality is proportional to the imaginary part of $\mathbf{E}^* \cdot \mathbf{B}$. This equation also provides two ways to enhance optical chirality. First is by reducing the angle between the electric and magnetic fields, and second is by increasing the electric or magnetic field. For the first case, the maximum value of optical chirality can be achieved when the directions between the electric and magnetic fields are parallel or anti-parallel as shown in Fig. 2.

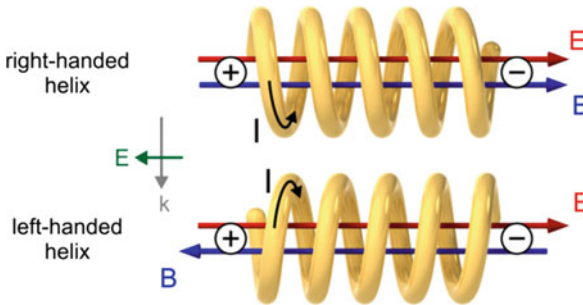


Fig. 2 Fundamental mode of a helical plasmonic nanoantenna exhibiting non-orthogonal electric and magnetic dipole moments. Given their nanostructure, the electric (red) and magnetic (blue) field vectors are mainly parallel, leading to a strong optical chirality and changes in the handedness of the structures, the relative orientation of vectors, and consequently the handedness of the chiral near-fields [26]

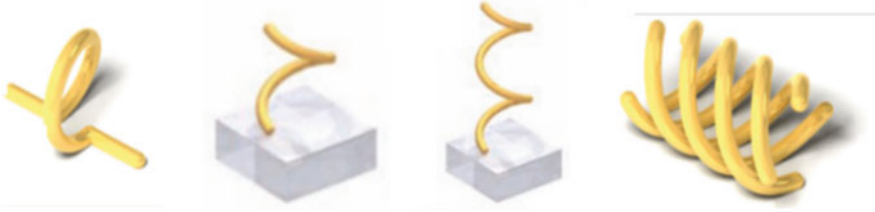


Fig. 3 Schematic of different helix nanostructures

Researchers recently proposed different plasmonic nanostructures to produce optical chirality and explored the reasons for the generation of optical chirality. Owing to the parallel directions of the electric field and the magnetic field in the spiral structure, the optical chirality is enhanced in the region surrounded by the wire. Therefore, different 3D nanostructures, such as loop-wire nanostructures [23–25] and multiple intertwined helices, have been employed to interact with circularly polarized light or linearly polarized light to generate optical chirality (Fig. 3) [11, 26]. The enhancement of optical chirality is due to the parallel electric and magnetic field components inside the spiral. The large pitch helix leads to a large volume that is enclosed by gold wires; hence, the multi-spiral nanostructure is used to improve the optical chirality as shown in Fig. 4. In general, the gold helix array is prepared by using laser to directly write photoresist and then electrochemically deposit the gold [25]. Preparing the precise helix nanostructure is extremely difficult. Therefore, the practical application of 3D devices is limited.

Layer-by-layer nanostructures composed of stacked and twisted planar nanostructures are designed to enhance local chirality depending on near-field enhancement. For this nanostructure, the enhancement of local chirality is strongest in the small gap between the upper and lower layer [18, 27, 28]. A layer-by-layer nanostructure composed of metal–dielectric–metal metasurface improves the local chirality through the interplay of the spatially separated and enhanced electric and magnetic fields with complementary profiles. In layer-by-layer nanostructures, one handed chiral field is obtained in the gap between the upper and lower layers, and the other handed chiral field surrounds the metal nanostructure [27]. The enhanced chiral near-field is located on the gap between the two nanostructured layers [27]. Unfortunately, it is difficult to use these strongly enhanced chiral fields in chiral molecular sensors. Layer-by-layer nanostructures are usually prepared through a multi-step advanced nanomanufacturing process. During the experiment, layer-by-layer nanostructures must be separated by dielectric layers, such as MgF_2 layers, so chiral molecules cannot be placed in areas where the chiral field is strongly enhanced between the interlayer spacing.

Planar polymer nanostructure illuminated with circularly polarization light is proposed to generate near-chiral fields for simplification. The chiral near-field is enhanced by boosting light–matter interaction. The improvement of local chirality originates from the simultaneous enhancement of magnetic and electric fields and

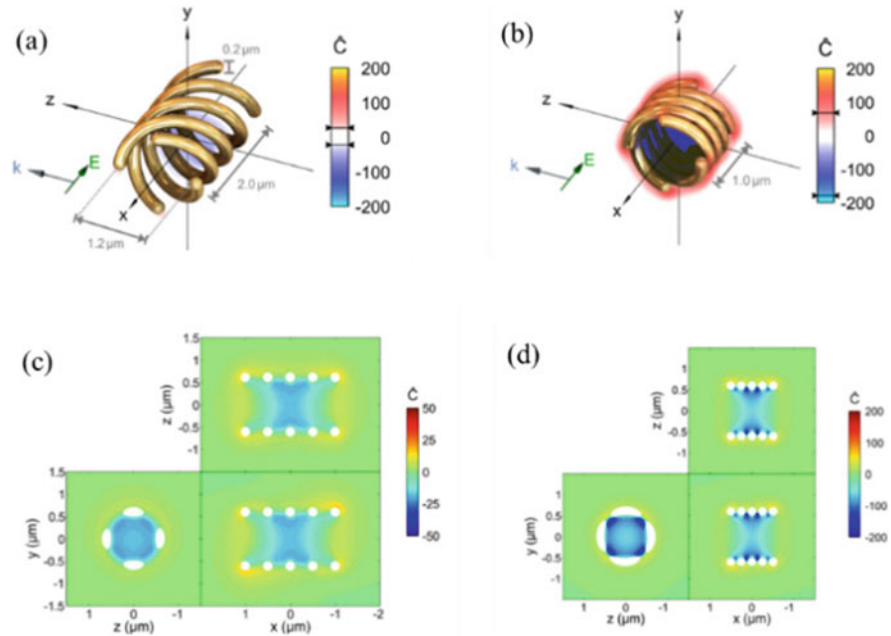


Fig. 4 (a) and (b) 3D optical chirality map for different pitch values showing chiral near-fields of one handedness in the whole interior of the nanostructure. (c) Optical chirality of slice plots for different pitch values. The slice plots confirm the confinement to the inner region [26]

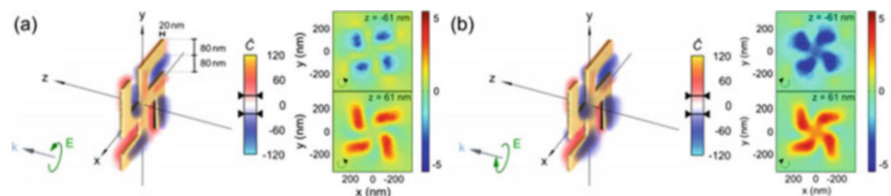


Fig. 5 Optical chirality enhancement by a planar gammadion structure illuminated with (a) LCP and (b) RCP at a wavelength of $2.01 \mu\text{m}$ [11]

their proper spatial overlap in the gap between polymer nanostructures as shown in Fig. 5 [29–33]. For example, optical chirality is generated around a swastika to achieve a chiral signal enhancement of 6 orders of magnitude. As a major difference, the gammadion shows both positive and negative values of optical chirality with similar absolute values, while for the helix the values corresponding to light with matching polarization are higher [20].

Optical chirality can be found around metal structures, and silicon (Si) nanoparticles also can generate large chiral electromagnetic fields. Si nanoparticles support electric and magnetic Mie resonances of substantial strength in the visible range of the electromagnetic spectrum [34–39]. These resonances originate from charge

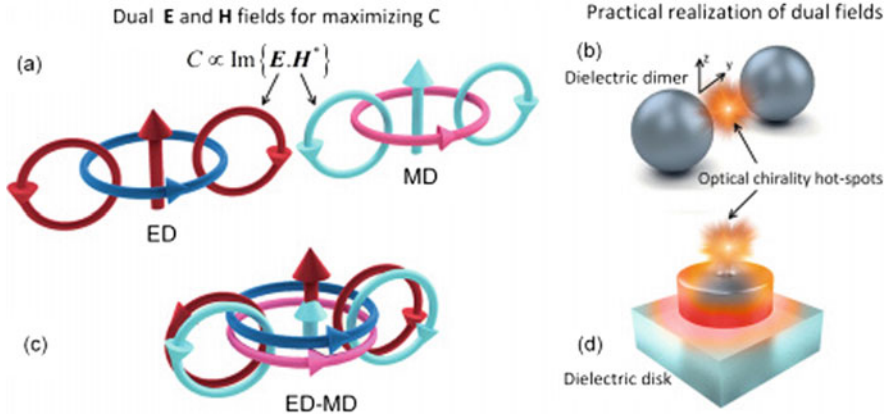


Fig. 6 (a) Duality of electromagnetic fields in a pair of electric and magnetic dipoles (ED and MD). The electric (red) and magnetic (blue) field lines of the electric dipole lie parallel with the corresponding magnetic (cyan) and electric (pink) field lines of the magnetic dipole. For comparison, similar color tones have been chosen for electric fields (red and pink) and magnetic fields (blue and cyan). (b) Realization of the dual dipoles in panel (a) by a dielectric nanodimer composed of two high refractive index spherical nanoparticles. (c) Overlapping electric and magnetic dual dipoles in a single nanoparticle by Kerker effect. (d) Holey dielectric disk could provide overlapped dipoles shown in panel (c) [36]

displacements in the high refractive index material. For Si nanodisks, the magnetic and electric dipole resonances are almost independently tunable via the aspect ratio [35, 36, 38, 40]. Solomon et al. investigated the near-field chirality enhancement in Si nanodisks with spectrally overlapping magnetic and electric dipole resonances as shown in Fig. 6 [41].

3 Far-Field Light-Matter Interactions

Artificial nanostructures provide a wealth of resources for designing customized optical responses. Different types of chiral structures have been designed with a common goal of using plasmons to enhance chiral responses. Under CPL illumination, artificial chiral metamaterials exhibit optical chirality due to the difference in refractive index and extinction coefficient of RCP and LCP. The chiral effects (CB, CD, and AT) are discussed for the far field of chiral plasmon and outlined in the following part of this chapter.

3.1 Circular Birefringence (CB)

CB refers to the optical rotation of polarization of the linearly polarized light transmitted through a chiral medium, in which the rotation direction (clockwise or counterclockwise) is determined by the handedness of the chiral material [42, 43]. Linearly polarized light can become circularly polarized light through a quarter glass and thus can be regarded as a combination of two circularly polarized lights (LCP and RCP). When RCP and LCP are transmitted in a chiral medium, linear polarization rotation occurs because their amplitudes are the same but their phase velocities are different. Kuwata–Gonokami et al. designed three sample—two enantiomorphs and an achiral pattern [31]. The measured achiral plasma structure and the rotation angle of the chiral plasma structure are shown in Fig. 7. Opposite rotation direction was observed with the left- and right-handed chiral structure, but no rotation was observed with the achiral structure.

Esposito et al. studied the hand optical properties of a 3D metal spiral system at light frequencies. A study focused on the optical activity of single nanowires and three nanowires under linear polarization and circular polarization and found that in the triple-helical nanowire configuration, the obtained pure CB can lead to a large optical activity of up to 8° , which is independent of the sample angle and extends in the visible light range in the 500 nm broad band [44].

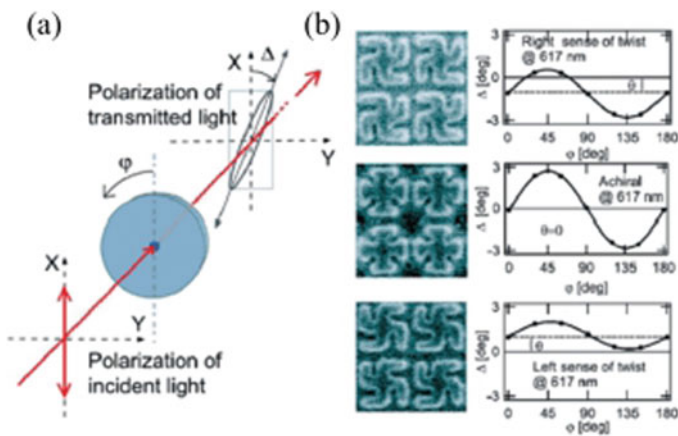


Fig. 7 (a) Schematic of CB measurement. (b) Optical rotation angles measured from plasmonic planar nanostructures with left-handedness, achiral geometry, and right-handedness [31]

3.2 Asymmetric Transmission

Circularly polarized light passing through the chiral structure is transformed into orthogonally polarized light. The conversion capacity of polarized light is called the transformation transmittance, and AT is the difference in transmittance between the two polarization states. For example, an RCP light is converted to an LCP light after passing through a chiral structure, and the quantitative relationship between the incoming RCP and the outgoing LCP is called the transformed transmittance (Fig. 8). When the incident light is LCP or RCP, the conversion transmittance is different. The conversion transmittance of the two kinds of polarized light is AT.

The AT of the circularly polarized light is defined as follows [46]:

$$AT = T_{-+} - T_{+-} = |t_{-+}|^2 - |t_{+-}|^2 = \begin{bmatrix} \text{Im}(t_{xx}) - \text{Im}(t_{yy}) \\ \text{Re}(t_{xy}) + \text{Re}(t_{yx}) \end{bmatrix} \begin{bmatrix} \text{Re}(t_{xy}) + \text{Re}(t_{yx}) \\ \text{Im}(t_{xy}) - \text{Im}(t_{yx}) \end{bmatrix} - \begin{bmatrix} \text{Re}(t_{xx}) + \text{Re}(t_{yy}) \\ \text{Im}(t_{xy}) - \text{Im}(t_{yx}) \end{bmatrix} \begin{bmatrix} \text{Im}(t_{xy}) - \text{Im}(t_{yx}) \\ \text{Re}(t_{xy}) + \text{Re}(t_{yx}) \end{bmatrix} \quad (7)$$

The AT effect was first discovered in metamaterials by Fedotov et al., who showed that this phenomenon is related to the direction of the light's propagation and the polarization state of the incident light. Under the strong interaction between electromagnetic waves and chiral metal structures, AT originates from the different polarized lights irradiated from the same polarized light in the opposite direction [47, 48]. This phenomenon is widely used in the design of polarization transformers and optical devices [49, 50]. At present, the AT effect of circularly polarized light excitation on many complex 3D has been studied. The AT effect of helical plasmonic nanostructures is the result of introducing spatial asymmetry into helical chiral nanostructures [13, 51].

The chiral plasmonic nanostructure of twist nanoslit-nanorod arrays can produce a remarkable AT effect (Fig. 9). Figure 10 illustrates that at the resonant wavelength, the spectra of T_{-+} and T_{+-} correspondingly present peaks and valleys, respectively, leading to a large AT effect. When the irradiation direction of polarized light is

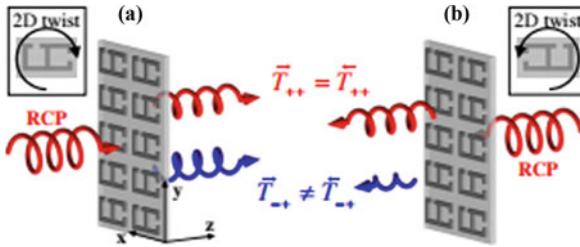


Fig. 8 (Color online) Asymmetric total transmission of a circularly polarized light incident on (a) front and (b) back side of a planar chiral metamaterial. The incident right-handed circularly polarized light (red spiral) is partially converted to the left-handed (blue spiral) polarization when propagating through the metamaterial [45]

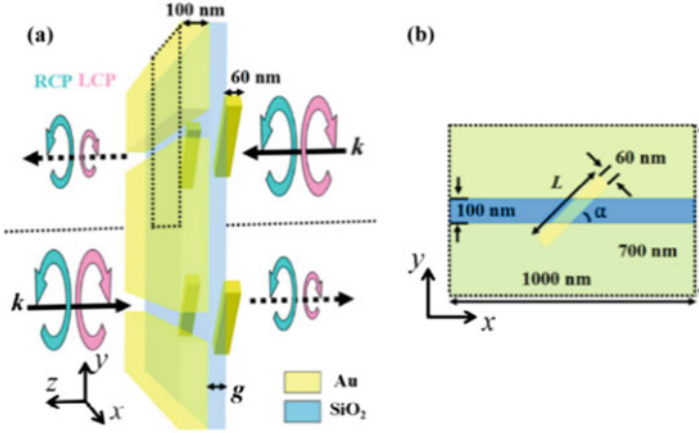


Fig. 9 (a) Schematic of TNNAs and (b) their unit cell with the associated geometric features [14]

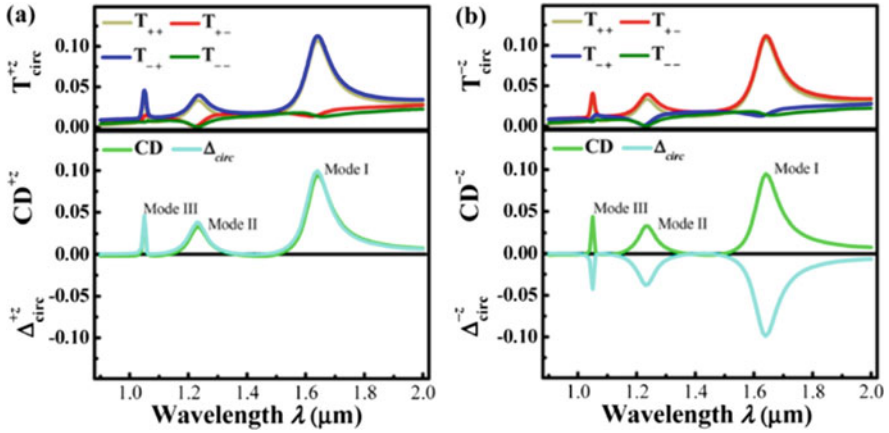


Fig. 10 Simulated $(T)_{circ}$ matrix, CD spectrum, and AT spectrum of TNNAs for $+z$ -direction light excitation (a) and $-z$ -direction light excitation (b). Three resonances labeled as mode I, II, and III [14]

changed, the spectra for T_{-+} and T_{+-} will produce reverse effects. The AT effect is highly dependent on the geometric parameters of the twist nanoslit-nanorod arrays.

The layer-by-layer structure is introduced to generate the AT effect of electromagnetic coupling between adjacent layers. Here, a composite chiral metamaterial composed of cut-wire pair and conjugated gammadion resonators is proposed (Fig. 11) [46]. Figure 11 shows that by changing the effective dielectric constant of composite chiral metamaterial medium, the electromagnetic behavior of the metamaterial can be controlled manually.

Spiral or multilayered chiral metamaterials are prepared using a complex process of bottom-up and top-down approach. Therefore, planar structures that produce AT

Fig. 11 (a) Scheme of a unit cell of the composite chiral metamaterial. (b) Photograph of the experimental sample [46]

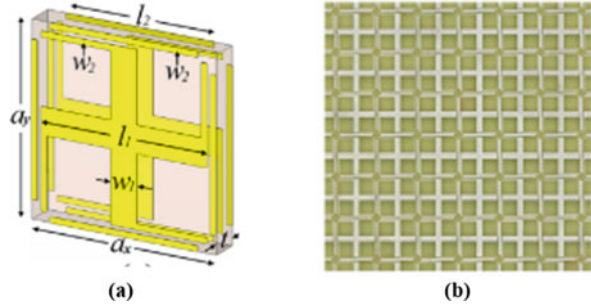
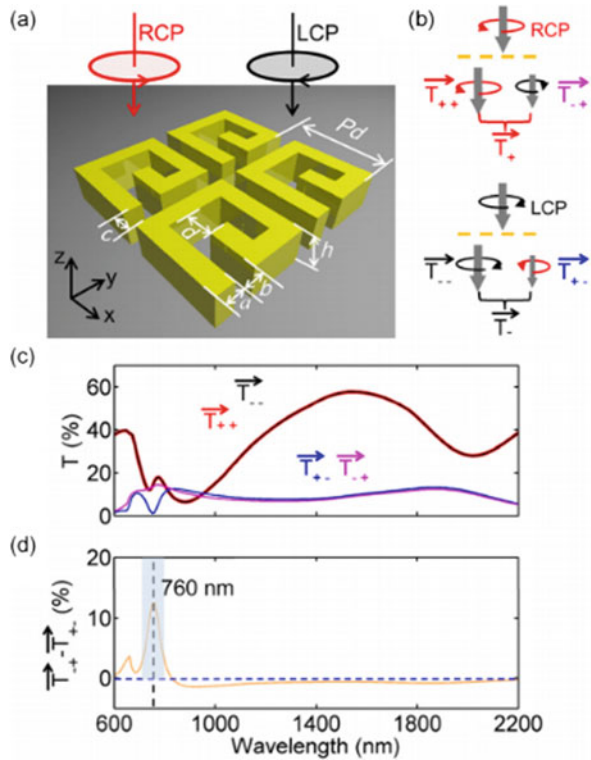


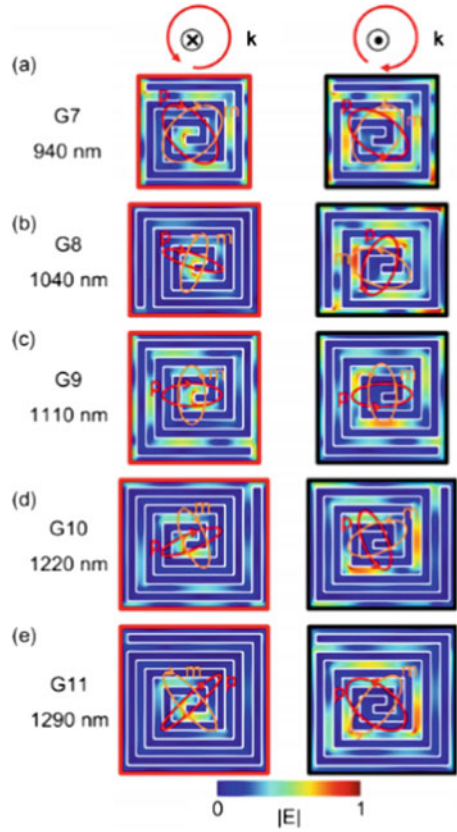
Fig. 12 (a) Design of the gold G-shaped chiral metamaterial suspended in air. (b) Illustration of transmission and polarization conversion of circularly polarized light partially directly transmit remaining the same handedness and partially convert to the opposite handed component. (c) Spectra for direct transmission T_{++} , T_{--} , circular polarization conversion T_{-+} , T_{+-} , and (d) circular polarization conversion dichroism $T_{-+} - T_{+-}$ [52]



effect, such as G-shaped structures, coupled cleavage resonators, and chiral fish-scale structures, have become research hotspots [52] (Fig. 12).

Broadband AT can be achieved in the spectral range using 2D monolayer spiral metamaterials. The AT effect with a bandwidth greater than 940 nm in the range of 965–1905 nm is realized by increasing the winding number of the element atoms (Fig. 13). Electric and MD have opposite chirality as incident lights. They radiate the counter-handed transmitted field component, which leads to the conversion from the incident RCP light to the transmitted LCP light.

Fig. 13 Electric field magnitude $|E|$ distributions excited by RCP light incident from opposite sides are presented by grey maps for structures G7 (a), G8 (b), G9 (c), G10(d), and G11 (e). Propagating directions of lights are indicated by the light vectors \mathbf{k} . The induce effective electric \mathbf{p} and magnetic \mathbf{m} dipoles in individual elements are given by solid black (red online) and grey (orange online) lines, respectively [52]



In contrast to the above protruding planar structures, metal films with nanoslits are easily and directly powered on as specific electrodes [53]. Such films can confine localized electric fields along the nanoslits (Figs. 14 and 15). Therefore, the design of nanoslits in thin films can aid in clarifying the mechanism of this effect and may show promising applications.

Tilted rectangular nanohole arrays (Fig. 16) in a square lattice have been proposed to produce AT effect. The AT properties of the tilted rectangular nanohole strongly depend on structural parameters, such as width, length, thickness, and tilted angle of tilted rectangular nanohole.

When the tilted rectangular nanohole is irradiated by circularly polarized light, the LSP and SPP appear around the tilted rectangular nanohole, thus producing the AT effect. In particular, the mechanism of SPPs provides another means to achieve AT effect, that is, when the array period matches the wavelength of the SPPs.

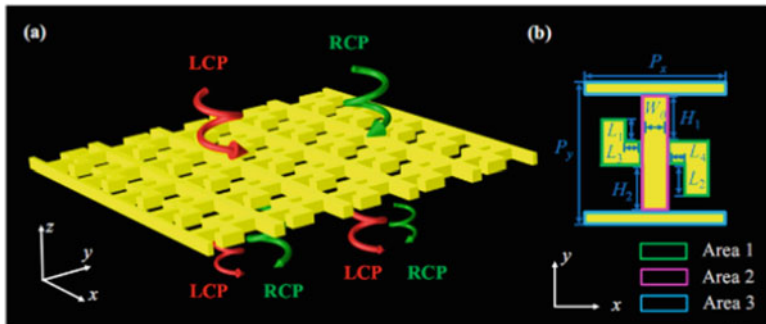


Fig. 14 (a) Schematic model of connected gammadion-shaped nanostructure arrays and (b) their unit cell with the associated parameter definition [54]

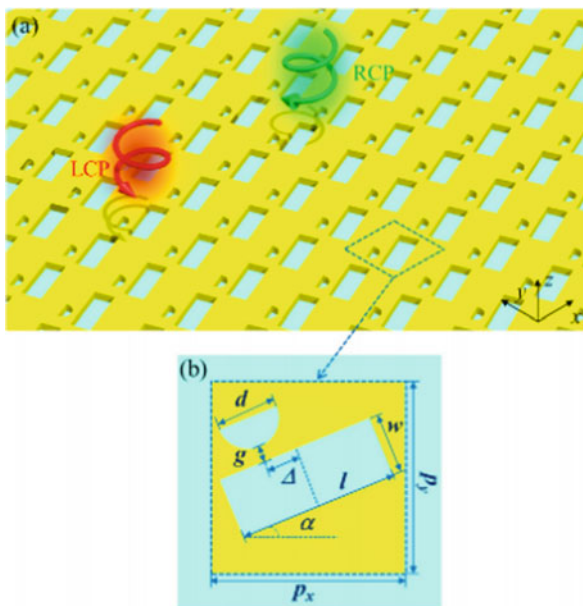


Fig. 15 (a) Schematic model of nanostructure arrays and (b) their unit cell with the associated parameter definition [55]

3.3 Circular Dichroism (CD)

CD points to the differential absorption or transmission of RCP or LCP light [57]. This parameter can identify enantiomers and is important in life science, analytical chemistry, biochemistry, and medical science. Compared with natural chiral molecules, such as DNA and proteins, artificially manufactured chiral plasmonic

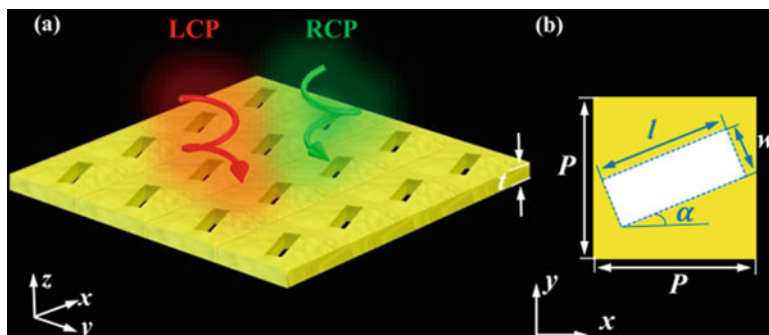


Fig. 16 (a) Schematic of tilted rectangular nanohole arrays with perforated gold film and (b) their unit cell with the associated geometric features [56]

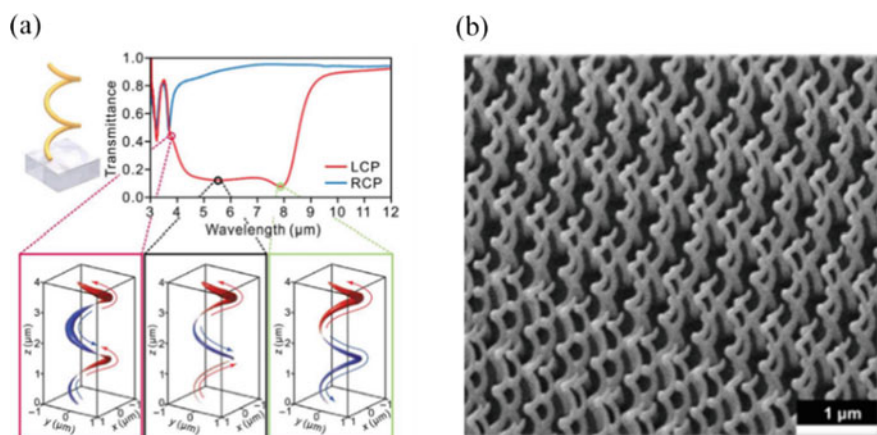


Fig. 17 (a) Simulated transmittance spectra and plasmonic modes of a metallic spiral with two pitches. The structures basically block LCP light while transmitting RCP light nearly without loss [25]. The observed plasmonic modes extend over the entire structure, thus being strongly handed themselves. (b) Platinum helices produced by focused ion and electron beam deposition [59]

nanostructures show larger CD response. Different strategies have been adopted to enhance the CD signal and improve detection sensitivity.

The helix is a typical chiral geometric structure and has attracted attention for CD effect enhancement. In 1940s, Kraus invented the helical antenna [58], which is widely used today. Gansel et al. proved that the vibration mode of the plasmon helix is a standing wave type. Figure 17a shows that the structures basically block LCP light while transmitting RCP light nearly without loss. Each of these modes has a distinct handedness and thus predominately interacts with the light of the same handedness [25]. Esposito et al. used focused ions and electron beam-induced deposition to prepare platinum helix with up to 22% CD in the visible spectrum as shown in Fig. 17b [59]. Helical nanostructures typically result in CD spectra in the

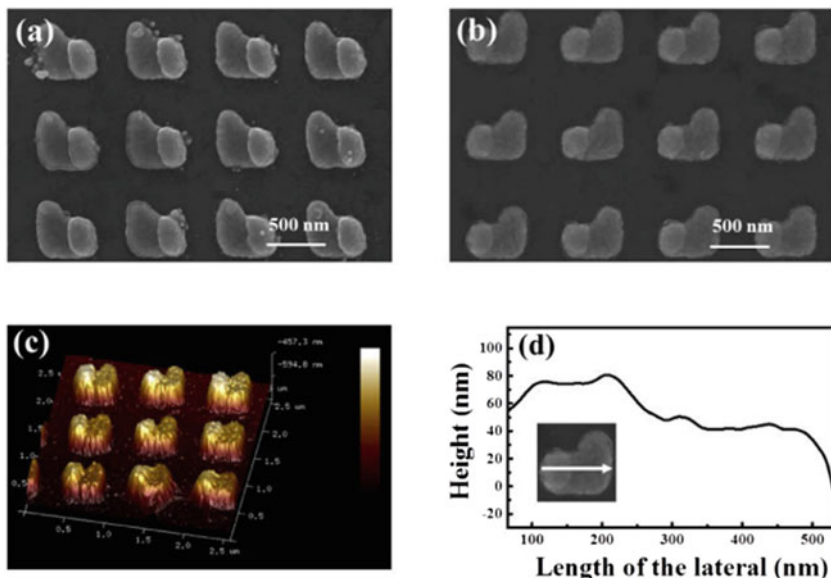


Fig. 18 (a) SEM images and 3D AFM measurement of nanostructure. (a), (b) SEM images of LH- and RH-LSNDH arrays; (c) 3D AFM image of RH-LSNDH arrays; (d) height profile of LSNDH in panel (a) along the cross-section line shown in the bottom left corner. The height of the arm with coverage layer height is approximately 60 nm [67]

visible and NIR regions; however, their cumbersome preparation process hinders their application.

Given that the helical structure is difficult to prepare, scientists have proposed different kinds of 3D structures to enhance the CD effect. Zhao et al. used the colloidal monolayer technology of PS beads and the glancing angle deposition (GLAD) technology to create 3D nanostructures. Helically stacked plasmonic layers [60] and fan-shaped nanostructures [61] (Fig. 18a) have partial characteristics of helical. By using a similar technique, Zhang et al. designed L-shaped chiral nanostructures with different thicknesses of the two slices [62], U-shaped tilted multilayer structures [60], and chiral L-shaped nanostructure added with an achiral nanorod [63]. In the U-shaped tilted multilayer structures, the thickness of the SiO₂ film served as the basis to control the phase difference [60]. The CD signal of the U-shaped 3D structure increases with the phase difference. A chiral L-shaped nanostructure at the bottom is coupled with an achiral nanorod acquiring different positions in the top layer with respect to the long and/or short arm of the chiral L-shaped nanostructure at the bottom layer [63]. The metastructure generates a giant CD signal resulting from the strong coupling of the multipolar and dipolar resonant modes on the two layers.

In addition to providing a certain spiral characteristic for the structure, other strategies can be employed to enhance the CD effect. In the Fabry–Perot (F–P)

cavity strategy, the CD effect can be enhanced by multiple reflections inside the dielectric spacer [64, 65]. Metal–insulator–metal (MIM) structures with periodic ordered patterns offer rich optical responses and CD effects from the coupling between the localized plasmon of nanoparticles and the surface plasmon mode sustained by the underlying metallic layer [66]. The CD effect can also be improved by the direct coupling of the upper metal and the lower metal. For example, L-shaped planar silver nanostructures were prepared using EBL and normal electron beam deposition, and the GLAD method was used to partially cover one arm of the L-shaped nanostructure as shown in Fig. 18 [67]. Simulations revealed that the height difference in the two arms of the L-shaped NDH causes a variation in the polarization directions of the LCP and RCP incident light, thereby generating CD effects.

In addition to the 3D nanostructures, the CD effect is also found in the layer-by-layer nanostructure. Decker et al. prepared chiral metamaterial structure composed of right-handed twisted gold crosses (Fig. 19a). Although single-layer crosses are not chiral, they develop chirality along the direction perpendicular to their surface when placed on top of another layer of cross and rotated on an angle [68]. Another typical structure is the U-shaped nanostructure, which is also called split ring resonator (SRR). Decker et al. prepared an array of SRRs, where the unit cell is made of four SRRs each rotated at 90° with respect to its neighbors as shown in Fig. 19b [69].

Compared with 3D and layer-by-layer structures, the chirality of the planar structure is relatively small because the former are a real chiral structure, whereas the chirality of the planar structure is mainly caused by the physical difference between the air sample and the sample–matrix interface. Although the chirality of

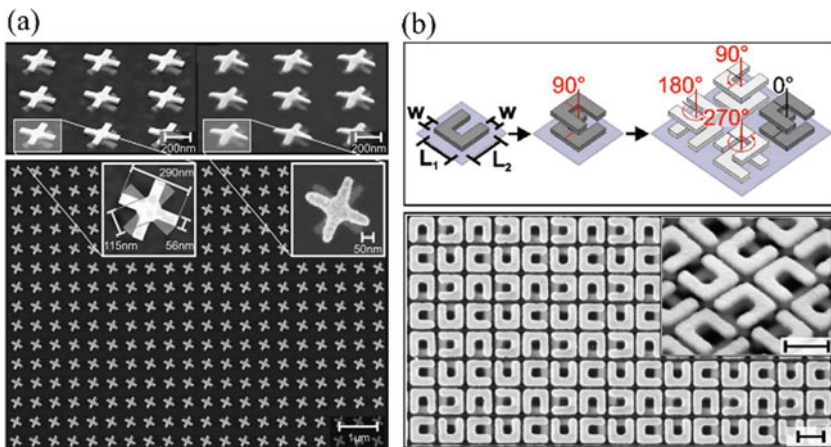


Fig. 19 (a) Scheme of the chiral metamaterial structure composed of right-handed twisted gold crosses [68]. (b) Schematic diagram and SEM image of a four-fold rotationally symmetric double-layer composed of U-shaped gold nanostructures [69]

planar structures is relatively small, planar chiral nanostructures can be combined with other materials through modern nanomanufacturing technology to open up new possibilities. For example, introducing 2D materials to the planar structure can produce strong surface electric field and lead to large CD effects [70]. For the most basic array composed of a single chiral structure, such as S-shaped [71] and gammadion-shaped [72] nanostructure, the CD effect occurs due to the LSP on the different parts of structures. Another common technique is the coupling between the two structures and the enhancement of the CD effect through the gap plasmon. The CD signal of planar heptamer gold nanostructures is due to the coupling between light and dark collective modes achieved by rotating the peripheral hexamer [29], thus providing large local electromagnetic field enhancements and strong near-field couplings.

4 Sensor

Chiral biomolecules are one of the basic units of life. Certain chiral molecular units are also important components of many drugs. Therefore, the detection and sensing of chiral molecules are particularly important. However, the weak chiral response of chiral molecules complicates the process of chiral molecular sensing. Chiral biomolecules can change some characteristics of chiral nanostructures and thus can be used for chiral sensing. This technique is easy to implement and is non-invasive to the analyte. Therefore, chiral plasmons have good application prospects in ultra-sensitive chiral molecular sensing.

The wavelength shift of chiral molecules can be achieved through the superchiral electromagnetic field capability generated by artificial chiral plasmonic nanostructures [73–78]. For example, the superchiral electromagnetic field generated by the optical excitation of plasmonic plane chiral metamaterial (PCM) is a highly sensitive probe of chiral supramolecular structure [78]. The PCM is prepared into a gamma-ray structure. The CD spectrum of the structure produces three resonance modes, which correspond to different localized surface plasmon resonances (LSPRs). When biomolecules are adsorbed, the gamma structure can be strongly coupled with chiral molecules. The refractive index change of LSPRs will displace the LSPRs, thereby changing the CD spectrum of PCM. The asymmetry of the refractive index of biomolecules can be extracted by the deviation of the CD spectrum. Therefore, the chirality of biomolecules can be judged, and the detection sensitivity can be greatly improved.

A low-cost and high-efficiency tilt angle deposition method has also been used to prepare large-area chiral molecular probes (in Fig. 20a) [76]. The plasmonic chiral conic nanoshell metallic nanostructure (CCNM), which is composed of three nanoshells of different heights, is synthesized by varying the incidence and orientation angles of deposition to achieve symmetry breaking. Such a conic nanoshell nanostructure can couple the incident light into the nanostructure, thus reducing the reflection and localizing the electromagnetic energy inside the nanoshell. This

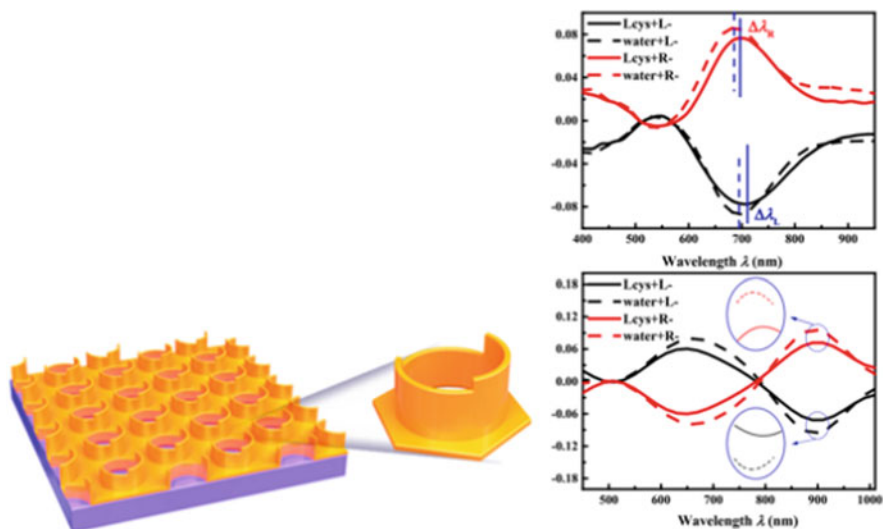


Fig. 20 (a) CCNM Structural diagram (b) experimental and simulated ΔT spectra of the R-CCNM and the L-CCNM in water (dashed line) and chiral L-cys solution (solid line). The shift of resonant peak from water to the chiral solution is defined as $\Delta\lambda$, and the inset is the amplified shift of the CD peak

structure can also achieve CD spectrum shift by adsorbing chiral molecules (in Fig. 20b) for chiral molecule detection.

In 1966, Bosnich showed that chiral molecules can induce CD at the absorption lines of achiral molecules with which they are closely interacting [79]. Induced circular dichroism (ICD) is the one which results from the interaction of chiral molecules with metal nanostructures, in this case the CD signal of chiral molecules lies between ultraviolet and visible bands. With monolayer inscribed graphene dual-rings arrays (IGDAs) and chiral molecular structures as examples, the ICD from the interaction of chiral molecules and metal nanostructures is shown in Fig. 21a, b. Figure 21c shows the T_{++} of chiral molecules, outer rings, inner rings, and IGDAs with chiral molecules. The T_{++} of chiral molecules, inner rings, and outer rings presents three resonant dips in $\lambda_0 = 0.192 \mu\text{m}$, $\lambda_{\text{IR}} = 22.084 \mu\text{m}$, and $\lambda_{\text{OR}} = 41.131 \mu\text{m}$, respectively. When the IGDAs composed of the inner ring and the outer ring are immersed in a chiral molecule, their transmission spectrum (black line) T_{++} ranges from $10 \mu\text{m}$ to $60 \mu\text{m}$ band and shows nine new resonance dips represented by λ_i (i from “1” to “9”). At the wavelength λ_i , the newly appeared CD signal is called an induced CD signal. Researchers have experimentally and theoretically studied the interaction between chiral molecules and metal nanostructures to induce molecular chiral signals from the ultraviolet band to the visible light band.

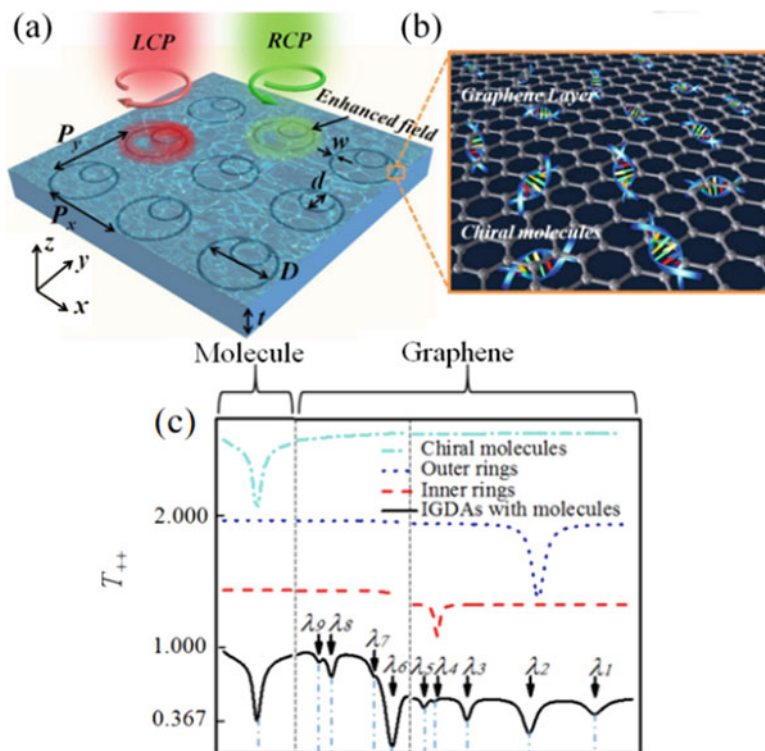


Fig. 21 (a) Schematic of IGDA immersed in chiral molecular solution and parameters definition; (b) the zoom cell presenting grapheme layer and chiral molecules; (c) T_{++} of chiral molecules, outer rings, inner rings, and IGDA with chiral molecules [80]

In theory, the plasma-enhanced CD is an ideal choice for detecting the chirality of molecules [81, 82] and can achieve the chirality detection of single-layer molecules or single molecules. As shown in Fig. 22a–c, gold nanorod dimers with chiral molecules fixed in the gap have stronger effect on resonance and non-resonance CD signals. For a gap size of 5 nm, an enhancement factor of up to 3000 can be expected. The CD enhancement factor is related to the average electric field in the gap [83]. Figure 22d–f shows that the CD spectra of individual chiral molecules and IGDA with chiral molecules almost overlap at $\lambda_0 = 0.192 \mu\text{m}$. However, the CD spectrum of IGDA with chiral molecules exhibits new CD signals in the microwave band. The wavelength of these newly emerged CD signals is almost the same as the resonance wavelength of IGDA. Hence, the resonance valley is determined by the chiral molecule.

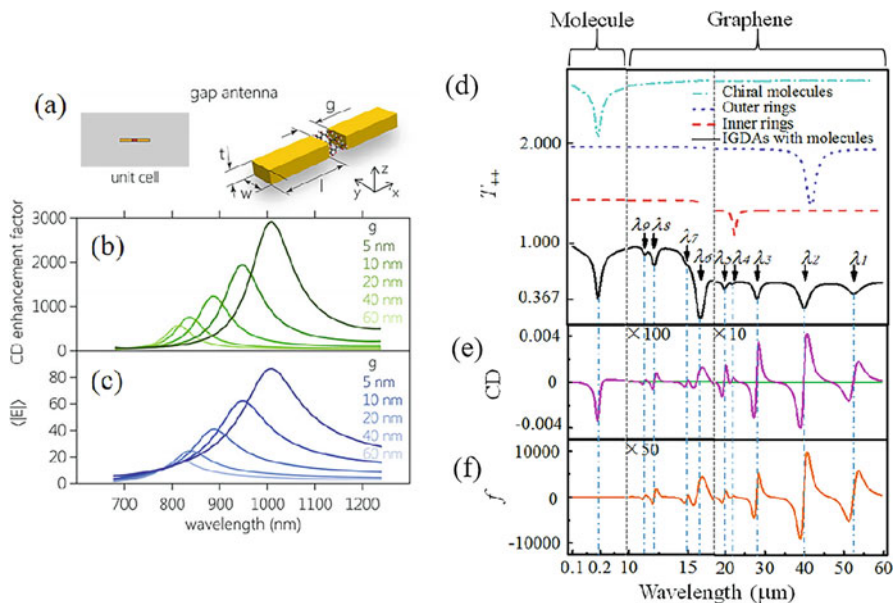


Fig. 22 (a) Schematics of gold nanorod dimer with chiral molecules immobilized in the gap; (b) calculated CD enhancement factor for different gap size; (c) corresponding values of average electric field in the gap volume [85]. (d) T_{++} of chiral molecules, outer rings, inner rings, and IGDA with chiral molecules; (e) CD spectra of chiral molecules alone (green line) and with IGDA (magenta line); (f) the CD enhancement factor f as the ratio between the values of magenta line and with green line [81]

Experimental analysis of the formation of chemical bonds revealed that molecular charges can be transferred to surface plasmonic nanostructures [85]. In addition, optical activity can be enhanced or inhibited through specially tailored nanostructures to customize optical activity [86]. As shown in Fig. 23, the formed achiral nanoparticles, namely, gold/silver core/shell nanocubes, can be used as chiral additional molecules of the plasma and can provide 2 orders of magnitude CD enhancement in the near visible region [87].

Chiral molecular sensing is important and is currently achieved by moving the chiral CD spectrum or inducing CD production. The self-assembly of plasmonic nanostructures triggered by chiral molecules is a promising method for chiral molecular sensing [74]. Therefore, chiral plasmons play an important role in chiral molecular sensing. Many possibilities and aspects worth studying remain unexplored.

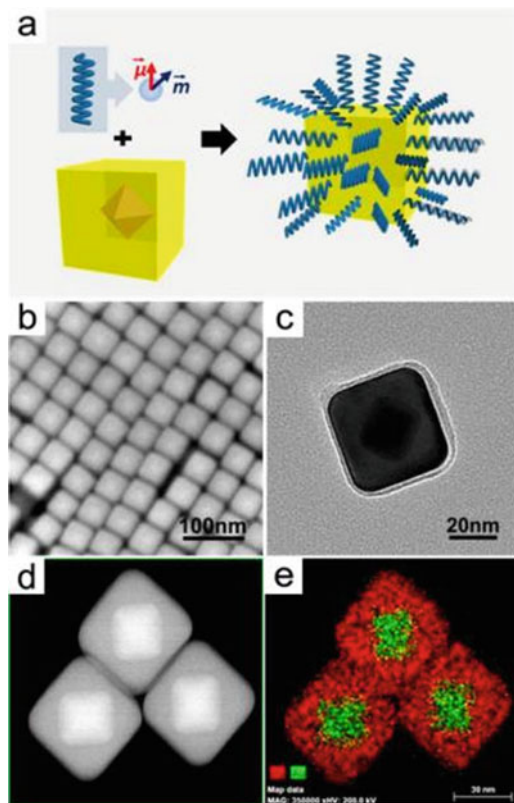


Fig. 23 Plasmonic nanoparticle with chiroptical activity, based on silver nanocube and DNA. (a) Design of “individual plasmonic chiral nanoparticle” using a gold/silver (Au/Ag) core–shell nanocube (namely, Ag NC) surface-functionalized with chiroptical molecules (e.g., DNA), theoretically expected to exhibit a plasmon- CD response. Structural characterizations of single-strand (ss) DNA-functionalized Ag NCs (b–e). (b) Low-magnification scanning electron microscopy (SEM) and (c) transmission electron microscopy (TEM) images show size and shape uniformity of nanocubes with edge length of 42 ± 2 nm. (d and e) Scanning transmission electron microscopy (STEM) and the corresponding energy dispersive X-ray (EDX) mapping images showing that the nanocube is made of an octahedral Au core embedded with thick cubic shell of Ag [87]

5 Outlook

Plasmonic chirality shows many unique characteristics in the near and far fields and provides many exciting possibilities for the sensing of molecular chirality for chirality improvement and CD induction. Different chiral metal nanostructures, such as 3D, multi-layer, and planar chiral nanostructures, have been prepared using some advanced methods, including top-down and bottom-up technology, and can be combined with different chiral molecules for various sensors. However, a tunable sensor is necessary for practical application. On the basis of their continuous

maturity in scientific research and their high electron mobility, 2D materials have shown good effects in the design and regulation of metal structures [88, 89]. Recent research indicated that surface plasmon effects can also be excited in semiconductors, such as InAs nanowires and carbon nanotubes [90–92]. Given the electrical tunability of semiconductors, electric fields can be used to control the light field and achieve the tunability of plasmons and chirality. These ideas can serve as references for the design of molecular sensors based on plasmonic chiral nanostructures in the future and provide new ideas for the generation of plasmonic chirality.

Plasmonic chirality is still evolving, and many phenomena and challenges remain undiscovered, such as circularly polarized luminescence, nonlinear chiral effects, chiral selective hot electron transfer, ultrafast detection, and chiral quantum optics. The research on plasmonic chirality plays a vital role in the future development of science and technology.

References

1. Thomson, W., & Kelvin, B. (2010). Lecture Xi. In *Baltimore lectures on molecular dynamics and the wave theory of light* (pp. 122–134). Cambridge University Press.
2. Hutt, A. J., & Tan, S. C. (1996). Drug chirality and its clinical significance. *Drugs*, 52(Suppl 5), 1–12.
3. Sharma, V., et al. (2009). Structural origin of circularly polarized iridescence in jeweled beetles. *Science*, 325(5939), 449–451.
4. Vignolini, S., et al. (2013). Analysing photonic structures in plants. *Journal of the Royal Society Interface*, 10(87), 20130394.
5. Coric, I., & List, B. (2012). Asymmetric spiroacetalization catalysed by confined Bronsted acids. *Nature*, 483(7389), 315–319.
6. Du, W., et al. (2019). Chiral plasmonics and enhanced chiral light-matter interactions. *Science China Physics, Mechanics & Astronomy*, 63(4), 1–11.
7. Collins, J. T., et al. (2017). Chirality and chiroptical effects in metal nanostructures: Fundamentals and current trends. *Advanced Optical Materials*, 5(16), 1700182.
8. Yoo, S., & Park, Q. H. (2019). Metamaterials and chiral sensing: A review of fundamentals and applications. *Nanophotonics*, 8(2), 249–261.
9. Luo, Y., et al. (2017). Plasmonic chiral nanostructures: Chiroptical effects and applications. *Advanced Optical Materials*, 5(16), 1700040.
10. Hentschel, M., et al. (2017). Chiral plasmonics. *Science Advances*, 3(5), e1602735.
11. Schäferling, M., et al. (2012). Tailoring enhanced optical chirality: Design principles for chiral plasmonic nanostructures. *Physical Review X*, 2(3), 031010.
12. Pfeiffer, C., et al. (2014). High performance bianisotropic metasurfaces: Asymmetric transmission of light. *Physical Review Letters*, 113(2), 023902.
13. Gansel, J. K., et al. (2010). Gold helix photonic metamaterials: A numerical parameter study. *Optics Express*, 18(2), 1059–1069.
14. Wang, Y., et al. (2016). Co-occurrence of circular dichroism and asymmetric transmission in twist nanoslit-nanorod arrays. *Optics Express*, 24(15), 16425–16433.
15. Tang, Y., & Cohen, A. E. (2011). Enhanced enantioselectivity in excitation of chiral molecules by superchiral light. *Science*, 332(6027), 333–336.
16. Tang, Y., & Cohen, A. E. (2010). Optical chirality and its interaction with matter. *Physical Review Letters*, 104(16), 163901.

17. Lipkin, D. M. (1964). Existence of a new conservation law in electromagnetic theory. *Journal of Mathematical Physics*, 5(5), 696–700.
18. Schäferling, M., et al. (2016). Reducing the complexity: Enantioselective chiral near-fields by diagonal slit and mirror configuration. *ACS Photonics*, 3(6), 1076–1084.
19. Schaeferling, M., Yin, X., & Giessen, H. (2012). Formation of chiral fields in a symmetric environment. *Optics Express*, 20(24), 26326–26336.
20. Meinzer, N., Hendry, E., & Barnes, W. L. (2013). Probing the chiral nature of electromagnetic fields surrounding plasmonic nanostructures. *Physical Review B*, 88(4), 041407.
21. Hendry, E., et al. (2012). Chiral electromagnetic fields generated by arrays of nanoslits. *Nano Letters*, 12(7), 3640–3644.
22. Davis, T. J., & Hendry, E. (2013). Superchiral electromagnetic fields created by surface plasmons in nonchiral metallic nanostructures. *Physical Review B*, 87(8), 085405.
23. Tretyakov, S. A., et al. (1996). Analytical antenna model for chiral scatterers: Comparison with numerical and experimental data. *IEEE Transactions on Antennas and Propagation*, 44, 1006–1014.
24. Rockstuhl, C., et al. (2009). Optical activity in chiral media composed of three-dimensional metallic meta-atoms. *Physical Review B*, 79(3), 035321.
25. Gansel, J. K., et al. (2009). Gold helix photonic metamaterial as broadband circular polarizer. *Science*, 325(5947), 1513–1515.
26. Schäferling, M., et al. (2014). Helical Plasmonic nanostructures as prototypical chiral near-field sources. *ACS Photonics*, 1(6), 530–537.
27. Rui, G., et al. (2019). Symmetric meta-absorber-induced superchirality. *Advanced Optical Materials*, 7(21), 1901038.
28. Decker, M., et al. (2007). Circular dichroism of planar chiral magnetic metamaterials. *Optics Letters*, 32(7), 856–858.
29. Zu, S., Bao, Y., & Fang, Z. (2016). Planar plasmonic chiral nanostructures. *Nanoscale*, 8(7), 3900–3905.
30. Papakostas, A., et al. (2003). Optical manifestations of planar chirality. *Physical Review Letters*, 90(10), 107404.
31. Kuwata-Gonokami, M., et al. (2005). Giant optical activity in quasi-two-dimensional planar nanostructures. *Physical Review Letters*, 95(22), 227401.
32. Horrer, A., et al. (2020). Local optical chirality induced by near-field mode interference in achiral plasmonic metamolecules. *Nano Letters*, 20(1), 509–516.
33. Eftekhari, F., & Davis, T. J. (2012). Strong chiral optical response from planar arrays of subwavelength metallic structures supporting surface plasmon resonances. *Physical Review B*, 86(7), 075428.
34. van de Groep, J., & Polman, A. (2013). Designing dielectric resonators on substrates: Combining magnetic and electric resonances. *Optics Express*, 21(22), 26285–26302.
35. Staude, I., et al. (2013). Tailoring directional scattering through magnetic and electric resonances in subwavelength silicon Nanodisks. *ACS Nano*, 7(9), 7824–7832.
36. Mohammadi, E., et al. (2019). Accessible superchiral near-fields driven by tailored electric and magnetic resonances in all-dielectric nanostructures. *ACS Photonics*, 6(8), 1939–1946.
37. García-Etxarri, A., & Dionne, J. A. (2013). Surface-enhanced circular dichroism spectroscopy mediated by nonchiral nanoantennas. *Physical Review B*, 87(23), 235409.
38. Butakov, N. A., & Schuller, J. A. (2016). Designing multipolar resonances in dielectric metamaterials. *Scientific Reports*, 6, 38487.
39. Bakker, R. M., et al. (2015). Magnetic and electric hotspots with silicon nanodimers. *Nano Letters*, 15(3), 2137–2142.
40. Evlyukhin, A. B., Reinhardt, C., & Chichkov, B. N. (2011). Multipole light scattering by nonspherical nanoparticles in the discrete dipole approximation. *Physical Review B*, 84(23), 235429.
41. Solomon, M. L., et al. (2018). Enantiospecific optical enhancement of chiral sensing and separation with dielectric Metasurfaces. *ACS Photonics*, 6(1), 43–49.

42. Takechi, H., et al. (2011). Chiroptical measurement of chiral aggregates at liquid-liquid interface in centrifugal liquid membrane cell by Mueller matrix and conventional circular dichroism methods. *Molecules*, *16*(5), 3636–3647.
43. Helgert, C., et al. (2011). Chiral metamaterial composed of three-dimensional plasmonic nanostructures. *Nano Letters*, *11*(10), 4400–4404.
44. Esposito, M., et al. (2015). Tailoring chiro-optical effects by helical nanowire arrangement. *Nanoscale*, *7*(43), 18081–18088.
45. Singh, R., et al. (2009). Terahertz metamaterial with asymmetric transmission. *Physical Review B*, *80*(15), 153104.
46. Song, K., et al. (2013). A frequency-tunable 90°-polarization rotation device using composite chiral metamaterials. *Applied Physics Letters*, *103*(10), 101908.
47. Plum, E., Fedotov, V. A., & Zheludev, N. I. (2009). Planar metamaterial with transmission and reflection that depend on the direction of incidence. *Applied Physics Letters*, *94*(13), 131901.
48. Fedotov, V. A., et al. (2007). Asymmetric transmission of light and enantiomerically sensitive plasmon resonance in planar chiral nanostructures. *Nano Letters*, *7*(7), 1996–1999.
49. Li, Z., et al. (2016). Tunable dual-band asymmetric transmission for circularly polarized waves with graphene planar chiral metasurfaces. *Optics Letters*, *41*(13), 3142–3145.
50. Han, J., et al. (2011). An ultrathin twist-structure polarization transformer based on fish-scale metallic wires. *Applied Physics Letters*, *98*(15), 151908.
51. Gansel, J. K., et al. (2012). Tapered gold-helix metamaterials as improved circular polarizers. *Applied Physics Letters*, *100*(10), 101109.
52. Pan, C., et al. (2014). Broadband asymmetric transmission of optical waves from spiral plasmonic metamaterials. *Applied Physics Letters*, *104*(12), 121112.
53. Wang, Y., et al. (2016). Direct and indirect coupling mechanisms in a chiral plasmonic system. *Journal of Physics D: Applied Physics*, *49*(40), 405104.
54. Bai, Y., et al. (2018). Asymmetric transmission of a planar metamaterial induced by symmetry breaking. *Journal of Physics. Condensed Matter*, *30*(11), 114001.
55. Bai, Y., et al. (2018). Splitting an asymmetric transmission peak by introducing magnetic-dipole oscillation on gold film. *Optical Materials Express*, *8*(9), 2743.
56. Aba, T., et al. (2018). Tunable asymmetric transmission through tilted rectangular nanohole arrays in a square lattice. *Optics Express*, *26*(2), 1199–1205.
57. Hu, Z., et al. (2019). Plasmonic circular dichroism of gold nanoparticle based nanostructures. *Advanced Optical Materials*, *7*(10), 1801590.
58. Kraut, J. (1949). The helical antenna*. *Proceedings of the IEEE*, *37*, 263–272.
59. Esposito, M., et al. (2014). Nanoscale 3D chiral Plasmonic helices with circular dichroism at visible frequencies. *ACS Photonics*, *2*(1), 105–114.
60. Wang, T., et al. (2017). Circular dichroism of a tilted U-shaped nanostructure. *Optics Letters*, *42*(14), 2842–2845.
61. He, Y., et al. (2014). Tunable three-dimensional helically stacked plasmonic layers on nanosphere monolayers. *Nano Letters*, *14*(4), 1976–1981.
62. Wang, Y., et al. (2016). Plasmonic chirality of L-shaped nanostructure composed of two slices with different thickness. *Optics Express*, *24*(3), 2307–2317.
63. Ullah, H., et al. (2020). Giant circular dichroism of chiral L-shaped nanostructure coupled with achiral nanorod: Anomalous behavior of multipolar and dipolar resonant modes. *Nanotechnology*, *31*(27), 275205.
64. Tang, B., et al. (2017). Chiral-selective Plasmonic Metasurface absorbers operating at visible frequencies. *IEEE Photonics Technology Letters*, *29*(3), 295–298.
65. Yang, Z.-J., et al. (2016). Enhanced chiral response from the Fabry–Perot cavity coupled metasurfaces. *Chinese Physics B*, *25*(8), 084201.
66. Li, J., et al. (2015). Nanoplasmonic sensors with various photonic coupling effects for detecting different targets. *The Journal of Physical Chemistry C*, *119*(52), 29116–29122.
67. Bai, Y., et al. (2020). Increasing the circular dichroism of the planar chiral nanostructure by inducing coupling between the coverage layer and the planar nanostructure. *Optics Express*, *28*(14), 20563–20572.

68. Decker, M., et al. (2009). Strong optical activity from twisted-cross photonic metamaterials. *Optics Letters*, 34(16), 2501–2503.
69. Decker, M., et al. (2010). Twisted split-ring-resonator photonic metamaterial with huge optical activity. *Optics Letters*, 35(10), 1593–1595.
70. Wang, Y., et al. (2019). Strong circular dichroism enhancement by plasmonic coupling between graphene and h-shaped chiral nanostructure. *Optics Express*, 27(23), 33869–33879.
71. Narushima, T., & Okamoto, H. (2013). Circular dichroism nano-imaging of two-dimensional chiral metal nanostructures. *Physical Chemistry Chemical Physics*, 15(33), 13805–13809.
72. Phua, W. K., et al. (2015). Study of circular dichroism modes through decomposition of planar nanostructures. *Plasmonics*, 11(2), 449–457.
73. Zhao, Y., et al. (2017). Chirality detection of enantiomers using twisted optical metamaterials. *Nature Communications*, 8, 14180.
74. Wu, X., et al. (2013). Unexpected chirality of nanoparticle dimers and ultrasensitive chiroplasmonic bioanalysis. *Journal of the American Chemical Society*, 135(49), 18629–18636.
75. Tullius, R., et al. (2015). “Superchiral” spectroscopy: Detection of protein higher order hierarchical structure with chiral plasmonic nanostructures. *Journal of the American Chemical Society*, 137(26), 8380–8383.
76. Qu, Y., et al. (2020). Chiral near-fields induced by plasmonic chiral conic nanoshell metallic nanostructure for sensitive biomolecule detection. *The Journal of Physical Chemistry C*, 124(25), 13912–13919.
77. Kumar, J., & Liz-Marzán, L. M. (2019). Recent advances in chiral plasmonics – Towards biomedical applications. *Bulletin of the Chemical Society of Japan*, 92(1), 30–37.
78. Hendry, E., et al. (2010). Ultrasensitive detection and characterization of biomolecules using superchiral fields. *Nature Nanotechnology*, 5(11), 783–787.
79. Ben-Moshe, A., et al. (2013). Chirality and chiroptical effects in inorganic nanocrystal systems with plasmon and exciton resonances. *Chemical Society Reviews*, 42(16), 7028–7041.
80. Wang, Y., et al. (2017). Induced chirality in micron wave through electromagnetic coupling between chiral molecules and graphene nanostructures. *Carbon*, 120, 203–208.
81. Govorov, A. O. (2011). Plasmon-induced circular dichroism of a chiral molecule in the vicinity of metal nanocrystals. Application to various geometries. *The Journal of Physical Chemistry C*, 115(16), 7914–7923.
82. Abudukelimu, A., et al. (2019). The causality of circular dichroism inducement by isotropic and anisotropic chiral molecules. *Journal of Physics D: Applied Physics*, 52(30), 305306.
83. Bochenkov, V. E., & Shabatina, T. I. (2018). Chiral plasmonic biosensors. *Biosensors (Basel)*, 8(4), 120.
84. Nesterov, M. L., et al. (2016). The role of plasmon-generated near fields for enhanced circular dichroism spectroscopy. *ACS Photonics*, 3(4), 578–583.
85. Le Ru, E. C., & Etchegoin, P. G. (2013). Quantifying SERS enhancements. *MRS Bulletin*, 38(8), 631–640.
86. Vestler, D., et al. (2018). Circular dichroism enhancement in plasmonic nanorod metamaterials. *Optics Express*, 26(14), 17841–17848.
87. Lu, F., et al. (2013). Discrete nanocubes as plasmonic reporters of molecular chirality. *Nano Letters*, 13(7), 3145–3151.
88. Yao, Y., et al. (2014). Wide wavelength tuning of optical antennas on graphene with nanosecond response time. *Nano Letters*, 14(1), 214–219.
89. Liu, T., Yi, Z., & Xiao, S. (2017). Active control of near-field coupling in a terahertz metal-graphene metamaterial. *IEEE Photonics Technology Letters*, 29(22), 1998–2001.
90. Zhou, Y., et al. (2018). Tunable low loss 1D surface plasmons in InAs nanowires. *Advanced Materials*, 30(35), e1802551.
91. Yin, X., et al. (2015). Active chiral plasmonics. *Nano Letters*, 15(7), 4255–4260.
92. Tian, X., et al. (2018). Improving Luttinger-liquid plasmons in carbon nanotubes by chemical doping. *Nanoscale*, 10(14), 6288–6293.

Epsilon-Near-Zero Plasmonics



Hosein Ghobadi, Zeinab Jafari, and Israel De Leon

Abstract Two exciting research fields in modern optics are the fields of plasmonics and the optics of materials with vanishing permittivity, also known as epsilon-near-zero (ENZ) materials. On the one hand, plasmonics allows us to confine light at deep sub-wavelength scales, enabling the possibility of light-matter interactions over nanoscale dimensions. On the other hand, ENZ materials exhibit interesting features such as wavelength elongation, decoupling of light's temporal and spatial properties, velocity divergence, and field enhancement. Indeed, as these two fields evolve, it has become clear that combining the properties of plasmonics and ENZ materials could open new avenues for manipulating light, offering an exciting road ahead for nanophotonics research. In this chapter, we review the recent progress in the field of ENZ plasmonics. We discuss fundamental aspects of ENZ media and its interaction with plasmonic systems, giving particular emphasis to nonlinear optical phenomena. We also review the various approaches to the realization of ENZ materials, mentioning the advantages and limitations of each.

Keywords Plasmonics · Nanophotonics · Epsilon near zero materials · Metamaterials · Metasurfaces · Nonlinear optics · Transparent conductive oxides

1 Introduction

Light-matter interactions are of great importance in several areas of science and technology. It is therefore essential to explore and understand methods to enhance and control such interactions. The field of plasmonics, for instance, studies to a large extent the use of surface plasmons for enhancing light-matter interactions at the nanoscale through the sub-wavelength field confinement and large optical intensities that they can achieve. On the other hand, epsilon-near-zero (ENZ) materials,

H. Ghobadi (✉) · Z. Jafari (✉) · I. De Leon (✉)
Tecnologico de Monterrey, Monterrey, Mexico
e-mail: a00827395@itesm.mx; zjafari@tec.mx; ideleon@tec.mx

i.e. materials with vanishing electric permittivity, promise exciting avenues for manipulating the properties of light and light-matter interactions, due to their interesting optical properties, which include strong optical field enhancements [1, 2], vanishing group velocity and phase-free propagation [3–5].

Both, plasmonics and ENZ materials, have recently attracted much attention on their own. For instance, plasmonic systems have been exploited for sensing applications [6, 7], surface enhanced Raman spectroscopy [8, 9], nanoscale field localization [10–12], and for manipulation of the properties of light through the use of nanostructured two- and three-dimensional plasmonic media commonly known as metasurfaces and metamaterials, respectively [13–16]. ENZ materials, on the other hand, have been recently used to demonstrate outstanding effects, such as enhanced nonlinear optical phenomena [17–20] and light-funneling through sub-wavelength channels [21, 22]. Given the demonstrated potential of plasmonics and ENZ materials, it is apparent that optical systems combining the essence of both fields could open new avenues for light control and for the enhancement of light-matter interactions, offering an exciting road ahead for nanophotonics research. Indeed, the available literature in the field reveals the rich physics of complex ENZ-plasmonic systems, as well as the important optical phenomena that they enable, such as perfect absorption [23–25], tailoring of radiation emission [26–28], enhanced nonlinear refraction [29], and optical frequency conversion [30–32].

This chapter summarizes the major theoretical and experimental progress achieved in the field of ENZ plasmonics. The chapter is organized as follows: Sect. 2 discusses the fundamental concepts of plasmonic and the ENZ materials, giving special attention to the description of fundamental optical phenomena in ENZ materials; Sect. 3 reviews the different material platforms that have been explored for the fabrication of ENZ media; in Sect. 4, we review and discuss the major theoretical and experimental studies on linear and nonlinear optical phenomena in ENZ-plasmonic systems; finally, the concluding remarks are presented in Sect. 5.

2 Fundamental Concepts

In this section we review the relevant concepts related to the field of plasmonics and ENZ materials. The topic of plasmonics is treated briefly, only discussing the most important aspects, while the reader is referred to selected scientific literature for a deeper understanding of the subject. Special attention is given to the subject of ENZ materials and their optical properties.

2.1 Plasmonics

The field of plasmonics studies the fundamental properties and applications of surface plasmons (SPs), which are transverse magnetic (TM) polarized optical

surface waves formed at the interface between a metal and a dielectric [33]. They are coupled excitations comprising a charge density wave in the metal and electromagnetic fields that peak at the interface and decay exponentially into both media. SPs can be casted in two main types: surface plasmon-polaritons (SPPs) and localized surface plasmons (LSPs) [34]. SPPs are propagating modes that exist on open metallic surfaces and can be excited over a continuous range of frequencies. In comparison, LSPs are resonant modes localized to metallic nanoparticles [33]; they can be excited at discrete resonance frequencies defined by the size, shape, and material composition of the nanoparticle. For both types of SPs, a negative real part of permittivity with a magnitude much larger than the permittivity's imaginary part is required [35].

Both SPPs and LSPs are capable of confining optical fields to dimension significantly smaller than the wavelength [35, 36], generating regions of large optical energy density where light-matter interactions can be dramatically enhanced. Specially, plasmonic nanostructures featuring nanoscale gaps (see Fig. 1a) [37] can confine optical fields to volumes well below the diffraction limit, reaching volumes as small as $\lambda^3/1000$ [38]. These important properties, hold promise for enabling controlled optical interactions with nano-scale objects [39–41], and for a wide range of applications such as photodetection, surface-enhanced Raman spectroscopy, optical microscopy, and on-chip communications [36, 42, 43].

2D arrays of metallic nanoparticles arranged in a specific fashion, known as plasmonic metasurfaces, have also revealed superior performance in tailoring the optical response (see Fig. 1b as an example). Engineering the orientation of the constituent nanoparticles and lattice parameters of such arrays offers additional flexibility in manipulating the amplitude, phase, and polarization of light [44]. A wealth of functional metasurfaces have been reported for the realization of ultrathin metalenses [45], waveplates [46], vortex beam and angular momentum generators [47, 48], and nanolasers [49], to name a few. Moreover, the enhanced fields and

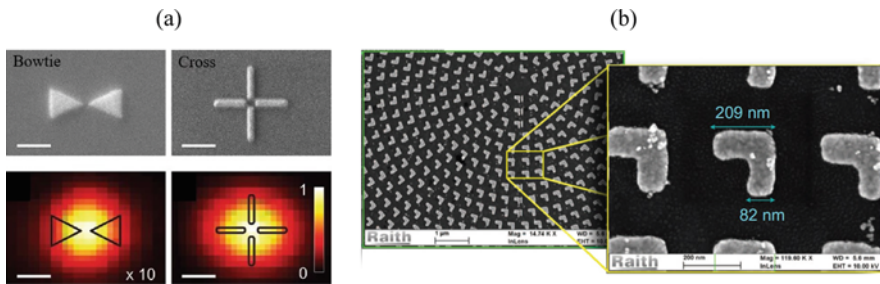


Fig. 1 (a) SEM images of plasmonic nanoantennas featuring nanoscale gaps (top panel) with the corresponding spatial maps of third harmonic generation intensity illustrating the regions of high energy densities (bottom panel). The numbers included in the bottom panel represent the magnification of the normalized intensity. (b) A metasurface composed of L-shaped gold nanoantennas used for generating optical angular momentum. (Panel (a) is adapted with permission from Ref. [37]. Copyright (2012) American Chemical Society. Panel (b) is adapted from Ref. [48])

relaxed phase-matching condition in ultrathin plasmonic metasurfaces are beneficial for efficient nonlinear applications [50–53].

The capabilities of the plasmonic nanostructures and metasurfaces in enhancing the field and controlling the properties of light when combined with the interesting properties of the ENZ media holds much promise for harnessing extraordinary optical phenomena. For a comprehensive understanding of the optical properties and applications of plasmonic systems, the interested reader is referred to a number of excellent review articles and books on the subject [33, 44, 54–57].

2.2 *Epsilon-Near-Zero Media*

ENZ materials are characterized by a vanishing real part of permittivity that occurs over a particular frequency range [58], typically referred to as the ENZ spectral region, or simply the ENZ region. These materials exhibit a number of unconventional optical properties that, together with the ability of plasmonic materials to confine light, enable the development of ENZ-plasmonic systems with an outstanding linear and nonlinear optical response [23, 26, 29, 30, 32]. In this section, we explain the fundamental properties of light in the ENZ region, which will be later required to describe interesting optical phenomena occurring in ENZ-plasmonic systems.

Decoupling of temporal and spatial properties An optical wave propagating through a material is characterized by the spatiotemporal coupling of the electric and magnetic fields and its oscillatory nature. In a source-free medium, this is captured by Maxwell’s curl equations (assuming $\exp(-i\omega t)$ harmonic convention),

$$\nabla \times \mathbf{E} = -i\omega\mu\mathbf{H} \quad (1)$$

$$\nabla \times \mathbf{H} = i\omega\epsilon\mathbf{E}, \quad (2)$$

where \mathbf{E} and \mathbf{H} are the electric and magnetic fields, and ϵ and μ are the permittivity and permeability of the medium, respectively [59]. However, when $\epsilon \rightarrow 0$, Eq. (2) reduces to $\nabla \times \mathbf{H} = 0$, indicating the electric and magnetic fields are decoupled [3, 60]. Furthermore, applying Gauss’s law we find that the electric field is described by Laplace’s equation, $\nabla^2\mathbf{E} = 0$, implying an electrostatic-like spatial distribution regardless of the oscillation frequency, ω . Thus, the fields in an ENZ medium are quasi-static, with decoupled electric and magnetic fields oscillating in time at the frequency ω [3, 61].

Wavelength expansion As a spatial property, the optical wavelength (λ) in a medium is related to frequency (f) and the phase velocity of the wave (v_p) by $\lambda = v_p/f$. The phase velocity depends on the constitutive parameters of the medium with

$$v_p = \frac{c}{n}, \quad (3)$$

where $n = \sqrt{\epsilon\mu}$ is the refractive index and c is the speed of light in vacuum. At optical frequencies $\mu = 1$; therefore, $v_p \rightarrow \infty$ when $\epsilon \rightarrow 0$. This divergence of the phase velocity results in a significant wavelength expansion in an ENZ medium [3, 58].

Another property of wave is the phase accumulated after propagation for a certain length (l) given as $\phi = 2\pi l/\lambda$. Replacing λ with λ_{ENZ} , it instantly becomes obvious that the phase acquired by a wave traveling inside an ENZ medium approaches zero ($\phi \rightarrow 0$) [5, 62]. This property of the ENZ material benefits nonlinear processes such as wave mixing where a phase mismatch-free propagation is critical for efficient constructive interaction among the waves [63].

Zero group velocity In a dispersive medium, waves with different frequencies propagate with different phase velocities. For an optical pulse, waves with various frequencies interfere and shape the envelope of the pulse that propagates with group velocity, v_g , given by [59]

$$v_g = \frac{\partial \omega}{\partial k} = \frac{2c\sqrt{\epsilon(\omega)}}{\omega} \frac{\partial \omega}{\partial \epsilon(\omega)}, \quad (4)$$

where $k = \omega\sqrt{\epsilon(\omega)}/c$ is the wavenumber in the medium. Equation (4) describes the group velocity of an unbounded ENZ medium, which becomes zero in the limit of $\epsilon = 0$. This means that a lossless unbounded material with zero permittivity does not transport energy [64, 65]. In reality, however, ENZ media have finite sizes and suffer from loss. As a consequence, they can have a small, but non-zero, group velocity [3]. As an example, $v_g = 0.08c$ is theoretically calculated for a narrow U-shaped ENZ channel, assuming a small optical loss [64].

Field enhancement An important property of ENZ media is the large field enhancement experienced by the longitudinal component of a transverse magnetic (TM) polarized light wave incident from a dielectric medium onto the surface of an ENZ material [66]. Boundary conditions dictate that at the interface of an ENZ medium the normal component of displacement field, $\mathbf{D} = \epsilon \mathbf{E}$, must be continuous. Therefore,

$$E_{\text{ENZ}}^\perp = \frac{\epsilon_i}{\epsilon_{\text{ENZ}}} E_i^\perp, \quad (5)$$

where E_i^\perp and E_{ENZ}^\perp are, respectively, the longitudinal component of fields outside and inside the ENZ medium, and ϵ_{ENZ} is the permittivity of the ENZ medium. The field intensity enhancement (FIE) in the ENZ material is given by the factor $|E_{\text{ENZ}}/E_i|^2 = |\epsilon_i/\epsilon_{\text{ENZ}}|^2$. In principle, as the permittivity of the ENZ medium

approaches zero, the FIE would approach infinity. However, in real ENZ materials the maximum FIE is limited by the unavoidable optical losses, which results in a non-zero value of $\text{Im}(\epsilon_{\text{ENZ}})$, and hence a non-zero value for ϵ_{ENZ} . From the above discussion, it is clear that in order to maximize the FIE, it is important to develop low-loss ENZ materials. One possible way to achieve this is through loss compensation by incorporating gain materials. Although fabrication of gain incorporated ENZ media is technologically challenging, a significant improvement of FIE could be realized in them [66]. An alternative path has recently been explored which considers the role of anisotropy in improving FIE [67, 68].

It is theoretically predicted that anisotropic ENZ media with a vanishing permittivity in the longitudinal direction reach larger FIE compared to isotropic ones [67, 68]. Taking into account the reflection at the interface, the FIE in longitudinal-ENZ media is given by [67]

$$\text{FIE}_{\text{LENZ}} \approx 4 \left| \frac{\epsilon_{\parallel}}{\epsilon_{\perp}} \right| \cos^2(\theta), \quad (6)$$

with θ being the incidence angle, and ϵ_{\parallel} and ϵ_{\perp} being the transverse and longitudinal components of complex permittivity tensor, respectively. According to Eq. (6), the FIE in a longitudinal-ENZ medium becomes considerably large when $\epsilon_{\perp} \rightarrow 0$, and grows further with pronounced anisotropy (larger $|\epsilon_{\parallel}|$) [67]. A comparison of the FIE between the longitudinal-ENZ and isotropic-ENZ cases is presented in Fig. 2a, which reveals a significantly larger enhancement for the longitudinal-ENZ case [67]. Moreover, the sensitivity of the FIE with respect to the optical losses seems to be relaxed in anisotropic ENZ media.

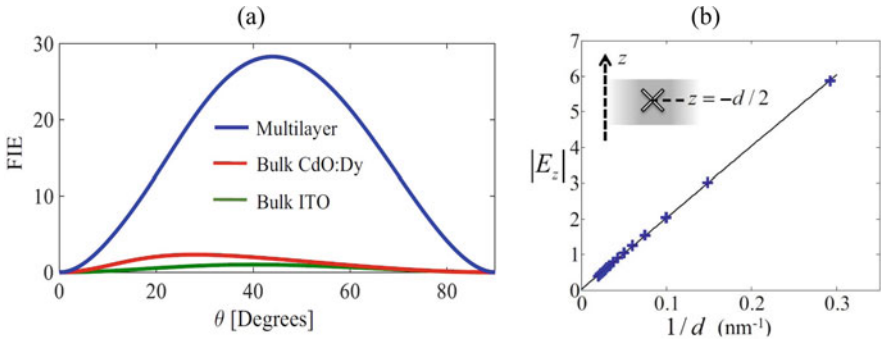


Fig. 2 (a) Variation of FIE with the angle of incidence in an anisotropic ENZ medium (blue) compared to that of isotropic ENZ media (red and green). The anisotropic medium is made of alternating layers of Si and Dysprosium-doped Cadmium Oxide (CdO:Dy) with $\epsilon_{\perp} = 0.26i$ and $\epsilon_{\parallel} = 5.98 + 0.065i$. (b) The thickness dependent magnitude of the longitudinal component of the electric field calculated at the center of an ENZ slab, $z = -d/2$, shown in the inset. (Panel (a) is adapted with permission from Ref. [67]. Copyright (2017) by the American Physical Society. Panel (b) is adapted with permission from Ref. [2]. Copyright (2015) by the American Physical Society)

The magnitude of the electric field inside the ENZ materials also depends on thickness (d). This dependence is theoretically shown to be linear $|E_{\text{ENZ}}| \propto 1/d$ (Fig. 2b) in ultrathin ENZ layers, which support the ENZ mode (see Sect. 4.1) [2]. However, the relation is not linear in real ENZ materials because of absorption losses at the wavelength of near-zero permittivity [69].

3 Material Platforms for ENZ Media

Materials with vanishing permittivity can be mainly categorized into natural and artificial media. A large portion of this section is dedicated to naturally occurring ENZ media due to their easy processing and availability over a wide range of frequencies. Our definition of natural media is limited to metals, transition metal nitrides, and transparent conducting oxides. For these materials, the near-zero permittivity is an intrinsic property achieved at their bulk plasma frequency. The frequency-dependent permittivity of natural ENZ materials, arising from the free electrons in the conduction band, is explained by the Drude model [33]

$$\epsilon(\omega) = \epsilon_{\infty} - \frac{\omega_p^2}{\omega^2 + i\gamma\omega}, \quad (7)$$

where ϵ_{∞} is the high-frequency permittivity and usually takes values between 1 and 10. The damping parameter (γ) and plasma frequency (ω_p) are given by

$$\gamma = \frac{e}{m^* \mu_{\text{opt}}} \quad (8)$$

$$\omega_p = \sqrt{\frac{Ne^2}{\epsilon_0 m^*}}, \quad (9)$$

in which N , m^* and μ_{opt} are volume density, effective mass, and optical mobility of free electrons, respectively. The quantity e is the fundamental charge of the electron and ϵ_0 is the vacuum permittivity. It is useful to write Eq. (7) in terms of its real and imaginary components,

$$\epsilon(\omega) = \text{Re}(\epsilon) + \text{Im}(\epsilon)i, \quad (10)$$

where,

$$\text{Re}(\epsilon) = \epsilon_{\infty} - \frac{\omega_p^2}{\omega^2 + \gamma^2}, \quad (11a)$$

$$\text{Im}(\epsilon) = \frac{\omega_p^2 \gamma}{\omega(\omega^2 + \gamma^2)}. \quad (11b)$$

Note that when ω is equal to the screened plasma frequency, $\tilde{\omega}_p = \omega_p / \sqrt{\epsilon_\infty}$, the real part of permittivity becomes zero, whereas the imaginary part takes a non-zero value. Therefore, $\text{Im}(\epsilon)$ needs to be decreased to acquire smaller values for the permittivity. For the rest of this chapter, the condition $\text{Re}(\epsilon) = 0$ will be referred to as zero-crossing with the corresponding wavelength λ_{ZC} .

Metals All metallic elements have a zero-crossing of real permittivity as an intrinsic property in the UV or visible range due to the high density of free electrons (10^{22} – 10^{23} cm^{-3}) [70–72]. Studies on the ENZ properties of metals are limited to gold and silver [73, 74] because their λ_{ZC} is in the range accessible by high power pulsed laser sources; zero-crossing wavelengths for Au and Ag are 520 and 362 nm, respectively [5]. However, the large optical losses, untunable zero-crossing wavelength, and low damage threshold of these materials impose serious limitations on their performance as ENZ materials. The low damage threshold, in particular, makes noble metals unsuitable for nonlinear applications where the media is typically illuminated by a high intensity laser. Moreover, attempts to further the λ_{ZC} of Ag and Au to longer wavelengths have had limited success with the cost of increased optical losses [75, 76].

Transition metal nitrides A substitute to metals in the visible range is transition metal nitrides such as Titanium nitride (TiN), Zirconium nitride (ZrN), and Hafenium nitride (HfN) [77]. Similar to metals, these materials possess relatively large losses [77–79]. Nevertheless, one of their advantages over metals is the tunability of optical properties by adjusting the fabrication parameters [79, 80]. In general, increasing metal:nitrogen ratio shifts λ_{ZC} to shorter wavelengths because of the increased electron density (see Eq. (9)) [78]. Furthermore, highly-crystalline thin films can be produced with these materials, leading to a reduction in optical losses [79]. Unlike metals, transition metal nitrides offer the advantage of being compatible with the standard CMOS technology.

Transparent Conducting Oxides (TCOs) TCOs are wide band gap semiconductors that show a metallic conductivity when degenerately doped with donor impurities. Typical free-electron density of TCOs is around 10^{20} cm^{-3} or larger [81], which locates their zero-crossing wavelength in the NIR [82]. Analogous to transition metal nitrides, the optical dispersion of TCOs can be tailored through material processing [83]. A wide tuning range of λ_{ZC} from 1280 to 2900 nm can be achieved in Tin-doped Indium Oxide (ITO) as a result of changes to free-electron density by simply annealing under different gasses and temperatures [84]. TCOs have the smallest losses among the natural ENZ media in the NIR; almost five times smaller than noble metals and at least an order of magnitude smaller than transition metal nitrides [78]. According to Eq. (8), the damping parameter is inversely proportional to optical mobility. Therefore, materials with higher electron mobility are expected to have smaller losses. It is possible to improve the optical mobility by growing highly-crystalline thin films through well-established techniques such as pulsed laser deposition. Another advantage of TCOs is their large damage threshold, allowing for a full realization of their nonlinear response in the ENZ region using

intense laser pulses (see Sect. 4.2) [17]. Furthermore, TCOs could potentially be used in CMOS fabrication processes.

Although a large number of TCOs has been reported for optoelectronic applications, only ITO [17], Aluminum-doped Zinc Oxide (AZO) [85], Gallium-doped Zinc Oxide (GZO) [86] and Indium-doped Cadmium Oxide (ICO) [87] have been explored as the ENZ media. This can be due partly to the fact that not all TCOs have small enough losses to be suitable for nanophotonics purposes. For instance, correlated metals with electron densities in the order of 10^{22} cm^{-3} are considered as alternatives to ITO for optoelectronic applications [88]. However, their large imaginary permittivity has to be reduced before any attempts to evaluate their ENZ properties.

Optical Metamaterials This class of materials refers to artificial 3D media consisting periodic sub-wavelength particles or layers. The constituent parts of metamaterials are engineered to manipulate the properties of light upon interaction. As a consequence, unusual and intriguing optical properties such as negative refraction, superlensing, and cloaking can be obtained [89–92]. Metamaterials can also provide a large degree of freedom in designing tunable ENZ media. For instance, stacking alternating layers of metal and dielectric together is a straightforward way of realizing a near-zero effective permittivity [93]. Metal-dielectric structures are characterized by an anisotropic permittivity with effective components parallel (ϵ_{\parallel}) and normal (ϵ_{\perp}) to the interface (Fig. 3a) given by [94]

$$\epsilon_{\parallel} = \frac{\epsilon_m d_m + \epsilon_d d_d}{d_m + d_d}, \quad \frac{1}{\epsilon_{\perp}} = \frac{d_m/\epsilon_m + d_d/\epsilon_d}{d_m + d_d} \quad (12)$$

where $\epsilon_m(\epsilon_d)$ and $d_m(d_d)$ represent, respectively, the permittivity and thickness of metallic (dielectric) component. At optical frequencies, the permittivity is negative for metals and positive for dielectrics. Therefore, by a proper choice of materials and thicknesses, one can tune the zero-crossing wavelength [93, 95].

Metal-dielectric structure with periodic air holes extending the entire thickness, known as fishnet structure, allows for manipulating both ϵ and μ at the same time. Refractive indices ranging from negative to positive are reported for these structures [96, 97]. A drawback of ENZ media comprising metallic components is the ohmic loss, which can be overcome in all dielectric structures. These are periodic metamaterials with a Dirac cone-like dispersion that acquire a near-zero index as a result of Mie resonances supported by dielectrics [98, 99]. All-dielectric metamaterials with an in-plane geometry enable the integration of zero-index media into on-chip photonic applications, offering flexibility in customizing the device shape and interaction length [100, 101]. A plasmonic waveguide operating at cut-off frequency may also be treated as an ENZ metamaterial, and is another approach to the realization of vanishing permittivity (Fig. 3b). It is shown that at the cut-off frequency, the electromagnetic field oscillates in phase inside a metal-insulator-metal waveguide [102]. That in turn means the wavenumber is zero ($k = 0$), in resemblance to the case of $n = 0$.

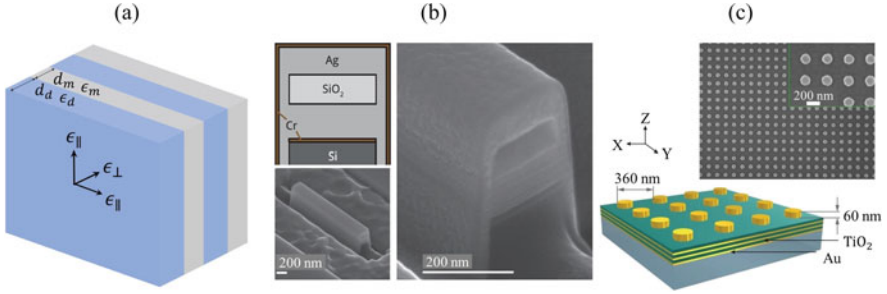


Fig. 3 (a) Schematic representation of a metal-dielectric multilayer structure labeled with the structural parameters used in Eq. (12). (b) A plasmonic metal-insulator-metal waveguide for realization of near-zero permittivity. (c) An ENZ-plasmonic metamaterial composed of a gold nanodisk array deposited on top of a metal-dielectric multilayer metamaterial. (Panel (b) is adapted with permission from Ref. [102]. Copyright (2013) by the American Physical Society. Panel (c) is adapted with permission from Ref. [27])

Metasurfaces which are the 2D equivalent of metamaterials have also attracted great attention due to their lower loss and ease of fabrication compared to the 3D structures. Integration of ENZ media with plasmonic metasurfaces offers extra degree of freedom in controlling the properties of light. An example of such a structure is shown in Fig. 3c, in which a metasurface of nanodisc antennas is fabricated on top of a metal-dielectric metamaterial. Moreover, plasmonic metasurfaces are of interest as they can augment the coupling of light to the ENZ mode and further enhance the field within the thin ENZ media [31, 32, 103–106] (see Sect. 4).

4 Linear and Nonlinear Optical Phenomena in ENZ Plasmonics

The interesting optical properties of ENZ and plasmonic media have ignited extensive research for understanding the physics behind the different optical phenomena in coupled ENZ-plasmonics systems. In this section, we review the major contributions thus far reporting linear and nonlinear optical phenomena in ENZ media incorporating plasmonic structures.

4.1 Linear Case

In this subsection, we review different linear optical phenomena observed in ENZ-plasmonic systems, including perfect optical absorption, tailoring of radiation emission, as well the strong coupling between plasmonic resonators and highly-confined quasi-static modes supported by ultra-thin ENZ materials.

Tailoring the radiation characteristics In a medium with vanishing permittivity, the wave can enter (or exit) the medium only at angles close to the normal. This is because the transverse component of the wavevector must be continuous at the interface between two media, i.e. $k_{it} = k_{\text{ENZ}t}$, where k_{it} and $k_{\text{ENZ}t}$ are the transverse component of wavevectors outside and inside the ENZ medium, respectively. Since $k_{\text{ENZ}t} \rightarrow 0$, k_{it} must approach zero, which is satisfied only in a range of angles centered around the normal to the interface [99, 107]. Following the same reasoning, one finds that the wave also leaves the ENZ media with high directionality. This phenomenon was reported in Ref. [107] for an ENZ metamaterial made of metallic grid network with a monopole source embedded inside. It was shown that the emission directionality of the structure is enhanced near the plasma frequency. In this work, the emission measurements in the far-field revealed a narrow lobe centered around the normal to the surface. A directional quantum dot emission from PbS semiconductor placed within an all-dielectric structure was also demonstrated [99].

The analytical expression predicting the angular bandwidth of the wave transmitted from a simple planar ENZ slab was developed and, in the lossless ENZ limit, is given by

$$\Delta\theta = 2 \frac{\sqrt{\epsilon_{\text{ENZ}}/\epsilon_0}}{k_0 d_{\text{ENZ}}}, \quad (13)$$

in which ϵ_{ENZ} and d_{ENZ} represent the permittivity and thickness of the ENZ slab, respectively [62]. According to Eq. (13), $\Delta\theta$ becomes narrower as ϵ_{ENZ} tends to zero or as the thickness grows. It needs to be noted that losses arising from the non-zero imaginary permittivity can broaden the angular bandwidth of transmission in realistic ENZ materials [62, 108]. Scattering losses as a consequence of structural imperfections can also broaden the angular bandwidth [108].

Highly directional emission from the ENZ material enables tailoring the radiation pattern through customizing the shape of exit side of the media. This was proposed theoretically [62, 109] and confirmed experimentally [110, 111]. In Ref. [109], simulation of an anisotropic 2D plano-concave waveguide illuminated on its flat side at cut-off frequency showed that the transmitted wave adapts the shape of exit face and the structure works as a lens focusing the wave at the focal point. Focusing phenomenon was also experimentally observed in a Dirac cone photonic crystal made of alumina nanorods [98].

The ability of ENZ media in modifying the radiation pattern of the wave passing through them can be used to influence the scattering characteristics of nearby objects. Studies on nanostructures composed of plasmonic metasurfaces deposited on top of ENZ media [26–28] reported that the resonance frequency of a plasmonic nanoantenna does not strongly depend on its dimension, when located in close proximity to an ENZ medium. Figure 4b illustrates the so-called resonance pinning effect for the nanorods deposited on Al:ZnO substrate, as shown in Fig. 4a. A considerably reduced red-shift of resonance wavelength versus nanorod length is evident for the ENZ-nanorod system [26]. This phenomenon is caused by a decrease in effective refractive index (n_{eff}) of the media surrounding the nanorod array, which

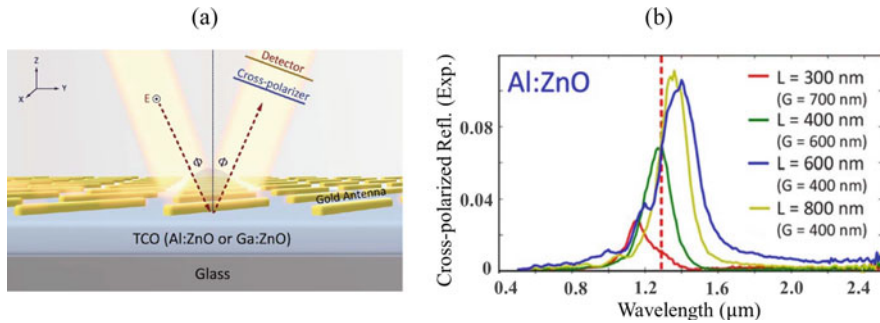


Fig. 4 (a) Schematic representation of gold nanoantenna array deposited on TCO layers, and (b) the corresponding reflection spectra for various antenna lengths. (Figures adapted with permission from Ref. [26] © The Optical Society)

compensates for the effect of increased nanorod length. Resonance pinning was also reported for a plasmonic nanodisk array developed on top of a metal-dielectric ENZ substrate [27], as shown in Fig. 3c. A 3-fold reduction of the resonance shift was observed when comparing the response of the nanodisk array on the ENZ substrate with that on a glass substrate. The resonance shift was smaller when the zero-crossing of the ENZ metamaterial coincided with the resonance frequency of nanodisks, further supporting the role of vanishing permittivity of the substrate in modifying the scattering from the plasmonic resonators.

ENZ mode Complex frequency modal analysis for a slab of gold with thickness d bounded with two semi-infinite free-spaces showed that the dispersion curve splits into symmetric and asymmetric modes for d values comparable to the skin depth. As d gets much smaller than the skin depth, the dispersion curve of the symmetric mode becomes flat at the zero-crossing frequency of the material [1, 2, 112]. This mode, usually referred to as ENZ mode, exhibits a quasi-static behavior, having a uniform field distribution strongly confined to within the slab, and a near-zero group velocity originating from its nearly-flat dispersion relation [1, 2]. In comparison, the field distribution inside a thick ENZ slab has a minimum at the center of the slab. A flat dispersion is only realized in a certain small range of transverse wavenumber $k_{||}$ values, given by $\omega_p/c < k_{||} < 0.4/d$ for the gold slab [2]. The ENZ mode is only excited by the longitudinal component of the electric field; hence, illumination with TM-polarized light at oblique incidence is required. Moreover, d has to be smaller than $\lambda_p/50$, where λ_p is the plasma wavelength [2].

A number of studies have reported a strong optical coupling between the resonance of plasmonic antennas and the ENZ mode of a thin ENZ film acting as a substrate [29, 103–106]. This occurs because the plasmonic antennas produce near-fields with a significant longitudinal component that can effectively excite the ENZ mode. For antennas with a resonance frequency overlapping with that of the ENZ mode, the strong coupling is manifested as a large splitting of the plasmonic resonance, typically observed in the transmission spectrum of the

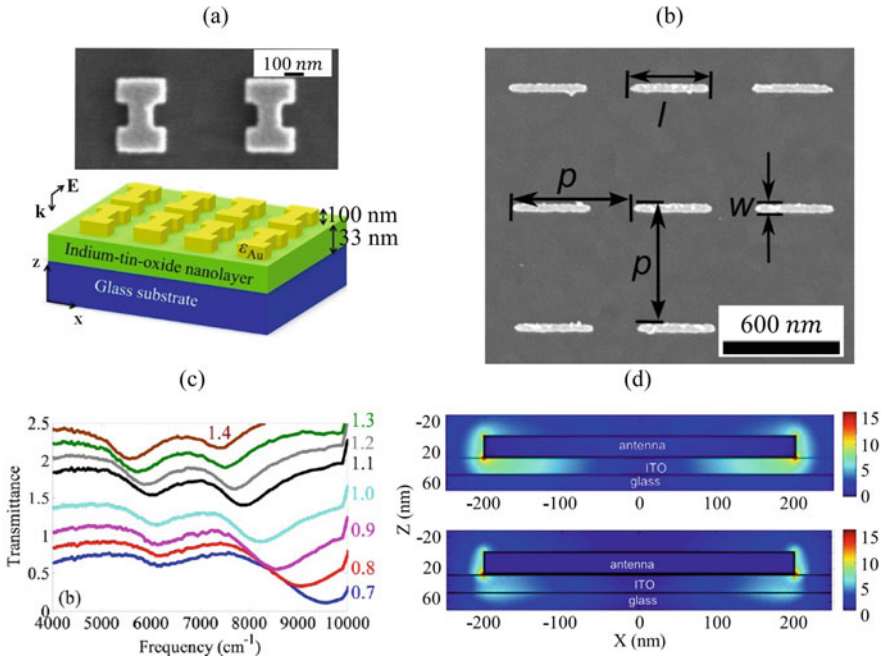


Fig. 5 (a) and (b) SEM images of the structures with strong optical coupling between the ENZ mode and gold nanoantenna resonance. (c) Transmission spectrum of the structure in (a), showing two largely separated resonances. (d) Top and bottom panels show the electric field magnitude for the coupled system in (b) at resonance frequencies in the ENZ region and away from it, respectively. (Panels (a) and (c) are adapted with permission from Ref. [106]. Copyright (2016) American Chemical Society. Panels (b) and (d) are adapted with permission from Ref. [105])

coupled structure (Fig. 5c) [106]. In these systems, the ENZ material is a TCO such as ITO (Fig. 5a and b), with its zero-crossing wavelength located in the NIR region of the spectrum. The possibility of adjusting the zero-crossing wavelength of TCOs by doping, and adjusting the plasmonic resonance frequency through the antenna’s dimensions makes this system particularly robust for exploring the coupling phenomenon [29, 30, 105, 106]. For instance, a resonance splitting as large as 30% of the zero-crossing frequency of ITO (Fig. 5c) was reported in Ref. [106]. The authors of Ref. [105] used a similar material system (Fig. 5b) to study the field enhancement in the ENZ layer induced by the plasmonic antenna. As shown in Fig. 5d, field enhancement in the order of 10 (intensity enhancements around 100) are estimated within the ENZ material. It was also noted that the resonance characteristics of the coupled system show a small dependence on the nanoresonator’s size [105]. Coupling to the ENZ mode was also obtained in the mid-IR region using an ultra-thin layer of n-type GaAs with a gold split-ring resonator array deposited on top [103]. A triple resonance splitting was reported in the mid-IR region for a structure that supports an ENZ mode and an optical phonon resonance

that are both coupled to the resonance of gold resonators. This in turn led to three distinct polariton branches in the transmission spectra of the coupled system. The authors also demonstrated the triple splitting due to the simultaneous coupling to an ENZ mode and a quantum-well intersubband transition. Moreover, an increased splitting was achieved by tuning the zero-crossing frequency of the ENZ layer to overlap with the intersubband transition [104].

Perfect absorption Research on perfect absorption (PA) is fueled because of its importance in many applications such as photovoltaics, photodetection and sensing. There is a number of ways to achieve PA [113]. Recently, it has been shown that ENZ media provide a new approach to realizing PA. A detailed theoretical and experimental study of TM-polarized light PA in a glass/ITO/Ag structure was performed in Ref. [114]. In this structure, or similar ones, the metallic capping acts as an opaque layer setting the transmission to zero. Therefore, $A = 1 - R$, where A and R represent the absorbance and reflectance, respectively. Surprisingly, a somewhat counter-intuitive relation among the thickness d_{PA} of ITO, its permittivity ϵ_2 and the angle of incidence θ_{PA} was drawn for the condition of PA [114], given by

$$\frac{2\pi d_{\text{PA}}}{\lambda_{\text{PA}}} = \left[\frac{\text{Re}(\epsilon_2)^2 + \text{Im}(\epsilon_2)^2}{\epsilon_1^{3/2} \text{Im}(\epsilon_2)} \right] \frac{1}{\tan\theta_{\text{PA}} \sin\theta_{\text{PA}}}, \quad (14)$$

in which ϵ_1 is the permittivity of glass substrate. The above equation predicts that as the angle of incidence increases or $\text{Re}(\epsilon_2)$ and $\text{Im}(\epsilon_2)$ simultaneously tend to zero, $d_{\text{PA}}/\lambda_{\text{PA}}$ becomes smaller, indicating that PA can be attained in films with deep sub-wavelength thickness. More interestingly, ITO layers with smaller loss need to be thinner to satisfy the conditions for PA [114]. This is in contrast with the case of conventional media, where the absorbed power increases exponentially with the thickness of the medium. The absorption measurements for the structure studied in Ref. [114] consisting a 53 nm-thick ITO layer revealed PA at 57.3° incidence angle. Moreover, simulation of the angle resolved absorption indicated that PA occurs at two different frequencies; one at a frequency slightly larger than zero-crossing frequency and another at a much larger frequency [114]. Complex wavenumber modal analysis showed that at these two frequencies the imaginary part of the propagation constant vanishes. At the frequencies of PA, the field distribution resembles that of an incident plane wave in medium 1 which is completely absorbed, and unlike the surface and leaky modes, it neither decays nor increases [114, 115]. Similar conditions were found for air/ENZ/metal structure featuring a uniaxially anisotropic ENZ medium, resulting in an equation analogous to Eq. (14), but with no dependency on the in-plane component of the permittivity [115]. Conditions leading to Eq. (14) also require $\text{Re}(\epsilon_2) > 0$, i.e. PA is obtained at frequencies larger than the zero-crossing frequency [87, 114–116]. Nonetheless, PA was experimentally shown at frequencies slightly smaller than the zero-crossing frequency [116, 117]. In these works, an overlap of the ENZ mode dispersion with the PA frequency along with a constant field distribution in the ENZ medium led the authors to link PA to the ENZ mode [117].

According to Eq. (14), the PA wavelength can be tuned with the proper choice of thickness, permittivity and the angle of incidence. However, the thickness and permittivity cannot be altered after fabrication. Therefore, PA can only occur at single wavelength unless the angle of incidence is dynamically tuned, which might not be of practical convenience. As a consequence, other strategies should be adapted to have broadband absorption at a fixed incidence angle. TCOs allow for broadband PA as their permittivity can be engineered to remain small in a wider range of wavelength by fabricating a multilayered film with each layer having different electron density [116, 117]. Employing this strategy, close to 100% absorption was demonstrated over 45 nm [116] and 300 nm [117] spectral bandwidth.

Broadband PA was also demonstrated in ENZ-plasmonic systems as a result of coupling between a gap plasmon mode and the ENZ mode supported by a thin ITO film [23]. The studied structure (Fig. 6a) was a metal-insulator-metal arrangement with the top metal layer patterned as an array of squared nanopatches, and a 12 nm ITO film deposited between the top metal and the insulator (SiO_2) region. Gap plasmons are supported between the top and bottom metallic layers. The thickness of the insulator was optimized in order to have a weak coupling between the gap plasmon and the ENZ mode to increase the PA bandwidth. Measured reflectivity data, shown in Fig. 6b, revealed a 246 nm bandwidth for PA. The distinguishable characteristic of the reflectivity curve is a flat PA over the entire bandwidth, which was not achieved in other designs. Based on a similar approach, broadband perfect absorption was also studied theoretically in Ref. [24], reporting 99% absorption over a 255 nm wavelength range.

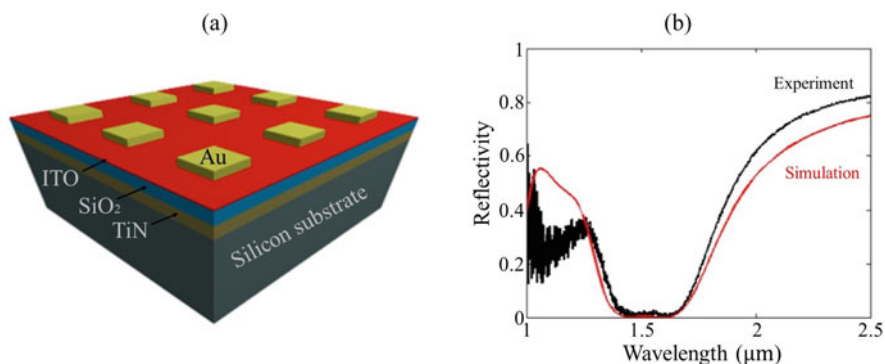


Fig. 6 (a) A metal-insulator-metal gap plasmon structure consisting an ultrathin ITO layer deposited in the gap region. (b) The reflectivity spectrum for the ENZ-plasmonic system in (a), exhibiting a flat top broadband PA. (Figures adapted with permission from Ref. [23]. Copyright (2018) American Chemical Society)

4.2 Nonlinear Case

Nonlinear optical phenomena are fundamental for applications such as telecommunications, optical data processing, microscopy, and spectroscopy [36, 118]. Yet, the performance of such applications is usually hindered by the weak nonlinear response of materials. It is, therefore, important to develop material systems with a large optical nonlinearity. Recently, it has been recognized that ENZ materials can possess an outstanding nonlinear optical response [17, 87, 130]. Moreover, several groups have taken advantage of plasmonic materials to enhance even further the nonlinear optical phenomena in coupled ENZ-plasmonic structures [29, 30, 32]. In what follows, we explain the main mechanisms contributing to the nonlinear optical response of ENZ materials, and review the main investigations reporting nonlinear optical phenomena in ENZ materials and ENZ-plasmonic systems.

Origins of boosted nonlinearity A number of mechanisms can contribute to the nonlinearity of ENZ media. Next we provide a brief description for each of them.

- **Field enhancement:** Nonlinear optical effects require the interaction of a material with an intense coherent optical field. Therefore, a possible way to achieve a stronger nonlinear optical effect without increasing the illumination power is by enhancing the optical intensity within the material. As discussed in Sect. 2.2, the continuity of the electric field displacement across a material boundary results in an enhancement of the longitudinal electric field component inside ENZ materials that is proportional to $|\epsilon_{\text{ENZ}}|^{-1}$ – see Eq. (5). Thus, a significant intensity enhancement can be achieved at the zero-crossing frequency for ENZ materials with low loss (small $\text{Im}(\epsilon_{\text{ENZ}})$). In addition, since only the longitudinal electric field component is affected, the intensity enhancement is highly dependent on the incidence angle, resulting in angle-dependent nonlinear effects. This enhancement mechanism is predicted to be further improved in thin films that have a real permittivity tensor with a vanishing out-of-plane component [67, 119]. Furthermore, as discussed in Sect. 4.1, ultra-thin ENZ films based on TCOs support quasi-static modes (ENZ mode) that exhibit large field enhancements that can significantly enhance the nonlinear optical response of these materials [1, 2]. Finally, the use of plasmonic structures to enhance the electric field nearby ENZ materials has been proven to be a powerful method to achieve efficient nonlinear responses in coupled ENZ-plasmonic systems [29, 30, 32].
- **Hot electrons:** A significant contribution to the nonlinear optical response of TCO-based ENZ materials comes from the generation of hot electrons in the non-parabolic conduction band [17, 120–123]. This mechanism affects mainly those nonlinear processes associated to an intensity-dependent permittivity, which can be described by the Drude model – see Eq. (7) – by taking intensity-dependent plasma frequency (ω_p) and damping constant (γ) parameters [122]. In TCOs, hot electrons are generated by raising the kinetic energy and temperature of free electrons through the intraband absorption of an optical pump (Fig. 7a). In

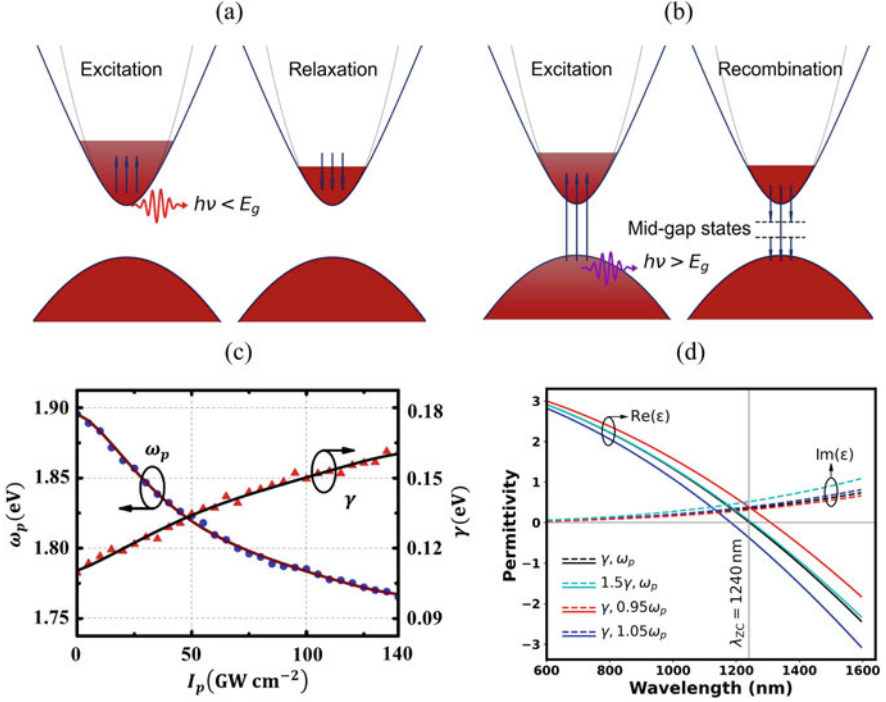


Fig. 7 Schematic representation of (a) intraband, and (b) interband excitation of TCOs featuring a non-parabolic conduction band (the parabolic band is shown in gray). (c) Variation of plasma frequency and damping parameter as a function of intensity in an ITO layer under intraband excitation. (d) Changes of $\text{Re}(\epsilon)$ and $\text{Im}(\epsilon)$ with ω_p and γ . The linear permittivity data reported in [17] was used for plotting the figure in panel (d). (Panel (c) is adapted with permission from Ref. [122]. Copyright (2020) by the American Physical Society)

turn, the energy increase of an electron in the non-parabolic conduction band results in an increment of its effective mass, m^* [121–123], and consequently a reduction of ω_p – see Eq. (9). Hot electrons also produce an increment in the value of γ . However, this parameter is limited by the high density of defects and ionized impurity scattering of TCOs; hence, its dependence on the intensity is usually assumed to be negligible [121, 123]. Since ω_p is much larger than γ , it follows from Eqs. (8), (9), (10), and (11) that the generation of hot electrons results in an increment (reduction) of the real (imaginary) part of the material permittivity and refractive index. This effect has been reported by several groups [17, 85, 87, 121] and can be summarized nicely by the results in Fig. 7c and d. It can be seen in Fig. 7d that even a large increase (50%) of γ has almost no effect on $\text{Re}(\epsilon)$ and slightly increases $\text{Im}(\epsilon)$. However, only 5% red-shift of ω_p increases $\text{Re}(\epsilon)$ by 0.4 at the zero-crossing wavelength. Smearing of the Fermi-level caused by hot electrons also contributes to the enhanced nonlinear response

of ENZ material. Nevertheless, the main contribution is from the dynamics of non-parabolic conduction band.

Temporal dynamics of the hot electrons is ultrafast (sub-picosecond), which is often explained by the two-temperature model [5, 17, 121]. This model takes into account the electron-electron (τ_{ee}) and electron-phonon (τ_{ep}) relaxation times. The intraband excitation causes electrons to be in thermal non-equilibrium. After a few femtoseconds, they arrive equilibrium through electron-electron scattering with the required time being determined by the scattering rate $\Gamma_{ee} = \tau_{ee}^{-1}$. Afterwards, the electron-phonon scattering gives rise to equilibrium between the hot electrons and the lattice ($\Gamma_{ep} = \tau_{ep}^{-1}$), which increases the lattice temperature. Finally, heat dissipates from the lattice to the surrounding environment. This last step takes a longer time than the previous ones.

- **Interband transitions:** Interband transitions occur when a material is illuminated by photons with energies large enough to promote the electrons from the valence band to the conduction band (Fig. 7b). In case of TCOs, the excited electrons add to the already existing population of free electrons in the conduction band. This in turn increases (reduces) the plasma frequency ($\text{Re}(\epsilon)$) – see Eq. (9) and Fig. 7d. The excited electrons return to their unperturbed state through a number of processes with the characteristic recombination time on the order of a few picoseconds [124, 125]. TCOs, however, feature a sub-picosecond relaxation time because of the mid-gap trap states that facilitate the recombination process [125, 126].

Intensity dependent refraction The intensity-dependent refractive index is arguably one of the most important nonlinear optical effects, because of its application in high-speed optical signal modulation, switching, and optical data processing. This effect is characterized by a refractive index of the form

$$n = n_0 + \Delta n, \quad (15)$$

where n_0 is the linear refractive index and $\Delta n = n_2 I$ is the intensity-dependent change in refractive index, with n_2 being the nonlinear refractive index and I being the optical intensity in the medium. Here, we are employing a more general definition of the nonlinear refractive index, $n_2 = \partial n / \partial I$, to be consistent with the terminology broadly used in the literature. However, note that under this definition n_2 is in general a function of the intensity [127] and not a constant value as it is typically the case for weakly nonlinear materials. It is desired for both n_2 and the maximum value of Δn , to be as large as possible. The latter describes the strength of the nonlinearity, which is typically limited by saturation effects; the former describes its efficiency, i.e. how large is the effect for a particular input intensity. Furthermore, for many applications such as telecommunications and optical signal processing, it is of utmost importance for the material to have an ultrafast (sub-picoseconds) nonlinear response.

For decades, there has been a great deal of work in this research line, aiming at developing materials with strong and ultrafast intensity-dependent refraction.

Recently, it has been demonstrated that TCO-based ENZ materials possess remarkable intensity-dependent refraction properties, featuring record reported values for n_2 and maximum Δn that can be several orders of magnitude larger than that of Arsenic Triselenide glass, which has the largest nonlinear coefficient previously reported [118, 128, 129]. Furthermore, it has been shown that the fast hot-electron dynamics in these materials results in an ultrafast intensity-dependent refractive index, with response times in the order of a few hundred femtoseconds [17, 85, 87, 126]. In addition to the hot-electron effect, the field enhancement mechanisms discussed earlier play an important role in defining the overall nonlinear optical response of the material.

A number of studies have reported large values of Δn in different TCOs [17, 85, 87, 125, 130]. The key findings of these works can be summarized as follows: (i) for a given angle of incidence, a larger change of refractive index is achieved near the zero-crossing wavelength (Fig. 8a); (ii) nonlinear response of the TCOs is further enhanced for an oblique incident TM-polarized light (Fig. 8a). This is due to an increase in the longitudinal field component, which causes larger field enhancements inside the ENZ material; (iii) the smaller heat capacity of free-electron for TCOs, compared to that of noble metals, gives rise to a higher electron temperature after an intense laser excitation. As a consequence, unforeseen values of Δn ($\Delta n/n_0$) as large as 0.45 (5) and 0.72 (1.7) have been obtained for AZO [130] and ITO [17], respectively; (iv) the large Δn is accompanied with a sub-picosecond response time as shown in Fig. 8b.

A significantly larger change of refractive index over a broader range of wavelengths was achieved in an ENZ-plasmonic structure composed of a gold nanoantenna array deposited on top of a 23 nm-thick ITO layer on glass (Fig. 8c) [29]. In this work, a strongly coupled system was realized by tuning the fundamental resonance of nanoantenna to overlap with that of the ENZ mode of the ITO layer. The linear transmittance spectrum of the coupled system featured a resonance splitting (see Sect. 4.1) with the main resonance centered at 1280 nm. Considerably large n_2 values over a broad spectral range of 1180–1560 nm were measured (Fig. 8d). The authors reported both positive and negative values of n_2 , corresponding to the measurements at wavelengths shorter and longer than the main resonance, respectively. The largest absolute value of $|n_2| = 3.73 \pm 0.56 \times 10^{-13} \text{ m}^2/\text{W}$ was 2000 times larger than that of the bare ITO film. Values of $|\Delta n|$ larger than 2.7 were also reported for a relatively low beam intensity of $0.150 \text{ GW}/\text{cm}^2$. The nonlinear response of this system is enhanced by two main factors: (i) an efficient coupling of the radiation into the ENZ material mediated by the nanoantennas, and (ii) a large intensity enhancement in the ENZ material due to the field localization around the nanoantennas. A 860 fs total response time was also measured using the degenerate pump-probe experiment. Compared to the bare ITO film, the response time of the coupled structure was relatively slower because of the resonant nature of the system [29].

Adiabatic frequency conversion Adiabatic frequency conversion (AFC) is a nonlinear process that shifts the frequency of light as a result of time-varying

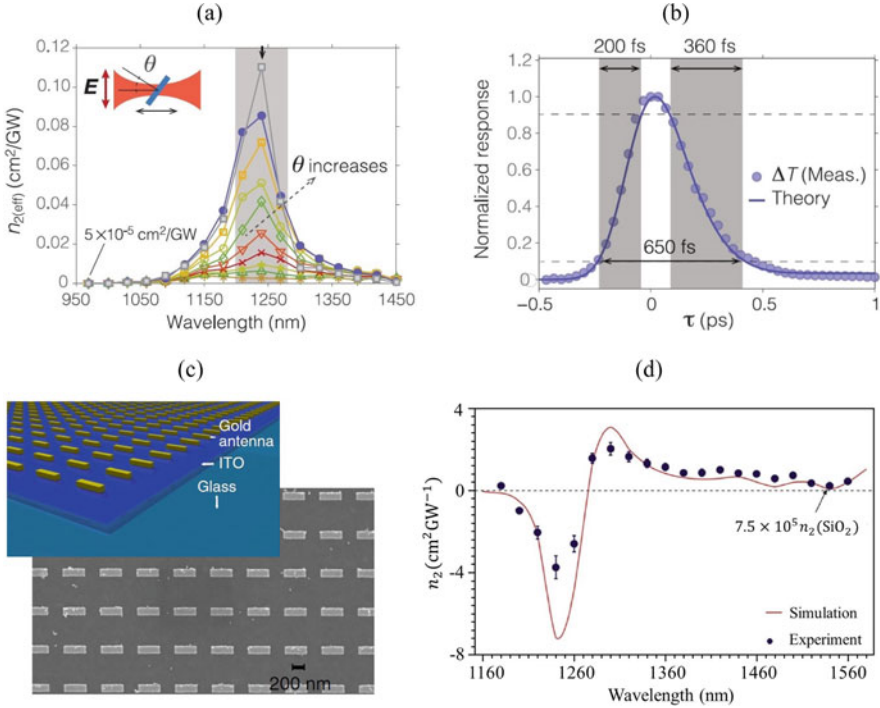


Fig. 8 (a) Wavelength and angle dependent nonlinear refractive index, and (b) the temporal response of hot electrons measured in ITO layer. (c) An array of gold nanorod deposited on top of a thin ITO film, and (d) the change in nonlinear refractive index as a function of wavelength reported for the structure in (c). (Panels (a) and (b) are adapted with permission from Ref. [17]. Panels (c) and (d) are adapted from Ref. [29])

refractive index ($\partial n/\partial t$). AFC is important for applications such as sensing, imaging, and telecommunication. Contrary to the spatially-varying refractive index, that is characterized by a constant frequency and a changing wavevector, a time-varying refractive index shifts the frequency while the wavevector remains constant [131, 132]. TCOs offer a large time-varying refractive index in the ENZ region, which induces a broadband adiabatic frequency conversion [133, 134].

Experimental studies performed on TCOs have resulted in a shift of the probe wavelength ($\Delta\lambda$) in the range of 12–58 nm [130–132, 135]. The wavelength can be either red- or blue-shifted, depending on the delay time between the pump and the probe (Fig. 9a). It has been shown that for a given pump intensity, the magnitude of the red-shift is larger than that of the blue-shift, as illustrated in Fig. 9b and c for the case of ITO [131]. When the probe precedes the pump, the probe signal experiences an increase in the refractive index, and a translation of the probe wavelength to the longer wavelengths occurs. This is because of the excitation of free electrons in the conduction band. On the other hand, the probe experiences a reducing refractive index during the relaxation process when it follows the pump. As

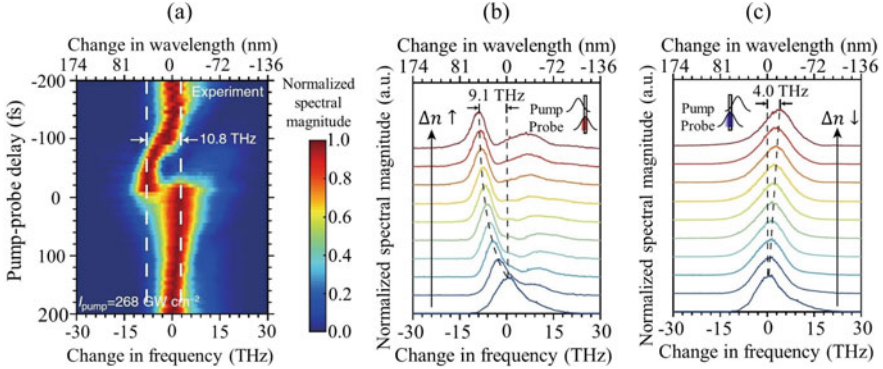


Fig. 9 (a) Measured probe spectra as a function of pump-probe delay time. Changes in probe frequency with the pump intensity in an ITO film for the cases of (b) red-shift and (c) blue-shift. (Figures adapted from Ref. [131], CC- BY-4.0)

a consequence, the probe wavelength undergoes a blue-shift. The faster dynamics of hot electrons during the excitation, compared to that during the relaxation (see Fig. 8b), leads to a larger change of refractive index with time. This in turn, results in the larger red-shifts than the blue-shifts measured in TCOs. Moreover, a larger wavelength shift is acquired when the central wavelength of the probe is near the zero-crossing wavelength of ENZ media. A blue-shift of $\Delta\lambda = 11$ nm in the probe central wavelength at a low pump intensity of 4 GW/cm^2 was measured in an ENZ-plasmonic structure composed of cross-shaped gold antennas on top of 65 nm-thick ITO layer on glass [30]. It is worth noting that comparable values of the blue-shift in bare ITO film required at least an order of magnitude larger pump intensity [131]. Moreover, in order to acquire similar values of the red-shift in bare AZO layers, 400 times larger pump intensities were utilized [135, 136].

Optical wave mixing This category of nonlinear phenomena refers to processes in which the interaction of photons in a nonlinear medium can lead to the generation of new photons with different frequencies [137]. Four-wave mixing (FWM), second harmonic generation (SHG), and third harmonic generation (THG) are among the most studied nonlinear phenomena in this category. Phase matching is critical to achieve efficient nonlinear wave mixing because multiple photons with different frequencies are involved in the process; however, its realization is typically challenging because of material dispersion [63, 137]. Recently, the feasibility of using ENZ media for perfect phase matching in SHG was theoretically studied [138], introducing a clever material design with ENZ regions at both fundamental and second-harmonic frequencies. In such a scenario, all photons carry zero momentum, enabling phase mismatch-free nonlinear interactions for any combination of photon directions. This concept was further investigated and experimentally demonstrated through degenerate FWM in a zero-index material [63]. Since the refractive index at the pump, signal, and idler frequencies was zero,

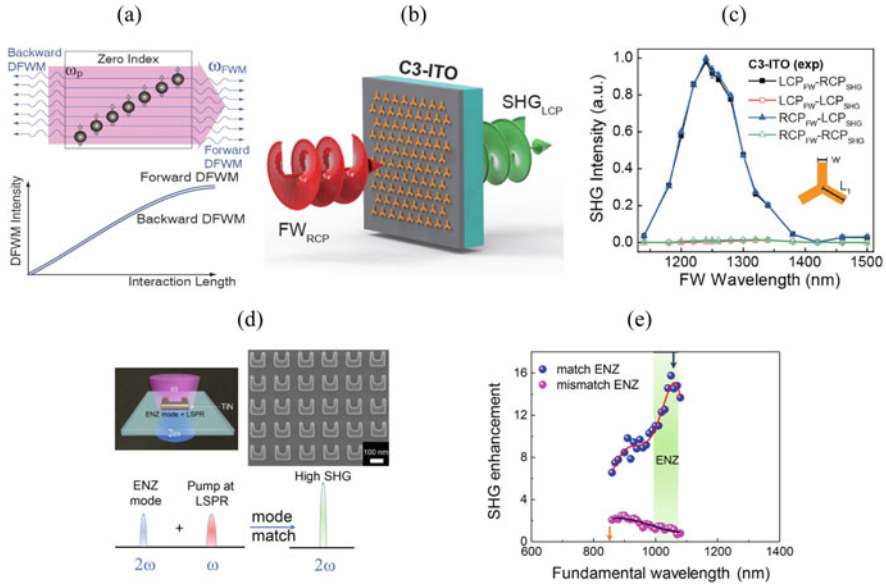


Fig. 10 (a) Phase mismatch-free propagation of light (top panel) and forward and backward idler intensities (bottom panel) in a zero-index medium. (b) Schematic representation of an ENZ-plasmonic system studied for SHG, and (c) the corresponding conversion efficiencies for different circularly polarized pumps. (d) TiN split ring resonator array supporting a resonance at the pump frequency and another at the second harmonic frequency. (e) SHG enhancement versus pump wavelength for the structure in (d); the blue and magenta dots show the experimental results for the horizontal and vertical polarization of the pump, respectively. (Panel (a) is adapted with permission from Ref. [63]. Copyright (2013) AAAS. Panels (b) and (c) are adapted with permission from [32]. Copyright (2018) American Chemical Society. Panels (d) and (e) are adapted with permission from [31]. Copyright (2018) American Chemical Society)

the phase-matching condition, $|\Delta k_{\pm}| = |2k_{\text{pump}} - k_{\text{signal}} \mp k_{\text{idler}}|$, was automatically fulfilled for both forward and backward idlers (Fig. 10a-top panel). As a result, the intensities of the counter-propagating idlers were almost equal (Fig. 10a-bottom panel), contrary to significantly different idler intensities typically obtained for FWM in conventional nonlinear media [63].

In addition to the advantages for phase matching, the strong field enhancement in ENZ media increases the conversion efficiency and lowers the required pump power [139]. Experimental studies of the SHG and THG in thin films of TCOs have shown several orders of magnitude larger conversion efficiencies when pumped at the [18, 19, 119, 140, 141]. Furthermore, high harmonic generation up to the 9th order was obtained in a 75 nm-thick ICO layer because of a large field enhancement in the ENZ region [20].

Much stronger SHG was realized in an ENZ-plasmonic structure made of plasmonic nanoantenna fabricated on top of ITO (Fig. 10b) [32]. The structure featured a conversion efficiency up to 4 orders of magnitude larger than that in

the bare ITO film for normally incident pumps. This was attributed to the efficient coupling of the pump to the ITO layer along with further enhancement of the field by the nanoantennas. In addition, the integration of rotationally symmetric nanoantennas with the ENZ medium provided the extra advantage of simultaneous polarization control for the second harmonic signal upon its generation. As shown in Fig. 10c, a right (left) circularly polarized pump resulted in generation of a left (right) circularly polarized harmonic signal. It is important to note that the conversion efficiency is not only dependent on the field enhancement at the pump frequency, but also on that in all other generated frequencies. Therefore, nonlinear materials with multiple resonances that coincide with the pump and the generated frequencies can ensure highly-efficient nonlinear interaction [31, 138]. For instance, an array of TiN split ring resonators that supports an ENZ mode in the visible and a localized surface plasmon resonance in the NIR (Fig. 10d) was employed for enhancing the electric field at the harmonic and pump frequencies [31]. As shown in Fig. 10e, the conversion efficiency was larger for the horizontally polarized pump, which was due to the excitation of the fundamental plasmonic mode. Moreover, a 16 times larger enhancement of SHG was measured for the resonator array compared to the thin layer of TiN.

5 Concluding Remarks

Over the past years, there has been a growing interest in studying a broad range of optical phenomena occurring in ENZ media and in ENZ media coupled to plasmonic structures. Indeed, it is clear from the current state of this research field that there is great deal of synergy between the fields of ENZ materials and plasmonics. In particular, the capacity of plasmonic structures to enhance optical interactions in ENZ materials through strongly localized near fields results in enhanced linear and nonlinear optical phenomena with rich physics. Various material platforms for ENZ media have been proposed so far, however, those based on TCOs appear to be the best candidates for devising coupled ENZ-plasmonic systems because of their ease of fabrication and readily integration with plasmonic structures through standard nanolithography methods. Through this approach, ENZ-plasmonic structures have already demonstrated exciting linear optical phenomena such as strong coupling between plasmonic and ENZ excitations, tailoring the optical scattering of plasmonic nanoparticles, and broadband perfect absorption. On the other hand, several convincing laboratory demonstrations have made clear the enormous nonlinear optical response of TCO-based ENZ materials, and the dramatic enhancement that such a nonlinear response can achieve by incorporating plasmonic structures. In addition to their strong nonlinearity, it has been demonstrated that coupled ENZ-plasmonic structures can feature a nonlinear optical response with sub-picosecond time scale, opening possibilities for creating advanced materials with strong and ultrafast nonlinearities. However, there are important challenges to solve, such as the detrimental impact of the losses in most applications and the low damage

threshold of conventional plasmonic materials, which would limit the performance of nonlinear optical devices. Despite these challenges, it is the opinion of the authors that the field of ENZ plasmonics has a bright future with vast opportunities for research activities and great potential for applications.

Acknowledgments This work was supported by Consejo Nacional de Ciencia y Tecnología (CONACyT) and by the Sectorial Research Fund for Education (Fondo Sectorial de Investigación para la Educación); project number 286150.

References

1. Vassant, S., Hugonin, J. P., & Marquier, F., et al. (2012). Berreman mode and epsilon near zero mode. *Optics Express*, *20*, 23971–23977.
2. Campione, S., Brener, I., & Marquier, F. (2015). Theory of epsilon-near-zero modes in ultrathin films. *Physical Review B*, *91*, 121408.
3. Liberal, I., & Engheta, N. (2017). Near-zero refractive index photonics. *Nature Photonics*, *11*, 149–158.
4. Reshef, O., De Leon, I., Alam, M. Z., et al. (2019). Nonlinear optical effects in epsilon-near-zero media. *Nature Reviews Materials*, *4*, 535–551.
5. Kinsey, N., DeVault, C., Boltasseva, A., et al. (2019). Near-zero-index materials for photonics. *Nature Reviews Materials*, *4*, 1–19.
6. Lal, S., Link, S., & Halas N. J. (2007). Nano-optics from sensing to waveguiding. *Nature Photonics*, *1*, 641–648.
7. Anker, J. N., Hall, W. P., Lyandres, O., et al. (2008). Biosensing with plasmonic nanosensors. *Nature Materials*, *7*, 442–453.
8. Wang, X., Huang, S. C., Hu, S., et al. (2020). Fundamental understanding and applications of plasmon-enhanced Raman spectroscopy. *Nature Reviews Physics*, *2*, 253–271.
9. D’Andrea, C., Bochterle, J., Toma, A., et al. (2013). Optical nanoantennas for multiband surface-enhanced infrared and Raman spectroscopy. *ACS Nano*, *7*, 3522–3531.
10. Stockman, M. I. (2004). Nanofocusing of optical energy in tapered plasmonic waveguides. *Physical Review Letters*, *93*, 137404.
11. Neacsu, C. C., Berweger, S., & Olmon, R. L. (2010). Near-field localization in plasmonic superfocusing: A nanoemitter on a tip. *Nano Letters*, *10*, 592–596.
12. Im, H., Bantz, K. C., Lindquist, N. C., et al. (2010). Vertically oriented sub-10-nm plasmonic nanogap arrays. *Nano Letters*, *10*, 2231–2236.
13. Meinzer, N., Barnes, W., & Hooper, I. (2014). Plasmonic meta-atoms and metasurfaces. *Nature Photonics*, *8*, 889–898.
14. Valentine, J., Zhang, S., Zentgraf, T., et al. (2008). Three-dimensional optical metamaterial with a negative refractive index. *Nature*, *455*, 376–379.
15. Liu, N., Guo, H., Fu, L., et al. (2008). Three-dimensional photonic metamaterials at optical frequencies. *Nature Materials*, *7*, 31–37.
16. Gansel, J. K., Thiel, M., Rill, M. S., et al. (2009). Gold helix photonic metamaterial as broadband circular polarizer. *Science*, *325*, 1513–1515.
17. Alam, M. Z., De Leon, I., & Boyd, R. W. (2016). Large optical nonlinearity of indium tin oxide in its epsilon-near-zero region. *Science*, *352*, 795–797.
18. Luk, T. S., De Ceglia, D., Liu, S., et al. (2015). Enhanced third harmonic generation from the epsilon-near-zero modes of ultrathin films. *Applied Physics Letters*, *106*, 151103.
19. Capretti, A., Wang, Y., Engheta, N., et al. (2015). Enhanced third-harmonic generation in Si-compatible epsilon-near-zero indium tin oxide nanolayers. *Optics Letters*, *40*, 1500–1503.

20. Yang, Y., Lu, J., Manjavacas, A., et al. (2019). High-harmonic generation from an epsilon-near-zero material. *Nature Physics*, *15*, 1022–1026.
21. Silveirinha, M., & Engheta, N. (2006). Tunneling of electromagnetic energy through sub-wavelength channels and bends using ϵ -near-zero materials. *Physical Review Letters*, *97*, 157403.
22. Edwards, B., Alù, A., Young, M. E., et al. (2008). Experimental verification of epsilon-near-zero metamaterial coupling and energy squeezing using a microwave waveguide. *Physical Review Letters*, *100*, 033903.
23. Hendrickson, J. R., Vangala, S., Dass, C., et al. (2018). Coupling of epsilon-near-zero mode to gap plasmon mode for flat-top wideband perfect light absorption. *ACS Photonics*, *5*, 776–781.
24. Meng, Z., Cao, H., & Wu X. (2019). New design strategy for broadband perfect absorber by coupling effects between metamaterial and epsilon-near-zero mode. *Optical Materials*, *96*, 109347.
25. Park, J., Kang, J. H., Liu, X., et al. (2015). Electrically tunable epsilon-near-zero (ENZ) metafilm absorbers. *Scientific Reports*, *5*, 15754.
26. Kim, J., Dutta, A., Naik, G. V., et al. (2016). Role of epsilon-near-zero substrates in the optical response of plasmonic antennas. *Optica*, *3*, 339–346.
27. Habib, M., Briukhanova, D., Das, N., et al. (2020). Controlling the plasmon resonance via epsilon-near-zero multilayer metamaterials. *Nanophotonics*, *6*, 3637–3644.
28. DeVault, C. T., Zenin, V. A., Pors, A., et al. (2018). Suppression of near-field coupling in plasmonic antennas on epsilon-near-zero substrates. *Optica*, *5*, 1557–1563.
29. Alam, M. Z., Schulz, S. A., Upham, J., et al. (2018). Large optical nonlinearity of nanoantennas coupled to an epsilon-near-zero material. *Nature Photonics*, *12*, 79–83.
30. Liu, C., Pang, K., Manukyan, K., et al. (2019). Resonance splitting and enhanced optical nonlinearities in ITO-based epsilon-near-zero metasurface with cross-shaped nanoantennas. CLEO: QELS_Fundamental Science, FW4B-5.
31. Wen, X., Li, G., Gu, C., et al. (2018). Doubly enhanced second harmonic generation through structural and epsilon-near-zero resonances in TiN nanostructures. *ACS Photonics*, *5*, 2087–2093.
32. Deng, J., Tang, Y., Chen, S., et al. (2020). Giant enhancement of second-order nonlinearity of epsilon-near-zero medium by a plasmonic metasurface. *Nano Letters*, *20*, 5421–5427.
33. Maier, S. A. (2007). *Plasmonics: Fundamentals and applications*. New York: Springer.
34. Zayats, A. V., & Smolyaninov, I. I. (2003). Near-field photonics: Surface plasmon polaritons and localized surface plasmons. *Journal of Optics A: Pure and Applied Optics*, *5*, S16.
35. Stockman, M. I. (2011). Nanoplasmonics: Past, present, and glimpse into future. *Optical Society of America*, *19*, 22029–22106.
36. Schuller, J. A., Barnard, E. S., Cai, W., et al. (2010). Plasmonics for extreme light concentration and manipulation. *Nature Materials*, *9*, 193–204.
37. Hanke, T., Cesar, J., Knittel, V., et al. (2012). Tailoring spatiotemporal light confinement in single plasmonic nanoantennas. *Nano Letters*, *12*, 992–996.
38. Zhang, S., Park, Y. S., Liu, Y., et al. (2010). Far-field measurement of ultra-small plasmonic mode volume. *Optics Express*, *18*, 6048–6055.
39. Novotny, L., & Van, H. N. (2011). Antennas for light. *Nature Photonics*, *5*, 83–90.
40. Kinkhabwala, A., Yu, Z., Fan, S., et al. (2009). Large single-molecule fluorescence enhancements produced by a bowtie nanoantenna. *Nature Photonics*, *3*, 654–657.
41. Taminiou, T. H., Stefani, F. D., Segerink, F. B., et al. (2008). Optical antennas direct single-molecule emission. *Nature Photonics*, *2*, 234–237.
42. Maier, S. A. (2006). Plasmonics: Metal nanostructures for subwavelength photonic devices. *IEEE*, *12*, 1214–1220.
43. Volker, J. S., Rupert, F. O., Ma, R. M., et al. (2012). Toward integrated plasmonic circuits. *MRS Bulletin*, *37*, 728–738.
44. Chen, H. T., Taylor, A. J., & Nanfang, Y. (2016). A review of metasurfaces: Physics and applications. *Reports on Progress in Physics*, *79*, 076401.

45. Chen, X., Huang, L., Mühlenbernd, H., et al. (2012). Dual-polarity plasmonic metalens for visible light. *Nature Communications*, *3*, 1198.
46. Yu, N., Aieta, F., Genevet, P., et al. (2012). A broadband, background-free quarter-wave plate based on plasmonic metasurfaces. *Nano Letters*, *12*, 6328–6333.
47. Yu, N., Genevet, P., Kats, M. A., et al. (2011). Light propagation with phase discontinuities: Generalized laws of reflection and refraction. *Science*, *334*, 333–337.
48. Karimi, E., Schulz, S., De Leon, I., et al. (2014). Generating optical orbital angular momentum at visible wavelengths using a plasmonic metasurface. *Light: Science & Applications*, *3*, e167.
49. Yang, A., Hoang, T., Dridi, M., et al. (2015). Real-time tunable lasing from plasmonic nanocavity arrays. *Nature Communications*, *6*, 6939.
50. Lee, J., Tymchenko, M., Argyropoulos, C., et al. (2014). Giant nonlinear response from plasmonic metasurfaces coupled to intersubband transitions. *Nature*, *511*, 65–69.
51. Rahimi, E., & Gordon, R. (2018). Nonlinear plasmonic metasurfaces. *Advanced Optical Materials*, *6*, 1800274.
52. Chen, S., Reineke, B., Li, G., et al. (2019). Strong nonlinear optical activity induced by lattice surface modes on plasmonic metasurface. *Advanced Nano Letters*, *19*, 6278–6283.
53. Jin, B., & Argyropoulos, C. (2016). Enhanced four-wave mixing with nonlinear plasmonic metasurfaces. *Scientific Reports*, *6*, 28746.
54. Gwo, S., Wang, C. Y., Chen, H. Y., et al. (2016). Plasmonic metasurfaces for nonlinear optics and quantitative SERS. *ACS Photonics*, *8*, 1371–1384.
55. Hsiao, H. H., Chu, C. H., & Tsai, D. P. (2017). Fundamentals and applications of metasurfaces. *Small Methods*, *1*, 1600064.
56. Ding, F., Pors, A., & Bozhevolnyi, S. I. (2018). Gradient metasurfaces: A review of fundamentals and applications. *Reports on Progress in Physics*, *71*, 026401.
57. Ding, F., Yang, Y., Deshpande, R. A., et al. (2018). A review of gap-surface plasmon metasurfaces: Fundamentals and applications. *Nanophotonics*, *7*, 1129–1156.
58. Engheta, N. (2013). Pursuing near-zero response. *Science*, *340*, 286–287.
59. Saleh, B. E. A., & Teich, M. C. (2007). *Fundamentals of photonics*. Hoboken: Wiley.
60. Ziolkowski, R. W. (2004). Propagation in and scattering from a matched metamaterial having a zero index of refraction. *Physical Review E*, *70*, 046608.
61. Niu, X., Hu, X., Chu, S., et al. (2018). Epsilon-near-zero photonics: A new platform for integrated devices. *Advanced Optical Materials*, *6*, 1701292.
62. Alu, A., Silveirinha, M. G., Salandrino, A., et al. (2007). Epsilon-near-zero metamaterials and electromagnetic sources: Tailoring the radiation phase pattern. *Physical Review B*, *75*, 155410.
63. Suchowski, H., O'Brien, K., Wong, Z. J., et al. (2013). Phase mismatch-free nonlinear propagation in optical zero-index materials. *Science*, *342*, 1223–1226.
64. Silveirinha, M. G., & Engheta, N. (2007). Theory of supercoupling, squeezing wave energy, and field confinement in narrow channels and tight bends using ϵ near-zero metamaterials. *Physical Review B*, *76*, 245109.
65. Javani, M. H., & Stockman, M. I. (2016). Real and imaginary properties of epsilon-near-zero materials. *Physical Review Letters*, *117*, 107404.
66. Campione, S., De Ceglia, D., Vincenti, M. A., et al. (2013). Electric field enhancement in ϵ -near-zero slabs under TM-polarized oblique incidence. *Physical Review B*, *87*, 035120.
67. Kamandi, M., Guclu, C., Luk, T. S., et al. (2017). Giant field enhancement in longitudinal epsilon-near-zero films. *Physical Review B*, *95*, 161105.
68. Vincenti, M. A., Kamandi, M., & de Ceglia, D. (2017). Second-harmonic generation in longitudinal epsilon-near-zero materials. *Physical Review B*, *96*, 045438.
69. Gurung, S., Anopchenko, A., Bej, S., et al. (2020). Atomic layer engineering of epsilon-near-zero ultrathin films with controllable field enhancement. *Advanced Materials Interfaces*, *7*, 2000844.
70. Johnson, P. B., & Christy, R. W. (1972). Optical constant of the noble metals. *Physical Review B*, *6*, 4370.

71. Johnson, P. B., & Christy, R. W. (1974). Optical constants of transition metals: Ti, v, cr, mn, fe, co, ni, and pd. *Physical Review B*, *9*, 5056.
72. McMahon, J. M., Schatz, G. C., & Gray, S. K. (2013). Plasmonics in the ultraviolet with the poor metals Al, Ga, In, Sn, Tl, Pb, and Bi. *Physical Chemistry Chemical Physics*, *15*, 5415–5423.
73. Smith, D. D., Yoon, Y., Boyd, R. W., et al. (1999). Z-scan measurement of the nonlinear absorption of a thin gold film. *Journal of Applied Physics*, *86*, 6200–6205.
74. Ricard, D., Roussignol, P., & Flytzanis, C. (1985). Surface-mediated enhancement of optical phase conjugation in metal colloids. *Optics Letters*, *10*, 511–513.
75. Zhang, C., Kinsey, N., Chen, L., et al. (2017). High-performance doped silver films: Overcoming fundamental material limits for nanophotonic applications. *Advanced Materials*, *29*, 1605177.
76. Ovidio, P. R., Caro, M., Rivera, A., et al. (2014). Optical properties of Au-Ag alloys: An ellipsometric study. *Optical Materials Express*, *4*, 403–410.
77. Karlsson, B., Shimshock, R. P., Seraphin, B. O., et al. (1983). Optical properties of CVD-coated TiN, ZrN and HfN. *Solar Energy Materials*, *7*, 401–411.
78. Naik, G. V., Kim, J., & Boltasseva, A. (2011). Oxides and nitrides as alternative plasmonic materials in the optical range. *Optical Materials Express*, *1*, 1090–1099.
79. Naik, G. V., Schroeder, J. L., Ni, X., et al. (2012). Titanium nitride as a plasmonic material for visible and near-infrared wavelengths. *Optical Materials Express*, *2*, 478–489.
80. Combadiere, L., & Mchet, J. (1997). Reactive magnetron sputtering deposition of TiN films. I. Influence of the substrate temperature on structure, composition and morphology of the films. *Surface and Coatings Technology*, *88*, 17–27.
81. Minami, T. (2005). Transparent conducting oxide semiconductors for transparent electrodes. *Semiconductor Science and Technology*, *20*, S35–S44.
82. Fujiwara, H., & Kondo, M. (2005). Effects of carrier concentration on the dielectric function of ZnO: Ga and In 2 O 3: Sn studied by spectroscopic ellipsometry: Analysis of free-carrier and band-edge absorption. *Physical Review B*, *71*, 075109.
83. Wang, H., Dai, X., Du, K., et al. (2020). Tuning epsilon-near-zero wavelength of indium tin oxide film via annealing. *Journal of Physics D: Applied Physics*, *53*, 225108.
84. Johns, B., Puthoor, N. M., Gopalakrishnan, H., et al. (2020). Epsilon-near-zero response in indium tin oxide thin films: Octave span tuning and IR plasmonics. *Journal of Applied Physics*, *127*, 043102.
85. Carnemolla, E. G., Caspani, L., DeVault, C., et al. (2016). Degenerate optical nonlinear enhancement in epsilon-near-zero transparent conducting oxides. *Optical Materials Express*, *8*, 3392–3400.
86. Tyborski, T., Kalusniak, S., Sadofev, S., et al. (2015). Ultrafast nonlinear response of bulk plasmons in highly doped ZnO layers. *Physical Review Letters*, *115*, 147401.
87. Yang, Y., Kelley, K., Sachet, E., et al. (2017). Femtosecond optical polarization switching using a cadmium oxide-based perfect absorber. *Nature Photonics*, *11*, 1–6.
88. Zhang, L., Zhou, Y., Guo, L., et al. (2016). Correlated metals as transparent conductors. *Nature Materials*, *15*, 204–210.
89. Jacob, J., Alekseyev, L. V., & Narimanov, E. (2006). Optical hyperlens: Far-field imaging beyond the diffraction limit. *Optics Express*, *14*, 8247–8256.
90. Smolyaninov, I. I., Hung, Y. J., & Christopher, C. D. (2007). Magnifying superlens in the visible frequency range. *Science*, *315*, 1699–1701.
91. Pendry, J. B., Schurig, D., & Smith, D. R. (2006). Controlling electromagnetic fields. *Science*, *312*, 1780–1782.
92. Xiao, S., Drachev, V., Kildishev, A., et al. (2010). Loss-free and active optical negative-index metamaterials. *Nature*, *466*, 735–738.
93. Subramania, G., Fischer, A. J., & Luk, T. S. (2012). Optical properties of metal-dielectric based epsilon near zero metamaterials. *Applied Physics Letters*, *101*, 241107.
94. Poddubny, A., Iorsh, I., Belov, P., et al. (2013). Hyperbolic metamaterials. *Nature Photonics*, *7*, 948–957.

95. Maas, R., Parsons, J., Engheta, N., et al. (2013). Experimental realization of an epsilon-near-zero metamaterial at visible wavelengths. *Nature Photonics*, 7, 907–912.
96. Valentine, J., Zhang, S., Zentgraf, T., et al. (2008). Three-dimensional optical metamaterial with a negative refractive index. *Nature*, 455, 376–379.
97. Yun, S., Jiang, Z. H., Xu, Q., et al. (2012). Low-loss impedance-matched optical metamaterials with zero-phase delay. *ACS Nano*, 6, 4475–4482.
98. Huang, X., Lai, Y., Hang, Z. H., et al. (2011). Dirac cones induced by accidental degeneracy in photonic crystals and zero-refractive-index materials. *Nature Materials*, 10, 582–586.
99. Moitra, P., Yang, Y., Anderson, Z., et al. (2013). Realization of an all-dielectric zero-index optical metamaterial. *Nature Photonics*, 7, 791–795.
100. Li, Y., Kita, S., Muñoz, P., et al. (2015). On-chip zero-index metamaterials. *Nature Photonics*, 9, 738–742.
101. Vulis, D. I., Li, Y., Reshef, O., et al. (2017). Monolithic CMOS-compatible zero-index metamaterials. *Optics Express*, 25, 12381–12399.
102. Vesseur, E. J. R., Coenen, T., Caglayan, H., et al. (2013). Experimental verification of $n=0$ structures for visible light. *Physical Review Letters*, 110, 013902.
103. Jun, Y. C., Reno, J., Ribaudo, T., et al. (2013). Epsilon-near-zero strong coupling in metamaterial-semiconductor hybrid structures. *Nano Letters*, 13, 5391–5396.
104. Campione, S., Liu, S., Benz, A., et al. (2015). Epsilon-near-zero modes for tailored light-matter interaction. *Physical Review Applied*, 4, 044011.
105. Schulz, S. A., Tahir, A. A., Alam, M. Z., et al. (2016). Optical response of dipole antennas on an epsilon-near-zero substrate. *Physical Review A*, 93, 063846.
106. Campione, S., Wendt, J. R., Keeler, G. A., et al. (2016). Near-infrared strong coupling between metamaterials and epsilon-near-zero modes in degenerately doped semiconductor nanolayer. *ACS Photonics*, 3, 293–297.
107. Enoch, S., Tayeb, G., Sabouroux, P., et al. (2002). A metamaterial for directive emission. *Physical Review Letters*, 89, 213902.
108. Alekseyev, L. V., Narimanov, E. E., Tumkur, T., et al. (2010). Uniaxial epsilon-near-zero metamaterial for angular filtering and polarization control. *Physical Review Letters*, 97, 131107.
109. Navarro, C. M., Beruete, M., Sorolla, M., et al. (2012). Lensing system and Fourier transformation using epsilon-near-zero metamaterials. *Physical Review B*, 86, 165130.
110. Torres, V., Orazbayev, B., Pacheco-Peña, V., et al. (2014). Experimental demonstration of a millimeter-wave metallic ENZ lens based on the energy squeezing principle. *IEEE Transactions on Antennas and Propagation*, 63, 231–239.
111. Soric, J. C., & Alù, A. (2015). Longitudinally independent matching and arbitrary wave patterning using ϵ -near-zero channels. *IEEE Transactions on Microwave Theory and Techniques*, 63, 3558–3567.
112. Vasant, S., Archambault, A., Marquier, F., et al. (2012). Epsilon-near-zero mode for active optoelectronic devices. *Physical Review Letters*, 109, 237401.
113. Baranov, D. G., Krasnok, A., Shegai, T., et al. (2016). Coherent perfect absorbers: linear control of light with light. *Nature Reviews Materials*, 2, 1–14.
114. Luk, T. S., Campione, S., Kim, I., et al. (2014). Directional perfect absorption using deep subwavelength low-permittivity films. *Physical Review B*, 90, 085411.
115. Feng, S., & Halterman, K. (2012). Coherent perfect absorption in epsilon-near-zero metamaterials. *Physical Review B*, 86, 165103.
116. Anopchenko, A., Tao, L., Arndt, C., et al. (2018). Field-effect tunable and broadband epsilon-near-zero perfect absorbers with deep subwavelength thickness. *ACS Photonics*, 5, 2631–2637.
117. Yoon, J., Zhou, M., Badsha, M. A., et al. (2015). Broadband epsilon-near-zero perfect absorption in the near-infrared. *Scientific Reports*, 5, 12788.
118. Eggleton, B. J., Luther-Davies, B., & Richardson, K. (2011). Chalcogenide photonics. *Nature Photonics*, 5, 141–148.

119. Vincenti, M. A., Ceglia, D. D., & Scalora, M. (2020). ENZ materials and anisotropy: Enhancing nonlinear optical interactions at the nanoscale. *Optics Express*, *28*, 31180–31196.
120. Liu, X., Park, J., Kang, J. H., et al. (2014). Quantification and impact of nonparabolicity of the conduction band of indium tin oxide on its plasmonic properties. *Applied Physics Letters*, *105*, 181117.
121. Guo, P., Schaller, R. D., Ketterson, J. B., et al. (2014). Ultrafast switching of tunable infrared plasmons in indium tin oxide nanorod arrays with large absolute amplitude. *Nature Photonics*, *10*, 267–273.
122. Wang, H., Du, K., Jiang, C., et al. (2019). Extended Drude model for intraband-transition-induced optical nonlinearity. *Physical Review Applied*, *11*, 064062.
123. Secondo, R., Khurgin, J., & Kinsey, N. (2020). Absorptive loss and band non-parabolicity as a physical origin of large nonlinearity in epsilon-near-zero materials. *Optical Materials Express*, *10*, 1545–1560.
124. Saha, S., Diroll, B. T., Shank, J., et al. (2020). Broadband, high-speed, and large-amplitude dynamic optical switching with Yttrium-doped Cadmium oxide. *Advanced Functional Materials*, *30*, 1908377.
125. Kinsey, N., DeVault, C., Kim, J., et al. (2015). Epsilon-near-zero Al-doped ZnO for ultrafast switching at telecom wavelengths. *Optica*, *2*, 616–622.
126. Clerici, M., Kinsey, N., DeVault, C., et al. (2017). Controlling hybrid nonlinearities in transparent conducting oxides via two-colour excitation. *Nature Communications*, *8*, 1–7.
127. Reshef, O., Giese, E., Alam, M. Z., et al. (2017). Beyond the perturbative description of the nonlinear optical response of low-index materials. *Optics Letters*, *42*, 3225–3228.
128. Harbold, J. M., Ilday, F., Wise, F. W., et al. (2002). Highly nonlinear As–S–Se glasses for all-optical switching. *Optics Letters*, *27*, 119–121.
129. Slusher, R. E., Lenz, G., Hodelin, J., et al. (2004). Large Raman gain and nonlinear phase shifts in high-purity As₂Se₃ chalcogenide fibers. *Journal of the Optical Society of America B*, *21*, 1146–1155.
130. Caspani, L., Kaipurath, R. P. M., Clerici, M., et al. (2016). Enhanced nonlinear refractive index in ϵ -near-zero materials. *Physical Review Letters*, *116*, 233901.
131. Zhou, Y., Alam, M. Z., Karimi, M., et al. (2020). Broadband frequency translation through time refraction in an epsilon-near-zero material. *Nature Communications*, *11*, 1–7.
132. Khurgin, J. B., Clerici, M., Bruno, V., et al. (2020). Adiabatic frequency shifting in epsilon-near-zero materials: The role of group velocity. *Optica*, *7*, 226–231.
133. Preble, S. F., Xu, Q., & Lipson, M. (2007). Changing the colour of light in a silicon resonator. *Nature Photonics*, *1*, 293–296.
134. Beggs, D. M., Krauss, T. F., Kuipers, L., et al. (2012). Ultrafast tilting of the dispersion of a photonic crystal and adiabatic spectral compression of light pulses. *Physical Review Letters*, *108*, 033902.
135. Carnemolla, E. G., Bruno, V., Caspani, L., et al. (2018). Giant nonlinear frequency shift in epsilon-near-zero aluminum zinc oxide thin films. CLEO: Science and Innovations, SM4D-7.
136. Ferrera, M., & Carnemolla, E. G. (2018). Ultra-fast transient plasmonics using transparent conductive oxides. *Journal of Optics*, *20*, 024007.
137. Boyd, R. W. (2008). *Nonlinear optics*. Amsterdam/Boston: Academic Press.
138. Argyropoulos, C., D’Aguanno, G., & Alu, A. (2014). Giant second-harmonic generation efficiency and ideal phase matching with a double ϵ -near-zero cross-slit metamaterial. *Physical Review B*, *89*, 235401.
139. Vincenti, M. A., De Ceglia, D., Ciattoni, A., et al. (2011). Singularity-driven second- and third-harmonic generation at ϵ -near-zero crossing points. *Physical Review A*, *84*, 063826.
140. Capretti, A., Wang, Y., Engheta, N., et al. (2015). Comparative study of second-harmonic generation from epsilon-near-zero indium tin oxide and titanium nitride nanolayers excited in the near-infrared spectral range. *ACS Photonics*, *2*, 1584–1591.
141. Passler, N. C., Rzdolski, I., Katzer, D. S., et al. (2019). Second harmonic generation from phononic epsilon-near-zero Berreman modes in ultrathin polar crystal films. *ACS Photonics*, *6*, 1365–1371.

Epsilon-Near-Zero Plasmonic Waveguides for Enhanced Coherent Optical Effects



Ying Li and Christos Argyropoulos

Abstract Plasmonic waveguides exhibit an effective epsilon-near-zero (ENZ) operation in their cut-off wavelength and Fabry-Pérot resonances at lower wavelengths. In this chapter, we demonstrate a scheme to realize nonlinear coherent perfect absorption (CPA) at the nanoscale using the ENZ plasmonic waveguide nanochannels. The strong and uniform field enhancement inside the nanochannels of the waveguides at the ENZ resonance can efficiently boost Kerr nonlinearities, resulting in a new all-optical switching intensity-dependent CPA phenomenon which can be tunable with ultrafast speed. Our findings provide a new platform to efficiently excite nonlinear phenomena at the nanoscale and design tunable coherent perfect absorbers.

In addition, we demonstrate the formation of exceptional points (EP) in a nanoscale open and lossy (non-Hermitian) nanophotonic system based on gain medium embedded inside the ENZ plasmonic waveguide nanochannels. Reflectionless transmission (perfect loss compensation) at the nanoscale is realized at the EP, which coincides with the ENZ cut-off frequency of the proposed plasmonic system. This special spectral degeneracy point (EP) is a unique feature of the presented nanoscale symmetric plasmonic ENZ configuration, different from most of the previous works that were mainly focused on asymmetric bulky micron-scale active photonic configurations. When we further increase the gain coefficient of the dielectric material loaded in the waveguides, a spectral singularity occurs leading to super scattering (lasing) response at both forward and backward directions. The presented results demonstrate that ENZ plasmonic waveguides can enhance different coherent optical effects that can find a plethora of new applications.

Y. Li

School of Physics and Optoelectronic Engineering, Nanjing University of Information Science and Technology, Nanjing, China

e-mail: ying@nuist.edu.cn

C. Argyropoulos (✉)

Department of Electrical and Computer Engineering, University of Nebraska-Lincoln, Lincoln, NE, USA

e-mail: christos.argyropoulos@unl.edu

© The Author(s), under exclusive license to Springer Nature Switzerland AG 2022

P. Yu et al. (eds.), *Plasmon-enhanced light-matter interactions*,

Lecture Notes in Nanoscale Science and Technology 31,

https://doi.org/10.1007/978-3-030-87544-2_3

Keywords Surface plasmon · Epsilon-near-zero · Plasmonics · Coherent optics · Exceptional point · Non-Hermitian

1 Introduction to Epsilon-Near-Zero (ENZ) Plasmonic Waveguides

Plasmonic nanostructures have received extensive attention due to their ability to generate surface plasmon resonances resulting in an efficient and realistic way to control and manipulate the light-matter interactions at the nanoscale [1–5]. Surface plasmon-polaritons (SPPs) are electromagnetic waves which are confined to metal-insulator interfaces and allow sub-wavelength confinement of light [6]. Applications of SPPs in optics and photonics are numerous, including light harvesting [7], plasmon focusing [8], waveguiding, cloaking [9, 10], plasmon-enhanced solar cells [11], and surface enhanced Raman spectroscopy [12].

During the recent years, few natural materials or metamaterials with permittivity or permeability near zero have been proposed with several exciting properties [13–16]. Such materials whose permittivity or dielectric constant become close to zero, are called *epsilon-near-zero (ENZ) materials*. Many materials in nature, such as metals, achieve ENZ permittivity at specific wavelengths. In this chapter, a free-standing waveguide structure is proposed to obtain an effective ENZ response [17–21]. It is based on periodic rectangularly-shaped plasmonic ultranarrow channels operating close to their cut-off frequency. This anomalous quasi-static response was originally proposed in [22] and can lead to very strong fields inside the ENZ plasmonic waveguides, characterized by uniform phase distribution and infinite phase velocity. It has been used for several applications, such as squeezing and tunneling of light [22], superradiance enhancement [17, 23], boosting optical nonlinearities [24–26], realizing quantum entanglement [20], and obtaining tunable coherent perfect absorbers [18].

In the following, we demonstrate that the proposed plasmonic waveguide channels can indeed achieve an effective ENZ response at their cut-off frequency. Figure 1 shows one unit cell of the periodic nanochannel geometry. As depicted in Fig. 1, a narrow rectangular slit filled with dielectric material with width w , height $t \ll w$, and length l , is carved in silver to create a waveguide. To further simplify our analysis, the dielectric slits are assumed to be composed of a material with no gain or loss. The relative permittivity of the passive dielectric material loaded in the narrow slit is chosen to be $\varepsilon = \varepsilon_r = 2.2$. Similar to the ENZ supercoupling effect presented in closed waveguides at optical [22, 23] and microwave frequencies [27, 28], the proposed approach to realize effective ENZ nanophotonic configurations consists of properly modulating the lateral width w of the plasmonic channels, such that each nanowaveguide operates at the cut-off of its dominant mode.

The lowest-order mode of such narrow orthogonal waveguide channels is a quasi-TE₁₀ mode, which is of a ‘quasi’ nature due to the non-negligible losses induced by the metallic (silver) waveguide walls at optical frequencies [24]. It can be evaluated

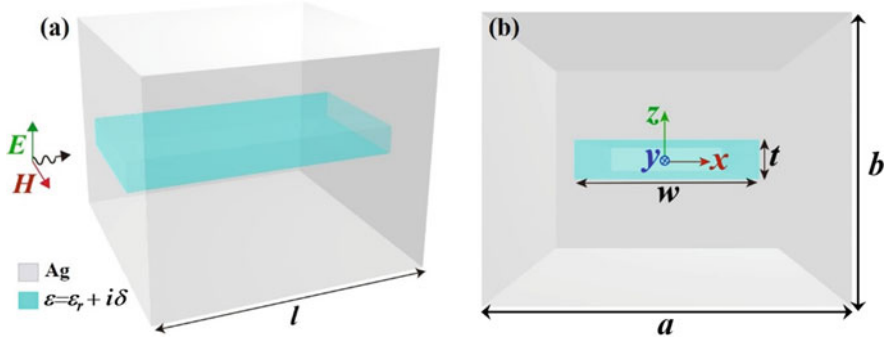


Fig. 1 Geometry of the silver plasmonic waveguide unit cell. The rectangular slits are loaded with a lossless passive dielectric material ($\varepsilon = \varepsilon_r + i\delta$, where $\delta = 0$) and are carved in the silver screen. The device is excited by a plane wave impinging at normal incidence. (Adapted with permission from Ref. [18]. © 2018 Optical Society of America)

by considering the transverse magnetic (TM) mode supported by a parallel-plate waveguide made of the upper and lower plates of the nanochannel, in combination with the transverse electric (TE) mode confined between the lateral walls [29]. In the limit $\varepsilon_{Ag} \rightarrow -\infty$ (assuming perfectly conducting metal), the effective permittivity for the quasi-TE₁₀ mode of the plasmonic nanowaveguide array system can be simply written as: $\varepsilon_{eff} = \varepsilon - \pi^2/k_0^2 w^2$, where k_0 is the wave vector of the propagating wave in free space and ε is the relative permittivity of passive dielectric material loaded in the narrow slit. As a result, the effective permittivity given by the approximate formula will become equal to zero leading to an effective ENZ resonant response only for a waveguide with width w equal to: $w = \pi/(\sqrt{\varepsilon}k_0)$, which is the classic cut-off condition of rectangular waveguides at microwave frequencies. Therefore, the effective ENZ operation can be obtained at the cut-off wavelength ($\lambda_c = 2w\sqrt{\varepsilon}$) of the dominant quasi-TE₁₀ mode, where $\text{Re}[\varepsilon_{eff}] = \text{Re}[\beta_{wg}] = 0$.

In order to further clarify the ENZ resonance features of the proposed plasmonic waveguide system, the transmittance from the system has been evaluated by using full-wave numerical simulations (COMSOL Multiphysics). The waveguide parameters are chosen to obtain the cut-off wavelength around $\lambda_c = 1012\text{nm}$, by using a slit height $t = 40\text{ nm}$ and width $w = 200\text{ nm}$. The grating period is selected to be equal to $a = b = 400\text{ nm}$. The transmittance results are computed and shown in Fig. 2 as a function of the incident wavelength for three different waveguide lengths: $l = 500\text{ nm}$ (solid line), $l = 700\text{ nm}$ (dashed line), and $l = 1\text{ }\mu\text{m}$ (dotted line). A strong transmission peak around the wavelength $\lambda = 1012\text{ nm}$ is always present, independent to the waveguide's length l values, which further proves that this is the cut-off wavelength of this waveguide. This cut-off wavelength is very close to the theoretical value computed by the theoretical analysis [19].

For longer wavelengths, the slits operate below cut-off and the incident waves are totally reflected back leading to zero transmittance, whereas for shorter wavelengths, several additional transmission peaks are observed that correspond to

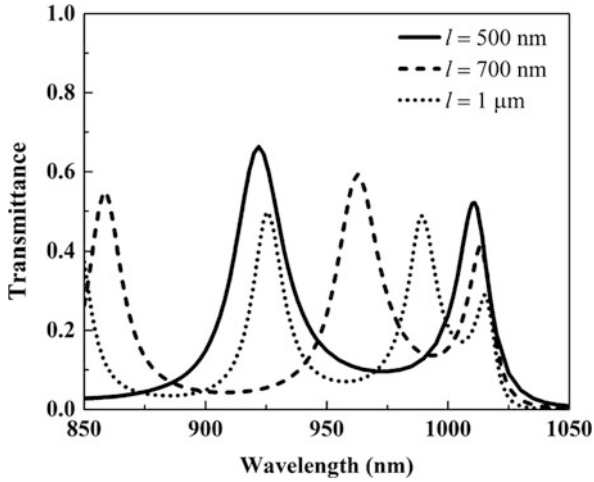


Fig. 2 Computed transmittance of the waveguide channels shown in Fig. 1 for three different values of channel thicknesses: $l = 500$ nm, 700 nm, and $1 \mu\text{m}$. (Adapted with permission from Ref. [19]. © 2019 American Physical Society)

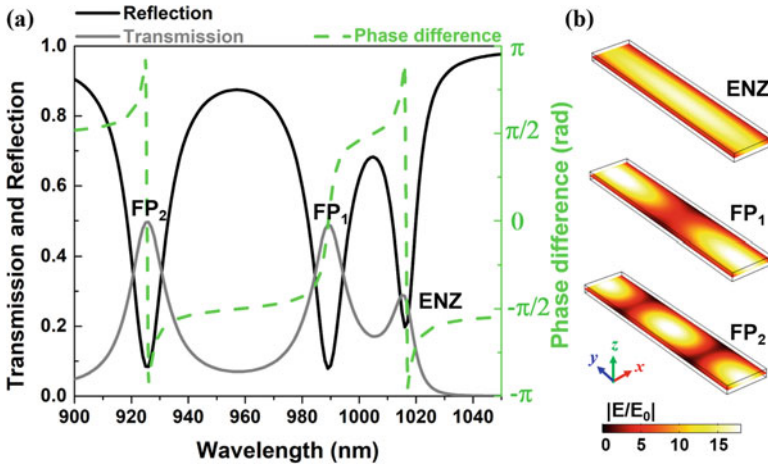


Fig. 3 (a) Transmission and reflection coefficients and phase difference between them for the plasmonic waveguide as a function of the incident wavelength. (b) The total electric field enhancement distribution in the channel's xy -plane operating at the ENZ, FP_1 , and FP_2 resonant wavelengths. (Adapted with permission from Ref. [18]. © 2018 Optical Society of America)

Fabry-Pérot (FP) resonances, which are strongly dependent on the waveguide's length l , as it can be seen in Fig. 3. In the next section, we will plot the field enhancement distributions at the ENZ operation and other higher-order FP resonances (see Fig. 3b). It is interesting that at the ENZ cut-off wavelength, large and uniform field enhancement is obtained inside the nanochannels due to the

effective infinitely elongated guided wavelength in each nanowaveguide (tunneling effect), since $\lambda_g = 2\pi / \text{Re}[\beta_{wg}]$ and $\text{Re}[\beta_{wg}] = 0$ at ENZ. Whereas for higher-order FP resonances, the fields have the typical characteristics of standing wave distributions, where sharp minima and maxima are observed along the waveguide length. The enhanced and homogeneous fields at the ENZ resonance are responsible to the boosting of several coherent optical effects, such as CPA.

2 Tunable Nonlinear Coherent Perfect Absorption (CPA) Based on Passive ENZ Plasmonic Waveguides

Recently, increased interest has been dedicated towards the design of different plasmonic nanostructures to control light in an efficient and coherent way. One example is the effect of coherent perfect absorption (CPA) leading to the interferometric all-optical control of absorption under the illumination of two counter-propagating coherent beams [30]. As the time-reversed counterpart of lasing, coherent perfect absorption, also known as “anti-lasing”, can be obtained by reversing the gain in a medium with absorption that will completely annihilate the incoming beams due to the formation of a standing wave distribution inside a lossy medium [31]. This interesting effect provides a new opportunity to dynamically modulate the absorption of a lossy medium by changing the relative phase between the two counter-propagating incident waves. CPA has been investigated and demonstrated in various nanostructures [32, 33] and new materials, such as graphene [34, 35]. Moreover, CPA is also related to the new physics of parity-time (PT) symmetric photonic systems. Spatially symmetric and balanced inclusions of loss and gain in photonic structures have led to PT-symmetric devices that simultaneously behave as a coherent perfect absorber and a laser oscillator (i.e., a CPA-laser) [36, 37]. More details about PT-symmetric structures are provided in the next Sect. 3 of this chapter. However, CPA so far has been mostly realized with bulky materials exhibiting linear absorption and only a few theoretical studies have been focused on the extension of the CPA effect to nonlinear absorptive media [38–40].

In a relative context, considerable research efforts have been dedicated during the recent years to realistic metamaterials with effective ENZ permittivity response due to their peculiar transmission properties that provide, in principle, infinite phase velocity combined with enhanced and uniform field confinement distribution [12–14]. Recently, some interesting works have been proposed that connects ENZ metamaterials, even zero index metamaterials (ZIM), with CPA [42–44]. However, none of these works is focused on the nonlinear extension of the CPA effect.

In this section, we propose a nonlinear ENZ plasmonic waveguide system to realize tunable nonlinear CPA in nanoscale dimensions. We first analyze the CPA conditions in linear plasmonic waveguides. This plasmonic configuration exhibits an effective ENZ response at its cut-off frequency and FP resonances at higher frequencies [25, 26]. In the vicinity of the ENZ resonance, it is found that perfect

CPA can be achieved under the illumination of two counter-propagating plane waves with appropriate amplitudes and phases. Next, we present an ultrafast and efficient way to switch ON or OFF the CPA process by incorporating Kerr nonlinear materials inside the ENZ plasmonic waveguide. Our findings can provide a new platform to excite nonlinear gap solitons [39], and design unidirectional CPA [45], optical switches [40], and ultrasensitive optical sensors.

2.1 Linear CPA by ENZ Plasmonic Waveguides

The geometry of the proposed plasmonic waveguide unit cell has been shown before in Fig. 1 in the previous Sect. 1. It is composed of a narrow periodic rectangular slit carved in a silver screen whose material permittivity dispersion follows derived experimental data [46]. The slits are loaded with a passive dielectric material ($\delta = 0$) with the linear part of permittivity $\varepsilon = \varepsilon_r = 2.2$. This free-standing waveguide geometry was originally introduced in [24] for several nonlinear applications and can sustain ENZ and FP resonances. The slit width w is designed to tune the cut-off wavelength of the dominant quasi-TE₁₀ mode along the channel. The guided wave number β of this mode has near-zero real part, resulting in effectively infinite guided wavelength and an anomalous impedance-matching phenomenon at the nanochannel. This effect is independent of the grating's periodicity and the waveguide channel's thickness [24]. Here, the slit dimensions of the rectangular channels are chosen to have width $w = 200$ nm, height $t = 40$ nm ($t \ll w$), and thickness $l = 1$ μ m, respectively.

Now we consider the linear operation of the plasmonic waveguide channel. This linear plasmonic waveguide is illuminated by a normal incident z -polarized plane wave and the simulated transmittance and reflectance are shown in Fig. 3 as a function of the incident wavelength. Resonant optical transmission peaks occur at the waveguide's cut-off wavelength and at lower wavelengths (gray solid line in Fig. 3). At the cut-off wavelength of the dominant quasi-TE₁₀ mode ($\lambda = 1016$ nm), the plasmonic waveguide behaves as an effective ENZ medium. An anomalous impedance-matching phenomenon occurs that leads to extraordinary transmission combined with large field enhancement and uniform electric field distribution inside each slit. The field distribution at the ENZ operation is shown in the upper caption of Fig. 3b. Below the cut-off wavelength, the first and second order FP resonances are observed at $\lambda = 989$ nm and $\lambda = 926$ nm, respectively, which have typical standing wave field distributions [middle and lower captions in Fig. 3b]. The dashed line in Fig. 3a refers to the computed phase difference $\Delta\phi$ between the transmission and reflection coefficients of the system. At the ENZ and lower FP resonances, the phase offset between the transmitted and reflected waves experience an abrupt transition from almost π to $-\pi$, typical behavior of resonating effects. We will show later that either $\Delta\phi = 0$ or $\Delta\phi = \pi$ is one of the required conditions to generate the CPA effect under the illumination of two coherent counter-propagating beams.

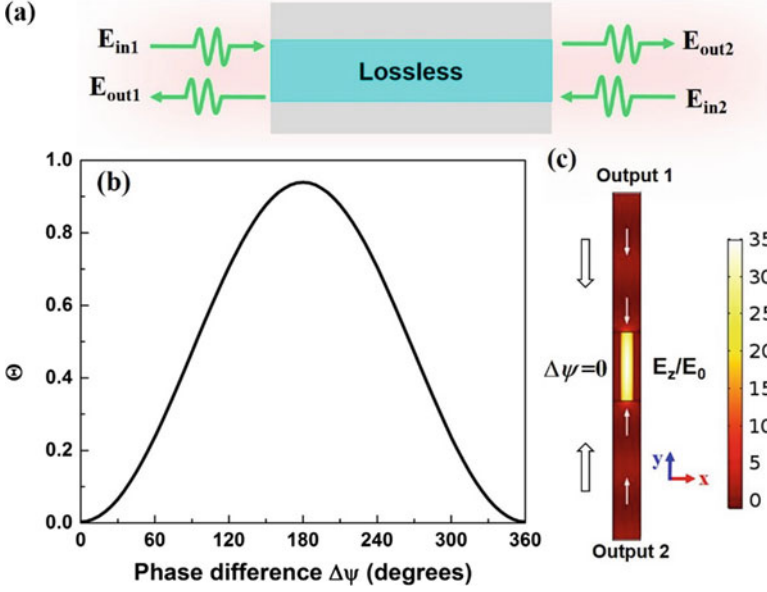


Fig. 4 (a) Plasmonic waveguide illuminated by two counter-propagating plane waves (E_{in1} , E_{in2}) from opposite sides. The two output plane waves (E_{out1} , E_{out2}) are also shown in the schematic. (b) Output coefficient Θ versus the phase difference $\Delta\psi$ of two incident waves operating very close to the ENZ wavelength. CPA occurs at $\Delta\psi = 0^\circ$ or 360° . (c) Field enhancement distribution of the real part of E_z in the channel's xy -plane at the ENZ wavelength in the case of $\Delta\psi = 0^\circ$ (CPA point). The white arrows depict the power flow direction. (Adapted with permission from Ref. [18]. © 2018 Optical Society of America)

Next, we illuminate the same nanowaveguide with two plane wave sources of equal intensity I_0 ($I_0 = |\mathbf{E}_{in1}|^2/2\eta_0 = |\mathbf{E}_{in2}|^2/2\eta_0$) launched from opposite sides, as illustrated in Fig. 4a. The transfer matrix method is used to investigate the role of interference from the two incident waves, which provides a relationship between the outgoing waves (E_{out1} , E_{out2}) and the input waves (E_{in1} , E_{in2}):

$$\begin{bmatrix} E_{out2} \\ E_{in2} \end{bmatrix} = \mathbf{M} \begin{bmatrix} E_{in1} \\ E_{out1} \end{bmatrix}, \quad (1)$$

where \mathbf{M} is the transfer matrix that has a unitary determinant for systems with time-reversal symmetry [47]. This quantity connects the fields at the output and input surfaces. The elements of the transfer matrix are related to the elements of the scattering matrix \mathbf{S} through the following relations [30]:

$$\mathbf{M} = \begin{bmatrix} M_{11} & M_{12} \\ M_{21} & M_{22} \end{bmatrix} = \begin{bmatrix} S_{21} - \frac{S_{22}S_{11}}{S_{12}} & \frac{S_{22}}{S_{12}} \\ -\frac{S_{11}}{S_{12}} & \frac{1}{S_{12}} \end{bmatrix}, \quad (2)$$

where S_{21} and S_{11} represent the transmission coefficient t and reflection coefficient r under a single normal incident plane wave, respectively. In a reciprocal and symmetric system, similar to the current case, $S_{11} = S_{22} = r$ and $S_{21} = S_{12} = t$. Perfect absorption occurs only when the outgoing waves from each side disappear, *i.e.*, $E_{out1} = E_{out2} = 0$, which means that the upper left transfer matrix element becomes $M_{11} = 0$, a relationship that can be directly derived from Eq. (1). Combining the relationship of M_{11} with the scattering matrix elements in Eq. (2), it implies that $t^2 = r^2$ [30], which is valid for reciprocal systems. Hence, in order to achieve CPA through destructive interference, the transmission and reflection coefficients not only should have equal amplitudes ($|t| = |r|$), but they must also have a particular phase difference $\Delta\phi$, which is equal to either 0 or $\pm\pi$ [30]. All these conditions are very difficult to be simultaneously satisfied in subwavelength plasmonic structures and usually large photonic structures are used instead with several wavelengths thicknesses [48]. For instance, in our design, we consider a dielectric slab with the real part of permittivity $\varepsilon = 2.2$ and very small thickness $l = 1 \mu\text{m}$. According to Eq. (7) in [30], for a given incident wavelength (around $1 \mu\text{m}$), CPA would occur only when the imaginary part of the permittivity of this ultrathin slab will reach 0.7, an extremely high dielectric loss value that does not exist in nature. Moreover, just a metallic slab will also not work to obtain CPA because it will reflect all the incident radiation from both sides.

However, the aforementioned CPA conditions can be easily fulfilled by the proposed plasmonic waveguide system that has a very small thickness ($l = 1 \mu\text{m}$) and is loaded with lossless dielectric material. As illustrated in Fig. 3a, at the wavelength point ($\lambda = 1017 \text{ nm}$), very close to the ENZ wavelength, the amplitude of the transmission is totally equal to the reflection amplitude ($|t| = |r|$) and the phase difference $\Delta\phi$ between the transmission and reflection coefficients (t and r) reaches nearly the desired value of $-\pi$. Therefore, CPA is expected to be obtained at this point when we illuminate the nanowaveguide with two coherent counter-propagating plane waves ($\mathbf{E}_{in1} = \sqrt{2\eta_0 I_0}$ and $\mathbf{E}_{in2} = \sqrt{2\eta_0 I_0} e^{i\Delta\psi}$), where $\eta_0 = 377\Omega$ is the surrounding free space impedance) that have equal intensity amplitudes I_0 and zero phase offset $\Delta\psi = 0$.

To quantitatively measure CPA, we define an output coefficient Θ as the ratio of the total outgoing light intensity to the total incoming light intensity impinging at the nanowaveguide [36, 49]: $\Theta = (|\mathbf{E}_{out1}|^2 + |\mathbf{E}_{out2}|^2) / (|\mathbf{E}_{in1}|^2 + |\mathbf{E}_{in2}|^2)$. Therefore, $\Theta = 0$ refers to CPA while $\Theta = 1$ refers to coherent perfect transmission (transparency). Figure 4b demonstrates the computed output coefficient Θ of the system as a function of the phase difference $\Delta\psi$ between the two counter-propagating incident waves (\mathbf{E}_{in1} and \mathbf{E}_{in2}). The input wavelengths of the two incident beams are fixed at $\lambda = 1017 \text{ nm}$ (the CPA point). Perfect CPA is obtained by using a phase offset $\Delta\psi$ value of either 0° or 360° . The total output power can be modulated from zero (perfect CPA) to high transmission just by changing the phase offset $\Delta\psi$ between the two incident waves. Note that the high transmission obtained close to $\Delta\psi = 180^\circ$ is counterintuitive compared to the low transmission values obtained for just one incident wave shown in Fig. 3a. Hence, the ENZ response becomes almost lossless in this case due to constructive interference and exhibits

close to unitary transmission, an effect which is surprisingly achieved by a passive lossy plasmonic system. The normalized real part of the electric field distribution (E_z , the main component) at the CPA point ($\psi = 0^\circ$) is shown in Fig. 4c, where the electric field outside of the plasmonic waveguide is nearly plus/minus unity (plane wave incidence), meaning that there are no reflections from either side and that all the incident radiation energy is completely absorbed by the proposed plasmonic waveguide (perfect CPA). This is another counterintuitive result, since the material at the core of the waveguide, where the electromagnetic energy is confined, is lossless. Note that the minimum field value used in the colorbar at Fig. 4c is -1 . The white arrows in Fig. 4c represent the total power flow direction of each counter-propagating wave and provide another clear indication of the vanishing outgoing waves.

In addition, it is interesting to note that the value of the field enhancement inside the nanochannels nearly doubles at the CPA point for the case of two incident waves, compared to the field enhancement at the ENZ resonance using only one incident wave (Fig. 3b). However, the field distribution still remains homogeneous because the CPA effect happens close to the ENZ resonance of the waveguide. The obtained large and uniform field distribution at the CPA point is advantageous in order to increase light-matter interactions. For example, it will lead to large and uniform local and non-local density of optical states inside the waveguide's nanochannel, which are ideal conditions to increase the collective coherent spontaneous emission rate of several emitters placed inside the channel leading to superradiance [17]. In this case, CPA is achieved with an extremely thin plasmonic structure (thickness $l = 1 \mu\text{m}$) and, interestingly, the area of the field enhancement is lossless while the losses are coming only from its metallic walls.

2.2 Tunable CPA by Nonlinear ENZ Plasmonic Waveguides

Now we consider the Kerr nonlinear effect in the proposed CPA ENZ plasmonic waveguide. The strong and uniform field enhancement at the CPA point can cause the plasmonic system to access the optical nonlinear regime, especially as we increase the intensity of the incident waves. Third-order nonlinear effects will make the CPA phenomenon become intensity-dependent, in addition to phase-dependent, and, as a result, tunable with ultrafast speed. The slits in Fig. 1 now are loaded with a standard nonlinear Kerr material, with relative permittivity $\varepsilon_{ch} = \varepsilon + \chi^{(3)}|\mathbf{E}_{ch}|^2$, where $\varepsilon = \varepsilon_r = 2.2$ represents the glass linear permittivity (same as the linear case), $\chi^{(3)} = 4.4 \times 10^{-20} \text{ m}^2/\text{V}^2$ is its third-order nonlinear susceptibility [50], and $|\mathbf{E}_{ch}|$ is the magnitude of local electric field in the nanochannel. The local electric field \mathbf{E}_{ch} at the ENZ CPA point will be very strong and homogeneous (Fig. 4c) and the Kerr nonlinear effect is expected to be enhanced and triggered by relative low input intensities. This will directly lead to a shift in the frequency where CPA is obtained. Slow thermal nonlinear effects are not expected to affect the performance of the proposed nonlinear CPA device because it will be excited by relative low input

intensities that will lead to low induced temperatures in the plasmonic structure [51].

Again, we illuminate the waveguide with two z -polarized plane waves (Fig. 4a) at the ENZ CPA point ($\lambda = 1017$ nm) and compute the output coefficient Θ now versus the input intensity I_0 of each beam. For a fixed input intensity I_0 , the phase difference $\Delta\psi$ of the two incident beams is set to vary from 0 to 2π . We record the maximum (coherent perfect transmission) and minimum (CPA) values of Θ in Fig. 5a. The CPA effect is always present [minimum $\Theta \sim 0$] as we gradually increase the input intensity I_0 before reaching to a threshold value of 30 MW/cm². Above this threshold low input intensity, the minimum Θ gradually approaches maximum Θ values ~ 1 , which directly indicates that the nonlinear CPA effect disappears just by increasing the illuminating input intensities. Interestingly, an absorption dip in the value of Θ down to 0.0017 is observed at $I_0 = 3.16$ MW/cm², attributed to the nearly perfect satisfaction of the CPA conditions at this point. It can be seen in Fig. 5b that for $I_0 = 0.01$ MW/cm² (solid line) the CPA is obtained at $\Delta\psi = 0^\circ$ and 360° [similar to the linear operation in Fig. 4b], while at a larger input intensity $I_0 = 1000$ MW/cm², the output coefficient becomes almost phase-insensitive [dashed line in Fig. 5b]. This can be explained by the fact that the third-order Kerr nonlinearity leads to a gradual change in the nonlinear permittivity of the dielectric medium and the system does not satisfy the aforementioned CPA conditions anymore. This effect is similar to nonlinear saturable absorption [22] but it works for waves illuminating the nonlinear structure from both sides and can lead to perfect transparency with relative low input intensities and in nanoscale dimensions. It can be used to achieve passive Q-switching for the envisioned compact nanolasers based on plasmonic structures [52–54]. It can also be utilized to design amplitude modulators for efficient all-optical routing of the electromagnetic radiation in nanoscale dimensions and to build adaptive optical filters. Such strong

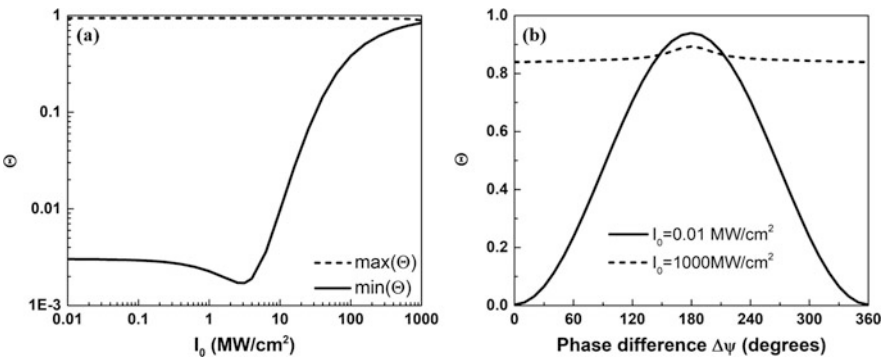
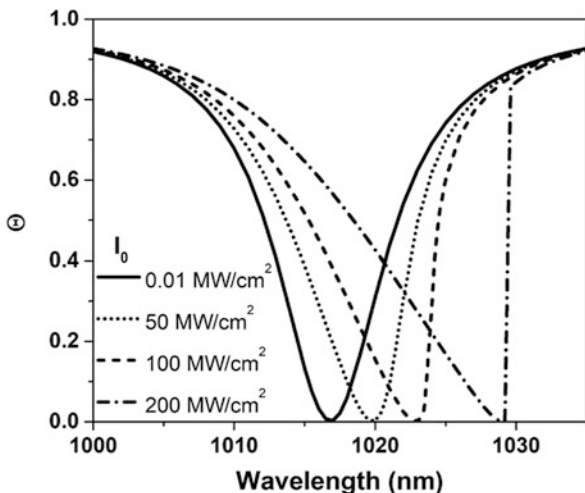


Fig. 5 (a) Nonlinear variation of the maximum and minimum values of the output coefficient Θ versus the input intensity I_0 for two incident counter-propagating waves operating very close to the ENZ wavelength. (b) The output coefficient Θ versus the phase difference $\Delta\psi$ for low 0.01 MW/cm² and high 1000 MW/cm² input intensity values. (Adapted with permission from Ref. [18]. © 2018 Optical Society of America)

Fig. 6 Output coefficient Θ versus the incident wavelength for four different input intensities: $I_0 = 0.01, 50, 100,$ and 200 MW/cm^2 . The phase difference $\Delta\psi$ is set equal to zero leading to CPA at the ENZ point. (Adapted with permission from Ref. [18], © 2018 Optical Society of America)



nonlinear tunable CPA response, achieved with relative low input intensities, is a unique feature of the proposed ENZ plasmonic structure. Note that regular elongated photonic CPA configurations will not be able to achieve this strong nonlinear response under such low input intensities due to the poor field confinement and enhancement inside their geometries.

Finally, we plot in Fig. 6 the nonlinear output coefficient Θ versus the incident wavelength around the ENZ resonance for four different input intensities. The phase difference $\Delta\psi$ of the two incident beams is now fixed and equal to zero, corresponding to perfect CPA. As we increase the input intensity I_0 from 0.01 MW/cm^2 to 200 MW/cm^2 , the CPA effect always exists close to the ENZ resonance and the absorption dip (perfect CPA point) is gradually shifted to larger wavelengths and becomes tunable. Finally, it is interesting to note that the abrupt transition of Θ obtained for 200 MW/cm^2 is a clear indication of optical bistable response [24].

3 Exceptional Points and Spectral Singularities by Active ENZ Plasmonic Waveguides

Exceptional points (EPs) are branch point singularities of the spectrum found in open non-Hermitian (lossy and/or active) Hamiltonian systems that correspond to the coalescence of both eigenvalues and eigenvectors [55]. They have been observed in parity-time (PT) symmetric non-Hermitian photonic systems and have led to several counterintuitive phenomena including unidirectional light propagation [56–59], loss-induced lasing [60], topological energy transfer [61], and asymmetric mode switching [62]. Not limited to PT-symmetric structures, EPs have also been

detected in other open non-Hermitian systems without gain (passive), such as metallic gratings [63], photonic crystal slabs [64], asymmetric plasmonic nanostructures [65, 66], lossy metamaterials [67], and graphene [68]. All these interesting systems exhibit some form of geometrical or material asymmetry in order to break parity reversal symmetry and achieve the EP response. A unique characteristic of EPs is that the reflection of the system becomes zero from different directions, which provides a strong indication of potential EP formation in the pursuit of their detection. Besides EPs, another class of irregular spectral points obtained only in active systems is the so-called spectral singularities that correspond to a lack of completeness of the system's eigenfunctions in a continuous spectrum [69]. They lead to distinct spectral degeneracies where the reflection and transmission of the system tend to infinity and have extremely narrow resonant bandwidth [70]. This interesting feature can be used for potential applications relevant to super scattering [71, 72], coherent perfect absorption and lasing [36, 37, 49], and saturable nonlinearity [73]. Note that the majority of the previous related works are focused on asymmetric nanoscale structures and the realization of EPs in symmetric plasmonic configurations have not been presented so far.

In parallel with the aforementioned research efforts, some interesting works have recently been proposed [44, 74–77] that connected active ENZ metamaterials, even ZIM, with PT-symmetry in order to realize the formation of EPs and spectral singularities or other degeneracies. However, the permittivity of the loss material in these systems needs to be equal to the conjugate of the permittivity of the gain medium to obtain efficient PT-symmetric effects, such as the EP formation. Note that, in the case of plasmonic nanoscale systems, it is very difficult to find optical active (gain) media with a positive imaginary part of permittivity equal to the usually large, especially for metals, optical losses associated to the negative imaginary part of the loss material permittivity [78]. Fortunately, the response of plasmonic waveguides operating near their cut-off frequency exhibiting effective ENZ response is accompanied by a uniform and strong field enhancement inside their nanochannels, where the gain material is located. This unique property is expected to trigger EPs and other PT-symmetric effects with minimum gain values, since the enhanced electromagnetic mode is evenly spread throughout the entire gain dielectric medium leading to a strong interaction with it. Hence, arrays of ENZ waveguides are anticipated to bring the formation of EPs and spectral singularities in symmetric plasmonic nanoscale systems one step closer to their practical implementation.

In this section, we propose a realistic design of a non-Hermitian nanophotonic system based on an array of ENZ waveguides loaded with active dielectric materials with low gain values with the goal to obtain PT-symmetric effects with spatially symmetric nanostructures. In the previous sections, it was demonstrated that this plasmonic configuration exhibits an effective ENZ response at its cut-off frequency and FP resonances at higher frequencies [22, 24, 41]. In this section, we study the effect of low gain in this system, which is induced by realistic active materials loaded inside the spatially symmetric plasmonic nanoslits. Our aim is to completely compensate the loss of the proposed plasmonic ENZ configuration and achieve

more complicated optical effects derived by PT-symmetry. Towards these goals, we numerically demonstrate and analytically prove the existence of an EP spectral degeneracy at the ENZ resonance that leads to reflectionless transparency combined with total loss compensation at the ENZ frequency point. In addition, a spectral singularity with super scattering (lasing) response is obtained by the same compact ENZ nanoscale system when active materials with slightly larger gain coefficients are introduced inside the nanochannels. The proposed active optical ENZ system has several additional unique features. For example, it is demonstrated that it can be used to dynamically modulate the output ENZ power from phase-controlled amplification to unidirectional absorption when the waveguide is illuminated by two counter-propagating plane waves. Finally, the proposed active ENZ configuration is also found to drastically boost several relative weak optical nonlinear effects, such as optical bistability and all-optical switching [79, 80]. It is interesting that all these effects are achieved by a purely symmetric plasmonic configuration that does not break parity reversal symmetry. Our findings provide a new platform to design lossless ENZ metamaterials, low threshold nanolasers, and unidirectional coherent perfect absorbers [45].

3.1 Numerical Modeling of Active ENZ Waveguides

The geometry of the unit cell of the proposed plasmonic non-Hermitian nanophotonic system is the same as the structure illustrated in Fig. 1. It is composed of an array of narrow periodic rectangular slits but loaded now with an active dielectric material carved in a silver screen. The loss is introduced in the proposed non-Hermitian system by the silver screen, in addition to the inherent radiation losses of the system. The silver permittivity dispersion values used in our simulations are taken by previously derived experimental data [46]. In this design, the slits are loaded with an active dielectric material exhibiting gain with a relative permittivity at steady-state equal to $\varepsilon = \varepsilon_r + i\delta$, where the real part is equal to $\varepsilon_r = 2.2$ and the imaginary part corresponds to the gain coefficient that, for now, is set to be an arbitrary variable with constant value δ . This is a valid approximation to model active materials with low gain coefficient values at the steady-state condition when equilibrium is reached [81, 82]. In addition, always an $\exp(i2\pi ft)$ time convention is assumed in the current simulations. The slit dimensions are chosen to have width $w = 200\text{nm}$, height $t = 40\text{nm}$ ($t \ll w$), and thickness $l = 500\text{nm}$, respectively, and the grating period is selected to be equal to $a = b = 400\text{nm}$. As it was explained in the previous Sect. 1, this free-standing waveguide geometry can sustain an ENZ resonance at the cut-off wavelength of its dominant quasi-TE₁₀ mode [24]. It has been proven that extraordinary optical transmission can occur at the ENZ wavelength combined with large field enhancement and uniform phase distribution inside the nanoslits [17]. This is due to an anomalous impedance matching phenomenon that depends only on the interface properties, i.e., on the

aperture to period ratio of the array, and is therefore independent to the grating's periodicity and each waveguide channel thickness.

The active plasmonic waveguide system is illuminated by a z -polarized plane wave. The contour plots of transmittance and reflectance as a function of the incident wavelength and small values of the active dielectric permittivity imaginary part δ are computed and shown in Fig. 7a, b, respectively. The wavelength in these plots varies very close to the ENZ cut-off frequency point of the system that was found to be approximately equal to $\lambda = 1011\text{nm}$ in the case of passive slits ($\delta = 0$). Interestingly, reflectionless ENZ response is observed for a very low gain value of $\delta = 0.011$ at $\lambda = 1011\text{ nm}$ [point A in Fig. 7b]. This is clearly shown in Fig. 8, where the computed transmittance and reflectance of both passive ($\delta = 0$) and active ($\delta = 0.011$) systems are plotted. In the absence of gain ($\delta = 0$ /black lines), resonant optical transmission occurs at two different frequency points: the ENZ cut-off wavelength ($\lambda = 1011\text{ nm}$) and the FP resonance $\lambda = 922\text{nm}$. The transmittances have relatively small values ($T \sim 0.5$) for these two wavelength points and cannot reach unity due to strong ohmic losses coming from the metallic (silver) walls of the waveguides. However, when an active dielectric material with small gain coefficient equal to $\delta = 0.011$ is included in the waveguide channels (gray lines in Fig. 8), perfect transmittance and zero reflectance are obtained at the ENZ wavelength point. This response offers a clear indication of an EP formation

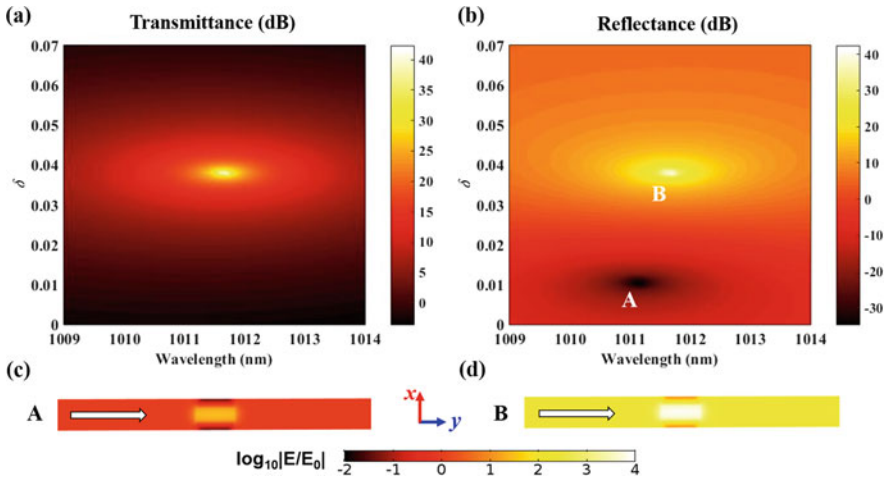


Fig. 7 (a) Transmittance and (b) reflectance as a function of the incident wavelength and the small imaginary part δ (gain) of the active dielectric material permittivity loaded in the waveguides. Reflectionless loss-compensated ENZ behavior is obtained at the exceptional point A. The super scattering (lasing) ENZ mode is obtained at the spectral singularity point B. Amplitude of the electric field enhancement distribution in the channel's xy -plane operating at (c) the reflectionless loss-compensated ENZ point A and (d) the super scattering (lasing) ENZ point B. The white arrows depict the incident wave direction. (Adapted with permission from Ref. [19]. © 2019 American Physical Society)

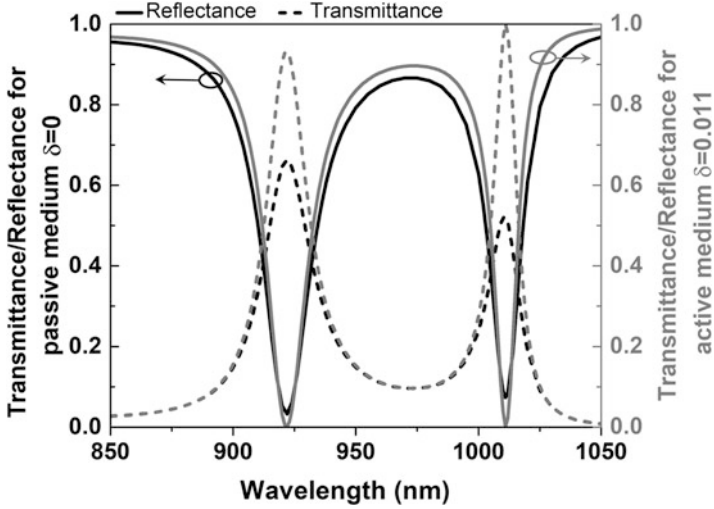


Fig. 8 Computed transmittance and reflectance of the plasmonic waveguide as a function of the incident wavelength with (gray) and without (black) gain. An active dielectric material permittivity with imaginary part $\delta = 0.011$ is used to obtain the reflectionless loss-compensated ENZ response shown by the exceptional point A in Fig. 7b. (Adapted with permission from Ref. [19]. © 2019 American Physical Society)

which is now obtained by a purely symmetric active nanoplasmonic structure. The proposed system is completely different than the usually used asymmetric active photonic microscale structures exhibiting PT-symmetry [57].

The corresponding amplitude of the electric field enhancement distribution at the reflectionless ENZ wavelength point A is shown in Fig. 7c along a cross-section of the waveguide unit cell. The fields inside the waveguide, plotted in Fig. 7c, are homogeneous and enhanced, a distinct characteristic of ENZ response. In this case, the transmitted field (right side of waveguide) has almost the same field values as the incident field (left side of waveguide), which means that there is no reflection and all the incident energy is perfectly transmitted through the matched nanochannel. We will prove in the next Sect. 3.2 that, indeed, an EP is formed at this wavelength (point A) where perfect loss-compensated ENZ response is achieved that is not affected by the losses of the plasmonic waveguide. The loss and gain parameters of the resistive metallic waveguides and the active dielectric material are perfectly balanced at this ENZ EP. Note that in the proposed open non-Hermitian system the radiation loss also needs to be included in the total loss of the system, in addition to the loss stemming from the plasmonic material. The presented perfect loss-compensated ENZ response can be used to further improve the enhancement of quantum effects, such as superradiance [17], and boost optical nonlinearities [24] by skipping the usual loss limitations of plasmonic systems. The EP response at the ENZ wavelength is relative similar to the unidirectional reflectionless transparency obtained before for larger microscale (not nanoscale) PT-symmetric photonic systems [57, 83].

However, in the currently proposed design the zero-reflection response is obtained from both sides due to the symmetric structure of the proposed active plasmonic waveguide system. In addition, and even more importantly, in the proposed unique ENZ configuration we obtain this effect by using a subwavelength active plasmonic configuration with an extremely thin thickness of just $l = 500$ nm.

Next, we further increase the imaginary part of the gain material permittivity loaded in the nanochannels. When a gain value of $\delta = 0.038$ is reached, the response of the proposed open non-Hermitian plasmonic system is totally different compared to the lower gain EP response presented before and is transformed to a spectral singularity [71]. A super scattering (lasing) response is observed at the spectral singularity point B ($\delta = 0.038$, $\lambda = 1011.7$ nm) in Fig. 7b, obtained in the vicinity of the passive system's ENZ resonance. Giant and narrow transmittance and reflectance are simultaneously achieved by the proposed active plasmonic system at point B, which are ideal conditions for nanolasing and sensor applications. The corresponding fields inside the active waveguides also diverge and the surrounding fields are enhanced by many orders of magnitude. The calculated normalized electric field enhancement distribution in this case is depicted in Fig. 7d. It is expected that the inherent nonlinear response of the gain material used in the proposed active system will eventually saturate the spectral singularity [73].

The gain loaded inside the nanochannels has a constant non-dispersive value and our next step will be to consider a more practical gain material model. To this end, we include the realistic frequency dispersion in the gain material that follows Kramers-Kronig relations [50]. Hence, the dielectric properties of the active medium are modeled with the Lorentz dispersion model with relative permittivity: $\varepsilon = \varepsilon_\infty + \frac{\varepsilon_{Lorentz}\omega_0^2}{(\omega_0^2 - 2i\omega\delta_0 - \omega^2)}$, where $\varepsilon_\infty = 2.175$, $\varepsilon_{Lorentz} = 0.06325$, $\omega_0 = 4.2 \times 10^{15}$ rad/s, $\delta_0 = 5.0 \times 10^5$ rad/s and $\omega = 2\pi f$ [45, 84]. Realistic gain materials that exhibit these dispersion values are dyes (for example Rhodamine) doped in dielectric materials [85, 86]. The corresponding active material dispersion curves around the operating wavelength are plotted in Fig. 9a. The real permittivity in this case is equal to $\varepsilon_r \approx 2.2$ and the imaginary part (gain) is approximately $\delta \approx 0.038$, which are ideal values to achieve the spectral singularity effect that was mentioned in the previous paragraph. The computed transmittance and reflectance of the active system loaded with the presented realistic gain material are plotted in Fig. 9b, where the black lines refer to the plasmonic channels loaded with a passive dielectric material ($\delta = 0$, also shown in Fig. 8), while the gray lines represent the channels loaded with the realistic active material characterized by the aforementioned Lorentzian dispersion model. As already mentioned, in the absence of the gain medium (black lines), resonant optical transmission occurs at the ENZ cut-off wavelength ($\lambda = 1011$ nm) and the FP resonance $\lambda = 922$ nm. The maximum transmission is accompanied by minimum reflection at these wavelengths points that consist a typical resonance behavior.

In the passive case, the summation of transmittance T and reflectance R is always less than one ($T + R < 1$), since the presented array of passive waveguides is a lossy system and part of the incident energy is absorbed by the ohmic losses

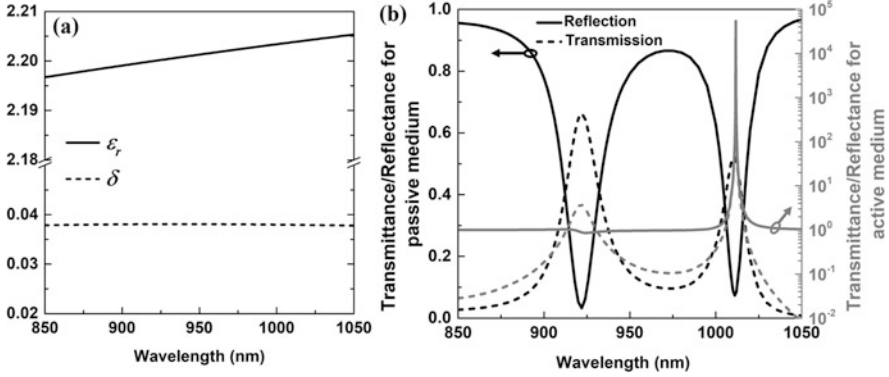


Fig. 9 (a) The Lorentz permittivity model of the dispersive realistic active (gain) dielectric material. (b) Transmittance and reflectance of the plasmonic waveguides as a function of the incident wavelength with (gray) and without (black) gain. The permittivity of the active material in this case follows the Lorentz model shown in (a). (Adapted with permission from Ref. [19]. © 2019 American Physical Society)

of the waveguides' metallic walls. However, this situation changes dramatically when the realistic active dielectric material with Lorentzian dispersion is included in the waveguide channel. An ultrasharp spectral singularity with giant and narrow transmittance and reflectance is obtained, interestingly, only at the ENZ resonance [gray lines in Fig. 9b] and not at the FP resonance. This response is similar to the one obtained in point B of Fig. 7 for the constant (not dispersive) gain coefficient. Hence, super scattering and lasing with a very small practical gain coefficient is achieved only at the ENZ resonance frequency point. This is in stark contrast to the FP resonance response $\lambda = 922$ nm of the same active system loaded with the same gain coefficient material, also shown by the gray lines in Fig. 9b, where there is no super scattering mainly due to the inhomogeneous and relative weak fields inside the plasmonic nanochannels.

3.2 Theoretical Analysis of Active ENZ Waveguides

The simulation results presented in the previous section provide a clear indication of EP formation and super scattering (lasing) response. The presented reflectionless transparency caused by the EP and the obtained divergent super scattering properties are further analyzed and scrutinized by using a transmission-line analytical model. This simple theoretical model can provide additional physical insights to the currently proposed active plasmonic system and can accurately verify the previously presented simulation results. The unit cell of the ENZ plasmonic waveguides section is described by a transmission line segment with length l , wavenumber β_{wg} , and characteristic impedance Z_{wg} . It is schematically depicted in Fig. 10a and is

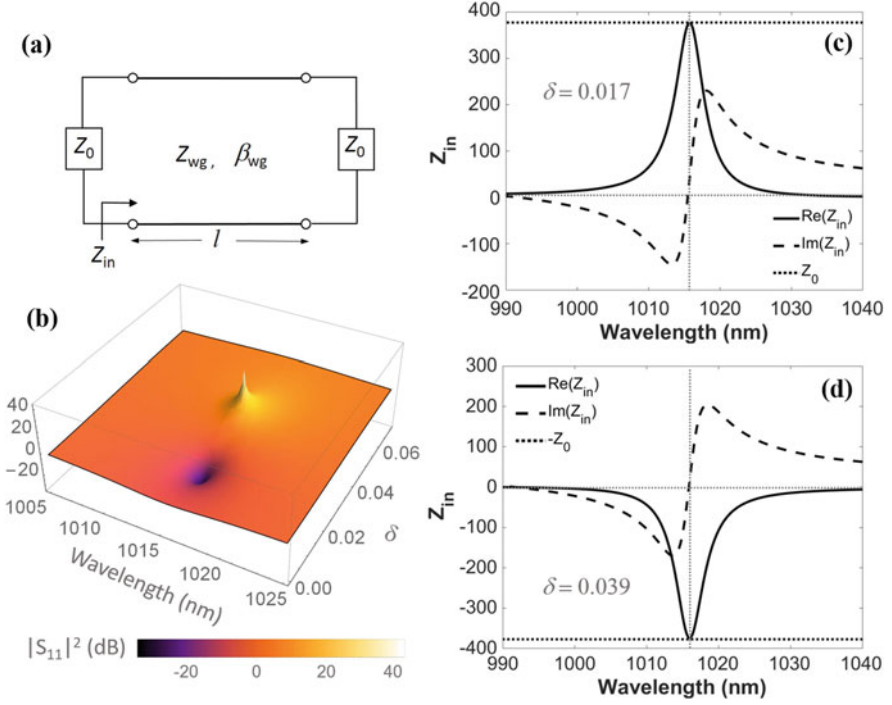


Fig. 10 (a) Transmission-line theoretical model of an active plasmonic waveguide Z_{wg} terminated by two loads with impedances Z_0 due to the surrounding free space. (b) Analytically computed 3D distribution of the amplitude of the scattering parameter $|S_{11}|^2$ (reflectance) versus the incident wavelength and gain coefficient δ . (c) The real and imaginary part of the input impedance Z_{in} versus the incident wavelength for a fixed gain coefficient $\delta = 0.017$. The condition of the reflectionless loss-compensated ENZ response given by Eq. (9) is perfectly satisfied at the exceptional point (vertical gray dotted line). (d) The real and imaginary part of the input impedance Z_{in} versus the incident wavelength for a fixed gain coefficient equal to $\delta = 0.039$. The condition of the super scattering ENZ response given by Eq. (10) is perfectly satisfied at the spectral singularity point (vertical gray dotted line). (Adapted with permission from Ref. [19]. © 2019 American Physical Society)

surrounded by free space with a constant impedance equal to $Z_0 = 377\Omega$. The guided wavenumber β_{wg} of the ENZ mode, which supports a dominant quasi- TE_{10} mode at the proposed plasmonic system, is calculated by solving the dispersion equation:

$$\tan\left(\sqrt{\beta_{pp}^2 - \beta_{wg}^2} \frac{w}{2}\right) = \frac{\sqrt{\beta_{wg}^2 - k_{Ag}^2}}{\sqrt{\beta_{pp}^2 - \beta_{wg}^2}}, \quad (3)$$

where $k_{Ag} = k_0\sqrt{\varepsilon_{Ag}}$ is the wavenumber of silver with relative Drude permittivity dispersion $\varepsilon_{Ag} = \varepsilon_\infty - \frac{f_p^2}{f(f-i\gamma)}$, $f_p = 2175\text{THz}$, $\gamma = 4.35\text{THz}$, $\varepsilon_\infty = 5$ [46], k_0 is the free space wavenumber, and β_{pp} is the guided wavenumber in an equivalent parallel-plate waveguide with the same height t but infinite width w that can be computed by the following dispersion formula [87]:

$$\tanh\left(\sqrt{\beta_{pp}^2 - \varepsilon k_0^2} \frac{t}{2}\right) = -\frac{\varepsilon}{\varepsilon_{Ag}} \frac{\sqrt{\beta_{pp}^2 - k_{Ag}^2}}{\sqrt{\beta_{pp}^2 - \varepsilon k_0^2}}, \quad (4)$$

where $\varepsilon = \varepsilon_r + i\delta$ is the relative permittivity of the active dielectric material loaded inside the nanochannels. Thus, the characteristic impedance of the dominant quasi-TE mode inside the plasmonic waveguide operating at the ENZ wavelength is defined as [28]:

$$Z_{wg} = \frac{\mu_0\omega}{\beta_{wg}}, \quad (5)$$

where $\omega = 2\pi f$ is the radial frequency. The effective permittivity of the active ENZ waveguide system can also be derived, in the limit $\varepsilon_{Ag} \rightarrow -\infty$ (assuming perfectly conducting metal) and $\beta_{pp} = k_0\sqrt{\varepsilon_r}$, to be equal to [24]: $\varepsilon_{eff} = \varepsilon_r - \frac{\pi^2}{k_0^2 w^2} + i\delta$. The real part of this formula will become equal to zero at the ENZ resonance for a waveguide width equal to $w = \pi/(\sqrt{\varepsilon_r}k_0)$, which is the classic cut-off condition of rectangular waveguides operating at microwave frequencies.

The proposed plasmonic configuration is a two-port network. In this case, we can use the guided wavenumber β_{wg} and characteristic impedance Z_{wg} to construct the 2×2 ABCD matrix that relates the total electric and magnetic fields at the output and input ports of this system. This matrix is written as [88]:

$$\begin{bmatrix} A & B \\ C & D \end{bmatrix} = \begin{bmatrix} \cos(\beta_{wg}l) & iZ_{wg} \sin(\beta_{wg}l) \\ iZ_{wg}^{-1} \sin(\beta_{wg}l) & \cos(\beta_{wg}l) \end{bmatrix}. \quad (6)$$

By computing the ABCD parameters, we can calculate all the elements of the scattering matrix \mathbf{S} that directly correspond to the reflection (S_{11}, S_{22}) and transmission (S_{21}, S_{12}) coefficients seen from both directions of the system [88]:

$$\begin{aligned} S_{11} &= \frac{A+B/Z_0-CZ_0-D}{\Delta}, \\ S_{12} &= \frac{2(AD-BC)}{\Delta}, \\ S_{21} &= \frac{2}{\Delta}, \\ S_{22} &= \frac{-A+B/Z_0-CZ_0+D}{\Delta}, \end{aligned} \quad (7)$$

where $\Delta = A + \frac{B}{Z_0 + CZ_0 + D}$ and $Z_0 = 377\Omega$ is the surrounding free space impedance. The currently system is symmetric and reciprocal leading to $S_{11} = S_{22}$ and $S_{21} = S_{12}$.

Based on the aforementioned transmission-line method, we analytically compute the three-dimensional (3D) distribution of the reflectance $|S_{11}|^2$ versus the incident wavelength and gain coefficient δ in the vicinity of the ENZ resonance. The results are demonstrated in Fig. 10b, where two interesting points with very high (divergent) and low (approximately zero) reflectance values are observed in the vicinity of the ENZ resonance depending on the value of the gain parameter δ . The analytical results are consistent with the previously demonstrated simulation results shown in Fig. 7b and prove that the presented transmission line model can accurately predict the performance of the proposed active ENZ nanophotonic system.

To gain even more physical insights, we further analyze the impedance matching conditions where the reflectionless ENZ and super scattering frequency points occur. The free space surrounding the plasmonic waveguide is represented by two parallel lumped impedance elements Z_0 connected to the transmission line segment of the waveguide, as it can be seen in Fig. 10a. The input impedance Z_{in} seen looking towards the back load Z_0 of the plasmonic waveguide system at a distance l from this load is given by [88]:

$$Z_{in} = Z_{wg} \frac{Z_0 + iZ_{wg} \tan(\beta_{wg}l)}{Z_{wg} + iZ_0 \tan(\beta_{wg}l)} \quad (8)$$

The reflection coefficient of the entire plasmonic ENZ system is analytically calculated by $r = (Z_{in} - Z_0)/(Z_{in} + Z_0)$, due to the front load Z_0 . The transmission coefficient of the same configuration is equal to $t = 2Z_{in}/(Z_{in} + Z_0)$ [88]. In order to obtain perfect transmission and reflectionless responses ($r = 0$ and $t = 1$) at the ENZ EP, the real part $[\text{Re}(Z_{in})]$ and imaginary part $[\text{Im}(Z_{in})]$ of the system's input impedance have to satisfy the following perfect impedance matching relationships:

$$\begin{aligned} \text{Re}(Z_{in}) &= Z_0, \\ \text{Im}(Z_{in}) &= 0, \end{aligned} \quad (9)$$

because $Z_0 = 377\Omega$ always takes real values. We plot in Fig. 10c the real and imaginary part of the input impedance Z_{in} versus the incident wavelength for a fixed gain coefficient equal to $\delta = 0.017$. It is interesting that exactly at the ENZ resonance ($\lambda = 1016$ nm), the input impedance Z_{in} perfectly satisfies the conditions given by Eq. (9). The presented impedance matching process results in perfect ENZ transmission combined with reflectionless ENZ propagation, as it was clearly demonstrated in Fig. 10b.

Similarly, in order to achieve simultaneously diverging reflection and transmission coefficients (super scattering), the denominators of r and t need to become equal

to zero. Therefore, the real and imaginary part of the system's input impedance should satisfy the following lasing conditions:

$$\begin{aligned} \operatorname{Re}(Z_{in}) &= -Z_0, \\ \operatorname{Im}(Z_{in}) &= 0. \end{aligned} \quad (10)$$

These interesting conditions are also verified by plotting the real and imaginary part of the input impedance, now for a higher gain coefficient $\delta = 0.039$, with results depicted in Fig. 10d. Note that the results obtained by the proposed analytical transmission line method are very close to the previously presented in Sect. 3.1 simulation results. Some minor discrepancies are expected and are mainly due to the numerical and analytical approximations that are inevitable made during the simulations and theory, respectively.

Next, we compute the eigenvalues and eigenvectors of the proposed plasmonic ENZ system to unambiguously prove that the presented reflectionless perfect ENZ transmission happens, indeed, at an EP. Towards this goal, we introduce the transfer matrix \mathbf{M} formalism, which provides a direct relationship between the outgoing and input waves of the system. The eigenvalues of the transfer matrix \mathbf{M} of the proposed plasmonic ENZ structure are computed by [71]:

$$\eta_{1,2} = \frac{M_{11} + M_{22}}{2} \pm \sqrt{\left(\frac{M_{11} + M_{22}}{2}\right)^2 - 1}, \quad (11)$$

where the transfer matrix components M_{11} and M_{22} are calculated by using the transfer and scattering matrix elements relationship which has been shown in Eq. (2). Equation (2) is derived if we assume that the determinant of the transfer matrix is unitary $\det(\mathbf{M}) = 1$ and the condition $M_{12} = -M_{21}$ is satisfied, which are valid relationships for reciprocal and symmetric systems, similar to the current case [71]. Hence, the product of the two eigenvalues of the system always needs to satisfy the relation $|\eta_1 \eta_2| = 1$, meaning that either each eigenvalue is unimodular or the eigenvalues form pairs with reciprocal moduli [37]. In contrast to the orthogonal eigenvectors of a Hermitian system, the eigenvectors of a non-Hermitian Hamiltonian system are biorthogonal given by the relation [71]:

$$\langle \varphi_1^l | \varphi_2^r \rangle = \langle \varphi_2^l | \varphi_1^r \rangle = 0, \quad (12)$$

where the left $\varphi_{1,2}^l$ and right $\varphi_{1,2}^r$ eigenvectors of the transfer matrix \mathbf{M} are computed by the following formulas:

$$\begin{aligned} \langle \varphi_{1,2}^l | &= \left(\frac{\eta_{1,2} - M_{22}}{M_{12}} \quad 1 \right), \\ | \varphi_{1,2}^r \rangle &= \begin{pmatrix} \frac{\eta_{1,2} - M_{22}}{M_{21}} \\ 1 \end{pmatrix}. \end{aligned} \quad (13)$$

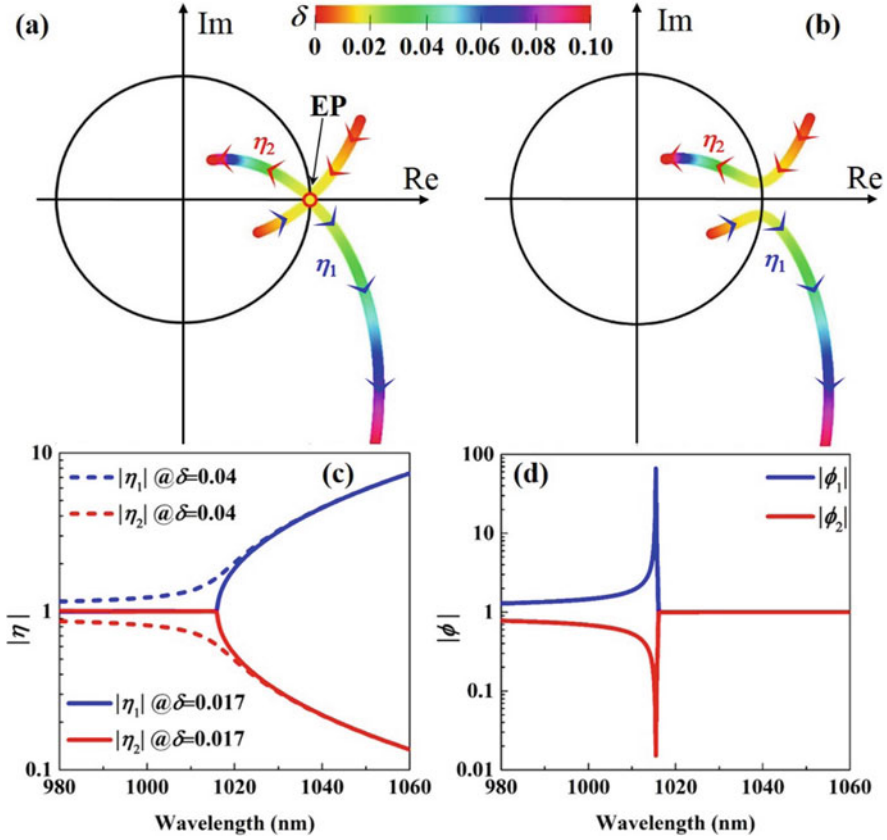


Fig. 11 (a–b) Evolution of the two complex eigenvalues η_1 and η_2 as a function of the gain coefficient δ at (a) the ENZ cut-off wavelength ($\lambda = 1016$ nm) and (b) slightly off the ENZ resonance wavelength ($\lambda = 1015.8$ nm). The two eigenvalues coalesce to form an EP degeneracy only at the ENZ cut-off wavelength which can be clearly seen in caption (a). (c) Absolute values of the two eigenvalues versus the wavelength for two different gain coefficients equal to $\delta = 0.017$ (solid lines) and $\delta = 0.04$ (dashed lines). (d) Absolute values of the two eigenvectors versus the wavelength for a fixed gain equal to $\delta = 0.017$. A clear bifurcation point is observed for both eigenvalues [caption (c)] and eigenvectors [caption (d)] for the gain value $\delta = 0.017$. This bifurcation point coincides with the ENZ wavelength, which is a clear indication of an EP spectral degeneracy formation. (Adapted with permission from Ref. [19]. © 2019 American Physical Society)

We present in Fig. 11a, b the evolution of the eigenvalues computed by Eq. (11) in the complex domain as a function of the gain coefficient δ at the ENZ resonance ($\lambda = 1016$ nm) and slightly off the ENZ wavelength ($\lambda = 1015.8$ nm), respectively. Interestingly, a clear EP degeneracy is observed for $\delta = 0.017$ at the ENZ cut-off resonance wavelength ($\lambda = 1016$ nm) (Fig. 11a), which is manifested by the collapse of the two eigenvalues into one along the unit circle only for this particular

gain coefficient value. On the contrary, the two eigenvalues are always separated and there is no EP formation at a wavelength slightly off the ENZ resonance (Fig. 11b).

We also compute and present in Fig. 11c the absolute values of the two eigenvalues, calculated again by using Eq. (11), as a function of the incident wavelength for two different gain coefficients: $\delta = 0.017$ (solid lines) and $\delta = 0.04$ (dashed lines). In the case of $\delta = 0.017$, a clear bifurcation point is observed at the ENZ resonance ($\lambda = 1016$ nm). The observed bifurcation point again coincides with the ENZ wavelength which is another clear indication of an EP formation. When the wavelength is smaller than the ENZ resonance, the computed eigenvalues are unimodular, implying that there is no net amplification nor dissipation. However, when the wavelength is larger than the resonance, the eigenvalues have reciprocal moduli, with one magnitude greater than one and the other less than one, corresponding to states of amplification and dissipation, respectively [71]. In between and exactly at the ENZ resonance wavelength, there is a clear bifurcation point that is equivalent to an EP formed only on the ENZ response of this particular ENZ system. On the contrary, in the case of higher gain $\delta = 0.04$, the computed eigenvalues are not unimodular and the EP degeneracy does not exist anymore.

The associated eigenvectors, computed by using Eq. (13), also coalesce at the ENZ resonance for a very small gain coefficient of $\delta = 0.017$, which is another unambiguous indication of an EP, and the results are shown in Fig. 11d. Therefore, the ohmic losses induced by the metallic waveguides in addition to the radiation losses of the proposed open non-Hermitian Hamiltonian system are completely compensated by the active dielectric material leading to the formation of an EP degeneracy, which, interestingly, is obtained by a purely symmetric nanoscale plasmonic configuration. The formation of the corresponding EP results in a totally lossless (or loss-compensated) ENZ response leading to the reflectionless transparency behavior shown in Fig. 10b. Both eigenvalues and associated eigenvectors coalesce at the presented bifurcation point that is analytically proven to be certainly an EP with intriguing properties [71].

In addition, the other interesting spectral degeneracy point shown in Fig. 10b exhibits divergent reflectance values and satisfies the condition $M_{22} = 0$ at the ENZ wavelength for slightly larger gain values $\delta = 0.039$. This is a necessary condition in order to obtain a spectral singularity leading to the calculation of a gain threshold value that will cause lasing operation [49, 70]. However, we have computed that $M_{11} \neq 0$ at the same ENZ wavelength, indicating that the anti-lasing (also known as coherent perfect absorption) condition cannot be satisfied at the same frequency point if we excite the plasmonic structure with two counter propagating beams [49]. Therefore, as the gain coefficient δ is increased from 0.017 to 0.039, the proposed open non-Hermitian active plasmonic system is transformed into a system where gain dominates its response; the transitional point (EP) is transformed to a spectral singularity, which is manifested as a super scattering (or lasing) response of the system. Interestingly, the transmission and reflection of the system decrease again to low values in the case of further gain increase above the lasing threshold (not shown here), a different response compared to typical lasing system configurations.

3.3 Applications of Active ENZ Plasmonic Waveguides

In this section, we use the proposed active ENZ plasmonic system to investigate some interesting applications stemming from its unique properties, including unidirectional absorption and the enhancement of third-order optical nonlinear effects. The same active plasmonic waveguides system, which exhibits super scattering spectral degeneracy and is characterized by the previously presented Lorentzian model (Fig. 9a), is illuminated by two counter-propagating plane waves with equal intensities I_0 and arbitrary phase difference $\Delta\psi = \psi_2 - \psi_1$, as illustrated in Fig. 12a. The computed phase dependent output power in port 1 (Output 1) and port 2 (Output 2) as a function of the phase difference $\Delta\psi$ is demonstrated in Fig. 12b when the incident wavelengths of the two beams are fixed slightly off the ENZ resonance ($\lambda = 1009$ nm). Interestingly, almost perfect directional absorption is obtained only from one side of the waveguide (either Output 1 or 2), surprisingly

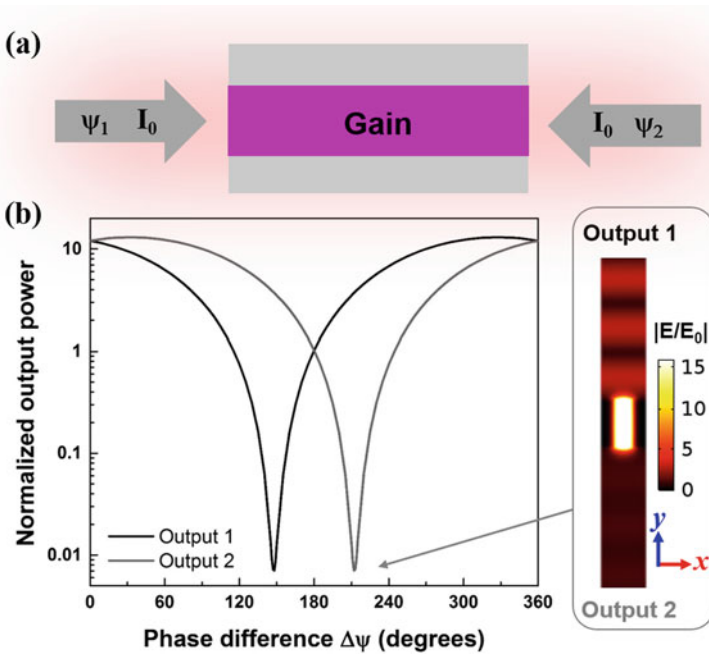


Fig. 12 (a) Active ENZ plasmonic waveguide illuminated by two counter-propagating plane waves. The phase difference of the two waves is $\Delta\psi = \psi_2 - \psi_1$. (b) Normalized output power computed at both sides of the active plasmonic system versus the phase difference $\Delta\psi$ plotted slightly off the ENZ resonance wavelength ($\lambda = 1009$ nm). The right inset caption demonstrates the amplitude of the normalized electric field distribution when $\Delta\psi = 212^\circ$. It can be clearly seen that the wave propagates only towards the output 1 in this case. (Adapted with permission from Ref. [19]. © 2019 American Physical Society)

by a perfectly symmetric structure, when a phase offset $\Delta\psi$ equal to either 148° or 212° is used.

The output power from both sides is modulated from amplification (super scattering) to perfect directional absorption just by carefully tuning the phase offsets between the two counter-propagating waves. It is noteworthy that the strong modulation between high to almost zero transmission happens with a purely reciprocal symmetric system with nanoscale subwavelength dimensions. The computed normalized electric field distribution at one of the directional absorption phase difference conditions ($\Delta\psi = 212^\circ$) is shown in the inset of Fig. 12b, where it can be seen that the power is mainly scattered unidirectional to the output port 1 and the transmission is almost zero at output port 2. Note that the field distribution inside the nanochannel is homogeneous and strong because we operate very close to the ENZ resonance. Such an efficient control of the radiation direction, achieved in subwavelength scale, is unprecedented. It is envisioned to have several all-optical switching and routing applications in integrated nanophotonic components and nanocircuits. Finally, we would like to stress that the currently proposed plasmonic system cannot work as a coherent perfect absorber under the illumination of two counter-propagating waves and can only work as a laser [49, 70]. The complex transmission and reflection coefficients t and r do not have equal amplitudes ($|t| \neq |r|$), even at the ENZ super scattering point shown in Fig. 9b, and the phase difference between transmission and reflection coefficients cannot be made equal to either 0 or $\pm\pi$ [18, 30]. These critical conditions are absolutely needed in order to achieve coherent perfect absorption, as it was explained in the previous Sect. 2, and cannot be realized with the currently proposed active ENZ plasmonic system.

The strong and uniform fields inside the waveguide channels at the ENZ EP (shown in Fig. 7c) are expected to naturally cause the proposed plasmonic system to access the optical nonlinear regime as the intensity values of the input illumination are increased. The triggered boosted third-order nonlinearity will make the system become intensity-dependent and bistable. Due to this reason, we study the third-order Kerr optical nonlinear effect in the active plasmonic waveguide system illuminated now by only one plane wave incident from one side. In this case, the slits in Fig. 1 are loaded with a Kerr nonlinear material with relative permittivity $\varepsilon_{ch} = \varepsilon + \chi^{(3)}|\mathbf{E}_{ch}|^2$, where $\varepsilon = 2.2 + 0.011i$ represents the active dielectric material with a gain coefficient $\delta = 0.011$ corresponding to the response demonstrated by point A in Fig. 7b, $\chi^{(3)} = 4.4 \times 10^{-20} \text{ m}^2/\text{V}^2$ is a typical third-order nonlinear dielectric material susceptibility [50], and \mathbf{E}_{ch} is the local electric field induced inside the nanochannels.

We illuminate the waveguides with a z-polarized plane wave (similar to Fig. 1) and compute the transmittance versus the wavelength for a fixed input intensity $I_0 = 1500 \text{ MW}/\text{cm}^2$. The result is shown in Fig. 13a, where we also present in the same figure the linear operation (dashed line) to better illustrate the effect of nonlinearity to the proposed ENZ system. In the case of linear operation, perfect reflectionless transmission is obtained at the ENZ EP ($\lambda = 1011 \text{ nm}$), similar to point A in Fig. 7b. In the nonlinear case (solid lines), a strong optical bistability or broad hysteresis appears which exhibits two stable transmission branches. The

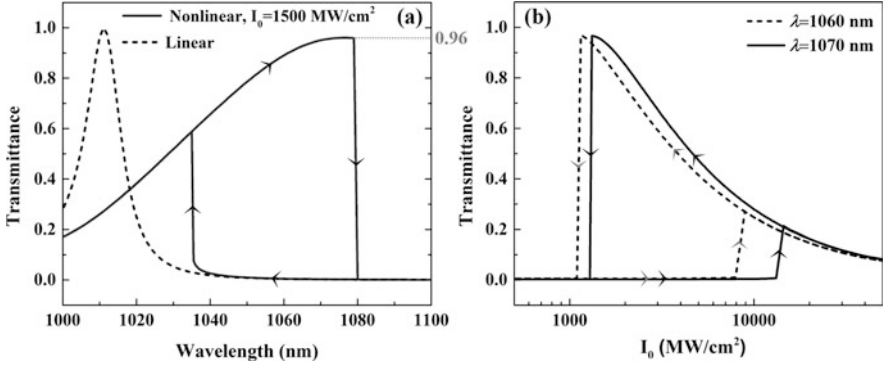


Fig. 13 Third-order optical nonlinear material introduced in the nanochannels of the active plasmonic waveguides. (a) Computed transmittance versus wavelength for both linear (dashed line) and nonlinear (solid line) operation when high input intensity $I_0 = 1500 \text{ MW/cm}^2$ is applied. (b) Bistable transmission versus the input intensity I_0 computed for two different wavelengths both of them with slightly larger values compared to the ENZ EP wavelength. (Adapted with permission from Ref. [19]. © 2019 American Physical Society)

peak of the upper transmission branch reaches very close to one values (total transmission) and, at the same time, the corresponding lower transmission branch reaches zero values. Perfect transmission (ON state) or total reflection (zero transmission-OFF state) is achieved with the same nonlinear structure just by increasing or decreasing the incident radiation's wavelength (shown by the arrows in Fig. 13). This interesting property consists the epitome of all-optical nonlinear switching behavior. Figure 13b demonstrates the variation in the transmission versus the input intensity I_0 for two different incident radiation wavelengths, both chosen to be slightly larger than the ENZ EP wavelength. Two broad nonlinear transmission hysteresis loops exist under relative low threshold input intensities (approximately 1000 MW/cm^2) and the peak transmission in both cases is almost one (total transmission). Hence, the proposed optical nonlinear active ENZ plasmonic design is an ideal platform to be used for tunable all-optical switching applications [24, 89, 90]. Note that the combination of nonlinearities and non-Hermitian Hamiltonian systems has been demonstrated before mainly with microscale bulk photonic structures, especially for nonlinear PT-symmetric photonic systems [91], but these interesting effects have not been presented yet with subwavelength nonlinear plasmonic systems.

Finally, it is interesting to mention that the proposed active ENZ plasmonic system is able to slow down the incident light at the ENZ EP, where the group velocity nearly vanishes [92]. The group velocity is defined as $v_g = (d\beta_{wg}/d\omega)^{-1}$, where the guided wavenumber β_{wg} at the ENZ wavelength of the proposed array of plasmonic waveguides is calculated by using Eq.(3). In the usual case of lossy ENZ plasmonic waveguides ($\delta = 0$), slow group velocity values of $v_g = c/7$ have been reported before close to the ENZ wavelength [26]. However, in the alternative current example of an active ENZ plasmonic waveguide with gain coefficient

$\delta = 0.017$, the group velocity becomes much smaller and reaches to $v_g = c/570$ (stopped light regime) at the ENZ EP degeneracy, where c is the velocity of light in free space. We have also considered the case of complex frequency excitation in the proposed active plasmonic devices leading to purely real wave numbers with very low values, which can retain their slow group velocity even in the presence of losses [93, 94]. Such slow group velocities at the ENZ EP may inspire new applications in temporal soliton excitation and in the design of slow light devices.

4 Conclusions

The goal of the research work presented in this chapter is to propose a new practical plasmonic metamaterial that promises to maximize coherence in various optical effects. It can serve as a novel platform to trigger, harness, and enhance coherent light-matter interactions at the nanoscale. To fulfill this goal, specialized ENZ plasmonic waveguides have been presented, which can efficiently control the intensity and phase of electromagnetic radiation, and engineer some of the coherent optical features of light. The proposed plasmonic screens are practical and can be fabricated by embedding them in a dielectric material that can serve as superstrate and substrate.

When we illuminate the passive waveguide with two counter-propagating waves, the CPA effect was found to exist around the ENZ cut-off wavelength leading to double field enhancement inside the nanochannels in comparison to the single incident wave case. The strong and uniform field enhancement at the ENZ-CPA point can cause the plasmonic system to access the optical nonlinear regime exhibiting boosted third-order optical nonlinear effects at the nanoscale. As a result, the phase-dependent CPA effect also becomes intensity-dependent and tunable with ultrafast speed due to the third-order nonlinear susceptibility of the dielectric nanochannels.

Finally, we explored the formation of an EP in a similar nanophotonic system consisting of an array of periodic nanowaveguides loaded now with a very low gain coefficient material. Reflectionless transmission (perfect loss compensation) and ultraslow group velocity values at the nanoscale were realized at the EP, which coincides with the ENZ cut-off frequency of the proposed plasmonic system. This special spectral degeneracy (EP) point was a unique feature of the presented nanoscale symmetric plasmonic active ENZ configuration, different from most of the previous works that were mainly focused on asymmetric bulky micron-scale active photonic configurations.

Acknowledgments This work was partially supported by the National Science Foundation (DMR-1709612) and the Nebraska Materials Research Science and Engineering Center (MRSEC) (grant no. DMR-1420645). Ying Li is supported by the National Natural Science Foundation of China (Grant No. 12104233). Christos Argyropoulos is partially supported by the National Science

Foundation/EPSCoR RII Track-1: Emergent Quantum Materials and Technologies (EQUATE) under Grant No. OIA-2044049.

References

1. Zayats, A. V., Smolyaninov, I. I., & Maradudin, A. A. (2005). Nano-optics of surface plasmon polaritons. *Physics Reports*, *408*, 131–314.
2. Gramotnev, D. K., & Bozhevolnyi, S. I. (2010). Plasmonics beyond the diffraction limit. *Nature Photonics*, *4*, 83–91.
3. Schuller, J. A., Barnard, E. S., Cai, W., Jun, Y. C., White, J. S., & Brongersma, M. L. (2010). Plasmonics for extreme light concentration and manipulation. *Nature Materials*, *9*, 193–204.
4. Meinzer, N., Barnes, W. L., & Hooper, I. R. (2014). Plasmonic meta-atoms and metasurfaces. *Nature Photonics*, *8*, 889–898.
5. Yao, K., & Liu, Y. (2014). Plasmonic metamaterials. *Nanotechnology Reviews*, *3*, 177–210.
6. Maier, S. A. (2007). *Plasmonics: Fundamentals and applications* (p. 250). Springer US.
7. Jiang, Y., Lu, W. B., Xu, H. J., Dong, Z. G., & Cui, T. J. (2012). A planar electromagnetic “black hole” based on graphene. *Physics Letters A*, *376*, 1468–1471.
8. Yin, L., Vlasko-Vlasov, V. K., Pearson, J., Hiller, J. M., Hua, J., Welp, U., Brown, D. E., & Kimball, C. W. (2005). Subwavelength focusing and guiding of surface plasmons. *Nano Letters*, *5*, 1399–1402.
9. Argyropoulos, C., Chen, P.-Y., Monticone, F., D’Aguanno, G., & Alù, A. (2012). Nonlinear plasmonic cloaks to realize giant all-optical scattering switching. *Physical Review Letters*, *108*, 263905.
10. Monticone, F., Argyropoulos, C., & Alù, A. (2012). Layered plasmonic cloaks to tailor the optical scattering at the nanoscale. *Scientific Reports*, *2*, 912.
11. Catchpole, K. R., & Polman, A. (2008). Plasmonic solar cells. *Optics Express*, *16*, 21793.
12. Le Ru, E. C., & Etchegoin, P. G. (2009). *Principles of surface-enhanced Raman spectroscopy*. Elsevier.
13. Engheta, N. (2013). Pursuing near-zero response. *Science*, *340*, 286–287.
14. Liberal, I., & Engheta, N. (2017). Near-zero refractive index photonics. *Nature Photonics*, *11*, 149–158.
15. Niu, X., Hu, X., Chu, S., & Gong, Q. (2018). Epsilon-near-zero photonics: A new platform for integrated devices. *Advanced Optical Materials*, *6*, 1701292.
16. Reshef, O., De Leon, I., Alam, M. Z., & Boyd, R. W. (2019). Nonlinear optical effects in epsilon-near-zero media. *Nature Reviews Materials*, *4*, 535–551.
17. Li, Y., & Argyropoulos, C. (2016). Controlling collective spontaneous emission with plasmonic waveguides. *Optics Express*, *24*, 26696.
18. Li, Y., & Argyropoulos, C. (2018). Tunable nonlinear coherent perfect absorption with epsilon-near-zero plasmonic waveguides. *Optics Letters*, *43*, 1806.
19. Li, Y., & Argyropoulos, C. (2019). Exceptional points and spectral singularities in active epsilon-near-zero plasmonic waveguides. *Physical Review B*, *99*, 075413.
20. Li, Y., Nemilentsau, A., & Argyropoulos, C. (2019). Resonance energy transfer and quantum entanglement mediated by epsilon-near-zero and other plasmonic waveguide systems. *Nanoscale*, *11*, 14635–14647.
21. Jin, B., & Argyropoulos, C. (2019). Nonreciprocal transmission in nonlinear PT-symmetric metamaterials using epsilon-near-zero media doped with defects. *Advanced Optical Materials*, *7*, 1901083.
22. Alù, A., & Engheta, N. (2008). Light squeezing through arbitrarily shaped plasmonic channels and sharp bends. *Physical Review B*, *78*, 035440.
23. Fleury, R., & Alù, A. (2013). Enhanced superradiance in epsilon-near-zero plasmonic channels. *Physical Review B*, *87*, 201101.

24. Argyropoulos, C., Chen, P.-Y., D'Aguanno, G., Engheta, N., & Alù, A. (2012). Boosting optical nonlinearities in ϵ -near-zero plasmonic channels. *Physical Review B*, *85*, 045129.
25. Argyropoulos, C., D'Aguanno, G., & Alù, A. (2014). Giant second-harmonic generation efficiency and ideal phase matching with a double ϵ -near-zero cross-slit metamaterial. *Physical Review B*, *89*, 235401.
26. Argyropoulos, C., Chen, P.-Y., D'Aguanno, G., & Alù, A. (2014). Temporal soliton excitation in an ϵ -near-zero plasmonic metamaterial. *Optics Letters*, *39*, 5566.
27. Silveirinha, M., & Engheta, N. (2006). Tunneling of electromagnetic energy through subwavelength channels and bends using ϵ -near-zero materials. *Physical Review Letters*, *97*, 157403.
28. Alù, A., Silveirinha, M. G., & Engheta, N. (2008). Transmission-line analysis of ϵ -near-zero-filled narrow channels. *Physical Review E*, *78*, 016604.
29. Gordon, R., & Brolo, A. G. (2005). Increased cut-off wavelength for a subwavelength hole in a real metal. *Optics Express*, *13*, 1933.
30. Chong, Y. D., Ge, L., Cao, H., & Stone, A. D. (2010). Coherent perfect absorbers: Time-reversed lasers. *Physical Review Letters*, *105*, 053901.
31. Baranov, D. G., Krasnok, A., Shegai, T., Alù, A., & Chong, Y. (2017). Coherent perfect absorbers: Linear control of light with light. *Nature Reviews Materials*, *2*, 17064.
32. Pirruccio, G., Ramezani, M., Rodriguez, S. R.-K., & Rivas, J. G. (2016). Coherent control of the optical absorption in a plasmonic lattice coupled to a luminescent layer. *Physical Review Letters*, *116*, 103002.
33. Wu, J.-H., Artoni, M., & La Rocca, G. C. (2016). Coherent perfect absorption in one-sided reflectionless media. *Scientific Reports*, *6*, 35356.
34. Zhang, J., Guo, C., Liu, K., Zhu, Z., Ye, W., Yuan, X., & Qin, S. (2014). Coherent perfect absorption and transparency in a nanostructured graphene film. *Optics Express*, *22*, 12524.
35. Fan, Y., Liu, Z., Zhang, F., Zhao, Q., Wei, Z., Fu, Q., Li, J., Gu, C., & Li, H. (2015). Tunable mid-infrared coherent perfect absorption in a graphene meta-surface. *Scientific Reports*, *5*, 13956.
36. Longhi, S. (2010). PT-symmetric laser absorber. *Physical Review A*, *82*, 031801.
37. Chong, Y. D., Ge, L., & Stone, A. D. (2011). PT-symmetry breaking and laser-absorber modes in optical scattering systems. *Physical Review Letters*, *106*, 093902.
38. Nireekshan Reddy, K., & Dutta Gupta, S. (2013). Light-controlled perfect absorption of light. *Optics Letters*, *38*, 5252.
39. Nireekshan Reddy, K., & Dutta Gupta, S. (2014). Gap solitons with null-scattering. *Optics Letters*, *39*, 2254.
40. Agarwal, G. S., Di, K., Wang, L., & Zhu, Y. (2016). Perfect photon absorption in the nonlinear regime of cavity quantum electrodynamics. *Physical Review A*, *93*, 1–6.
41. Alù, A., & Engheta, N. (2011). Emission enhancement in a plasmonic waveguide at cut-off. *Materials (Basel)*, *4*, 141–152.
42. Feng, S., & Halterman, K. (2012). Coherent perfect absorption in epsilon-near-zero metamaterials. *Physical Review B*, *86*, 165103.
43. Kim, T. Y., Badsha, M. A., Yoon, J., Lee, S. Y., Jun, Y. C., & Hwangbo, C. K. (2016). General strategy for broadband coherent perfect absorption and multi-wavelength all-optical switching based on epsilon-near-zero multilayer films. *Scientific Reports*, *6*, 22941.
44. Bai, P., Ding, K., Wang, G., Luo, J., Zhang, Z., Chan, C. T., Wu, Y., & Lai, Y. (2016). Simultaneous realization of a coherent perfect absorber and laser by zero-index media with both gain and loss. *Physical Review A*, *94*, 063841.
45. Baum, B., Alaeian, H., & Dionne, J. (2015). A parity-time symmetric coherent plasmonic absorber-amplifier. *Journal of Applied Physics*, *117*, 063106.
46. Johnson, P. B., & Christy, R. W. (1972). Optical constants of the Noble metals. *Physical Review B*, *6*, 4370–4379.
47. Markoš, P., & Soukoulis, C. M. (2008). *Wave propagation. From electrons to photonic crystals and left-handed materials* (Vol. 50, Student ed.). Princeton University Press.
48. Wan, W., Chong, Y., Ge, L., Noh, H., Stone, D., & Cao, H. (2011). Time-reversed lasing and interferometric control of absorption. *Science (80-.)*, *331*, 889–892.

49. Wong, Z. J., Xu, Y.-L., Kim, J., O'Brien, K., Wang, Y., Feng, L., & Zhang, X. (2016). Lasing and anti-lasing in a single cavity. *Nature Photonics*, *10*, 796–801.
50. Boyd, R. W. (2008). *Nonlinear optics* (3rd ed.). Academic.
51. Argyropoulos, C., & Li, Y. (2018). Epsilon-near-zero plasmonic waveguides to enhance nonlinear coherent light-matter interactions. In G. S. Subramania & S. Foteinopoulou (Eds.), *Active photonic platforms X* (Vol. 1072106, p. 5). SPIE.
52. Noginov, M. A., Zhu, G., Belgrave, A. M., Bakker, R., Shalae, V. M., Narimanov, E. E., Stout, S., Herz, E., Suteewong, T., & Wiesner, U. (2009). Demonstration of a spaser-based nanolaser. *Nature*, *460*, 1110–1112.
53. Oulton, R. F., Sorger, V. J., Zentgraf, T., Ma, R.-M., Gladden, C., Dai, L., Bartal, G., & Zhang, X. (2009). Plasmon lasers at deep subwavelength scale. *Nature*, *461*, 629–632.
54. Khajavikhan, M., Simic, A., Katz, M., Lee, J. H., Slutsky, B., Mizrahi, A., Lomakin, V., & Fainman, Y. (2012). Thresholdless nanoscale coaxial lasers. *Nature*, *482*, 204–207.
55. Heiss, W. D. (2012). The physics of exceptional points. *Journal of Physics A: Mathematical and Theoretical*, *45*, 444016.
56. Regensburger, A., Bersch, C., Miri, M.-A., Onishchukov, G., Christodoulides, D. N., & Peschel, U. (2012). Parity–time synthetic photonic lattices. *Nature*, *488*, 167–171.
57. Feng, L., Xu, Y.-L., Fegadolli, W. S., Lu, M.-H., Oliveira, J. E. B., Almeida, V. R., Chen, Y.-F., & Scherer, A. (2012). Experimental demonstration of a unidirectional reflectionless parity-time metamaterial at optical frequencies. *Nature Materials*, *12*, 108–113.
58. Yin, X., & Zhang, X. (2013). Unidirectional light propagation at exceptional points. *Nature Materials*, *12*, 175–177.
59. Wang, W., Wang, L.-Q., Xue, R.-D., Chen, H.-L., Guo, R.-P., Liu, Y., & Chen, J. (2017). Unidirectional excitation of radiative-loss-free surface plasmon polaritons in PT -symmetric systems. *Physical Review Letters*, *119*, 077401.
60. Peng, B., Özdemir, Ş. K., Rotter, S., Yilmaz, H., Liertzer, M., Monifi, F., Bender, C. M., Nori, F., & Yang, L. (2014). Loss-induced suppression and revival of lasing. *Science*, *346*, 328–332.
61. Xu, H., Mason, D., Jiang, L., & Harris, J. G. E. (2016). Topological energy transfer in an optomechanical system with exceptional points. *Nature*, *537*, 80–83.
62. Doppler, J., Mailybaev, A. A., Böhm, J., Kuhl, U., Girschick, A., Libisch, F., Milburn, T. J., Rabl, P., Moiseyev, N., & Rotter, S. (2016). Dynamically encircling an exceptional point for asymmetric mode switching. *Nature*, *537*, 76–79.
63. Cui, H.-X., Cao, X.-W., Kang, M., Li, T.-F., Yang, M., Guo, T.-J., Guo, Q.-H., & Chen, J. (2013). Exceptional points in extraordinary optical transmission through dual subwavelength metallic gratings. *Optics Express*, *21*, 13368–13379.
64. Zhen, B., Hsu, C. W., Igarashi, Y., Lu, L., Kaminer, I., Pick, A., Chua, S.-L., Joannopoulos, J. D., & Soljačić, M. (2015). Spawning rings of exceptional points out of Dirac cones. *Nature*, *525*, 354–358.
65. Kodigala, A., Lepetit, T., & Kanté, B. (2016). Exceptional points in three-dimensional plasmonic nanostructures. *Physical Review B*, *94*, 201103.
66. Park, J.-H., Ndao, A., Cai, W., Hsu, L., Kodigala, A., Lepetit, T., Lo, Y.-H., & Kanté, B. (2020). Symmetry-breaking-induced plasmonic exceptional points and nanoscale sensing. *Nature Physics*, *16*, 462–468.
67. Kang, M., Zhu, W., Wang, H.-T., & Premaratne, M. (2017). Spawning a ring of exceptional points from a metamaterial. *Optics Express*, *25*, 18265.
68. Liu, Q., Wang, B., Ke, S., Long, H., Wang, K., & Lu, P. (2017). Exceptional points in Fano-resonant graphene metamaterials. *Optics Express*, *25*, 7203.
69. Ramezani, H., Li, H.-K., Wang, Y., & Zhang, X. (2014). Unidirectional spectral singularities. *Physical Review Letters*, *113*, 263905.
70. Mostafazadeh, A. (2009). Spectral singularities of complex scattering potentials and infinite reflection and transmission coefficients at real energies. *Physical Review Letters*, *102*, 220402.
71. Feng, S. (2016). Loss-induced super scattering and gain-induced absorption. *Optics Express*, *24*, 1291.

72. Zhang, W., Wu, T., & Zhang, X. (2017). Tailoring eigenmodes at spectral singularities in graphene-based PT systems. *Scientific Reports*, 7, 11407.
73. Liu, X., Gupta, S. D., & Agarwal, G. S. (2014). Regularization of the spectral singularity in PT-symmetric systems by all-order nonlinearities: Nonreciprocity and optical isolation. *Physical Review A*, 89, 013824.
74. Savoia, S., Castaldi, G., Galdi, V., Alù, A., & Engheta, N. (2014). Tunneling of obliquely incident waves through PT-symmetric epsilon-near-zero bilayers. *Physical Review B*, 89, 085105.
75. Savoia, S., Castaldi, G., Galdi, V., Alù, A., & Engheta, N. (2015). PT-symmetry-induced wave confinement and guiding in ϵ -near-zero metamaterials. *Physical Review B*, 91, 115114.
76. Fu, Y., Xu, Y., & Chen, H. (2016). Zero index metamaterials with PT symmetry in a waveguide system. *Optics Express*, 24, 1648.
77. Fu, Y., Zhang, X., Xu, Y., & Chen, H. (2017). Design of zero index metamaterials with PT symmetry using epsilon-near-zero media with defects. *Journal of Applied Physics*, 121, 094503.
78. Čtyroký, J., Kuzmiak, V., & Eyderman, S. (2010). Waveguide structures with antisymmetric gain/loss profile. *Optics Express*, 18, 21585.
79. Ramezani, H., Kottos, T., El-Ganainy, R., & Christodoulides, D. N. (2010). Unidirectional nonlinear PT-symmetric optical structures. *Physical Review A*, 82, 043803.
80. Bender, N., Factor, S., Bodyfelt, J. D., Ramezani, H., Christodoulides, D. N., Ellis, F. M., & Kottos, T. (2013). Observation of asymmetric transport in structures with active nonlinearities. *Physical Review Letters*, 110, 234101.
81. Fleury, R., Sounas, D. L., & Alù, A. (2014). Negative refraction and planar focusing based on parity-time symmetric metasurfaces. *Physical Review Letters*, 113, 023903.
82. Veltri, A., Chipouline, A., & Aradian, A. (2016). Multipolar, time-dynamical model for the loss compensation and lasing of a spherical plasmonic nanoparticle spaser immersed in an active gain medium. *Scientific Reports*, 6, 33018.
83. Lin, Z., Ramezani, H., Eichelkraut, T., Kottos, T., Cao, H., & Christodoulides, D. N. (2011). Unidirectional invisibility induced by PT-symmetric periodic structures. *Physical Review Letters*, 106, 213901.
84. Fang, A., Huang, Z., Koschny, T., & Soukoulis, C. M. (2011). Overcoming the losses of a split ring resonator array with gain. *Optics Express*, 19, 12688.
85. Campione, S., Albani, M., & Capolino, F. (2011). Complex modes and near-zero permittivity in 3D arrays of plasmonic nanoshells: Loss compensation using gain [Invited]. *Optical Materials Express*, 1, 1077.
86. Sun, L., Yang, X., & Gao, J. (2013). Loss-compensated broadband epsilon-near-zero metamaterials with gain media. *Applied Physics Letters*, 103, 201109.
87. Alù, A., & Engheta, N. (2006). Optical nanotransmission lines: Synthesis of planar left-handed metamaterials in the infrared and visible regimes. *Journal of the Optical Society of America B: Optical Physics*, 23, 571.
88. Pozar, D. M. (2011). *Microwave engineering* (4th ed.). Wiley.
89. Argyropoulos, C., Ciraci, C., & Smith, D. R. (2014). Enhanced optical bistability with film-coupled plasmonic nanocubes. *Applied Physics Letters*, 104, 063108.
90. Huang, Z., Baron, A., Larouche, S., Argyropoulos, C., & Smith, D. R. (2015). Optical bistability with film-coupled metasurfaces. *Optics Letters*, 40, 5638.
91. Konotop, V. V., Yang, J., & Zezyulin, D. A. (2016). Nonlinear waves in PT-symmetric systems. *Reviews of Modern Physics*, 88, 035002.
92. Goldzak, T., Mailybaev, A. A., & Moiseyev, N. (2018). Light stops at exceptional points. *Physical Review Letters*, 120, 013901.
93. Tsakmakidis, K. L., Pickering, T. W., Hamm, J. M., Page, A. F., & Hess, O. (2014). Completely stopped and dispersionless light in plasmonic waveguides. *Physical Review Letters*, 112, 167401.
94. Tsakmakidis, K. L., Hess, O., Boyd, R. W., & Zhang, X. (2017). Ultraslow waves on the nanoscale. *Science*, 358, eaan5196.

Topological Insulator Plasmonics and Enhanced Light-Matter Interactions



Hua Lu, Dikun Li, Yangwu Li, Zengji Yue, and Jianlin Zhao

Abstract Topological insulators with Dirac conducting surface state and insulating bulk state offer a promising platform for plasmonics with a broad operating frequency range from ultraviolet (UV) to terahertz (THz). Topological insulator plasmonics (TIPs) has become a quickly developing branch of plasmonics since the terahertz (THz) Dirac plasmons was observed from Bi_2Te_3 topological insulator microribbons in 2013. This chapter mainly introduces plasmonic effects generated in three-dimensional (3D) topological insulator materials as well as their application potentials in light-matter interactions. The effects mainly contain Dirac plasmons, surface plasmon resonances (SPRs), localized plasmon resonances (LPRs), and magnetic plasmon resonances (MPRs) occurring in structured topological insulators. TIPs with the field confinement and enhancement acts as a promising platform for reinforced light-matter interactions. Here, we also discuss the recently reported applications of TIPs, especially in refractive index monitoring, photoluminescent emission, and light harvesting. These results will not only help us to understand plasmonic behaviors and characters of topological insulators, but also provide guidance for exploring their applications in light control and functional devices.

Keywords Topological insulators · Surface plasmons · Light-matter interactions

H. Lu (✉) · D. Li · Y. Li · J. Zhao (✉)

MOE Key Laboratory of Material Physics and Chemistry under Extraordinary Conditions, Key Laboratory of Light-Field Manipulation and Information Acquisition, Ministry of Industry and Information Technology, and Shaanxi Key Laboratory of Optical Information Technology, School of Physical Science and Technology, Northwestern Polytechnical University, Xi'an, China
e-mail: hualu@nwpu.edu.cn; jlzhao@nwpu.edu.cn

Z. Yue

Institute for Superconducting & Electronic Materials and ARC Centre of Excellence in Future Low-Energy Electronics, University of Wollongong, North Wollongong, NSW, Australia

1 Introduction

Surface plasmons (SPs) are electromagnetic waves coupled to collective electron oscillations on the metal surface, presenting the high light confinement, strong near-field enhancement, and beyond the traditional diffraction limit of light [1–4]. SPs generated in metallic micro/nanoscale structures enable the realization of novel optical physics and devices. For example, extraordinary optical transmission can be observed in the metallic gratings/arrays with the generation of SPs [1, 3]. The metallic nanoparticles can support localized plasmon resonances (LPRs) [5]. The coupling between metallic nanoparticles enables the formation of plasmon-induced transparency (PIT) and Fano resonances [6–8]. The plasmonic slow light and rainbow trapping effects were observed in the graded metallic gratings [9, 10]. The magnetic resonances were found in the metallic nanoparticle-film structures [11]. The subwavelength light confinement of SPs makes the metallic waveguides a promising platform for miniaturization and integration of optical devices [12, 13]. Metasurfaces composed of nanoscale metallic elements with flexible control of light polarization and phase were used for the vector beam generation [14]. These plasmonic effects also contribute to the realization of optical devices, for instance logical gates [15], multiplexers [16, 17], filters [18, 19], and perfect absorbers [20]. Particularly, the plasmonic electric field with several orders of magnitude enhancement is beneficial for boosting light-matter interactions. The plasmonic enhancement results in the realization of high-sensitive sensors [5, 8, 21], nanoscale lasers [22, 23], ultrafast optical switches [24, 25], high-responsivity photodetectors [26], highly efficient nonlinear optical conversion [27], and improved light harvesting and emission [28, 29]. Even so, metal-based plasmonics faces some drawbacks and difficult challenges in practical devices and integration, such as the large intrinsic ohmic loss at optical frequencies, chemical instability in the environments, incompatibility with standard silicon manufacturing processes, and poor tunability [30].

The alternative materials have attracted great attentions for broadening actual applications of SPs. For example, the semiconductors with a heavy doping can increase free carriers to make the materials produce negative real permittivity at the frequencies of interest [31]. However, the complicated doping has the challenge of efficient introduction of dopants into semiconductors for a high carrier concentration [30]. Transparent conducting oxides (e.g. indium tin oxide) with the heavy doping present metal-like characteristics in the near-infrared region [32]. Graphene with two-dimensional (2D) massless Dirac electrons has been demonstrated to exhibit pronounced plasmonic response [34–37]. Graphene plasmonics (GPs) gradually draws broad attentions for nanoscale light control and integrated devices [34–37]. This is attributed to the advantages of graphene, such as the high charge carrier mobility, electric tunability, and compatibility with standard semiconductor technology [34, 35, 38, 39]. Even so, the operating frequency of GPs is limited to the mid-infrared (MIR) and THz regions [33–37]. To achieve plasmonic response in the near-infrared (NIR), graphene should be heavily doped for a large Fermi level

[40]. The doping operation inevitably hinders the actual applications of graphene in high-frequency plasmonic devices.

Topological insulators are a new type of materials that play critical role in current electronics and condensed matter physics due to the fantastic electric properties [41–43]. Different from conventional materials, topological insulators present the conducting edge/surface state and insulating bulk state [44]. The topologically-protected nontrivial edge/surface state with the time-reversal symmetry enables the avoidance of the backscattering as the carriers encounter the impurities without magnetism [43]. The topological property was predicted and confirmed in the 2D CdTe/HgTe/CdTe quantum wells [41, 42]. In 2009, the topological surface states were reported in the 3D materials with layered structures, such as Bi₂Se₃, Bi₂Te₃, and Sb₂Te₃ [45]. The compound materials (Bi_xSb_{1-x})₂Te₃ and Bi_{2-x}Sb_xTe_{3-y}Se_y were proposed to achieve the tunable topological insulators by adjusting the ratio of elements Bi, Sb, Te, and Se [46, 47]. Recently, thousands of materials have been reported to possess the topological properties [48, 49]. Topological insulators with unique band structure will advance the development of spintronics, quantum computing, and low-energy-consumption devices [43, 46, 47, 50, 51]. In 2013, the THz Dirac plasmons like GPs was observed in the microribbons of 3D topological insulator Bi₂Se₃ [52]. In recent years, various plasmonic behaviors have been found in topological insulators containing Bi₂Se₃, Bi₂Te₃, Sb₂Te₃, Bi₂Te₂Se, and Bi_{1.5}Sb_{0.5}Te_{1.8}Se_{1.2} in an ultrawide range from the UV to THz [53–65]. After GPs, topological insulator plasmonics (TIPs) becomes a new branch of plasmonics. TIPs will provide a promising platform for advancing optical physics and applications in light-matter interactions, light control, photonic integration, and optoelectronic devices. Here, we introduce the fabrications, optical constants, plasmonic effects of 3D topological insulators, and discuss their applications in plasmon-enhanced light-matter interactions.

2 Fabrications and Optical Constants of Topological Insulators

2.1 Fabrications of Topological Insulators

The binary sesquichalcogenides Bi₂Se₃, Bi₂Te₃, and Sb₂Te₃ are the main members of reported 3D topological insulators. As shown in Fig. 1a, these materials have layered crystal structure with space group $D^5_{3d} (R\bar{3}m)$, whose unit cell is composed of five alternative layers with Se (Te) and Bi (Sb) along c-axis direction, namely quintuple layer (QL) [45]. QLs are bonded together via van der Waals forces along the c axis. Each QL is about 1 nm thickness, in which the atom layers are strongly coupled [45]. As depicted in Fig. 1b, topological insulators exhibit surface state with spin-momentum locking and a gapless Dirac cone dispersion in the bandgap of bulk state [41–47]. The bulk bandgaps are relatively small. For example, the

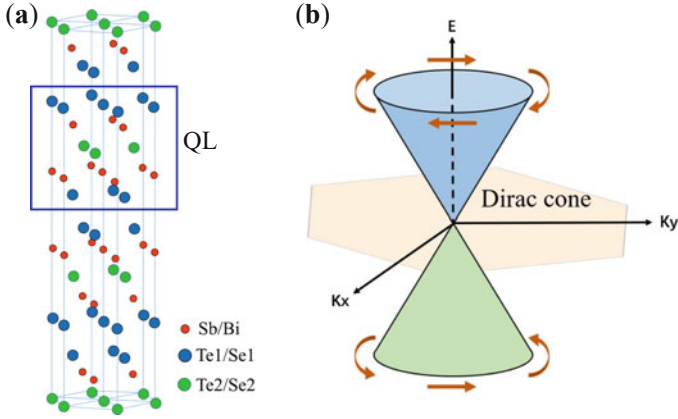


Fig. 1 (a) Crystal structure of 3D topological insulators Bi_2Se_3 , Bi_2Te_3 , and Sb_2Te_3 . The square denotes a quintuple layer (QL) with five-atom layers. (b) Energy dispersion of the surface state for 3D topological insulators with the 2D Dirac cone and spin-momentum locking

bandgap is ~ 0.3 eV for Bi_2Se_3 [45]. With the unusual band structure, topological insulators will not only play critical role in next-generation electric devices, but also present exciting potential for new optical and optoelectronic applications [46, 50, 51, 66–69]. Particularly, various plasmonic response has been found in the fabricated structures based on topological insulators [52–65]. The topological insulator materials can be synthesized using a variety of methods for different fabrication technologies. Here, we simply introduce some methods to grow typical 3D topological insulators.

The melting and slow-cooling (MSC) method can be used to fabricate the high-quality topological insulator single crystals [65, 70]. We take Sb_2Te_3 as an example to simply describe the growth process. As the starting materials, the high-purity Te and Sb powders are sealed in a quartz tube with an atom ratio of 3:2. The single crystals can be grown in a vertical furnace. The procedures are described as follows: Firstly, the Te and Sb powders are mixed and heated to 900 °C until completely melted. Secondly, the mixture temperature is quickly decreased to 650 °C with the 60 °C/h rate, and then slowly to 550 °C with the 2 °C/h rate. Thirdly, the furnace is naturally cooled down to the room temperature, and thus the Sb_2Te_3 single crystals can be fabricated along the c -oriented growth direction. It should be noting that the temperatures may be different for other topological insulators. Some of them could be doped with other elements to modulate the crystal and electronic structures [70]. The topological insulator thin films are easy to be exfoliated from bulk single crystals with the weak van der Waals forces between QLs. In this way, the quality of topological insulator films is high, but the area is limited.

The atomic layer deposition (ALD) method enables the growth of topological insulator film with the nanoscale precision and relatively large area at relatively low temperatures [62, 63]. This method is compatible with complementary metal-

oxide-semiconductor (CMOS) technology [62]. For example, the Sb_2Te_3 film can be synthesized through the chemical equation: $3[(\text{CH}_3)_3\text{Si}]_2\text{Te} + \text{Sb}(\text{OC}_2\text{H}_5)_3 \rightarrow 6(\text{CH}_3)_3\text{Si-OC}_2\text{H}_5 + \text{Sb}_2\text{Te}_3$. For the precursors of the chemical materials $3[(\text{CH}_3)_3\text{Si}]_2\text{Te}$ and $\text{Sb}(\text{OC}_2\text{H}_5)_3$, the injection (purge) time is set as 0.1 (9) s and 0.75 (9) s, respectively. To improve the gasification process of $\text{Sb}(\text{OC}_2\text{H}_5)_3$ precursor, an Ar gas booster can be employed on the cylinder. The chamber temperature and vacuum are set as 70 °C and 2×10^{-2} Torr, respectively. The Sb_2Te_3 growth rate is 0.01 nm per cycle [62]. The ALD growth time is about 5 h for depositing a 50 nm Sb_2Te_3 film [63].

The pulsed laser deposition (PLD) method can also be used to fabricate large-area topological insulator film. The detailed growth process of Sb_2Te_3 film can be seen in [71]. Compared with ALD, PLD can grow topological insulator film faster, but with the relatively high roughness. Another predominant method to fabricate topological insulator film is the molecular beam epitaxy (MBE) growth [72]. The MBE method is able to grow ultrathin Sb_2Te_3 film (even 1 QL), but effusion cells are employed and heated to high temperatures for the evaporation of elements [72]. The chemical vapor deposition (CVD) methods have been generally used to synthesize few-layer topological insulator nanoplates [60, 73]. Recently, some approaches were used to produce topological insulator nanoparticles for the investigation of plasmonic resonances, for example the solvothermal synthesis method [59, 74], facile solution-based method [58, 75]. There are some common-used technologies for clarifying the chemical composition, crystalline character, and quality of 3D topological insulators. They contain the Raman shift spectrum, energy-dispersive X-ray spectroscopy (EDS), X-ray diffraction (XRD), high-resolution transmission electron microscopy (HRTEM)/selected area electron diffraction (SAED) [55, 58, 63, 65, 70–72, 76]. The structural profile and surface roughness can be characterized by optical microscope, scanning electron microscope (SEM), TEM, and atomic force microscope (AFM) imaging [55, 58, 59, 63, 65, 76]. The AFM image presents the highest precision for recognizing the detailed surface structures. To explore optical properties and applications of topological insulators, it is of particular importance to know their optical constants.

2.2 Optical Constants of Topological Insulators

The first-principles electronic structure calculations and angle-resolved photoemission spectroscopy (ARPES) experiments have revealed the Dirac surface states of Bi_2Te_3 , Bi_2Se_3 , and Sb_2Te_3 [45, 77–79]. The existing surface states complicate the measurement of optical constants for this kind of topological insulators. Several methods have been proposed to measure the refractive indices or relative permittivities of topological insulators in different wavelength ranges. The permittivities at short wavelengths (e.g. from the UV to NIF region) of topological insulator films and single crystals can be measured by spectroscopic ellipsometer [53, 57, 62, 63, 65]. As shown in the inset of Fig. 2a, topological insulators can be seemed as

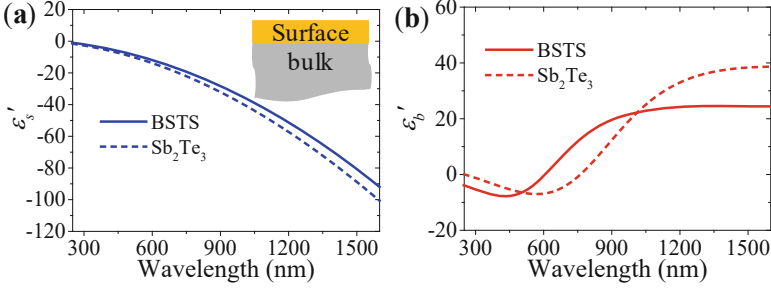


Fig. 2 (a–b) Surface and bulk permittivities of $\text{Bi}_{1.5}\text{Sb}_{0.5}\text{Te}_{1.8}\text{Se}_{1.2}$ (BSTS) and Sb_2Te_3 single crystals in the UV, VIS, and NIF ranges. The fitted permittivities of the topological insulators are obtained by fitting the ellipsometer data with a layer-on-bulk model, as shown in the inset of (a)

an insulating (or semiconductor-like) bulk covered with a thin Drude conducting surface [63, 65]. The surface and bulk permittivities of topological insulators can be obtained by fitting the ellipsometer data with the Drude and Tauc-Lorentz dispersion models, respectively [53]. The bulk permittivities are primarily derived from the interband transition and can be described using the Kramers-Kronig equations [80–82]. The imaginary and real bulk permittivities (ε_b'' and ε_b') can be written as

$$\varepsilon_b''(E) = \frac{AC E_0 (E - E_g)^2}{C^2 E^2 + (E^2 - E_0^2)^2} \cdot \frac{\Theta(E - E_g)}{E}, \quad (1)$$

$$\varepsilon_b'(E) = \varepsilon_{b,\infty} + \frac{2}{\pi} P \int_{E_g}^{\infty} \frac{\varepsilon_b''(\xi) \xi}{\xi^2 - E^2} d\xi, \quad (2)$$

where $\Theta(E - E_g) = 1$ for $E > E_g$ and 0 for $E < E_g$. The physical parameter A stands for the absorption peak amplitude, C is the broadening factor, and E_0 is the peak in joint density of states, and E_g is the bandgap energy of bulk state. $E = \hbar\omega$ represents the energy of incident photons, and $\omega = 2\pi c/\lambda$ is the angular frequency of incident photons. $\varepsilon_{b,\infty}$ is the relative permittivity at high frequency, and P is the Cauchy principal part for the integral [81]. The surface permittivities of topological insulators can be modeled by the Drude dispersion:

$$\varepsilon_s(\omega) = \varepsilon_{s,\infty} - \frac{\omega_p^2}{\omega^2 + i\omega\Gamma_d}, \quad (3)$$

where $\varepsilon_{s,\infty}$ stands for the surface permittivity at the high frequency, ω_p is bulk plasma frequency, and Γ_d is electron collision frequency (damping rate) of surface state [53, 63, 65]. With the spectroscopic ellipsometer, the ellipsometric angles Ψ and Δ (or I_S and I_c) can be measured by impinging light on the smooth surface of topological insulator at a fixed angle (e.g. 70°). The entire real and imaginary

Table 1 Fitting parameters in Drude and Tauc-Lorentz models for surface and bulk of topological insulators

Material	S_t (nm)	E_g (eV)	$\epsilon_{b,\infty}$	A (eV)	E_0 (eV)	C (eV)	$\epsilon_{\infty,s}$	ω_p (eV)	Γ_d (eV)	Range (μm)
BSTS [53]	1.5	0.25	0	65.9	1.94	1.94	1.3	7.5	0.05	0.2 ~ 1.6
Sb ₂ Te ₃ [56]	2.6	0.33	3.28	89.5	1.39	1.40	1.0	7.98	0.16	0.25 ~ 2.065

BSTS Bi_{1.5}Sb_{0.5}Te_{1.8}Se_{1.2}, S_t Surface thickness

permittivities of topological insulators can be achieved. Then, the surface and bulk are set as a surface-on-bulk double layer model with Drude and Tauc-Lorentz dispersion relations, respectively [53, 63, 65]. Through fitting the experimental data in the software, the surface, bulk, and entire permittivities can be obtained for topological insulators. Table 1 depicts the fitting parameters of Bi_{1.5}Sb_{0.5}Te_{1.8}Se_{1.2} and Sb₂Te₃ single crystals in the Drude and Tauc-Lorentz models. It should be noting that the thickness of conducting surface is unknown and also set as a fitting parameter. Generally, the surface thickness is a few nanometers, and thus the topological insulator surface should be smooth enough for ensuring the accuracy of results. Figure 2 show the surface and bulk dispersion curves, which are plotted according to the fitting results of topological insulators in Table 1. It shows that the real surface permittivity is negative ($\epsilon_s' < 0$) at the UV, visible (VIS), and NIF wavelengths, similar to noble metals [53, 65]. The bulk also exhibits negative real permittivities ($\epsilon_b' < 0$) at the UV and part VIS wavelengths. This mainly stems from the interband electronic transitions of bulk, similar to the semiconductors [83]. Due to the intraband transition of Dirac electrons, the surface permittivity is also negative at the long wavelengths [64, 82]. The negative real permittivities of topological insulators provide the possibility for the generation of plasmonic behaviors over an extremely wide spectral range [83]. At the UV and part VIS wavelengths, the topological insulators exhibit plasmonic figures of merit (FOM) superior to noble metals [53, 62].

Actually, limited by the detection range of spectrometer in ellipsometer, it is not easy to measure the optical constants of materials at the long wavelengths (e.g. the MIF region). The reflection and transmission spectra also enable the calculations of surface and bulk permittivities for topological insulator films. In the calculations, the Drude and Tauc-Lorentz models can also be used to fit the experimental spectra for the surface and bulk layers, respectively [64]. For measuring the MIF permittivities, the optical spectra of topological insulators can be achieved by Fourier-transform infrared spectroscopy (FTIR) [64]. The spectroscopic ellipsometry data and NIF-to-MIF reflection spectra were employed to calculate the dielectric constants of topological insulator in the UV-to-MIF range [82]. It has been found that topological insulators Bi₂Te₃ possess ultrahigh refractive indices (>7) at the infrared wavelengths, offering a new platform for the light control and functionalities. From optical constants of 3D topological insulators, we can see

that plasmonic response is attributed to the surface and bulk states in the UV and VIS regions, while mainly Dirac surface state at the infrared region [64]. The first-principles density functional theory (DFT) is a powerful scheme to theoretically study the electronic band structures and optical constants of topological insulators in $\text{Bi}_x\text{Sb}_{1-x}\text{Te}_y\text{Se}_{1-y}$ family [83]. The DFT calculations are significant for the clarification of the ellipsometric measurements [82, 83].

At the THz wavelengths, there exist the phonon modes in the topological insulator (e.g. Bi_2Se_3) films. When the film is thin and its thickness H is smaller than lateral dimensions, the optical response of the film can be described using effective conductance $G(\omega)$ with neglecting nonlocal effects. In the region around optical phonons, the topological insulator permittivity can be approximately written as [84, 85].

$$\varepsilon_T(\omega) = \varepsilon_\infty + \frac{S_{ph}^2}{\omega_{ph}^2 - \omega(\omega + i\gamma_{ph})}, \quad (4)$$

where ε_∞ stands for the permittivity at high frequency. ω_{ph} and γ_{ph} are the phonon frequency and width, respectively. The permittivity of topological insulator film can also be written as the form of conductivity $\sigma(\omega)$: $\varepsilon_T = 1 + 4\pi i\sigma(\omega)/\omega$. The 2D conductance $G(\omega)$ related to $H\sigma(\omega)$ can be expressed as [85].

$$G(\omega) = \frac{e^2}{\hbar} \frac{i\omega_e}{\omega + i\gamma_e} + \frac{i\omega H}{4\pi} \left[\frac{S_{ph}^2}{\omega(\omega + i\gamma_{ph}) - \omega_{ph}^2} + (1 - \varepsilon_\infty) \right], \quad (5)$$

where γ_e is the intrinsic decay rate of electronic excitations for topological insulator surface, and ω_e is a characteristic frequency. If there is no overlap between the two metallic regions, ω_e should rather not depend on the film thickness H and dielectric environment. The above parameters of surface conductance can be extracted from the extinction spectra of topological insulator film on a substrate as following [85].

$$E(\omega) = 1 - \frac{1}{[1 + Z_0 G'(\omega)/(n+1)]^2 + [Z_0 G''(\omega)/(n+1)]^2}. \quad (6)$$

Here, Z_0 is the impedance in free space ($Z_0 = 377 \Omega$). $G'(\omega)$ and $G''(\omega)$ is the real and imaginary parts of surface conductance $G(\omega)$, respectively. n is the refractive index of the substrate at the THz frequencies.

3 Plasmonic Behaviors of Topological Insulators

3.1 Dirac Plasmons

Topological insulator plasmonic response was firstly observed in the THz range from microribbon arrays of Bi_2Se_3 with the 2D electron gas at the surface [52]. This plasmonic response was regarded as Dirac plasmons like plasmons in graphene with massless Dirac electrons. Figure 3a depicts the microribbon structure of MBE-grown Bi_2Se_3 , which were fabricated by electron-beam lithography (EBL) and reactive ion etching (RIE). From Fig. 3b, we can see that there exist two extinction coefficient peaks at 1.85 and 4.0 THz, which correspond to two phonon modes, namely α mode and β mode [52]. The frequencies of phonon modes are independent on the structure and the polarization of incident electric field. However, when the

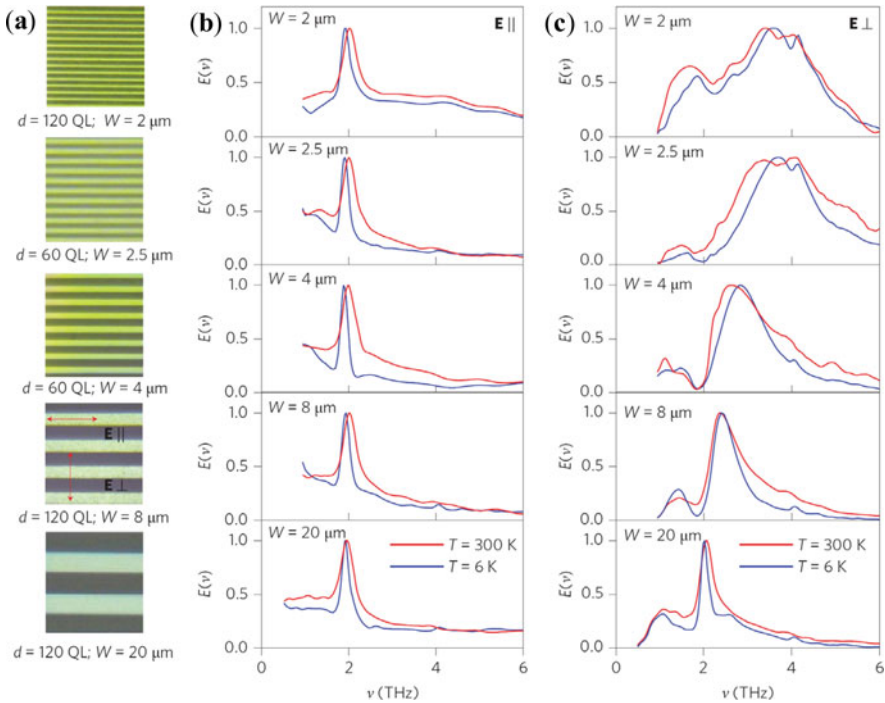


Fig. 3 (a) Optical microscope images of the Bi_2Se_3 microribbons with different widths W and periods $P = 2W$. The arrows denote the direction of the electric field \mathbf{E} . d stands for the thickness of Bi_2Se_3 film, and QL is quintuple layer (1QL ~ 1 nm). (b) Normalized extinction coefficients of the Bi_2Se_3 microribbons at 6 and 300 K when the electric field is parallel to the microribbons. (c) Normalized extinction coefficients of the microstructures when the electric field is perpendicular to the microribbons. (Reprinted with permission from Ref. [52] © 2013 Macmillan Publishers Limited, part of Springer Nature)

polarization of incident light is perpendicular to the ribbons, the phonon peak of α mode disappears and is replaced by new peaks in the spectrum, as depicted in Fig. 3c. The new peaks are derived from the generation of plasmonic mode that interacts with α phonon mode. The plasmonic and phonon modes can be extracted from the spectral curves by fitting with the coupling equation (see Eq. 1 in [52]). The fitting results showed that the plasmonic mode had a red shift with increasing the array width, while the frequency of phonon mode was unchanged. Similar to traditional SPs, the microribbon arrays were used to offer the reciprocal-lattice vectors to satisfy the wavevector matching condition between the incident light and topological insulator plasmons. The Dirac dispersion of plasmon frequency in the long wavelength limit ($k \rightarrow 0$) can be described as [52, 86].

$$v_D = \frac{1}{2\pi} \sqrt{k} \left(\frac{e^2}{4\pi \epsilon_0 \epsilon \hbar} v_F \sqrt{2\pi n_D} \right)^{1/2}, \quad (7)$$

where the wavevector k is equal to π/W , and W is the microribbon width. $n_D = 3 \pm 1 \times 10^{13} \text{ cm}^{-2}$ and $v_F = 6 \pm 1 \times 10^7 \text{ cm/s}$ for Bi_2Se_3 thin films [87]. The above equation does not include the permittivity and thickness of the Bi_2Se_3 film, while contains the surrounding permittivities with $\epsilon = (\epsilon_1 + \epsilon_2)/2$. Here, ϵ_1 and ϵ_2 are the permittivities of air and substrate, respectively [52]. At the highest wavevectors, the form of Eq. (7) is not proper for the description of experimental data. With considering the permittivity ϵ_T and film thickness H of topological insulator Bi_2Se_3 film, the equation can be modified as [86].

$$v_D = \frac{1}{2\pi} \sqrt{k} \left(\frac{e^2}{4\pi \epsilon_0 \epsilon \hbar} v_F \sqrt{2\pi n_D} \right)^{1/2} \left[1 + \frac{kH\epsilon_T}{2\epsilon} \right]^{-1/2}. \quad (8)$$

At the THz wavelengths, Dirac plasmons can also be observed in the Bi_2Se_3 microring arrays with strong plasmon-phonon hybridization and interference [85]. The excitations and properties of the THz Dirac plasmons in Bi_2Se_3 microstructures were concluded and discussed by Lupi et al. in [86].

Marta et al., reported the modulation of THz plasmons under the condition of external magnetic field (i.e., magnetoplasmonics) in the Bi_2Se_3 microribbon arrays [56]. Plasmonic response induced by Dirac surface state were detected in the MIF region on topological insulator Bi_2Te_3 nanosheets using scattering-type scanning near-infrared optical microscopy (s-SNOM) [60]. The plasmonic near-field properties of Bi_2Te_3 nanosheets can be tuned by supplying an external gate bias. The propagating plasmons at $10.6 \mu\text{m}$ wavelength were also observed on topological insulator $\text{Bi}_2\text{Te}_2\text{Se}$ flakes through SNOM [64]. The wavelength of MIF plasmonic wave on the topological insulator exceeds 100 times smaller than that of incident light. This is different from visible SPs, whose wavelengths are on the order of incident light [64].

3.2 Surface Plasmon Resonances

The Kretschmann structure is a simple and effective method to excite SPs, which has a broad application in plasmonic sensors [88]. In this configuration, the light beam impinging into the prism can satisfy the wavevector matching condition with SPs. The incident light couples with SPs via the evanescent field and induce surface plasmon resonance (SPR) on the metal nanofilm. An obvious dip will appear in the reflection spectrum at the SPR excitation angle or wavelength. To excite SPR on the topological insulators, the Sb_2Te_3 films with a 50 nm thickness were grown on the glass substrate using the ALD method [63]. Figure 4a shows an optical path to study the SPR generation on the Sb_2Te_3 film. Here, the Sb_2Te_3 film replaces

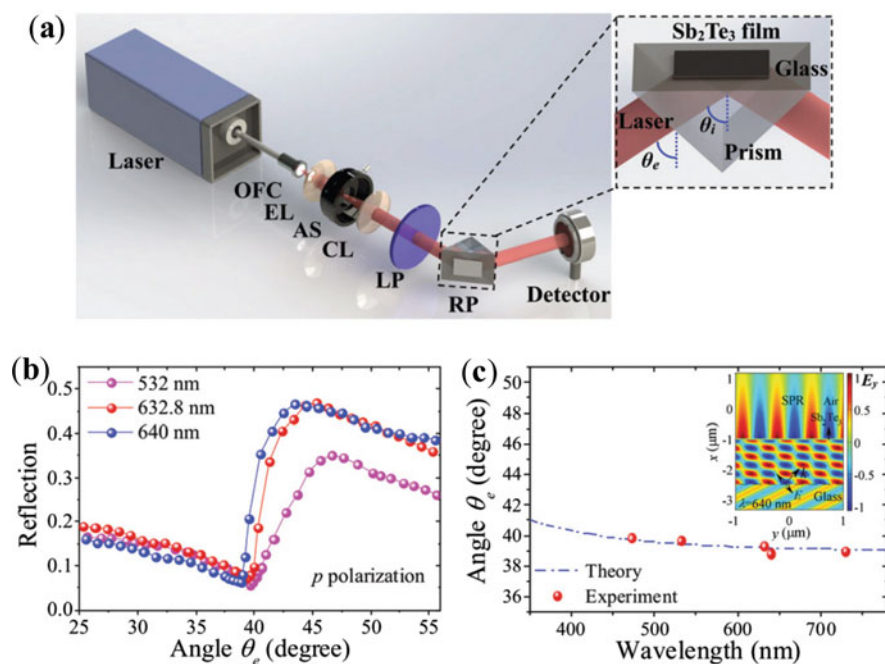


Fig. 4 (a) Optical path for the SPR generation on the Sb_2Te_3 film. The inset shows the ALD-grown Sb_2Te_3 film on the glass substrate adhered to a rectangular prism. The experimental setup contains optical fiber coupler (OFC), expanding lens (EL), aperture stop (AS), collimator lens (CL), linear polarizer (LP), and rectangular prism (RP). (b) Measured reflection intensities of p -polarized light in the Sb_2Te_3 -based Kretschmann structure at different incident angles θ_e for the 532, 632.8 and 640 nm incident beam. (c) SPR excitation angles of the Sb_2Te_3 film in the Kretschmann structure at the different wavelengths. The circles and curve represent the experimental and theoretical results, respectively. The inset depicts the field distribution of E_y in the Kretschmann structure with the Sb_2Te_3 film. Here, a p -polarized light with the 640 nm wavelength is obliquely illuminated at the SPR excitation angle. The field distribution is simulated by finite-difference time-domain (FDTD) method. (Reprinted with permission from Ref. [63] © 2019 The Royal Society of Chemistry)

the traditional metal film in the Kretschmann structure, as can be seen in the inset of Fig. 4a. The experimental setup includes the laser source, optical fiber coupler, expanding lens, aperture stop, collimator lens, linear polarizer, rectangular prism, and detector. The linear polarizer enables the control of the polarization for incident light beam. The glass substrate with the Sb_2Te_3 film on top is adhered to the prism (K9) by employing the refractive index matching liquid ($n = 1.516$). The detector can record the power of light beam reflected from the Sb_2Te_3 film. By rotating the prism on a rotator, the reflected intensities of incident light at different angles can be measured. θ_e (θ_i) represents the external (internal) incident angle. Figure 4b depicts the reflection intensities from Kretschmann configuration at different incident angle θ_e . The p -polarized light with the 640 nm wavelength presents a distinct reflection dip at $\theta_e \approx 38.8^\circ$. But the reflection is not sensitive to the incident angle of s -polarized light. The reflection dip of p -polarized light is derived from the SPR excitation on the Sb_2Te_3 film at 640 nm wavelength. To prove it, the SPR angles of the Sb_2Te_3 film are theoretically calculated for different incident wavelengths. As depicted in Fig. 4c, the SPR angle decreases with the increase of the incident wavelength. The theoretical results agree well with the experimental measurement. The visible SPR on topological insulator Sb_2Te_3 mainly stems from the conducting property of surface and the optical conductivity due to the interband transition of bulk [61]. As shown the inset of Fig. 4c, when a p -polarized light is incident at the excitation angle, the SPR electric field can be observed on the Sb_2Te_3 film. Similar to $\text{Bi}_{1.5}\text{Sb}_{0.5}\text{Te}_{1.8}\text{Se}_{1.2}$, the topological insulator Sb_2Te_3 will also support the plasmonic generation in the UV region due to the negative permittivity [53]. The topological insulator-based SPR possesses the smaller excitation angle and stronger field penetration in air, compared to metal-based SPR. These properties will benefit for the sensing of refractive index. The generation and propagation of visible SPs on the ALD-grown Sb_2Te_3 nanofilm was confirmed by the SNOM measurement [62].

3.3 Localized Plasmon Resonances

Localized plasmon resonances (LPRs) commonly occur in the metallic nanoparticles and are well known from some fantastic phenomena, for example Lycurgus glass cup [89]. The cup with embedded small Au nanoparticles has different color for transmitted and reflection light. The spectral response (e.g. position, profile, and strength) of plasmonic resonances relies on the shape, material, size, and surrounding refractive index of the metallic nanoparticles. The resonantly enhanced near fields are promising for applications of metallic nanoparticles in light-matter interactions [29, 89]. The LPR effect was also observed in topological insulator $\text{Bi}_{1.5}\text{Sb}_{0.5}\text{Te}_{1.8}\text{Se}_{1.2}$ (BSTS) nanocone arrays in the UV and VIS regions [57]. With the conducting surface and insulating bulk, the BSTS nanocones display the intrinsically core-shell structures. The ellipsometry results demonstrate that the refractive index of BSTS can approach 5.5 at the NIF wavelengths [57]. Figure 5a shows a unit of BSTS nanocones with intrinsically core-shell structures. The red part

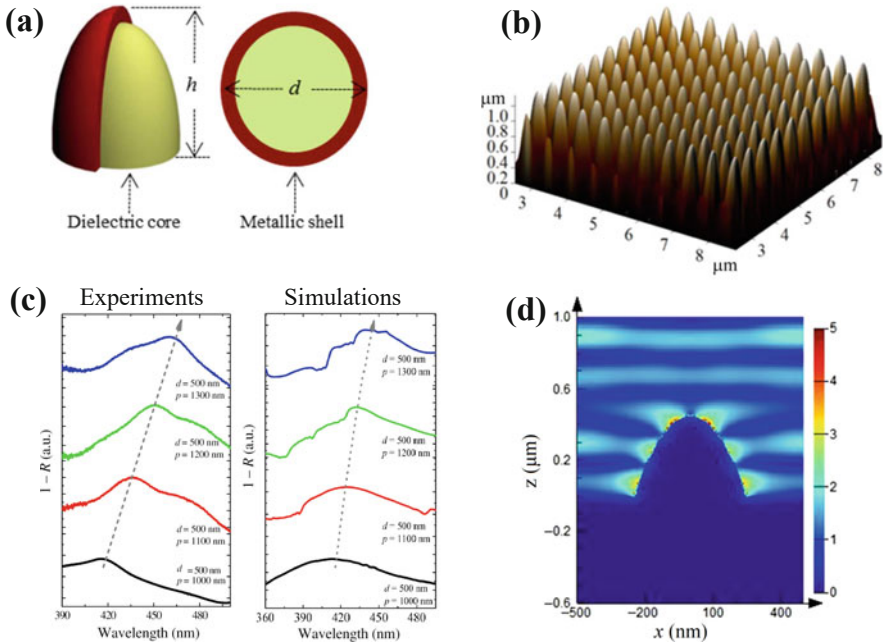


Fig. 5 (a) Schematic diagram of a BSTS nanocone with the intrinsically core-shell structure. The red and yellow parts are a metallic shell and a dielectric core, respectively. (b) 3D AFM image of a BSTS nanocone array with the width $d = 300$ nm, height $h = 450$ nm, and pitch $p = 600$ nm. (c) Experiment and simulation results of normalized absorption spectra from BSTS nanocone arrays with different p when $d = 500$ nm. (d) FDTD simulated field distribution of BSTS nanocone arrays with $d = 500$ nm and $p = 1000$ nm at the resonance wavelength of 411 nm. (Reprinted with permission from Ref. [57] © 2017, AAAS)

is a metallic (metal-like) shell, and the yellow part is an insulating core. In Fig. 5b, we can see the 3D AFM image of a nanocone array fabricated on flat BSTS flakes using the focused ion beam (FIB) milling method. The width, height, and pitch of the nanocone array is set as $d = 300$ nm, $h = 450$ nm, and $p = 600$ nm, respectively. The light reflection from the BSTS nanostructures can be measured by the FTIR equipped with a microscope system. Figure 5c depicts the normalized absorption spectra from the BSTS nanocone arrays. The absorption spectra can be calculated through $A = 1 - R$. It shows that there exist the distinct absorption peaks in the UV and VIS regions. The simulation results are in good agreement with the experimental measurements. The absorption peaks are derived from the generation of LPRs on the nanocones. This can be verified by the FDTD simulated field distribution. As shown in Fig. 5d, the plasmonic resonance is localized on the BSTS nanocone surface as the light is incident on the structure at the wavelength of absorption peak. Moreover, the resonance wavelength has a red shift with the increase of the pitch p , enabling the selection of LPR wavelength. The LPR response in topological insulator BSTS

nanocones results from both the bulk charge carriers induced by interband transition and the surface charge carriers [57].

The VIS and NIR plasmonic resonances were also observed in the Bi_2Te_3 hexagonal nanoplates synthesized by solvothermal method [59]. Meanwhile, it was found that the Se doping could be used to tailor the spectrum of plasmonic resonance in Bi_2Te_3 nanoplates. With increasing the portion of Se, the resonance wavelength presented a clear blue shift [59]. Especially, the crystalline-amorphous phase change of Bi_2Te_3 material enables the dynamic modulation of the intensity for the plasmonic resonance. The plasmonic behavior similar to LPRs was also found in the Bi_2Se_3 hierarchical nanoflowers composed of a large number of nanocrystals. The plasmonic resonance was proposed to effectively produce enhanced photothermal conversion effect [58]. Actually, the Dirac plasmons in Bi_2Se_3 microribbons and microrings belong to the topological insulator LPRs [52, 85].

3.4 Magnetic Plasmon Resonances

Artificially structured materials composed of metallic atoms (e.g. split rings) attract broad attention due to the exciting strong magnetism. The artificial magnetism plays an important role in the realization of negative refractive index and cloaking [90, 91]. But the magnetic response induced by conduction current loops mainly exists at the relatively low frequencies. Broadening artificial magnetism to high frequencies is limited by the magnetic response saturation of metallic rings [92]. Plasmon-assisted magnetic resonances in special metallic structures can achieve the high-frequency artificial magnetism with the formation of displacement current loops [93]. The metallic nanopillar pairs, nanoclusters, and nanoparticle-film structures were reported to acquire plasmon-assisted magnetic resonances [93–95]. The plasmon-assisted magnetic resonances were also named magnetic plasmon resonances (MPRs) [96]. MPRs are not only capable of engineering magnetism and controlling light at nanoscale, but also in favor of enhancing light-matter interactions [93–95]. Currently, magnetic resonances draw special attentions in other materials, especially new-emerging materials for improving the characters and application range. Graphene split rings were proposed to produce stronger magnetic resonances than metallic structures in the far-infrared region [97]. The topological insulator materials presented plentiful plasmonic behaviors at high frequencies due to the surface conducting and bulk conductivity. This makes the generation of MPRs in topological insulator structures possible.

Figure 6a shows a topological insulator nanogroove grating structure with a width d , height h , and pitch p . θ is the polarization angle of light incident on the nanostructure. Figure 6b depicts the SEM image of a nanogroove grating fabricated on the Sb_2Te_3 single crystal by the FIB milling method [65]. The Sb_2Te_3 single crystal is grown by the MSC method and mechanically transferred onto a silicon substrate. The reflection spectra of Sb_2Te_3 nanogroove grating structures were measured by a home-made micro-spectrometer system. As shown in Fig. 6c, an

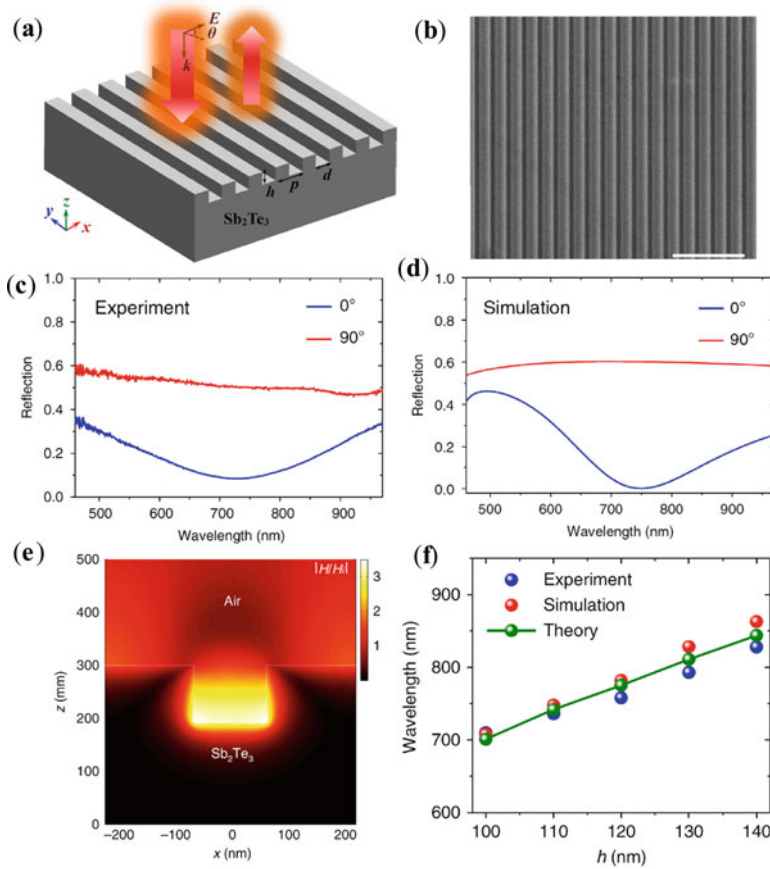


Fig. 6 (a) Schematic diagram of a Sb_2Te_3 nanogroove grating with the width d , height h , and pitch p . The incident light has a polarization angle of θ . (b) SEM image of the fabricated Sb_2Te_3 nanogroove grating. The scale bar is $2 \mu\text{m}$. (c–d) Measured and simulated reflection spectra from the nanogroove grating with $h = 110 \text{ nm}$, $d = 130 \text{ nm}$, and $p = 450 \text{ nm}$ when $\theta = 0^\circ$ and 90° . (e) Field distribution of $|H/H_i|$ in the Sb_2Te_3 nanogrooves at the wavelength of reflection dip when $\theta = 0^\circ$. (f) Resonance wavelengths of Sb_2Te_3 nanogrooves with different depth h . The theoretical, simulation, and experiment results are achieved using the MLC circuit model, FDTD method, and micro-spectrometer, respectively. (Reprinted with permission from Ref. [65] © 2020 Springer Nature)

obvious reflection dip appears at the wavelength of $\sim 736 \text{ nm}$ when the polarization of incident light is vertical to the nanogrooves ($\theta = 0^\circ$). There is no reflection dip for the incident light with the polarization parallel to the nanogrooves ($\theta = 90^\circ$). The FDTD simulations agree well with the experiment results, as shown in Fig. 6d. This effect was attributed to the excitation of visible-range magnetic resonance, similar to MPR in metallic nanogrooves [96]. The field distribution in Fig. 6e clarifies the generation of MPR-like effect in the Sb_2Te_3 nanogrooves. The MPR

wavelength presents a nearly linear redshift with increasing the nanogroove depth. The experimental measurements are consistent with the simulation and theoretical calculations, as depicted in Fig. 6f. This visible-range magnetic resonance will open a new door for exploring topological insulator optical functionalities and high-frequency artificial magnetic materials.

4 Plasmon-Enhanced Light-Matter Interactions

4.1 Refractive Index Monitoring

Due to the surface sensitivity, SPRs enable the realization of sensing, monitoring, and measuring of the refractive index [98]. The SPR sensing in the Kretschmann structure is generally attributed to the change of reflection intensity when the surrounding refractive index alters. It is worth noting that the reflection phase also plays a critical role in the refractive index sensing [99]. Digital holography (DH) is an advanced technology to simultaneously acquire the phase and intensity information of the objects. DH has the advantages of non-intrusive and dynamic measurement [100]. SPR DH is able to measure the near-field refractive index from the recorded holograms in the far field [98, 100]. The phase and intensity information of the specimen can be reconstructed using the angular spectrum method [63, 100]. The principle of double-exposure holographic interferometry can be used to measure the phase differences of reconstructed object waves and intensity ratios (reflection intensities) at different time t . The phase difference is described as $\Delta\phi_{O_t} = \phi_{O_t} - \phi_{O_0} = \arg(O_t/O_0)$. Here, ϕ_{O_t} and ϕ_{O_0} denote the phases of object waves at different time t and start time, respectively. O_t is the reconstructed object waves at time t , and O_0 is the reference object wave at start time. The intensity ratios can be calculated by $IR_t = |O_t/O_0|^2$.

The SPR response on the Sb_2Te_3 film will advance the practical applications of topological insulators in environmental and biochemical sensing. Combining with DH, the topological insulator SPR was proposed to realize the real-time monitoring of the refractive index variation [63]. Figure 7a shows an experimental setup of the SPR holographic imaging for monitoring refractive index variation of ethanol-water mixtures. The ethanol and deionized water are mixed with a ratio of 1:1 as a specimen. When the ethanol volatilizes, the refractive index will alter from 1.350 to 1.331 for the mixture. The 640 nm laser beam with a 45° polarization is obliquely incident into the Kretschmann structure. When a mixture droplet is dripped on the Sb_2Te_3 film, the incident light beam can excite SPR at a certain angle. The reflected light will carry the information of droplet specimen and be projected on the CCD after penetrating a Wollaston prism (WP) and a linear polarizer. The WP can split the p - and s -polarized components of reflected light with a small angle for recording off-axis holograms. With the excitation of SPR, the p -polarized component can sense the refractive index variation of the droplet on the Sb_2Te_3

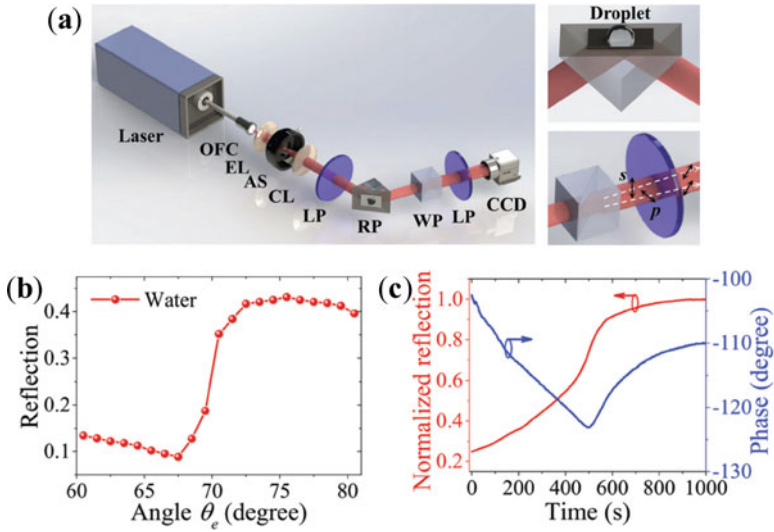


Fig. 7 (a) Experimental setup for the common-path DH with the SPR on the Sb_2Te_3 film for measuring the variation of refractive index, which contains Wollaston prism (WP) and charge-coupled device (CCD) besides the elements in Fig. 4a. The upper-right inset depicts a mixture droplet adhered to the Sb_2Te_3 film on the prism. The lower-right inset shows the *s*- and *p*-polarized light components that are split through the WP. (b) Measured reflection intensities at different angles of incident light in the Kretschmann structure with a deionized water droplet on the Sb_2Te_3 film. (c) Normalized reflection intensities and phase shift differences of DH reconstructed images varying with time. (Reprinted with permission from Ref. [63] © 2019 The Royal Society of Chemistry)

film. But, the SPR excitation is prohibited for the *s*-polarized component, which does not carry the droplet information. The *p*- and *s*-polarized components can be regarded as the object and reference waves, respectively. After passing through the linear polarizer, the two split light beams have the same polarization direction. Thus, the two light beams generate interference (holograms) on the target plane of CCD. As shown in Fig. 7b, the SPR angle θ_e is around 67.5° for the water droplet. Thus, the excitation angle θ_i is 59.6° , which is smaller than $\sim 70^\circ$ in the Kretschmann structure with gold film [101]. This benefits for reducing distortion of holographic images. The angle sensitivity of SPR is defined as $S_\theta = d\theta_e/dn$, which is estimated as $88.5^\circ/\text{RIU}$ for the Sb_2Te_3 film [63]. This value is comparable to the traditional gold-based SPR systems [102]. Here, θ_e is set as 71.3° to excite SPR on the Sb_2Te_3 film with a mixture droplet. To monitor the refractive index variation of this droplet, 1000 holograms are recorded with 3 s time interval as the ethanol in the mixture volatilizes. The phase- and intensity-contrast holographic images of mixture droplet can be acquired from the holograms by the numerical reconstruction [63]. Figure 7c shows that the reflection intensity rapidly rises before 600 s and then becomes relatively flat. This is because the volatilization of ethanol in the mixture droplet is quick in the initial stage and then slow. The intensity sensitivity

of SPR is defined as $S_r = dR/dn$. It depends on the recording time and is largest at ~ 501 s. The average sensitivity is $\sim 15.8 \text{ RIU}^{-1}$. As the mixture droplet volatilizes before 501 s, the phase difference has a nearly linear decrease and then gradually increases. The phase sensitivity is lowest at 501 s, when the intensity sensitivity is highest. This kind of SPR DH systems facilitates the realization of the real-time, full-view, nondestructive, and distortion-reduced monitoring of near-field refractive index variation [63, 98, 100].

4.2 Enhanced Photoluminescence Emission

Plasmonic resonances with strong field enhancement have broad applications in light-matter interactions, for example enhanced photoluminescence (PL) emission [29, 59, 65]. The MPR effect in topological insulator nanogrooves can give rise to significantly strong electric field [65]. It provides a pathway for reinforcing light interactions with 2D materials. As a kind of 2D materials, transition metal dichalcogenides (TMDCs) present semiconductor-like band structures with excellent electric, optical, and mechanical characters [103–105]. For instance, molybdenum disulfide (MoS_2) as a typical TMDC exhibits the state transition of a 1.2 eV indirect bandgap for bulk, while a 1.8 eV direct bandgap for monolayer [103]. Monolayer MoS_2 with the direct bandgap contributes to the realization of the field effect transistors with ultra-high on/off ratio [105]. Meanwhile, the PL response of monolayer MoS_2 attract particular interests due to the chemical stability, photoemission, and excitonic binding [29, 65, 106, 107]. But, the atomic-layer thickness of MoS_2 is not beneficial for light-matter interactions and restricts the light emission. The significant enhancement of light-matter interactions is crucial for MoS_2 optoelectronic devices. Monolayer MoS_2 was proposed to integrate with the Sb_2Te_3 nanogroove grating for tailoring and reinforcement of PL emission [65]. As shown in Fig. 8a, a mechanically exfoliated MoS_2 flake is transferred on the Sb_2Te_3 nanogrooves by using fixed-point transfer method. The inset of Fig. 8b shows SEM image of the Sb_2Te_3 nanogrooves after the transfer of a MoS_2 flake. The nanogroove grating with $d = 130$ nm, $h = 50$ nm, and $p = 400$ nm was fabricated on an exfoliated Sb_2Te_3 single crystal with a thickness of ~ 200 nm. The Raman shift spectra show that the vibrational modes E_{2g}^1 and A_{1g} of MoS_2 on Sb_2Te_3 has a frequency difference of $\sim 18.5 \text{ cm}^{-1}$ with the excitation of a 532 nm laser [65]. This verifies the monolayer character of MoS_2 . The nanogrooves exhibit a magnetic resonance at the wavelength of ~ 532 nm when $\theta = 0^\circ$. The PL spectra in Fig. 8b show that two PL peaks appear at 680.5 and 638.0 nm wavelengths for MoS_2 on the Sb_2Te_3 nanogrooves when $\theta = 0^\circ$. The two peaks are close to the positions of A and B direct excitonic transitions of MoS_2 [106, 108]. Sb_2Te_3 cannot solely excite the distinct PL emission. It illustrates that the PL emission comes from MoS_2 . The primary PL peak of MoS_2 on the Sb_2Te_3 nanogrooves is about 21-fold higher than that of MoS_2 on Sb_2Te_3 . This is mainly attributed to the enhanced electric

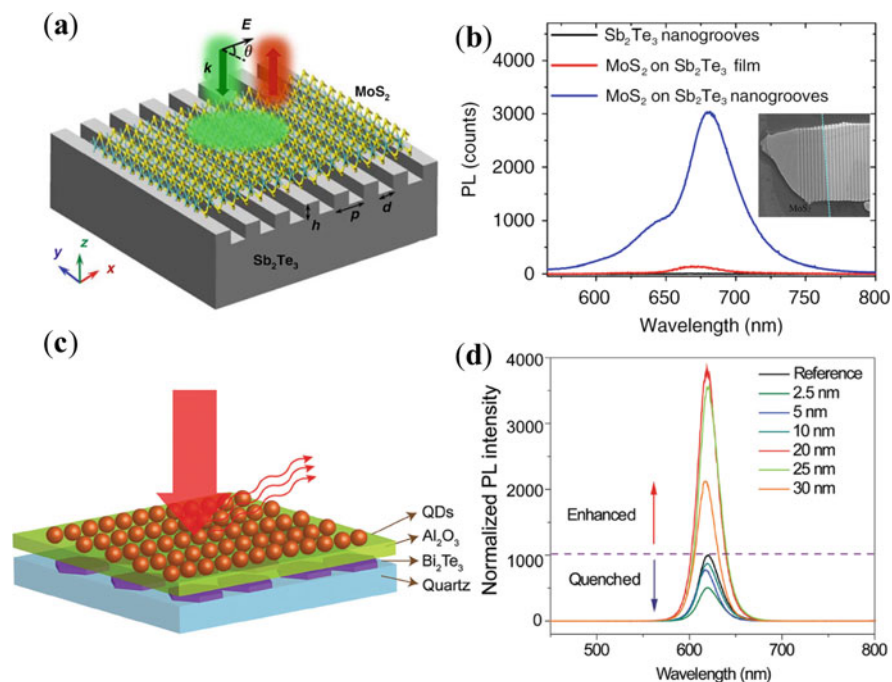


Fig. 8 (a) Schematic diagram of the Sb_2Te_3 TI nanogroove grating with a monolayer MoS_2 on top. (b) PL emission from the Sb_2Te_3 nanogrooves and monolayer MoS_2 on the Sb_2Te_3 film/nanogrooves. The inset shows SEM image of Sb_2Te_3 nanogrooves with transferring MoS_2 flake. (Reprinted with permission from Ref. [65] © 2020 Springer Nature). (c) Schematic diagram of the Bi_2Te_3 nanoplates coated with the CdSe/ZnS QDs and an Al_2O_3 spacing layer. (d) Normalized PL intensity of QDs with different thicknesses of the Al_2O_3 layer. (Reprinted with permission from Ref. [59] © 2016 WILEY-VCH Verlag GmbH & Co. KGaA, Weinheim)

field induced by the generation of MPR in the Sb_2Te_3 nanogrooves at ~ 532 nm wavelength. When $\theta = 90^\circ$, the PL emission is seriously suppressed due to the vanishment of magnetic resonance [65]. The doping of MPR-excited hot electrons can increase the level of A- trions in MoS_2 and cause the redshift of PL peaks [65, 108].

The plasmonic resonance in solvothermal method-synthesized Bi_2Te_3 nanoplates was proposed to enhance the fluorescence emission of CdSe/ZnS quantum dots (QDs) [59]. Figure 8c shows the CdSe/ZnS QD structure for PL emission assisted by the Bi_2Te_3 nanoplates with the hexagonal shape. An Al_2O_3 spacer is introduced between the QDs and Bi_2Te_3 nanoplates. The QD emission peak locates at 610 nm wavelength, overlapping with the SP energy of Bi_2Te_3 [59]. With the excitation of a 410 nm laser, the PL intensity of QDs is dependent on the thickness of Al_2O_3 spacer, as depicted in Fig. 8c. As the thickness is smaller than 10 nm, QD PL emission is quenched compared to the case without the Bi_2Te_3 nanoplates. The quenching of PL emission was attributed to the dominant nonradiative energy transfer from

the QDs to Bi₂Te₃ nanoplates. As the thickness is 20 nm, the PL intensity reaches the highest value with a 3.8-fold reinforcement. This results from the plasmon-enhanced electric field and enhanced radiative rate due to the Purcell effect [29, 59, 108]. As the spacer thickness further increases, the PL emission descends with the weakening of electric field and Purcell effect [59]. The enhanced UV PL emission of ZnO was also observed with the excitation of SPs existing at the ZnO/Bi₂Te₃ interface [109]. The plasmonic effects in topological insulator materials enable the enhancement of light-matter interactions, which will broaden the applications of topological insulators in photonics and optoelectronics, especially light emission and sources.

4.3 Enhanced Light Harvesting

The strong plasmon-induced electric field has also been widely applied in boosting light harvesting for high-performance photodetectors and solar cells [26, 28]. As mentioned above, the plasmonic resonance can be supported in the topological insulator nanocone arrays and nanoplates at the UV and VIS wavelengths [57, 59]. This holds potential to reinforce the light absorption and conversion efficiency of photovoltaic devices. Figure 9a shows a designed a-Si solar cell with BSTS nanocone arrays. The BSTS nanocones are integrated into the back of a-Si thin film and act as the back electrode of the solar cell. Figure 9b depicts the light absorption of the a-Si thin-film solar cells without and with the BSTS nanocone arrays. We can see that the BSTS nanocone arrays can achieve a broadband light absorption enhancement in the VIS range. The light absorption of a-Si thin-film solar cell can be enhanced by 15% in the entire range with the integration of BSTS nanocone arrays. The enhancement reaches the maximum value of 55% at the wavelength of 325 nm. Besides the plasmonic resonance, the high light absorption efficiency also arises from the strong backward scattering of BSTS nanocone arrays, which increases the path length of light [57].

Zhao et al., reported a plasmon-enhanced Si/PEDOT:PSS solar cell integrated with the Bi₂Te₃ nanoplates [59]. As shown in the inset of Fig. 9c, there exists a Schottky junction at the Si-PEDOT:PSS film interface. Meanwhile, a built-in potential forms around the interface due to the difference between the conduction band of n-Si and the work function of PEDOT:PSS film. The aluminum electrode and silver-grid top act as the electrodes. The PEDOT:PSS film can help to collect and transfer the holes separated in the internal electric field. The PEDOT:PSS layer was fabricated through spin-coating the mixture of Bi₂Te₃ nanoplates and PEDOT:PSS solution on n-doped Si plane [59]. Figure 9c shows the plasmon-enhanced performance of the solar cell with the introduction of Bi₂Te₃ nanoplates. The curves denote the current-density-voltage (J - V) properties of the solar cells without and with Bi₂Te₃ nanoplates (1.04% weight percentage). The incorporation of Bi₂Te₃ can contribute to the significant reinforcement of short-circuit current density (J_{sc}) from 21.75 to 27.08 mA/cm² [59]. Figure 9d shows the incident

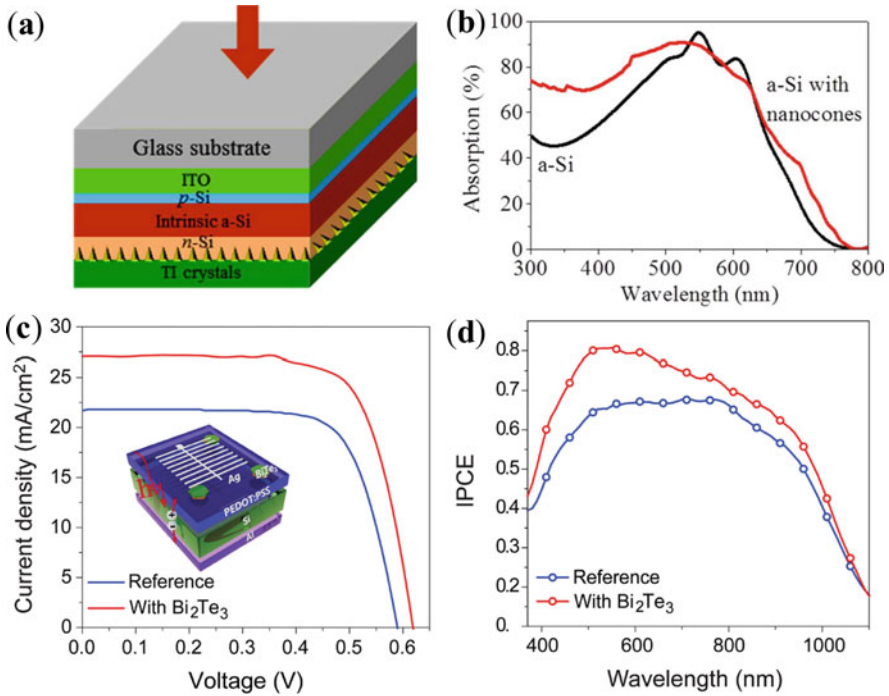


Fig. 9 (a) Schematic diagram of the a-Si solar cell with a BSTS nanocone array integrated into a-Si thin film. The BSTS nanostructure also acts as the back electrode of solar cell. (b) Light absorption in a-Si thin-film solar cell with (red curve) and without (black curve) the BSTS nanocone array. (Reprinted with permission from Ref. [57] © 2017, AAAS). (c–d) Current-density-voltage and incident photon-to-charge carrier efficiency (IPCE) of a solar cell without and with Bi₂Te₃ nanoplates (1.04% weight percentage). The inset in (c) shows the schematic diagram of the Bi₂Te₃-incorporated solar cell. (Reprinted with permission from Ref. [59] © 2016 WILEY-VCH Verlag GmbH & Co. KGaA, Weinheim)

photon-to-charge carrier efficiency (IPCE) of the solar cell device with and without the Bi₂Te₃ nanoplates. The Bi₂Te₃-involved solar cell presents a significantly enhanced IPCE in the entire visible range. The enhanced light absorption effects stem from the plasmonic resonance in the Bi₂Te₃ nanoplates. The strong local electric fields of plasmonic resonance can promote the creation of electron-hole pairs and boost the absorption of incident light near the Si layer. Meanwhile, the light scattering from the Bi₂Te₃ nanoplates can also enhance light absorption in Si layer and IPCE at the short wavelengths from 400 to 500 nm. The plasmon-enhanced light absorption of the Si layer results in the improvement of the short-circuit current density in the solar cell with the Bi₂Te₃ nanoplates. Topological insulator-based plasmonics can enhance not only light interaction with semiconductors, but also light absorption of topological insulators. For example, Tamm plasmons generated in BSTS-Bragg mirrors is able to improve light-BSTS interaction with a three-fold enhancement of BSTS light absorption [110].

5 Conclusions

Topological insulators, as new states of quantum matter, have attracted broad attentions in electronics and condensed matter physics due to the generation of phenomena, for instance quantum spin Hall effect, superconductivity, and Majorana fermions [41–43]. These exotic phenomena are attributed to the special band structures of topological insulators. Topological insulators exhibit topologically-protected conducting edge/surface state and insulating bulk state [44]. Due to the band inversion induced by strong spin-orbit coupling, the surface state forms a gapless Dirac cone in the bandgap of bulk. Besides the electronic capacities, the unique optical characteristics and functionalities have been found in topological insulators. For instance, the intrinsic surface-on-bulk structures of topological insulators facilitated the achievement of ultrathin holographic imaging [50]. At the infrared wavelengths, the topological insulators possess ultrahigh refractive indices (see Table 2), larger than traditional infrared materials Si and Ge [57, 65, 82, 111]. With the high-refractive-index topological insulator, the photonic type I Weyl points were observed at optical frequencies [51]. Moreover, the high nonlinear refractive coefficients were reported in topological insulators (see Table 2), larger than the nonlinear coefficient of graphene [66, 112, 113]. The nonlinear features are helpful for the realization of broadband wavelength converters and optical Kerr switchers [66]. The Dirac conducting surface and semiconductor-like bulk contributes to the ultrabroad plasmonic behaviors from the UV to THz region [52–65]. As mentioned above, the 3D topological insulators have exhibited some attractive plasmonic effects, such as Dirac plasmons, SPRs, LPRs, and MPRs [52, 57, 63, 65]. The plasmonic resonances with near-field enhancement promote the application potential of topological insulators in improving light-matter interactions, especially the refractive index monitoring, PL emission, and light harvesting [57, 59, 63, 65]. Meanwhile, TIPs can be used to achieve the CMOS-compatible OAM nanometrology, which is generally unavailable for novel metal-based plasmonics [62]. Different from novel metals, the optical properties of topological insulators can be dynamically tuned through controlling the temperature, light intensity,

Table 2 Refractive indices and nonlinear refractive coefficients of 3D topological insulators at optical wavelengths

Material	Refractive index						Nonlinear refractive coefficient (cm ² /W)
	850 nm		1310 nm		1550 nm		
	<i>n</i>	<i>k</i>	<i>n</i>	<i>k</i>	<i>n</i>	<i>k</i>	
BSTS [53]	4.6	3.0	5.0	1.7	4.9	1.5	
Bi ₂ Te ₃ [82]	5.0	4.5	6.7	3.6	6.9	3.1	~9.16 × 10 ⁻⁶ @ 1526 nm [66]
Sb ₂ Te ₃ [65]	3.8	4.1	6.1	3.2	6.2	2.5	2.606 × 10 ⁻⁵ @ 632.8 nm [112]
BTS [64]	5.6	3.6	6.1	2.2	5.9	2.1	
Bi ₂ Se ₃ [111]	6.1	2.1	5.8	0.8	5.6	0.7	2.26 × 10 ⁻¹⁰ @ 800 nm [113]

BSTS Bi_{1.5}Sb_{0.5}Te_{1.8}Se_{1.2}, BTS Bi₂Te₂Se

and magnetic field [54, 56, 59, 111]. An ultrahigh modulation depth of 2400% was achieved in the Bi₂Se₃ microribbon arrays by tailoring THz plasmon-phonon interference with an optical pump injection [54]. With these advantages, plasmonics in topological insulators will open a new door for optical physics and functional devices. TIPS will become a rapidly developing branch of plasmonics and may find significant applications in nonlinear optics, integrated photonics, and optoelectronics.

Acknowledgements The authors would like to thank the funding support from the National Key R&D Program of China (2017YFA0303800), National Natural Science Foundation of China (11974283, 61705186, 11774290, and 11634010), and Natural Science Basic Research Plan in Shaanxi Province of China (2020JM-130).

References

1. Ebbesen, T., Lezec, H. J., Ghaemi, H. F., Thio, T., & Wolff, P. A. (1998). Extraordinary optical transmission through sub-wavelength hole arrays. *Nature*, *391*, 667–669.
2. Barnes, W. L., Dereux, A., & Ebbesen, T. W. (2003). Surface plasmon subwavelength optics. *Nature*, *424*, 824–830.
3. Genet, C., & Ebbesen, T. W. (2007). Light in tiny holes. *Nature*, *445*, 39–46.
4. Gramotnev, D., & Bozhevolnyi, S. (2010). Plasmonics beyond the diffraction limit. *Nature Photonics*, *4*, 83.
5. Mayer, K. M., & Hafner, J. H. (2011). Localized surface plasmon resonance sensors. *Chemical Reviews*, *111*, 3828–3857.
6. Zhang, S., Genov, D. A., Wang, Y., Liu, M., & Zhang, X. (2008). Plasmon-induced transparency in metamaterials. *Physical Review Letters*, *101*, 047401.
7. Rahmani, M., Luk'yanchuk, B., & Hong, M. (2013). Fano resonance in novel plasmonic nanostructures. *Laser & Photonics Reviews*, *7*, 329–349.
8. Zhan, Y., Lei, D. Y., Li, X., & Maier, S. A. (2014). Plasmonic Fano resonances in nanohole quadrumers for ultrasensitive refractive index sensing. *Nanoscale*, *6*, 4705–4715.
9. Gan, Q., Ding, Y., & Bartoli, F. (2009). ‘Rainbow’ trapping and releasing at telecommunication wavelengths. *Physical Review Letters*, *102*, 056801.
10. Wang, G., Lu, H., & Liu, X. (2012). Trapping of surface plasmon waves in graded grating waveguide system. *Applied Physics Letters*, *101*, 013111.
11. Meng, Y., Zhang, Q., Lei, D., Li, Y., Li, S., Liu, Z., Xie, W., & Leung, C. (2020). Plasmon-induced optical magnetism in an ultrathin metal nanosphere-based dimer-on-film nanocavity. *Laser & Photonics Reviews*, *14*, 2000068.
12. Sorger, V., Oulton, R. F., Ma, R., & Zhang, X. (2012). Toward integrated plasmonic circuits. *MRS Bulletin*, *37*, 728–738.
13. Lu, H., Gan, X., Mao, D., & Zhao, J. (2017). Graphene-supported manipulation of surface plasmon polaritons in metallic nanowaveguides. *Photonics Research*, *5*, 162.
14. Yu, P., Chen, S., Li, J., Cheng, H., Li, Z., Liu, W., Xie, B., Liu, Z., & Tian, J. (2015). Generation of vector beams with arbitrary spatial variation of phase and linear polarization using plasmonic metasurfaces. *Optics Letters*, *40*, 3229–3232.
15. Wei, H., Wang, Z., Tian, X., Käll, M., & Xu, H. X. (2011). Cascaded logic gates in nanophotonic plasmon networks. *Nature Communications*, *2*, 387.
16. Lu, H., Liu, X., Gong, Y., Mao, D., & Wang, L. (2011). Enhancement of transmission efficiency of nanoplasmonic wavelength demultiplexer based on channel drop filters and reflection nanocavities. *Optics Express*, *19*, 12885.

17. Ren, H., Li, X., Zhang, Q., & Gu, M. (2016). On-chip noninterference angular momentum multiplexing of broadband light. *Science*, *352*, 805.
18. Xiao, S., Liu, L., & Qiu, M. (2006). Resonator channel drop filters in a plasmon-polaritons metal. *Optics Express*, *14*, 2932.
19. Lu, H., Liu, X., Mao, D., Wang, L., & Gong, Y. (2010). Tunable band-pass plasmonic waveguide filters with nanodisk resonators. *Optics Express*, *18*, 17922–17927.
20. Li, J., Yu, P., Tang, C., Cheng, H., Li, J., Chen, S., & Tian, J. (2017). Bidirectional perfect absorber using free substrate plasmonic metasurfaces. *Advanced Optical Materials*, *5*, 1700152.
21. Lu, H., Liu, X., Mao, D., & Wang, G. (2012). Plasmonic nanosensor based on Fano resonance in waveguide-coupled resonators. *Optics Letters*, *37*, 3780–3782.
22. Oulton, R. F., Sorger, V. J., Zentgraf, T., Ma, R. M., Gladden, C., Dai, L., Bartal, G., & Zhang, X. (2009). Plasmon lasers at deep subwavelength scale. *Nature*, *461*, 629–632.
23. Ding, K., & Ning, C. (2012). Metallic subwavelength-cavity semiconductor nanolasers. *Light: Science & Applications*, *1*, e20.
24. Kauranen, M., & Zayats, A. V. (2012). Nonlinear plasmonics. *Nature Photonics*, *6*, 737–748.
25. Lu, H., Liu, X., Wang, L., Gong, Y., & Mao, D. (2011). Ultrafast all-optical switching in nanoplasmonic waveguide with Kerr nonlinear resonator. *Optics Express*, *19*, 2910–2915.
26. Berini, P. (2014). Surface plasmon photodetectors and their applications. *Laser & Photonics Reviews*, *8*, 197.
27. Liu, S., Leong, E., Li, G., Hou, Y., Deng, J., Teng, J., Ong, H., & Lei, D. (2016). Polarization-independent multiple Fano resonances in plasmonic nonamers for multimode-matching enhanced multiband second-harmonic generation. *ACS Nano*, *10*, 1442.
28. Zhang, Y., Stokes, N., Jia, B., Fan, S., & Gu, M. (2014). Towards ultra-thin plasmonic silicon wafer solar cells with minimized efficiency loss. *Scientific Reports*, *4*, 4939.
29. Butun, S., Tongay, S., & Aydin, K. (2015). Enhanced light emission from large-area monolayer MoS₂ using plasmonic nanodisk arrays. *Nano Letters*, *15*, 2700.
30. Naik, G. V., Shalae, V. M., & Boltasseva, A. (2013). Alternative plasmonic materials: Beyond gold and silver. *Advanced Materials*, *25*, 3264–3294.
31. Shahzad, M., Medhi, G., Peale, R. E., Buchwald, W. R., Cleary, J. W., Soref, R., Boreman, G. D., & Edwards, O. (2011). Infrared surface plasmons on heavily doped silicon. *Journal of Applied Physics*, *110*, 123105.
32. Naik, G., & Boltasseva, A. (2010). Semiconductors for plasmonics and metamaterials. *Physica Status Solidi RRL*, *4*, 295–297.
33. Jablan, M., Buljan, H., & Soljačić, M. (2009). Plasmonics in graphene at infrared frequencies. *Physical Review B*, *80*, 245435.
34. Fei, Z., Rodin, A. S., Andreev, G. O., Bao, W., McLeod, A. S., Wagner, M., Zhang, L. M., Zhao, Z., Thieme, M., Dominguez, G., Fogler, M. M., Castro Neto, A. H., Lau, C. N., Keilmann, F., & Basov, D. N. (2012). Gate-tuning of graphene plasmons revealed by infrared nano-imaging. *Nature*, *487*, 82–85.
35. de Abajo, F. J. G. (2014). Graphene plasmonics: Challenges and opportunities. *ACS Photonics*, *1*, 135–152.
36. Lu, H., Zeng, C., Zhang, Q., Liu, X., Hossain, M. M., Reineck, P., & Gu, M. (2015). Graphene-based active slow surface plasmon polaritons. *Scientific Reports*, *5*, 8443.
37. Rodrigo, D., Limaj, O., Janner, D., Etezadi, D., García de Abajo, F. J., Pruneri, V., & Altug, H. (2015). Mid-infrared plasmonic biosensing with graphene. *Science*, *349*, 165–168.
38. Gan, X., Shiu, R., Gao, Y., Meric, I., Heinz, T., Shepard, K., Hone, J., Assefa, S., & Englund, D. (2013). Chip-integrated ultrafast graphene photodetector with high responsivity. *Nature Photonics*, *7*, 883–887.
39. Pospischil, A., Humer, M., Furchi, M. M., Bachmann, D., Guider, R., Fromherz, T., & Mueller, T. (2013). CMOS-compatible graphene photodetector covering all optical communication bands. *Nature Photonics*, *7*, 892–896.

40. Zhang, Q., Li, X., Hossain, M. M., Xue, Y., Zhang, J., Song, J., Liu, J., Turner, M. D., Fan, S., Bao, Q., & Gu, M. (2015). Graphene surface plasmons at the near-infrared optical regime. *Scientific Reports*, *4*, 6559.
41. Bernevig, B., Hughes, T., & Zhang, S. (2006). Quantum spin Hall effect and topological phase transition in HgTe quantum wells. *Science*, *314*, 1757–1761.
42. König, M., Wiedmann, S., Brüne, C., Roth, A., Buhmann, H., Molenkamp, L., Qi, X., & Zhang, S. (2007). Quantum spin Hall insulator state in HgTe quantum wells. *Science*, *318*, 766–770.
43. Hasan, M., & Kane, C. (2010). Colloquium: Topological insulators. *Reviews of Modern Physics*, *82*, 3045–3067.
44. Moore, J. E. (2010). The birth of topological insulators. *Nature*, *464*, 194.
45. Zhang, H., Liu, C., Qi, X., Dai, X., Fang, Z., & Zhang, S. (2009). Topological insulators in Bi₂Se₃, Bi₂Te₃ and Sb₂Te₃ with a single Dirac cone on the surface. *Nature Physics*, *5*, 438–442.
46. Ando, Y. (2013). Topological insulator materials. *Journal of the Physical Society of Japan*, *82*, 102001.
47. Kong, D., Chen, Y., Cha, J., Zhang, Q., Analytis, J. G., Lai, K., Liu, Z., Hong, S., Koski, K., Kwan, S., Hussain, Z., Fisher, I., Shen, Z., & Cui, Y. (2011). Ambipolar field effect in the ternary topological insulator (Bi_xSb_{1-x})₂Te₃ by composition tuning. *Nature Nanotechnology*, *6*, 705–709.
48. Tang, F., Po, H., Vishwanath, A., & Wan, X. (2019). Comprehensive search for topological materials using symmetry indicators. *Nature*, *566*, 486.
49. Vergniory, M., Elcoro, L., Felser, C., Bernevig, B., & Wang, Z. (2019). A complete catalogue of high-quality topological materials. *Nature*, *566*, 480.
50. Yue, Z., Xue, G., Liu, J., Wang, Y., & Gu, M. (2017). Nanometric holograms based on a topological insulator material. *Nature Communications*, *8*, 15354.
51. Goi, E., Yue, Z. J., Cumming, B. P., & Gu, M. (2017). Observation of type I photonic Weyl points in optical frequencies. *Laser & Photonics Reviews*, *12*, 1700271.
52. Pietro, P., Ortolani, M., Limaj, O., Gaspare, A., Giliberti, V., Giorgianni, F., Brahlek, M., Bansal, N., Koirala, N., Oh, S., Calvani, P., & Lupi, S. (2013). Observation of Dirac plasmons in a topological insulator. *Nature Nanotechnology*, *8*, 556.
53. Ou, J., So, J., Adamo, G., Sulaev, A., Wang, L., & Zheludev, N. (2014). Ultraviolet and visible range plasmonics in the topological insulator Bi_{1.5}Sb_{0.5}Te_{1.8}Se_{1.2}. *Nature Communications*, *5*, 5139.
54. Sim, S., Jang, H., Koirala, N., Brahlek, M., Moon, J., Sung, J., Park, J., Cha, S., Oh, S., Jo, M., Ahn, J., & Choi, H. (2015). Ultra-high modulation depth exceeding 2,400% in optically controlled topological surface plasmons. *Nature Communications*, *6*, 9814.
55. Zhao, M., Bosman, M., Danesh, M., Zeng, M., Song, P., Darma, Y., Rusydi, A., Lin, H., Qiu, C., & Loh, K. (2015). Visible surface plasmon modes in single Bi₂Te₃ nanoplate. *Nano Letters*, *15*, 8331–8335.
56. Autore, M., Engelkamp, H., Apuzzo, F., Gaspare, A., Pietro, P., Vecchio, I. L., Brahlek, M., Koirala, N., Oh, S., & Lupi, S. (2015). Observation of magnetoplasmons in Bi₂Se₃ topological insulator. *ACS Photonics*, *2*, 1231–1235.
57. Yue, Z., Cai, B., Wang, L., Wang, X., & Gu, M. (2016). Intrinsically core-shell plasmonic dielectric nanostructures with ultrahigh refractive index. *Science Advances*, *2*, e1501536.
58. Guozhi, J., Peng, W., Yanbang, Z., & Kai, C. (2016). Localized surface plasmon enhanced photothermal conversion in Bi₂Se₃ topological insulator nanoflowers. *Scientific Reports*, *6*, 25884.
59. Zhao, M., Zhang, J., Gao, N., Song, P., Bosman, M., Peng, B., Sun, B., Qiu, C., Xu, Q., Bao, Q., & Loh, K. (2016). Actively tunable visible surface plasmons in Bi₂Te₃ and their energy-harvesting applications. *Advanced Materials*, *28*, 3138–3144.
60. Yuan, J., Ma, W., Zhang, L., Lu, Y., Zhao, M., Guo, H., Zhao, J., Yu, W., Zhang, Y., Zhang, K., Hoh, H., Li, X., Loh, K., Li, S., Qiu, C., & Bao, Q. (2017). Infrared nanoimaging reveals the surface metallic plasmons in topological insulator. *ACS Photonics*, *4*, 3055–3062.

61. Dubrovkin, A., Adamo, G., Yin, J., Wang, L., Soci, C., Wang, Q., & Zheludev, N. (2017). Visible range plasmonic modes on topological insulator nanostructures. *Advanced Optical Materials*, 5, 1600768.
62. Yue, Z., Ren, H., Wei, S., Lin, J., & Gu, M. (2018). Angular-momentum nanometrology in an ultrathin plasmonic topological insulator film. *Nature Communications*, 9, 4413.
63. Lu, H., Dai, S., Yue, Z., Fan, Y., Cheng, H., Di, J., Mao, D., Li, E., Mei, T., & Zhao, J. (2019). Sb₂Te₃ topological insulator: Surface plasmon resonance and application in refractive index monitoring. *Nanoscale*, 11, 4759–4766.
64. Venuthurumilli, P. K., Wen, X., Iyer, V., Chen, Y. P., & Xu, X. (2019). Near-field imaging of surface plasmons from the bulk and surface state of topological insulator Bi₂Te₂Se. *ACS Photonics*, 6, 2492–2498.
65. Lu, H., Yue, Z., Li, Y., Zhang, Y., Zhang, M., Zeng, W., Gan, X., Mao, D., Xiao, F., Mei, T., Zhao, W., Wang, X., Gu, M., & Zhao, J. (2020). Magnetic plasmon resonances in nanostructured topological insulators for strongly enhanced light-MoS₂ interactions. *Light: Science & Applications*, 9, 191.
66. Chen, S., Miao, L., Chen, X., Chen, Y., Zhao, C., Datta, S., Li, Y., Bao, Q., Zhang, H., Liu, Y., Wen, S., & Fan, D. (2015). Few-layer topological insulator for all-optical signal processing using the nonlinear Kerr effect. *Advanced Optical Materials*, 3, 1769–1778.
67. Mao, D., Jiang, B., Gan, X., Ma, C., Chen, Y., Zhao, C., Zhang, H., Zheng, J., & Zhao, J. (2015). Soliton fiber laser mode locked with two types of film-based Bi₂Te₃ saturable absorbers. *Photonics Research*, 3, A43–A46.
68. Yue, Z., Wang, X., & Gu, M. (2019). Topological insulator materials for advanced optoelectronic devices. *arXiv: Optics*, 45–70.
69. Miao, R., Hu, Y., Ouyang, H., Tang, Y., Zhang, C., You, J., Zheng, X., Xu, Z., Cheng, X., & Jiang, T. (2019). A polarized nonlinear optical response in a topological insulator Bi₂Se₃-Au nanoantenna hybrid-structure for all-optical switching. *Nanoscale*, 11, 14598.
70. Yue, Z., Zhao, W., Cortie, D., Yang, G., Li, Z., & Wang, X. (2019). Modulation of crystal and electronic structures in topological insulators by rare-earth doping. *ACS Applied Electronic Materials*, 1, 1929–1936.
71. Liu, T., Deng, H., Zhou, H. W., Zhang, J., Liu, J., Yang, P., & Chu, J. (2015). Structural, optical and electrical properties of Sb₂Te₃ films prepared by pulsed laser deposition. *Journal of Crystal Growth*, 416, 78–81.
72. Lanius, M., Kampmeier, J., Kölling, S., Mussler, G., Koenraad, P. M., & Grützmacher, D. (2016). Topography and structure of ultrathin topological insulator Sb₂Te₃ films on Si(111) grown by means of molecular beam epitaxy. *Journal of Crystal Growth*, 453, 158–162.
73. Kong, D., Dang, W., Cha, J., Li, H., Meister, S., Peng, H., Liu, Z., & Cui, Y. (2010). Few-layer nanoplates of Bi₂Se₃ and Bi₂Te₃ with highly tunable chemical potential. *Nano Letters*, 10, 2245–2250.
74. Song, J., Xia, F., Zhao, M., Zhong, Y., Li, W., Loh, K. P., Caruso, R. A., & Bao, Q. (2015). Solvothermal growth of bismuth chalcogenide nanoplatelets by the oriented attachment mechanism: An in Situ PXRD Study. *Chemistry of Materials*, 27, 3471–3482.
75. Mntungwa, N., Rajasekhar, P., Ramasamy, K., & Revaprasadu, N. (2014). A simple route to Bi₂Se₃ and Bi₂Te₃ nanocrystals. *Superlattices and Microstructures*, 69, 226–230.
76. Tan, C., Wang, Q., & Fu, X. (2014). Topological insulator Sb₂Te₃ as an optical media for the generation of ring-shaped beams. *Optical Materials Express*, 4, 2016.
77. Chen, Y., Analytis, J., Chu, J., Liu, Z., Mo, S., Qi, X., Zhang, H., Lu, D. H., Dai, X., Fang, Z., Zhang, S. C., Fisher, I. R., Hussain, Z., & Shen, Z. (2009). Experimental realization of a three-dimensional topological insulator, Bi₂Te₃. *Science*, 325, 178–181.
78. Xia, Y., Qian, D., Hsieh, D., Wray, L., Pal, A., Lin, H., Bansil, A., Grauer, D., Hor, Y. S., Cava, R. J., & Hasan, M. Z. (2009). Observation of a large-gap topological-insulator class with a single Dirac cone on the surface. *Nature Physics*, 5, 398–402.

79. Hsieh, D., Xia, Y., Qian, D., Wray, L., Meier, F., Dil, J. H., Osterwalder, J., Patthey, L., Fedorov, A. V., Lin, H., Bansil, A., Grauer, D., Hor, Y. S., Cava, R. J., & Hasan, M. Z. (2009). Observation of time-reversal-protected single-Dirac-cone topological-insulator states in Bi_2Te_3 and Sb_2Te_3 . *Physical Review Letters*, *103*, 146401.
80. Palik, E. D. (1991). *Handbook of optical constant of solids II* (pp. 151–166). Academic.
81. Jellison, G., & Modine, F. (1996). Parameterization of the optical functions of amorphous materials in the interband region. *Applied Physics Letters*, *69*, 371.
82. Krishnamoorthy, H., Adamo, G., Yin, J., Savinov, V., Zheludev, N. I., & Soci, C. (2020). Infrared dielectric metamaterials from high refractive index chalcogenides. *Nature Communications*, *11*, 1692.
83. Yin, J., Krishnamoorthy, H., Adamo, G., Dubrovkin, A. M., Chong, Y., Zheludev, N., & Soci, C. (2017). Plasmonics of topological insulators at optical frequencies. *NPG Asia Materials*, *9*, e425.
84. Dressel, M., & Grüner, G. (2002). *Electrodynamics of solids*. Cambridge University Press.
85. Autore, M., D'Apuzzo, F., Gaspare, A. D., Giliberti, V., Limaj, O., Roy, P., Brahlek, M., Koirala, N., Oh, S., Abajo, F. J. G., & Lupi, S. (2015). Plasmon-phonon interactions in topological insulator microrings. *Advanced Optical Materials*, *3*, 1257–1263.
86. Autore, M., Pietro, P., Gaspare, A., Apuzzo, F., Giorgianni, F., Brahlek, M., Koirala, N., Oh, S., & Lupi, S. (2017). Terahertz plasmonic excitations in Bi_2Se_3 topological insulator. *Journal of Physics: Condensed Matter*, *29*, 183002.
87. Cao, Y., Waugh, J., Zhang, X., Luo, J., Wang, Q., Reber, T., Mo, S., Xu, Z., Yang, A., Schneeloch, J., Gu, G., Brahlek, M., Bansal, N., Oh, S., Zunger, A., & Dessau, D. (2013). Mapping the orbital wavefunction of the surface states in three-dimensional topological insulators. *Nature Physics*, *9*, 499–504.
88. Zayats, A., & Smolyaninov, I. (2003). Near-field photonics: Surface plasmons polaritons and localized surface plasmons. *Journal of Optics A: Pure and Applied Optics*, *5*, S16.
89. Maier, S., & Atwater, H. (2005). Plasmonics: Localization and guiding of electromagnetic energy in metal/dielectric structures. *Journal of Applied Physics*, *98*, 011101.
90. Smith, D., Pendry, J., & Wiltshire, M. (2004). Metamaterials and negative refractive index. *Science*, *305*, 788–792.
91. Yen, T., Padilla, W., Fang, N., Vier, D. C., Smith, D. R., Pendry, J., Basov, D. N., & Zhang, X. (2004). Terahertz magnetic response from artificial materials. *Science*, *303*, 1494–1496.
92. Zhou, J., Koschny, T., Kafesaki, M., Economou, E. N., Pendry, J. B., & Soukoulis, C. (2005). Saturation of the magnetic response of split-ring resonators at optical frequencies. *Physical Review Letters*, *95*, 223902.
93. Grigorenko, A., Geim, A., Gleeson, H., Zhang, Y., Firsov, A., Khrushchev, I., & Petrovic, J. (2005). Nanofabricated media with negative permeability at visible frequencies. *Nature*, *438*, 335.
94. Shafiei, F., Monticone, F., Le, K., Liu, X., Hartsfield, T., Alù, A., & Li, X. (2013). A subwavelength plasmonic metamolecule exhibiting magnetic-based optical Fano resonance. *Nature Nanotechnology*, *8*, 95–99.
95. Chen, S., Zhang, Y., Shih, T., Yang, W., Hu, S., Hu, X., Li, J., Ren, B., Mao, B., Yang, Z., & Tian, Z. (2018). Plasmon-induced magnetic resonance enhanced Raman spectroscopy. *Nano Letters*, *18*, 2209.
96. Sarychev, A., Shvets, G., & Shalaev, V. (2006). Magnetic plasmon resonance. *Physical Review E*, *73*, 036609.
97. Papasimakis, N., Thongrattanasiri, S., Zheludev, N., & Abajo, F. (2013). The magnetic response of graphene split-ring metamaterials. *Light: Science & Applications*, *2*, e78.
98. Dai, S., Lu, H., Zhang, J., Shi, Y., Dou, J., Di, J., & Zhao, J. (2019). Complex refractive index measurement for atomic-layer materials via surface plasmon resonance holographic microscopy. *Optics Letters*, *44*, 2982–2985.
99. Kabashin, A. V., Patskovsky, S., & Grigorenko, A. (2009). Phase and amplitude sensitivities in surface plasmon resonance bio and chemical sensing. *Optics Express*, *17*, 21191–21204.

100. Dai, S., Zhang, J., Lu, H., Xi, T., Ma, C., Li, Y., Di, J., & Zhao, J. (2018). Integrated digital holographic microscopy based on surface plasmon resonance. *Optics Express*, *26*, 25437–25445.
101. Li, S., & Zhong, J. (2012). Simultaneous amplitude-contrast and phase-contrast surface plasmon resonance imaging by use of digital holography. *Biomedical Optics Express*, *3*, 3190–3202.
102. Abbas, A., Linman, M., & Cheng, Q. (2011). Sensitivity comparison of surface plasmon resonance and plasmon-waveguide resonance biosensors. *Sensors & Actuators, B: Chemical*, *156*, 169–175.
103. Xia, F., Wang, H., Xiao, D., Dubey, M., & Ramasubramaniam, A. (2014). Two-dimensional material nanophotonics. *Nature Photonics*, *8*, 899–907.
104. Sun, Z., & Chang, H. (2014). Graphene and graphene-like two-dimensional materials in photodetection: Mechanisms and methodology. *ACS Nano*, *8*, 4133.
105. Lopez-Sanchez, O., Lembke, D., Kayci, M., Radenovic, A., & Kis, A. (2013). Ultrasensitive photodetectors based on monolayer MoS₂. *Nature Nanotechnology*, *8*, 497–501.
106. Splendiani, A., Sun, L., Zhang, Y., Li, T., Kim, J., Chim, C., Galli, G., & Wang, F. (2010). Emerging photoluminescence in monolayer MoS₂. *Nano Letters*, *10*, 1271.
107. Liao, F., Yu, J., Gu, Z., Yang, Z., Hasan, T., Linghu, S., Peng, J., Fang, W., Zhuang, S., Gu, M., & Gu, F. (2019). Enhancing monolayer photoluminescence on optical micro/nanofibers for low-threshold lasing. *Science Advances*, *5*, eaax7398.
108. Li, J., Ji, Q., Chu, S., Zhang, Y., Li, Y., Gong, Q., Liu, K., & Shi, K. (2016). Tuning the photo-response in monolayer MoS₂ by plasmonic nano-antenna. *Scientific Reports*, *6*, 23626.
109. Liao, Z., Han, B., Wu, H., Yashina, L., Yan, Y., Zhou, Y., Bie, Y., Bozhko, S., Fleischer, K., Shvets, I., Zhao, Q., & Yu, D. (2012). Surface plasmon on topological insulator/dielectric interface enhanced ZnO ultraviolet photoluminescence. *AIP Advances*, *2*, 022105.
110. Lu, H., Li, Y., Yue, Z., Mao, D., & Zhao, J. (2019). Topological insulator based Tamm plasmon polaritons. *APL Photonics*, *4*, 040801.
111. Whitcher, T., Silly, M., Yang, M., Kumar Das, P., Peyrot, D., Chi, X., Eddrief, M., Moon, J., Oh, S., Castro-Neto, A., Breese, M., Wee, A., Silly, F., & Rusydi, A. (2020). Correlated plasmons in the topological insulator Bi₂Se₃ induced by long-range electron correlations. *NPG Asia Materials*, *12*, 37.
112. Liu, J., Liu, S., & Wei, J. (2010). Origin of the giant optical nonlinearity of Sb₂Te₃ phase change materials. *Applied Physics Letters*, *97*, 261903.
113. Lu, S., Zhao, C., Zou, Y., Chen, S., Chen, Y., Li, Y., Zhang, H., Wen, S., & Tang, D. (2013). Third order nonlinear optical property of Bi₂Se₃. *Optics Express*, *21*, 2072–2082.

Advanced Applications of Nonlinear Plasmonics



Ming Fang, Qun Ren, Jianwei You, Zhihao Lan, Zhixiang Huang,
and Wei E. I. Sha

Abstract The nonlinear optical effects originating from the light-matter interaction under intense light excitations have enabled numerous novel applications, such as frequency conversion, all-optical modulation, and ultrafast optical switching. Recent years, the development of metamaterials, photonic crystals, and topological optics allow unconventional enhanced nonlinear effects that may potentially exceed traditional nonlinear materials. In this chapter, we discuss the concepts of nonlinear optical effects and introduce several nonlinear optical applications, including broadband terahertz source based on plasmonic metasurfaces, nonlinear Fano resonances, and nonlinear interaction of topological graphene plasmons.

Keywords Nonlinear optics · Plasmonic metamaterials · Terahertz generation · Fano resonances · Topological optics · Graphene

M. Fang · Z. Huang

Key Laboratory of Intelligent Computing and Signal Processing, Ministry of Education, Anhui University, Hefei, Anhui, China

Institute of Physical Science and Information Technology, Anhui University, Hefei, Anhui, China

Key Laboratory of Electromagnetic Environmental Sensing, Department of Education of Anhui Province, Hefei, Anhui, China

Q. Ren

School of Electrical and Information Engineering, Tianjin University, Tianjin, China

J. You

State Key Laboratory of Millimeter Waves, Southeast University, Nanjing, Jiangsu, China

Z. Lan

Department of Electronic and Electrical Engineering, University College London, London, UK

W. E. I. Sha (✉)

State Key Laboratory of Modern Optical Instrumentation, College of Information Science and Electronic Engineering, Zhejiang University, Hangzhou, China

e-mail: weisha@zju.edu.cn

© The Author(s), under exclusive license to Springer Nature Switzerland AG 2022

P. Yu et al. (eds.), *Plasmon-enhanced light-matter interactions*,

Lecture Notes in Nanoscale Science and Technology 31,

https://doi.org/10.1007/978-3-030-87544-2_5

1 Introduction

With the development of lasers, the nonlinear interaction between light and matter becomes accessible. Despite the weakness of the nonlinear response, intrinsic nonlinear effect of materials is essential for optical signal processing in photonic integrated circuits and provide opportunities to develop numerous modern applications from the second- and third-order nonlinear processes, optical parametric amplification lasers to optical solitons, holography, and self-modulation of optical signals, as well as parametric down-conversion. Recent developments of plasmonic modes in metals and their nanostructures have been widely used to improve the efficiency of linear light-matter interaction [1–7]. The excitation of plasmonic modes, either surface plasmon plasmons (SPPs) or localized surface plasmons (LSPs) in metal nanoparticles, enables electromagnetic field confinement near metal-dielectric interfaces, leading to the local field enhancement. The presence of plasmonic resonances, strongly enhanced near the metal-dielectric interface, has profound implications for nonlinear optics, which depends on the linear field intensity in a superlinear manner [8, 9].

Recent developments of nonlinear plasmonics take advantages of the linear plasmonic resonances described above and operate linear and nonlinear dynamics on subwavelength scales; Thus, they are naturally compatible with integrated optics. There are two concepts to utilize plasmonic excitations in nonlinear plasmonic systems. One scenario is to enhance the nonlinear conversion efficiency of dielectrics by the strong localized field near the metal interface in the metal-dielectric hybrid system. The other is to generate the nonlinear response from the dynamic motion of free electrons in metals then harvest the nonlinearity of metal itself. Both concepts are explored to enhance coherent nonlinear interaction and require a universal description of complex linear and nonlinear dynamics of free electrons.

A full hydrodynamic consideration of free electrons reveals key contributions to the nonlinear effects caused by the interplay between the nonlinear response of the fermionic gas and metallic structures with arbitrary geometries, allowing for investigation of nonlinearities in plasmonics. In this chapter, we first present efficient and broadband terahertz (THz) generation from plasmonic metasurfaces. The THz generation due to optical rectification (OR) originating from the second-order nonlinearity of symmetry-breaking meta-atoms is numerically investigated by a first-principle calculation. Then we give an overall review of the nonlinear plasmonic response and their intrinsic connections with bound states in the continuum (BIC) modes in plasmonic nanomaterials, which can extend the lifetime of plasmonic excitation and therefore enhance the nonlinear optical processes such as second harmonic generation (SHG), third harmonic generation (THG), and surface enhanced Raman scattering (SERS). Finally, we show that topologically protected one-way edge nonlinear plasmons up to infrared frequencies could be realized in a periodically nanostructured graphene monolayer under the time-reversal-symmetry breaking induced by a static magnetic field.

2 Broadband THz Generation from Nonlinear Metasurfaces

A novel broadband THz source based on a single layer metasurface made of gold split-ring resonators (SRRs) has been reported in a recent experimental study [10]. The SRRs with a just 40 nm thickness were designed to have magnetic-dipole resonances around the optical communication wavelength of 1550 nm. By exciting the metasurface with an infrared femtosecond laser pulse, efficient THz emission can be observed due to the nonlinear optical rectification in SRRs. The measured THz conversion efficiency from the metasurface is in the same order as the zinc telluride nonlinear crystals which are generally used for broadband THz generation. The single-layer metasurface is made of gold and glass, making it have deficient absorption in the THz frequency region. Thus, the metasurface can be used to generate broadband THz signals. In an analytical theory, we can predict the generated THz wave from the metasurface by omitting the thickness of the metasurface. The wave equation can describe the generated THz field in a nonlinear medium with the second-order nonlinear susceptibility $\chi^{(2)}$ propagating in the z -axis

$$\frac{\partial^2 E_{THz}(z, t)}{\partial z^2} - \frac{n_{THz}^2}{c^2} \frac{\partial^2 E_{THz}(z, t)}{\partial t^2} = \frac{1}{\epsilon_0 c^2} \frac{\partial^2 P_{THz}^{(2)}(z, t)}{\partial t^2} = \frac{\chi^{(2)}}{c^2} \frac{\partial^2 |E_0(z, t)|^2}{\partial t^2}, \quad (1)$$

where n is the medium refractive index at the THz frequencies, c is the speed of light. The THz polarization is proportional to the power of the pump laser $|E_0(z, t)|^2$. The pump laser is a temporal Gaussian pulse $E_0(t) = \cos(\omega_0 t + \phi)g_\sigma(t)$ $E(t) = \cos(\omega_0 t + \phi)g(t)$. Here $g_\sigma(t) = e^{-\frac{1}{2}\sigma^2 t^2} \iff g_\sigma(\omega) = \left(\sqrt{2\pi}/\sigma\right) e^{-\frac{\omega^2}{2\sigma^2}}$ is a Gaussian envelope. ω_0 is the center frequency of the pump pulse, and ϕ is a phase delay. The full width at half maximum (FWHM) of the pump pulse is $\Delta f_{FWHM}^{pump} \approx 2.335\sigma$ $\Delta t_{FWHM}^{pump} \approx 2.355\sigma$. THz generation from the infinitesimal thin nonlinear metasurface can be expressed as

$$\begin{aligned} P^{(2)}(t) &\sim E^2(t) = \cos(2\omega_0 t + 2\phi) g_\sigma^2(t) + g_\sigma^2(t) \iff \\ P^{(2)}(\omega) &\sim e^{2i\phi} g_{\frac{1}{\sqrt{2}\sigma}}(w - 2w_0) + e^{-2i\phi} g_{\frac{1}{\sqrt{2}\sigma}}(-w - 2w_0) + g_{\frac{1}{\sqrt{2}\sigma}}(w). \end{aligned} \quad (2)$$

We can see the first two terms are the SHG with a center frequency of $2\omega_0$; the last term is the origin of the THz emission; thus, the THz emission only depends on the temporal Gaussian envelope. Consequently, the emitted THz field is written as

$$\begin{aligned} E^{(THz)}(\omega) &\sim c^{(2)}(-i\omega)^2 g_{\frac{1}{\sqrt{2}\sigma}}(w) = c^{(2)}\omega^2 e^{-\frac{\omega^2}{4\sigma^2}} \iff \\ E^{(THz)}(t) &\sim -c^{(2)}\partial_t^2 g_{\sqrt{2}\sigma}(t) = c^{(2)}\sigma^2 (1 - 2\sigma^2 t^2) e^{-\sigma^2 t^2}. \end{aligned} \quad (3)$$

From Eq. (3), we can see that the bandwidth of THz emission is limited mainly by the duration of the incident pulse. The THz emission has a peak frequency

$f_0^{THz} = 2\sigma f_0^{THz} = 2\sigma$ and a bandwidth $\Delta f_{FWHM}^{THz} = 2.31\sigma \Delta f_{FWHM}^{THz} \approx 2.31\sigma$. We can theoretically estimate the peak frequency and bandwidth of the THz emission by the bandwidth of pump pulse, i.e., $\Delta f_{FWHM}^{THz} \approx 0.98\Delta f_{FWHM}^{pump}$, $\Delta f_{FWHM}^{THz} \approx 0.98\Delta f_{FWHM}^{pump}$ and $f_0^{THz} \approx 0.85\Delta f_{FWHM}^{pump}$, $f_0^{THz} \approx 0.85\Delta f_{FWHM}^{pump}$. The bandwidth of the generated THz spectrum can be tuned by changing the duration of the incident Gaussian pulse. One can see that THz emission bandwidth and central frequency scale linearly with the pump pulse bandwidth. Comparing with the nonlinear crystals, the single-layer metasurface emitter is free from the limitation of the Reststrahlen region [11]. Therefore, it can achieve tunable THz bandwidth by changing the pump pulse duration. Moreover, the fundamental pumping frequency of the metasurface THz emitter is flexible and can easily be scaled to arbitrary operation frequencies by optimizing the dimensions of the SRR unit.

However, due to the fact that the upper cut-off frequency of the inorganic crystal detector used in the experiments is much smaller than the emitted THz signal, the measured bandwidth of the THz signal was much narrower than expected from the analytical solution. Consequently, it is important to investigate the mechanism of the THz emission from nonlinear metasurfaces by a first-principle method. When an intense electromagnetic field illuminates a plasmonic nanostructure, it can interact with free electrons in the plasmonic material resulting in intrinsic nonlinear behaviors. The nonlinear response of the conduction-band electrons in plasmonic structures can be modeled by self-consistently solving Maxwell's equations and hydrodynamic model. The interaction of electromagnetic fields with an arbitrary nonmagnetic material can be described by Maxwell's equation:

$$\begin{aligned}\nabla \times \mathbf{H} &= \varepsilon_0 \partial_t \mathbf{E} + \mathbf{J} \\ \nabla \times \mathbf{E} &= -\mu_0 \partial_t \mathbf{H},\end{aligned}\quad (4)$$

where ε_0 and μ_0 are the vacuum permittivity and permeability. The hydrodynamic model can describe the complex dynamics of electrons in metallic/plasmonic materials driven by an external field (Lorentz force):

$$\begin{aligned}[\partial_t + \mathbf{v} \cdot \nabla] \mathbf{v} &= -\gamma \mathbf{v} - \frac{e}{m_e} [\mathbf{E} + \mathbf{v} \times \mathbf{B}] - \frac{\nabla p}{n} \\ \partial_t n &= -\nabla \cdot (n\mathbf{v}).\end{aligned}\quad (5)$$

Maxwell's equation and hydrodynamic equations can be coupled through the polarization density, electron density, and velocity:

$$\mathbf{J} = \partial_t \mathbf{P} = -en\mathbf{v}.\quad (6)$$

With the help of the FDTD algorithm, Eqs. (4), (5) and (6) can be solved self-consistently, and both linear, nonlocal, and nonlinear responses can be captured [12–17].

The efficient and compact metasurface THz emitter is shown in Fig. 1a. The gold SRRs are arranged periodically in both x and y directions and supported by

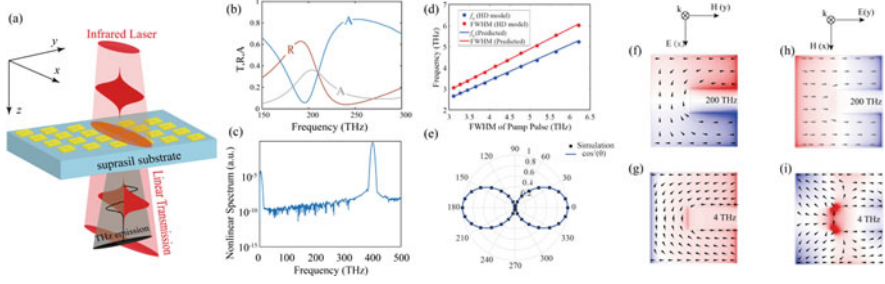


Fig. 1 (a) Layout of a metasurface consisting of a periodic array of SRRs. (b) The feature size of a unit cell. (c) Semilog plot of the nonlinear signal spectrum. (d) The FWHM of pump pulse versus the generated THz spectral bandwidth (red dots) and peak frequency (blue dots). The straight lines are the predicted analytical results. (e) Polar plot of the peak-to-peak amplitude of THz emission as a function of the polarization angle. (f–i) Current and charge density distributions in two SRRs at the frequencies of linear response (200 THz) and THz generation (4 THz)

a glass substrate coated with ITO. The thickness of the gold film, ITO, and SiO₂ substrates are 40 nm, 6 nm, and 200 nm, respectively. The glass substrate and ITO layer are chosen as non-dispersive dielectric materials of relative permittivities 2.25 and 3.8. The parameters for gold are taken to be $n_0 = 5.92 \times 10^{28} \text{ m}^{-3}$ and $\gamma = 10.68 \times 10^{13} \text{ rad/s}$. The dimensions of the SRRs are the same as the experimental sample [10], for which the magnetic dipole can be excited around 200 THz as shown in Fig. 1b. An x-polarized infrared laser pulse propagating in the z-direction. We describe the pump laser by a Gaussian pulse of the form $E(t) = E_0 \exp[-2 \ln 2(t - t_0)^2/\tau^2] \cos(\omega t)$. Here, the driving frequency, temporal width and peak amplitude are chosen as $\omega = 1.257 \times 10^{15} \text{ rad/s}$, $\tau = 140 \text{ fs}$ and $E_0 = 2 \times 10^7 \text{ V/m}$, respectively. Figure 1c shows the second-order nonlinear spectrum with the two peaks: the sum-frequency generation has a peak around 400 THz and difference-frequency generation spectrum shows a peak in the THz region. Figure 1d compares the THz emission bandwidth $\Delta f^{\text{THz}}/\Delta f^{\text{THz}}$ and central frequency $f_0^{\text{THz}}/f_0^{\text{THz}}$ from the metasurface versus the incident pulse bandwidth $\Delta f^{\text{inc}} \approx 0.44/\tau \Delta f^{\text{inc}} \approx \frac{0.44}{\tau}$. The first-principle FDTD calculation results agree well with the analytical solution. In contrast, when the polarization is perpendicular to the gap of SRRs (along the x-axis), the excitation of the circular current is forbidden by symmetry and only straight-line linear currents are induced in the SRR arms. Then, the nonlinear currents in the two arms show reverse flow directions along the x-axis, leading to the vanishing of radiation in the far-field. Consequently, the proposed THz emitter indeed has a polarization dependence. Figure 1e shows the polar plot of the peak-to-peak amplitude of THz signals versus the polarization angle. We can see that the simulated results fit very well with $\cos^2(\theta)$, consistent with the polarization control from SRR metasurface reported in [10].

The calculated charge and current distributions at the frequencies of 4 THz and 200 THz were plotted in Figs. 1f–i. Figures 1f, h shows the fundamental field distributions for the normal incidence to the SRR. When the polarization of the

incident wave is parallel to the gap of SRRs (along the x -direction), the nonlinear currents in both arms are parallel along the y -direction and thus strong radiation fields can be observed in the far field as depicted in Fig. 1g. Differently, when the polarization is perpendicular to the gap of SRRs, the nonlinear currents show reverse flow directions along the y -direction, leading to a vanishing radiation in the far field as shown in Fig. 1i.

Despite of being a seminal progress toward compact tailorable THz sources benefiting next-generation computation and communication, the nonlinear optical response reported in [10] is still fairly weak. Therefore, a fundamental improvement in nonlinear efficiency with metasurface-based devices is critical. In order to improve the THz conversion efficiency, instead of driving the SRR directly, a resonant dark bound state in a silicon film with a sub-wavelength thickness was used to create local field enhancement and the strong evanescent surface fields of this quasisurface mode then drive the SRRs [18]. The low-loss dielectric dark state allows to concentrate intense field energy in the metasurface leading to a strong local field enhancement. Figure 2a shows the schematic unit of dark-state metasurface THz source. Two gold SRRs oriented in the same direction asymmetrically sit on the two sides of a thin Si slab, which is periodically punctuated by metal walls. The two SRRs are not only the key element for THz emission via difference frequency generation, but also serve as a bridge coupling the incident wave into the dark element (Si slab). The introduction of metal walls is to quantize the modes of the dielectric slab achieving a set of discrete resonant dark states (see Fig. 2b). The $TE_{2,0}$ mode marked by a red circle in Fig. 2b, which gives an antisymmetric profile of the electric field as shown in Fig. 2a. By shifting the positions of the two SRRs, i.e., Δx_1 and Δx_2 , the energy of excitation exchanged to the dark state indeed can be controlled purposely. Upon the excitation of the $TE_{2,0}$ mode in the Si slab, out-of-phase polarization currents \mathbf{I}_1 and \mathbf{I}_2 are induced in the two SRRs, which can be decomposed to symmetric (corresponding to an electric moment along the y axis) and antisymmetric (corresponding to a magnetic moment along the x axis) polarization sets, respectively, as shown in Fig. 2c. Consequently, the proposed metasurface can be regarded as the superposition of an electric current sheet and a magnetic current sheet with conductivities $\sigma_s^{(e)}$ and $\sigma_s^{(m)}$, while the scattering properties of the metasurface, i.e., reflectance (R) and transmittance (T), can be given by [19]

$$R = \frac{2 \left(\zeta \sigma_s^{(e)} - \zeta^{-1} \sigma_s^{(m)} \right)}{4 + 2\zeta \sigma_s^{(e)} + 2\zeta^{-1} \sigma_s^{(m)} + 2\sigma_s^{(e)} \sigma_s^{(m)}}, \quad (7)$$

$$T = \frac{4 - \sigma_s^{(e)} \sigma_s^{(m)}}{4 + 2\zeta \sigma_s^{(e)} + 2\zeta^{-1} \sigma_s^{(m)} + 2\sigma_s^{(e)} \sigma_s^{(m)}}, \quad (8)$$

where ζ is the wave impedance. An ideal perfect absorbing sheet should fulfill the condition $\zeta \sigma_s^{(e)} = \zeta^{-1} \sigma_s^{(m)} = 2$. For the dark-state metasurface, the sheet

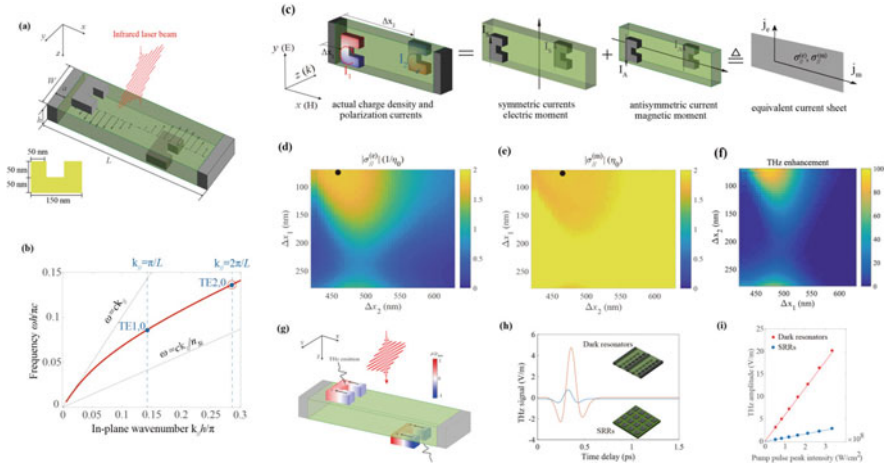


Fig. 2 (a) Schematics of the meta-atom of designed metasurface THz emitter. The geometric parameters of the unit are designed to have the length $L = 800$ nm and thickness $h = 100$ nm, so the operation wavelength is tailored within typical high-speed telecommunications range as round $1.5 \mu\text{m}$, and the thickness of SRRs is set as $t = 50$ nm. (b) Dispersion diagram of the system. The solid (red) line shows the lowest TE branch and vertical dashed (blue) lines indicate the quantization of eigenmodes. The blue dots are the quantized eigenstates of the lowest TE branch, and the red circle indicates the TE_{2,0} mode adopted in the dark-state metasurface. (c) Polarization currents on two SRRs (\mathbf{I}_1 and \mathbf{I}_2) can be decomposed into the set of symmetric (\mathbf{I}_S) and antisymmetric (\mathbf{I}_A) currents, equivalently described by electric $\sigma_s^{(e)}$ and magnetic $\sigma_s^{(m)}$ sheet conductivities. (d), (e) Maps of $\sigma_s^{(e)}$ and $\sigma_s^{(m)}$ in dependence of positions of the two SRRs. Black dots indicate the optimized case of the system showing the highest absorption. (f) THz intensity enhancement map of our design. (g) Distributions of THz currents (black arrows) and charge density (color plot) of the SRRs. “+” and “-” indicate charge accumulation. (h) Time trace of THz radiation from design (red) compared to that from traditional SRR metasurface (blue). (i) THz peak-to-peak amplitude in dependence of pump power for our design (red squares) and for bare SRRs metasurface [10] (blue dots)

conductivities in dependence of $(\Delta x_1, \Delta x_2)$ are shown in Figs. 2d, e, from which, an optimized case may be picked at $\Delta x_1 \cong 70$ nm and $\Delta x_2 \cong 470$ nm with $\zeta|\sigma_s^{(e)}| = \zeta^{-1}|\sigma_s^{(m)}| \cong 1.8$ and the corresponding absorption reaches as high as 95%. In the dark-state meta-atom, two SRRs driven by the out-of-phase field, the linear responses of the two SRRs are opposite and get canceled, while the nonlinear responses of the two SRRs are in phase and interfere constructively as shown in Fig. 2g. Therefore, the THz radiation from the SRRs has negligible phase delay and will be coherent. Figure 2h gives the typical time-domain trace for the dark-state metasurface THz emitter compared to that for the bare SRR metasurface [10]. Upon increasing the pump pulse intensity, the generated THz signal amplitude increases linearly as presented in Fig. 2i. By properly optimizing the two SRRs, more than 120-fold enhancement in THz emission power compared to the reference case can be achieved.

3 Nonlinear Fano Resonances and Plasmonic BICs

Periodic media supports both leaky and non-leaky modes respectively for each supported resonant Bloch wave (as extended wave solutions of periodic potentials) if the lattice is symmetric. The non-leaky mode is associated with BICs (or embedded eigenvalues), which provides a physical mechanism for trapping electromagnetic energy for a long time [20, 21]. Ideally, BICs exhibit an infinitesimal value of the resonance spectral width (or infinite Q factor). In the case of plasmonic materials, BICs can be realized as quasi-BICs (or supercavity mode) [22], where both the Q factor and resonance width become finite. Nevertheless, BIC-based localization of light in plasmonic materials still makes it possible to realize high- Q quasi-BIC modes. Therefore, BIC-based plasmonic resonances exhibit strong light-matter interaction, which could enhance the light-matter interactions as well as the optical nonlinearities.

Research on BICs initially dates from quantum mechanics [23]. Recently, all dielectric nanostructures have been extensively studied for optical BICs [24–32]. Both symmetry-protected and non-symmetry-protected BICs have been proposed. Symmetry-protected BICs are often found in a system with a reflection or rotational symmetry. On the other hand, non-symmetry-protected BICs can be formed by the destructive interference of interacting optical resonances. BICs provide a way to confine light in a mini structure via destructive interference. They provide new avenue for designing high- Q optical nano devices, which is important for lasers, nonlinear optical enhancement, optical sensing, as well as for the enhancement of general light-matter interactions [33].

However, BICs in plasmonic nanostructures were less reported, especially in experiments. Plasmonic structures have unique advantages in light confinement [34, 35]. In addition, the strong near-field and large local density of optical states (LDOSs) in plasmonic materials enable the efficient coupling of light emission from nearby emitters [36–39]. Nevertheless, plasmonic nanostructures suffer from significant metal absorption and radiation losses. Therefore, increasing concerns on the suppression of radiative dissipation in plasmonic nanostructures have been taken in several reports [40–42]. The strong coupling interaction between plasmonic and photonic modes have been theoretically investigated, which realizes hybrid plasmonic BICs in nanostructures [43, 44]. In the strong coupling regime, such a hybrid BIC mode occurs near the band anti-crossing point via the destructive interference, under a Friedrich-Wintgen condition [45].

In the section, we will discuss in detail the nonlinear plasmonic BICs in nanostructures and the inherent connections between the Fano resonances and physics of BICs. Particularly, when the frequency converting materials are positioned near the localized electromagnetic field induced by plasmons, the nonlinear responses of this hybrid structures can be further enhanced at the resonance modes where the constructive interference occurs. Potential applications of BIC-inspired plasmonic resonances are also discussed in this section.

Plasmonic BICs can be categorized with respect to the physical origin of radiation suppression [46]: The coupling interaction between the resonant mode and all radiation channels of the surroundings could vanish due to the spatial symmetry, which is called as the symmetry-protected BICs [47–52]. In contrast to the symmetry-protected BICs, another is the accidental BICs, whose formation is due to the accidental vanishing of the coupling to the radiation waves via continuous tuning of one or several parameters (Perot-type) or the destructive interference of several leaky waves (Friedrich-Wintgen scenario) [53]. There are more specific examples of BICs, such as anisotropic [54], Floquet [55] or PT symmetric systems [56, 57].

In connection with the high- Q resonances supported by BICs, the light-matter interaction and the nonlinear optical effects would be greatly enhanced, which is currently under active study [44, 52, 58, 59]. The reason is that nonlinear optics at the nanoscale is governed by strong field confinement and resonant response, [60] and is not limited by phase matching [61]. As a result, the processes of optical nonlinearity can be boosted dramatically since they scale as $(Q/V)^n$, where n is the nonlinear process order and V is the mode volume [62]. Therefore, the giant increase of the nonlinear efficiency is expected in isolated subwavelength nanoantennas which are tuned to the BIC regime. This prediction was recently demonstrated for the case of the SHG in AlGaAs nanodisks [63].

In this section, several research works on nonlinear BIC-based metasurfaces are reviewed. The frequency conversion efficiency of BIC-based metasurfaces can be boosted dramatically by smart engineering the asymmetry parameter in the vicinity of the quasi-BICs. The physics is that the optical metasurfaces with broken-symmetry (incidence or meta atom) could enhance substantially the Q factor of the structures when tuning to the BIC conditions. Additionally, the applications of these BIC-based ideas will also be discussed.

BICs are commonly considered as an effective means to dramatically elongate the trapping time of light. However, light-matter interaction depends not only on the lifetime of an optical mode, but also on its mode volume. Yi et al. [44] proposed a novel hybrid plasmonic-dielectric structure to manipulate the mode volume of BICs. Strong localization of electric field can be achieved along the surface normal direction for the symmetry-protected BICs, leading to one order of magnitude reduction of mode volume in one unit cell compared with the conventional symmetry-protected BICs of all-dielectric structure. The proposed hybrid photonic system could provide an ideal flat platform for advanced manipulation of light-matter interaction.

Very large two photon absorption (2PA) and three photon absorption (3PA) enhancement can be achieved at ~ 730 nm, as shown in Fig. 3b, where the leaky resonance associated with the FW-BIC appears. The corresponding electromagnetic field distribution for this leaky resonance is shown in the inset, where the electromagnetic field is mainly located inside the nanoparticle, leading to enhancement factors as large as 3500 and 250 for the 3PA and 2PA compared with the single dielectric nanoparticle case, respectively. The dependence of the 2PA and 3PA on the lattice constant of the hybrid structure was also examined, as shown in Fig. 3c.

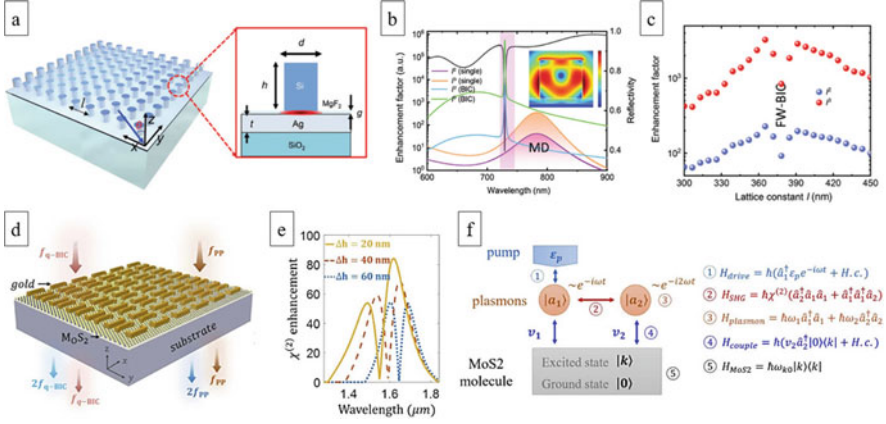


Fig. 3 (a) Schematic of the hybrid plasmonic-photonic system, which is composed of a periodic array of Si nanopillars, a thin MgF₂ spacer layer, a thin Ag film and a SiO₂ substrate. (b) Reflection spectrum of the hybrid structure, and the electric field distribution of unit cell in the inset. (c) Dependence of the nonlinear optical absorption (2PA and 3PA) on the lattice constant [44]. (d) Schematics of the nonlinear plasmon-assisted MoS₂ metasurfaces with multiple radiation channels orienting towards nonlinear multiplexing. (e) Wavelength dependence of the enhancement of second-order susceptibility determined for the asymmetric parameters. (f) Hamiltonian of the nonlinear optical process [58]

Significant enhancement of the 2PA and 3PA of Si nanopillars can also be achieved in the hybrid structures close to the FW-BIC condition owing to the dramatical increase of radiative Q factor.

The spectrum of nonlinear optical response is typically determined from the linear optical resonance. To settle this matter, a wavelength-multiplexed nonlinear plasmon-MoS₂ hybrid metasurface with suppression phenomenon was proposed [64], where multiple nonlinear signals could be simultaneously processed and optionally tuned. As shown in Fig. 3d, a typical planar array of split metal frames is placed on monolayer MoS₂ for exciting singularity-associated light-trapping resonances via symmetry breaking. The presence of a quantum oscillator is adopted to both suppress and enhance the nonlinear quasi BICs, which makes the optical nonlinearity exhibit as Fig. 3e. This selectable nonlinear BIC-based suppression and enhancement effect can optionally block the undesired modes, resulting in narrower linewidth as well as smaller quantum decay rates.

The Hamiltonian of plasmonic nonlinear system is described in Fig. 3f, which involves with the incident wave, fundamental and nonlinear mode plasmons, as well as the quantum oscillator brought by MoS₂ molecule. The relationship between the second harmonic generated mode and the fundamental mode tells the phenomenon of enhancement and suppression, whose underlying physics is the destructive interference effect.

The enhancement of optical nonlinearity in BIC-based nanostructures derived from the boosted light confinement and strong light-matter interactions. For the

plasmonic nanostructures, there are three factors, multiplying each other, provide for the enhancement of nonlinear processes [65]: (i) Localization of the incident radiation into hot spots can increase the local intensity 5 orders of magnitude. The enhanced intensity also amplifies the nonlinear processes, which is the major contribution to the nonlinear enhancement [66–69]; (ii) Fano resonances in the linear response can enhance the localized field. Nonlinear interactions as well as the surface-to-volume ratio can be enhanced via breaking the symmetry of both the materials on a nanoscopic level and the optical fields. This further enhancement in the hot spot field enhances the nonlinear process more [70]; (iii) Finally, multiplying (i) and (ii), originates from the constructive interference effect of the frequency conversion paths. Particularly, among various plasmonic nanostructures, plasmonic metasurfaces resolve the phase-matching issue due to the thin-film nature. Additionally, since the resonant properties of nanostructured plasmonic metasurfaces depend strongly on the geometries of the unit cells, the resonances can be both spatially and temporally tuned by varying the nanoscale geometries across the metasurfaces, and the interplay between the linear and nonlinear properties can be exploited for more complex spatiotemporal nonlinear beam shaping and control.

4 Nonlinear Interaction of Topological Graphene Plasmons

Graphene plasmon is promising for the development of efficient photonic devices at the nanoscale due to its deeply subwavelength optical field confinement and extremely long intrinsic relaxation times in the terahertz and up to mid-infrared frequency range. Recent works [71, 72] have shown that topologically protected one-way edge plasmons operable up to infrared frequencies could be realized in periodically nanostructured monolayer graphene under time-reversal-symmetry breaking induced by a static magnetic field. These topological graphene plasmons are immune to backscattering from structural defects, thus hold great potentials in the advancement of topologically robust chiral plasmonic devices and provide new opportunities for nonlinear graphene plasmonics, such as harmonic generation, plasmonic nanolaser, and plasmonic soliton propagation. Especially, recent works [73–74] demonstrate that due to the significant nonlinearity enhancement and large life time of graphene plasmons, a net gain of four-wave mixing interaction of plasmonic edge states can be achieved with a pump power of less than 10 nW; and what is more, the effective nonlinear edge-waveguide coefficient could reach as large as $1.1 \times 10^{13} \text{ W}^{-1} \text{ m}^{-1}$, which is more than 10 orders of magnitude larger than that of commonly used, highly nonlinear silicon photonic nanowires.

In the work of [73], the authors considered a graphene plasmonic metasurface consisting of a periodic nanohole array with hexagonal symmetry, which is placed in a static magnetic field B . At infrared and terahertz frequencies, graphene placed

in a static magnetic field can be characterized as an electrically gyrotropic material with the surface conductivity tensor given by

$$\sigma_s = \begin{bmatrix} \sigma_L & \sigma_H \\ -\sigma_H & \sigma_L \end{bmatrix} \quad (9)$$

where the diagonal elements σ_L and the off-diagonal elements σ_H at room temperature and for frequencies below the visible-light region can be written as

$$\sigma_L = \sigma_0 \frac{1 - i\omega\tau}{(\omega_c\tau)^2 - (i + \omega\tau)^2} \quad (10)$$

$$\sigma_H = -\sigma_0 \frac{\omega_c\tau}{(\omega_c\tau)^2 - (i + \omega\tau)^2} \quad (11)$$

where $\sigma_0 = e^2 E_F \tau / (\pi h^2)$, τ is the relaxation time (plasmon lifetime), $\omega_c \approx eB_\perp v_F^2 / E_F$ is the cyclotron frequency, with B_\perp , v_F , and E_F being the external static magnetic field perpendicular onto the graphene surface, the graphene Fermi velocity, and the Fermi energy, respectively. Because of the time reversal symmetry breaking induced by the magneto-optical response of graphene under an external magnetic field, this plasmonic system could host a topological bandgap. To demonstrate this, the authors calculated the photonic band structure using a numerical approach based on the finite element method. The unit cell (with lattice constant a and air hole radius r) and the first Brillouin zone of the system used in the numerical calculations are shown in Figs. 4a, b. The band diagrams of the system at $a = 400$ nm, $r = 120$ nm under different magnetic fields $B = 0, 2, 5, 7, 10$ T are given in Fig. 4c, where the parameters of the graphene are set to be $E_F = 0.2$ eV, $v_F = 10^6$ ms⁻¹, and $\tau = 50$ ps.

As can be seen from Fig. 4c, without the external magnetic field (i.e., $B = 0$), due to the hexagonal symmetry of the metasurface structure, Dirac cones protected by the parity (P) inversion and time reversal (T) symmetries exist at K and K' symmetry points of the Brillouin zone. When $B > 0$, the time reversal symmetry of the system is broken and, consequently, the Dirac cones are gapped out, resulting in a topological nontrivial bandgap. Moreover, the width $\Delta\nu$ of this bandgap increases as the amplitude of the magnetic field increases. The topological properties of the bandgap could be characterized by the so-called gap Chern number, whose magnitude indicates the number of topological edge modes, whereas the sign shows the direction of propagation and the gap Chern number was calculated to be -1 for the bandgap shown in Fig. 4c.

To confirm the topologically protected edge modes will emerge within the topological bandgap, the authors calculated the projected band diagrams of a finite graphene metasurface as shown in Fig. 4d, which has 20 unit cells along the y axis and is periodic along the x axis. The projected band diagrams along K_x , determined for $B = 0, 2, 5, 7, 10$ T, are depicted in Fig. 4e. From the figure, one can see apart

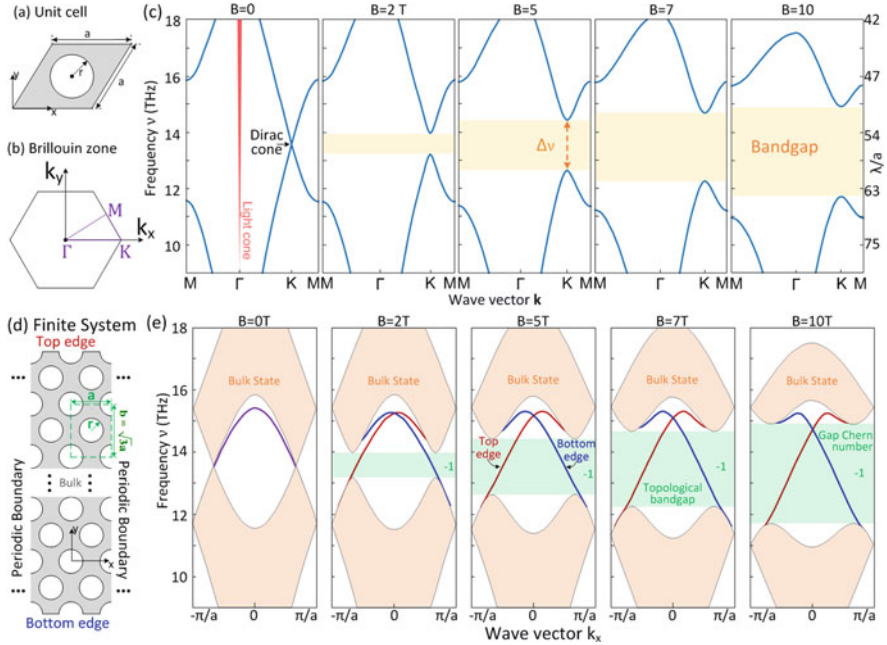


Fig. 4 (a) Unit cell and (b) the first Brillouin zone of the graphene plasmonic metasurface. (c) Band diagrams of the metasurface at $B = 0, 2, 5, 7, 10$ T. As the Dirac cone is below the air light cone, surface plasmons can exist at deep-subwavelength scale ($\lambda Ja > 40$). Moreover, a topological bandgap is opened in the presence of an external static magnetic field. (d) Geometry of the finite graphene metasurface, where the number of unit cells (green dashed frame) is finite along the y axis and infinite along the x axis. (e) Projected band diagrams of the metasurface at $B = 0, 2, 5, 7,$ and 10 T, where the edge modes on the top and bottom boundaries are depicted by red and blue curves, respectively. Since the gap Chern number characterizes the number of edge modes in the gap, there is a single edge mode at each boundary

from the bandgap also shown in the bulk band diagrams of Fig. 4c, there are two additional edge modes at the top (red) and bottom (blue) boundaries of the finite graphene system. These two edge modes connect the bulk bands located above and below the bandgap and cannot be moved out of the bandgap into the bulk bands as long as the bandgap exists, i.e., they are topologically protected by the bandgap.

The existence of one-way topological edge plasmons in the nanostructured graphene metasurface makes the system ideal for studying nonlinear frequency conversion. This is because in addition to the typical plasmonic effects, such as local field enhancement and field confinement, the local field can be further confined to the edge of the graphene plasmonic system, leading to a marked enhancement of the nonlinear optical response of the graphene system. Furthermore, in contrast to the frequently used bulk modes for nonlinear frequency mixing processes, where several modes with different wave vectors usually exist at a given frequency, the one-way topological edge mode has a unique wave vector at a fixed frequency. Therefore, the

phase matching condition can be achieved and implemented experimentally much more easily, as in this case only one mode can be excited at a specific frequency.

Taking these advantages, the authors studied the nonlinear four-wave mixing interaction of the topological edge plasmons as illustrated in Fig. 5a, where the system is excited by an external source at the pump frequency ω_p . Because of the strong third-order nonlinearity of graphene, a degenerate four-wave mixing process could take place, where two photons in a pump mode will generate a pair of photons at the signal and idler frequencies, ω_s and ω_i , respectively. As a result, the energy of the pump mode (green) in Fig. 5a is transferred to the (seeded) signal (blue) and idler (red) modes, leading to the pump decay and the amplification of the signal and idler. The four waves participating the degenerate four-wave mixing process are labeled in Fig. 5b. To gain deeper insights into the physical properties of plasmonic bulk and edge modes of the graphene metasurface, the near-field distributions of these modes propagating in a finite graphene plasmonic metasurface were studied by using full-wave simulations as shown in Figs. 5c, d. Note, in these computations, a perfectly matched layer was used at the left side of the graphene structure, whereas

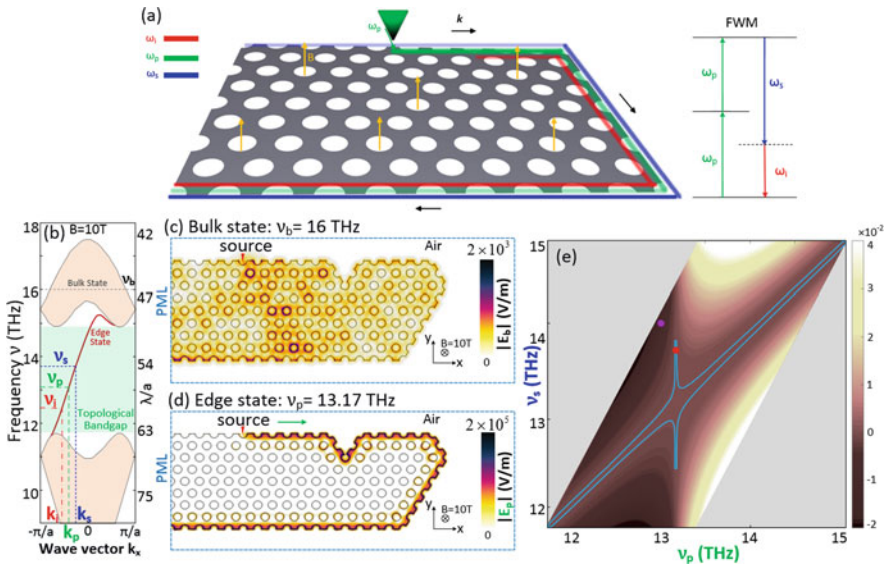


Fig. 5 (a) Four-wave mixing (FWM) of topologically protected one-way edge plasmons in a graphene metasurface consisting of a periodic nanohole array with hexagonal symmetry in a static magnetic field and the corresponding energy level diagram of a degenerate four-wave mixing process. (b) Band diagram of the graphene metasurface at $B = 10$ T. (c) Field profile of a bulk mode excitation at $v_b = 16$ THz, showing that the optical field spreads throughout the bulk region. (d) Field profile of an edge mode excitation at $v_p = 13.17$ THz, illustrating its unidirectional and defect-immune propagation along the system edge ($\tau \rightarrow \infty$). (e) Dispersion map of the normalized wave vector mismatch Δk . The blue contour is defined by the condition $\Delta k = 10^{-5}$ whereas the red and magenta dots correspond to a nearly phase-matched ($\Delta k = 5.16 \times 10^{-6}$) and a phase-mismatched ($\Delta k = 1.75 \times 10^{-2}$) four-wave mixing process, respectively

at the other sides, scattering boundary conditions were imposed so as to mimic infinite air space. The source to excite the finite graphene system is marked by a red triangle in Fig. 5c. In the case of the bulk mode, the corresponding optical field excited by the source spreads throughout the graphene structure as shown in Fig. 5c. In the case of the excitation of an edge mode as presented in Fig. 5d, the optical field does not penetrate in the bulk region and only propagates unidirectionally along the edge of the graphene metasurface. In addition, because of the chiral nature of the edge mode, this unidirectional propagation is robust against structural defects, which allows it to circumvent defects (e.g., sharp bends) without producing backscattering. As there is only a single-edge mode with a unique wave vector at a given frequency (see Fig. 5b), the phase matching could be achieved more easily. To analyze the circumstances in which the phase matching condition in a degenerate four-wave mixing of one-way edge modes can be fulfilled, the authors calculated the normalized wave vector mismatch, $\Delta k = \alpha(2k_p - k_s - k_i)$, corresponding to a four wave mixing process in which a pump edge mode with wave vector k_p gives rise to signal and idler edge modes with wave vectors k_s and k_i , respectively. The dispersion map of the normalized wave vector mismatch is given in Fig. 5e and from the contour defined by $\Delta k = 10^{-5}$, the authors found that for frequencies inside the domain defined by the contour, energy could be transferred from the pump to the signal and idler over a distance of about $10^{-5}\pi$ lattice constants.

The nonlinear dynamics of the four-wave mixing process was studied by full-wave simulations, in which a point indicated with a red dot in Fig. 5e characterized by $\nu_p = 13.17$ THz, $\nu_s = 13.72$ THz and $\nu_i = 12.62$ THz was chosen and the input intensity of the signal was considered to be much smaller than that of the pump, whereas the input intensity of the idler was set to zero. The nonlinearity of graphene under the influence of a magnetic field of 10 T is described by a third-order susceptibility with value of $\chi^{(3)} = 5 \times 10^{-10} \text{m}^2 \text{V}^{-2}$. The calculated near-field profiles at the frequencies of the pump, signal, and idler, are given in Figs. 6a, b, from which one can see as a result of the nonlinear four-wave mixing interaction, the signal is amplified upon propagation, whereas an edge mode is generated at the idler frequency. Since the frequency of all the interacting edge modes is located in the topological bandgap, both signal and idler modes are topologically protected and exhibit unidirectional and defect-immune propagation along the system edge. The dependences on the propagation distance of the power carried by the three edge modes, calculated by integrating the corresponding Poynting vector across the transverse section of the mode, are given in Figs. 6c, d, corresponding to the case of near phase matching and a case when the four-wave mixing process is not phase matched (marked by the magenta point in Fig. 5e). Figure 6c, d show that the power of both the signal and idler modes is amplified upon propagation, due to the energy conversion from the pump mode and the growth rate of the signal and idler modes in the case of the nearly phase-matched four-wave mixing is larger than when the four-wave mixing interaction is not phase matched, which means that the energy conversion is more efficient in the former case. Furthermore, the predictions of the coupled-mode theory were shown to agree very well with the rigorous results obtained using full-wave simulations of the nonlinear mode

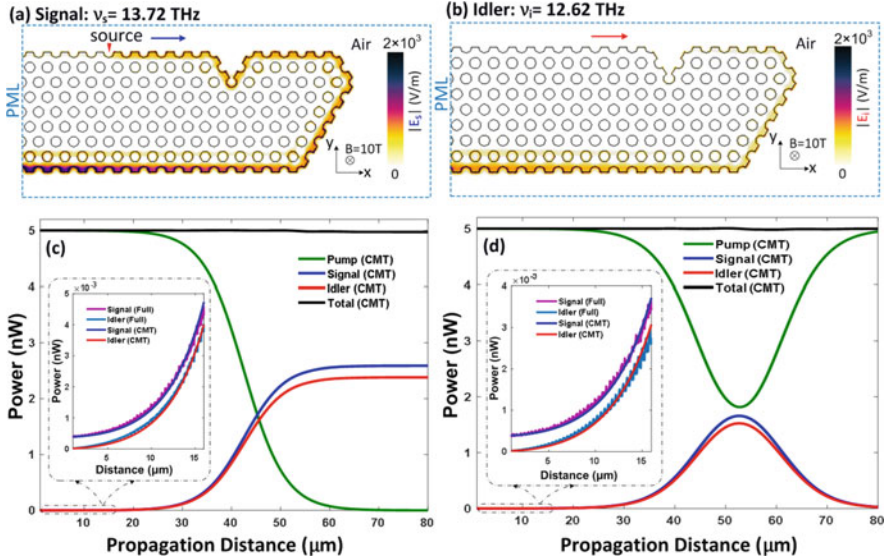


Fig. 6 (a) Field profile at the signal frequency, $\nu_s = 13.72$ THz. (b) Field profile at the idler frequency, $\nu_i = 12.62$ THz. (c) Dependence on the propagation distance of the mode power of the pump, signal, and idler corresponding to the field profiles shown in (a) and (b), determined using the coupled mode theory (CMT) when the four-wave mixing process is phase matched. Also shown in the insets are the same mode powers determined using the coupled mode theory and full-wave simulations. The black curve corresponds to the total power and shows that the energy is conserved in the four-wave mixing interaction. (d) The same as in (c), but corresponding to a case when the four-wave mixing interaction is not phase matched

interaction, despite the fact that the optical fields at the three frequencies are strongly confined at deep-subwavelength scale and significantly enhanced. Most importantly, the coupled-mode theory predicts that the effective nonlinear four-wave mixing coefficient $\gamma_{FWM} \approx 2.4 \times 10^{13} \text{ W}^{-1}\text{m}^{-1}$, which is more than 10 orders of magnitude larger than that of silicon photonic wire waveguides and 5 orders of magnitude larger than that of a graphene nanoribbon waveguide. This remarkable result is a consequence of the particularly large third-order susceptibility of graphene, which is further enhanced by the plasmon-induced enhancement and extreme confinement of the optical field of the edge modes. In particular, the size of the unit cell of the graphene metasurface is much smaller than the operating wavelength, namely, $\lambda/a > 50$ in the four-wave mixing process, a notable feature that can facilitate the design of low-power, ultracompact active photonic nanodevices. The findings in [73] pave a new way for developing ultralow-power-consumption, highly integrated, and robust active photonic systems at deep-subwavelength scale for applications in quantum communications and information processing.

5 Conclusion

The recent advances in nonlinear plasmonics, including difference frequency generation for terahertz source, multiple photon absorption and multiplexing enhanced by Fano-resonance and BICs, and four-wave mixing in topological graphene structure, have been briefly reviewed in this chapter. The nonlinearities in metallic and graphene plasmons are greatly enhanced and highly tunable by using the state-of-art principles and designs. In future, the nonlinear plasmonics will emerge into quantum regime. The nonlinear plasmonic processes could be manipulated at few photon levels and even under vacuum fluctuation scenarios.

Acknowledgments This work was supported by National Science Foundation of China (NSFC) (Nos. 61901001, U20A20164, 61971001, 61871001, 61975177) and Anhui Province (No. 1908085QF259).

References

1. Barnes, W. L., Dereux, A., & Ebbesen, T. W. (2003). *Nature*, *424*, 824.
2. Zayats, A. V., Smolyaninov, I. I., & Maradudin, A. A. (2005). *Physics Reports*, *408*, 131.
3. Bozhevolnyi, S. I. (Ed.). (2009). *Plasmonic nanoguides and circuits*. Pan Stanford Publishing Pte. Ltd..
4. Zayats, A. V., & Maier, S. (Eds.). (2013). *Active plasmonics and tuneable plasmonic metamaterials* (1st ed.). Wiley.
5. Cai, W., & ShalaeV, V. (Eds.). (2009). *Optical metamaterials: Fundamentals and applications*. Springer.
6. Maradudin, A. A., Sambles, J. R., & Barnes, W. L. (Eds.). (2014). *Modern plasmonics*. Elsevier.
7. Schuller, J. A., Barnard, E. S., Cai, W. S., Jun, Y. C., White, J. S., & Brongersma, M. L. (2010). *Nature Materials*, *9*, 193.
8. Kauranen, M., & Zayats, A. V. (2012). *Nature Photonics*, *6*, 737.
9. Boardman, A. D., & Zayats, A. V. (2014). In A. A. Maradudin, J. R. Sambles, & W. L. Barnes (Eds.), *Modern plasmonics* (p. 329). Elsevier.
10. Luo, L., Chatzakis, I., Wang, J., Niesler, F. B. P., Wegener, M., Koschny, T., & Soukoulis, C. M. (2014). *Nature Communications*, *5*, 3055.
11. Feng, K., StreYer, W., Zhong, Y., Hoffman, A. J., & Wasserman, D. (2015). *Optics Express*, *23*(24), A1418–A1433.
12. Yee, K. S. (1966). *IEEE Transactions on Antennas and Propagation*, *14*(3), 302–307.
13. Taflove, A., & Hagness, S. C. (2005). *Computational electrodynamics: The finite-difference time-domain method* (3rd ed.). Artech House.
14. Fang, M., Huang, Z., Sha, W. E. I., Xiong, X. Y. Z., & Wu, X. (2016). *Progress in Electromagnetics Research*, *157*, 63–78.
15. Liu, J., BriO, M., Zeng, Y., Zakharian, A. R., Hoyer, W., Koch, S. W., & Moloney, J. V. (2010). *Journal of Computational Physics*, *229*(17), 5921–5932.
16. Fang, M., Huang, Z., Sha, W. E. I., & Wu, X. (2017). *IEEE Journal on Multiscale and Multiphysics Computational Techniques*, *2*, 194–201.
17. Fang, M., Niu, K., Huang, Z., Wei, E. I., Wu, X., Koschny, T., & Soukoulis, C. M. (2018). *Optics Express*, *26*(11), 14241–14250.

18. Fang, M., Shen, N. H., Wei, E. I., Huang, Z., Koschny, T., & Soukoulis, C. M. (2019). *Physical Review Letters*, *122*(2), 027401.
19. Tassin, P., Koschny, T., & Soukoulis, C. M. (2012). *Physica B (Amsterdam)*, *407*, 4062.
20. Kodigala, A., Lepetit, T., Gu, Q., Bahari, B., Fainman, Y., & Kanté, B. (2017). *Nature*, *541*, 196.
21. Rho, J., Pertsch, T., & Kivshar, Y. (2020). *MRS Bulletin*, *45*, 210–220.
22. Rybin, M., & Kivshar, Y. S. (2017). *Nature*, *541*, 165.
23. Neumann, J. V., & Wigner, E. P. (1929). *Physikalische Zeitschrift*, *30*, 465.
24. Marinica, D. C., Borisov, A. G., & Shabanov, S. V. (2008). *Physical Review Letters*, *100*, 183902.
25. Hsu, C. W., Zhen, B., Lee, J., et al. (2013). *Nature*, *499*, 188.
26. Azzam, S. I., & Kildishev, A. V. (2020). *Advanced Optical Materials*, *9*, 2001469.
27. Mylnikov, V., Ha, S. T., Pan, Z., Valuckas, V., Paniagua-Domínguez, R., Demir, H. V., & Kuznetsov, A. I. (2020). *ACS Nano*, *14*, 7338–7346.
28. Ha, S. T., Fu, Y. H., Emami, N. K., et al. (2018). *Nature Nanotechnology*, *13*, 1042.
29. Sadrieva, Z. F., Sinev, I. S., Koshelev, K. L., et al. (2017). *ACS Photonics*, *4*, 723.
30. Rybin, M. V., Koshelev, K. L., Sadrieva, Z. F., et al. (2017). *Physical Review Letters*, *119*, 243901.
31. Taghizadeh, A., & Chung, I. S. (2017). *Applied Physics Letters*, *111*, 031114.
32. Doleman, H. M., Monticone, F., Hollander, W., Alù, A., & Koenderink, A. F. (2018). *Nature Photonics*, *12*, 397.
33. Seo, I. C., Kim, S., Woo, B. H., Chung, I. S., & Jun, Y. C. (2020). *Nanophotonics*, *9*, 4565–4577.
34. Schuller, J. A., Barnard, E. S., Cai, W., Jun, Y. C., White, J. S., & Brongersma, M. L. (2010). *Nature Materials*, *9*, 193.
35. Maier, S. A. (2007). *Plasmonics: Fundamentals and applications*. Springer.
36. Törmä, P., & Barnes, W. L. (2015). *Reports on Progress in Physics*, *78*, 013901.
37. Sukharev, M., & Nitzan, A. (2017). *Journal of Physics: Condensed Matter*, *29*, 443003.
38. Jun, Y. C., Kekatpure, R. D., White, J. S., & Brongersma, M. L. (2008). *Physical Review B*, *78*, 153111.
39. Jun, Y. C., Huang, K. C. Y., & Brongersma, M. L. (2011). *Nature Communications*, *2*, 283.
40. Min, B., Ostby, E., Sorger, V., et al. (2009). *Nature*, *457*, 455.
41. Zhu, W., Xu, T., Wang, H., et al. (2017). *Science Advances*, *3*, e1700909.
42. Monticone, F., & Alù, A. (2014). *Physical Review Letters*, *112*, 213903.
43. Azzam, S. I., Shalaev, V. M., Boltasseva, A., & Kildishev, A. V. (2018). *Physical Review Letters*, *121*, 253901.
44. Xiang, J., Xu, Y., Chen, J. D., & Lan, S. (2020). *Nano*, *9*, 133.
45. Friedrich, H., & Wintgen, D. (1989). *Physical Review A*, *32*, 3231.
46. Paddon, P., & Young, J. F. (2000). *Physical Review B*, *61*, 2090–2101.
47. Tikhodeev, S. G., Yablonskii, A. L., Muljarov, E. A., et al. (2002). *Physical Review B*, *66*, 045102.
48. Shipman, S. P., & Venakides, S. (2005). *Physical Review E*, *71*, 026611.
49. Bulgakov, E. N., & Sadreev, A. F. (2014). *Optics Letters*, *17*, 5212–5215.
50. Bulgakov, E., Sadreev, A. F., & Maksimov, D. (2017). *Applied Sciences*, *7*, 147.
51. Sadrieva, Z. F., Belyakov, M. A., Balezin, M. A., Kapitanova, P. V., Nenasheva, E. A., Sadreev, A. F., & Bogdanov, A. A. (2019). *Physical Review A*, *99*, 053804.
52. Hsu, C. W., Zhen, B., Chua, S.-L., Johnson, S. G., Joannopoulos, J. D., & Soljačić, M. (2013). *Light: Science & Applications*, *2*, e84.
53. Gomis-Bresco, J., Artigas, D., & Torner, L. (2017). *Nature Photonics*, *11*, 232.
54. Zhong, H. H., Zhou, Z., Zhu, B., et al. (2017). *Chinese Physics Letters*, *34*, 070304.
55. Longhi, S. (2014). *Optics Letters*, *39*, 1697–1700.
56. Kartashov, Y. V., Milian, C., Konotop, V. V., et al. (2018). *Optics Letters*, *43*, 575–578.
57. Poddubny, A. N., & Smirnova, D. A. (2018). *arXiv*, 1808.04811.

58. Ren, Q., Feng, F., Yao, X., Xu, Q., Xin, M., Lan, Z., Xiao, X., Wei, E., & Sha, I. (2021). *Optics Express*, 29, 5384–5396.
59. Liu, Y., Zhu, S., Zhou, Q., Cao, Y., Fu, Y., Gao, L., Chen, H., & Xu, Y. (2020). *Optics Express*, 28, 13234–13242.
60. Smirnova, D., & Kivshar, Y. S. (2016). *Optica*, 3, 1241–1255.
61. Kauranen, M. (2013). *Science*, 342, 1182–1183.
62. Notomi, M. (2011). *Proceedings of the IEEE*, 99, 1768–1779.
63. Carletti, L., Koshelev, K., De Angelis, C., et al. (2018). *Physical Review Letters*, 121, 033903.
64. Stillinger, F. H., & Herrick, D. R. (1975). *Physical Review A*, 11, 446–454.
65. Manjappa, M., Srivastava, Y. K., Cong, L., Al-Naib, I., & Singh, R. (2017). *Advanced Materials*, 29, 1603355.
66. Kauranen, M., & Zayats, A. V. (2012). *Nature Photonics*, 6, 737–748.
67. Ren, M. L., Liu, S. Y., Wang, B. L., Chen, B. Q., Li, J., & Li, Z. Y. (2014). *Optics Express*, 22, 28653–28661.
68. Poutrina, E., Ciraci, C., Gauthier, D. J., & Smith, D. R. (2012). *Optics Express*, 20, 11005–11013.
69. Le Ru, E. C., Blackie, E., Meyer, M., & Etchegoin, P. G. (2007). *Journal of Physical Chemistry C*, 111, 13794–13803.
70. Stockman, M. I. (2010). *Nature*, 467, 541–542.
71. Jin, D., Christensen, T., Soljacic, M., Fang, N. X., Lu, L., & Zhang, X. (2017). *Physical Review Letters*, 118, 245301.
72. Pan, D., Yu, R., Xu, H., & de Abajo, F. J. G. (2017). *Nature Communications*, 8, 1243.
73. You, J. W., Lan, Z., & Panoiu, N. C. (2020). *Science Advances*, 6, eaaz3910.
74. Smirnova, D., Leykam, D., Chong, Y., & Kivshar, Y. (2020). *Applied Physics Reviews*, 7, 021306.

Evolutionary Algorithms for Molding with Bezier Curves: A Novel Way to Obtain Optimized Structures at Nanoscale



Ramon Diaz de Leon-Zapata, Ivan Alberto Cruz-Garcia,
Ariel B. de la Rosa-Zapata, Javier Mendez-Lozoya, Gabriel Gonzalez,
and F. Javier Gonzalez

Abstract The use of evolutionary algorithms for optimization has been applied in various aspects of nanosciences and nanotechnologies. These algorithms emulate the biological course of action such as inheritance, mutation, genetic load, etc., and transfer these to the field of computer programming to accelerate million-year long natural processes, and to solve them in just a minimum fraction of time, depending on the complexity of the simulation. In this chapter, a novel way to apply the genetic algorithm is presented, where the geometry of nanostructures, made up of Bezier curves, is optimized by evolving their surface (2D) or volume (3D), which allows considering the structure as a moldable clay that can take virtually any possible shape. The advantages of this new technique are also discussed.

Keywords Bezier curves for molding nanostructure geometries · Evolutionary algorithms · Geometry as optimization issue

R. D. de Leon-Zapata (✉) · A. B. de la Rosa-Zapata
Electrics, Electronics, and Mechatronics Department, Tecnológico Nacional de México, Instituto Tecnológico de SLP, San Luis Potosí, Mexico

I. A. Cruz-Garcia
Electrics, Electronics, and Mechatronics Department, Tecnológico Nacional de México, Instituto Tecnológico de SLP, San Luis Potosí, Mexico

Mechatronics Department, Tecnológico Nacional de México, Instituto Tecnológico Superior de SLP, San Luis Potosí, Mexico

J. Mendez-Lozoya · G. Gonzalez · F. J. Gonzalez
LANCYTT—Terahertz National Laboratory, Universidad Autónoma de San Luis Potosí, San Luis Potosí, Mexico

1 Introduction

Multiple factors can yield optimal nanostructure. These factors are dependent functions of certain variables such as geometric shape, material combinations, operating frequencies, and so on. If it is assumed that a maximum, or a minimum, optimum is required (for example, maximum absorption at a specific frequency or minimum loss of power), then the value of a variable or a set of variables that make that specific attainable (optimal) condition is usually unknown. Furthermore, if the optimal conditions are a combination of these functions, then, each variable with its maximum or independent minimums do not converge at the same point; therefore, it will be impossible or possibly impractical to find the final solution due to the large computational time that leads towards a difficult process for accurate calculation.

In particular, concerning to nanoantennas, an alternative has been suggested to obtain an acceptable value for their performance (not necessarily optimal performance). This consists in changing the design and manufacturing characteristics from the macroscopic (radio frequency antennas for telecommunications) to the micro and nanometric scale, although it is necessary to understand that the behavior of these devices can be significantly different.

One property of antennas that is usually transferred to the micro and submicron scale is its ‘geometry’. It has been considered that the suitable behavior of these antennas exhibited at “conventional” scales would be the same at any other scale. However, it has been shown that at least in the geometric aspect [1] the optimum turned out to be geometrically different to the macroscopic counterparts. Consequently, questions arise about the optimal geometry characteristics or how to obtain (among other possible variables) an optimal geometry for a nanometric scale model, since this has only been imported from telecommunications antennas and is yet to be tested or studied.

Geometric optimization processes with evolutionary algorithms at different scales have been proposed [2, 3]. In general terms, very complex figures are obtained, which are difficult to manufacture with precision or are built up with a hollow or a ‘filled’ space. Other equivalents, such as a matrix or a grid of material can be considered, though their fabrication could be more complex due to the resolution limit to create filled or empty spaces aside from the resonances and/or parasitic capacitances caused by the interactions of those void spaces within the antenna material.

An alternative to obtain solid, continuous, completely malleable geometric figures, both two- and three-dimensional, is to assume that the material can take any shape because it can be conceived as plasticine and thus it is ideal to adopt its construction with Bezier curves [1]. Figure 1 depicts a brief comparison between a classical dipole nanoantenna (a), an evolutionary-non-continuous nanoantenna (b), an evolutionary segmented dipole satellite antenna (c), and an evolutionary-continuous nanoantenna (d).

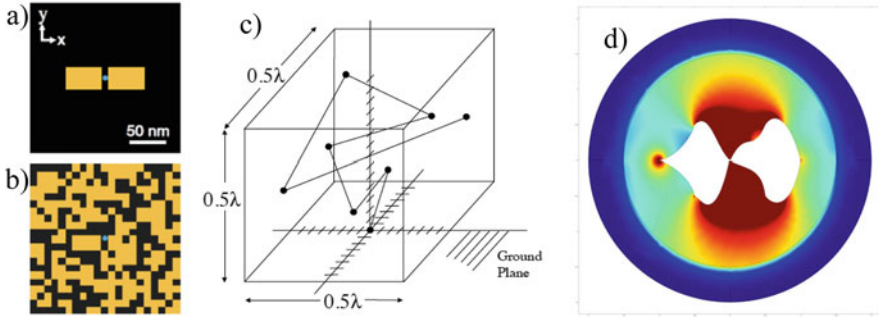


Fig. 1 Classical dipole nanoantenna (a), evolutionary-non-continuous nanoantenna (b) evolutionary segmented dipole satellite antenna (c), and evolutionary-continuous nanoantenna (d)

2 Use of Bezier Curves in Nanostructures

Bezier curves are a tool to manipulate polynomial surfaces with applications in computer-aided geometric design [4], trajectory generation [5], and model reconstruction [6]. This tool is formed of a straight line defined between two points (initial and final) and it can have one or more so-called ‘control points’ that adjust to form a curve instead of a straight line, and join all the involved points (the initial, the final and control points). A first-degree Bezier curve contains a single control point, a second-degree Bezier curve contains two control points, and so on, making it a function of the number of control points (Fig. 2).

The junction of several curves can form an initial open or closed geometry, with as many curves as necessary to achieve the desired resolution or smoothing (quality) effect of the final geometry. In this matter, flexible polynomial curves are called rational Bezier curves. Figure 3 shows a surface composed of several Bezier curves (a) and how that surface can be deformed by changing the control points (b).

The Bezier curves of degree n are defined as:

$$b(t) = \sum_{i=0}^n b_i B_i^n(t), \quad (0 \leq t \leq 1) \quad (1)$$

where $b_i \in \mathfrak{R}^2$ in a set of $n + 1$ where the control points are defined.

A rational Bezier curve R_n of degree n with control points $b_i \in \mathfrak{R}^2$ and positive weights $\omega_i \in \mathfrak{R}$ is defined as:

$$R_n(t) = \frac{\sum_i^n \omega_i b_i B_i^n(t)}{\sum_i^n \omega_i B_i^n(t)}, \quad (0 \leq t \leq 1) \quad (2)$$

Equation (2) is often used in reconstruction for 2D and 3D geometrical designs [7].

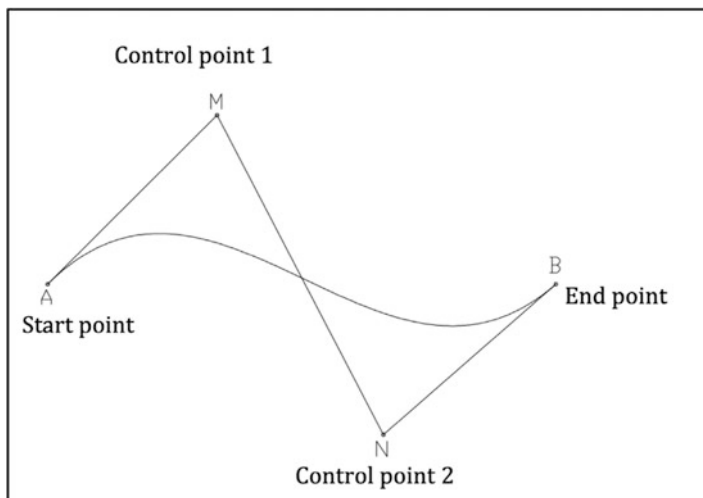


Fig. 2 Second-degree Bezier curve

As previously mentioned, the geometry or figure, in many engineering fields, plays a fundamental role in the performance of the conceived devices as supported by the argument of references [8, 9]. Particularly, although not limited to the case of the geometries of structures of nanometric dimensions (field of nanotechnology), the behavior of electromagnetic radiation with matter depends significantly on geometry [10].

3 Application of Evolutionary Algorithms in the Optimization of Nanostructures

With the premise that surfaces or volumes can be molded using geometrical curves, the next query is how to find the geometry that generates the optimal resonance considering only the geometric optimization.

The seek for geometries that optimize parameters of interest has led to the use of optimization algorithms such as evolutionary ones, particularly genetic ones, both single and multi-objective [1, 11].

Evolutionary algorithms try to imitate nature, where all living organisms exist in a given environment. The genetic material is stored in chromosomes, which contain all the organism-specific genetic information (characteristics) encoded in genes, also known as the genotype. Through reproduction, the organisms transfer their characteristics to new generations. Nonetheless, the newly created living beings are unique, as a consequence of the combination and crossover of maternal and paternal chromosomes. Moreover, mutations may also occur, altering the

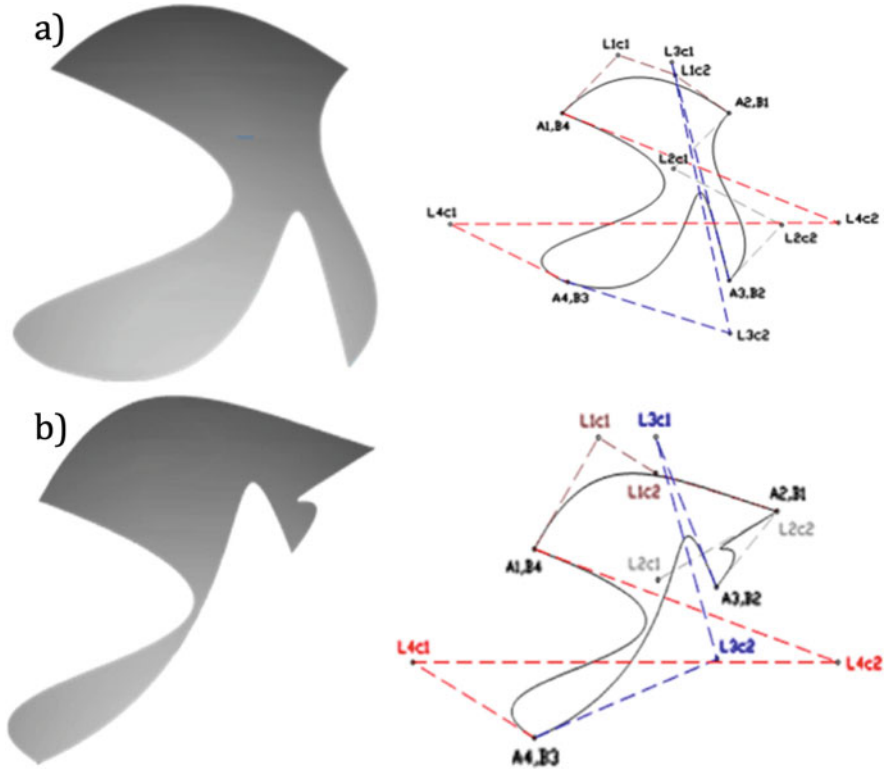


Fig. 3 Bezier curves conforming surfaces (left) and their respective control points (right). An arbitrary surface (a), can be molded by modifying their original Bezier’s control points producing a new surface (b)

information contained within the genes. The new organism begins its life in an environment that is not significantly different from that of its parents; it grows and develops to survive and transfer its genome, which allows the species to persist in such environment. An organism that cannot adapt to its environment will struggle to survive and to transfer its genes to new generations.

These ideas can be modified and used for optimization of problem solutions. An analog of this process can be implemented based on numerical calculations, assuming that the environment is defined based on known values and characteristics. The population of organisms constitutes potential solutions to the given problem, thus the solution already exists within the environment.

An adequate mathematical function must be chosen to define the fitness of any given organism representing how well adapted they are to their environment. Living beings will exchange genetic materials and mutations will occur during the genetic crossover process. Therefore, an optimal solution that best suits a given environment will be created [1].

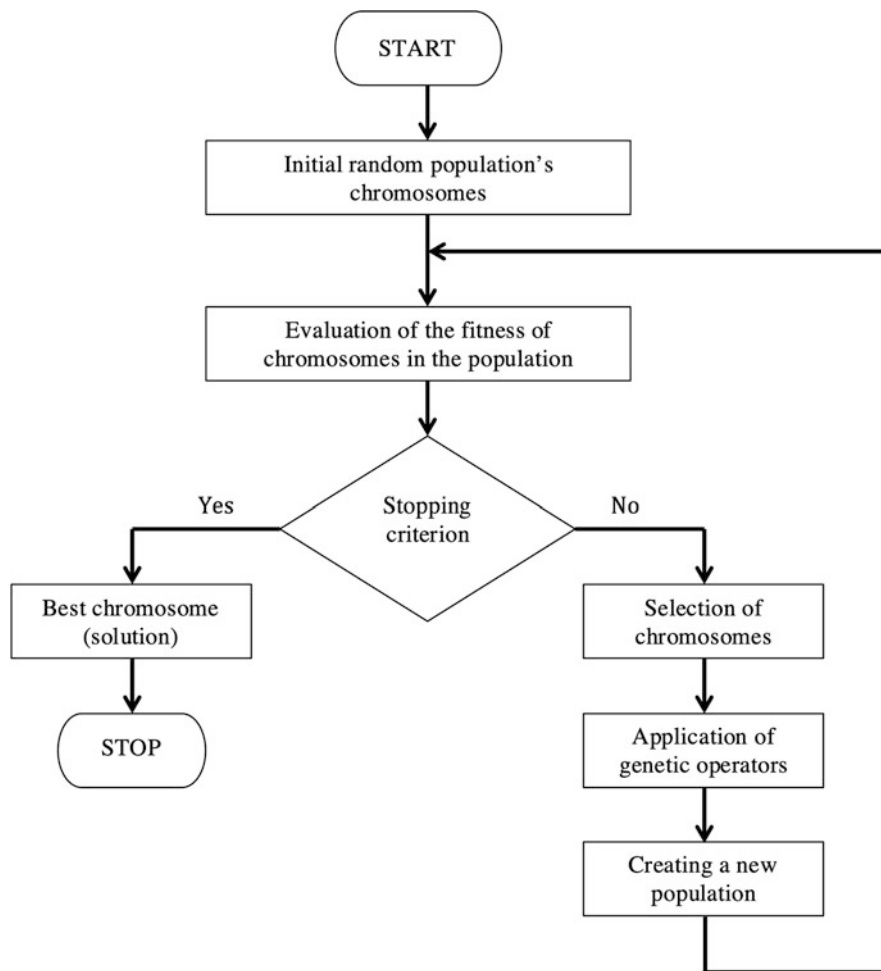


Fig. 4 Generic flow diagram of a genetic algorithm

A flow diagram of the algorithm is presented in Fig. 4.

Interesting results have been obtained through the application of this technique, as those presented in the references [2, 3]. A novel variant has also been applied to this technique, in which it is considered that the geometric modeling by evolutionary algorithms is no longer the placement or absence of material (organisms of the population) that generated discontinuous patterns. Due to the nanometric dimensions, smooth and continuous geometry ease the manufacture process and provide material continuity, which avoids possible interactions or parasitic (plasmonic) resonances in discontinuous cases.

In the case of micro and submicrometric geometries, each organism is considered as one of the control points that shape a Bezier curve. Afterwards, a complete and typically closed geometry (area or volume) is formed of several of these curves.

In the case of this algorithmic variant, the chromosomes are considered to be geometrically positioned in two or three dimensions depending on the application and are named by the letters x , y , and z .

In nanoantennas built by self-assembly techniques [12, 13], which are used in the thin surface, it is not relevant to consider the thickness within the optimization variables; however, in the case of plasmonics [14, 15] the height (z) of the geometry is a parameter that must be considered, as for some cases of meta-surface design. Assuming the simplest evolutionary model of the genetic algorithm, the so-called “Holland genetic algorithm” [16] (although others may be applied depending on the particular application), a population of at least ten times the number of original organisms that make up a pattern is started and considered to be sufficiently flexible (several Bezier curves such that an arbitrary geometry can be molded). For instance, 16 third-degree (three control points) Bezier curves can be sufficient for the construction of a dipole nanoantenna, besides its respective start and end points. This number, to a certain arbitrary point at the moment, is being analyzed by this same research group to quantitatively determine the minimum value of necessary curves and is part of future work.

A population ten times greater than the number of original organisms, which is necessary to construct an initial geometry, is useful and essential to guarantee genetic variation. Furthermore, genetic variation avoids the production of unhealthy organisms during the cross genetic operation, that do not contribute to the convergence of the fitness function.

Given that, for any antenna (including nanoantennas), the objective is that if they can present the maximum concentration or emission of electromagnetic radiation in a specific range of frequencies, one could try to select it as a fitness function for the maximum emission or reception according to the radiation source. However, these structures at the nanometric level present amplified resonances that are not necessarily the maximum if their simulated or experimental value is unknown. Therefore, in reality, the health function will be changed to that which represents the minimum losses in the range of frequencies of interest and depending on the dimensions of the nanoantenna. Consequently, the fitness function can be expressed as shown in Eq. (3):

$$f_{\text{fitness}} = \min \left(\frac{1}{2} \operatorname{Re} (\sigma \mathbf{E} \cdot \mathbf{E}_{\text{tot}}) \right) \quad (3)$$

where

$$\mathbf{E}_{\text{tot}} = \mu_0 \int \left(\mathbf{J} + \varepsilon_0 \frac{\partial \mathbf{E}}{\partial t} \right) da \quad (4)$$

Similar to any ecosystem, there is the possibility that organisms can go through mutation. These alterations to the chromosomes are introduced into the computational algorithms to prevent them from cycling. Consequently, it does not achieve the convergence or demonstrates a point of the function different from its true maximum or minimum, which is often known as false convergence. The value assigned in the percentage of mutation is usually very different between biological species. For instance, a higher breed of animals such as humans, statistically presents an extremely low mutation index, while certain bacteria and viruses have a higher proportion [17, 18]. In practice, this value is usually adjusted empirically after executing the algorithm for a few times to establish the one that best corresponds. Nonetheless, a present value in many practical cases has been 0.1%, which has perfectly suited the expected results for the tests carried out in previously published works.

There are other biological analogies for genetic algorithm; however, it is not included in the scope of this work. Following this background, Table 1 presents a summary of the variables and their respective values.

Figure 5 shows the results of the algorithm execution where the first geometry is obtained in the first iteration (of more than 30). Additionally, the classical dipole (for comparative effects) and the last geometries generated by the algorithm can be seen. It can also be noted that all are two-dimensional geometries (nanoantennas) because of their simplest nature; however, the algorithm is easily applicable to three-dimensional cases (plasmons). For the case of surface plasmons, unless the design situation is different, it is intended that most of the electromagnetic field is concentrated on the surface normal to the plane of incidence, which in this case is normal to the x, y plane (hence, the name of plasmon surface resonance). Furthermore, it can be seen in Fig. 5 that the first iteration, which generated a completely random geometry, is capable of significantly concentrating the electromagnetic field but not in a uniform or normal way to the plane of incidence. Finally, in the last iteration, the maximum concentration is observed on the normal surface of the nanoantenna (see intense red color in the center).

Table 1 General values for the experimental genetic algorithm

Parameter	Value
Population size	200
Elite count	0.05*Population size
Crossover fraction	0.8
Stop criteria	100*number of variables or 0.01% of losses (first thing happens)
Number of variables	22 (Bezier control points and start and end curve points)

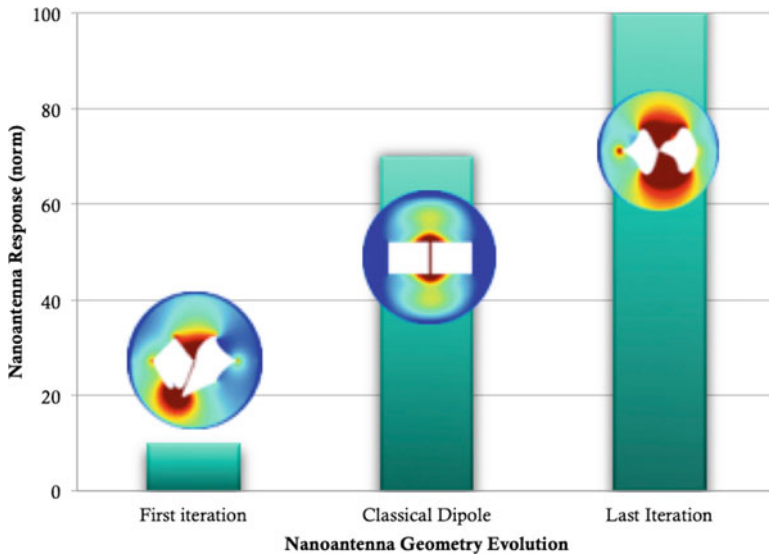


Fig. 5 2D nanoantenna evolution and comparison with a classical dipole geometry

After demonstrating the success of the evolutionary algorithms application to optimize a single parameter, in this case geometry (single-objective evolutionary algorithms), the next step is to search for optimization that involves more parameters simultaneously (multi-objective).

The multi-objective genetic algorithm was used by the authors to obtain nanoparticles with optimized geometry, current density, and electric field strength for maximum plasmon resonance simultaneously. Because the problem involved the boundary conditions of the plasmon and its interaction with the semiconductor substrate, it was convenient to add restrictions that led to the “multi-objective restricted genetic algorithm” application [19], which can be established in general terms as follows:

$$\left. \begin{aligned}
 &\text{Minimize/ Maximize } f_m(x), \quad m = 1, 2, \dots M; \\
 &\text{Subject to } g_j(x) \geq 0, \quad j = 1, 2, \dots J; \\
 &\quad \quad \quad h_k(x) = 0, \quad k = 1, 2, \dots K; \\
 &\quad \quad \quad x_i^L \leq x_i \leq x_i^U, \quad i = 1, 2, \dots n
 \end{aligned} \right\} \quad (5)$$

where the constraints divide the search space of the solution into feasible and non-feasible regions.

As with a single-objective optimization, all Pareto optimal solutions must be feasible (the Pareto optimal solution means that there is no way of improving any objective without degrading at least one other objective) [20]. The constraints can be equality or inequality type. Equation (5) shows that there are J inequalities and K equalities in the problem. The constraints can also be hard or soft. The hard

constraints must be satisfied for the solution to be acceptable. A soft constraint, however, is less demanding and does not determine if the solution is acceptable but the result might lose some accuracy. Therefore, in this type of algorithm, the constraints by equality h_k will be omitted. It is important to note that this relaxation in the constraint requirement does not mean that the algorithm cannot handle equality constraints but that the inequality constraints must be treated as a convergence toward equality.

For the proposed case, Eq. (5) takes the following form:

$$\left. \begin{array}{l} \text{Optimize } f_1(x), \\ \text{Minimize } f_2(x), \\ \text{Maximize } f_3(x), \\ \text{Subject to } g_1(x) \text{ (see table 2)} \end{array} \right\} \quad (6)$$

The objective functions $f_1(x)$, $f_2(x)$ and $f_3(x)$ are:

$$f_1(x) = \text{optimum Geometry}(x) \quad (7)$$

$$f_2(x) = \min \left(\frac{1}{2} \text{Re} (\mathbf{J}_{tot} \cdot \mathbf{E}_{tot}) \right) \quad (8)$$

$$f_3(x) = \max (-\sigma \nabla \mathbf{V}) \quad (9)$$

Equation (7) is a function that determines the geometry of the plasmon: the optimal geometry at the end of the execution of the multi-objective genetic algorithm. Equation (8) is a function that determines the power losses of the electric field (minimization function), and Eq. (9) is a function that returns the current density in the plasmon; at lower power losses and higher current density, there is higher plasmon efficiency [21]. x represents the twenty-two variables ($x_{1,2,\dots,22}$) that form the geometry. Some of them are the control points of the Bezier curves, and others represent the height, scale deformations, inclination angle, etc. (see Table 2). This allows for a geometric evolution of the plasmon as if it was clay or plasticine, which offers the advantage of obtaining a continuous figure that is easier to manufacture [1]. \mathbf{J}_{tot} is the total electric current density over the whole geometry obtained by the genetic algorithm,

$$\mathbf{J}_{tot} = \sigma \mathbf{E} \quad (10)$$

where σ is the electrical conductivity and \mathbf{E}_{tot} is the electric field over the whole geometry shown in Eq. (4) and \mathbf{V} is the electric potential on the bottom and top ends of the obtained geometry.

For electric current conduction, the flux physically signifies the total number of electrons flowing through the cross-section per time unit (referred to as current

Table 2 Constraint values for $g_1(x)$

Range	Units	Comments
$0 \leq x_i \leq 200$	nm	Bezier control points (Parameter x_i goes from x_1 to x_{16})
$0 \leq x_{17} \leq 200$	nm	Height of the geometry
$0 \leq x_{18} \leq 1.2$	Dimensionless	Scaling factor in x
$0.1 \leq x_{19} \leq 1.2$	Dimensionless	Scaling factor in y
$0 \leq x_{20} \leq 200$	nm	Displacement x
$0 \leq x_{21} \leq 200$	nm	Displacement y
$0 \leq x_{22} \leq 90$	Degrees	Twisting in the geometry (twisting along the Z axis)

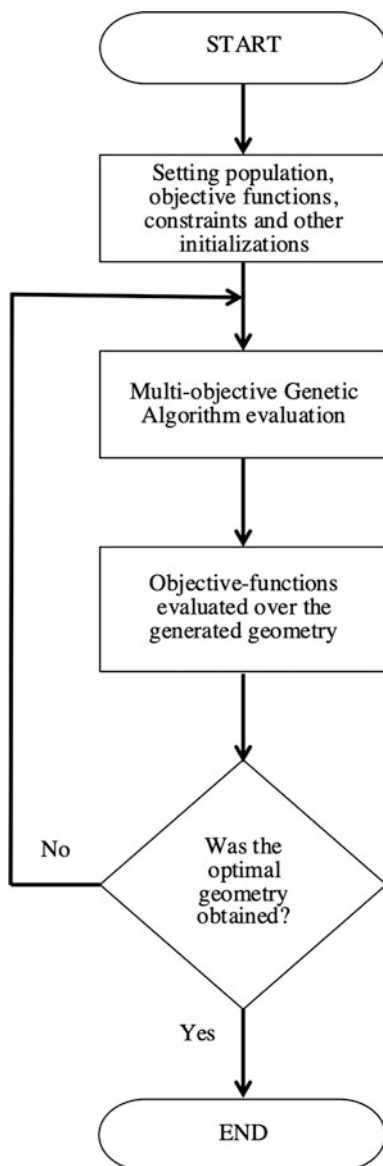
density). The multi-objective genetic algorithm was implemented in Matlab[®], and the evaluation of the objective functions, as well as the characterization via numerical simulation of the nanostructure, was performed in COMSOL Multiphysics[®] through iterations between these programs with the aid of the LiveLink-for-Matlab[®] module by creating a fully automated process, which eliminated errors due to human intervention and ensured optimal results. Figure 6 shows the flowchart of the process.

The search for more complex optimal nanostructures, such as Seebeck antennas [22], which are formed by the union of two materials with different Seebeck coefficients (hence their name), forced us to think about other parameters which can affect their performance (apart from the geometric appearance). The combination of materials is precisely the additional aspect of interest for this new optimization model, since the geometric optimization and the previously analyzed parameters were not enough, despite it can be assumed *a priori* that the best combination of materials is the one that has the largest opposite Seebeck coefficients. The largest positive Seebeck coefficient and the largest negative Seebeck coefficient is not a guarantee that the other parameters will turn out to be adequate for those materials.

The outcome of an executed multi-objective algorithm with 2 geometries (each one of different material) joined in a relatively small region are shown below. As already mentioned, these materials must have a different sign in their Seebeck coefficient. For this particular example, an electromagnetic wave with a frequency of 1TH is applied, which is a frequency of specific interest for telecommunications and other applications. As described in reference [23] two measurements were carried out, the normalized electric field and the density of total power dissipation in W/m^3 . The objective was to find the best pair of geometries with their combination of materials for which the best Seebeck effect is attained.

In this case, it is necessary to increase the number of organisms in the initial population because the solution space increases significantly with the increase from a single material (in the previous studies) to nine combinations of materials; materials that are, on the one hand, the most common ones, and on the other hand, those that have an available data to conduct a numerical simulation. For this purpose, it is required to utilize a greater genetic diversity like 100 organisms with

Fig. 6 Process flow diagram for the optimized by multi-objective-algorithm nanoparticle



a number of proposed generations of 40. After executing the algorithm with these characteristics, Fig. 7 shows the follow-up of the offspring of an organism.

It can be noted from Fig. 7 that the difference between the generation 1 (a) and generation 2 (b), is only in the shape of the geometries since the combination of materials in the first two generations of silver and nickel was the same, and it is the case where the “offspring” (b) exhibits a minimized response of the normalized

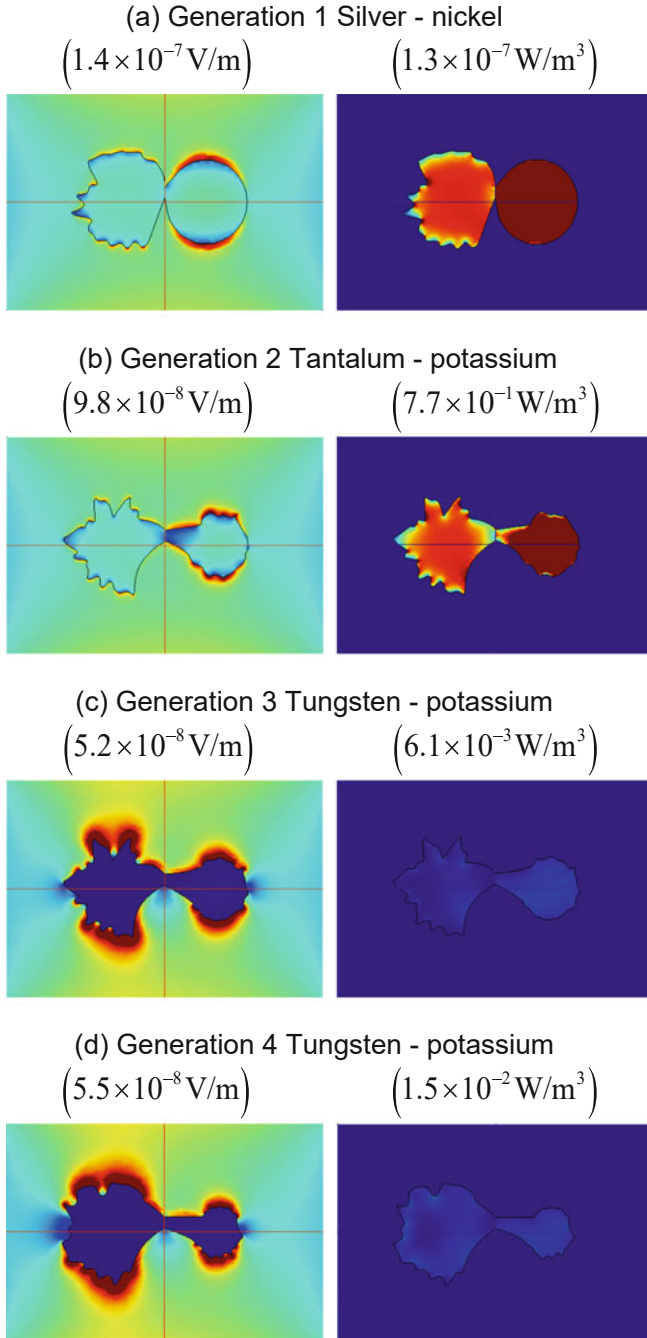
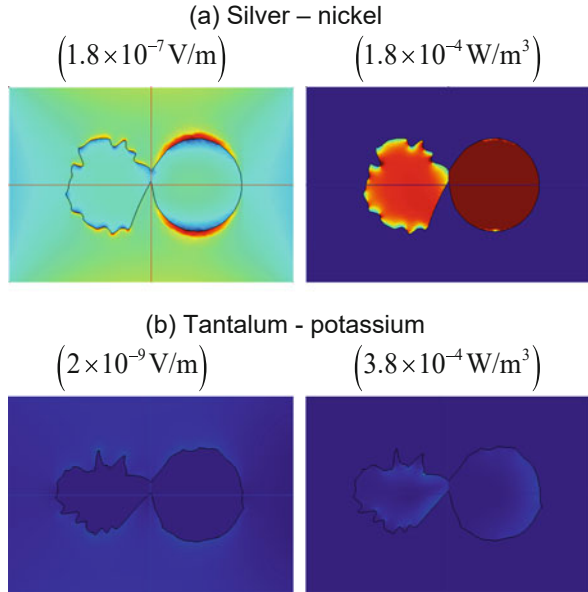


Fig. 7 Descendants of an organism over 4 generations. On the left: the representation of the normalized electric field response; on the right: the representation of the total power dissipation density response

Fig. 8 (a) Pair of geometries of silver-nickel material. (b) Pair of geometries of tantalum-potassium material. Left side represents the total power dissipation density; right side represents the normalized electric field



electric field and the total power dissipation density to the concerning “ancestor” (a). However, for generation 3 (c), there is already a change in the materials (tantalum and potassium) and it is an important reduction in the two responses, even when the changes in the shape of the geometries are small. Figure 8 shows the contrast of the responses between the pair of geometries with the lowest normalized electric field and total power dissipation density (b), and the pair of geometries with the highest normalized electric field and total power dissipation density (a) after running the multi-objective genetic algorithm with an initial population of 100 individuals and 40 generations.

Complementary optimization studies have been reported where the concept of evolution with Bezier curves has been applied. One of these studies shows an improvement in the thermoelectric efficiency of nanoantennas [24]. In this study, the design of the nanoantennas was obtained and characterized in the first instance by numerical simulation. The aim was to identify if the antennas would present any significant improvement as compared to classical dipole antennas before the fabrication process. The results of these simulations can be seen in Fig. 9.

Once the numerical simulation indicated that there was an increase in thermal efficiency, it was fabricated according to the mentioned specifications which are summarized in Fig. 10 as the results of the real thermoelectric characterization of the device, and the reference with the classical dipole.

The technique exposed here, is being applied to interdigital capacitors (Fig. 11a) with similar positive results. A preliminary geometry obtained with the evolutive algorithm can be seen in Fig. 11b).

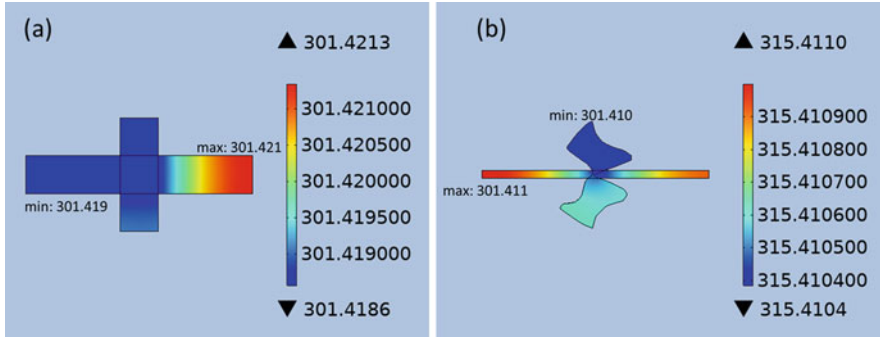


Fig. 9 Numerical simulation and its respective comparison, between a classical dipole geometry and an evolutionary geometry subjected to thermoelectric analysis

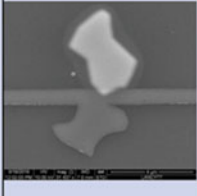
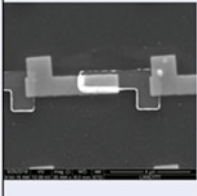
Nanoantenna	9x9 Array	Voc(V)	Isc(A)	Pmax(W)
EDN		0.09194	1.209E-7	4.005E-9
CDN		0.03047	4.095E-7	3.125E-9

Fig. 10 Thermoelectric characterization of a Classical Dipole Nanoantenna (CDN) and an Evolutionary Dipole Nanoantenna (EDN)

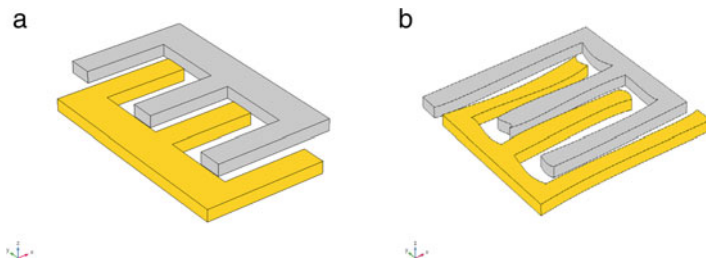


Fig. 11 (a) Classical interdigital capacitor. (b) Evolutive interdigital capacitor

RD would like to acknowledge support from “Tecnológico Nacional de México” through grant “PROYECTOS DE INVESTIGACIÓN CIENTÍFICA”, projects 5083.19-P and 9977.21-P.

GG would like to acknowledge support by the program Cátedras Conacyt through proyecto 1757 and from project A1-S-43579 of SEP-CONACYT Ciencia Básica and Laboratorio Nacional de Ciencia y Tecnología de Terahertz (LANCYTT).

References

1. Díaz de León-Zapata, R., Gonzalez, G., Flores-García, E., & Gonzalez, J. (2016). Evolutionary algorithm geometry optimization of optical antennas. *International Journal of Antennas and Propagation*, 2016(3156702), 7.
2. Derek, L. S. (2002). Antenna design using genetic algorithms. In *Presented at the genetic and evolutionary computation conference (GECCO)*. New York, NY.
3. Feichtner, T., Selig, O., Kiunke, M., & Hecht, B. (2012). Evolutionary optimization of optical antennas. *Physical Review Letters*, 109(127701), 5.
4. Gómez-Collado, M. C., Puchalt, J., Sarrió, J., & Trujillo, M. (2013). Designing an architectural work from a mathematical viewpoint. *Pensamiento matemático*, 3(1), 155–165.
5. Vicent Girbés, J. D. (2010). Generación de trayectorias de curvatura continua para el seguimiento de líneas basado en visión artificial, Master, Ingeniería de sistemas y automatización (DISA), Ingeniería de sistemas y computación (DICSA), Valencia, España.
6. Avila Torres, A. (2012). Reconstrucción de curvas B-spline y de Bezier mediante selección clonal, Master, Facultad de Ciencias, Universidad de Cantabria, Santander, Spain.
7. Galdames Bravo, O. (2011). Modelización con curvas y superficies de Bezier. *Modelling in Science Education and Learning*, 4(14), 181.
8. Santiago-Valentín, E., Portilla-Flores, E. A., Mezura-Montes, E., Vega-Alvarado, E., Calva-Yáñez, M. B., & Pedroza-Villalba, M. (2019). A graph-theory-based method for topological and dimensional representation of planar mechanisms as a computational tool for engineering design. *IEEE Access*, 7, 9.
9. Johansson, S., et al. (2019). Combining spectral induced polarization with X-ray tomography to investigate the importance of DNAPL geometry in sand samples. *Geophysics*, 84(3), E173–E188.
10. Papari, G. P., Koral, C., & Andreone, A. (2019). Geometrical dependence on the onset of surface Plasmon Polaritons in THz grid Metasurfaces. *Scientific Reports*, 2019(9), 12.
11. Díaz de León-Zapata, R., González-Fernández, J. V., Flores-García, E., De La Rosa Zapata, A. B., & Lara-Velázquez, I. (2018). Multi-objective evolutionary algorithm as a method to obtain optimized nanostructures. *European Physical Journal – Applied Physics*, 83(2), 8. <https://doi.org/10.1051/epjap/2018170408>
12. Zhang, J. (Ed.). (2003). *Self-assembled nanostructures*. Springer.
13. Sanchez, J. E., et al. (2017). Silver/zinc oxide self-assembled nanostructured bolometer. *Infrared Physics & Technology*, 81(2017), 5.
14. Anuj, K. S., Ankit Kumar, P., & Baljinder, K. (2018). A review of advancements (2007–2017) in plasmonics-based optical fiber sensors. *Optical Fiber Technology*, 43(2018), 14.
15. Maier, S. A. (2010). *Plasmonics fundamentals*. Springer.
16. Whitley, D. (2019). Next generation genetic algorithms: A user’s guide and tutorial. In m. gendreau & J. Y. Potvin (Eds.), *Handbook of metaheuristics. International series in operations research & management science* (Vol. 272). Springer.
17. Charlesworth, B., Charlesworth, D., & Morgan, M. T. (1990). Genetic loads and estimates of mutation rates in highly inbred plant populations. *Nature*, 347, 3.

18. Zhu, Y. O., Siegal, M. L., Hall, D. W., & Petrov, D. A. (2014). Precise estimates of mutation rate and spectrum in yeast. *Proceedings of the National Academy of Sciences of the United States of America*, 22, E2310–E2318.
19. Deb, K. (2009). *Multi-objective optimization using evolutionary algorithms*. Wiley.
20. Mehdi, K.-P., & IGI Global (Eds.). (2018). *Encyclopedia of information science and technology* (1st ed.). IGI Global.
21. Datta, S. (2014). Computing Total Normal flux on a planar surface. In *COMSOL* (Vol. 2016) ed. U. S. A.: COMSOL, A. B.
22. Cuadrado, A., Briones, E., González, F. J., & Alda, J. (2014). Polarimetric pixel using Seebeck Nanoantennas. *Optics Express*, 22(11), 11.
23. Díaz de León-Zapata, R., Flores-García, E., Lara-Velázquez, I., & Gonzalez, F. J. (2017). Geometry of nanostructures analyzed for terahertz applications. In *Presented at the 42nd international conference on infrared, millimeter, and terahertz waves (IRMMW-THz)*. Cancun, Mexico.
24. Mendez-Lozoya, J., Diaz de Leon-Zapata, R., Guevara, E., Gonzalez, G., & Gonzalez, F. J. (2019). Thermoelectric efficiency optimization of nanoantennas for solar energy harvesting. *Journal of Nanophotonics*, 13(2), 1.

Plasmon-Induced Hot Electrons in Metallic Nanoparticles



Lei Yan, Zhengkun Fu, and Zhenglong Zhang

Abstract Plasmon-induced hot electrons have attracted much recent attention due to its promising potential in photocatalysis and other light harvesting applications. Surface plasmon of metal nanoparticles decays nonradiatively to generate energetic electrons, referred to as hot electrons. Since hot electrons can be transferred to a chemically attached acceptor, this process is potentially useful for technological applications. Plasmon-induced hot-electron transfer is known to occur via two key mechanisms: indirect transfer and direct transfer. For hot-electron-driven catalysis, the energy of hot electrons needs to overlap with the unoccupied orbitals of the reactant, and the particular chemical channel can be selectively enhanced by controlling the energy distribution of hot electrons. High-energy hot electrons generated by plasmon decay also could contribute to nonlinear responses, which is essential for fundamental understanding of the optical nonlinearity associated with quantum and nonlocal effects on the atomic level. This chapter focuses on the recent advances in the understanding of plasmon-induced hot electrons and highlights its application in photocatalysis.

Keywords Surface plasmon · Hot electrons · Photocatalysis · Electron transfer · Nonlinearity

1 Introduction

The photoelectric effect was discovered by H. Hertz in 1887 when studying the effects of ultraviolet light on electrical discharge from metallic electrodes [1]. The key explanation of the phenomenon was provided in 1905 by A. Einstein [2], who suggested that a beam of light consists of a set of photons, each with a quantized energy E linked to their frequency ν [3]. This bold proposal explained why light

L. Yan (✉) · Z. Fu · Z. Zhang

School of Physics and Information Technology, Shaanxi Normal University, Xi'an, China
e-mail: yanlei@snnu.edu.cn

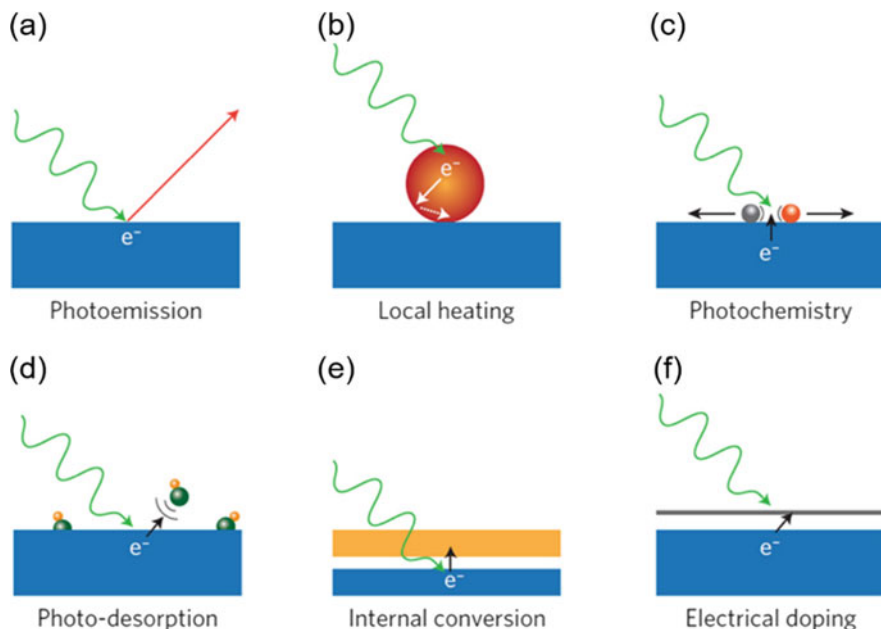


Fig. 1 Effects from the photoexcitation of hot electrons in a metal (blue). (a) Photoemission of electrons from a metal surface into vacuum can occur when the electron energy exceeds the metal's work function. (b) Photoexcited hot electrons can remain trapped inside a metallic nanostructure and cause local heating of its surroundings. (c) Hot electrons can interact with molecules on a surface and induce photochemistry. (d) The energy of hot electrons can be used to photo-desorb small molecules from the surface. (e) Photo-ejected electrons from a metal can be captured by a counter-electrode (orange) to generate useful current. (f) Photo-ejected electrons can be captured by an ultrathin semiconductor layer or two-dimensional materials (grey) and electrically dope them [4]

cannot eject an electron from a metal surface regardless of the intensity below a certain threshold frequency. The process requires a minimum photon energy equal to the metal's work function. These historical events provided the initial sparks for the quantum revolution and inspired a diverse set of fundamental research efforts aimed at elucidating the complex physical and chemical processes that can be stimulated with energetic, photoexcited 'hot' electrons [4]. Figure 1 shows the possible hot electron effects.

The photoemission process (Fig. 1a), where the energy of an incident photon is used to eject an electron, is arguably the most well-studied phenomenon involving hot electrons. The energy and angular dependent photoemitted electrons provide important information about the surface properties and the electronic structure of solids [5]. Hot electrons stimulate useful physical and chemical processes, but their ability to do so is limited by rapid relaxation processes where the electron's energy is converted into heat. On the other side, the relaxation provides an opportunity to heat nanostructures effectively (Fig. 1b) [4], which has many practical applications.

Hot electrons can have positive or negative energy depending on their position with respect to the vacuum level. The negative-energy hot electrons are bound to the nanostructure but can have energies that are larger than those arising from thermal excitations. In this sense, they are of particular importance in chemical applications. Such electrons can transfer into nearby structures and induce photochemical transformations (Fig. 1c) or photo-desorption (Fig. 1d). These are discussed in the section on the ‘Hot-electron-driven catalysis’. Finally, there is an opportunity to harvest the hot electrons for a number of device applications in photodetection (Fig. 1e, f) [4].

The birth of each photogenerated hot electron is a photon absorption event. Plasmon provides ways to manipulate light absorption with nanometre-scale precision and at sub-femtosecond timescales enabling new levels of control of hot electron processes. The outstanding light-trapping and electromagnetic-field-concentrating properties of surface plasmons open up a wide range of applications in the field of plasmonics [6]. Localized surface plasmon resonance (LSPR) can occur in noble metal nanoparticles (NPs) in which confined free electrons oscillate with the same frequency as the incident radiation and eventually enter resonance, giving rise to highly localized electromagnetic fields [7]. Consequently, such nanostructures have been proposed as efficient light-trapping components that can be integrated in photovoltaic cells to increase the efficiency of conventional architectures considerably [8]. Recent investigations have shown that plasmonic nanostructures can also directly convert the collected light into electrical energy by generating hot electrons [9, 10]. After light absorption in the nanostructures and LSPR excitation, plasmons can decay and produce highly energetic electrons, also known as ‘hot electrons’, which can be collected by chemically attached acceptor via indirect or direct electron transfer [11]. This process has been believed to promote the chemical reactions and as an essential step for artificial photosynthesis toward a sustainable energy future [12]. The hot electrons ultimately dissipate by coupling to phonon modes of the metal nanoparticles, resulting in a higher lattice temperature. Local heat generated by hot electrons can be harvested to drive a wide range of physical and chemical processes [13]. These are discussed in the section on the ‘Plasmon-induced hot electrons’. High-energy hot electrons generated by plasmon decay also could contribute to nonlinear responses, which is discussed in the section ‘Hot-electron-induced nonlinearity’. This chapter provides the recent theoretical and experimental advances in the understanding of plasmon-induced hot electrons and highlights its application in photocatalysis.

2 Plasmon-Induced Hot Electrons

The LSPR excitation of metal NPs produces strong light–matter interaction, resulting in highly localized electromagnetic fields on the surface of the NP (Fig. 2c) [14]. Plasmonic resonant energy is controllable by tuning their size, shape, material, and surrounding medium across the entire visible spectrum (Fig. 2b) [14]. Following

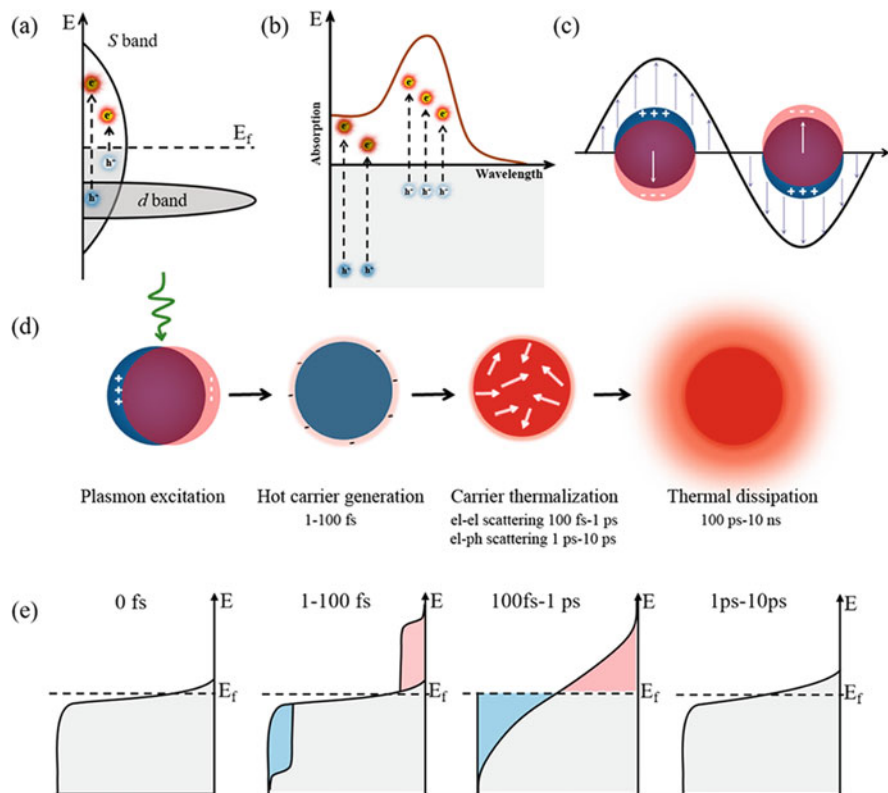


Fig. 2 Surface plasmon excitation (a–c) and decay (d, e). (a) Density of states of a plasmonic metal and the photoexcitation of intraband s-to-s and interband d-to-s transitions [19]. (b) Absorption spectrum of plasmonic metals [14]. (c) Coherent oscillation of electrons, resulting in a highly elevated plasmonic field at the surface of the NP [14]. (d) Schematic showing the photoexcitation and subsequent relaxation processes of the LSPR [4]. (e) Time evolution and energy distribution of hot carriers generated from plasmon decay [12]. E_f is the Fermi energy, and the gray shading indicates filled electronic states

plasmon excitation, electromagnetic decay takes place on a femtosecond timescale, either radiatively through re-emitted photons [15] or non-radiatively by transferring the energy to hot electrons [16] (Fig. 2d). The branching ratio between these two decay mechanisms is determined by the radiance of the plasmon mode, which can be suppressed for structures supporting dark plasmon modes [17]. Non-radiative decay can take place on the timescale of ranging from 1 to 100 fs through intraband excitations within the conduction band or through interband excitations caused by transitions between other bands (for example, d bands) and the conduction band. A possible carrier distribution is illustrated in Fig. 2a. The distribution of the carriers depends on the plasmon energy, the particle size, the symmetry of the plasmon mode, and the electronic structure and density of states of the material [18].

Since the work functions of standard plasmonic metals are larger than their plasmonic energies $\hbar\omega_P$, hot electrons will have negative energies ranging from the Fermi level E_F up to $E_F + \hbar\omega_P$ (Fig. 2e) and cannot escape into vacuum. The hot electrons generated from plasmon decay will quickly redistribute their energy among many lower-energy electrons via electron–electron scattering processes [20], forming a Fermi–Dirac-like distribution characterized by a large effective electron temperature (Fig. 2d). Time-resolved studies [21, 22] suggested relaxation times for extended metal surfaces around 100 fs to 1 ps (Fig. 2e). Then the hot distribution cools via the coupling between the “hot electrons” and the phonons of the metal lattice, which elevates the lattice temperature over a longer timescale of 1 ps ~ 10 ps [23]. In a final step, heat is transferred to the surroundings of the metallic structure. Taking from 100 ps to 10 ns depending on the material, the particle size, and the thermal conduction properties of the environment (Fig. 2d) [4].

2.1 Hot-Electron Generation and Relaxation

The basic understanding of physical processes behind plasmon-induced hot electron generation is essential for the design and optimization of novel devices capable of fully exploiting the properties of hot electrons [24]. Figure 3a shows the the energy of the hot electrons and holes generated by silver nanoparticles using different hot carrier lifetimes by a theoretical model. Experimental measurements of excited

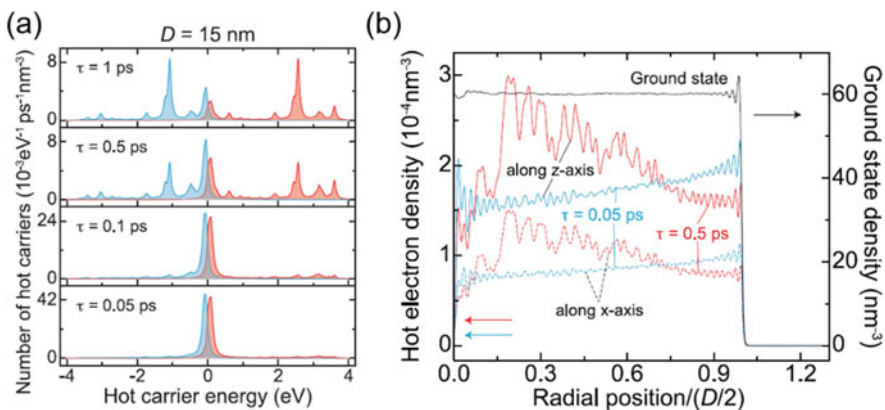


Fig. 3 (a) The number of hot electrons (red lines) and hot holes (blue lines) generated per unit of time and volume as a function of their energy with hot carrier lifetimes τ ranging from 0.05 to 1 ps for a silver nanoparticle with diameters $D = 15$ nm. Zero energy refers to the Fermi level [18]. (b) Local density of hot electrons generated in a silver nanoparticle of $D = 25$ nm at the plasmon frequency calculated along the axis parallel (solid lines) and perpendicular (dashed lines) to the external field polarization for $\tau = 0.5$ ps (red lines) and $\tau = 0.05$ ps (blue lines). For comparison, the ground state density (black line) is also shown [18]

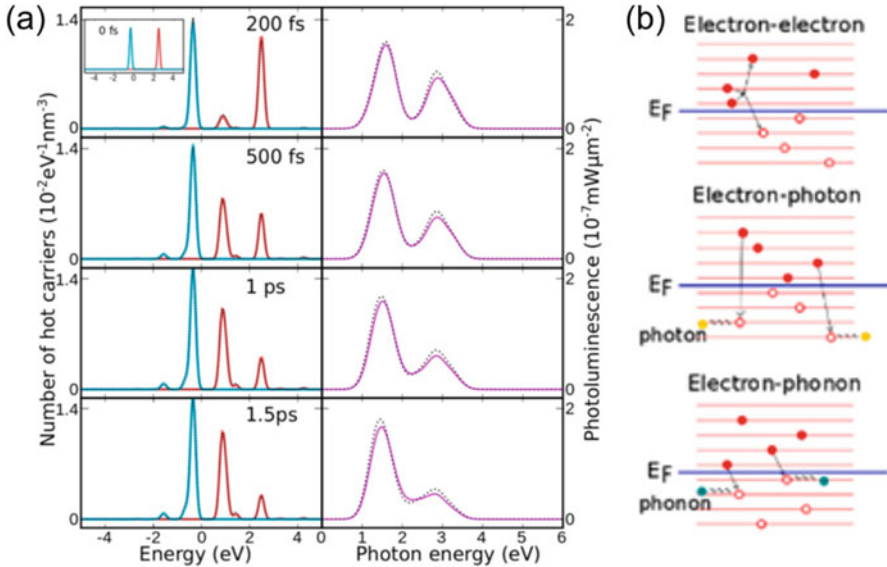


Fig. 4 (a) Instantaneous hot-electron (red), hot-hole (blue) distribution, and photoluminescence for a silver jellium sphere with diameter of 1.5 nm (100 electrons) illuminated for 10 fs with light intensity of $1 \text{ mW}/\mu\text{m}^2$ [26]. The inset shows the carrier distribution immediately after plasmon decay. (b) Illustration of the decay channels for hot-electron relaxation: electron–electron, electron–photon, and electron–phonon scattering [26]

carrier lifetimes have shown that hot carrier lifetimes can range from 0.05 to 1 ps [25]. Interestingly, the actual value of the lifetime turns out to be of crucial importance since the energy distribution of the hot carriers changes dramatically as this magnitude is varied within that range. In particular, long lifetimes result in the generation of carriers with large energies. On the contrary, smaller values favor the generation of carriers near the Fermi level. In addition, the plasmon-induced hot electrons are not distributed uniformly across the nanoparticle volume. Figure 3b shows the hot electron density distribution across the nanoparticle at the plasmon frequency. Hot electrons are primarily generated in the region of the sphere along the polarization direction. Shorter lifetimes result in more homogeneous spatial distributions, similar to the ground state.

After excitation, the hot electrons start to relax through electron–electron, electron–photon, and electron–phonon scattering as depicted in Fig. 4b [26]. Electron–electron relaxation is shown to be the dominant scattering mechanism from numerical simulations using quantum mechanical model and results in efficient carrier multiplication where the energy of the initial hot electron–hole pair is transferred to other multiple electron–hole pair excitations of lower energies. Specially, instantaneous hot-electron distribution following a pulsed laser excitation of the plasmon in a small nanosphere calculated using numerical integration for the electron–electron scattering matrix element is shown in Fig. 4a [26]. Plasmon decay

predominantly results in cold holes and hot electrons in two states located around 1 and 2 eV above the Fermi level. Within the first picosecond, the electrons in the 2 eV state begin to scatter into the 1 eV state and to some extent, into a state located around 1.5 eV. As the electrons scatter into these lower energy states, a small but finite fraction of electrons scatter into luminescent states where they can recombine radiatively with holes by emission of photons. The energy of the emitted photons is found to follow the energies of the electrons and thus redshifts monotonically during the relaxation process. The electron–photon rate is around 6 orders of magnitude smaller than the electron–electron scattering rate.

When the energies of the electrons approach the Fermi level, electron–phonon interaction becomes dominant and results in heating of the nanoparticle. While no conclusive experimental measurements of the time scales for relaxation have been reported so far, it is generally believed that electron–electron interactions occur on a time scale of 200–500 fs [27] and that electron–phonon coupling to equilibrate electron and lattice temperatures takes a few picoseconds [28] in gold and silver. The involved process can be addressed in the experiment using transient absorption spectroscopy. Minutella et al. [29] has investigated hot-electron relaxation times on the excitation wavelength on gold nanoparticles to differentiate between inter- and intraband transitions, and found that interband transitions result in significantly longer electron–phonon (e-ph) coupling times than solely plasmonic excitations, stemming from higher initial temperatures. Excitation-power independent electron–phonon relaxation times were observed in both experiments and calculations [29, 30]. In scope of the importance of hot electrons for photocatalytic reactions and photovoltaics, this result revealed that the possibility of interband transitions is an important factor that has to be considered.

2.2 *Size and Shape Effect of Nanostructure*

The size and shape of plasmonic nanostructures are among the most important parameters for LSPR excitation and hot-electron generation. They affect not only the wavelength at which LSPR takes place, but also the efficiency of the charge separation process [7]. As mentioned above, surface plasmons decay by either radiative emission of photons (the dominant process in large Au and Ag NPs with the size of 20–40 nm [31]) or through non-radiative excitation of hot electrons (the dominant process for smaller nanostructures [10]). The nanostructure size at which radiative decay starts becoming the predominant process strongly depends on the optical characteristics of the material. Langhammer et al. [32] investigated this dependence in lithography-patterned Ag, Pt and Pd nanodisks with sizes ranging from 38 to 530 nm. Interestingly, non-radiative decay was found to be the dominant process for Pd and Pt nanodisks for all the investigated sizes, whereas it disappeared for Ag nanodisks larger than 110 nm. Yu et al. [33] observed larger photocurrents for 15-nm-diameter nanoparticles than in nanoparticles with larger diameters because of more efficient decay of surface plasmons into hot electrons in the 15-nm-diameter

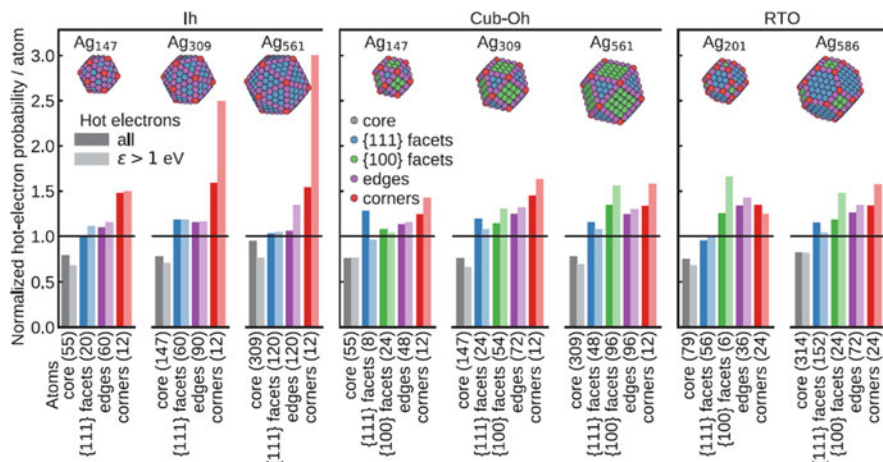


Fig. 5 Atomic-scale distributions of hot electrons in silver nanoparticles. Spatial distribution of hot electrons generated on different atomic sites in icosahedral (Ih), cuboctahedral (Cub-Oh), and regularly truncated octahedral (RTO) NPs. Sites with lower coordination exhibit a higher proportion of hot electrons than core sites. A spatially uniform distribution corresponds to a normalized probability of unity. The insets show the atomic structures with the different atomic sites colored [38]

nanoparticles. Specifically, larger nanoparticle sizes and shorter lifetimes result in higher carrier production rates but smaller energies, and vice versa [18].

In addition, spherical nanoparticles exhibit a single plasmon resonance peak, whereas structures such as nanorods exhibit two characteristic peaks that correspond to longitudinal and transverse modes. This phenomenon has been investigated in periodically distributed Au rods nanopatterned on TiO_2 single-crystal substrates [34, 35] and in nanorod-based plasmonic systems [36]. Double-peaked extinction spectra allow the optical absorption range to be extended, which is typically in the visible range for Au nanostructures to the near-infrared region. Strikingly, the photoelectric conversion efficiency obtained with these plasmonic structures increases with increasing temperature, in contrast to the general trend of semiconductor-based solar cells. Plasmonic energy conversion could thus solve the overheating problem that afflicts conventional photovoltaic cells [37].

A more quantitative view is obtained by considering the total per-atom occupation probability of hot electrons at a particular atomic site in comparison to the total per-atom occupation probability throughout the system (Fig. 5). Overall, hot electrons with more than 1 eV constitute 30–60% of all hot electrons depending on the system. Although the details of the distribution depend on particle size and shape, as a general trend, lower-coordinated surface sites such as corners, edges, and {100} facets exhibit a higher proportion of hot electrons than higher-coordinated surface sites such as {111} facets or the core sites. Thereby, hot electrons could be tailored by careful design of atomic-scale structures in nanoscale systems [38].

Several works have provided insights into the localization of hot-electron generation in plasmonic nanostructures. Kazuma et al. [39, 40] showed that sites in Ag nanorods on TiO₂ exposed to higher electromagnetic fields generate more hot electrons. After LSPR excitation and hot-electron generation, the oxidized ions diffuse in the water layer, and eventually recombine with electrons from TiO₂, leading to the formation of satellite islands. This effect was observed in rods with different aspect ratios that sustained different multipole plasmon modes. Islands appeared in locations where the LSPR electromagnetic field was more intense, confirming the hypothesis that the charge generation process is induced by the intense electromagnetic fields in the plasmonic nanostructures. Optimizing the design of plasmonic nanostructures so as to maximize the electromagnetic fields will increase hot-electron generation [7].

2.3 Direct and Indirect Electron Transfer

Since hot electrons by plasmon decay can be transferred to a chemically attached acceptor such as a semiconductor or a molecule, this process is potentially useful for technologies such as photovoltaics, photodetection, and photocatalysis [8, 12, 41]. The initially generated hot electrons go through the thermalization process forming a hot Fermi–Dirac distribution, and then transfer into the acceptor via inelastic electron tunneling (Fig. 6a). This two-step transfer process, termed indirect electron transfer, is the primary excitation pathway in plasmonic catalysis, which shows a relatively high transfer efficiency due to the continuous distribution of hot electrons near the Fermi level [13]. However, the energy of hot electrons cannot be effectively controlled by the excitation light, ultimately limiting the ability to selectively enhance specific chemical pathways. Resonant excitation of the LSPR would only enhance the efficiency of electron excitation without having much impact on the electron distribution of adsorbed molecules. Hot electrons generated in the metal can quickly relax back to the Fermi level via electron–electron scattering before being transferred to the acceptor (Fig. 6c), which leads to a low efficiency of hot-electron catalysis [42].

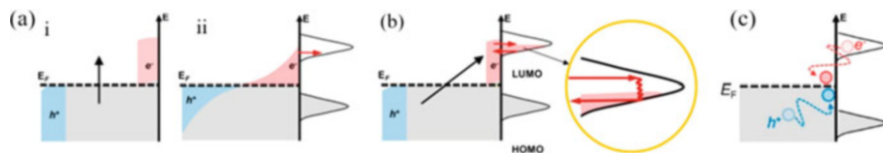


Fig. 6 Plasmon-induced hot electron transfer from the metal to the adsorbed molecule. (a) Two-step indirect electron transfer mechanism. (b) Direct electron transfer mechanism. (c) Recombination of hot electron–hole pairs in metals with the adsorbed molecule. E_F is the Fermi energy, and the gray shading indicates filled electronic states [14]

When there are strongly interacting reactants such as chemically adsorbed molecules or semiconductors, hybridized surface states can be formed at the interface as a result of the interactions between the metal and the reactants [43]. The formed interface states provide an additional pathway for plasmon dephasing through the coupling between the hybridized states and the plasmon, which induces the direct generation of hot electrons in the electron-accepting orbitals of the adsorbate, leaving hot holes in the electron-donating states on the metal surface (Fig. 6b). Without electron–electron scattering in the metal before its transfer, this process can significantly reduce the energy loss of the hot electron and accelerate the overall plasmon dephasing process [44]. Compared with the indirect mechanism, this direct electron transfer process shows a lower efficiency because of the relatively small transition dipole moments of molecule–metal composites and the required formation of hybridized surface states. In addition, the energy overlap between the excited LSPR and the energy gap of the hybridized surface states is also important for the direct transfer process, which allows for a direct resonant transition from occupied to unoccupied orbitals of the molecule–NP complex [45].

Since direct transfer occurs on an ultrafast time scale and is experimentally difficult to distinguish from indirect transfer that operates in parallel, the hot-electron transfer mechanism remains poorly understood at the atomic scale [46, 47]. It has been particularly challenging to isolate direct-transfer transitions, understand their characteristics, and quantify them accurately. Fortunately, theoretical calculations could help in this direction, and there is a methodology to address these issues rooted in a rigorous first-principles approach [42]. Zhang et al. investigated photon-induced electron injection from small metal clusters Au₅₅ into a MoS₂ monolayer, employing nonadiabatic molecular dynamics simulations [48]. The spatial distributions of the hot-carrier states in the Au₅₅/MoS₂ heterostructure are shown in Fig. 7. The transverse mode (Fig. 7a (i)) indicates that the charge distribution of the plasmonic oscillation is parallel to the MoS₂ monolayer, while the longitudinal mode (Fig. 7a (ii)) means that the charge distribution of the plasmonic oscillation is perpendicular to the MoS₂ plane. The interfacial delocalization between the Au₅₅ cluster and the MoS₂ monolayer differs strongly for the two states. For the transverse state, the photoexcited state is mainly localized (~65%) on the Au₅₅ cluster at $t = 0$ fs. At the initial stage (~50 fs), the localization on the cluster decreases rapidly to 35% (Fig. 7a (iii)). This process can be assigned to the hot-electron transfer after the photoexcited plasmonic state decays into electron–hole pairs in the indirect transfer mechanism. Sequentially, the injected electron transfers back from the MoS₂ monolayer to the Au₅₅ cluster in 600 fs. The longitudinal state follows a similar trend with the crossover at 47 fs in the direct transfer mechanism (Fig. 7a (iv)), faster than the transverse state. Notably, both time scales are faster than the time scale of energy relaxation inside the Au₅₅ cluster. Two electron transfer mechanisms can coexist in a nanoparticle–semiconductor hybrid nanomaterial, both leading to faster transfer than the recombination.

Furthermore, Kumar et al. [42] have isolated and quantified the direct-transfer process at a model metal–acceptor (Ag₁₄₇–Cd₃₃Se₃₃) interface based on real-time time-dependent density-functional theory (TDDFT) [49]. Figure 7b shows

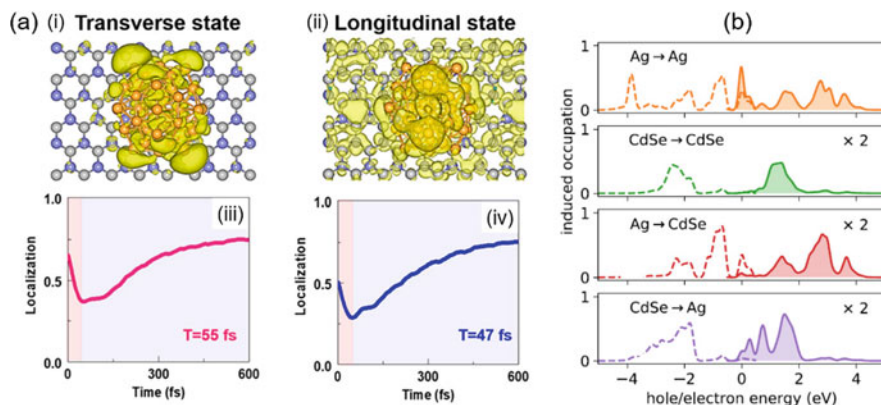


Fig. 7 (a) Charge distributions of the transverse and longitudinal states for Au_{55} on the MoS_2 monolayer at the top view (i, ii). The longitudinal state has a much larger delocalization between the Au_{55} cluster and the MoS_2 monolayer, forming a coherent superposition between the two components. The localization of the hot electron on the Au_{55} as a function of time after optical excitation of the transverse (iii) and longitudinal state (iv) [48]. (b) Partial hot-electron (solid lines and shaded) and hot-hole (dotted lines and unshaded) distributions for the $\text{Ag}_{147} - \text{Cd}_{33}\text{Se}_{33}$ system [42]

the partial hot-carrier distributions in this system at 21 fs, i.e., immediately after plasmon decay. A total probability of 43.4% for the plasmon decays, inducing intraband and interband transitions, is observed in Ag nanoparticles ($\text{Ag} \rightarrow \text{Ag}$). Intra-acceptor excitation [45] occurs when plasmons directly excite electrons from occupied states of the acceptor to unoccupied states of the acceptor with the probability of 12.2% in this structure ($\text{CdSe} \rightarrow \text{CdSe}$). The probabilities of direct hot-electron transfer ($\text{Ag} \rightarrow \text{CdSe}$) and hot-hole transfer ($\text{CdSe} \rightarrow \text{Ag}$) are 23.0% and 21.4%, respectively. Thus, direct transfer contributes up to 44.4% of the total plasmon decay, demonstrating that it could play a significant role at metal–acceptor interfaces [42]. Ma et al. [50] found that hot electrons are more efficient than the hot holes in the charge injection due to different interfacial couplings, and over 40% of the hot electron–hole pairs are separated spatially from the $\text{Ag}_{20} - \text{TiO}_2$ interface, which are in line with the direct electron transfer mechanism.

3 Hot-Electron-Driven Catalysis

Plasmon driven photocatalysis, as a route to concentrate and channel the energy of visible light into adsorbed molecules, has gained increasing attention thanks to its potential to drastically improve energy conversion technologies [4]. Many experimental and theoretical groups have proposed several mechanisms underlying plasmon-induced catalysis, including plasmon-field-driven catalysis [51, 52], heat-driven [53, 54], indirect hot-carrier transfer [55, 56], direct charge transfer [57, 58]

and intramolecular charge transfer, which can be distinguished by their timescales [59]. In this section, we focus on the catalysis mediated by indirect and direct charge transfer. Plasmon-mediated hot electrons can be transferred to the molecules through a transient electronic exchange between the metal and reactant [14]. With electronic exchange, transient negative ions (molecules with the addition of high energy electrons) are created and survive on the metal surface for tens of femtoseconds, which is sufficient to induce a chemical reaction or add vibrational energy to the molecule [4].

3.1 Catalysis Mediated by Indirect Electron Transfer

To date, most of the reported plasmonic catalysis is believed to occur through a conventional indirect hot electron transfer mechanism [60, 61]. Yan et al. [56] investigated the atomic scale mechanism and real time dynamics of H_2 photosplitting on a silver atomic chain irradiated by laser pulses (Fig. 8a) using *ab initio* TDDFT [49]. Femtosecond laser pulses provide a powerful tool to engineer electronic excitations and to study the ultrafast dynamics of chemical reactions [62]. Laser field polarized in the x direction along the chain shaped by a Gaussian wave packet is shown in Fig. 8b (i) with laser frequency of 1.74 eV as the plasmonic resonant frequency for $N_{Ag} = 6$. With the strength of laser field gradually increasing in time, H-H bond length in Ag- H_2 system gradually deviates from its original value. With the laser frequency of 1.74 eV, the dissociation of H_2 is obvious. While for other frequencies, no dissociation is observed within the simulation time (Fig. 8b (ii)). Therefore, the splitting of H_2 is induced by Ag-chain plasmon.

The H_2 splitting dynamics also exhibits dependence on the field strength (Fig. 8b (iii)). When laser field strength increasing, H_2 splitting shows an enhanced behavior. To understand the intensity dependence of plasmon-induced H_2 splitting, the dynamic charge transfer from Ag atomic chains to H_2 molecule upon laser excitation is analyzed (Fig. 8b (iv)). Calculated charge around H_2 denoted as Q_{HH} is obtained by integrating total charge density above the plane between H_2 and Ag chain. The increase in Q_{HH} by 0.5–0.8e at $t = 20$ fs results in a transient negative H_2^- state and subsequent H_2 splitting dynamics. To confirm that hot electrons transfer to the anti-bonding (AB) state of absorbed H_2 , indirect charge-transfer mechanism is proposed from time-evolved occupation of KS states (Fig. 8c). Projection of the time-dependent KS states on the anti-bonding eigenstate of H_2 shows that the antibonding state is partially occupied and the occupation is increasing during the dynamic evolution. There are sufficient couplings between the high-energy Ag states and H_2 antibonding state during the dynamic evolution after plasmonic excitation. Therefore, the laser pulse drives electrons to the excited states of silver chain, and then excited electrons transfer to the antibonding state of H_2 facilitating the reaction, which is a typical indirect charge-transfer process. This result is in general accordance with the mechanism speculated for plasmon-induced photochemistry reactions [63, 64].

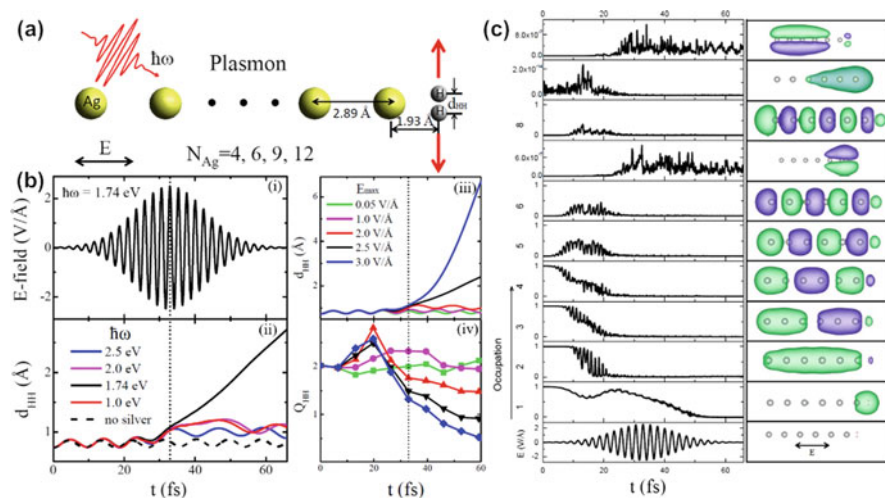


Fig. 8 (a) Schematic showing plasmon-induced H_2 splitting on Ag atomic chain with variable number of Ag atoms N_{Ag} . (b) H_2 dissociation on the silver chain with $N_{Ag} = 6$: (i) Time-dependent field strength of the laser pulse. The maximum amplitude E_{max} is 2.5 V/\AA and laser frequency is 1.74 eV ; (ii) Time evolution of bond length d_{HH} under laser illumination with different frequency. The dashed line is the case for isolated H_2 in vacuum, and the vertical dotted line denotes the time at which laser field reaches its maximum strength; (iii) Time evolution of d_{HH} and (iv) charge around H_2 for the same frequency 1.74 eV . (c) Time-dependent occupations of the ground-KS states, based on the sum of squares of the projections of the td-KS states onto static eigenstates for $E_{max} = 2.5 \text{ V/\AA}$

3.2 Catalysis Mediated by Direct Electron Transfer

The existence of the direct transfer process was demonstrated by the atomic-scale mechanism and real-time ultrafast electron–nuclear dynamics study of water splitting on Au NPs upon exposure to femtosecond laser pulses (Fig. 9a) [57]. The maximum field strength of laser pulse is set to $E_{max} = 1.6 \text{ V/\AA}$ and frequency $\hbar\omega = 2.62 \text{ eV}$ (Fig. 9b). This frequency matches the plasmonic absorption peak at 2.62 eV calculated for the Au NP. In the Fig. 9c, the O atom is almost static and the H atom pointing to the NP oscillates in a 10 fs period during the simulation timespan. The height of the other H first oscillates, then keeps increasing from 3.7 \AA at $t = 10 \text{ fs}$ to 6.4 \AA at $t = 33 \text{ fs}$. The corresponding OH bond length increases from 1.12 to 2.84 \AA . That is, water molecule splits into hydroxyl group (OH) and hydrogen (H) within 30 fs. In contrast, for an isolated water molecule in the same laser field, two OH bonds oscillate continuously and never break. Therefore, water splitting is mediated by plasmon excitation in the Au NP.

Further evidence implicating plasmon-induced reaction can be drawn from wavelength-dependent photocatalytic rates shown in Fig. 9d. For the Au NP with diameter of $D = 1.6 \text{ nm}$, the absorption spectrum shows double peaks due to quantum size effect. Reaction rates also exhibit two major peaks, closely following

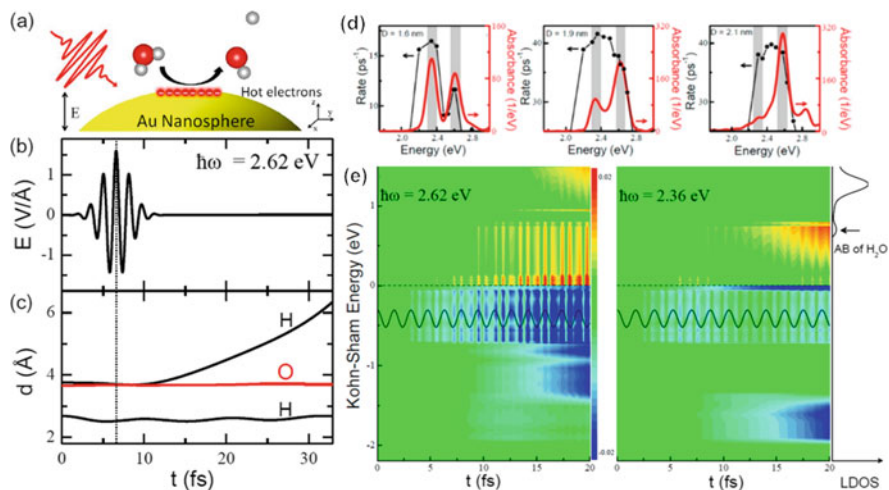


Fig. 9 (a) The schematic showing plasmon-induced water splitting on Au nanosphere ($D = 1.9$ nm) under the laser field polarized in the z direction. (b) Time evolution of the applied field and (c) atomic distance d of water along the z direction to the Au surface. The vertical dotted line denotes the time $t_0 = 6.6$ fs at which laser field reaches its maximum strength. (d) Water splitting rates (black dots) on Au NP with varied laser frequency. The connected line is the guide to eyes. Corresponding absorption spectrum (red lines) of Au NP to an impulse excitation is superimposed for comparison. (e) Time-evolved changes in the occupation of Kohn–Sham (KS) states for Au NP ($D = 1.9$ nm) when driven by continuous plane-wave laser. Black line denotes laser field oscillations, and calculated localized density of states (LDOS) of water is added in the right panel. Horizontal dashed line denotes the Fermi level [57]

the absorption spectrum. However, surprising contrast in reaction rate and photo absorption is found for Au NP of larger size. For Au NP with $D = 1.9$ nm, the intensity for absorption at resonance frequency $\hbar\omega = 2.62$ eV is almost doubled compared to that for $\hbar\omega = 2.36$ eV. The reaction rate with laser frequency $\hbar\omega = 2.62$ eV, however, is only 36 ps^{-1} , even smaller than the rate of 42 ps^{-1} at $\hbar\omega = 2.36$ eV. Again, for $D = 2.1$ nm, the reaction rate at $\hbar\omega = 2.63$ eV, where the maximum absorption is reached, is almost same with that at $\hbar\omega = 2.30$ eV with only weak absorption. Above simulations strongly suggest that the rate of water splitting depends not only on optical absorption of Au NP, but also on its plasmonic excitation mode. For the mode at $\hbar\omega = 2.36$ eV, the oscillation period of induced charge density is odd. While the mode at $\hbar\omega = 2.62$ eV is even-period plasmon excitation. Upon water adsorption, the odd mode indeed induces more electrons around water than the even mode.

To further understand photo-excitations associated with odd and even modes, Yan et al. analyzed time-evolved change in the occupation of KS states in Fig. 9e. For $\hbar\omega = 2.62$ eV, there exist strong oscillations in the occupation of states near the Fermi level, which is designated as electron “sloshing” [65], and electron excitations from deep states with the energy at -1.43 to about -0.72 eV to the

states at 1.40 ~ 1.50 eV, called “inversion” motion [65]. The “sloshing” behavior around Fermi level results in oscillations in the charge density near the NP surface [66], while “inversion” is responsible for plasmon decaying into hot electrons and hot holes [67]. Compared with even mode, the variation in the occupation of KS orbitals for the odd mode at $\hbar\omega = 2.36$ eV is minor, and there mainly exhibits electron inversion from the orbitals between -1.90 eV and -1.50 eV to those at $0.58 \sim 0.79$ eV. The AB state of water appears at the energy of 0.64 eV, overlapping well with the KS orbitals of Au NP which are newly partly occupied upon excitation at $\hbar\omega = 2.36$ eV. The energy match promotes resonant charge transfer from Au NP to water for the odd mode. Thereby, direct charge-transfer enhancement by better energy overlap between plasmon-induced hot electrons and the adsorbate’s unpopulated state is crucial for plasmon-enhanced reactions.

4 Hot-Electron-Induced Nonlinearity

Boosting nonlinear optical and electronic effects at the nanoscale is an important subject of extensive theoretical and experimental studies. Since the photon–photon interaction is intrinsically weak, nonlinear effects can be generated only with very high light intensities before significant material damage occurs, limiting the choice of materials [68]. A promising route for circumventing this difficulty and achieving efficient nonlinear responses is to strengthen the localized optical field through the excitation plasmon. LSPR can be exploited to dramatically enhance light–matter interaction, enabling nonlinear effects observable with low incident light intensity [69, 70]. Nonlinear plasmonics is a fast-growing field of research due to its potential applications in energy [71], optoelectronic devices [72], and biological imaging and sensing [73]. LSPR could boost nonlinear optical effects by tuning the shape of the nanostructures such as non-centrosymmetric gold nanocup [74] for enhanced second-harmonic generation (SHG) and gold bowtie antenna [75] for third-harmonic generation (THG).

The nonlinear response of a model plasmonic system, a linear silver chain coupled to molecules (Fig. 10a (i)), is investigated using *ab initio* TDDFT [76]. The laser field polarized along the chain direction is shaped as a Gaussian wave packet. Laser frequency is set to the plasmon resonance frequency 1.69 eV and intensity is 0.01 V/Å. The tunneling current I_t is collected at the central plane between the end atom of the silver chain and water molecule in $\text{Ag}_6\text{H}_2\text{O}$, and it is at the same position for the isolated chain Ag_6 . The variation in the current can be related to experimentally measurable quantities such as emission of high-energy photoelectrons or localized high harmonic generation [77].

In the isolated silver chain, the tunneling current coherently oscillates following the external field and continues to oscillate with negligible decay after field attenuation (Fig. 10a (ii)). With a water molecule adsorbed, the tunneling current exhibits phase shifts in the oscillations and shows the emergence of high-frequency modulation (Fig. 10a (iii)). Figure 10b shows the spectra of tunneling current

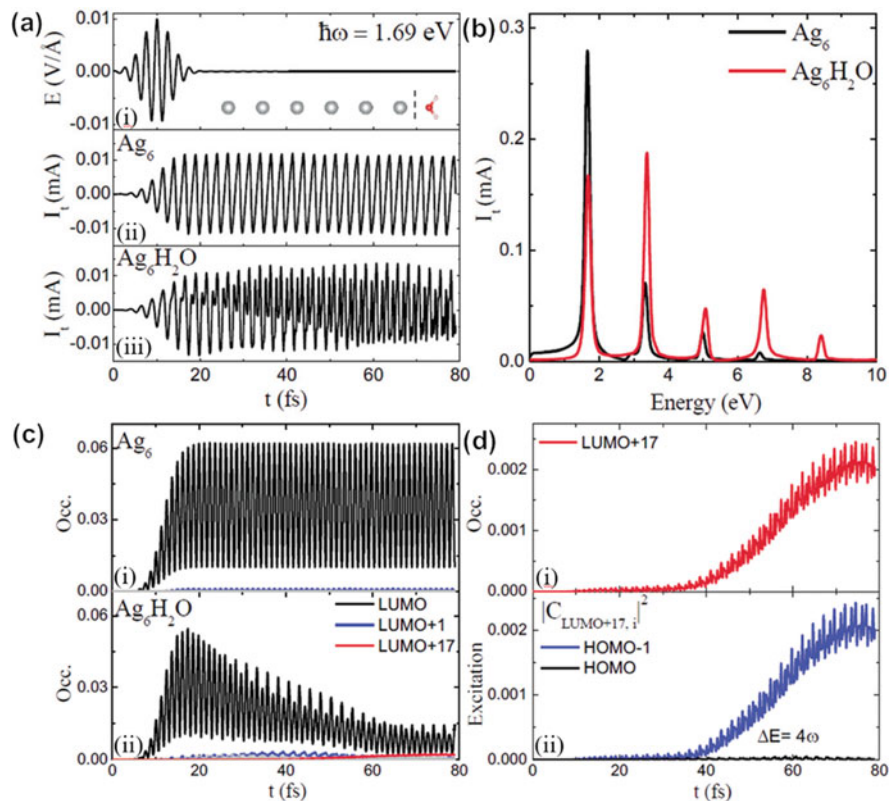


Fig. 10 (a) Time evolution of the applied laser field (i) and tunnel currents for Ag_6 (ii) and $\text{Ag}_6\text{H}_2\text{O}$ (iii). The maximum laser intensity E_{max} is 0.01 V/Å with a resonant frequency of 1.69 eV. (b) Corresponding tunneling current spectra for Ag_6 and $\text{Ag}_6\text{H}_2\text{O}$. (c) Time-evolved occupation of initially unoccupied KS states in (i) Ag_6 and (ii) $\text{Ag}_6\text{H}_2\text{O}$ driven by the laser pulse. (d) Zoomed-in plot for the occupation of the LUMO+17 state shown in panel (c). (d) Corresponding time-dependent transition coefficient from all occupied states i to the LUMO+17 state for $\text{Ag}_6\text{H}_2\text{O}$ [76]

obtained by the Fourier transform of its time evolution. In addition to Mie resonance and SHG, the third, fourth, and fifth-order excitations emerge for $\text{Ag}_6\text{H}_2\text{O}$. The SHG peak is even stronger than that for Mie resonance. In contrast, for the isolated silver chain, Mie resonance dominates the spectrum, and nonlinear responses are weaker than those for $\text{Ag}_6\text{H}_2\text{O}$. Therefore, adsorbing polar molecule such as a water molecule at the end of nanoparticle could greatly enhance the nonlinear responses.

To gain a deeper insight into plasmon-induced nonlinear responses, the time-evolved occupation of KS states (Fig. 10c) is calculated by projecting time-dependent KS states onto the ground state. For the silver chain, the occupation of the lowest unoccupied molecular orbital (LUMO) oscillates coherently and increases to 0.06 (i.e., $\sim 0.12e$), and continuously oscillates without decay after laser falling

off (Fig. 10c (i)). For $\text{Ag}_6\text{H}_2\text{O}$, the occupation of LUMO starts to decline upon laser field attenuation (Fig. 10c (ii)), different from the case of Ag_6 . Therefore, water adsorption at the end of the silver chain greatly accelerates plasmon decay. In addition, the occupation of LUMO decreases exponentially leading to the excitation of high-energy electrons. Therefore, plasmon decay of the silver chain into high-energy electron-hole pairs is identified as nonradiative Landau damping [78].

Interestingly, the occupations of a few high-energy orbitals of $\text{Ag}_6\text{H}_2\text{O}$, particularly the LUMO+17 state, change significantly. Within the timespan of laser excitation, the occupation of LUMO+17 is almost zero (Fig. 10d (i)). With laser decay, the occupation increases drastically. Figure 10d (ii) displays the transition coefficients from occupied states to initial LUMO+17 state. The transition mainly comes from the HOMO-1 state, suggesting the generation of hot electrons promoted from HOMO-1 to LUMO+17. Moreover, the energy difference between HOMO-1 and LUMO+17 is 6.70 eV, which is approximately four times the incident laser frequency (1.69 eV). That is, the fourth-order nonlinear response is estimated to be originated from electron transitions from HOMO-1 to LUMO+17 through Landau damping during plasmon decay. Other nonlinear responses including SHG and THG have similar origins. The results shed light on the atomistic mechanisms regarding how hot electrons generated by plasmon decay contribute to nonlinear responses.

5 Summary

This chapter has covered the fundamentals of hot electrons in plasmonic nanostructures and its applications in photocatalysis. Optimizing the size and shape of nanostructure so as to maximize the electromagnetic fields would increase hot-electron generation. Direct or indirect hot-electron transfer occurs when plasmonic metal contact with the attached acceptor. Specially, charge-transfer enhancement by better energy overlap between plasmon-induced hot electrons and the adsorbate's unpopulated state is crucial for plasmon-enhanced reactions. In addition, high-energy hot-electrons from plasmon decay could drive the optical nonlinear effect with a wide range of practical plasmonic applications. Meanwhile, it is a big challenge to provide a holistic description of the photocatalytic process and atomic mechanism [79]. With the advances in nanotechnology and nanoscale characterization in the future, plasmon-induced hot electrons will be ripe in designing highly tunable and selective catalytic systems along with carrying out significant improvement in the effective use of solar energy.

Acknowledgments This work was supported by the National Key R&D Program of China (Grant No. 2020YFA0211300), the National Natural Science Foundation of China (Nos. 92050112, 12074237 and 12004233), and the Fundamental Research Funds for Central Universities (GK201701008).

References

1. Hertz, H. (1887). Ueber einen Einfluss des ultravioletten Lichtes auf die electriche Entladung. *Annals of Physical Chemistry*, 267, 983–1000.
2. Einstein, A. (1905). Über einen die Erzeugung und Verwandlung des Lichtes betreffenden heuristischen Gesichtspunkt. *Annals of Physics*, 322, 132–148.
3. Planck, M. (1901). Ueber das gesetz der energieverteilung im normalspectrum. *Annals of Physics*, 309, 553–563.
4. Brongersma, M. L., Halas, N. J., & Nordlander, P. (2015). Plasmon-induced hot carrier science and technology. *Nature Nanotechnology*, 10, 25–34.
5. Hüfner, S. (2003). *Photoelectron spectroscopy: Principles and applications*. Springer.
6. Atwater, H. A. (2007). The promise of plasmonics. *Scientific American*, 296, 56–62.
7. Clavero, C. (2014). Plasmon-induced hot-electron generation at nanoparticle/metal-oxide interfaces for photovoltaic and photocatalytic devices. *Nature Photonics*, 8, 95–103.
8. Atwater, H. A., & Polman, A. (2010). Plasmonics for improved photovoltaic devices. *Nature Materials*, 9, 205–213.
9. Tian, Y., & Tatsuma, T. (2005). Mechanisms and applications of plasmon-induced charge separation at TiO₂ films loaded with gold nanoparticles. *Journal of the American Chemical Society*, 127, 7632–7637.
10. Linic, S., Christopher, P., & Ingram, D. B. (2011). Plasmonic-metal nanostructures for efficient conversion of solar to chemical energy. *Nature Materials*, 10, 911–921.
11. Wu, K., Chen, J., McBride, J. R., & Lian, T. (2015). Efficient hot-electron transfer by a Plasmon-induced interfacial charge-transfer transition. *Science*, 349, 632–635.
12. Linic, S., Aslam, U., Boerigter, C., & Morabito, M. (2015). Photochemical transformations on plasmonic metal nanoparticles. *Nature Materials*, 14, 567–576.
13. Zhang, Z., Zhang, C., Zheng, H., & Xu, H. (2019). Plasmon-driven catalysis on molecules and nanomaterials. *Accounts of Chemical Research*, 52, 2506–2515.
14. Zhang, Y., He, S., Guo, W., Hu, Y., Huang, J., Mulcahy, J. R., & Wei, W. D. (2018). Surface-Plasmon-driven hot electron photochemistry. *Chemical Reviews*, 118, 2927–2954.
15. Sönnichsen, C., et al. (2002). Drastic reduction of plasmon damping in gold nanorods. *Physical Review Letters*, 88, 077402.
16. Lehmann, J., et al. (2000). Surface plasmon dynamics in silver nanoparticles studied by femtosecond time-resolved photoemission. *Physical Review Letters*, 85, 2921–2924.
17. Hao, F., et al. (2008). Symmetry breaking in plasmonic nanocavities: Subradiant LSPR sensing and a tunable Fano resonance. *Nano Letters*, 8, 3983–3988.
18. Manjavacas, A., Liu, J., Kulkarni, V., & Nordlander, P. (2014). Plasmon-induced hot carriers in metallic nanoparticles. *ACS Nano*, 8, 7630–7638.
19. Aslam, U., Rao, V. G., Chavez, S., & Linic, S. (2018). Catalytic conversion of solar to chemical energy on plasmonic metal nanostructures. *Nature Catalysis*, 1, 656–665.
20. Watanabe, K., Menzel, D., Nilius, N., & Freund, H. J. (2006). Photochemistry on metal nanoparticles. *Chemical Reviews*, 106, 4301–4320.
21. Lisowski, M., et al. (2004). Ultra-fast dynamics of electron thermalization, cooling and transport effects in Ru(001). *Applied Physics A: Materials Science & Processing*, 78, 165–176.
22. Inouye, H., Tanaka, K., Tanahashi, I., & Hirao, K. (1998). Ultrafast dynamics of nonequilibrium electrons in a gold nanoparticle system. *Physical Review B*, 57, 11334–11340.
23. Fang, Z., Zhen, Y. R., Neumann, O., Polman, A., Garcia de Abajo, F. J., Nordlander, P., & Halas, N. J. (2013). Evolution of light-induced vapor generation at a liquid-immersed metallic nanoparticle. *Nano Letters*, 13, 1736–1742.
24. Frischkorn, C., & Wolf, M. (2006). Femtochemistry at metal surfaces: Nonadiabatic reaction dynamics. *Chemical Reviews*, 106, 4207–4233.
25. Du, L., Furube, A., Hara, K., Katoh, R., & Tachiya, M. (2013). Ultrafast Plasmon induced electron injection mechanism in gold-TiO₂ nanoparticle system. *Journal of Photochemistry and Photobiology, C: Photochemistry Reviews*, 15, 21–30.

26. Liu, J. G., Zhang, H., Link, S., & Nordlander, P. (2018). Relaxation of Plasmon-induced hot carriers. *ACS Photonics*, *5*, 2584–2595.
27. Link, S., & El-Sayed, M. (1999). Spectral properties and relaxation dynamics of surface plasmon electronic oscillations in gold and silver nanodots and nanorods. *The Journal of Physical Chemistry B*, *103*, 8410–8426.
28. Dowgiallo, A. M., & Knappenberger, K. L. (2011). Ultrafast electron-phonon coupling in hollow gold Nanospheres. *Physical Chemistry Chemical Physics*, *13*, 21585–21592.
29. Minutella, E., Schulz, F., & Lange, H. (2017). Excitation-dependence of Plasmon-induced hot electrons in gold nanoparticles. *Journal of Physical Chemistry Letters*, *8*, 4925–4929.
30. Su, M., et al. (2019). Ultrafast electron dynamics in single aluminum nanostructures. *Nano Letters*, *19*, 3091–3097.
31. Kreibig, U., & Vollmer, M. (1995). *Optical properties of metal clusters*. Springer.
32. Langhammer, C., Yuan, Z., Zorić, I., & Kasemo, B. (2006). Plasmonic properties of supported Pt and Pd nanostructures. *Nano Letters*, *6*, 833–838.
33. Yu, K., Tian, Y., & Tatsuma, T. (2006). Size effects of gold nanoparticles on plasmon-induced photocurrents of gold–TiO₂ nanocomposites. *Physical Chemistry Chemical Physics*, *8*, 5417–5420.
34. Nishijima, Y., et al. (2012). Near-infrared plasmon-assisted water oxidation. *Journal of Physical Chemistry Letters*, *3*, 1248–1252.
35. Nishijima, Y., Ueno, K., Yokota, Y., Murakoshi, K., & Misawa, H. (2010). Plasmon-assisted photocurrent generation from visible to near-infrared wavelength using a Au-nanorods/TiO₂ electrode. *Journal of Physical Chemistry Letters*, *1*, 2031–2036.
36. Mubeen, S., et al. (2013). An autonomous photosynthetic device in which all charge carriers derive from surface plasmons. *Nature Nanotechnology*, *8*, 247–251.
37. Skoplaki, E., & Palyvos, J. A. (2009). On the temperature dependence of photovoltaic module electrical performance: A review of efficiency/power correlations. *Solar Energy*, *83*, 614–624.
38. Rossi, T. P., Erhart, P., & Kuisma, M. (2020). Hot-carrier generation in Plasmonic nanoparticles: The importance of atomic structure. *ACS Nano*, *14*, 9963–9971.
39. Kazuma, E., Sakai, N., & Tatsuma, T. (2011). Nanoimaging of localized plasmon-induced charge separation. *Chemical Communications*, *47*, 5777–5779.
40. Kazuma, E., & Tatsuma, T. (2013). Photoelectrochemical analysis of allowed and forbidden multipole plasmon modes of polydisperse Ag nanorods. *Journal of Physical Chemistry C*, *117*, 2435–3441.
41. Knight, M. W., Sobhani, H., Nordlander, P., & Halas, N. J. (2011). Photodetection with active optical antennas. *Science*, *332*, 702–704.
42. Kumar, P. V., et al. (2019). Plasmon-induced direct hot-carrier transfer at metal-acceptor interfaces. *ACS Nano*, *13*, 3188–3195.
43. Chen, Y.-C., Hsu, Y.-K., Popescu, R., Gerthsen, D., Lin, Y. G., & Feldmann, C. (2018). Au@Nb@HxK1–xNbO3 nanopeapods with near-infrared active plasmonic hot-electron injection for water splitting. *Nature Communications*, *9*, 232.
44. Foerster, B., Joplin, A., Kaefer, K., Celiksoy, S., Link, S., & Sonnichsen, C. (2017). Chemical Interface damping depends on electrons reaching the surface. *ACS Nano*, *11*, 2886–2893.
45. Kazuma, E., Jung, J., Ueba, H., Trenary, M., & Kim, Y. (2018). Real-space and real-time observation of a plasmon-induced chemical reaction of a single molecule. *Science*, *360*, 521–525.
46. Wu, K., Chen, J., McBride, J. R., & Lian, T. (2015). Efficient hot-electron transfer by a Plasmon-induced interfacial charge-transfer transition. *Science*, *349*, 632–635.
47. Tan, S., Dai, Y., Zhang, S., Liu, L., Zhao, J., & Petek, H. (2018). Coherent electron transfer at the Ag/Graphite heterojunction interface. *Physical Review Letters*, *120*, 126801.
48. Zhang, J., Guan, M., Lischner, J., Meng, S., & Prezhdo, O. V. (2019). Coexistence of different charge-transfer mechanisms in the hot-carrier dynamics of hybrid Plasmonic nanomaterials. *Nano Letters*, *19*, 3187–3193.
49. Runge, E., & Gross, E. K. U. (1984). Density-functional theory for time-dependent systems. *Physical Review Letters*, *52*, 997–1000.

50. Ma, J., & Gao, S. (2019). Plasmon-induced electron–hole separation at the Ag/TiO₂(110) Interface. *ACS Nano*, *13*, 13658–13667.
51. Liu, Z. W., Hou, W. B., Pavaskar, P., Aykol, M., & Cronin, S. B. (2011). Plasmon resonant enhancement of photocatalytic water splitting under visible illumination. *Nano Letters*, *11*, 1111–1116.
52. Yan, L., Xu, J., Wang, F., & Meng, S. (2018). Plasmon-induced ultrafast hydrogen production in liquid water. *Journal of Physical Chemistry Letters*, *9*, 63–69.
53. Golubev, A. A., Khlebtsov, B. N., Rodriguez, R. D., Chen, Y., & Zahn, D. R. T. (2018). Plasmonic heating plays a dominant role in the Plasmon-induced photocatalytic reduction of 4-Nitrobenzenethiol. *Journal of Physical Chemistry C*, *122*, 5657–5663.
54. Zhang, C., Lu, J., Jin, N., Dong, L., Fu, Z., Zhang, Z., & Zheng, H. (2019). Plasmon driven rapid in-situ formation of luminescence single crystal nanoparticle. *Small*, *15*, 1901286.
55. Christopher, P., Xin, H., & Linic, S. (2011). Visible-light-enhanced catalytic oxidation reactions on plasmonic silver nanostructures. *Nature Chemistry*, *3*, 467–472.
56. Yan, L., Ding, Z., Song, P., Wang, F., & Meng, S. (2015). Plasmon-induced dynamics of H₂ splitting on a silver atomic chain. *Applied Physics Letters*, *107*, 083102.
57. Yan, L., Wang, F., & Meng, S. (2016). Quantum mode selectivity of Plasmon-induced water splitting on gold nanoparticles. *ACS Nano*, *10*, 5452–5458.
58. Kale, M. J., Avanesian, T., Xin, H., Yan, J., & Christopher, P. (2014). Controlling catalytic selectivity on metal nanoparticles by direct photoexcitation of adsorbate–metal bonds. *Nano Letters*, *14*, 5405–5412.
59. Langhammer, C., Kasemo, B., & Zoric, I. (2007). Absorption and scattering of light by Pt, Pd, Ag, and Au nanodisks: Absolute cross sections and branching ratios. *The Journal of Chemical Physics*, *126*, 194702.
60. Naldoni, A., Montini, T., Malara, F., Mróz, M. M., Beltram, A., Virgili, T., Boldrini, C. L., Marelli, M., Romero-Ocaña, I., Delgado, J. J., Dal Santo, V., & Fornasiero, P. (2017). Hot electron collection on Brookite Nanorods lateral facets for Plasmon-enhanced water oxidation. *ACS Catalysis*, *7*, 1270–1278.
61. Sakamoto, H., Ohara, T., Yasumoto, N., Shiraishi, Y., Ichikawa, S., Tanaka, S., & Hirai, T. (2015). Hot-electron-induced highly efficient O₂ activation by Pt nanoparticles supported on Ta₂O₅ driven by visible light. *Journal of the American Chemical Society*, *137*, 9324–9332.
62. Lupetti, M., Hengster, J., Uphues, T., & Scrinzi, A. (2014). Attosecond photocopy of plasmonic excitations. *Physical Review Letters*, *113*, 113903.
63. Mukherjee, S., Libisch, F., Large, N., Neumann, O., Brown, L. V., Cheng, J., Lassiter, J. B., Carter, E. A., Nordlander, P., & Halas, N. J. (2013). Hot electrons do the impossible: Plasmon-induced dissociation of H₂ on Au. *Nano Letters*, *13*, 240–247.
64. Seemala, B., Therrien, A. J., Lou, M., Li, K., Finzel, J. P., Qi, J., Nordlander, P., & Christopher, P. (2019). Plasmon-mediated catalytic O₂ dissociation on Ag nanostructures: Hot electrons or near fields? *ACS Energy Letters*, *4*, 1803–1809.
65. Townsend, E., & Bryant, G. W. (2014). Which resonances in small metallic nanoparticles are Plasmonic? *Journal of Optics*, *16*, 114022.
66. Townsend, E., & Bryant, G. W. (2012). Plasmonic properties of metallic nanoparticles: The effects of size quantization. *Nano Letters*, *12*, 429–434.
67. Ma, J., Wang, Z., & Wang, L. W. (2015). Interplay between Plasmon and single-particle excitations in a metal nanocluster. *Nature Communications*, *6*, 10107.
68. Grinblat, G., Li, Y., Nielsen, M. P., Oulton, R. F., & Maier, S. A. (2016). Enhanced third harmonic generation in single germanium Nanodisks excited at the Anapole mode. *Nano Letters*, *16*, 4635.
69. Mohamed, M. B., Volkov, V., Link, S., & El-Sayed, M. A. (2000). The ‘lightning’ gold nanorods: Fluorescence enhancement of over a million compared to the gold metal. *Chemical Physics Letters*, *317*, 517.
70. Kauranen, M., & Zayats, A. V. (2012). Calculated absorption and scattering properties of gold nanoparticles of different size, shape, and composition: Applications in biological imaging and biomedicine. *Nature Photonics*, *6*, 737.

71. Narang, P., Sundararaman, R., Jermyn, A. S., Goddard, W. A., & Atwater, H. A. (2016). Cubic nonlinearity driven up-conversion in high-field plasmonic hot carrier systems. *Journal of Physical Chemistry C*, *120*, 21056.
72. Van Sark, W., de Wild, J., Rath, J. K., Meijerink, A., & Schropp, R. E. I. (2013). Upconversion in solar cells. *Nanoscale Research Letters*, *8*, 81.
73. Arppe, R., Näreoja, T., Nylund, S., Mattsson, L., Koho, S., Rosenholm, J. M., Soukka, T., & Schäferling, M. (2014). Photon upconversion sensitized nanoprobles for sensing and imaging of pH. *Nanoscale*, *6*, 6837.
74. Zhang, Y., Grady, N. K., Ayala-Orozco, C., & Halas, N. J. (2011). Three-dimensional nanostructures as highly efficient generators of second harmonic light. *Nano Letters*, *11*, 5519.
75. Hanke, T., Cesar, J., Knittel, V., Trügler, A., Hohenester, U., Leitenstorfer, A., & Bratschitsch, R. (2012). Tailoring spatiotemporal light confinement in single plasmonic nanoantennas. *Nano Letters*, *12*, 992.
76. Yan, L., Guan, M., & Meng, S. (2018). Plasmon-induced nonlinear response of silver atomic chains. *Nanoscale*, *10*, 8600.
77. Li, S., & Jones, R. R. (2016). High-energy electron emission from metallic nano-tips driven by intense single-cycle terahertz pulses. *Nature Communications*, *7*, 13405.
78. Kale, M. J., Avanesian, T., & Christopher, P. (2014). Direct photocatalysis by plasmonic nanostructures. *ACS Catalysis*, *4*, 116.
79. Cortés, E., Besteiro, L. V., Alabastri, A., Baldi, A., Tagliabue, G., Demetriadou, A., & Narang, P. (2020). Challenges in plasmonic catalysis. *ACS Nano*, *14*, 16202–16219.

Plasmon-Enhanced Optical Forces and Tweezers



Domna G. Kotsifaki, Viet Giang Truong, and Sile Nic Chormaic

Abstract In 2018, the Swedish Academy of Sciences awarded one half of the Nobel Prize in Physics to Arthur Ashkin for his pioneering work on optical tweezers and their applications in biology. Since then, the manipulation of small particles using optical forces has gained significant attention and generated a wide interest across the fields of physics, chemistry, and medicine. This chapter describes the underlying physics governing the plasmon-enhanced optical forces generated by the integration of optical tweezers with plasmonic nanostructures. The aim of this chapter is to provide the reader with the basic ideas and mathematical expressions that can be used to understand the nature of optical forces at the nanoscale. We also discuss some of the important applications of nano-enhanced optical manipulation techniques in life sciences.

Keywords Optical forces · Maxwell's stress tensor · Metallic nanostructures · Plasmonic optical tweezers · Optothermal plasmonic tweezers

1 Introduction

In 1970, Ashkin discovered that a slightly focussed laser beam could attract small objects towards the beam centre [1]. The particles, in this case, are confined to the optical axis, and propelled in the direction of light propagation. Ashkin demonstrated optical guiding of particles suspended in a liquid, as well as in air, and trapped the particles by balancing the radiation pressure against the gravitational force using an inverted geometry [1]. Moreover, he demonstrated the three-dimensional confinement of particles using counter-propagating laser beams. The single-beam gradient optical tweezers was first demonstrated in 1986 by Ashkin

D. G. Kotsifaki (✉) · V. G. Truong · S. Nic Chormaic (✉)
Light-Matter Interactions for Quantum Technologies Unit, Okinawa Institute of Science and
Technology Graduate University, Onna-son, Okinawa, Japan
e-mail: domna.kotsifaki@oist.jp; v.g.truong@oist.jp; sile.nicchormaic@oist.jp

© The Author(s), under exclusive license to Springer Nature Switzerland AG 2022
P. Yu et al. (eds.), *Plasmon-enhanced light-matter interactions*,
Lecture Notes in Nanoscale Science and Technology 31,
https://doi.org/10.1007/978-3-030-87544-2_8

177

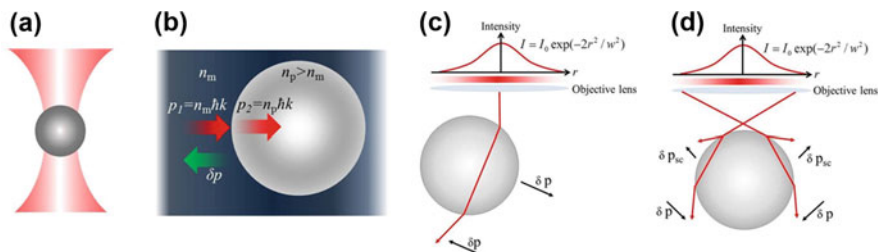


Fig. 1 (a) Schematic of a particle trapped at the centre of a laser beam. (b) Momentum, \mathbf{p} , of the photons impinging on a particle at normal incidence. (c, d) Ray diagrams illustrating the origin of the optical gradient force for non-normal incident rays in a tightly focussed Gaussian beam. Symbols: n_p is the refractive index of the particle, n_m is the refractive index of the surrounding medium, the wavenumber, $k = 2\pi n_m/\lambda$, where λ is the wavelength of light, \hbar is the reduced Planck's constant, δp is a momentum difference, w is the Gaussian beam waist, I is the intensity of the Gaussian beam, and δp_{sc} is the component of momentum transfer that contributes to the scattering force. (Figure reproduced with permission from Ref. [19]; copyright 2016 American Chemical Society)

and coworkers [2]. Since then, several applications of this technique have been proposed and developed [3]. In the last few years, the optical trapping technique has been advanced even further, and optical tweezers have become important tools in the fields of biology [4], physics [5], and biophysics [6]. The physics behind optical tweezers has been understood for a long time [7–11]. Therefore, a single-beam gradient trap can be created by focussing a laser beam onto a diffraction-limited spot using an objective lens with a high numerical aperture (NA) as illustrated in Fig. 1. The strong field gradient near the focus creates a potential well, in which a particle can be trapped in three dimensions. A variety of particles including atoms [12–16], dielectric particles [17–21], small metal particles [22, 23], nanoplastics [24, 25] and living bio-entities [26–33], with sizes ranging from several nanometres to tens of micrometres, can be trapped and manipulated using optical tweezers. However, the gradient force vary with the cube of the particle size; hence, smaller particles require higher laser powers for stable trapping. At such high laser powers, more than 100 mW [34], the trapped particles typically undergo rapid optical damage. Furthermore, Abbe's diffraction limit restricts the minimum particle size that can be trapped efficiently. These obstacles make trapping and manipulating nanometre-sized particles particularly challenging.

Optical tweezers based on metallic nanostructures [35–45] were developed to overcome the limitations imposed by free-space diffraction as well as to enhance the local optical intensity within the trap. In Sect. 2 of this chapter, we introduce the fundamental concepts underlying optical tweezers based on the classical electromagnetic wave theory. The physics behind optical trapping involves a net exchange of linear momentum between the light field and the scattered object that is described by Maxwell's equations. Consequently, as per the law of conservation of linear momentum, a force is exerted on the object by the light beam. Particles much smaller than the beam wavelength behave similarly to an electric dipole; hence, a

simple description is used to derive the optical forces acting on the dipole. Such particles undergo Rayleigh scattering. In contrast, particles with a size comparable to or larger than the beam wavelength undergo Lorentz-Mie scattering, wherein the optical forces are modelled using classical electromagnetic theory. The Maxwell stress tensor method is used to determine the net optical force or torque exerted by the beam on particle size in Lorentz-Mie regime. Moreover, the Langevin equation, which predicts the motion of the particle near the focussed beam and describes its behaviour in the optical trap, is presented.

In Sect. 3, we discuss the limitations encountered by conventional optical tweezers when dealing with nanometre-sized objects. Section 4 highlights the geometries of the metallic nanostructures (disks, nano-antennas, nanoholes, etc.) that have been used to enhance the optical forces in the nanoscale regime. In Sect. 5, applications of plasmonic optical tweezers (POTs) in the life sciences, especially to manipulate biomolecules such as proteins and nucleic acids, are addressed. A review of optothermal plasmonic trapping field is presented in Sect. 6 and, finally, Sect. 7 summarises the main conclusions from the current state-of-the-art techniques in optical manipulation and provides future perspectives in this field.

2 Optical Forces and Torque

2.1 Maxwell's Stress Tensor

The derivation of the optical forces generated owing to the interaction between an electromagnetic field and an object is based on the conservation of linear momentum, which, in turn, can be derived using Maxwell's equations in vacuum [46], given by:

$$\nabla \times \mathbf{E}(\mathbf{r}, t) = -\frac{\partial \mathbf{B}(\mathbf{r}, t)}{\partial t}, \quad (1)$$

$$\nabla \times \mathbf{B}(\mathbf{r}, t) = \frac{1}{c^2} \frac{\partial \mathbf{E}(\mathbf{r}, t)}{\partial t} + \mu_0 \mathbf{j}(\mathbf{r}, t), \quad (2)$$

$$\nabla \cdot \mathbf{E}(\mathbf{r}, t) = \frac{1}{\varepsilon_0} \rho(\mathbf{r}, t), \quad (3)$$

$$\nabla \cdot \mathbf{B}(\mathbf{r}, t) = 0, \quad (4)$$

where ε_0 and μ_0 are the dielectric permittivity and magnetic permeability in vacuum, respectively, $\mathbf{E}(\mathbf{r}, t)$ is the electric field, $\mathbf{B}(\mathbf{r}, t)$ is the magnetic field, $\rho(\mathbf{r}, t)$ is the total electric charge density, $\mathbf{j}(\mathbf{r}, t)$ is the total electric current density and c

is the speed of light. The Lorentz force, $\mathbf{F}(\mathbf{r}, t)$, exerted on a particle of charge q and moving with velocity $\mathbf{v}(\mathbf{r}, t)$ through an electric field, $\mathbf{E}(\mathbf{r}, t)$, and magnetic field, $\mathbf{B}(\mathbf{r}, t)$, is defined as [47]:

$$\begin{aligned}\mathbf{F}(\mathbf{r}, t) &= q [\mathbf{E}(\mathbf{r}, t) + \mathbf{v}(\mathbf{r}, t) \times \mathbf{B}(\mathbf{r}, t)] \\ &= \int_V [\rho(\mathbf{r}, t) \mathbf{E}(\mathbf{r}, t) + \mathbf{j}(\mathbf{r}, t) \times \mathbf{B}(\mathbf{r}, t)] dV.\end{aligned}\quad (5)$$

The Minkowski form of Maxwell's stress tensor, $\overset{\leftrightarrow}{\mathbf{T}}$, in a medium is defined as [47]:

$$\overset{\leftrightarrow}{\mathbf{T}} = \varepsilon_0 \varepsilon \mathbf{E} \mathbf{E} + \mu_0 \mu \mathbf{H} \mathbf{H} - \frac{1}{2} (\varepsilon_0 \varepsilon E^2 + \mu_0 \mu H^2) \overset{\leftrightarrow}{\mathbf{I}}, \quad (6)$$

where the notation $\mathbf{E} \mathbf{E}$ denotes the outer product, E^2 and H^2 are the electric and magnetic field ($\mathbf{H}(\mathbf{r}, t) = \frac{1}{\mu} \mathbf{B}(\mathbf{r}, t)$) strengths, respectively, $\overset{\leftrightarrow}{\mathbf{I}}$ denotes the unit tensor, ε and μ are the non-dispersive dielectric permittivity and magnetic permeability in surrounding medium, respectively. An alternative definition of Maxwell's stress tensor, proposed by Max Abraham [48], does not consider the material properties, such that the resultant momentum represents the momentum stored in the electromagnetic field only [49]. In contrast, the Minkowski definition includes the momentum of the matter that interacts with the electromagnetic field and hence, is particularly useful when calculating the interaction between light and matter, and the resultant optical force [50]. Using Maxwell's Eqs. (1, 2, 3, and 4) and integrating over an arbitrary volume, V , we obtain:

$$\begin{aligned}\int_V \nabla \cdot \overset{\leftrightarrow}{\mathbf{T}} dV &= \frac{1}{c^2} \frac{d}{dt} \int_V (\mathbf{E}(\mathbf{r}, t) \times \mathbf{H}(\mathbf{r}, t)) dV \\ &+ \int_V (\rho(\mathbf{r}, t) \mathbf{E}(\mathbf{r}, t) + \mathbf{j}(\mathbf{r}, t) \times \mathbf{B}(\mathbf{r}, t)) dV.\end{aligned}\quad (7)$$

The last term of Eq. (7) can be recognized as the mechanical force (see Eq. (5)). The volume integral can be transformed into a surface integral using Gauss's law, such that:

$$\int_V \nabla \cdot \overset{\leftrightarrow}{\mathbf{T}} dV = \int_{\partial V} \overset{\leftrightarrow}{\mathbf{T}}(\mathbf{r}, t) \cdot \mathbf{n}(\mathbf{r}) da = \frac{d[\mathbf{P}_{field} + \mathbf{P}_{mech}]}{dt}, \quad (8)$$

where dV denotes the surface enclosing the V , \mathbf{n} is the unit vector perpendicular to the surface, da is an infinitesimal surface element, and \mathbf{P}_{field} and \mathbf{P}_{mech} are the electromagnetic and mechanical momenta, respectively. In Eq. (8), we have used

Newton's second law to derive the mechanical force and a similar definition to derive the electromagnetic momentum, which describes the momentum carried by the electromagnetic field within a volume V . Assuming harmonic electromagnetic fields, the time-averaged optical force, $\langle \mathbf{F} \rangle$, acting on the scattered object is defined as:

$$\langle \mathbf{F} \rangle = \int_{\partial V} \langle \vec{\mathbf{T}}(\mathbf{r}, t) \rangle \cdot \mathbf{n}(\mathbf{r}) da. \quad (9)$$

Note that Eq. (9) is generally valid and is used to calculate the mechanical force acting on an object within the closed surface, ∂V .

2.2 Dipole Approximation Regime

The Rayleigh scattering or dipole approximation regime applies when the diameter of the particle is smaller than the wavelength of light ($d < \lambda$), where d is the radius of the particle. Therefore, a general expression for the optical force can be derived by considering the interaction of the electromagnetic field of the laser beam with the particle itself, which is treated as a point dipole. If we consider two oppositely charged particles separated by a small distance and irradiated by an arbitrary monochromatic electromagnetic wave with frequency ω , then the total force acting on the system of particles is given by [47]:

$$\mathbf{F} = (\mathbf{p} \cdot \nabla) \mathbf{E}(\mathbf{r}, t) + \mathbf{p} \times (\nabla \times \mathbf{E}(\mathbf{r}, t)) + \frac{d}{dt} (\mathbf{p} \times \mathbf{B}(\mathbf{r}, t)). \quad (10)$$

In Eq. (10) the force consists of the term originates from the interaction of the particles with an inhomogeneous electric field and the Lorentz force. Note that Eq. (10) represents the mechanical force exerted by the electromagnetic field on the two particles that are represented by the dipole moment \mathbf{p} . To derive the basic equations for a particle in an optical trap, we consider the simple case of a particle oscillating in a classical radiation field. The time average of the force can be written as [47]:

$$\langle \mathbf{F} \rangle = \sum_i \langle p_i(t) \nabla E_i(t) \rangle, \quad (11)$$

where $i = x, y, z$ denotes the Cartesian components. We assume the following: there is a linear relationship between the dipole and electric field, the dipole oscillates with the same frequency as the driving frequency, and the particle has no static dipole moment. Then, the induced dipole moment, \mathbf{p} , is proportional to the electric field at the particle position, r , and is given by the following equation [47]:

$$\underline{\mathbf{p}} = \alpha(\omega) \underline{\mathbf{E}}(\mathbf{r}_0), \quad (12)$$

where $\alpha(\omega)$ is a tensor of rank two that denotes the polarisability of the particle, and the underline denotes the complex amplitudes. Using Eq. (12) in Eq. (11), the average force owing to the radiation field acting on the oscillator becomes [47]:

$$\langle \mathbf{F} \rangle = \frac{\alpha'}{2} \sum_i \Re \{ \underline{E}_i^* \nabla \underline{E}_i \} + \frac{\alpha''}{2} \sum_i \Im \{ \underline{E}_i^* \nabla \underline{E}_i \}, \quad (13)$$

where $\alpha = \alpha' + i\alpha''$. Note that the real part of Eq. (13) accounts for the gradient force, while the imaginary part accounts for the absorption and longitudinal component of the scattering force. Therefore, the gradient force is proportional to the dispersive part of the complex polarisability, whereas the scattering force is proportional to the dissipative part of the complex polarisability. The gradient force originates from field inhomogeneities, while the scattering force arises because of momentum transfer from the radiation field to the particle. The gradient force accelerates the polarisable particles toward the extremes of the radiation field. Therefore, a tightly focussed laser beam can trap particles in all dimensions at its focus. However, the scattering force pushes the particles in the direction of laser propagation; if the focus of the trapping laser is not sufficiently concentrated, then the particles can be pushed out of the trap. Note that, for an evanescent field plane wave and non-absorbing particles, the last term in Eq. (13) is zero [47]. Moreover, the imaginary part of $\alpha(\omega)$ is often assumed to be zero for dielectric, transparent particles. In the Rayleigh scattering regime, the polarisability is defined as [19]:

$$\alpha(\omega) = \frac{\alpha_0(\omega)}{1 - \frac{1}{6\pi\epsilon_0} ik^3 \alpha_0(\omega)}, \quad (14)$$

where α_0 is the Clausius-Mossotti relation defined as:

$$\alpha_0(\omega) = 4\pi n_m^2 \epsilon_0 \left(\frac{d}{2} \right)^3 \left(\frac{m^2 - 1}{m^2 + 2} \right). \quad (15)$$

The quantity $m = \frac{n_p}{n_m}$ is the ratio of the refractive indices of the particle, n_p , and the surrounding medium, n_m , and d is the particle diameter. Consequently, the gradient force is given by [51]:

$$\langle \mathbf{F}_{grad}(\mathbf{r}, t) \rangle = 4\pi n_m^2 \epsilon_0 \left(\frac{d}{2} \right)^3 \left(\frac{m^2 - 1}{m^2 + 2} \right) \frac{1}{2} \nabla E^2(\mathbf{r}, t). \quad (16)$$

The scattering force is obtained by substituting the imaginary part of the polarisability Eq. (13), as follows [51]:

$$\langle \mathbf{F}_{scat}(\mathbf{r}, t) \rangle = \frac{n_m}{c} \frac{8\pi}{3} \left(k \frac{d}{2} \right)^4 \left(\frac{d}{2} \right)^2 \left(\frac{m^2 - 1}{m^2 + 2} \right)^2 \mathbf{I}(\mathbf{r}). \quad (17)$$

The trapping potential depth, U_{trap} , is the key factor determining whether the trapping is stable and it must be large compared to the thermal energy, $k_B T$. The trapping potential is obtained by integrating the optical force as follows [52]:

$$U_{trap} = \int_{\infty}^{surface} \pi \varepsilon \left(\frac{d}{2} \right)^3 \frac{\varepsilon_p - \varepsilon}{\varepsilon_p + 2\varepsilon} \nabla |E|^2 dx = \pi \varepsilon \left(\frac{d}{2} \right)^3 \frac{\varepsilon_p - \varepsilon}{\varepsilon_p + 2\varepsilon} \nabla |E_{surface}|^2, \quad (18)$$

where ε_p , and ε are the dielectric constants of the particle and the surrounding medium, respectively. Note that the field intensity on the surface determines the depth of the trapping potential.

2.3 Optical Torque

The torque due to the gradient force does not act on a spherical particle; rather, it acts on a particle for which the associated polarisability tensor matrix is asymmetric with respect to its three components [53]. A simple example of a nonspherical particle is one with cylindrical symmetry, such as a rod. In this case, the diagonal elements of the polarisability matrix have different values, $\alpha_{||}$ and α_{\perp} , for the longitudinal and transverse directions, respectively. Note that in a prolate ellipsoid, $\alpha_{||}$ has a larger magnitude because it corresponds to a larger electron shift [53]. Such particles experience a torque in response to a linearly polarised radiation field and align themselves with their long axis parallel to the polarisation plane, which is at right angles to the direction of light propagation. The expression for the nanoscale torque, $\boldsymbol{\tau}$ is given by [53]:

$$\boldsymbol{\tau} = (\alpha_{||} - \alpha_{\perp}) (E_y \mathbf{i} - E_x \mathbf{j}) E_z, \quad (19)$$

where E_x , E_y , and E_z are the electric fields in the x , y , and z directions, respectively and \mathbf{i} and \mathbf{j} denote x and y directions, respectively.

Note that optical torque can also arise from the transfer of orbital angular momentum (OAM) and spin angular momentum (SAM) from the trapping beam to the particle. In 1936, Beth [54] demonstrated the angular momentum transfer from an optical beam to irradiated particles. He measured the torque on a suspended

birefringent half-plate as circularly polarised light passed through it. Since then, several experiments have been performed [18], demonstrating that optical beams with non-vanishing OAM can be used to transform a trapped particle into a spinning state. SAM is strongly dependent on the polarisation state of the light beam and can thus arise for beams that are either fully or partially circularly polarised; moreover, the induced torque can be reduced if there is beam scattering and reflection [53].

2.4 Additional Forces on Dielectric Particles

The gradient force has a range of several hundred nanometres and attracts the particles toward the centre of the optical trap. Based on the fact that the particle has mass and is usually suspended in liquid, as well as considering the Hookean nature of the gradient force, an equation of motion for the particle with respect to the trapping position can be written as [11]:

$$m_p \frac{d^2 \mathbf{r}}{dt^2} = \mathbf{F}_{drag} + \mathbf{F}_g + \mathbf{F}_B + \mathbf{F}_{opt} + \mathbf{F}_{other}, \quad (20)$$

where \mathbf{F}_{drag} , is the drag force [11], \mathbf{F}_g , represents gravity as well as the buoyant force [11], \mathbf{F}_B is the Brownian force [55], \mathbf{F}_{opt} is the optical gradient force [47], and \mathbf{F}_{other} represents any thermophoretic force that may be present. The drag force can be calculated using the following equation [11]:

$$\mathbf{F}_{drag} = \frac{m_p 9\eta}{2\rho_p \left(\frac{d}{2}\right)^2} (\mathbf{u} - \mathbf{v}), \quad (21)$$

where η is the viscosity of the surrounding medium, ρ_p is the density of the particle, d is the particle diameter, \mathbf{u} is the fluid velocity, and \mathbf{v} is the particle velocity. \mathbf{F}_g is calculated using the following equation [11]:

$$\mathbf{F}_g = m_p \mathbf{g} \frac{(\rho_p - \rho)}{\rho_p}, \quad (22)$$

where ρ is the solution density and \mathbf{g} is the acceleration due to gravity. The Brownian force is modeled as Gaussian white noise and is given by [55]:

$$\mathbf{F}_B = \zeta \sqrt{\frac{12\pi k_B \eta T \frac{d}{2}}{\Delta t}}, \quad (23)$$

where T is the fluid temperature in Kelvin, k_B is the Boltzmann constant, Δt is the time step, and ζ is a Gaussian random number with zero mean and unit variance. The optical force is given by Eq. (16). If we assume that no thermophoretic force is present, and that gravity along with buoyancy are negligible, then the motion of the particle can be described by the overdamped Langevin equation, such that:

$$\frac{d\mathbf{x}(t)}{dt} = \frac{k_{tot}}{\gamma} \mathbf{x}(t) + \left(\frac{2k_B T}{\gamma} \right)^{1/2} \zeta(t), \quad (24)$$

where γ [18] is the viscous damping, $\mathbf{x}(t)$ is the displacement of the particle from the equilibrium point, and k_{tot} is the total trap stiffness. In the absence of damping, Eq. (24) describes an ideal oscillator; however when there is damping, a response that is equivalent to that of a low-pass filter is generated.

Plasmon Resonance Shift Induced by Optical Trapping The resonance wavelength of a metallic nanocavity is highly sensitive to its dielectric environment, such that even a small modification of its optical near-field by nanoparticles or biomolecules in the cavity causes the resonance peaks to shift [56–58]. A general expression for the relationship between the sensitivity of the nanocavity and the material properties is important for understanding, analysing, and developing trapping-assisted nanostructures. Zhang and Martin [59] derived an expression to predict the resonance frequency shift of subwavelength plasmonic nanocavities interacting with a nanoparticle located in the near-field zone of the nanocavity itself, as illustrated in Fig. 2. Using perturbation theory and Green’s tensor technique, the authors derived the following expression for the nanoparticle trapping-induced shift in resonance frequency, $\Delta\omega_i$, of a metallic nanocavity:

$$\Delta\omega_i = -\alpha_{NP} \frac{d\omega_i}{d\varepsilon_{ca}} \frac{|\mathbf{E}(\mathbf{r}_{NP})|^2}{\int_{cavity} |\mathbf{E}(\mathbf{r})|^2 d\mathbf{r}}, \quad (25)$$

where α_{NP} is the polarisability of the nanoparticle, ε_{ca} is the permittivity of the nanocavity, and \mathbf{r}_{NP} is the location of the trapped nanoparticle or the absorbed biomolecule. Equation (25) provides a general relation for the shift in resonance frequency for subwavelength cavities made of dispersive materials.

The relationship between the resonance shift and the trapping potential of a 10 nm gold (Au) particle trapped in a metallic nanocavity [59] is shown in Fig. 2d. Specifically, the 10 nm Au particle is trapped in a gold dimer nanocavity of dimensions 60 nm \times 40 nm \times 40 nm with a 25 nm cavity gap (see Fig. 2c). The local field distribution of the nanocavity without the nanoparticle is enhanced in the gap region due to the presence of the particle. The corresponding optical force and trapping potential are calculated based on this field distribution along the minor axis of the nanocavity gap as shown in Fig. 2d. Note that the trapping potential depth attains its maximum value at the centre of the nanocavity, where the net optical force

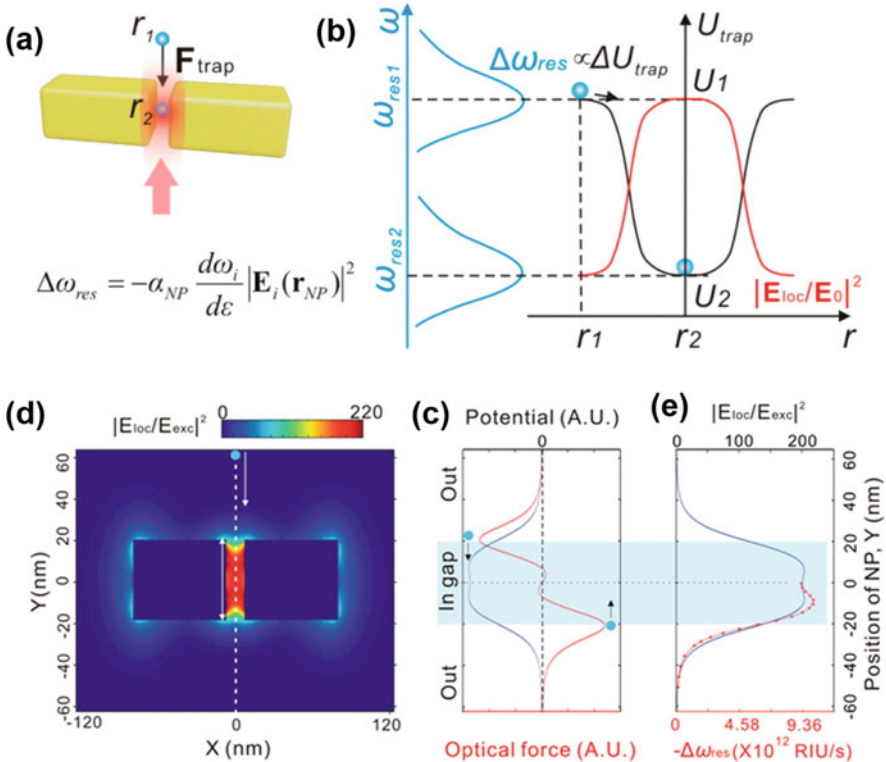


Fig. 2 (a) Schematic showing nanoparticle trapping in a metallic nanocavity, (b) Optical trapping induced cavity resonance shift (blue curves on the left) and changes in energy (right). (c) Local field intensity map of the nanocavity. (d) Optical trapping potential (blue curve) and corresponding optical force (red curve) of a 10 nm gold particle trapped along the minor axis of the nanocavity (dashed line in (c)), (e) Optical trapping potential (blue curve) and trapping-induced shift in resonance frequency (red curve) of the nanocavity along the dashed line in (a). (Figures reproduced with permission from Ref. [59]; copyright 2015 American Chemistry Society)

is zero. However, as the trapped nanoparticle attempts to leave the potential well, the optical force pulls it back to the equilibrium position (see the blue dots in Fig. 2d). The nanoparticle trapping-induced resonance shift of the coupled nanosystem as a function of the location of the trapped nanoparticle is also shown in Fig. 2e.

3 From Conventional to Plasmonic Tweezers

Although conventional optical tweezers have been extensively employed to manipulate micron-scale particles, it is difficult to stably trap and hold particles that are much smaller than the wavelength of light. The precise manipulation of such small

particles is critical in bioscience [60, 61] as well as in atomic physics [62, 63]. Therefore, it is crucial to enhance the trapping forces acting on particles in the nanoscale regime. The main issue regarding trapping nanoparticles is the magnitude of the gradient force, which decreases significantly with decreasing particle size. This results in a shallower potential well and the particles escape quickly from the trap. Therefore, a high-intensity laser is needed to create optical forces that are strong enough to overcome Brownian motion. For example, conventional optical tweezers can trap micron-sized particles with laser powers less than 1 mW. However, laser powers in the range 10 mW–1 W are required to stably hold particles with sizes in the range 100–10 nm [2]. Such high-power lasers cause damage to the trapped particles owing to thermal effects. Meanwhile, Abbe's diffraction limit prevents the confinement of propagating light beyond a fraction of its wavelength and thus hinders accurate trapping. Therefore, using lenses with a higher NA or increasing the laser power does not significantly improve the optical trapping performance.

Plasmonic optical tweezers [35, 41, 64] that are based on surface plasmon polaritons (SPPs) offer an alternative approach to manipulate particles at the nanoscale. SPPs are coherent collective oscillations that exist at the interface between a flat metal and a dielectric (SPPs) or bound electron plasmas on nanoparticles (LSPs) [65]. The excitation of SPPs can be used to focus light energy far beyond the diffraction limit which in turn can greatly increase the precision of optical manipulation. Another merit of SPPs is that the evanescent field decays rapidly away from the interface, thus inducing strong gradient forces and making the trapping more stable. Novotny et al. [64] first suggested the theoretical possibility of nanometric optical trapping using surface plasmons on a sharply pointed metal tip under laser illumination. They proposed that this new trapping approach could generate highly confined evanescent fields that significantly reduce the trapping volume, as shown in Fig. 3. This results in a large trapping force as well as enhancement of the field, thereby reduces the laser power illumination and radiation damage to the trapped objects [64].

Optical trapping using SPPs was experimentally realised using metal/dielectric interfaces, where surface plasmons were confined to subwavelength scales [66, 67]. Volpe et al. [66] observed and measured plasmon radiation forces on dielectric particles using a linearly polarised beam that impinged upon the metal-water interface through a prism thereby generating surface plasmons. A photonic force microscope, which can yield the optical force by analysing the Brownian motion of a trapped particle, was used to trap the probe particle and detect its position. Another experiment was performed by Wang et al. [67], who placed gold nanoparticles close to a gold film to effectively manipulate them using optical forces and test their usefulness for biophysical investigations. Because of the proximity of the gold particles to the gold film, the resultant near-field coupling greatly enhanced the field, as shown in Fig. 4.

Although POTs can increase the local intensity by focussing the laser light to a smaller cross-sectional area, a fundamental drawback is the thermal effect generated as a result of the frequency-dependent absorption of this light by the metallic nanostructures. Heating limits the maximum laser power that can be used as well as

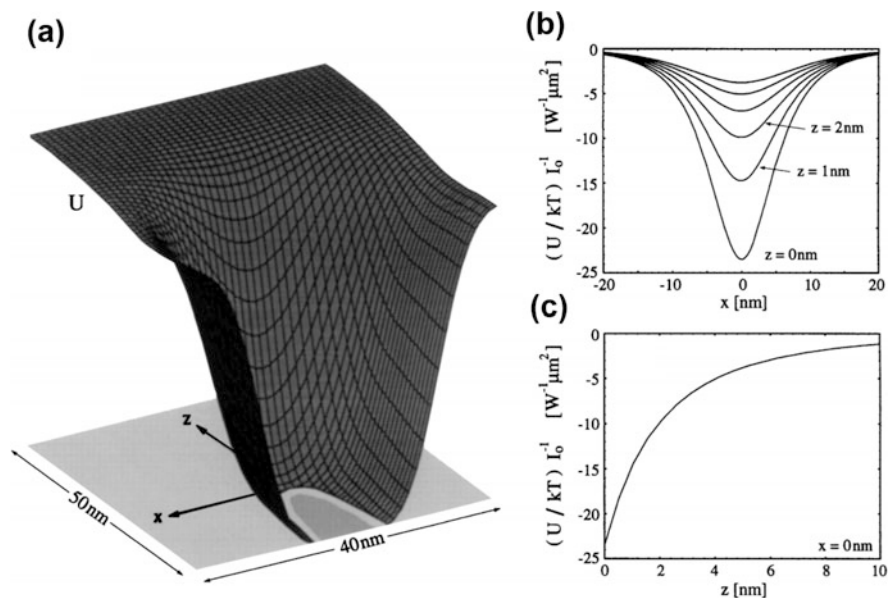


Fig. 3 (a) Potential energy surface of a 10 nm diameter particle in the x, y, z plane. Cross-sections of the trapping potential along the (b) forward and (c) transverse directions of the metallic film. (Figure reproduced with permission from Ref. [64]; copyright 1997 American Physical Society)

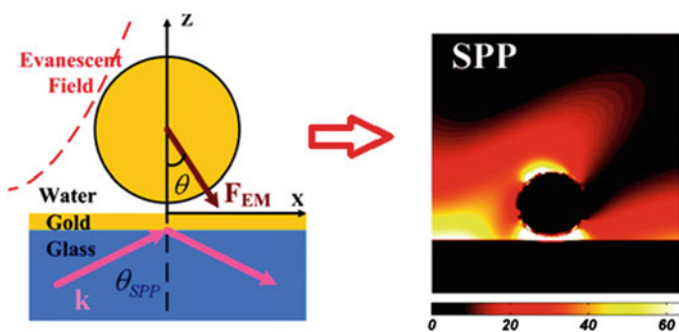


Fig. 4 Schematic representation and power flow magnitudes of the optical manipulation of a gold nanoparticle using SPPs. (Figure reproduced with permission from Ref. [67]; copyright 2009 American Chemistry Society)

the magnitude of the optical force or trap stiffness that can be achieved. In addition, the heat generated by the metallic nanostructures gives rise to bubble formation and particle migration along the temperature gradient, thereby enhancing Brownian motion that affects the stability of the trapping process [68–70]. Such photothermal effects have been studied in POT designs [44, 71–75], and several approaches have also been demonstrated to suppress them. For example, a POT configuration on a heat sink [70] was proposed to trap and rotate 200 nm particles. In this

approach, the thermal energy generated by the absorption of the optical energy in the water solution surrounding the near-field trap was dissipated through the underlying copper film and silicon substrate. Plasmonic-induced heating is expected to become an important tool for several applications because of its simple optics, versatile and low-power operation, applicability to diverse nanoparticles, and tunable working wavelengths [74].

4 Optical Manipulation Using Plasmonic Nanostructures

The first experimental implementation of POTs was by Garcés-Chávez et al. [76]; they achieved self-assembly of microparticles at the flat gold/water interface (see Fig. 5a) using the Kretschmann–Raether configuration (see Fig. 5b). In the same year, Volpe et al. [66] measured the momentum transfer from SPPs to microbeads using a photonic force microscope. They noted that the modulus of the optical force undergoes exponential decay with respect to the distance from the interface, similar to the exponential decay of the plasmon field (see Fig. 5c). Two years after the first experimental demonstration of POTs, Grigorenko et al. [77] verified the use of a localised electromagnetic field to trap 200 nm dielectric particles. They achieved particle confinement with one order of magnitude higher trapping force (2 nN for 1 μm particle near the nanostructure) than that of conventional tweezers. Gold optical nanoantennas with a narrow gap have also shown to improve trapping efficiency and have been used to trap live bacteria with laser intensities that are much lower than the damage threshold, as shown in Fig. 5d [78]. A similar dipole nanoantenna was later used for the trapping and sensing of 10 nm gold nanoparticles [56] as well as 40 nm fluorescent nanodiamonds [79].

An array of bowtie nanostructures consisting of two symmetric triangular structures facing tip-to-tip with a nanogap has also been used to trap submicron particles in water [81] and buffer solutions [82] (see Fig. 6a). Although the electric field enhancement in bowtie nanostructures is smaller than that in dipole antennas, the former can support multiple resonances [83]. Yoon et al. [84] performed label-free nanoscopic monitoring of a single trapped nanoparticle by illuminating it with a pair of nonlinear point-like sources in a tapered plasmonic nanoantenna. In this work, a pair of oscillating point-like nonlinear optical sources were used to illuminate the quantum dot (QD) trapped between two potential wells formed in the bowtie nano-apertures (Fig. 6b). The authors measured Kramers hopping by analysing the high-contrast nonlinear optical spikes generated [84, 85]. Figure 6c shows pyramidal nanostructures that are used to trap various particles such as QDs [86], λ -DNA [87], and polymer chains [88]. An interesting approach with diabolo geometry has also been demonstrated through the first nano-optical vortex trapping of a silica particle with a refractive index smaller than that of its surrounding [89]. Moreover, the trapping efficiency and thermal side effects of POTs can be further improved using aperture-based nanostructures, where the self-induced back-action (SIBA) effect can also be examined. In SIBA optical trapping, the trapped

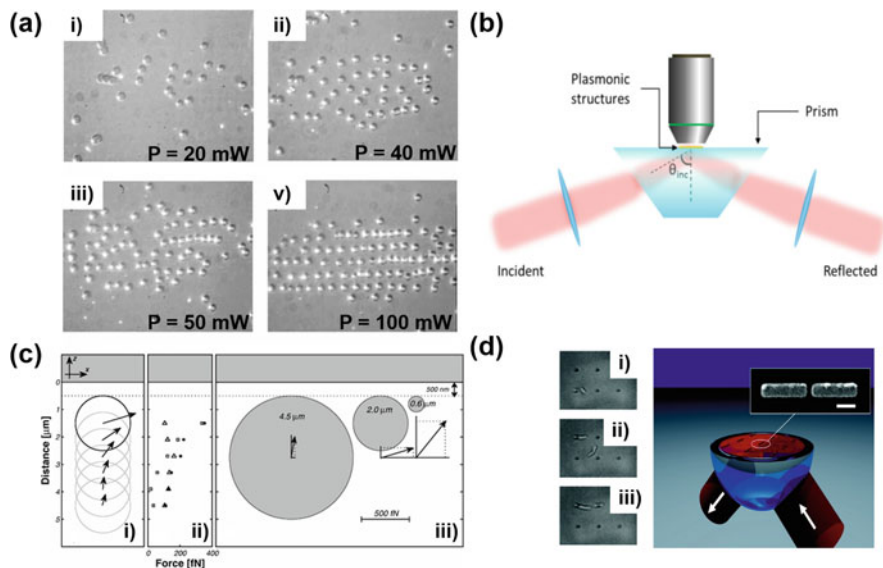


Fig. 5 (a) Successive frames showing the formation of linear arrays of $5\ \mu\text{m}$ particles owing to an enhanced optical interaction resulting from SPP excitation using a Kretschmann-Raether prism. (Figure reproduced with permission from Ref. [76]; copyright 2006 America Physical Society). (b) Schematic of the Kretschmann-Raether configuration. (Figure reproduced with permission from Ref. [80]; copyright 2016 IOP Science Publishing Ltd). (c) The radiation force (i) vector and (ii) modulus acting on a $2\ \mu\text{m}$ particle as a function of the distance from the metal surface. (iii) Force vectors for three different sizes of the particle when the distance between the metal layer and upper surface of the particle is $500\ \text{nm}$. (Figure reproduced with permission from Ref. [66]; copyright 2006 America Physical Society). (d) Frames showing optical trapping of *E.coli* bacteria using periodically arranged gold nanoantennas [78]; copyright 2009 American Chemistry Society

particle strongly influences the degree of local field enhancement and thereby plays an active role in the trapping process [90–93]. To date, several theoretical and experimental studies on near-field optical tweezers involving the SIBA approach have been discussed [90–96]. For example, a coaxial nano-aperture with a $10\ \text{nm}$ gap in a gold film was fabricated to trap nanoparticles and proteins (see Fig. 6d). In the double nanohole (DNH) configuration (see Fig. 6e) trapping occurs at the cusps where the holes overlap. This can lead to a very small trapping volume and is therefore efficient in handling sub- $10\ \text{nm}$ particles [97, 98]. Apart from single biomolecule trapping [98], DNH optical tweezers have also been applied to trap and manipulate dielectric [99], silica [97], and magnetic [100] nanoparticles.

A smart design of the optical landscape is required for the dynamic manipulation of nanoparticles in short-range plasmonic near-fields. Chen et al. [101] demonstrated a plasmon-enhanced optical lattice to guide and arrange nanoparticles over a distance of a few micrometres. In their work, the plasmonic lattice was illuminated by a resonant Gaussian beam, which created a periodic optical potential that was used to trap and transport nanoparticles simultaneously, as shown in Fig.

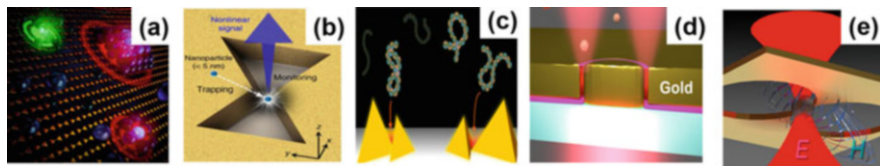


Fig. 6 (a) An array of bowtie nanostructures. (Figure reproduced with permission from Ref. [81]; copyright 2011 America Chemistry Society). (b) Bowtie nano-aperture configuration. (Figure reproduced with permission from Ref. [84]; copyright 2018 Springer Nature). (c) Nanopyramidal dimer array nanostructure. (Figure reproduced with permission from Ref. [87]; copyright 2013 America Chemistry Society). (d) Coaxial nano-aperture. (Figure reproduced with permission from Ref. [95]; copyright 2018 America Chemistry Society). (e) DNH nanostructure. (Figure reproduced with permission from Ref. [100]; copyright 2016 America Chemistry Society)

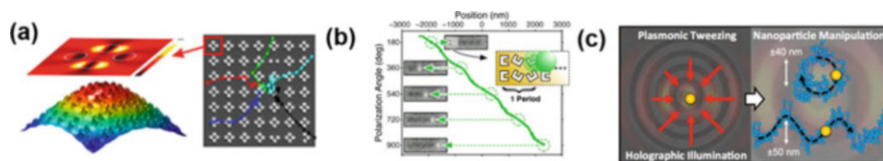


Fig. 7 (a) Intensity enhancement and profile of an optical lattice created under Gaussian illumination as a 500 nm particle enters at the edge of the array and is attracted towards the central region. (Figure reproduced with permission from Ref. [101]; copyright 2013 America Chemistry Society). (b) Nano-optical conveyor belt generated by the controlling polarisation. (Figure reproduced with permission from Ref. [102]; copyright 2014 America Chemistry Society). (c) Holographic plasmonic tweezers. 200 nm diameter particles can be moved in arbitrary patterns by shifting the phase of the plasmon waves in space. (Figure reproduced with permission from Ref. [104]; copyright 2014 America Chemistry Society)

7a. Following this work, Hansen et al. [102] theoretically proposed and Zheng et al. [103] experimentally demonstrated a nano-optical conveyor belt, in which closely placed optical traps were activated in a sequential manner to transport a trapped particle to adjacent traps using optical peristalsis (see Fig. 7b). An all-optical technique was proposed by Huft et al. [104], in which the dynamic trapping and manipulation of nanoparticles was demonstrated using plasmonic holograms (see Fig. 7c). In their work, a focussed hot spot was created by modifying the incident illumination pattern with a spatial light modulator through plasmon wave interference and could be used to manoeuvre trapped 200 nm dielectric particles across a surface.

Several studies have demonstrated the use of plasmonic nanoring arrays, which enable tunability of the resonance frequency in the near-infrared region for optical trapping and sorting of nanoparticles [80, 105, 106]. These studies investigated the trapping performance of plasmonic nanostructures by manipulating 100 nm polystyrene particles with a low incident trapping power of 1 mW [80]. Moreover, they found that, by using the abrupt phase changes of the proposed plasmonic nanostructures, the detection sensitivity can be improved by a factor of ten compared to that in excitation spectra methods [80].

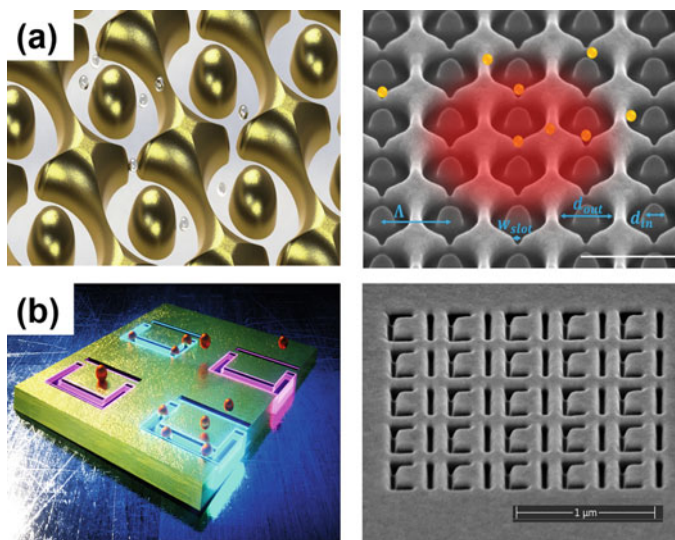


Fig. 8 (a) **Left:** Schematic of an array of nanoring nano-apertures. **Right:** Scanning electron microscope (SEM) image which also illustrates the concept of nanoparticle trapping. (Figure produced with permission from Ref. [107]; copyright 2021 IOP Science). (b) **Left:** Schematic of an array of asymmetric split-ring nano-apertures. **Right:** SEM image of the metamaterial. (Figure reproduced with permission from Ref. [108]; copyright 2020 America Chemistry Society)

Han et al. [105, 106] demonstrated optical trapping of micro- and nanoparticles using a POT based on annular nano-aperture arrays. The authors performed sequential single-particle trapping within specific trapping sites and concluded that their proposed POT configuration had the potential to be used in lab-on-a-chip devices for efficient nanoparticle trapping with high tenability [106]. However, the trapping or sensing of nanoparticles using nanostructures suffers from an intrinsic problem of low-throughput, as the particle delivery process is often diffusion-limited. More recently, the same research group trapped nanoparticles both quickly and efficiently in arrays of plasmonic coaxial nano-apertures with different inner ring sizes, as illustrated in Fig. 8a. By illuminating an array of nanorings with an inner disk diameter of 149 nm, a 20 nm dielectric particle was trapped in 8 s [107]; this helps bridge the gap between optical manipulation and nanofluidics. For nanostructures that are small compared to the wavelength of the incident light, only plasmons having finite moments can be excited. The symmetry breaking of the nanostructures introduces interference between the dark modes and broad bright modes, leading to a Fano resonance peak. Fano resonance peaks are quantum phenomena due to the interference of discrete state with a continuum [109]. These resonances are also demonstrated in the artificial nanostructures that support both the radiative (bright) and localized (dark) modes [110]. Photons in the bright modes have large radiative loss to the incident electromagnetic light, resulting in broad spectral bandwidths. On the other hand, photons in dark modes have small radiative loss, leading to narrow

spectral bandwidths and high quality factors of the resonances. This Fano resonant peak is highly sensitive to modifications of the surrounding medium, rendering these nanostructures particularly attractive for optical trapping and sensing applications. Therefore, an array of asymmetric split nano-apertures (ASR) (see Fig. 8b) was fabricated to improve the trapping performance by several factors and reduce the diffusion time [108, 111]. The ASR nano-aperture configuration increased the on-resonance trap stiffness by a factor of 60 compared to the off-resonance trap stiffness owing to the ultrasmall mode volume, which enables large near-field strengths.

Hybrid photonic-plasmonic tweezers that are based on plasmon excitation have gained considerable attention as they enable efficient optical manipulation of trapped nanoparticles in lab-on-a-chip devices and enhance light-matter interactions between trapped nanoparticles and integrated photonic systems [112–114]. Recently, a periodic chain of gold nanorods coupled to a silicon photonic waveguide was demonstrated to trap single nanoparticles and form well-defined, self-assembled nanoparticle clusters [112]. The authors showed that a single plasmonic trap on a silicon waveguide can generate a pattern equivalent to that of seven traps with comparable trap stiffnesses which is achieved through the balance of optical forces, surface topography, and electrostatic interactions [112].

5 Applications of Plasmonic Optical Trapping in Life Sciences

Nano-aperture optical trapping has emerged as an essential approach to detect and identify biological entities and their interactions at the single-particle level. Compared with other single-molecule detection approaches [115] such as fluorophore-based methods [116] or single-molecule fluorescence resonance energy transfer (FRET) microscopy [117], biosensing with nano-optical tweezers offers intrinsic information about the trapped biomolecule, and allows label-free and low-cost operation. Hence, plasmonic nanostructures with large local field intensities and high transmission efficiencies have emerged as the most promising architectures for biological applications.

In the last few years, DNH nanoholes in metallic films have been extensively used to trap, hold and sense biomolecules and dielectric nanoparticles (see Fig. 9). Using DNH optical tweezers integrated with an inverted microscope trapping system (see Fig. 9a), Gordon et al. [40] successfully demonstrated the detection and identification of biomolecules and their interactions. By employing a platform of DNH nanotweezers, Pang and Gordon [98] experimentally demonstrated the trapping and unfolding of a single bovine serum albumin (BSA) molecule with a radius of 3.4 nm. The transition of the BSA molecule between the normal and fast forms upon trapping was also confirmed by experiments using various optical powers, as well as by changing the ionic concentration of the solution [98]. The ease of trapping a single protein molecule with this plasmonic tweezers platform has

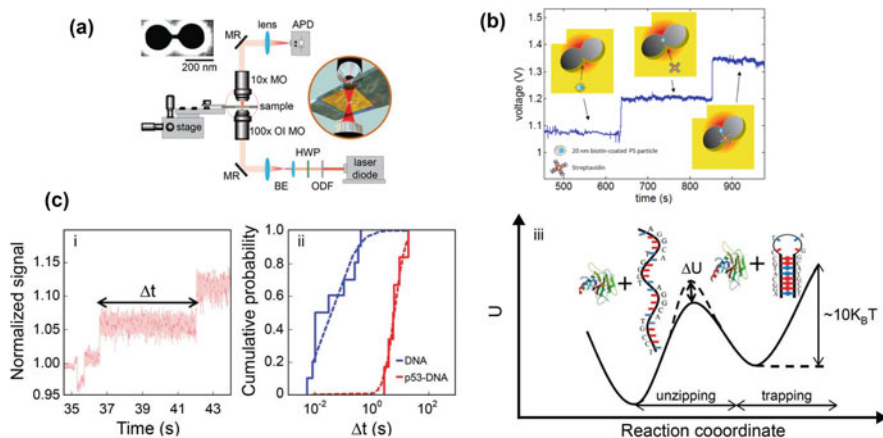


Fig. 9 (a) POTs based on a DNH aperture. The top left corner shows the SEM image of the DNH fabricated using a focussed ion beam (FIB). The circular inset shows a gold DNH with 20 nm polystyrene spheres suspended in water. (Figure reproduced with permission from Ref. [99]; copyright 2014 American Chemistry Society). (b) Time trace of optical transmission through the DNH, with the insets showing the trapping of a 20 nm biotin-coated polystyrene particle and the binding process between the polystyrene particle and streptavidin. (Figure reproduced with permission from Ref. [118]; copyright 2013 Optical Society). (c) Suppression of DNA hairpin unzipping by tumor suppressor protein p53: (i) wild type p53 suppresses the unzipping of the DNA hairpin with a delay of approximately 10 s, (ii) cumulative probability as a function of unzipping time Δt for p53-DNA complex and DNA alone, and (iii) energy reaction diagram showing increased energy barrier ΔU . (Figure reproduced with permission from Ref. [119]; copyright 2014 Optical Society)

prompted researchers to hypothesise a possible development of this configuration in a biosensor for single protein detection [98]. Following this work, Balushi et al. [118] experimentally demonstrated the trapping of 20 nm biotin-coated dielectric particles and their binding with streptavidin molecules by measuring the optical transmission through a DNH aperture. Biotin–streptavidin binding was detected by an increase in the optical transmission through the DNH aperture (see Fig. 9b). To ensure that the observed increase in optical transmission was owing to the specific binding of streptavidin to biotin, the authors also performed two control experiments using saturated streptavidin and non-functionalised dielectric particles; neither of the control experiments resulted in a similar optical transmission behavior [118]. By adopting the same trapping system, Kotnala and Gordon [119] studied the interaction between the tumor suppressor p53 protein and 10 base pair single stranded DNA-hairpins (see Fig. 9c). They demonstrated the unzipping of individual 10 base pair DNA-hairpins and quantified the unzipping delay by the p53 protein. The long unzipping delay implies a strong binding between the p53 protein and the DNA molecule (see Fig. 9c inset (i)). The cumulative probability shown in Fig. 9c inset (ii) shows that, for a given probability range, the unzipping time is always greater than 10 s for the wild-type p53-DNA complex compared to DNA

alone [119]. The energy barrier to the unzipping suppression was found to be approximately $\Delta G = 2 \times 10^{-20}$ J, which is lower than the binding energy of p53 ($\Delta G = 6.9 \times 10^{-20}$ J) [119]. Although the authors did not discuss the mechanism of interaction between the DNA and p53 molecules, they revealed the capability of DNH optical nanotweezers to study the interaction between proteins and short DNA molecules directly without the need for tethers of fluorescence labels, as is typically employed in experiments performed using conventional optical tweezers.

Furthermore, DeWolf and Gordon [120] and Wheaton et al. [121] demonstrated extraordinary acoustic Raman (EAR) spectroscopy to directly measure the Raman-active vibrations of single trapped biomolecules and nanoparticles, respectively, by integrating two trapping lasers having tunable frequency differences with DNH optical tweezers. The vibrational modes of biomolecules reflect their structure and conformations; in the case of proteins, these provide valuable information about their allostery, which in turn is associated with various diseases. The physical mechanism behind EAR is based on the electrostriction force that leads to heating and increased Brownian motion of the trapped biomolecule at the trapping site. In one case, when the protein was trapped in the DNH [121], the lasers were detached from each other, creating a tunable beat frequency between them. This beat frequency was then used to modulate the electrostriction force on the trapped protein in the nanohole. When the beat frequency matched the frequency of one of the protein's acoustic modes, the resonance motion of the protein increased the temperature of the system, leading to an increase in the root mean squared (RMS) variation of the transmission signal. This increase in the RMS was recorded to detect resonance and create a Raman spectrum by plotting the RMS of the signal against the beat frequency between the two laser sources. The spectra of two proteins, streptavidin and conalbumin, are shown in the left column of Fig. 10. Additionally, a theoretical anisotropic elastic network model was developed to associate the protein modes and calculate the Raman intensity by treating the protein as a polarisable ellipsoid [120]. Figure 10 shows the experimentally obtained EAR spectra (left) and computationally modeled Raman spectra (right) of the two proteins. The intensity and frequency of the major peaks, as well as some of the minor peaks, obtained using the theoretical model are in agreement with the experimental results. Thus, EAR spectroscopy is an important tool for studying the acoustic modes of bio-entities in the nanometre regime.

At present, nanopore-based detection platforms rely on the modulation of an ionic current to report small changes in the physical size of the analyte during its passage through the nanopore [123]. However, the requirement of individual current amplifiers for the read-out of each nanopore, the lack of full motion control of the biomolecules, and the low temporal resolution, limit the platform density for scalable integration of the chip [123]. Some strategies to reduce these limitations have been employed, but these require labelling and fail to demonstrate the full external motion control of the biomolecules. Alternatively, POTs have demonstrated the capacity to retain small particles in their sensing volume through optical trapping. Therefore, Verschueren et al. [122, 124] have combined POTs with metallic nanopores to create a new method for single-molecule manipulation. They

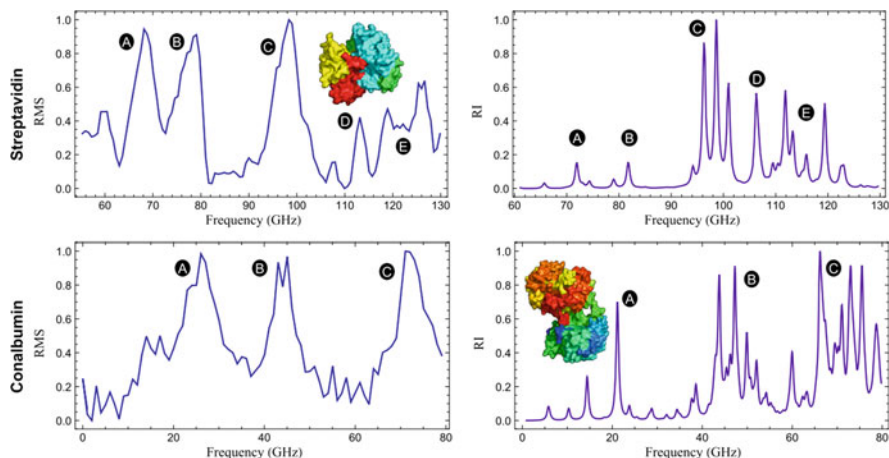


Fig. 10 **Left column:** Acoustic Raman spectra of five proteins obtained using DNH optical tweezers and two trapping lasers to create a beat frequency. The increase in noise amplitude as a function of the beat frequency is plotted. **Right column:** The theoretical Raman intensity, calculated by applying an elastic network Raman ellipsoid polarisability model. (Figure reproduced with permission from Ref. [120]; copyright 2016 American Physical Society)

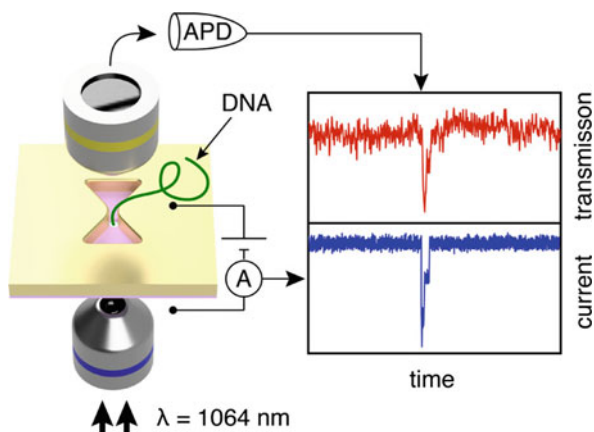


Fig. 11 [t]Schematic of an inverted bowtie plasmonic nanopore optical tweezers. The light transmission is monitored by sandwiching the plasmonic nanostructure in between two objective lenses, one for excitation and one for collection of the transmitted light. The ionic current is observed simultaneously using a convective current amplifier. (Figure reproduced with permission from Ref. [122]; copyright 2018 American Physical Society)

integrated a nanopore at the feed gap of an inverted bowtie-shaped nano-aperture to achieve simultaneous ionic current and optical transmission based detection of single-molecule DNA translocations [122] and beta-amylase protein [124], as shown in Fig. 11. The electrophoretic force from the nanopore and the gradient

force from the plasmonic nanostructure constitute two independent control handles at the single-molecule level that pull the molecules towards the sensor and retain them there. They also confirmed the presence and reported the conformation of the biomolecules by monitoring the changes in the light intensity transmitted through a resonant nanoscale aperture [124].

6 Optothermal Plasmonic Optical Tweezers

A large temperature gradient can cause a repulsive force between the trapped particle and the high-temperature zone. To address this drawback, Ndukaife et al. [68, 125] introduced a hybrid electro-thermo-plasmonic nanotweezers. They demonstrated long-range nanoparticle trapping by exploiting the synergistic effects of an externally applied electric field and the plasmonic field enhancement of an array of subwavelength nanoholes in a gold film. Specifically, by illuminating metallic nanostructures, the localised heating of the fluid creates a local gradient in the fluid’s electrical permittivity and conductivity. When an AC electric field is applied in the presence of these gradients, it gives rise to an electric force that in turn impacts the drag force on the suspended particles and transports them to the plasmonic hot spots at a significant speed. Figure 12 shows the thermoplasmonic platform in which an electrothermoplasmonic (ETP) flow arises from the combined

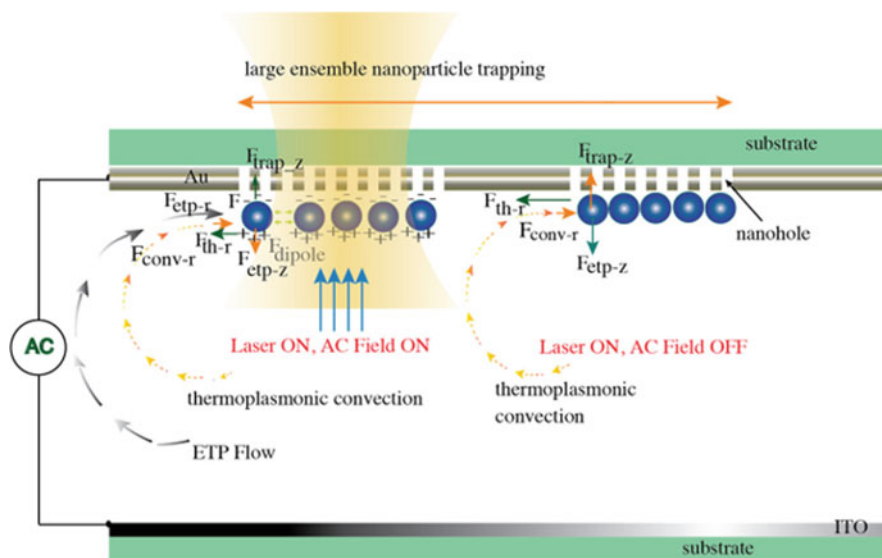


Fig. 12 A hybrid electrothermoplasmonic tweezers platform where the forces present when the laser illumination is “ON” and AC electric field is either “ON” or “OFF”. (Figure reproduced with permission from Ref. [125]; copyright 2018 American Chemistry Society)

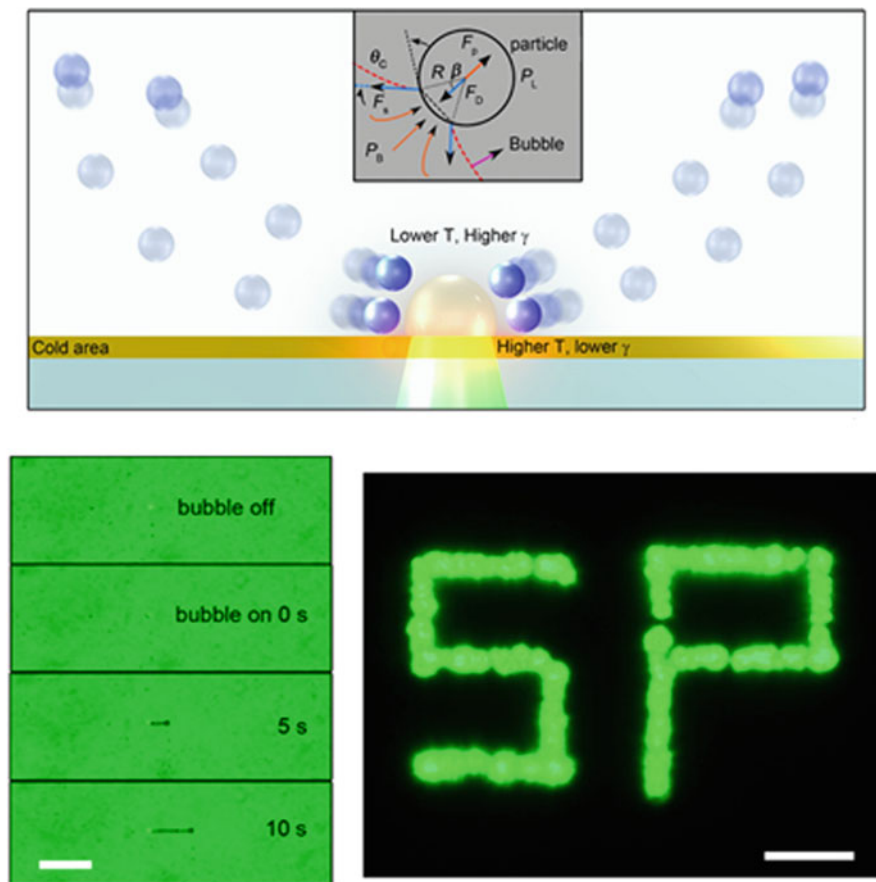


Fig. 13 *Top*: Particle trapping at the microbubble generated by a plasmon-enhanced photothermal effect. *Bottom*: By controlling the laser beam, the microbubble is moved to create patterns of particles dictated by the trajectories of bubble movement. Left: Time-resolved process for drawing a straight line using 540 nm dielectric particles on a gold nano-island substrate. Right: Dark-field optical image of the surface plasmon pattern composed of 540-nm dielectric particles. (Figure reproduced with permission from Ref. [127]; copyright 2016 American Chemistry Society)

action of the induced thermal gradient and the applied AC electric field [125]. Note that this method is limited to fluids with low ionic concentrations, thereby excluding most biofluids, whereas the localised nature of the plasmonic hot spots limits the dynamic manipulation of the POT.

Recently, Lin et al. [126] developed an opto-thermoelectric trapping technique that exploits plasmonic-induced heating. By optically heating a metallic substrate, a light-directed thermoelectric field can be generated owing to the spatial separation of the dissolved ions within the heating laser spot. This enables the manipulation of nanoparticles of various of materials having, sizes and shapes with single-

particle resolution [126]. The developed optothermal manipulation techniques based on microbubbles and optothermal POTs are advantageous for controlling the fabrication of plasmonic nanostructures, and they offer diverse functionalities, including optothermal assembly and printing [127]. Plasmonic heating of a gold-coated substrate generates microbubbles on the illuminated area, which creates a Marangoni convective flow because of the surface tension gradient at the vapour–liquid interface (see Fig. 13). The microbubbles can be exploited to manipulate and assemble the colloidal particles on the substrate, where they are immobilised owing to van der Waals interactions [127]. Note that manipulation with optothermal POTs is reversible in nature, such that they can trap particles in the presence of a thermal gradient and release them when the gradient is absent.

Most recently, Kotnala et al. [75] demonstrated nano-aperture-based plasmonic tweezers for the dynamic manipulation of nanoparticles in short-range plasmonic near-fields. By enhancing the local temperature through the collective heating of closely spaced plasmonic nano-apertures, a robust convective fluid flow was generated that moved the tracer particles close to the trapping region. This technique used Rayleigh–Bénard convection to create a convection-assisted trap for POTs with a low trap stiffness while the bubble-induced Marangoni convection was used to create a bubble-assisted trap for POTs with a high trap stiffness [75]. By using thermal activation, this technique facilitates rapid delivery of analytes with an increased concentration to the functional surfaces of the nanostructures, thus improving the overall sensitivity and throughput.

7 Future Perspectives

The manipulation of nanoparticles is critical for investigating single-particle processes in physics, chemistry, and the life sciences, as well as for the construction of nanodevices and molecular machines. However, molecular manipulation is strongly suppressed by Brownian motion. Therefore, an *in situ* single-molecule identification technique is essential for detecting single-molecule trapping events. By changing the wavelength, polarisation, and intensity of the incident light, the surface plasmon-enhanced electromagnetic field can play a critical role in single-molecule trapping [58], while achieving precise selectivity. Moreover, plasmonic optical trapping brings new opportunities to the field of molecular electronics [128], such as constructing optically controlled single-molecule junctions, which can achieve an increased detection efficiency.

Additionally, molecular chirality is strongly related to biological functions and is critical for several applications. Improvements over state-of-the-art techniques are required to detect and achieve enantiopurity for pharmaceutical and agrochemical applications. This necessitates further enhancements in chiral optical near-fields in the mid- to near-ultraviolet regimes, where most molecules of interest exhibit electron resonances. Existing separation methods rely on unique ways in which each molecule in an enantiomeric pair interacts with other chiral molecules. However,

these chemical processes may introduce unwanted side products. In contrast, using POTs, enantioselective optical trapping can be achieved at the nanoscale by combining chiral optical forces with efficient metallic nanostructures [129, 130].

The ability to completely control crystallisation from a solution impacts several scientific and industrial fields. This is because the functionalities of the resulting crystalline materials are influenced by the crystallisation process, and detailed exploration of the fundamental mechanism behind this process often demands a spatiotemporally predictable nucleation mechanism that has a stochastic nature. The plasmonic optical trapping-induced crystallisation of acetaminophen provides insight into crystallisation control [131] and paves the way for an alternative approach to design the crystallisation process from a solution. In this example, crystallisation occurs in a gold nanolattice pattern because of the excitation of the surface plasmons, such that the crystals are transformed to a highly concentrated droplet [131]. The position of the crystals was manipulated by changing the focal spot position [131]. These results highlight that the plasmonic optical trapping achieved by designed near-field and temperature distributions can manipulate both the molecular assembly and the creation of functional crystalline materials at the nanoscale. In summary, POTs have been widely studied and applied, but further efforts are still needed for their commercialization.

Acknowledgements The authors would like to thank the Okinawa Institute of Science and Technology Graduate University for funding this work. DGK acknowledges support from the JSPS Grant-in-Aid for Scientific Research (C) Grant Number GD1675001 and the Sumitomo Foundation Grant for Basic Science Research Project.

References

1. Ashkin, A. (1970). Acceleration and trapping of particles by radiation pressure. *Physical Review Letters*, 24(4), 156–159.
2. Ashkin, A., Dziedzic, J. M., Bjorkholm, J. E., & Chu, S. (1986). Observation of a single-beam gradient force optical trap for dielectric particles. *Optics Letters*, 11(5), 288–290.
3. Grier, D. G. (2003). A revolution in optical manipulation. *Nature*, 424(6950), 810–816.
4. Polimeno, P., Magazzù, A., Iatì, M. A., Patti, F., Saija, R., Esposti Boschi, C. D., Donato, M. G., Gucciardi, P. G., Jones, P. H., Volpe, G., & Maragò, O. M. (2018). Optical tweezers and their applications. *Journal of Quantitative Spectroscopy and Radiative Transfer*, 218, 131–150.
5. Daly, M., Sergides, M., & Nic Chormaic, S. (2015). Optical trapping and manipulation of micrometer and submicrometer particles. *Laser & Photonics Reviews*, 9(3), 309–329.
6. Arbore, C., Perego, L., Sergides, M., & Capitanio, M. (2019). Probing force in living cells with optical tweezers: from single-molecule mechanics to cell mechanotransduction. *Biophysical Reviews*, 11(5), 765–782.
7. Ashkin, A. (1997). Optical trapping and manipulation of neutral particles using lasers. *Proceedings of the National Academy of Sciences*, 94(10), 4853–4860.
8. Ashkin, A. (1992). Forces of a single-beam gradient laser trap on a dielectric sphere in the ray optics regime. *Biophysical Journal*, 61(2), 569–582.

9. Mazolli, A., Neto, P. A. M., & Nussenzeig, H. M. (2003). Theory of trapping forces in optical tweezers. *Proceedings of the Royal Society of London, Series A: Mathematical, Physical and Engineering Sciences*, 459(2040), 3021–3041.
10. Nieminen, T. A., Knöner, G., Heckenberg, N. R., & Rubinsztein-Dunlop, H. (2007). Physics of optical tweezers. In *Methods in cell biology* (Vol. 82, pp. 207–236). Academic.
11. Bui, A. A. M., Stilgoe, A. B., Lenton, I. C. D., Gibson, L. J., Kashchuk, A. V., Zhang, S., Rubinsztein-Dunlop, H., & Nieminen, T. A. (2017). Theory and practice of simulation of optical tweezers. *Journal of Quantitative Spectroscopy and Radiative Transfer*, 195, 66–75.
12. Chu, S. (1998). Nobel Lecture: The manipulation of neutral particles. *Reviews of Modern Physics*, 70, 685–706.
13. Muldoon, C., Brandt, L., Dong, J., Stuart, D., Brainis, E., Himsforth, M., & Kuhn, A. (2012). Control and manipulation of cold atoms in optical tweezers. *New Journal of Physics*, 14(7), 073051.
14. Daly, M., Truong, V. G., Phelan, C. F., Deasy, K., & Nic Chormaic, S. (2014). Nanostructured optical nanofibres for atom trapping. *New Journal of Physics*, 16(5), 053052.
15. Saskin, S., Wilson, J. T., Grinkemeyer, B., & Thompson, J. D. (2019). Narrow-line cooling and imaging of ytterbium atoms in an optical tweezer array. *Physical Review Letters*, 122, 143002.
16. Delić, U., Reisenbauer, M., Dare, K., Grass, D., Vuletić, V., Kiesel, N., & Aspelmeyer, M. (2020). Cooling of a levitated nanoparticle to the motional quantum ground state. *Science*, 367(6480), 892–895.
17. Kotsifaki, D., Makropoulou, M., & Serafetinides, A. (2009). *Optical tweezers and manipulation of PMMA beads in various conditions* (Vol. 7373). SPIE.
18. Maimaiti, A., Truong, V. G., Sergides, M., Gusachenko, I., & Nic Chormaic, S. (2015). Higher order microfibre modes for dielectric particle trapping and propulsion. *Scientific Reports*, 5(1), 9077.
19. Spesyvtseva, S. E. S., & Dholakia, K. (2016). Trapping in a material world. *ACS Photonics*, 3(5), 719–736.
20. Liu, J., & Li, Z. (2018). Controlled mechanical motions of microparticles in optical tweezers. *Micromachines*, 9(5), 232.
21. Choi, K. H., Kang, D. W., Kim, K. H., Kim, J., Lee, Y., Im, S. H., & Park, B. J. (2019). Direct measurement of electrostatic interactions between poly(methyl-methacrylate) microspheres with optical laser tweezers. *Soft Matter*, 15, 8051–8058.
22. Svoboda, K., & Block, S. M. (1994). Optical trapping of metallic Rayleigh particles. *Optics Letters*, 19(13), 930–932.
23. Nan, F., & Yan, Z. (2018). Sorting metal nanoparticles with dynamic and tunable optical driven forces. *Nano Letters*, 18(7), 4500–4505.
24. Gillibert, R., Balakrishnan, G., Deshoules, Q., Tardivel, M., Magazzù, A., Donato, M. G., Maragò, O. M., Lamy de La Chapelle, M., Colas, F., Lagarde, F., & Gucciardi, P. G. (2019). Raman tweezers for small microplastics and nanoplastics identification in seawater. *Environmental Science & Technology*, 53(15), 9003–9013.
25. Ripken, C., Kotsifaki, D. G., & Nic Chormaic, S. (2021). Analysis of small microplastics in coastal surface water samples of the subtropical island of Okinawa, Japan. *Science of the Total Environment*, 760, 143927.
26. Svoboda, K., & Block, S. M. (1994). Biological applications of optical forces. *Annual Review of Biophysics and Biomolecular Structure*, 23(1), 247–285.
27. Bayouth, S., Mehta, M., Rubinsztein-Dunlop, H., Heckenberg, N. R., & Critchley, C. (2013). Micromanipulation of chloroplasts using optical tweezers. *Journal of Microscopy*, 203(2), 214–222.
28. Kotsifaki, D., Makropoulou, M., & Serafetinides, A. (2007). *Ultra-violet laser microbeam and optical trapping for cell micromanipulation* (Vol. 6535). SPIE.
29. Kotsifaki, D., Makropoulou, M., & Serafetinides, A. (2013). *Near infrared optical tweezers and nanosecond ablation on yeast and algae cells* (Vol. 8770). SPIE.

30. Capitanio, M., & Pavone, F. S. (2013). Interrogating biology with force: Single molecule high-resolution measurements with optical tweezers. *Biophysical Journal*, *105*(6), 1293–1303.
31. Agrawal, R., Sherwood, J., Chhablani, J., Ricchhariya, A., Kim, S., Jones, P. H., Balabani, S., & Shima, D. (2016). Red blood cells in retinal vascular disorders. *Blood Cells, Molecules, and Diseases*, *56*(1), 53–61.
32. Favre-Bulle, I. A., Stilgoe, A. B., Rubinsztein-Dunlop, H., Scott, E. K., et al. (2017). *Nature Communications*, *8*(1), 630.
33. Torre-Mapa, M. L., Veldhuis, L., Ploschner, M., Dholakia, K., & Gunn-Moore, F. (2010). Transient transfection of mammalian cells using a violet diode laser. *Journal of Biomedical Optics*, *15*(4), 041506.
34. Peterman, E. J. G., Gittes, F., & Schmidt, C. F. (2003). Laser-induced heating in optical traps. *Biophysical Journal*, *84*(2), 1308–1316.
35. Juan, M. L., Righini, M., & Quidant, R. (2011). Plasmon nano-optical tweezers. *Nature Photonics*, *5*, 349.
36. Tsuboi, Y. (2016). A long arm and a tight grip. *Nature Nanotechnology*, *11*(1), 5–6.
37. Kotsifaki, D. G., Kandyala, M., & Lagoudakis, P. G. (2016). Plasmon enhanced optical tweezers with gold-coated black silicon. *Scientific Reports*, *6*, 26275.
38. Gao, D., Ding, W., Nieto-Vesperinas, M., Ding, X., Rahman, M., Zhang, T., Lim, C., & Qiu, C.-W. (2017). Optical manipulation from the microscale to the nanoscale: Fundamentals, advances and prospects. *Light: Science & Applications*, *6*, e17039.
39. Ma, Y., Rui, G., Gu, B., & Cui, Y. (2017). Trapping and manipulation of nanoparticles using multifocal optical vortex metalens. *Scientific Reports*, *7*(1), 14611.
40. Gordon, R. (2019). Biosensing with nanoaperture optical tweezers. *Optics & Laser Technology*, *109*, 328–335.
41. Kotsifaki, D. G., & Nic Chormaic, S. (2019). Plasmonic optical tweezers based on nanostructures: Fundamentals, advances and prospects. *Nanophotonics*, *8*(7), 1227–1245.
42. Kim, J., & Martin, O. J. F. (2019). Studying the different coupling regimes for a plasmonic particle in a plasmonic trap. *Optics Express*, *27*(26), 38670–38682.
43. Solomon, M. L., Saleh, A. A. E., Poulidakos, L. V., Abendroth, J. M., Tadesse, L. F., & Dionne, J. A. (2020). Nanophotonic platforms for chiral sensing and separation. *Accounts of Chemical Research*, *53*(3), 588–598.
44. Jiang, Q., Rogez, B., Claude, J.-B., Baffou, G., & Wenger, J. (2020). Quantifying the role of the surfactant and the thermophoretic force in plasmonic nano-optical trapping. *Nano Letters*, *20*(12), 8811–8817.
45. Jiang, Q., Claude, J.-B., & Wenger, J. (2021). Plasmonic nano-optical trap stiffness measurements and design optimization. *Nanoscale*, *13*(7), 4188–4194.
46. Maxwell, J. C. (1873). *A treatise on electricity and magnetism* (Vol. 2). Oxford University Press.
47. Novotny, L. H. B. (2019). *Principles of nano-optics*. Cambridge.
48. Abraham, M. (1909). Zur Elektrodynamik bewegter Körper. *Rendiconti del Circolo Matematico di Palermo (1884–1940)*, *28*(1).
49. Ramos, T., Rubilar, G. F., & Obukhov, Y. N. (2015). First principles approach to the Abraham–Minkowski controversy for the momentum of light in general linear non-dispersive media. *Journal of Optics*, *17*(2), 025611.
50. Pfeifer, R. N. C., Nieminen, T. A., Heckenberg, N. R., & Rubinsztein-Dunlop, H. (2007). Colloquium: Momentum of an electromagnetic wave in dielectric media. *Reviews of Modern Physics*, *79*, 1197–1216.
51. Harada, Y., & Asakura, T. (1996). Radiation forces on a dielectric sphere in the Rayleigh scattering regime. *Optics Communications*, *124*(5), 529–541.
52. Wang, K., & Crozier, K. B. (2012). Plasmonic trapping with a gold nanopillar. *ChemPhysChem*, *13*(11), 2639–2648.
53. Bradshaw, D. S., & Andrews, D. L. (2017). Manipulating particles with light: Radiation and gradient forces. *European Journal of Physics*, *38*(3), 034008.

54. Beth, R. A. (1936). Mechanical detection and measurement of the angular momentum of light. *Physical Review*, *50*, 115–125.
55. Kim, M. M., & Zydney, A. L. (2004). Effect of electrostatic, hydrodynamic, and Brownian forces on particle trajectories and sieving in normal flow filtration. *Journal of Colloid and Interface Science*, *269*(2), 425–431.
56. Zhang, W., Huang, L., Santschi, C., & Martin, O. J. F. (2010). Trapping and sensing 10 nm metal nanoparticles using plasmonic dipole antennas. *Nano Letters*, *10*(3).
57. Lin, S., & Crozier, K. B. (2013). Trapping-assisted sensing of particles and proteins using on-chip optical microcavities. *ACS Nano*, *7*(2), 1725–1730.
58. Al Balushi, A. A., & Gordon, R. (2014). A label-free untethered approach to single-molecule protein binding kinetics. *Nano Letters*, *14*(10), 5787–5791.
59. Zhang, W., & Martin, O. J. F. (2015). A universal law for plasmon resonance shift in biosensing. *ACS Photonics*, *2*(1), 144–150.
60. Ashkin, A., Dziedzic, J. M., & Yamane, T. (1987). Optical trapping and manipulation of single cells using infrared laser beams. *Nature*, *330*, 769.
61. Ashkin, A., & Dziedzic, J. M. (1987). Optical trapping and manipulation of viruses and bacteria. *Science*, *235*(4795), 1517–1520.
62. Ashkin, A., & Gordon, J. P. (1979). Cooling and trapping of atoms by resonance radiation pressure. *Optics Letters*, *4*(6), 161–163.
63. Kasevich, M., & Chu, S. (1992). Laser cooling below a photon recoil with three-level atoms. *Physical Review Letters*, *69*, 1741–1744.
64. Novotny, L., Bian, R. X., & Xie, X. S. (1997). Theory of nanometric optical tweezers. *Physical Review Letters*, *79*(4), 645–648.
65. Kravets, V. G., Kabashin, A. V., Barnes, W. L., & Grigorenko, A. N. (2018). Plasmonic surface lattice resonances: A review of properties and applications. *Chemical Reviews*, *118*(12), 5912–5951.
66. Volpe, G., Quidant, R., Badenes, G., & Petrov, D. (2006). Surface plasmon radiation forces. *Physical Review Letters*, *96*(23), 238101.
67. Wang, K., Schonbrun, E., & Crozier, K. B. (2009). Propulsion of gold nanoparticles with surface plasmon polaritons: Evidence of enhanced optical force from near-field coupling between gold particle and gold film. *Nano Letters*, *9*(7), 2623–2629.
68. Ndukaife, J. C., Kildishev, A. V., Nnanna, A. G. A., Shalaev, V. M., Wereley, S. T., & Boltasseva, A. (2015). Long-range and rapid transport of individual nano-objects by a hybrid electrothermoplasmonic nanotweezer. *Nature Nanotechnology*, *11*, 53.
69. Berry, D. W., Heckenberg, N. R., & Rubinsztein-dunlop, H. (2000). Effects associated with bubble formation in optical trapping. *Journal of Modern Optics*, *47*(9), 1575–1585.
70. Wang, K., Schonbrun, E., Steinvurzel, P., & Crozier, K. B. (2011). Trapping and rotating nanoparticles using a plasmonic nano-tweezer with an integrated heat sink. *Nature Communications*, *2*, 469.
71. Roxworthy, B. J., Bhuiya, A. M., Vanka, S. P., & Toussaint, K. C., Jr. (2014). Understanding and controlling plasmon-induced convection. *Nature Communications*, *5*, 3173.
72. Baffou, G., Berto, P., Bermúdez Ureña, E., Quidant, R., Monneret, S., Polleux, J., & Rigneault, H. (2013). Photoinduced heating of nanoparticle arrays. *ACS Nano*, *7*(8), 6478–6488.
73. Jiang, Q., Rogez, B., Claude, J.-B., Baffou, G., & Wenger, J. (2019). Temperature measurement in plasmonic nanoapertures used for optical trapping. *ACS Photonics*, *6*(7), 1763–1773.
74. Baffou, G., Cichos, F., & Quidant, R. (2020). Applications and challenges of thermoplasmonics. *Nature Materials*, *19*, 946–958.
75. Kotnala, A., Kollipara, P. S., Li, J., & Zheng, Y. (2020). Overcoming diffusion-limited trapping in nanoaperture tweezers using Opto-thermal-induced flow. *Nano Letters*, *20*(1), 768–779.
76. Garcés-Chávez, V., Quidant, R., Reece, P. J., Badenes, G., Torner, L., & Dholakia, K. (2006). Extended organization of colloidal microparticles by surface plasmon polariton excitation. *Physical Review B*, *73*(8), 085417.

77. Grigorenko, A. N., Roberts, N. W., Dickinson, M. R., & Zhang, Y. (2008). Nanometric optical tweezers based on nanostructured substrates. *Nature Photonics*, 2(6), 365–370.
78. Righini, M., Ghenuche, P., Cherukulappurath, S., Myroshnychenko, V., Garcia de Abajo, F. J., & Quidant, R. (2009). Nano-optical trapping of Rayleigh particles and Escherichia coli bacteria with resonant optical antennas. *Nano Letters*, 9(10), 3387–3391.
79. Geiselmann, M., Marty, R., Renger, J., García de Abajo, F. J., & Quidant, R. (2014). Deterministic optical-near-field-assisted positioning of nitrogen-vacancy centers. *Nano Letters*, 14(3), 1520–1525.
80. Sergides, M., Truong, V. G., & Nic Chormaic, S. (2016). Highly tunable plasmonic nanoring arrays for nanoparticle manipulation and detection. *Nanotechnology*, 27(36), 365301.
81. Roxworthy, B. J., Ko, K. D., Kumar, A., Fung, K. H., Chow, E. K. C., Liu, G. L., Fang, N. X., & Toussaint, K. C., Jr. (2012). Application of plasmonic Bowtie nanoantenna arrays for optical trapping, stacking, and sorting. *Nano Letters*, 12(2), 796–801.
82. Roxworthy, B. J., Johnston, M. T., Lee-Montiel, F. T., Ewoldt, R. H., Imoukhuede, P. I., & Toussaint, K. C., Jr. (2014). Plasmonic optical trapping in biologically relevant media. *PLoS One*, 9(4), e93929.
83. Fischer, H., & Martin, O. J. F. (2008). Engineering the optical response of plasmonic nanoantennas. *Optics Express*, 16(12), 9144–9154.
84. Yoon, S. J., Lee, J., Han, S., Kim, C.-K., Ahn, C. W., Kim, M.-K., & Lee, Y.-H. (2018). Non-fluorescent nanoscopic monitoring of a single trapped nanoparticle via nonlinear point sources. *Nature Communications*, 9(1), 2218.
85. Yoon, S. J., Song, D. I., Lee, J., Kim, M.-K., Lee, Y.-H., & Kim, C.-K. (2020). Hopping of single nanoparticles trapped in a plasmonic double-well potential. *Nanophotonics*, 9(16), 4729.
86. Tsuboi, Y., Shoji, T., Kitamura, N., Takase, M., Murakoshi, K., Mizumoto, Y., & Ishihara, H. (2010). Optical trapping of quantum dots based on gap-mode-excitation of localized surface plasmon. *The Journal of Physical Chemistry Letters*, 1(15), 2327–2333.
87. Shoji, T., Saitoh, J., Kitamura, N., Nagasawa, F., Murakoshi, K., Yamauchi, H., Ito, S., Miyasaka, H., Ishihara, H., & Tsuboi, Y. (2013). Permanent fixing or reversible trapping and release of DNA micropatterns on a gold nanostructure using continuous-wave or femtosecond-pulsed near-infrared laser light. *Journal of the American Chemical Society*, 135(17), 6643–6648.
88. Shoji, T., Sugo, D., Nagasawa, F., Murakoshi, K., Kitamura, N., & Tsuboi, Y. (2017). Highly sensitive detection of organic molecules on the basis of a poly(N-isopropylacrylamide) microassembly formed by plasmonic optical trapping. *Analytical Chemistry*, 89(1), 532–537.
89. Kang, J.-H., Kim, K., Ee, H.-S., Lee, Y.-H., Yoon, T.-Y., Seo, M.-K., & Park, H.-G. (2011). Low-power nano-optical vortex trapping via plasmonic diabolite nanoantennas. *Nature Communications*, 2, 582.
90. Lukas, N., Romain, Q., & Darrick, E. C. (2015). Self-induced back-action optical trapping in nanophotonic systems. *New Journal of Physics*, 17(12), 123008.
91. Juan, M. L., Gordon, R., Pang, Y., Eftekhari, F., & Quidant, R. (2009). Self-induced back-action optical trapping of dielectric nanoparticles. *Nature Physics*, 5, 915.
92. Berthelot, J., Acimovic, S. S., Juan, M. L., Kreuzer, M. P., Renger, J., & Quidant, R. (2014). Three-dimensional manipulation with scanning near-field optical nanotweezers. *Nature Nanotechnology*, 9(4), 295–299.
93. Mestres, P., Berthelot, J., Acimović, S. S., & Quidant, R. (2016). Unraveling the optomechanical nature of plasmonic trapping. *Light: Science & Applications*, 5, e16092.
94. Chen, C., Juan, M. L., Li, Y., Maes, G., Borghs, G., Van Dorpe, P., & Quidant, R. (2012). Enhanced optical trapping and arrangement of nano-objects in a plasmonic nanocavity. *Nano Letters*, 12(1), 125–132.
95. Yoo, D., Gurunatha, K. L., Choi, H.-K., Mohr, D. A., Ertsgaard, C. T., Gordon, R., & Oh, S.-H. (2018). Low-power optical trapping of nanoparticles and proteins with resonant coaxial nanoaperture using 10 nm gap. *Nano Letters*, 18(6), 3637–3642.

96. Saleh, A. A. E., & Dionne, J. A. (2012). Toward efficient optical trapping of sub-10-nm particles with coaxial plasmonic apertures. *Nano Letters*, *12*(11), 5581–5586.
97. Pang, Y., & Gordon, R. (2011). Optical trapping of 12 nm dielectric spheres using double-nanoholes in a gold film. *Nano Letters*, *11*(9), 3763–3767.
98. Pang, Y., & Gordon, R. (2012). Optical trapping of a single protein. *Nano Letters*, *12*(1), 402–406.
99. Kotnala, A., & Gordon, R. (2014). Quantification of high-efficiency trapping of nanoparticles in a double nanohole optical tweezer. *Nano Letters*, *14*(2), 853–856.
100. Xu, H., Jones, S., Choi, B.-C., & Gordon, R. (2016). Characterization of individual magnetic nanoparticles in solution by double nanohole optical tweezers. *Nano Letters*, *16*(4), 2639–2643.
101. Chen, K. Y., Lee, A. T., Hung, C. C., Huang, J. S., & Yang, Y. T. (2013). Transport and trapping in two-dimensional nanoscale plasmonic optical lattice. *Nano Letters*, *13*(9), 4118–4122.
102. Hansen, P., Zheng, Y., Ryan, J., & Hesselink, L. (2014). Nano-optical conveyor belt, part I: Theory. *Nano Letters*, *14*(6), 2965–2970.
103. Zheng, Y., Ryan, J., Hansen, P., Cheng, Y.-T., Lu, T.-J., & Hesselink, L. (2014). Nano-optical conveyor belt, part II: Demonstration of handoff between near-field optical traps. *Nano Letters*, *14*(6), 2971–2976.
104. Huft, P. R., Kolbow, J. D., Thweatt, J. T., & Lindquist, N. C. (2017). Holographic plasmonic nanotweezers for dynamic trapping and manipulation. *Nano Letters*, *17*(12), 7920–7925.
105. Han, X., Truong, V. G., & Nic Chormaic, S. (2018). Efficient microparticle trapping with plasmonic annular apertures arrays. *Nano Futures*, *2*(3), 035007.
106. Han, X., Truong, V. G., Thomas, P. S., & Nic Chormaic, S. (2018). Sequential trapping of single nanoparticles using a gold plasmonic nanohole array. *Photonics Research*, *6*(10), 981–986.
107. Bouloumris, T. D., Kotsifaki, D. G., Han, X., Nic Chormaic, S., Truong, V. G., et al. (2020). *Nanotechnology*, *32*(2), 025507.
108. Kotsifaki, D. G., Truong, V. G., & Nic Chormaic, S. (2020). Fano-resonant, asymmetric, metamaterial-assisted tweezers for single nanoparticle trapping. *Nano Letters*, *20*(5), 3388–3395.
109. Fano, U. (1961). Effects of configuration interaction on intensities and phase shifts. *Physical Review*, *124*, 1866–1878.
110. Luk'yanchuk, B., Zheludev, N. I., Maier, S. A., Halas, N. J., Nordlander, P., Giessen, H., & Chong, C. T. (2010). The Fano resonance in plasmonic nanostructures and metamaterials. *Nature Materials*, *9*(9), 707–715.
111. Kotsifaki, D. G., Truong, V. G., & Nic Chormaic, S. (2021). Dynamic multiple nanoparticle trapping using metamaterial plasmonic tweezers. *Applied Physics Letters*, *118*(2), 021107.
112. Pin, C., Magno, G., Ecarnot, A., Picard, E., Hadji, E., Yam, V., de Fornel, F., Dagens, & Cluzel, B. (2020). Seven at one blow: Particle cluster stability in a single plasmonic trap on a silicon waveguide. *ACS Photonics*, *7*(8), 1942–1949.
113. Ecarnot, A., Magno, G., Yam, V., & Dagens, B. (2018). Ultra-efficient nanoparticle trapping by integrated plasmonic dimers. *Optics Letters*, *43*(3), 455–458.
114. Conteduca, D., Reardon, C., Scullion, M. G., Dell'Olio, F., Armenise, M. N., Krauss, T. F., & Ciminelli, C. (2017). Ultra-high Q/V hybrid cavity for strong light-matter interaction. *APL Photonics*, *2*(8), 086101.
115. Zhao, D., Liu, S., & Gao, Y. (2018). Single-molecule manipulation and detection. *Acta Biochimica et Biophysica Sinica*, *50*(3), 231–237.
116. Michalet, X., & Weiss, S. (2002). Single-molecule spectroscopy and microscopy. *Comptes Rendus Physique*, *3*(5), 619–644.
117. Sekar, R. B., & Periasamy, A. (2003). Fluorescence resonance energy transfer (FRET) microscopy imaging of live cell protein localizations. *Journal of Cell Biology*, *160*(5), 629–633.

118. Al Balushi, A. A., Zehtabi-Oskuie, A., & Gordon, R. (2013). Observing single protein binding by optical transmission through a double nanohole aperture in a metal film. *Biomedical Optics Express*, 4(9), 1504–1511.
119. Kotnala, A., & Gordon, R. (2014). Double nanohole optical tweezers visualize protein p53 suppressing unzipping of single DNA-hairpins. *Biomedical Optics Express*, 5(6), 1886–1894.
120. DeWolf, T., & Gordon, R. (2016). Theory of acoustic Raman modes in proteins. *Physical Review Letters*, 117, 138101.
121. Wheaton, S., Gelfand, R. M., & Gordon, R. (2014). Probing the Raman-active acoustic vibrations of nanoparticles with extraordinary spectral resolution. *Nature Photonics*, 9, 68.
122. Verschueren, D. V., Pud, S., Shi, X., De Angelis, L., Kuipers, L., & Dekker, C. (2018). Label-free optical detection of DNA translocations through plasmonic nanopores. *ACS Nano*, 13(1), 61–70.
123. Garoli, D., Yamazaki, H., Maccaferri, N., & Wanunu, M. (2019). Plasmonic nanopores for single-molecule detection and manipulation: Toward sequencing applications. *Nano Letters*, 19(11), 7553–7562.
124. Verschueren, D., Shi, X., & Dekker, C. (2019). Nano-optical tweezing of single proteins in plasmonic nanopores. *Small Methods*, 3(5), 1800465.
125. Ndukaife, J. C., Xuan, Y., Nnanna, A. G. A., Kildishev, A. V., Shalae, V. M., Wereley, S. T., & Boltasseva, A. (2018). High-resolution large-ensemble nanoparticle trapping with multifunctional thermoplasmonic nanohole metasurface. *ACS Nano*, 12(6), 5376–5384.
126. Lin, L., Kollipara, P. S., Kotnala, A., Jiang, T., Liu, Y., Peng, X., Korgel, B. A., & Zheng, Y. (2010). Opto-thermoelectric pulling of light-absorbing particles. *Light: Science & Applications*, 9(1), 34.
127. Lin, L., Peng, X., Mao, Z., Li, W., Yogeesh, M. N., Rajeeva, B. B., Perillo, E. P., Dunn, A. K., Akinwande, D., & Zheng, Y. (2016). Bubble-Pen lithography. *Nano Letters*, 16(1), 701–708.
128. Xu, B., & Tao, N. J. (2003). Measurement of single-molecule resistance by repeated formation of molecular junctions. *Science*, 301(5637), 1221–1223.
129. Zhao, Y., Saleh, A. A., & Dionne, J. A. (2016). Enantioselective optical trapping of chiral nanoparticles with plasmonic tweezers. *ACS Photonics*, 3(3), 304–309.
130. Li, Y., Rui, G., Zhou, S., Gu, B., Yu, Y., Cui, Y., & Zhan, Q. (2020). Enantioselective optical trapping of chiral nanoparticles using a transverse optical needle field with a transverse spin. *Optics Express*, 28(19), 27808–27822.
131. Niinomi, H., Sugiyama, T., Uda, S., Tagawa, M., Ujihara, T., Miyamoto, K., & Omatsu Plasmonic, T. (2019). Trapping-induced crystallization of acetaminophen. *Crystal Growth & Design*, 19(2), 529–537.

Plasmon-Enhanced Optical Tweezing Systems: Fundamental and Applications



Mohammad Hazhir Mozaffari

Abstract Optical tweezing systems have heralded a revolution in nanoparticle science while they pose unique challenges, mainly due to low optical gradient force. A promising candidate that can provide the highly concentrated field intensity and vastly enhances the gradient force is surface plasmon. Hence, plasmon-enhanced tweezers have matured to a stage where today become increasingly attractive for optical manipulation applications. In this chapter, first, the physics behind the optical tweezing with focusing on plasmonic tweezers is explained, and as an example, a nano-bowtie plasmonic tweezer is simulated while its capability in the trapping of the nanoparticle is investigated. According to finite-difference-time-domain (FDTD) simulations, the device exerts a trapping force of 150 pNW^{-1} on a 40 nm virus-like-particle. Next, the applicable types of plasmon-enhanced tweezers are briefly introduced through a classification of these devices in two main generations. Finally, an intuitive overview of some of the widest applications of optical and plasmonic tweezing systems have found in various fields, is presented.

Keywords Optical tweezer · Plasmonic tweezer · Optical force · Trapping force · Optical trapping · Manipulation of nanoparticles

1 Introduction

The light can exert a force is now well understood. This force was predicted by J. C. Maxwell in 1873 whereas an experimental demonstration of radiation pressure from light was performed before the idea of a photon was suggested [1]. The radiation pressure was inferred from the concept of light being a wave.

With the appearance of quantum mechanics, and the definition of photons as the minimum unit of energy carried by a light beam, the force exerted by light could

M. H. Mozaffari (✉)

Department of Electrical Engineering, Sanandaj Branch, Islamic Azad University, Sanandaj, Iran
e-mail: mh.mozaffari@iausdj.ac.ir

be described as the transfer of a photon's momentum to a scattering or absorbing object.

The optical force arises from objects changing either the magnitude or direction of the momentum vector:

$$F = \frac{dp}{dt} \quad (1)$$

where p is the momentum vector, F is the optical force vector and t is time.

Everyday experience tells us that if there is an optical force, it must be particularly small. It is therefore perhaps predictable that the phenomenon has found application in nanoscience. An object's volume, and therefore mass, scales with the cube of its radius, meaning a factor of a million reduction in radius gives a 10^{18} reduction in mass. The first observation of microscopic particles being influenced by light came in 1969. Ten years after the invention of the laser, Ashkin, and coworkers [2] demonstrated that a laser could accelerate microscopic particles at 10^5 times acceleration due to gravity. In their experiment, thermal effects were evaded by using transparent particles that did not absorb light, nonetheless did deflect the light since the particles having a higher refractive index as compared to the surrounding fluid index. Ashkin described that the particles were drawn into the beam axis and accelerated in the direction of the light, which hints at the presence of two mechanisms, one to pull the particle in and one to push the particle upwards. As a result, an optical tweezer is defined as a device that uses tightly focused light to trap and move particles. Developed by Ashkin in 1986, and originally termed as a "gradient force optical trap," optical tweezers represented a significant development in optical trapping [3]. The key feature of this technique is the focusing of the beam, which makes use of the propensity of light to pull high refractive index objects into high-intensity regions. Hence, we need a highly localized field intensity gradient to increase the gradient force and consequently to realize stable optical trapping. In recent years, the use of metal nanostructures with localized surface plasmon resonances (LSPRR) has gained many achievements in making optical tweezers. In fact, they can provide intense and highly concentrated resonant fields smaller than the radiation wavelength (near field) that leads to an increased gradient force. This increased gradient force can, potentially, overcome the restrictions and drawbacks of conventional optical tweezers.

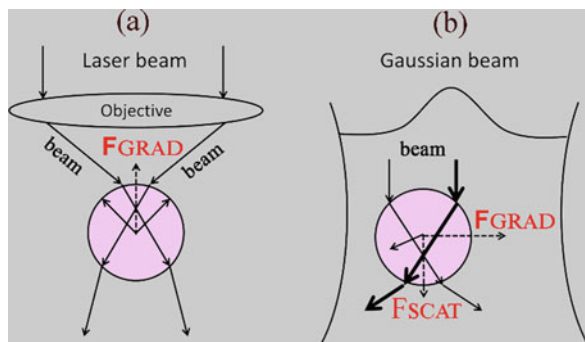
In this chapter, the theoretical aspects of these plasmonic tweezers are explained. For reaching this goal, first, we explain that how optical tweezers work and then focus on concepts of surface plasmon to explain plasmon-enhanced optical tweezers while as an example of plasmonic tweezer, we simulate a nano-bowtie tweezing system and investigate its ability in the trapping of the nanoparticle. After that, the applicable types of plasmonic tweezers are briefly introduced through a classification of these devices in two main generations. Finally, various applications of state-of-the-art tweezing systems are described.

2 Theoretical Aspects of Plasmonic Tweezers

As mentioned, the ability of light to exert a force for manipulation and trapping of particles was being founded by Ashkin. Basically, light not only has power but also has a momentum according to the electromagnetic theory. When light illuminates an object, there is a momentum change due to the scattering of the incident photons, then an optical radiation pressure is exerted on the illuminated object. When the object is a transparent dielectric particle, there are reflections inside the particle, and a trapping force may be exerted on this particle. A typical optical tweezers system is formed through a laser beam being focused onto a particle by an objective lens. Take Gaussian beam as an example, as shown in Fig. 1. Optical trapping can be broken down into two parts, namely, axial trapping and lateral trapping. In axial trapping, the particle will experience a force due to scattering and refraction.

The force is composed of two components. One is scattering force, which usually pushes the particle along the light propagation direction. It is proportional to the Poynting vector of the optical field. The other is gradient force, which normally attracts the particle to the laser focus area. It is proportional to the gradient of the light intensity. To realize optical manipulation, the gradient force must overtake the scattering force as well as other destructive forces such as the force resulting from the kinetic energy of matter and the Brownian motion. Lateral trapping is also indispensable for 3 dimensional (3D) manipulation. The axial gradient force pulls the particle towards the focal spot, overcoming the scattering force, the gravity, and the buoyancy of the particle. When the particle comes to the Gaussian laser beam, the light at the center of the beam is usually stronger than the light at the edge, so the gradient force will pull the particle to the center of the beam (Fig. 1). In other words, the gradient force pulls the particle in the direction of maximum focalized laser beam intensity and the scattering force gets the particle out from the beam focal point in the direction of the incident light. Equations (2) and (3) show the scattering force and the gradient force generated by a focalized beam emits to a spherical dielectric particle in the Rayleigh regime in which the particle radius (R) is much smaller than the radiation wavelength ($R < \lambda_0/10$) [4].

Fig. 1 Schematic diagram of (a) axial trapping and (b) lateral trapping of a dielectric particle in a laser beam (Gaussian beam) focused by an objective. (F_{GRAD} is the gradient force, and F_{SCAT} is scattering force)



$$\vec{F}_{scattering}(\vec{r}) = \vec{z} \left(\frac{n_{md}}{C} \right) C_{scat} I(\vec{r}) = \vec{z} \frac{128\pi^5 R^6}{3 C \lambda_0^4} \left(\frac{m^2 - 1}{m^2 + 1} \right)^2 n_{md}^5 I(\vec{r}) \quad (2)$$

$$\vec{F}_{gradient}(\vec{r}) = [\vec{p}(\vec{r}.t) \cdot \nabla] \vec{E}(\vec{r}.t) = \frac{2\pi n_{md} R^3}{C} \left(\frac{m^2 - 1}{m^2 + 1} \right) \nabla I(\vec{r}) \quad (3)$$

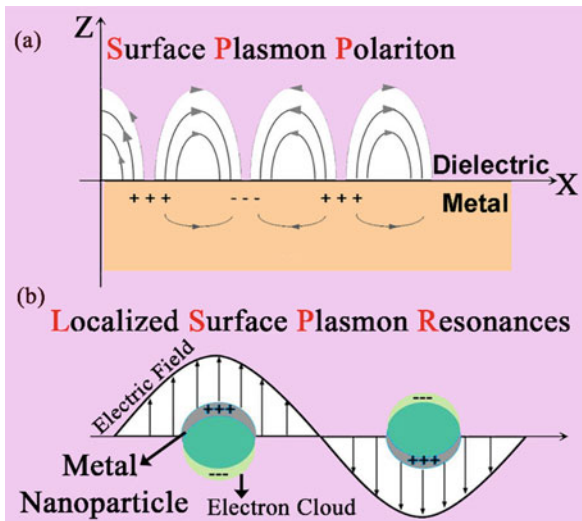
In these equations, n_{md} is the refractive index of the environment, C is the speed of light in a vacuum, C_{scat} represents the scattering cross-section, R is the radius of the particle, m is the particle refractive index/medium refractive index ratio, $I(\vec{r})$ is the intensity of the beam, Z is the propagation axis, $\vec{p}(\vec{r}.t)$ is the induced dipole of the particle caused by the instantaneous electric field ($\vec{E}(\vec{r}.t)$) of the beam and the beam wavelength is λ_0 . According to these equations, the scattering force changes with the sixth power of the particle radius while the gradient force is related to the third power of the particle radius. Therefore, as the particle size increases, the scattering force increases intensely and, can overtake the gradient force, leads to instability in optical tweezing. In contrast, the excessive reduction of the particle size will be associated with two significant effects that both lead to the tweezing instability [5]: First, reducing the particle radius, in turn, decreases the gradient force proportional to the third power of the particle radius, and secondly, the viscous drag is reduced, which raises the Brownian motion. Therefore, optical tweezers are useful for trapping and manipulating particles of a certain size range. This known as stability range ($R_{min} < R_{stability} < R_{max}$), and only when the target particle is in this range the optical tweezing can be accomplished merely. The first term of Eq. (3) cannot be improved and is the constant part of the equation. However, the second term, the $\nabla I(\vec{r})$, can be changed in order to enhance the gradient force. Increasing this part can increase the particle stability range; i.e. it can lessen the dependence of the tweezing stability on the particle radius variation. Thus, the intensity gradient, ($\nabla I(\vec{r})$), should be very high that the product of these two parts yields an adequate gradient force of the order of femto or pico-Newton. Therefore, the optical tweezer needs a highly localized electric field for providing adequate gradient force and to realize proper manipulation.

One promising candidate that can provide the highly concentrated field intensity is surface plasmons and an optical tweezer that works on this principle is known as a plasmonic tweezer.

The surface plasmon occurs in two main forms which are illustrated in Fig. 2: (1) surface plasmon polaritons (SPPs) and (2) localized surface plasmon resonances (LSPRRs).

Surface plasmons are the collective oscillations in the electron density at the interface of the two mediums with different electric constant where the zero electric constant allows the coupling of surface charge oscillations to electromagnetic

Fig. 2 Schematic illustration of (a) SPPs on the interface between a dielectric and metal and (b) LSPRRs around metal nanoparticles



waves. A mixture of a surface plasmon and a photon excitation is called an SPP. Consider a plane interface between two media, one having a complex frequency-dependent dielectric function $\epsilon_1(\omega)$ and the other having a real dielectric function $\epsilon_2(\omega)$. If the interface is at the plane $z = 0$, the electric field of the surface polariton propagating at the interface ($z = 0$) in the x -direction can be expressed as [6]:

$$E_{sp}(x, z) = E_0 e^{ik_{sp}x - k_z|z|} \tag{4}$$

This field proposes a surface plasmon mode propagating along the interface with wavevector k_{sp} and exponentially decaying from the interface with decay constant k_z . E_0 is the electric field at beginning of the path and the wavevector k_{sp} and normal component k_z are as follows:

$$K_{sp}^2 = \left(\frac{\omega}{C}\right)^2 \frac{\epsilon_1 \epsilon_2}{\epsilon_1 + \epsilon_2} \tag{5}$$

$$K_{j,z}^2 = \left(\frac{\omega}{C}\right)^2 \frac{\epsilon_j^2}{\epsilon_1 + \epsilon_2} \quad (j = 1, 2) \tag{6}$$

To have a sustainable solution, the normal component has to be purely imaginary in both media giving rise to exponentially decaying solutions. The following conditions must be satisfied [7]:

$$\varepsilon_1(\omega) \times \varepsilon_1(\omega) < 0 \quad (7)$$

$$\varepsilon_1(\omega) + \varepsilon_1(\omega) < 0 \quad (8)$$

meaning that the SPPs can exist only at the metal-dielectric interface, where metal has a large negative real part of the dielectric constant.

In addition to SPPs, the second fundamental excitation of plasmonic is called LSPRR, which are non-propagating excitations of the conduction electrons of metallic nanostructures coupled to the electromagnetic field. LSPR is the result of the confinement of surface plasmon. LSPR can also be described by the localization of free electrons induced by external excitation. It leads to a strong electric field enhancement. The frequency of LSPR can be determined through solving Laplace's equation while invoking proper boundary conditions. If the size of the nanostructure is much smaller than the wavelength corresponding to the frequency of LSPR, then quasi-electrostatic approximation is applicable in solving the equation. If a spherical metallic particle of size a is much smaller than the wavelength of light, a quasi-static approximation can be applied to solve for the electric field inside and outside the particle which described in Eq. 9, and Eq. 10.

$$E_{in} = E_0 \frac{3\varepsilon_m}{\varepsilon + 3\varepsilon_m} \quad (9)$$

$$E_{out} = E_0 + \frac{3n(n.p) - p}{4\pi\varepsilon_0\varepsilon_m r^3} \quad (10)$$

Where p is the induced oscillating dipole moment:

$$p = \varepsilon_0\varepsilon_m\alpha E_0 \quad (11)$$

and the polarizability is defined as:

$$\alpha = 4\pi a^3 \frac{\varepsilon - \varepsilon_m}{\varepsilon + 2\varepsilon_m} = \frac{\varepsilon' + i\varepsilon'' - \varepsilon_0}{\varepsilon' + i\varepsilon'' + 2\varepsilon_0} \quad (12)$$

where ε' and ε'' represent the real and imaginary parts of the permittivity of the nanosphere respectively. According to these equations, the polarizability of the metallic nanoparticle experiences a resonant enhancement under the circumstance that $|\varepsilon + 2\varepsilon_m|$ is a minimum, simply $\text{Re}[\varepsilon(\omega)] = -2\varepsilon_m$. This relationship is called the Fröhlich condition, and the associated mode is called the dipole surface plasmon of the metal nanoparticle. The magnitude of the electric field outside the

nanosphere will be maximum when $\varepsilon' + 2\varepsilon_0 = 0$. This is the resonance equation of the dispersion relation for a nanosphere. This case can be described as:

$$\alpha = \frac{-2\varepsilon_0 + i\varepsilon'' - \varepsilon_0}{i\varepsilon''} = 1 + \frac{3\varepsilon_0}{\varepsilon''}i \quad (13)$$

According to this equation, the polarizability is positively correlated to the dielectric constant of the ambient environment and negatively correlated to the imaginary part of the permittivity of the nanosphere. Thus we can either increase the refractive index of the environment or decrease ε'' to obtain a stronger electric field.

When the size of the nanosphere size increases, the contribution from higher multipole, especially the quadruple term, becomes more and more significant. The calculation of LSPR in higher-order mode can be obtained by simulation or by Mie scattering theory.

As mentioned, the surface plasmon resonance is largely dictated by α , and hence is the resonant enhancement of both internal and external fields. This field-enhancement is the key to many applications of metal nanoparticles in optical devices and sensors [7]. Surface plasmon can break the optical diffraction limit and has a near-field enhancement effect. With these two characteristics, it can improve the performance of the traditional optical device, induce many novel physical phenomena, and realize new device functionality. Developed in the last 10 years, the plasmonic tweezer is a novel technique in optical manipulation using surface plasmon. The surface plasmon field can significantly improve the gradient force, greatly reduce the requirement of the intensity of the light source, and solve the problem of the weak field in the evanescent wave tweezers system. LSPR excited among metallic particles can have a coupling with the surface plasmon excited in the plasmonic tweezers system, thus enhancing the electric field and the gradient force. Therefore, particles are more easily to trap by plasmonic tweezers. In 1997, it was demonstrated that a sharp metal tip excited by a laser beam could create sufficient optical force to trap nanoparticles close to the surface of the metal tip [8]. Under certain conditions, the charge concentrations, due to geometrical properties of the metal structure, generate highly localized evanescent field intensity that damps exponentially as get away from the interface, thus exerting strong gradient forces providing efficient optical trapping and manipulation. These fields due to surface plasmon can increase the confinement and the depth of the tweezing potential, making the tweezing more stable in the nanometer regime. Two years later, Okamoto and coworkers [9] proposed a plasmonic tweezer employing the confined light which is transmitted through a sub-wavelength aperture in an opaque metallic film. Based on these important early works, the coming-of-age of plasmon-enhanced tweezers occurred a decade later when small particles were trapped by the use of low-power exciting lasers [10], opening new frontiers for trapping and manipulation of nanoparticles.

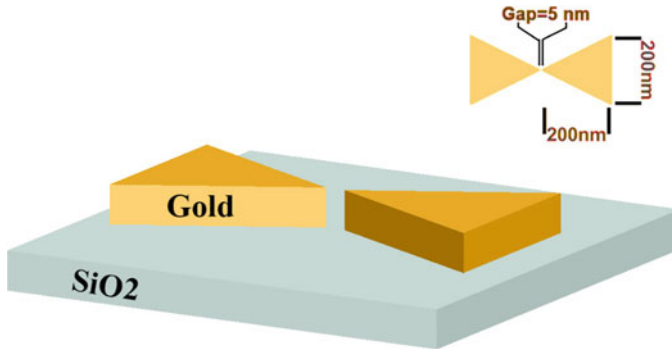


Fig. 3 Schematic illustration of a gold bowtie plasmonic tweezer

As an example of plasmonic tweezer here we simulate a nano-bowtie tweezing system and investigate its ability in the trapping of the nanoparticle. The schematic of the proposed tweezer is depicted in Fig. 3 where a gold nano-bowtie with a thickness of 70 nm has been located on a 50 nm-thick SiO₂ substrate. The altitude and the base of the coupled triangles are 200 nm while the gap between them is considered to be 5 nm. To mimic practical conditions in our simulations, the bowtie is considered to be immersed in the deionized water (effective refractive index = 1.33) with a height of 200 nm above the tweezer top surface.

In our 3D FDTD simulations, a perfectly matched layer (PML) boundary condition with 32 PML layers and the mesh size of 2 nm are considered whereas a horizontally polarized Gaussian laser beam (10 mW) located close to the chip top surface (2 μm) is employed for exciting the resonant modes. The results of the simulations are illustrated in Fig. 4 where the distribution profile of the LSPRR field intensity within the sample bowtie plasmonic tweezer is illustrated. As shown in both 2D and 3D profiles, the LSPRR field intensity is purely confined in the gap between the two nano-antennas on the interface between gold nano-antenna and the dielectric.

To examine the tweezing capability of this plasmon-enhanced tweezer, we calculated the total optical force exerted on a suspended bioparticle placed at close proximity of the chip top surface (20 nm above nano-antennas). It is worth noting that optical force exerted on a particle embedded in a viscous medium can be calculated by different approaches, which can be derived by integrating the momentum flux over a closed surface surrounding the particle. The main method of optical force calculation is based on a potential or the Maxwell stress tensor method [11].

We calculated the force exerted on a nanoparticle with a radius of 20 nm by integrating the Maxwell stress tensor. The spherical nanoparticle with an effective refractive index of 1.45 is modeled in the simulation to mimic virus-like particles. The results are presented in Fig. 5. As shown, the maximum retainable longitudinal trapping force is about 150 pN μm^{-1} . It is worth noting that the state-of-the-art

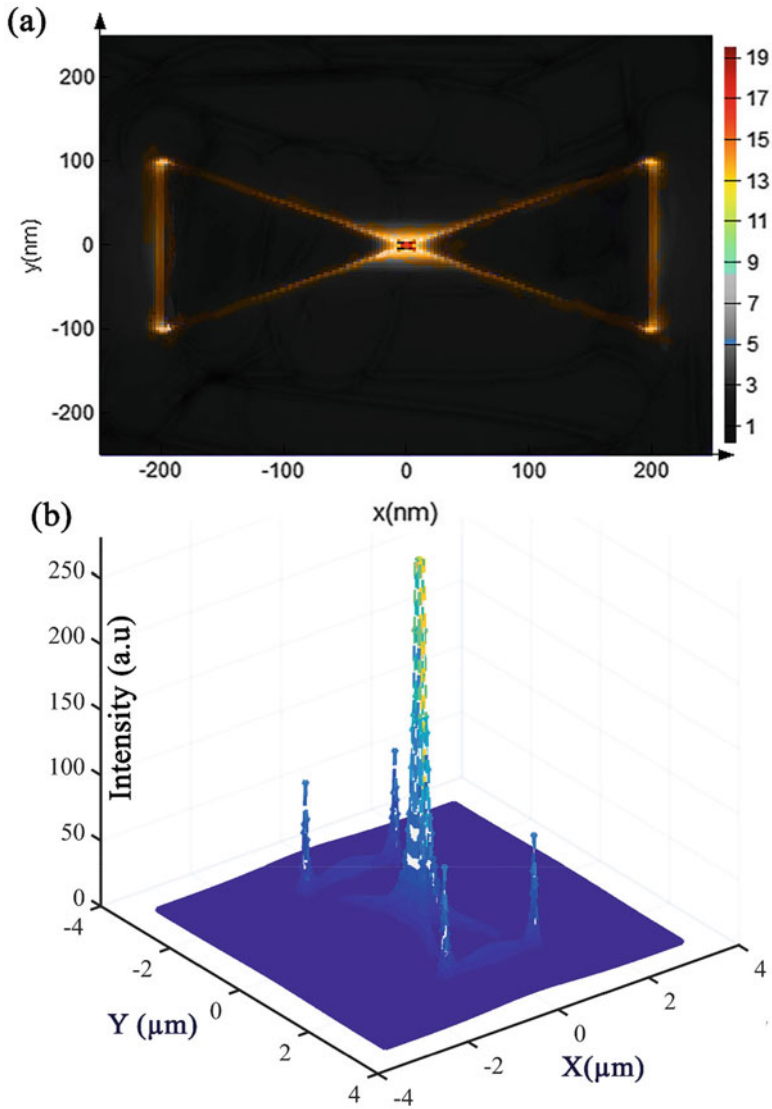
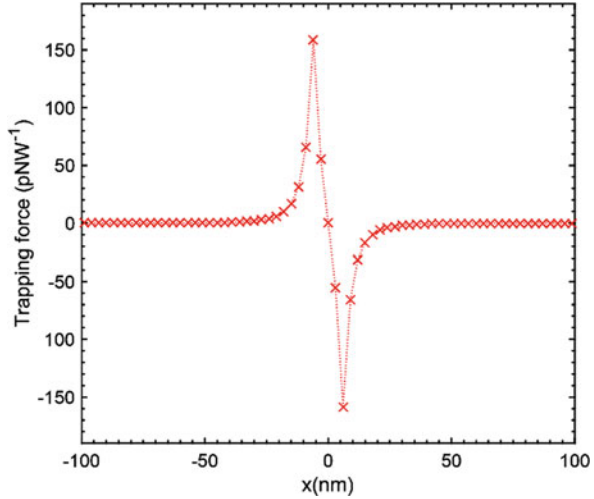


Fig. 4 (a) 2-dimensional, and (b) 3-dimensional distribution of optical-electrical field intensity within a sample nano-bowtie plasmonic tweezer

plasmon-enhanced tweezers demonstrate trapping force of 652 pN W^{-1} on a 20 nm diameter particle [12], $\sim 0.3 \text{ nN W}^{-1}$ on a $2.5 \text{ }\mu\text{m}$ diameter particle [13], $\sim 0.53 \text{ nN W}^{-1}$ on a $10 \text{ }\mu\text{m}$ diameter particle [14], 9.8 pN W^{-1} on a $10 \text{ }\mu\text{m}$ diameter particle [15], and 3.23 nN W^{-1} on a suspended bioparticle with a radius of 10 nm [16].

Fig. 5 Total trapping force exerted on a 40 nm particle as a function of the x position when $y = 0$ and $z = 20$ nm in a sample plasmonic nano bowtie tweezer



3 Types of Plasmonic Tweezers

In view of trapping forces, the plasmon-enhanced tweezers can be classified into two generations [17]. The first generation works on the surface evanescent plasmonic field with a nanostructured substrate. However, biosamples may be affected by the photothermal convection caused by surface plasmon resonances. The second generation of plasmonic tweezers in an effort to reduce the destructive effect of photothermal convection merge the plasmonic enhancement and photothermal effect as a combined trapping force.

3.1 First Generation

As stated before, the concept of plasmonic tweezers was theoretically proposed in 1997. After that, the main aim of this device was to enhance the plasmonic force provided by LSPRR in metal nanostructures known as nano-antennas. By employing a pair of nano-antennas in front of each other with a specified distance, the resonant field generated in the gap between them is usually strengthened. A point in which resonant electric field is strong known as the plasmonic hotspot [18] which provides the optical tweezing and manipulation of the nanoparticles. The plasmonic modes are influenced by various parameters such as the geometry, size, and optical properties of nano-antennas [19]. Thus, several plasmonic tweezing systems based on metallic nanoparticles such as nano-bowtie [20, 21], nano-rod [22], nano-ring [23], double nano-hole [24], and nano-bowtie ring [16] have so far been proposed in the first generation of plasmonic tweezer.

Table 1 Properties of some novel works in the first generation of plasmonic tweezers

Nanostructure/material	Wavelength (nm)	Size of the trapped object (nm)	Year
Bowtie + ring/Au	250–700	10	2019[16]
Nanowire/Ag	800	150	2019[28]
Nanohole/Graphene	8800	10	2016[29]
Cap/Au	717/767/817	100	2019[30]
Double nanohole/Au	975	20	2011[31]
Bowtie notch with curved grooves/Ag	1064	100	2021[32]

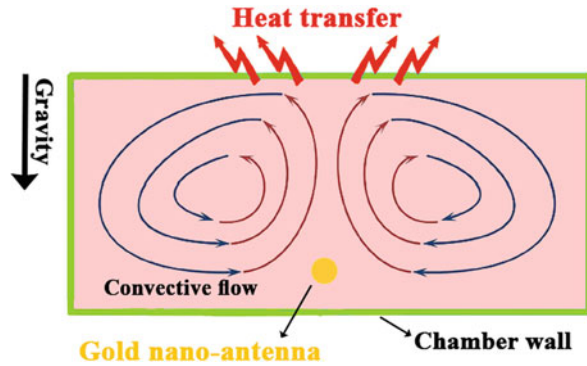
Since in visible wavelengths the metal shows highly reflective behavior it may block the illumination pathways, this disadvantage can be overcome by the use of graphene because of its high transmittance, which is an alternative plasmonic.

material to gold and silver [25, 26]. Graphene as a one-atom-thick layer is transparent in wide wavelengths, and its energy absorption is only 2.3–8.7%. Moreover, in graphene plasmonic tweezers by changing the chemical potential and conductivity of the graphene, the field enhancement can be controlled for a fixed incident laser intensity. As an experimental evidence, Lee and co-workers demonstrated that particles could be trapped by graphene nano-holes, with a local field enhancement factor of 35.8 which was more than enhancement factors of gold-based plasmonic structures [27]. Some state-of-the-art plasmonic optical tweezers that can be classified in first-generation are summarized in Table 1, providing a detailed comparison between the different trapping platforms.

3.2 Second Generation

As mentioned, the main shortcoming of first-generation plasmonic tweezers in bio-analysis applications is photothermal convection, which will potentially damage the biosamples. The illumination of plasmonic nanostructures with light leads to Joule heating due to absorption. This generally complicates the trapping process because it can result in convection currents, water boiling (in which the trapping is performed), and to damage of the sample at high laser intensities [33]. Some approaches that have been explored to mitigate this include the introduction of a high thermal conductivity substrate (i.e., heat sink design) or by off-resonance illumination to minimize the light absorption. For example, Wang et al. illustrated that heating can be decreased about 100-fold by introducing a gold-copper-silicon heat sink design with plasmonic nanoantennas [34]. On the other hand, the heating that accompanies plasmon resonance can be turned into an advantage. Examples include plasmonic photothermal therapies, the optical trapping and versatile manipulation of NPs and biological cells using thermophoretic nanotweezers [35], and the long-range and rapid transport of nanoparticles by the electrothermoplasmonic (ETP) flow [18]. Surface plasmon excitation can be accompanied by strong absorption, leading to

Fig. 6 Schematic illustration of thermal convection



local temperature increases. This in turn results in a large temperature gradient, causing the thermal convection and thermophoresis or even boiling of the water. Thermal convection, also commonly known as free convection or natural convection of a fluid (usually water), takes place through the net displacement of the fluid that is caused by buoyancy because the fluid density varies with the temperature. In optical trapping experiments, since there are no any external sources (like a pump, fan, etc.), the convection is only natural. The water that surrounds a plasmonic nanotweezers structure is heated and thus flows upward due to buoyancy. Then this hot water cools down via heat (or energy) exchange with the non-heated microfluidic chamber walls and finally flows back to the plasmonic nanotweezers structure, thus establishing a convective flow pattern which schematically is shown in Fig. 6.

Thermophoresis (also known as the Soret effect) moves particles along temperature gradients of the background fluid [36]. The direction in which the particles move by thermophoresis depends on the nanoparticle material. Polystyrene NSs, for example, move from hotter to colder areas. However, this effect can be reversed for very small particles (e.g., molecules) and at low temperatures (e.g., a few degrees Celsius).

The main aim of the second-generation plasmonic tweezers is to present a hybrid mechanism that combines the plasmonic enhancement and photothermal effect through the mixed forces of thermal convection, thermophoresis, and optical force. For example, Tsuboi and co-workers [37] founded that there is an optimum LSPR excitation intensity for the stable tweezing of the nanospheres. Above the optimum intensity, photothermal behavior such as thermophoresis disturbed the trapping process. In comparison, by use of a gold film deposited on a cleaved single-mode fiber, Ho and co-workers [38] fabricated a second-generation tweezer for trapping *Escherichia coli* cells. In this design, stable trapping was attributed to the force components, comprising thermophoresis, long-range converging lateral thermal convective flow, and near-field optical force under 980 nm laser.

In another work a research group fabricated an original hybrid electro-thermo-plasmonic nano-tweezers, that uses the interactive effects of LSPRR enhancement and an A.C. electric field, providing fast trapping of particles through a complex

interplay between thermal and optical forces [18]. In summary, during the past decade some research groups work on the second generation plasmonic tweezers by use of LSPRR induced by various nanoantenna structures and combining the related optical force with the thermal force that facilitates the precise and non-invasive tweezing of living biosamples even on the nanoscale, therefore will potentially become mainstream bioparticle manipulation and trapping device in the future.

4 Applications of Plasmonic Tweezers

Exerting force on nanoparticles enables plasmonic tweezers in optical manipulation, trapping, etc. Here we are describing the most apparent applications of this device:

4.1 Cell Biology

One of the most critical pieces of equipment that leads us to understand complex cellular processes is optical tweezers. They can probe forces that are relevant to cell biology in a minimally invasive way to search mechanical action and reaction between cells or their environments. Combination of optical tweezers and cell biology techniques help to the explanation of signaling pathways which is regulating process like as binding or growth. Modify and control cell behavior are occupied by using optical tweezers. As the size of the trapping target decreases, the main concern to consider is the synchronously reduced radiation pressure. Moreover, the thermal fluctuation will be comparable to the radiation force [39]. Plasmon-enhanced tweezers because of their enhanced optical force can overcome both issues. In the following, we illustrate some applications of plasmon-enhanced tweezers in cell biology such as measurement of cellular adhesion forces, adhesion and structure of bacterial pili, and guiding the growth of neurons.

4.1.1 Cellular Adhesion Forces

In cellular functions like endocytosis and migration, cellular adhesion has always played an essential role. Adhesion occurs is caused by specific and non-covalent binding between transmembrane receptors, such as integrins, and either counter-receptors on other cells or extracellular ligands. As dynamic bonds, cellular bonds, and their association and dissociation rates change by environmental factors for instance mechanical stress. One of the important features in cellular dynamics is regulation like spreading or migration. Exerting force by a cell on a substrate depends on the linkage of the cytoskeleton to the extracellular matrix via the integrin complex. To probe these forces, plasmonic optical tweezers are used either by

trapping the cells themselves or by trapping microscopic colloidal probe particles. The following two examples present this content:

- (i) Optical tweezers were used by Thoumine and coworkers [40] to probe the interaction between integrins and the extracellular matrix protein fibronectin in fibroblasts. k_{on} represents the association and k_{off} is used for dissociation rates of receptors and ligands. These rates control the time evolution of the probability $p_1(t)$ that a single receptor is bound as follows:

$$p_1(t) = \frac{k_{on}}{k_{on} + k_{off}} \left[1 - e^{-(k_{on} + k_{off})t} \right] \quad (14)$$

if adhesion bonds form independently, the probability, $p_n(t)$, that n out of a total population of N receptors are bound at time t , would give by a binomial distribution. Moreover, the probability that the cell attaches to the surface evolves as Eq. (15) in which N_a is the number of bonds necessary for adhesion.

$$p_a(t) = \sum_{n=N_a}^N p_n(t) = 1 - \sum_{n=0}^{N_a-1} p_n(t) \quad (15)$$

Optical tweezers hold Fibroblasts and bring them into contact with a fibronectin-coated coverslip for a set time. When the trap location wants to separate from the cell, the microscope stage moves fast, so an optical force F_{pull} acts to detach the cell from the surface. The function of cell-to-surface contact time in the adhesion probability for low ($F_{pull} \leq 13$ pN) and high ($F_{pull} \geq 28$ pN) force fit the theoretical time evolution of the adhesion probability which retrieves the association and dissociation rates in Eq. (15). $N_a = 1$ bonds represent the time evolution of adhesion probability for pulling with a low force which is given rates of $k_{on} = 1.64 \times 10^{-6} \text{ s}^{-1}$ and $k_{off} = 0.06 \text{ s}^{-1}$ and, for high force, with $N_a = 2$ with rates of $k_{on} = 2.50 \times 10^{-6} \text{ s}^{-1}$ and $k_{off} = 0.21 \text{ s}^{-1}$. To demonstrate the adhesion probability between $F_{pull} = 13$ and 28 pN, need to transition from one to two bonds that presented the strength of a single receptor-ligand bond lies within this range.

- (ii) Optical tweezers were used to probe the interaction of the cytoplasmic tail of integrins with the cytoskeleton by Jiang et al. [41]. The trimer of the fibronectin–integrin-binding domain is used as a coat for Silica beads (0.64 μm diameter) and holds in optical tweezers, they are in contact with the leading edge of the lamellipodia of a motile fibroblast. If the concentration of fibronectin trimer on the surface is sufficiently low, then the probability of the binding being a result of a single trimer is more than 80%. The beads have been steadily moved backward with a speed of 60 nm/s, away from the leading edge, as a result, the bead in the optical tweezers pulling away from equilibrium, and the load on the link between the bead and the cytoskeleton

were increased. The bead will be pulled back to the center of the trap by the optical trapping force if the link was broken, whenever it is free to form another bond and again be pulled out of the optical trap. Thoumine's group measured the fibronectin–integrin bond strength and it was considerably higher than was measured previously. The theory that the connection between the cytoplasmic tail of the integrin and the actin cytoskeleton has been broken was presented by Jiang's group.

4.1.2 Adhesion and Structure of Bacterial Pili

During colonization and infection processes, bacteria stick to tissues. Pili are hair-like structures on the surface of the bacterium, they mediate bacterial adhesion. For instance, the bacterium *Escherichia coli* which consists of a long helical rod with a short flexible fibrillum tip introduced the P pilus. The P pilus fimbrial adhesins and disaccharides stick together on the surface of epithelial cells in the urinary tract and make a route to colonization and infection. A plasmon-enhanced optical tweezer force transducer system can measure the strength of *E. coli* adhesion. The bacteria have been attached to the surface of large carboxyl polystyrene beads which were immobilized on a glass coverslip. By use of galabiose which is binding specifically to the P pilus adhesin, smaller polystyrene beads can be functionalized. To pull the bacterium away from the plasmonic tweezers, the force has been applied to the bond. For this purpose, the large bead was moved by using a piezo stage at a constant speed [39].

4.1.3 Directed Neuronal Growth

One of the subjects that have been the target for the researchers is the mechanical properties of cell membranes. Extension and distortion of the cell membrane are necessary for the growth and motility of cells. While during the deformation of the cytoskeleton the membrane is passive, motility and growth of the cell and deformation depend on the mechanical properties of the membrane certainly. Pulling the membrane into elongated tethers by optical tweezers is the way that has been used to study the mechanics of the membrane of a neuronal growth cone [42]. Plasmonic optical tweezers can trap spheres (0.5 μm diameter) coated with immunoglobulin G (IgG) then has been held against the surface of the growth cone of chick dorsal root ganglia (DRGs), signal to the spinal cord was carried by the clusters of sensory neurons. When the optical trap is moving at a constant velocity caused pulls the sphere away from the surface. Formative of an elongated membrane or the bead pulls out of the trap and remains on the surface, are the result of this process. A force pulling can back the membrane exists when the tethers retract during on release from the optical tweezers. If the displacement of the bead in the calibrated optical tweezers measure, the force acting on it during the pulling out of the tether will found.

4.2 Spectroscopy

Optical spectroscopy is a formidable technique to characterize materials and biological samples. For instants, Raman spectroscopy can measure chemical and physical in material science, geology, microelectronics, and biology. In the regulation of optical tweezers integrate spectroscopic functionalities can be possible. Nanoparticles such as viruses, bacteria, etc. have been analyzed and manipulated by spectroscopic plasmonic optical tweezers. In the following we briefly describe some important applications of plasmonic tweezers in spectroscopy:

4.2.1 Absorption and Photoluminescence Spectroscopy

The interaction between light and matter is basically defined by the energy levels of the inner degrees of freedom of the fabric system. As an example, Demtroder has found that the electronic energy levels during an atom and therefore the motion of atoms in a molecule the vibrational and rotational energy levels of the molecule are determined by the motion of electrons [43]. If a molecule is excited by a photon from its ground state to an excited state, then optical absorption will occur. The wavelength of the absorption process usually happens in the UV spectral region (approximately from 200 to 400 nm) or visible range (approximately 400–800 nm) when the transition involves different electronic states. Accordingly, the electronic structure of a system can be probed by spectroscopy in the UV and visible spectral regions. Molecules are excited to higher vibrational/rotational levels by photons.

A process that is involving the transition from an exciting level to a lower energy level of the molecular system which is resulting in the emission of a photon is called optical emission which can be classified as stimulated or spontaneous. A single photon can cause optical absorption and emission processes too. The scattering process is one of the classes of phenomena crucial in optical spectroscopy and can be elastic or inelastic depends on the energy of the scattered photon. Rayleigh scattering is defined if the energy of the scattered photon is identical to the energy of the incident photon and in the different levels of the energy Raman scattering is shown. By using plasmon-enhanced tweezers, the chemical properties of a single particle by probing its vibrational (Raman), electronic, plasmonic (extinction, thermal), (fluorescence/photoluminescence), or nonlinear (e.g., two-photons photoluminescence) properties in situ can be studied. Two optical beams one to trap the particle and one to excite it are in a typical tweezer setup. One of the optical methods which are used to probe the electronic and structural properties of materials integrated into optical tweezers is Photoluminescence spectroscopy. As well, holographic optical tweezers are used by Wang et al. [44] to scan the excitation spot along the nanowires, mapping structural inhomogeneities and enabling sorting of specific particles.

4.2.2 Raman Spectroscopy

If the light is scattered from a molecule, the majority of photons will elastically be diffused in which the scattered photons and the incident ones have the same energy. The linear Raman effect is shown when a small fraction of the light (around 1 in 10^7 photons) has been scattered at energies lower than the incident light energy. When the sample is illuminated by a laser beam, one can detect inelastically scattered light from a sample by Raman spectroscopy. By calculating the energy shift, information on the vibrational and rotational energies of molecular bonds as long as the chemical species forming those bonds is provided. The Raman spectra are the unique chemical property of molecules and reveal their interaction with the environment. In bioanalytical applications, this facilitates chemical identification of particular components in tissues, organisms, and cells.

At the first time, Raman tweezers were used to investigate biological materials, for instance, they were able to distinguish between living and dead yeast cells [45]. Next, Raman tweezers have been demonstrated to trap and analyze individual nanostructures like 40 nm polystyrene beads [46]. With the aim of plasmon-enhanced gradient force, they demonstrated more potential in the monitoring of blood diseases and analyze and manipulate nanostructures in liquid in carbon nanotubes. In Rodgers group work [47], Raman tweezers have been used to selectively trap and aggregate single-walled carbon nanotubes with specific chiralities. Also, Raman tweezers would be a suitable device to trap, manipulate and sort individual graphene flakes in solution while by the use of Raman spectroscopy, structural and electronic information on individual flakes can be extracted [48].

Exploiting the LSPRR to amplify the Raman signal is known as surface-enhanced Raman spectroscopy (SERS) that shows the enhanced gradient force provided by the plasmon-enhanced effect and allows high-sensitivity and label-free analyzing of molecular species [49]. The most efficient substrates for SERS to adsorb a molecule are the combination of optically and metal nanoparticles. Optical tweezers are an effective tool to create SERS-active metal nano colloid aggregates. As biomolecules, like proteins or nucleic acids, naturally function in a liquid environment, with the use of plasmon-enhanced Raman tweezers, rapid, ultrasensitive, and label-free detection of pathology biomarkers in body fluids can be organized whereas the contactless, label-free, three-dimensional capability of operation in liquids has been provided by SERS optical tweezers in high molecular sensitivity [39]. While probes that are functionalized allow selective interaction with specific sample sites, SERS-active probes can be highly specific. Therefore, SERS optical tweezers are a promising tool to develop next-generation biosensors which is capable to detect biomolecules and investigate biological samples in their natural environment.

4.3 *Optofluidics and Lab-on-a-Chip*

Optofluidics is known as the synergic combination of microfluidics and optics [50]. In this field, we can provide a platform for enhanced optical sensing and manipulation of different types of samples that are of interest to interdisciplinary science [51]. A deeper vision is the lab-on-a-chip (LOC) model which includes the scaling down of a complete laboratory to fit on a chip with biological, chemical, physical, and optical sensing abilities. In this context, optical forces find their perfect place, affording the possibility to trap, manipulate, sort, and characterize samples without mechanical contact. Here, we explain that how plasmonic tweezers can be exploited in optofluidics and LOC systems.

4.3.1 **Optical Sorting**

One of the important functions of optofluidic experiments is the isolation or separation of particles and cells. Using a microfluidic system, biosamples can be selected and delivered to a sensing or imaging location [52]. The first work in this area was introduced simply with the use of scattering forces to achieve sorting exploits the controlled propulsion and used this technique to sort Chinese hamster ovary cells [53]. Then, Imasaka and coworkers combined radiation pressure with an opposing fluid flow led to the realization of optical chromatography [54], and Hart et al. [55] separated particles in a microfluidic channel by radiation pressure. Some research groups were achieved to the optical separation of particles based on size and refractive index containing spores of *Bacillus anthracis* and *Bacillus thuringiensis* [56]. Moreover, a recent application of radiation pressure sorting is its application to chiral structures such as liquid crystal microdroplets or chiral solid microresonators [57]. The polarization-dependent interaction of light with chiral particles is made by optomechanical chiral forces that provide chiral optical sorting of cholesteric liquid crystal droplets using the radiation pressure of counter-propagating beams with opposite circular polarization crossing a microfluidic channel.

To create periodically modulated optical potentials that allow particles to be directionally locked a couple of research groups proposed arrays of holographic optical tweezers. Continuous and reconfigurable fractionation at the mesoscale which is dependent on the particles' properties, such as size and refractive index, with the part-per-thousand resolution is produced by ratchet potentials [58]. To sort particle which is dependent on size and refractive index, speckle fields have been used to create random optical potentials [59]. While microfluidic flow use extended static and time-varying speckle fields, optical sieving, guiding, and sorting is achieved by the statistical interaction between particles and random optical potentials.

4.3.2 Monolithic Integration

The miniaturization and integration on a single substrate of several functionalities for chemical, physical and biological analysis can be achieved by the LOC. If particles and cells are suspended, a small amount of fluid (from the microlitre down to the femtolitre range) is mixed, sorted, analyzed, and delivered by microfluidic channels [60]. The monolithic integration of the various optical elements which are necessary to trap, manipulate and characterize different samples is the basic element of the LOC concept. Full integration of microdevices is providing the construction of automated, low-cost, compactable, and portable microfluidic systems. The monolithic integration in a glass of both microchannels for microfluidics and optical waveguides can be provided by femtosecond laser micro structuring to deliver and collect light for spectroscopic detection [61]. As an example, a fully integrated system is achieved by sculpting elements directly on optical fibers providing miniaturized optofluidic and LOC fiber-based optical tweezers by fabricating micro-prism beam deflectors using two-photon lithography at the tip of bundled fibers. The light conducted in the fibers is reflected by the micro-prisms near the bundle axis, forming a trapping spot, where cells can be analyzed and trapped [62]. The fiber-bundle micro-tweezers have been used to trap red blood cells and collect fluorescence and Raman spectra of cancer cells towards the goal of a LOC-fiber concept that opens perspectives for diagnosis and screening purposes *in vivo*. It is worth noting that the integration of optofluidics with optical microcavities has great potential as a LOC device [63, 64]. Due to the properties of some cavities such as photonic crystals [65] or ring resonators [66], and the ability to integrate them into optofluidic and lab-on-a-chip applications, they are suitable for near-field light providing and trapping manipulation, and sensing. Because of the silicon substrate, photonic crystals are entailed negligible heating effects compare to plasmonic tweezers.

4.4 Trapping of Atoms

During the last decades, optical trapping at the atomic scale has seen enormous progress. Control accurately of light-matter and couple mechanically were caused neutral atoms, ions, and molecules to trap and cool and reach to the lower temperature. Three Nobel Prizes have been received for this fabulous progress: for the realization of Bose-Einstein condensation (BEC) of neutral atoms (2001), and for the manipulation of individual quantum systems (2012) [39]. As mentioned earlier, plasmonic tweezers due to their enhanced optical force compared to conventional optical tweezers can provide the acceptable gradient force of the order of femto or pico-Newton leads to stable optical trapping.

4.5 *Microchemistry*

One of the most important applications of plasmon-enhanced optical tweezing systems is the manipulation of droplets, vesicle membranes, and vesicles as movable reaction vessels comprising tiny amounts of desired reagents.

4.5.1 **Liquid Droplets**

Microchemical reaction vessels are used by measuring reactant concentration in aqueous droplets, reactants spread freely within a confined space, mimicking the environment in which biochemical processes occur in a cell. It is possible to optically trap aqueous droplets and manipulated them as aerosols. Light-scattering behavior and chemical activity are regulated by distributing the size of aerosols. Cavity-enhanced Raman scattering (CERS) has been used to study the coagulation and mixing of aerosols [67]. By monitoring CERS spectra, one can control the mixing of aerosol droplets of different compositions. Ideal reaction vessels can be caused by micron-sized aqueous droplets for femto liter volumes containing small numbers of molecules. Volume detection of a microscope without the need for surface attachment can confine the molecule. Aqueous droplets have dispersed in a suspending fluorocarbon, which is optically trapped, unlike the aerosol trap.

4.5.2 **Vesicle and Membrane Manipulation**

A (quasi-)spherical membrane that is surrounded by a liquid reservoir is called a vesicle [68]. The membrane material consists of a lipid (if the vesicle refers to as a liposome), a surfactant (noisome), or a block copolymer (polymersome). The membrane protects the contents of the vesicle to transport to a targeted location and potentially release on demand. Optical manipulation tools can transport the vesicle and release the cargo. One of the challenges to provide a vesicle is a stable optical trap because the refractive index is similar in the encapsulated material and external medium. Plasmonic tweezers electric field gradient is applied to a point on the surface of a large vesicle which is pulled the lipid membrane material towards the trap and hence in laser-induced surface tension in the membrane. Surface tension in optical tweezers is on the order of a few pico-newtons per micrometer. A research group report on their ability to optically trap vesicles with a diameter as small as 50 nm containing 1 M sucrose solution [69].

Line optical tweezers are used to induce a budding transition in multilamellar liposomes with the use of transforming the trapping laser beam into an elliptical cross-section by cylindrical lenses. It is worth noting, however, that other mechanisms caused by the heating induced by the trapping laser and the resulting changed permeability of the membrane may also play a role in this mechanism.

4.5.3 Vesicle Fusion

In a similar technique to that for aqueous droplets, a whole vesicle and membrane material can be optically trapped and manipulated by tweezing systems while aqueous droplets show some advantages in this regard, such as spontaneous fusion, encapsulation within a vesicle more closely replicates the partitioning between the inside and outside of a cell formed by the cell membrane. Giant multilamellar vesicles can be manipulated by the use of plasmon-enhanced optical tweezers and an additional pulsed ultraviolet laser when two vesicles are brought into contact [39]. Experiment studies have shown that the fused vesicle has a shape of spherical and that the volume of the vesicles was conserved during the fusion process. Since the surface area of the vesicles has been conserved by unilamellar vesicles, it is not possible for the final vesicle to be spherical without the uptake of additional fluid from the surroundings, so we can conclude that the membranes might be multilamellar.

4.6 Aerosol Science

Microscopic solid or liquid particles that are dispersed in a gas are called Aerosols. They are an important material in fields like combustion science and atmospheric chemistry. The chemical and physical state of the aerosol characteristics can be measured by holding them in optical tweezers and help its action on the environment. These properties are including, nucleation rates, mass and heat transfer, and particle composition, size, and mixing state. Because of the very low viscosity of the suspending medium aerosols manipulating and optical trapping are a big challenge and cause important inertial effects, bring the possibility to discover new phenomena like photophoretic forces.

The first optical tweezers which are suitable for airborne particles have been published by Omori et al. [70]. They presented micrometer-sized solid glass spheres with the use of driving the surface with a piezoelectric from a glass surface also reported a relatively low axial trapping efficiency ($Q_z = 0.01$) for $2.5 \mu\text{m}$ -radius spheres trapped using 40 mW of laser power. The first optically trapped (rather than optically levitated) liquid aerosols was reported in 2003 [71].

Optical tweezing particles in a liquid and gas have several important differences that are caused by the dissimilar viscosities of the media. While in a liquid medium, inertial effects might be neglected if Brownian motion is typically overdamped, for instance at relatively long-time scales (from a fraction of a millisecond upwards), in a gaseous medium, it is underdamped and inertial effects become important. Controlling the position of trapped aerosols is highly demanded like conventional optical tweezers in liquid media. The majority of aerosols are not transparent, for example, black carbon which arises from combustion processes. Due to the presence of overwhelming scattering optical forces, conventional optical trapping could not possible for these airborne particles, because of the light absorption. Shvedov and

coworkers introduced an alternative scheme to trap and guide absorbing aerosols based on radiometric forces (photophoresis). In this device, carbon clusters with sizes ranging from less than a micron to over 10 μm were trapped, and the guiding of particles up to 2 mm along the axis of the trap is realized [72].

5 Conclusion

The ability of light to exert forces leads to the invention of optical tweezers. In this chapter, we briefly explained how these devices work, and how plasmonics can overcome the limitation and drawbacks of the conventional optical tweezer. For reaching this goal, in addition to describing the theoretical aspects of optical forces, we investigated the role of LSPRR in enhancing the gradient force required in tweezing systems. The results of the simulation of a gold nano-bowtie LSPRR tweezer demonstrated that by the confinement of the high-intensity optical-electrical field, an optical force as strong as 150 pNW^{-1} can be exerted on a 40 nm virus-like particle. Moreover, the wide range of applications of the optical tweezer from cell biology to aerosol science was expressed.

References

1. Nichols, E. F., & Hull, G. F. (1901). A preliminary communication on the pressure of heat and light radiation. *Physical Review (Series I)*, 13(5), 307.
2. Ashkin, A. (1970). Acceleration and trapping of particles by radiation pressure. *Physical Review Letters*, 24(4), 156.
3. Ashkin, A., Dziedzic, J. M., Bjorkholm, J. E., & Chu, S. (1986). Observation of a single-beam gradient force optical trap for dielectric particles. *Optics Letters*, 11(5), 288–290.
4. Li, T. (2013). Physical principle of optical tweezers. In *Fundamental tests of physics with optically trapped microspheres* (pp. 9–20). Springer.
5. Quidant, R. (2012). Plasmonic tweezers—The strength of surface plasmons. *MRS Bulletin*, 37(8), 739–744.
6. Zayats, A. V., & Smolyaninov, I. I. (2003). Near-field photonics: Surface plasmon polaritons and localized surface plasmons. *Journal of Optics A: Pure and Applied Optics*, 5(4), S16.
7. Novotny, L., & Hecht, B. (2012). *Principles of nano-optics*. Cambridge University Press.
8. Martin, O. J., & Girard, C. (1997). Controlling and tuning strong optical field gradients at a local probe microscope tip apex. *Applied Physics Letters*, 70(6), 705–707.
9. Okamoto, K., & Kawata, S. (1999). Radiation force exerted on subwavelength particles near a nanoaperture. *Physical Review Letters*, 83(22), 4534.
10. Juan, M. L., Righini, M., & Quidant, R. (2011). Plasmon nano-optical tweezers. *Nature Photonics*, 5(6), 349.
11. Jain, P. K., Huang, W., & El-Sayed, M. A. (2007). On the universal scaling behavior of the distance decay of plasmon coupling in metal nanoparticle pairs: A plasmon ruler equation. *Nano Letters*, 7(7), 2080–2088.
12. Lin, P.-T., Chu, H.-Y., Lu, T.-W., & Lee, P.-T. (2014). Trapping particles using waveguide-coupled gold bowtie plasmonic tweezers. *Lab on a Chip*, 14(24), 4647–4652.

13. Zhang, Y., Dou, X., Dai, Y., Wang, X., Min, C., & Yuan, X. (2018). All-optical manipulation of micrometer-sized metallic particles. *Photonics Research*, 6(2), 66–71.
14. Kampmann, R., Sinzinger, S., & Korvink, J. (2018). Optical tweezers for trapping in a microfluidic environment. *Applied Optics*, 57(20), 5733–5742.
15. Xin, H., Xu, R., & Li, B. (2012). Optical trapping, driving, and arrangement of particles using a tapered fibre probe. *Scientific Reports*, 2, 818.
16. Mokri, K., & Mozaffari, M. H. (2019). Numerical design of a plasmonic nano-tweezer for realizing high optical gradient force. *Optics & Laser Technology*, 119, 105620.
17. Tan, H., Hu, H., Huang, L., & Qian, K. (2020). Plasmonic tweezers for optical manipulation and biomedical applications. *Analyst*, 145(17), 5699–5712.
18. Ndukaife, J. C., Kildishev, A. V., Nnanna, A. G. A., Shalaev, V. M., Wereley, S. T., & Boltasseva, A. (2016). Long-range and rapid transport of individual nano-objects by a hybrid electrothermoplasmonic nanotweezer. *Nature Nanotechnology*, 11(1), 53.
19. Vincenzo, A., Roberto, P., Marco, F., Onofrio, M. M., & Maria Antonia, I. (2017). Surface plasmon resonance in gold nanoparticles: A review. *Journal of Physics: Condensed Matter*, 29(20), 203002.
20. Roxworthy, B. J., Ko, K. D., Kumar, A., Fung, K. H., Chow, E. K., Liu, G. L., Fang, N. X., & Toussaint, K. C., Jr. (2012). Application of plasmonic bowtie nanoantenna arrays for optical trapping, stacking, and sorting. *Nano Letters*, 12(2), 796–801.
21. Samadi, M., Vasini, S., Darbari, S., Khorshad, A. A., Reihani, S. N. S., & Moravvej-Farshi, M. K. (2019). Hexagonal arrays of gold triangles as plasmonic tweezers. *Optics Express*, 27(10), 14754–14766.
22. Grigorenko, A., Roberts, N., Dickinson, M., & Zhang, Y. (2008). Nanometric optical tweezers based on nanostructured substrates. *Nature Photonics*, 2(6), 365.
23. Kang, Z., Zhang, H., Lu, H., Xu, J., Ong, H.-C., Shum, P., & Ho, H.-P. (2012). Plasmonic optical trap having very large active volume realized with nano-ring structure. *Optics Letters*, 37(10), 1748–1750.
24. Ghorbanzadeh, M., Jones, S., Moravvej-Farshi, M. K., & Gordon, R. (2017). Improvement of sensing and trapping efficiency of double nanohole apertures via enhancing the wedge plasmon polariton modes with tapered cusps. *ACS Photonics*, 4(5), 1108–1113.
25. Moradiani, F., Farmani, A., Mozaffari, M. H., Seifouri, M., & Abedi, K. (2020). Systematic engineering of a nanostructure plasmonic sensing platform for ultrasensitive biomaterial detection. *Optics Communications*, 474, 126178.
26. Ghasemi, H., & Mozaffari, M. H. (2020). *A simple proposal to reduce self-heating effect in SOI MOSFETs* (pp. 1–10). Silicon.
27. Kim, J.-D., & Lee, Y.-G. (2016). Graphene-based plasmonic tweezers. *Carbon*, 103, 281–290.
28. Nan, F., & Yan, Z. (2019). Silver-nanowire-based interferometric optical tweezers for enhanced optical trapping and binding of nanoparticles. *Advanced Functional Materials*, 29(7), 1808258.
29. Zhang, J., Liu, W., Zhu, Z., Yuan, X., & Qin, S. (2016). Towards nano-optical tweezers with graphene plasmons: Numerical investigation of trapping 10-nm particles with mid-infrared light. *Scientific Reports*, 6(1), 1–7.
30. Chai, R.-H., Zou, W.-J., Qian, J., Chen, J., Sun, Q., & Xu, J.-J. (2019). Plasmonic optical trapping of nanoparticles with precise angular selectivity. *Optics Express*, 27(22), 32556–32566.
31. Pang, Y., & Gordon, R. (2011). Optical trapping of 12 nm dielectric spheres using double-nanoholes in a gold film. *Nano Letters*, 11(9), 3763–3767.
32. Li, Z.-S., Lu, T.-W., Huang, P.-R., & Lee, P.-T. (2021). Efficient nano-tweezers via a silver plasmonic bowtie notch with curved grooves. *Photonics Research*, 9(3), 281–288.
33. Donner, J. S., Baffou, G., McCloskey, D., & Quidant, R. (2011). Plasmon-assisted optofluidics. *ACS Nano*, 5(7), 5457–5462.
34. Wang, K., Schonbrun, E., Steinvurzel, P., & Crozier, K. B. (2011). Trapping and rotating nanoparticles using a plasmonic nano-tweezer with an integrated heat sink. *Nature Communications*, 2(1), 1–6.

35. Lin, L., Wang, M., Peng, X., Lissek, E. N., Mao, Z., Scarabelli, L., Adkins, E., Coskun, S., Unalan, H. E., & Korgel, B. A. (2018). Opto-thermoelectric nanotweezers. *Nature Photonics*, *12*(4), 195–201.
36. Piazza, R., & Parola, A. (2008). Thermophoresis in colloidal suspensions. *Journal of Physics: Condensed Matter*, *20*(15), 153102.
37. Shoji, T., Shibata, M., Kitamura, N., Nagasawa, F., Takase, M., Murakoshi, K., Nobuhiro, A., Mizumoto, Y., Ishihara, H., & Tsuboi, Y. (2013). Reversible photoinduced formation and manipulation of a two-dimensional closely packed assembly of polystyrene nanospheres on a metallic nanostructure. *The Journal of Physical Chemistry C*, *117*(6), 2500–2506.
38. Chen, J., Kang, Z., Kong, S. K., & Ho, H.-P. (2015). Plasmonic random nanostructures on fiber tip for trapping live cells and colloidal particles. *Optics Letters*, *40*(17), 3926–3929.
39. Jones, P. H., Maragò, O. M., & Volpe, G. (2015). *Optical tweezers: Principles and applications*. Cambridge University Press.
40. Thoumine, O., Kocian, P., Kottelat, A., & Meister, J.-J. (2000). Short-term binding of fibroblasts to fibronectin: Optical tweezers experiments and probabilistic analysis. *European Biophysics Journal*, *29*(6), 398–408.
41. Jiang, G., Giannone, G., Critchley, D. R., Fukumoto, E., & Sheetz, M. P. (2003). Two-piconewton slip bond between fibronectin and the cytoskeleton depends on talin. *Nature*, *424*(6946), 334–337.
42. Dai, J., & Sheetz, M. P. (1995). Mechanical properties of neuronal growth cone membranes studied by tether formation with laser optical tweezers. *Biophysical Journal*, *68*(3), 988–996.
43. Demtröder, W. (2013). *Laser spectroscopy: Basic concepts and instrumentation*. Springer Science & Business Media.
44. Wang, F., Toe, W. J., Lee, W. M., McGloin, D., Gao, Q., Tan, H. H., Jagadish, C., & Reece, P. J. (2013). Resolving stable axial trapping points of nanowires in an optical tweezers using photoluminescence mapping. *Nano Letters*, *13*(3), 1185–1191.
45. Xie, C., Dinno, M. A., & Li, Y.-Q. (2002). Near-infrared Raman spectroscopy of single optically trapped biological cells. *Optics Letters*, *27*(4), 249–251.
46. Ajito, K., & Torimitsu, K. (2002). Single nanoparticle trapping using a Raman tweezers microscope. *Applied Spectroscopy*, *56*(4), 541–544.
47. Rodgers, T., Shoji, S., Sekkat, Z., & Kawata, S. (2008). Selective aggregation of single-walled carbon nanotubes using the large optical field gradient of a focused laser beam. *Physical Review Letters*, *101*(12), 127402.
48. Ferrari, A. C., & Basko, D. M. (2013). Raman spectroscopy as a versatile tool for studying the properties of graphene. *Nature Nanotechnology*, *8*(4), 235–246.
49. Kneipp, K., Moskovits, M., & Kneipp, H. (2006). *Surface-enhanced Raman scattering: Physics and applications* (Vol. 103). Springer Science & Business Media.
50. Aliee, M., Mozaffari, M. H., & Saghaei, H. (2020). Dispersion-flattened photonic quasicrystal optofluidic fiber for telecom C band operation. *Photonics and Nanostructures – Fundamentals and Applications*, *40*, 100797.
51. Farmani, A., Soroosh, M., Mozaffari, M. H., & Daghooghi, T. (2020). Chapter 25: Optical nanosensors for cancer and virus detections. In B. Han, V. K. Tomer, T. A. Nguyen, A. Farmani, & P. Kumar Singh (Eds.), *Nanosensors for smart cities* (pp. 419–432). Elsevier.
52. Fan, X., & White, I. M. (2011). Optofluidic microsystems for chemical and biological analysis. *Nature Photonics*, *5*(10), 591.
53. Buican, T. N., Smyth, M. J., Crissman, H. A., Salzman, G. C., Stewart, C. C., & Martin, J. C. (1987). Automated single-cell manipulation and sorting by light trapping. *Applied Optics*, *26*(24), 5311–5316.
54. Imasaka, T., et al. (1998). *Analisis*, *26*(5), 53–53.
55. Hart, S. J., Terray, A., Arnold, J., & Leski, T. A. (2007). Sample concentration using optical chromatography. *Optics Express*, *15*(5), 2724–2731.
56. Terray, A., Arnold, J., & Hart, S. (2005). Enhanced optical chromatography in a PDMS microfluidic system. *Optics Express*, *13*(25), 10406–10415.

57. Tkachenko, G., & Brasselet, E. (2014). Optofluidic sorting of material chirality by chiral light. *Nature Communications*, 5(1), 1–7.
58. Xiao, K., & Grier, D. G. (2010). Multidimensional optical fractionation of colloidal particles with holographic verification. *Physical Review Letters*, 104(2), 028302.
59. Volpe, G., Kurz, L., Callegari, A., Volpe, G., & Gigan, S. (2014). Speckle optical tweezers: Micromanipulation with random light fields. *Optics Express*, 22(15), 18159–18167.
60. Mozaffari, M. H., Ebnali-Heidari, M., Abaeiani, G., & Moravvej-Farshi, M. K. (2018). Designing a miniaturized photonic crystal based optofluidic biolaser for lab-on-a-chip biosensing applications. *Organic Electronics*, 54, 184–191.
61. Osellame, R., Hoekstra, H. J., Cerullo, G., & Pollnau, M. (2011). Femtosecond laser microstructuring: An enabling tool for optofluidic lab-on-chips. *Laser & Photonics Reviews*, 5(3), 442–463.
62. Liberale, C., Cojoc, G., Bragheri, F., Minzioni, P., Perozziello, G., La Rocca, R., Ferrara, L., Rajamanickam, V., Di Fabrizio, E., & Cristiani, I. (2013). Integrated microfluidic device for single-cell trapping and spectroscopy. *Scientific Reports*, 3(1), 1–7.
63. Mozaffari, M. H., Ebnali-Heidari, M., & Moravvej-Farshi, M. K. (2019). A proposal for ultra-sensitive intensity-based biosensing via photonic crystal optofluidic biolaser. *Laser Physics*, 29(3), 035803.
64. Mozaffari, M. H., Ebnali-Heidari, M., Abaeiani, G., & Moravvej-Farshi, M. K. (2017). Photonic crystal optofluidic biolaser. *Photonics and Nanostructures – Fundamentals and Applications*, 26, 56–61.
65. Eivazi, S., & Mozaffari, M. H. (2018). Numerical design and investigation of an optically pumped 1.55 μm single quantum dot photonic crystal-based laser. *Photonics and Nanostructures – Fundamentals and Applications*, 32, 42–46.
66. Mozaffari, M. H., & Farmani, A. (2020). On-chip single-mode optofluidic microresonator dye laser sensor. *IEEE Sensors Journal*, 20(7), 3556–3563.
67. Buajarern, J., Mitchem, L., Ward, A. D., Nahler, N. H., McGloin, D., & Reid, J. P. (2006). Controlling and characterizing the coagulation of liquid aerosol droplets. *The Journal of Chemical Physics*, 125(11), 114506.
68. Vasdekis, A. E., Scott, E. A., Roke, S., Hubbell, J. A., & Psaltis, D. (2013). Vesicle photonics. *Annual Review of Materials Research*, 43(1), 283–305. <https://doi.org/10.1146/annurev-matsci-071312-121724>
69. Bendix, P. M., & Oddershede, L. B. (2011). Expanding the optical trapping range of lipid vesicles to the nanoscale. *Nano Letters*, 11(12), 5431–5437.
70. Omori, R., Kobayashi, T., & Suzuki, A. (1997). Observation of a single-beam gradient-force optical trap for dielectric particles in air. *Optics Letters*, 22(11), 816–818.
71. Magome, N., Kohira, M. I., Hayata, E., Mukai, S., & Yoshikawa, K. (2003). Optical trapping of a growing water droplet in air. *The Journal of Physical Chemistry B*, 107(16), 3988–3990.
72. Shvedov, V. G., Desyatnikov, A. S., Rode, A. V., Krolikowski, W., & Kivshar, Y. S. (2009). Optical guiding of absorbing nanoclusters in air. *Optics Express*, 17(7), 5743–5757.

Plasmon-Enhanced Optothermal Manipulation



Zhihan Chen, Jingang Li, and Yuebing Zheng

Abstract Plasmon-enhanced optical heating can synergize optics and thermal fields to offer a versatile platform for optothermal manipulation of colloidal particles and living cells. By exploiting entropically favorable photon-phonon conversion and universal heat-directed migration, various optothermal tweezing techniques have been developed. Under the thermal gradient field enabled by plasmonic heating, opto-thermophoretic tweezers harness the permittivity gradient at particle-solvent interfaces to direct particles and cells toward the plasmonic hotspot via thermophoresis. Opto-thermoelectric tweezers can manipulate charged colloidal particles with various sizes, materials, and shapes in a localized electric field that is generated by the plasmon-enhanced electrolyte Seebeck effect. In addition, conventional plasmonic trapping can be significantly improved by three types of plasmon-enhanced optothermal-hydrodynamics, *i.e.*, thermo-plasmonic convection, Marangoni convection, and electrothermoplasmonic flow. These plasmon-enhanced optothermal convective flows can rapidly transport or concentrate free-dispersed objects to the plasmonic nanostructures, which significantly enhance the trapping efficiency of micro- and nano-objects. With their low operational power, simple optics, and wide applicability, plasmon-enhanced optothermal manipulation techniques can be applied to optothermal assembly of colloidal matter, non-invasive manipulation of cells and biological objects, and *in-situ* characterization of optical coupling in colloidal superstructures for a wide range of applications in photonics, materials science, colloidal science, biology, and medical engineering.

Z. Chen · J. Li

Materials Science & Engineering Program and Texas Materials Institute, The University of Texas at Austin, Austin, TX, USA

Y. Zheng (✉)

Materials Science & Engineering Program and Texas Materials Institute, The University of Texas at Austin, Austin, TX, USA

Walker Department of Mechanical Engineering, The University of Texas at Austin, Austin, TX, USA

e-mail: zheng@austin.utexas.edu

© The Author(s), under exclusive license to Springer Nature Switzerland AG 2022

233

P. Yu et al. (eds.), *Plasmon-enhanced light-matter interactions*,

Lecture Notes in Nanoscale Science and Technology 31,

https://doi.org/10.1007/978-3-030-87544-2_10

Keywords Plasmonic heating · Thermophoresis · Electrolyte thermoelectricity · Thermo-plasmonic convection · Marangoni convection · Electrothermoplasmonic flow · Colloidal particles · Cells

1 Introduction

Since Ashkin and co-workers first proposed to exploit light to manipulate micro- and nano-objects in 1986 [1], optical tweezers have been developed rapidly in the last 35 years and were awarded the Nobel Prize in Physics in 2018. Conventional optical tweezers can trap biological objects, plasmonic particles, and various dielectric particles in both two-dimensional (2D) and three-dimensional (3D) spaces [2–8]. However, trapping subwavelength objects via optical tweezers is challenging due to the diffraction limit of the incident light [9], which stimulated the development of plasmonic tweezers to overcome this limitation [10–15]. In brief, plasmonic tweezers rely on the interaction between incident light and plasmonic nanostructures consisting of noble metals [16–19] (or titanium nitride [20], graphene [21, 22], etc.) to trigger local near-field enhancement and strong gradient forces to trap nano-objects beyond the diffraction limit. However, the inherent Joule heating of metallic nanostructures upon laser irradiation in plasmonic tweezers sometimes leads to the failure of stable trapping or even thermal damages to the target objects [23, 24] because of the undesired thermophoresis, heat-induced convection, and/or the high temperature at the surface.

Apart from preventing heat generation or dissipating the heat via materials or structural designs [11, 25, 26], more strategies were proposed to reversely take advantage of the plasmonic heating to improve the manipulation efficiency of plasmonic tweezers [27, 28]. For instance, as the plasmonic heating occurs, a temperature gradient field is established in the vicinity of the plasmonic nanostructure, where the thermophoretic motions of suspended objects along or against the temperature gradient can be exploited for particle trapping and manipulation [29, 30]. In an ionic solution, differentiated thermophoretic motions of cations and anions can further facilitate the formation of thermoelectric fields to enabling opto-thermoelectric trapping of charged objects [31]. With an increasing irradiation intensity or illumination area, two types of optothermal flows, namely thermo-plasmonic and Marangoni convective flow, can take effect to deliver distant suspended particles towards the irradiated nanostructures, improving the trapping efficiency of plasmonic tweezers at low particle concentrations [32]. Moreover, local plasmonic heating also triggers a gradient of permittivity and electrical conductivity of the heated fluid. By applying an external a.c. electric field, the electrothermoplasmonic (ETP) flow is established and can be exploited for effective nano-object manipulation [33].

In this chapter, we first introduce the mechanism of plasmonic heating and feature several representative plasmonic heating substrates. Subsequently, plasmon-enhanced optothermal trapping and tweezing based on thermophoresis, thermo-

electricity, and thermo-plasmonic/Marangoni/ETP convective flows are discussed, respectively, including their working principles and applications. Finally, we give the summary and outlook of the plasmon-enhanced photothermal trapping and tweezing.

2 Plasmonic Photothermal Effect

Plasmonic photothermal effect is commonly initiated by the photoexcitation of metallic nanostructures [34]. When electromagnetic waves irradiate the metallic nanostructures with proper wavelength(s), the conduction electrons in the metal can oscillate collectively, known as localized surface plasmon resonance (LSPR). LSPR then leads to an intense electromagnetic field on the nanostructure surface, which can decay radiatively and non-radiatively. Specifically, radiative decay induces reemission of light, while non-radiative decay can be achieved via electron-electron collisions or electron-lattice phonon coupling, resulting in light-to-heat conversion (Fig. 1). Note that the heating of metallic nanostructures based on light irradiation can be quantitatively described by a value called absorption cross-section, $C_{\text{abs}} = Q/I$, where Q is the heat generated by the plasmonic nanostructure and I represents the intensity of incident light. Since the plasmonic photothermal effect relies on the coupling between light and electronic oscillations of metallic nanostructures, C_{abs} is a function of the shape and composition of plasmonic nanostructures and can also vary with the wavelength of the incident light.

Once the heat is generated by metallic nanostructures upon laser irradiation, a heat flux is created within the surrounding medium and the resultant temperature field is given by [34, 35]

$$\rho C_P \frac{\partial T(\mathbf{r})}{\partial t} - \nabla \cdot [\tau \nabla T(\mathbf{r})] = q \tag{1}$$

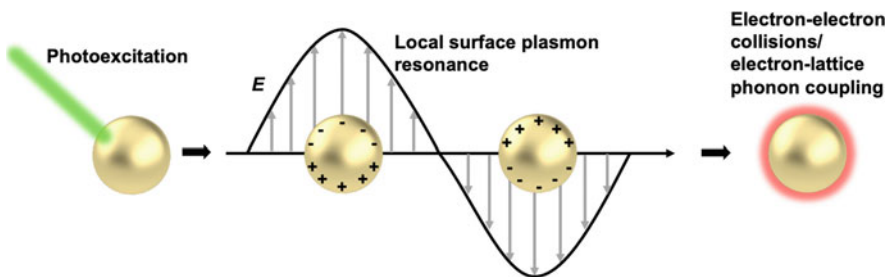


Fig. 1 Schematic of plasmonic photothermal effects. When laser irradiates metallic nanoparticles with suitable wavelengths, localized surface plasmon resonance is activated and the collective oscillation of electrons increases the frequency of collisions for the formation of local heating

where ρ , C_P and τ are the density, specific heat capacity at constant pressure and thermal conductivities of the corresponding regions, respectively. q is the heat power density of the plasmonic nanostructure. Since the metallic nanostructures possess high thermal conductivity while the environmental medium, typically aqueous solutions, has a low thermal conductivity, the temperature field within a single nanostructure will be uniform while a temperature gradient field is attained in the vicinity of the nanostructure. The continuous laser irradiation leads to a steady temperature distribution, which is established at nanosecond timescales. At the steady state, Eq. (1) can be written as $\nabla \cdot [\tau \nabla T(\mathbf{r})] = -q$. Besides, Q and q can be associated according to Poynting's theorem [36]:

$$Q = \iiint q dV \quad (2)$$

where $q = \frac{1}{2} \text{Re}(\mathbf{J} \cdot \mathbf{E}^*)$, $\mathbf{J} = \sigma \mathbf{E}$ and \mathbf{E} represent the electronic current density and electric field inside the metallic nanostructure, respectively; σ is the conductivity of the structure. Accordingly, numerical simulations can be performed to explore the C_{abs} and the temperature distribution based on the material properties of certain nanostructures [37].

As for trapping and tweezing of particles via plasmonic photothermal effects, plasmonic substrates composed of nano-sized metallic components are usually exploited for efficient heat generation and retention [38–40]. One popular type of plasmonic substrates called gold nano-islands (AuNIs) is shown in Fig. 2a, which consist of quasi-continuous Au nanoparticles fabricated by annealing Au thin films [38, 41]. Compared with Au thin films, AuNIs can create stronger temperature gradient fields upon laser irradiation due to the localized plasmonic resonances and the low thermal conductivity among each isolated Au nanoparticles (Fig. 2b) [38, 42]. The surface plasmon resonance wavelength of certain AuNIs can be tuned through adjusting the annealing temperature, rate of annealing, and thickness of original Au films.

More precise heat management of plasmonic substrates can be achieved by rationally designing the shape and spatial distribution of metallic nanoparticles. For instance, Au nanorods (AuNRs) on glass substrates have been successfully fabricated and exploited for heat-mediated particle manipulation (Fig. 2c) [39]. When the laser beam irradiates on certain AuNRs, a high-resolution temperature gradient field is established around the AuNRs (Fig. 2d). Similar to AuNIs, the surface plasmon resonance wavelength can be changed by the aspect ratio and size of AuNRs. In addition, the temperature gradient field of AuNRs can be further tuned by the polarization of incident light because the activated resonance modes, e.g., transversal and longitudinal resonances, is relevant to the relative angle between the electric field vector of incident light and the long axis of rods (Fig. 2e). Moreover, local plasmonic heating can also be achieved by metallic nanohole arrays [27, 40, 43]. Due to the in-plane Bloch mode surface plasmon polaritons [44, 45] and localized surface plasmon resonance of the individual nanoholes, the excitation of electric fields and resultant temperature gradient fields are usually concentrated

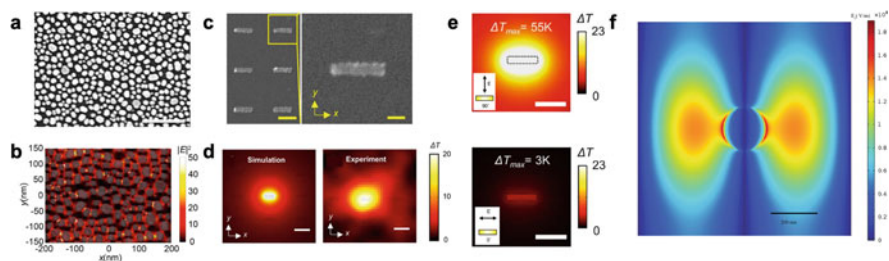


Fig. 2 Three representative metallic nanostructures for plasmon-enhanced optothermal manipulation. (a) Scanning electron microscopy (SEM) image of gold nano-islands. Scale bar: 200 nm. Adapted with permission from Ref. [28]. Copyright 2018 Springer Nature. (b) Simulated electric field distribution of AuNIs upon laser irradiation by finite-difference time-domain (FDTD) simulations. The model for the substrate was imported from the SEM image of AuNIs. Adapted with permission from Ref. [46]. Copyright 2017 American Chemical Society. (c) SEM images and (d) temperature field distribution of gold nanorods. (e) Simulated temperature field distribution with the electric field of incident light perpendicular (top) and parallel (bottom) to the long axis of the nanorod. The temperature fields were obtained from the FDTD-simulated electromagnetic fields. Scale bar: (c) left 300 nm, (c) right 100 nm, (d) 1 μm and (e) 500 nm. Adapted with permission from Ref. [39]. Copyright 2018 American Chemical Society. (f) Electric field distribution of nanohole arrays. The simulated temperature fields were modelled by finite element method (COMSOL Multiphysics). Scale bar: 200 nm. (Adapted with permission from Ref. [40]. Copyright 2018 American Chemical Society)

near the rims and interspace of nanoholes (Fig. 2f). In addition to nanorods and nanoholes, many other metallic nanostructures (such as nanobowties) have been designed and fabricated [34] for subtle control of local plasmonic heating.

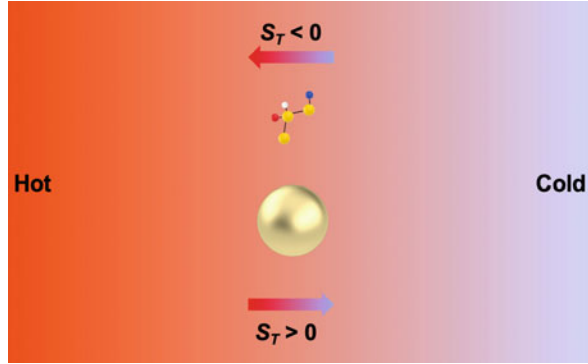
3 Opto-Thermophoretic Manipulation

Opto-thermophoretic manipulation relies on the thermophoretic motion of targeted objects under optically generated temperature gradient fields. Depending on the thermophobicity and thermophilicity of targeted objects, different plasmonic nanostructures have been designed to create highly localized temperature gradient fields with either hot or cold center to trap molecules and colloidal particles.

3.1 Mechanism

Thermophoresis, also known as the Soret effect, describes the directed migration of suspended colloidal particles or micelles along a temperature gradient (Fig. 3) [47–49]. The drift velocity of colloidal particles is given by

Fig. 3 Schematic of thermophoresis. Suspended particles or molecules with different signs of the Soret coefficient S_T show directed migration toward cold/hot regions



$$\mathbf{u} = -D_T \nabla T \quad (3)$$

where D_T is the thermophoretic mobility and ∇T is the temperature gradient. As for dilute suspensions in a steady state, the concentration gradient ∇c is expressed as [48]

$$\nabla c = -c \frac{D_T}{D} \nabla T = -c S_T \nabla T \quad (4)$$

where c is the concentration of the suspended particles, D is the Brownian diffusion coefficient, and S_T is the Soret coefficient. Since D of different components in a solution varies significantly, the Soret coefficient S_T is commonly utilized for the description of thermophoresis. Specifically, $S_T > 0$ describes that suspended objects are thermophobic and migrate toward the cold regions along the temperature gradient while $S_T < 0$ implies that suspended objects are thermophilic, which move to the hot region under ∇T .

3.2 Techniques and Applications

Most colloidal particles and molecules are thermophobic [50–52], moving from the hot to the cold regions. In order to stably trap suspended objects with $S_T > 0$ via thermophoretic migration, a localized “temperature well” should be created with the center being cold [29, 53, 54], which can be established when a non-absorbing region is surrounded by plasmonic nanostructures while a focused laser beam illuminates on the rim of the nanostructure selectively. Accordingly, Braun et al. have demonstrated opto-thermophoretic trapping of single DNA molecules within a hole surrounded by gold thin films based on feedback-controlled laser illumination (Fig. 4a) [29]. The effective potential energy $U_{eff}(\vec{r})$ of thermophoretic trapping is given by [29]

$$U_{eff}(\vec{r}) = k_B T_0 S_T \Delta T(\vec{r}) \quad (5)$$

where k_B is Boltzmann constant, T_0 is ambient temperature, and $\Delta T(\vec{r})$ is the local temperature increment. Since the effective potential is mainly determined by the temperature profile, a feedback control rule about steering the focused laser beam has been adopted to increase the temperature gradient within the metallic hole structure (Fig. 4b), which improves the trapping stiffness by a factor of 12. Specifically, compared with simply heating the whole rim of the Au nanostructure, the optically heating spot is dynamically controlled based on an acousto-optic deflector by analyzing the real-time position of the targeted object, whose width of the Gaussian position distribution can decrease by a factor of 3.5, and unwanted temperature rises at the trapping center can be alleviated. Moreover, different trapping modes, i.e., off-center trapping, two-position trapping, circular line trapping, and trapping at an expanded area, were also achieved based on different feedback laser manipulation protocols (Fig. 4c). Recently, Cichos and co-workers exploited similar methods to thermophoretically trap single amyloid fibril for the observation of fibril growth, secondary nucleation and/or fibril breakup [54].

The above opto-thermophoretic trapping enables the manipulation of single and multiple thermophobic macromolecules or colloids by elaborating the plasmon-enhanced temperature gradient field. However, targeted objects can only be trapped inside a plasmonic nanostructure, lacking dynamic manipulation over large areas. Opto-thermophoretic tweezers can be achieved if suspended objects become thermophilic, i.e., the objects can be attracted toward and stably trapped at the plasmonic heating region. Recently, Lin et al. have demonstrated opto-thermophoretic tweezers by exploiting the entropic responses and permittivity gradients at the particle-solvent interface under a plasmon-enhanced thermal gradient field [55]. Since the Brownian diffusion coefficient D is always positive, the key to opto-thermophoretic tweezers is to make targeted particles have negative D_T . The thermophoretic mobility is given by [56]

$$D_T = -\frac{\varepsilon}{2\eta T} \frac{2\Lambda_1}{2\Lambda_1 + \Lambda_p} \left(1 + \frac{\partial \ln \varepsilon}{\partial \ln T}\right) \zeta^2 \quad (6)$$

where ε is the solvent permittivity, η is the solvent viscosity, T is the temperature, Λ_1 and Λ_p is the thermal conductivities of the solvent and the particle, and ζ is the zeta potential of the particle, respectively. In bulk water, $\tau = \frac{\partial \ln \varepsilon}{\partial \ln T}$ is equal to -1.4 at room temperature, which indicates that the suspended particles are thermophobic. However, for charged particles, polarized water molecules can be confined in the electric double layer and enable abnormal permittivity, which is smaller than that of bulk water and leads to a positive τ value (Fig. 5a). Therefore, suspended charged particles have a negative D_T , which will be attracted and trapped at the heating spot. By exploiting Au nanodisk arrays as the heating substrate, plasmonic hotspots can be created selectively over large areas, and charged polystyrene beads can be dynamically transported (Fig. 5b). It is worth noting that plasmon-enhanced optical

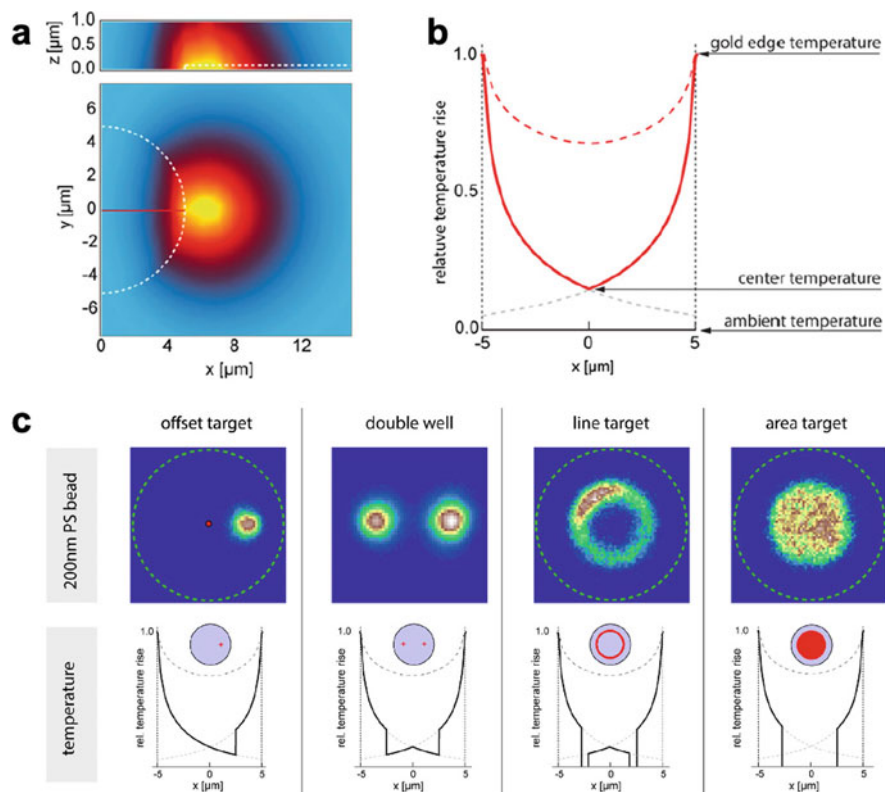


Fig. 4 Opto-thermophoretic trapping of objects with $S_T > 0$. (a) Simulated temperature profile with a focused laser beam illuminating at the rim of a gold structure. The white dash line indicates the boundary between the gold thin film and the glass. (b) Calculated relative temperature rise profile. The red dash line corresponds to the steady-state profile when the whole gold structure is heated. The solid line depicts the scaled temperature rise profile when the focused laser beam is controlled by a feedback program. The grey dash line extends the solid red line to indicate the profile without position feedback, i.e., only one spot is heated. (c) Different thermophoretic trapping potentials generated by different feedback rules. The simulated temperature fields were modelled by finite element method (COMSOL Multiphysics). (Adapted with permission from Ref. [29]. Copyright 2015 American Chemical Society)

force is excluded here since the calculated optical force is only 4 fN for a 500 nm PS particle with the same laser power, which is insufficient to trap the particle. Opto-thermophoretic tweezers are also applicable to biological objects due to the existence of phospholipid bilayers and the resultant negative surface charge (Fig. 5c) [46, 57]. Parallel manipulation of yeast cells has been achieved by exploiting a digital micromirror device (DMD) (Fig. 5d). Recently, Peng et al. studied opto-thermophoretic trapping of colloidal particles in different non-ionic liquids and reveal that the driving forces of opto-thermophoretic tweezers stem from a layered structure of solvent molecules at the particle-solvent interface. The trapping stability

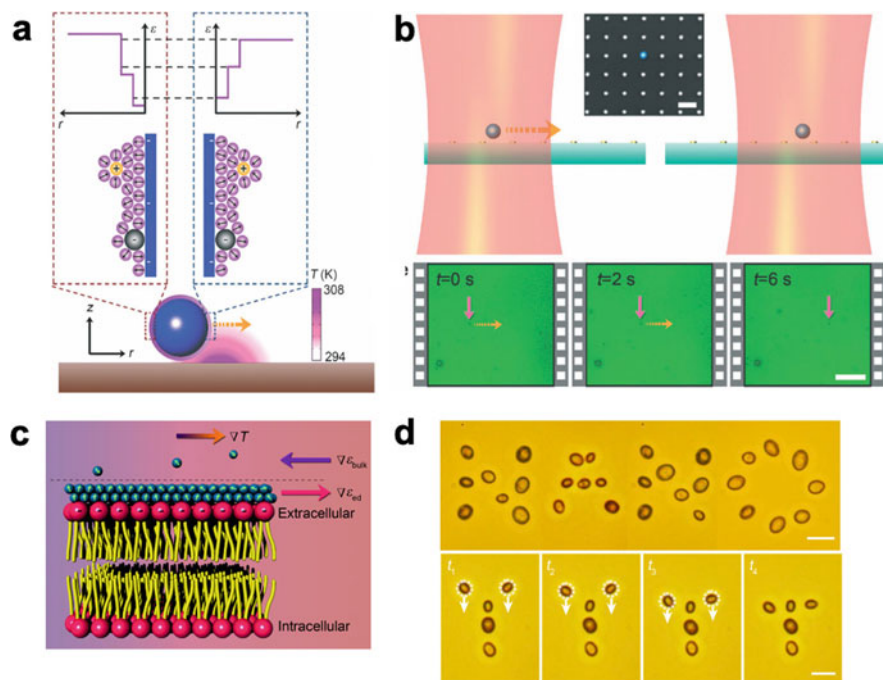


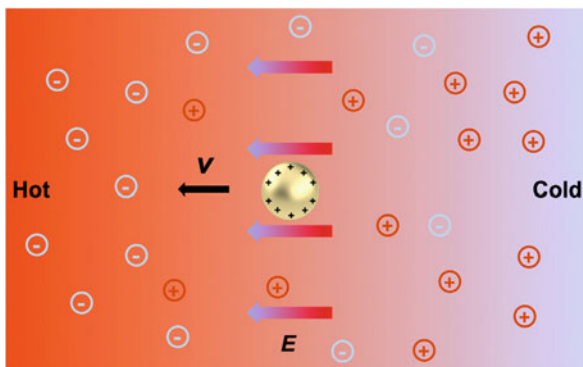
Fig. 5 Opto-thermophoretic trapping of objects with $S_T < 0$. (a) Schematic of the working principle of entropy-driven opto-thermophoretic tweezers. The purple balls correspond to the water molecules with their dipole orientations. The charged balls indicate anions and cations, respectively. (b) Schematic and optical images show light-directed thermophoretic transport of a single 500 nm polystyrene (PS) bead over Au nanodisk arrays. Scale bar: 10 μm . (Adapted with permission from Ref. [55]. Copyright 2017 The Royal Society of Chemistry). (c) Schematic shows the change of the permittivity in the electric double layer on a cell membrane under a temperature gradient field. (d) Parallel thermophoretic manipulation of yeast cells in “NANO” patterns (top) and “Y” to “T” transformation (bottom). Scale bar: 10 μm . (Adapted with permission from Ref. [46]. Copyright 2017 American Chemical Society)

of particles can be enhanced by designing the particle hydrophilicity, particle surface charge, solvent type, and ionic strength on the layered interfacial structures [58].

4 Opto-Thermoelectric Manipulation

Plasmon-enhanced thermophoresis can not only be directly exploited for particle manipulation but also enables the controlled migration of cations and anions, leading to the formation of thermoelectric fields in solutions. By engineering the plasmonic nanostructures and electrolyte composition, the opto-thermo-electro-mechanical coupling can be utilized to achieve opto-thermoelectric trapping and tweezing with low operational optical power, simple optical setup, and applicability to a wide range of polymers, metals, semiconductors, and dielectric nanostructures

Fig. 6 Schematic of liquid thermoelectricity. Cations (red circles with “+” symbols) and anions (blue circles with “-” symbols) have thermophoretic motions under a temperature gradient. The resultant thermoelectric field E induces directed migration of suspended charged particles (golden spheres with “+” symbols)



with different sizes and shapes. Compared to the conventional one-dimensional heating approach [20], exploiting plasmonic nanostructures can lead to radially shaped opto-thermoelectric fields, enabling particle manipulation at single-particle resolution.

4.1 Mechanism

When a localized temperature gradient field is formed in a solution, cations and anions drift towards either the hot or the cold region with different velocities based on their different S_T Eq. (4). As the ionic redistribution reaches a steady state, an electric field is built along the temperature gradient, driving suspended charged particles drifting directionally (Fig. 6). The underlying principle of the particle migration in aqueous environments is termed liquid thermoelectricity or the electrolyte Seebeck effect. Generally, the thermoelectric field can be given by [59, 60]

$$\mathbf{E}_{\text{TE}} = \frac{k_B T \nabla T}{e} \frac{\sum_i Z_i n_i S_{Ti}}{\sum_i Z_i^2 n_i} \quad (7)$$

where i indicates the ionic species, k_B is the Boltzmann constant, T is the environmental temperature, e is the elemental charge, and Z_i (± 1 for positive and negative monovalent ions), n_i , as well as S_{Ti} represent the charge number, the concentration, and the Soret coefficient of i species, respectively. Moreover, the thermophoretic mobility D_T of charged particles under the thermoelectric field is obtained via [59, 61]

$$D_T = \frac{\varepsilon \zeta^2}{3\eta T} - \frac{\varepsilon \zeta}{\eta} S \quad (8)$$

where ε and η are the permittivity and viscosity of the solution respectively, ζ is the surface potential of the particle, and S is the Seebeck coefficient that can be expressed as $S = E_{TE} / \nabla T$. It should be noted that the first term is always positive, which is related to the thermo-osmotic flow [62, 63]; while the second term can either be positive or negative, depending on the thermoelectric field and the surface charge of suspended particles. Therefore, according to Eq. (3), charged objects can move toward the hot/cold regions due to the liquid thermoelectricity, which can be tuned as a function of the electrolyte composition [64], ionic strength [49], temperature [65, 66], particle-solvent interface [50], colloidal size [67], and particle concentration [68, 69].

4.2 Techniques and Applications

Opto-thermoelectric effect has been proposed to achieve directional transportation of colloidal particles [64], micelles [70], DNA [60], and so forth [56, 71, 72]. Localized plasmonic heating is usually exploited to build inward/outward thermoelectric fields in the vicinity of the illuminated plasmonic nanostructures. Since the direction of the thermoelectric field is mainly determined by the electrolyte solution, opto-thermoelectric trapping is limited to either positively or negatively charged particles. Recently, Lin et al. overcame this challenge and developed opto-thermoelectric tweezers by exploiting cetyltrimethylammonium chloride (CTAC) solutions to manipulate various colloidal particles with different sizes, shapes and materials regardless of their original surface charge properties [28]. When colloidal particles are suspended in CTAC solutions, the CTA^+ molecules can not only self-assemble into positive micellar ions but also modify all particles with positive surface charges (Fig. 7a). As the laser beam illuminates on the plasmonic nanostructures (AuNIs), the difference in the Soret coefficients of positive micellar ions and negative Cl^- ions ($S_T(\text{micelle}) \gg S_T(Cl^-)$) leads to the spatial charge separation and a resultant thermoelectric field pointing toward the laser beam (Fig. 7b). Therefore, positively charged colloidal particles are attracted and stably trapped at the laser-illuminated region [73, 74]. Since AuNIs is quasi-continuous, opto-thermoelectric manipulation of colloidal particles is achieved by moving the heating laser or the sample stage. Parallel manipulation of metallic nanoparticles was further realized with a DMD that can generate multiple laser beams, i.e., simultaneously creating several plasmonic heating spots (Fig. 7c). When the AuNIs are implanted to the tapered optical fiber, the nanoparticles can be trapped at the fiber tip and transported to targeted objects in a 3D manner (Fig. 7d) [75].

To overcome the optical diffraction limit for higher spatial resolution of opto-thermoelectric manipulation, Liu et al. applied Au nanoantennas to trap nanoparticles at subwavelength resolution [39]. Since the thermoplasmonic response of nanoantennas depends on the polarization of incident laser beam relative to the long axis of nanoantennas, the intensity of thermoelectric fields and resultant trapping stiffness can be tuned by the polarization of the laser beam. Accordingly,

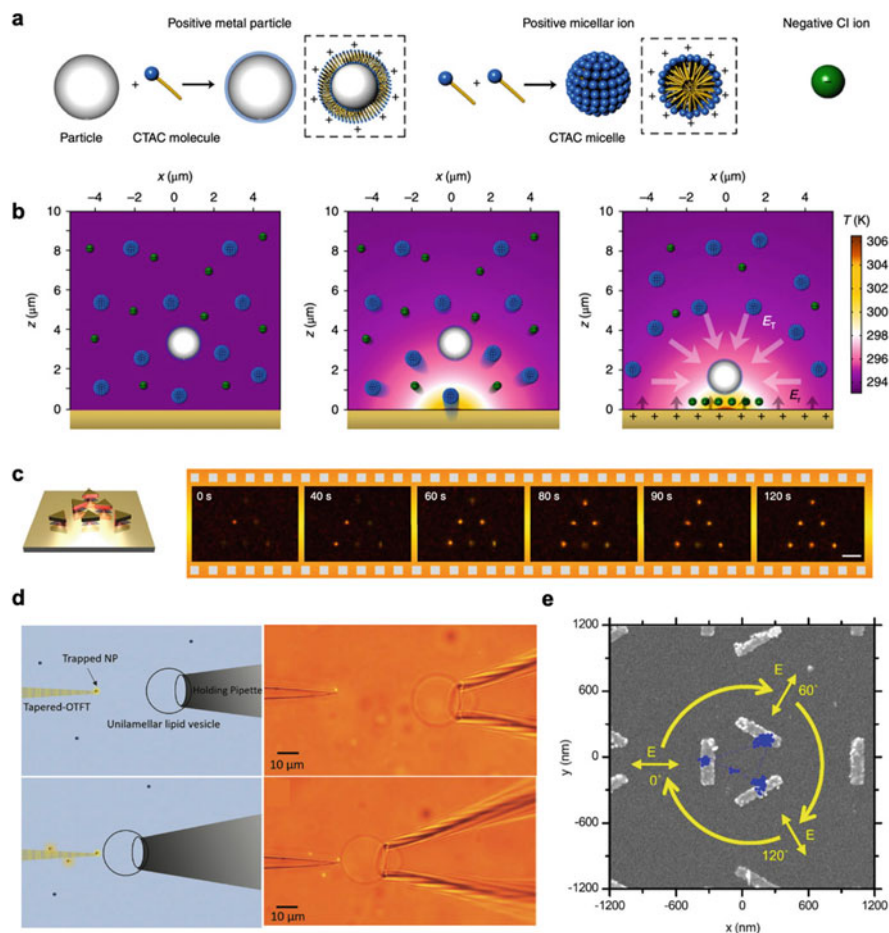


Fig. 7 Opto-thermoelectric trapping and manipulation. (a) Schematic shows the surface modification process of suspended particles by CTAC molecules and the formation of positively charged CTAC micelles through self-assembly. (b) Schematic demonstrates the formation of localized thermoelectric fields in the vicinity of a laser-induced plasmonic hotspot. (c) Schematic and dark-field optical images show an array made of anisotropic Au nanotriangles. Scale bar: 5 μm . (Adapted with permission from Ref. [28]. Copyright 2018 Springer Nature). (d) Schematics and optical images demonstrate three-dimensional nanoparticle delivery through fiber-based opto-thermoelectric trapping. (Adapted with permission from Ref. [75]. Copyright 2019 De Gruyter). (e) Opto-thermoelectric manipulation of nanoparticles based on plasmonic nanoantennas. Particles are circularly transported among different nanoantennas by changing the light polarization. (Adapted with permission from Ref. [39]. Copyright 2018 American Chemical Society)

circular transportation among three Au nanoantennas was achieved by altering the polarization angle of the laser beam (Fig. 7e).

Moreover, the CTAC molecules can serve as depletants to induce depletion forces for opto-thermoelectric assembly [76–80]. Specifically, when multiple particles

are trapped at the hotspot closely, CTAC micelles escape from interparticle gaps, creating concentration gradients and exerting an osmotic pressure on the particles to bond the particles. Different nanostructures, including chiral metamolecules [76] and 3D colloidal structures [78], are precisely fabricated in a bottom-up fashion and can be further immobilized by photocurable hydrogels [79]. More details can be found in other relevant reviews [30, 81–84].

5 Thermo-plasmonic Convection-Assisted Manipulation

Plasmonic tweezers have been developed for over a decade as an evolutionary optical manipulation technique because of their sub-diffraction-limited resolution [10–12]. However, since the near-field optical gradient force only takes effect within a nanoscale working distance, it is challenging for plasmonic tweezers to effectively trap suspended particles in solution with low particle concentrations (e.g. 2×10^7 particles·ml⁻¹). Recently, thermo-plasmonic convection generated by plasmonic nanostructures has been exploited to achieve fast transport of particles towards plasmonic hotspots, which significantly improves the trapping efficiency of plasmonic trapping.

5.1 Mechanism

Thermo-plasmonic convection describes a type of natural convection induced by local heated fluid. Specifically, when a thermal gradient is built around a plasmonic nanostructure via laser irradiation, the fluid density surrounding the heated structure decreases as the fluid temperature increases, leading to upward motion because of buoyancy. Subsequently, owing to the fluidic continuity, the fluid neighboring the local heated fluid flows towards the hotspot, being heated and moving upwardly again. Thus, a convective flow is generated in the vicinity of the laser-illuminated plasmonic nanostructure (Fig. 8a and 8b), which can be exploited for rapid particle delivery.

Donner et al. conducted a comprehensive study to analyze the plasmon-enhanced natural convection theoretically and numerically [85]. It has been validated that for thermoplasmonics occurring at the macro- or nano-scale in water-like media (i.e., the fluidic flow possessing small Reynolds number and Rayleigh number), the temperature distribution of fluid in the vicinity of heated nanostructures can be simplified as [85]

$$\partial_t T(\mathbf{r}, t) - \alpha \nabla^2 T(\mathbf{r}, t) = 0 \quad (9)$$

where $T(\mathbf{r}, t)$ represents the temperature distribution of the fluid, and α is the fluid diffusivity. Meanwhile, the Navier-Stoke equation describing the fluid velocity [86] is further reduced to [85]

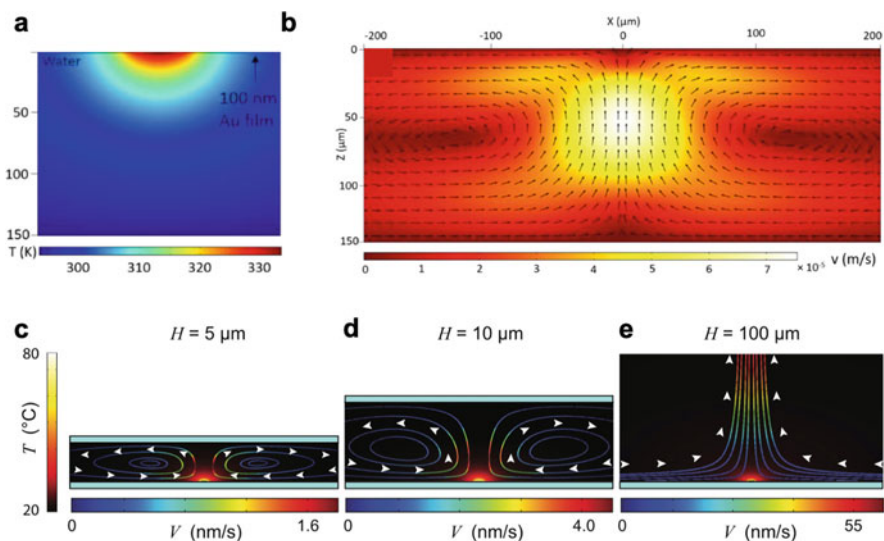


Fig. 8 Formation of thermo-plasmonic convection based on microscale plasmonic heating. (a) Simulated temperature distribution around a single nanoaperture on a 100 nm Au film that is irradiated over a circular area with diameter $\sim 60 \mu\text{m}$ and (b) corresponding simulated convective flow velocity distribution. The temperature field was obtained from the FDTD-simulated electromagnetic field, and the fluid velocity map was achieved by computational fluid dynamics (CFD) simulations. (Adapted with permission from Ref. [27]. Copyright 2019 American Chemical Society). (c)–(e) Simulated velocity distribution with various chamber heights H . The plasmonic nanostructure is a gold disk of radius $r = 250 \text{ nm}$ and $T = 80 \text{ }^\circ\text{C}$. The velocity field was obtained by using finite element method (COMSOL Multiphysics). (Adapted with permission from Ref. [85]. Copyright 2011 American Chemical Society)

$$\partial_t \mathbf{v}(\mathbf{r}, t) - \nu \nabla^2 \mathbf{v}(\mathbf{r}, t) = \mathbf{f}_t(T(\mathbf{r}, t)) \quad (10)$$

where $\mathbf{v}(\mathbf{r}, t)$ is the fluid velocity, ν is the fluid viscosity and $\mathbf{f}_t(T(\mathbf{r}, t))$ represents the force per unit mass due to temperature gradient that is commonly given as $\mathbf{f}_t(T) = \beta g(T(\mathbf{r}, t) - T_\infty) \mathbf{u}_z$ with g being the gravitational acceleration, β being the dilatation coefficient of water and \mathbf{u}_z demonstrating the unit vector along the z -direction.

It's worth noting that the fluid velocity generated by single plasmonic nanostructures with a typical size below 200 nm is estimated to be less than 10 nm/s even if the fluid temperature is close to the boiling point, which can hardly be exploited for effective particle delivery owing to the existence of Brownian motions or thermophoresis. Thus, thermo-plasmonic convection-assisted trapping usually requires micro-sized plasmonic nanostructures to be illuminated. Moreover, the shape and velocity of fluid can also be tuned by the height of the chamber (Fig. 8c-8e).

5.2 Techniques and Applications

Since thermo-plasmonic convection induced by plasmon-enhanced thermal effect often works under large-area illumination, it can be utilized for quick delivery and local concentration of targeted objects in solution over large volumes, especially for ultra-low concentration conditions. Recently, Kotnala et al. adopted thermo-plasmonic convection to facilitate plasmonic trapping and sensing of particles within an ultralow concentration ($< 2 \times 10^7$ particles·ml⁻¹) [27]. As shown in Fig. 9a, a multimode optical fiber coupled with a 532 nm laser beam illuminates a Au nanoaperture to generate the thermo-plasmonic convection with high velocity ($\sim 10\text{--}20 \mu\text{m}\cdot\text{s}^{-1}$). Dispersed particles were transported toward the plasmonic nanoaperture via the convective flow and got trapped with a 1020 nm laser beam (Fig. 9b). Compared with diffusion-limited plasmonic trapping, thermo-plasmonic convection-assisted trapping can reduce the trapping time by five-fold and 15-fold for particle concentrations of 2×10^8 and 2×10^7 particles·ml⁻¹, respectively (Fig. 9c). The particle delivery time can further be decreased by increasing the flow velocity. However, the convective velocity should be determined by the trapping laser intensity so that the drag force does not dominate over the near-field optical gradient force, which leads to the failure of single-particle trapping at the nanoaperture (Fig. 9d).

As the convective flow can have a vertical velocity component perpendicular to the substrate, it can also be utilized to assist 3D optical manipulation of colloidal particles and biological objects [87–89]. Cong et al. exploited a gold-coated micro-well array for efficient optical trapping and single-cell analysis [89]. In this work, the laser heating not only triggers thermo-plasmonic convective flow to facilitate the upward movement of a single living cancer cell, but also offers a constant temperature environment for recombinase polymerase amplification reaction of nucleic acid markers. In addition, thermo-plasmonic convective flow can also be generated by mobile plasmonic nanoparticles dispersed in solution, which assists the concentration and patterning of nanoparticles for photothermal convection lithography on generic substrates [90].

6 Marangoni Convection-Assisted Manipulation

In addition to thermo-plasmonic convection, Marangoni convection is another approach to facilitating long-range particle delivery for effective plasmonic trapping of nano-objects. Different from thermo-plasmonic convection induced by density gradient of a heated solution, Marangoni convection relies on the gradient of surface tension at the interface between two fluids, which usually have higher flow velocity. Moreover, the Marangoni convection induced by plasmonic heating can also be directly used for particle trapping and manipulation.

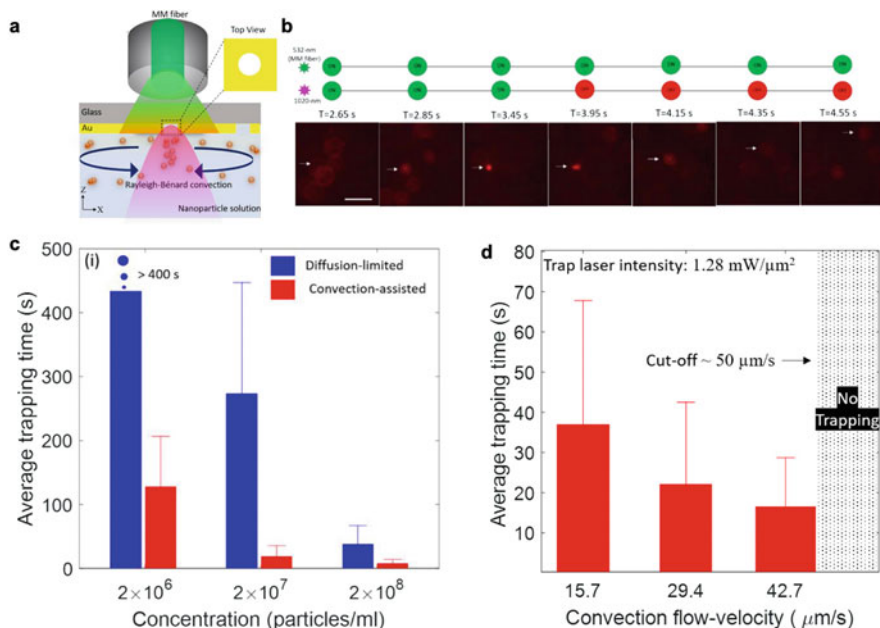


Fig. 9 Thermo-plasmonic convection-assisted trapping and tweezing. (a) Schematic shows that a multimode fiber illuminates a large area of AuNIs with nanoapertures for the formation of thermo-plasmonic convection. (b) Dark-field images demonstrate thermo-plasmonic convection-assisted trapping and release of a single 200-nm fluorescent polystyrene nanoparticle within a circular nanoaperture surrounded by AuNIs. 532-nm laser is used to generate the convective flow while 1020-nm laser is for the plasmonic optical trapping. Scale bar is 25 μm . (c) Comparison of average trapping time of diffusion-limited and convection-assisted trapping at three different particle concentrations. (d) Diagram represents the impact of convection-flow velocity on the average particle-trapping time. (Adapted with permission from Ref. [27]. Copyright 2019 American Chemical Society)

6.1 Mechanism

Marangoni convection describes mass transfer along with an interface between two fluids due to a gradient of the surface tension, which can be attributed to the concentration gradient or temperature gradient, where the latter type is also termed as thermocapillary convection [91]. In brief, when a laser beam irradiates the plasmonic nanostructures with a relatively high power intensity, abundant heat is generated at the hotspot, leading to water evaporation and resultant vapor bubble nucleation at the liquid-substrate interface [92, 93]. As the surface tension is inversely related to the temperature, a gradient of surface tension exists at the liquid-vapor interface due to the temperature gradient (Fig. 10a). Thus, a convective flow is generated around the microbubble because of the fluid's continuity (Fig. 10b). The temperature distribution and flow velocity pattern are different if the relative size between the diameter of the bubble and the chamber thickness changes (Fig.

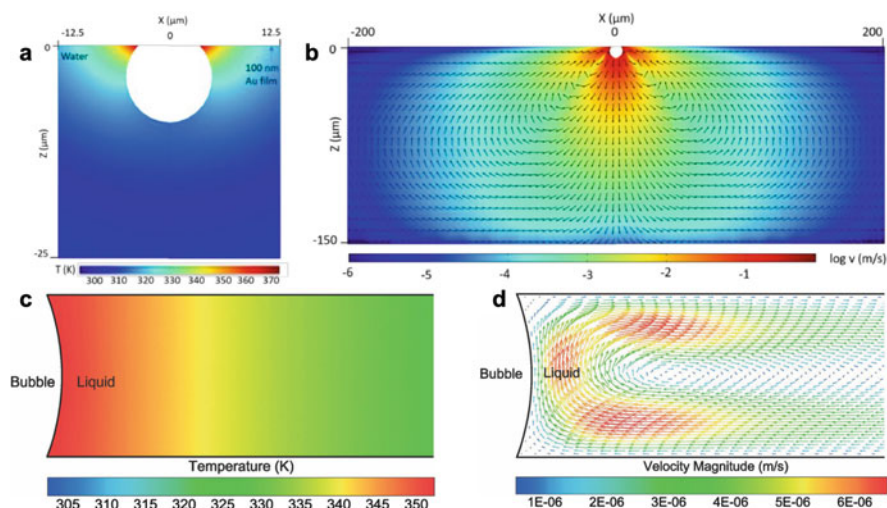


Fig. 10 Formation of Marangoni convection based on plasmonic heating. (a) Simulated temperature distribution and (b) simulated flow velocity around a 10 μm bubble generated upon laser irradiation on AuNIs. The temperature field was obtained from the FDTD-simulated electromagnetic field, and the fluid velocity map was achieved by CFD simulations. (Adapted with permission from Ref. [27]. Copyright 2019 American Chemical Society). (c) Simulated temperature distribution and (d) simulated flow velocity of a 60 μm vapor bubble generated in a chamber with height being 70 μm . The temperature distribution and fluid velocity map were achieved by CFD simulations (ANSYS Fluent). (Adapted with permission from Ref. [95]. Copyright 2014 Royal Society of Chemistry)

10c, d). Besides, it's worth noting that the plasmonic heating-induced Marangoni convection can also occur at the planar air-liquid interface via floating plasmonic nanoparticles [94].

6.2 Techniques and Applications

Similar to thermo-plasmonic convection, Marangoni convection has also been exploited for rapid delivery of nanoparticles toward the plasmonic hotspot for efficient plasmonic trapping (Fig. 11a). Kotnala et al. employed two laser beams to actuate Marangoni convection and plasmonic trapping, respectively, which significantly enhanced the trapping efficiency of conventional nanoaperture-based plasmonic tweezers [27]. Specifically, a 532 nm laser is used for plasmonic heating and bubble generation, while a 1020 nm laser works for plasmonic trapping. It's worth noting that the 532 nm laser beam should be turned off after the bubble emerges for 1–2 s in case that the nanoparticles are directly printed on the substrate by the strong Marangoni convective flow [96]. Due to the long-range delivery of nanoparticles via Marangoni convection, the average particle-trapping time can

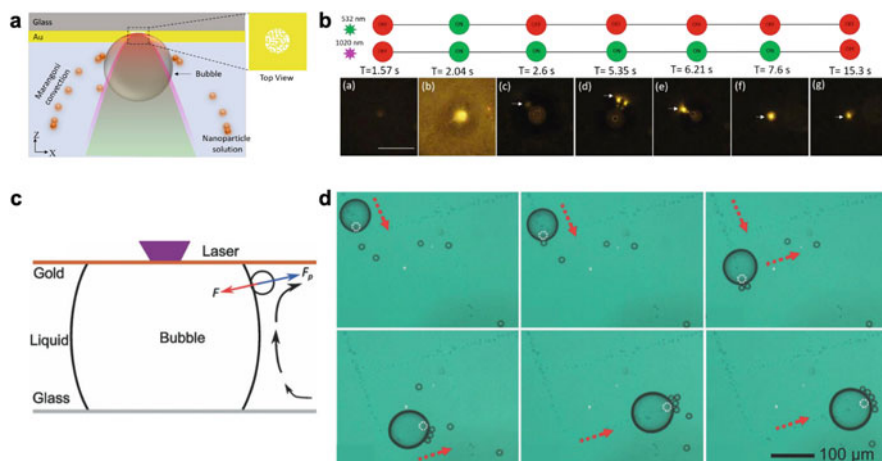


Fig. 11 Marangoni convection-assisted trapping and tweezing. (a) Schematic shows suspended nanoparticles being delivered to the nanoaperture via bubble-based Marangoni convection and get trapped by plasmonic tweezers. (b) Time-evolved dark-field images demonstrates bubble-assisted trapping and release of a single 200 nm fluorescent PS nanoparticle. 532 nm laser is exploited for the bubble generation while 1020 nm laser is specifically for plasmonic trapping. Scale bar: 10 μm . (Adapted with permission from Ref. [27]. Copyright 2019 American Chemical Society). (c) Schematic shows that particle get stabilized on the bubble surface via the balance between the pressure force (F_p) and the surface tension force (F). (d) Time-lapse optical images show the particle collection process via the movement of the bubble. (Adapted with permission from Ref. [95]. Copyright 2014 The Royal Society of Chemistry)

be reduced by 40 ~ 80 folds compared with that of diffusion-limited trapping. Moreover, since the position of the gas bubble can follow the movement of the heating laser on continuous plasmonic nanostructures [97], suspended particles can be patterned on the plasmonic substrate continuously for nanoparticle writing, namely bubble printing [98–102].

In addition to particle concentration, Marangoni convective flow can also facilitate precise trapping and manipulation of colloidal particles and biological cells [95, 103–105]. Zhao et al. developed single-particle trapping and manipulation based on the optothermal bubble [95]. When the bubble is generated upon laser irradiation on a gold thin film, neighboring suspended particles are attracted towards the bubble due to the Marangoni convection. Once the particle is attached to the bubble surface, it will be trapped stably through the balance among the surface tension force, pressure force and drag force (Fig. 11c). Particle collection and transportation were further demonstrated via directly manipulating the bubbles as a shuttle (Fig. 11d).

7 Electrothermoplasmonic Flow-Assisted Manipulation

When a laser beam irradiates a plasmonic nanostructure, in addition to thermophoresis and natural convection take effect, a gradient of permittivity and electrical conductivity can also be obtained in the vicinity of the nanostructure due to the local temperature gradient. Once an additional a.c. electric field is applied, electric body force is triggered and the force can be given by $f = \rho_f \mathbf{E}_l - \frac{1}{2} |\mathbf{E}_l|^2 \nabla \epsilon_m$ for an electrically linear incompressible fluid [106, 107], where ρ_f is the volume density of induced free charges, \mathbf{E}_l represents the local electric field, while $\nabla \epsilon_m$ is the gradient of the fluid's permittivity. The electric body force can trigger a new type of fluidic flow termed as ETP flow, which can also be exploited for trapping and tweezing of objects at single-particle resolution.

7.1 Mechanism

ETP flow describes a new type of opto-microfluidic flow for particle and molecule manipulation, which mainly stems from the electric body force in the fluids with assistance from plasmon-enhanced thermal effects [33, 40, 43]. Specifically, when a laser beam irradiates on plasmonic nanostructures, the plasmonic heating creates a local gradient of fluid's permittivity and electrical conductivity. Through applying an external a.c. electric field, an electrical body force per unit volume in the locally heated fluid is significantly enhanced. The resultant motion of the fluid will then exert a drag force on suspended particles, which can transport suspended particles toward the plasmonic hotspot (Fig. 12a). Although the plasmonic optothermal effect can intrinsically lead to buoyancy force for the generation of thermo-plasmonic convection [108], the electric body force plays an essential role in the ETP flow, which is given as [33]

$$\langle F_{\text{ETH}} \rangle = \frac{1}{2} \epsilon \left[\frac{(\alpha - \gamma)}{1 + (\omega\tau)^2} (\nabla T \cdot \mathbf{E}) \mathbf{E} - \frac{1}{2} \alpha |\mathbf{E}|^2 \nabla T \right] \quad (11)$$

where $\alpha = (1/\epsilon)(\partial\epsilon/\partial T)$, $\gamma = (1/\sigma)(\partial\sigma/\partial T)$, $\tau = \epsilon/\sigma$, ϵ and σ are the fluid's permittivity and electrical conductivity, respectively, and ω is the frequency of the a.c. electric field. Accordingly, the ETP flow can not only be tuned by the plasmonic heating but also the frequency and amplitude of the a.c. electric field. Numerical simulations further confirm that the ETP flow scales linearly with applied laser power but scales quadratically with the a.c. electric field. The fluid radial velocity of the ETP flow is validated to be two orders of magnitude larger than that of thermo-plasmonic convection, implying that the ETP flow is dominant here for on-demand long-range and rapid delivery of single nano-objects.

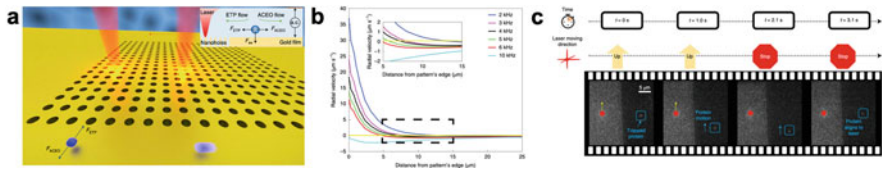


Fig. 12 Demonstration of electrothermoplasmonic flow-assisted trapping and tweezers. (a) Schematic shows the working mechanism of opto-thermo-electrohydrodynamic tweezers. (b) Simulated radial velocity under different a.c. frequencies along the direction perpendicular to the length of the nanohole array. The inset shows the zoom-in black dash box. The position of the stagnation zone can be tuned by the a.c. frequency. (c) Optical images show the dynamic manipulation of a single bovine serum albumin (BSA) protein molecule. (Adapted with permission from Ref. [43]. Copyright 2020 Springer Nature)

7.2 Techniques and Applications

ETP flow can transport suspended nano-objects towards the plasmonic nanoantenna at the fluid's velocity $\sim 10\text{--}15 \mu\text{m s}^{-1}$ [33], which can then be trapped at the nanostructure surface via the optical gradient force [11]. Once the targeted object is trapped at the surface, there have three options for subsequent manipulation: (1) laser on but electric field off: maintain the object being trapped via optical gradient force with minimum energy consumption; (2) both laser and electric field off: release the object; (3) laser on but switch a.c. field to d.c. field temporarily: immobilize the object on the nanoantenna. The immobilization mechanism, in brief, is that the d.c. electric field triggers the mobile ions in the electrical double layer of the trapped object moving and then pushing the particle closer to the surface until the short-range attractive forces take effect to bind the object onto the nanoantenna surface.

Moreover, when the plasmonic nanoantenna is replaced with the nanohole array, the applied a.c. electric field is distorted by the nanoholes, resulting in both normal and tangential a.c. field components. The tangential component drives the diffuse charges in the electrical double layer at the interface between the nanohole array and the fluid, triggering localized a.c. electro-osmotic flow that has an opposite direction against the ETP flow (Fig. 12a) [109]. Recently, Ndukaife and co-workers have synergized the ETP flow and a.c. electro-osmotic flow to develop opto-thermo-electrohydrodynamic tweezers for the trapping and manipulation of sub-10 nm objects [43]. Since the strength of the a.c. electro-osmotic flow is increased faster than that the ETP flow at a lower a.c. frequency, the trapping distance of targeted objects relative to the laser position, i.e., the stagnation zone, can be adjusted by tuning the a.c. frequency (Fig. 12b). Thus, the object can be trapped several micrometers away from the laser focus, alleviating potential optical and thermal damage for safe biological sensing or single-molecule analysis. Furthermore, the trapped object can also be dynamically manipulated by translating the laser beam, like other optical-based tweezers (Fig. 12c).

8 Conclusion

By taking advantage of plasmonic optothermal effects, researchers have developed various heat-mediated optical tweezing techniques in recent years, enabling a versatile platform for precise manipulation of micro- and nano-objects. Thermophoretic tweezers trap the objects in the solution by exploiting the directed thermal migration of suspended objects under a laser heating-generated temperature gradient. Optothermal tweezers present a more general approach to manipulate all kinds of colloids through the coordination of liquid thermoelectricity and surfactant modification of objects. To improve the trapping efficiency of plasmonic tweezers in dilute solution, various convection flows have been exploited to rapidly deliver particles toward the plasmonic hotspot. First, thermo-plasmonic convection can transport suspended particles mildly but usually requires large-area illumination for actuation, somehow sacrificing manipulation precision. Second, Marangoni convection enables more rapid delivery, but the target object might be directly printed on the substrate. In addition, the high temperature around the vapor bubble could cause damages to biological target objects. Last, ETP flow is newly developed in the last 5 years, which can transport suspended particles toward the trapping site rapidly and safely. However, an external electric field is required for ETP, which perplexes the experimental setup.

We expect the further developments of plasmon-enhanced optothermal manipulation in multiple directions to enhance the functions for the broader applications. Firstly, the capability of plasmon-enhanced optothermal manipulation in 3D will be improved. Due to the difficulty of optothermally constructing stable trapping potentials along the direction perpendicular to the plasmonic substrates, most single-particle manipulations have been limited to the in-plane directions along the substrates. Some methods have already been proposed to trap and manipulate particles in 3D via plasmon-induced optothermal fields. For instance, the plasmonic nanostructures were transferred onto optical fibers to realize 3D optothermal manipulation by simply controlling the position of the fiber tips [75]. Secondly it has been challenging to simultaneously achieve both high throughput and high precision for the plasmon-enhanced optothermal manipulation. To address the challenge, a spatial light modulator or digital micromirror device can be used to generate multiple laser beams for parallel manipulation of multiple particles [28]. Alternatively, the plasmonic nanostructures can be further elaborated to achieve multiple trapping potentials. Lastly, plasmon-enhanced optothermal manipulation has been mainly applied for particle assembly [76, 78] and *in vitro* sensing [39]. We envision that, with the further progress in the rational design of plasmonic nanostructures and heating source, in combination with additional external fields, the plasmon-enhanced optothermal trapping and tweezing will find more applications in materials science, biology, colloidal sciences, nanorobotics, and nanomanufacturing [110–112].

Acknowledgments The authors acknowledge the financial supports of the National Science Foundation (NSF-CMMI-1761743; NSF-ECCS-2001650), the National Aeronautics and Space Administration (80NSSC17K0520), and the National Institute of General Medical Sciences of the National Institutes of Health (DP2GM128446).

References

1. Ashkin, A., Dziedzic, J. M., Bjorkholm, J. E., & Chu, S. (1986). Observation of a single-beam gradient force optical trap for dielectric particles. *Optics Letters*, *11*, 288–290.
2. Jauffred, L., Richardson, A. C., & Oddershede, L. B. (2008). Three-dimensional optical control of individual quantum dots. *Nano Letters*, *8*, 3376–3380. <https://doi.org/10.1021/nl801962f>
3. Ashkin, A., Dziedzic, J. M., & Yamane, T. (1987). Optical trapping and manipulation of single cells using infrared laser beams. *Nature*, *330*, 769–771. <https://doi.org/10.1038/330769a0>
4. Ashkin, A., & Dziedzic, J. M. (1987). Optical trapping and manipulation of viruses and bacteria. *Science*, *235*, 1517. <https://doi.org/10.1126/science.3547653>
5. Urban, A. S., et al. (2014). Optical trapping and manipulation of Plasmonic nanoparticles: Fundamentals, applications, and perspectives. *Nanoscale*, *6*, 4458–4474. <https://doi.org/10.1039/C3NR06617G>
6. Wright, W. H., Sonek, G. J., & Berns, M. W. (1993). Radiation trapping forces on microspheres with optical tweezers. *Applied Physics Letters*, *63*, 715–717. <https://doi.org/10.1063/1.109937>
7. Preece, D., et al. (2011). Optical tweezers: Wideband microrheology. *Journal of Optics*, *13*, 044022.
8. He, H., Heckenberg, N., & Rubinsztein-Dunlop, H. (1995). Optical particle trapping with higher-order doughnut beams produced using high efficiency computer generated holograms. *Journal of Modern Optics*, *42*, 217–223.
9. Grigorenko, A. N., Roberts, N. W., Dickinson, M. R., & Zhang, Y. (2008). Nanometric optical tweezers based on nanostructured substrates. *Nature Photonics*, *2*, 365–370. <https://doi.org/10.1038/nphoton.2008.78>
10. Juan, M. L., Righini, M., & Quidant, R. (2011). Plasmon nano-optical tweezers. *Nature Photonics*, *5*, 349–356. <https://doi.org/10.1038/nphoton.2011.56>
11. Wang, K., Schonbrun, E., Steinvurzel, P., & Crozier, K. B. (2011). Trapping and rotating nanoparticles using a plasmonic nano-tweezer with an integrated heat sink. *Nature Communications*, *2*, 469. <https://doi.org/10.1038/ncomms1480>
12. Yoo, D., et al. (2018). Low-power optical trapping of nanoparticles and proteins with resonant coaxial nanoaperture using 10 nm gap. *Nano Letters*, *18*, 3637–3642.
13. Righini, M., Zelenina, A. S., Girard, C., & Quidant, R. (2007). Parallel and selective trapping in a patterned Plasmonic landscape. *Nature Physics*, *3*, 477–480.
14. Roxworthy, B. J., et al. (2012). Application of plasmonic bowtie Nanoantenna arrays for optical trapping, stacking, and sorting. *Nano Letters*, *12*, 796–801.
15. Berthelot, J., et al. (2014). Three-dimensional manipulation with scanning near-field optical Nanotweezers. *Nature Nanotechnology*, *9*, 295–299.
16. Kotsifaki, D. G., Kandyła, M., & Lagoudakis, P. G. (2015). Near-field enhanced optical tweezers utilizing femtosecond-laser nanostructured substrates. *Applied Physics Letters*, *107*, 211111.
17. Mundoor, H., et al. (2018). Tuning and switching a Plasmonic quantum dot “Sandwich” in a Nematic line defect. *ACS Nano*, *12*, 2580–2590.
18. Huft, P. R., Kolbow, J. D., Thweatt, J. T., & Lindquist, N. C. (2017). Holographic Plasmonic Nanotweezers for dynamic trapping and manipulation. *Nano Letters*, *17*, 7920–7925.

19. Kotsifaki, D. G., Kandyla, M., & Lagoudakis, P. G. (2016). Plasmon enhanced optical tweezers with gold-coated black silicon. *Scientific Reports*, 6, 26275. <https://doi.org/10.1038/srep26275>
20. Vigolo, D., Rusconi, R., Stone, H. A., & Piazza, R. (2010). Thermophoresis: Microfluidics characterization and separation. *Soft Matter*, 6, 3489–3493.
21. Kim, J.-D., & Lee, Y.-G. (2016). Graphene-based Plasmonic tweezers. *Carbon*, 103, 281–290.
22. Zhang, J., Liu, W., Zhu, Z., Yuan, X., & Qin, S. (2016). Towards nano-optical tweezers with graphene plasmons: Numerical investigation of trapping 10-nm particles with mid-infrared light. *Scientific Reports*, 6, 1–7.
23. Jiang, Q., Rogez, B., Claude, J.-B., Baffou, G., & Wenger, J. (2019). Temperature measurement in plasmonic nanoapertures used for optical trapping. *ACS Photonics*, 6, 1763–1773.
24. Jones, S., Andr n, D., Karpinski, P., & K ll, M. (2018). Photothermal heating of plasmonic nanoantennas: Influence on trapped particle dynamics and colloid distribution. *ACS Photonics*, 5, 2878–2887. <https://doi.org/10.1021/acsp Photonics.8b00231>
25. Juan, M. L., Gordon, R., Pang, Y., Eftekhari, F., & Quidant, R. (2009). Self-induced Back-action optical trapping of dielectric nanoparticles. *Nature Physics*, 5, 915–919.
26. Righini, M., et al. (2009). Nano-optical trapping of Rayleigh particles and escherichia coli bacteria with resonant optical antennas. *Nano Letters*, 9, 3387–3391.
27. Kotnala, A., Kollipara, P. S., Li, J., & Zheng, Y. (2019). Overcoming diffusion-limited trapping in Nanoaperture tweezers using opto-thermal-induced flow. *Nano Letters*, 20, 768–779.
28. Lin, L., et al. (2018). Opto-thermoelectric Nanotweezers. *Nature Photonics*, 12, 195–201. <https://doi.org/10.1038/s41566-018-0134-3>
29. Braun, M., Bregulla, A. P., G nther, K., Mertig, M., & Cichos, F. (2015). Single molecules trapped by dynamic inhomogeneous temperature fields. *Nano Letters*, 15, 5499–5505.
30. Lin, L., Hill, E. H., Peng, X., & Zheng, Y. (2018). Optothermal manipulations of colloidal particles and living cells. *Accounts of Chemical Research*, 51, 1465–1474. <https://doi.org/10.1021/acs.accounts.8b00102>
31. Chen, Z., Kollipara, P. S., Ding, H., Pughazhendi, A., & Zheng, Y. (2021). Liquid Optothermoelectrics: Fundamentals and applications. *Langmuir*, 37, 1315–1336.
32. Chen, J., et al. (2020). Thermal Optofluidics: Principles and applications. *Advanced Optical Materials*, 8, 1900829. <https://doi.org/10.1002/adom.201900829>
33. Ndukaife, J. C., et al. (2016). Long-range and rapid transport of individual nano-objects by a hybrid Electrothermoplasmonic nanotweezer. *Nature Nanotechnology*, 11, 53–59. <https://doi.org/10.1038/nnano.2015.248>
34. Jauffred, L., Samadi, A., Klingberg, H., Bendix, P. M., & Oddershede, L. B. (2019). Plasmonic heating of nanostructures. *Chemical Reviews*, 119, 8087–8130.
35. Baffou, G., Quidant, R., & Garc a de Abajo, F. J. (2010). Nanoscale control of optical heating in complex Plasmonic systems. *ACS Nano*, 4, 709–716.
36. Quinten, M. (2010). *Optical properties of nanoparticle systems: Mie and beyond*. Wiley.
37. Parsons, J., Burrows, C., Sambles, J., & Barnes, W. (2010). A comparison of techniques used to simulate the scattering of electromagnetic radiation by metallic nanostructures. *Journal of Modern Optics*, 57, 356–365.
38. Kang, Z., et al. (2015). Trapping and assembling of particles and live cells on large-scale random gold nano-Island substrates. *Scientific Reports*, 5, 9978. <https://doi.org/10.1038/srep09978>
39. Liu, Y., et al. (2018). Nanoradiator-mediated deterministic opto-thermoelectric manipulation. *ACS Nano*, 12, 10383–10392.
40. Ndukaife, J. C., et al. (2018). High-resolution large-ensemble nanoparticle trapping with multifunctional thermoplasmonic nanohole metasurface. *ACS Nano*, 12, 5376–5384. <https://doi.org/10.1021/acsnano.8b00318>

41. Lin, L., et al. (2018). Optothermoplasmonic nanolithography for on-demand patterning of 2d materials. *Advanced Functional Materials*, 28, 1803990. <https://doi.org/10.1002/adfm.201803990>
42. Sun, H., Yu, M., Wang, G., Sun, X., & Lian, J. (2012). Temperature-dependent morphology evolution and surface plasmon absorption of ultrathin Gold Island films. *The Journal of Physical Chemistry C*, 116, 9000–9008.
43. Hong, C., Yang, S., & Ndukaife, J. C. (2020). Stand-off trapping and manipulation of sub-10 nm objects and biomolecules using opto-thermo-electrohydrodynamic tweezers. *Nature Nanotechnology*, 15, 908–913. <https://doi.org/10.1038/s41565-020-0760-z>
44. Ebbesen, T. W., Lezec, H. J., Ghaemi, H., Thio, T., & Wolff, P. A. (1998). Extraordinary optical transmission through sub-wavelength hole arrays. *Nature*, 391, 667–669.
45. Popov, E., Neviere, M., Enoch, S., & Reinisch, R. (2000). Theory of light transmission through subwavelength periodic hole arrays. *Physical Review B*, 62, 16100.
46. Lin, L., et al. (2017). Thermophoretic tweezers for low-power and versatile manipulation of biological cells. *ACS Nano*, 11, 3147–3154.
47. Eslahian, K. A., Majee, A., Maskos, M., & Würger, A. (2014). Specific salt effects on thermophoresis of charged colloids. *Soft Matter*, 10, 1931–1936. <https://doi.org/10.1039/C3SM52779D>
48. Parola, A., & Piazza, R. (2004). Particle thermophoresis in liquids. *The European Physical Journal E*, 15, 255–263. <https://doi.org/10.1140/epje/i2004-10065-5>
49. Piazza, R., & Guarino, A. (2002). Soret effect in interacting micellar solutions. *Physical Review Letters*, 88, 208302. <https://doi.org/10.1103/PhysRevLett.88.208302>
50. Braibanti, M., Vigolo, D., & Piazza, R. (2008). Does Thermophoretic mobility depend on particle size? *Physical Review Letters*, 100, 108303.
51. Wiegand, S. (2004). Thermal diffusion in liquid mixtures and polymer solutions. *Journal of Physics: Condensed Matter*, 16, R357.
52. Dühr, S., Arduini, S., & Braun, D. (2004). Thermophoresis of DNA determined by microfluidic fluorescence. *The European Physical Journal E*, 15, 277–286.
53. Braun, M., & Cichos, F. (2013). Optically controlled Thermophoretic trapping of single nano-objects. *ACS Nano*, 7, 11200–11208. <https://doi.org/10.1021/nn404980k>
54. Fränzl, M., et al. (2019). Thermophoretic trap for single amyloid fibril and protein aggregation studies. *Nature Methods*, 16, 611–614.
55. Lin, L., et al. (2017). Interfacial-entropy-driven thermophoretic tweezers. *Lab on a Chip*, 17, 3061–3070.
56. Putnam, S. A., Cahill, D. G., & Wong, G. C. (2007). Temperature dependence of Thermodiffusion in aqueous suspensions of charged nanoparticles. *Langmuir*, 23, 9221–9228.
57. Hill, E. H., Li, J., Lin, L., Liu, Y., & Zheng, Y. (2018). Opto-thermophoretic attraction, trapping, and dynamic manipulation of lipid vesicles. *Langmuir*, 34, 13252–13262.
58. Peng, X., et al. (2018). Optothermophoretic manipulation of colloidal particles in nonionic liquids. *The Journal of Physical Chemistry C*, 122, 24226–24234. <https://doi.org/10.1021/acs.jpcc.8b03828>
59. Majee, A., & Würger, A. (2013). Thermocharge of a hot spot in an electrolyte solution. *Soft Matter*, 9, 2145–2153.
60. Reichl, M., Herzog, M., Götz, A., & Braun, D. (2014). Why charged molecules move across a temperature gradient: The role of Electric fields. *Physical Review Letters*, 112, 198101. <https://doi.org/10.1103/PhysRevLett.112.198101>
61. Würger, A. (2010). Thermal non-equilibrium transport in colloids. *Reports on Progress in Physics*, 73, 126601.
62. Ruckenstein, E. (1981). Can phoretic motions be treated as interfacial tension gradient driven phenomena? *Journal of Colloid and Interface Science*, 83, 77–81.
63. Bregulla, A. P., Würger, A., Günther, K., Mertig, M., & Cichos, F. (2016). Thermo-osmotic flow in thin films. *Physical Review Letters*, 116, 188303. <https://doi.org/10.1103/PhysRevLett.116.188303>

64. Würger, A. (2008). Transport in charged colloids driven by thermoelectricity. *Physical Review Letters*, *101*, 108302. <https://doi.org/10.1103/PhysRevLett.101.108302>
65. Würger, A. (2009). Temperature dependence of the soret motion in colloids. *Langmuir*, *25*, 6696–6701.
66. Sehnem, A., et al. (2015). Temperature dependence of the soret coefficient of ionic colloids. *Physical Review E*, *92*, 042311.
67. Morthomas, J., & Würger, A. (2008). Thermoelectric effect on charged colloids in the Hückel limit. *The European Physical Journal E*, *27*, 425–434.
68. Majee, A., & Würger, A. (2011). Collective Thermoelectrophoresis of charged colloids. *Physical Review E*, *83*, 061403.
69. Lüsebrink, D., & Ripoll, M. (2012). Collective thermodiffusion of colloidal suspensions. *The Journal of Chemical Physics*, *137*, 194904.
70. Vigolo, D., Buzzaccaro, S., & Piazza, R. (2010). Thermophoresis and thermoelectricity in surfactant solutions. *Langmuir*, *26*, 7792–7801. <https://doi.org/10.1021/la904588s>
71. Majee, A., & Würger, A. (2012). Charging of heated colloidal particles using the electrolyte seebeck effect. *Physical Review Letters*, *108*, 118301. <https://doi.org/10.1103/PhysRevLett.108.118301>
72. Iacopini, S., & Piazza, R. (2003). Thermophoresis in protein solutions. *Europhysics Letters (EPL)*, *63*, 247–253. <https://doi.org/10.1209/epl/i2003-00520-y>
73. Ding, H., Kollipara, P. S., Lin, L., & Zheng, Y. (2020). Atomistic modeling and rational Design of Optothermal Tweezers for targeted applications. *Nano Research*. <https://doi.org/10.1007/s12274-020-3087-z>
74. Kollipara, P. S., Lin, L., & Zheng, Y. (2019). Thermo-electro-mechanics at individual particles in complex colloidal systems. *The Journal of Physical Chemistry C*, *123*, 21639–21644.
75. Kotnala, A., & Zheng, Y. (2019). Opto-Thermophoretic fiber tweezers. *Nano*, *8*, 475–485.
76. Lin, L., et al. (2019). All-optical reconfigurable chiral meta-molecules. *Materials Today*, *25*, 10–20.
77. Lin, L., et al. (2016). Light-directed reversible assembly of plasmonic nanoparticles using plasmon-enhanced thermophoresis. *ACS Nano*, *10*, 9659–9668. <https://doi.org/10.1021/acsnano.6b05486>
78. Lin, L., et al. (2017). Opto-thermophoretic assembly of colloidal matter. *Science Advances*, *3*, e1700458.
79. Peng, X., Li, J., Lin, L., Liu, Y., & Zheng, Y. (2018). Opto-thermophoretic manipulation and construction of colloidal superstructures in photocurable hydrogels. *ACS Applied Nano materials*, *1*, 3998–4004.
80. Lin, L., Peng, X., & Zheng, Y. (2017). Reconfigurable opto-thermoelectric printing of colloidal particles. *Chemical Communications*, *53*, 7357–7360. <https://doi.org/10.1039/C7CC03530F>
81. Lin, L., Kollipara, P. S., & Zheng, Y. (2019). Digital manufacturing of advanced materials: Challenges and perspective. *Materials Today*, *28*, 49–62. <https://doi.org/10.1016/j.mattod.2019.05.022>
82. Li, J., Hill, E. H., Lin, L., & Zheng, Y. (2019). Optical nanoprinting of colloidal particles and functional structures. *ACS Nano*, *13*, 3783–3795. <https://doi.org/10.1021/acsnano.9b01034>
83. Li, J., Lin, L., Inoue, Y., & Zheng, Y. (2018). Opto-Thermophoretic tweezers and assembly. *Journal of Micro and Nano-Manufacturing*, *6*. <https://doi.org/10.1115/1.4041615>
84. Pughazhendi, A., Chen, Z., Wu, Z., Li, J., & Zheng, Y. (2020). Opto-thermoelectric tweezers: Principles and applications. *Frontiers in Physics*, *8*. <https://doi.org/10.3389/fphy.2020.580014>
85. Donner, J. S., Baffou, G., McCloskey, D., & Quidant, R. (2011). Plasmon-assisted optofluidics. *ACS Nano*, *5*, 5457–5462.
86. Guyon, E., Hulin, J.-P., Petit, L., & Mitescu, C. D. (2001). *Physical hydrodynamics*. Oxford University Press.
87. Liu, Y., & Poon, A. W. (2010). Flow-assisted single-beam optothermal manipulation of microparticles. *Optics Express*, *18*, 18483–18491. <https://doi.org/10.1364/OE.18.018483>

88. Chen, J., Kang, Z., Kong, S. K., & Ho, H.-P. (2015). Plasmonic random nanostructures on fiber tip for trapping live cells and colloidal particles. *Optics Letters*, *40*, 3926–3929. <https://doi.org/10.1364/OL.40.003926>
89. Cong, H., et al. (2019). Target trapping and in situ single-cell genetic marker detection with a focused optical beam. *Biosensors and Bioelectronics*, *133*, 236–242.
90. Jin, C. M., Lee, W., Kim, D., Kang, T., & Choi, I. (2018). Photothermal convection lithography for rapid and direct assembly of colloidal plasmonic nanoparticles on generic substrates. *Small*, *14*, 1803055. <https://doi.org/10.1002/sml.201803055>
91. Scriven, L., & Sternling, C. (1960). The Marangoni effects. *Nature*, *187*, 186–188.
92. Li, X., et al. (2019). Plasmonic bubble nucleation and growth in water: Effect of dissolved air. *The Journal of Physical Chemistry C*, *123*, 23586–23593. <https://doi.org/10.1021/acs.jpcc.9b05374>
93. Wang, Y., et al. (2018). Giant and explosive Plasmonic bubbles by delayed nucleation. *Proceedings of the National Academy of Sciences*, *115*, 7676–7681. <https://doi.org/10.1073/pnas.1805912115>
94. Giroto, A., et al. (2016). Motion of optically heated spheres at the water–Air interface. *Langmuir*, *32*, 2687–2697.
95. Zhao, C., et al. (2014). Theory and experiment on particle trapping and manipulation via Optothermally generated bubbles. *Lab on a Chip*, *14*, 384–391. <https://doi.org/10.1039/C3LC50748C>
96. Kim, Y., Ding, H., & Zheng, Y. (2020). Enhancing surface capture and sensing of proteins with low-power Optothermal bubbles in a biphasic liquid. *Nano Letters*, *20*, 7020–7027. <https://doi.org/10.1021/acs.nanolett.0c01969>
97. Miniewicz, A., Quintard, C., Orlikowska, H., & Bartkiewicz, S. (2017). On the origin of the driving force in the Marangoni propelled gas bubble trapping mechanism. *Physical Chemistry Chemical Physics*, *19*, 18695–18703.
98. Rajeeva, B. B., et al. (2019). Accumulation-driven unified spatiotemporal synthesis and structuring of immiscible metallic nanoalloys. *Matter*, *1*, 1606–1617. <https://doi.org/10.1016/j.matt.2019.10.017>
99. Bangalore Rajeeva, B., et al. (2017). High-resolution bubble printing of quantum dots. *ACS Applied Materials & Interfaces*, *9*, 16725–16733. <https://doi.org/10.1021/acsami.7b04881>
100. Rajeeva, B. B., et al. (2017). Patterning and fluorescence tuning of quantum dots with haptic-interfaced bubble printing. *Journal of Materials Chemistry C*, *5*, 5693–5699. <https://doi.org/10.1039/C7TC00454K>
101. Rajeeva, B. B., et al. (2018). “Point-and-shoot” synthesis of metallic ring arrays and surface-enhanced optical spectroscopy. *Advanced Optical Materials*, *6*, 1701213. <https://doi.org/10.1002/adom.201701213>
102. Lin, L., et al. (2016). Bubble-pen lithography. *Nano Letters*, *16*, 701–708. <https://doi.org/10.1021/acs.nanolett.5b04524>
103. Hu, W., Fan, Q., & Ohta, A. T. (2013). An opto-thermocapillary cell micromanipulator. *Lab on a Chip*, *13*, 2285–2291. <https://doi.org/10.1039/C3LC50389E>
104. Chikazawa, J.-I., Uwada, T., Furube, A., & Hashimoto, S. (2019). Flow-induced transport via optical heating of a single gold nanoparticle. *The Journal of Physical Chemistry C*, *123*, 4512–4522. <https://doi.org/10.1021/acs.jpcc.8b11575>
105. Dai, L., Ge, Z., Jiao, N., & Liu, L. (2019). 2d to 3d manipulation and assembly of microstructures using Optothermally generated surface bubble microrobots. *Small*, *15*, 1902815. <https://doi.org/10.1002/sml.201902815>
106. Stratton, J. A. (2007). *Electromagnetic theory* (Vol. 33). Wiley.
107. Melcher, J., & Electric, R. (1974). Fields and moving media. *IEEE Transactions on Education*, *17*, 100–110.
108. Roxworthy, B. J., Bhuiya, A. M., Vanka, S. P., & Toussaint, K. C. (2014). Understanding and controlling Plasmon-induced convection. *Nature Communications*, *5*, 3173. <https://doi.org/10.1038/ncomms4173>

109. Squires, T. M., & Bazant, M. Z. (2004). Induced-charge electro-osmosis. *Journal of Fluid Mechanics*, *509*, 217–252.
110. Li, J., et al. (2021). Tunable chiral optics in all-solid-phase reconfigurable dielectric nanostructures. *Nano Letters*, *21*, 973–979. <https://doi.org/10.1021/acs.nanolett.0c03957>
111. Li, J., et al. (2019). Optical nanomanipulation on solid substrates via optothermally-gated photon nudging. *Nature Communications*, *10*, 5672. <https://doi.org/10.1038/s41467-019-13676-3>
112. Kotnala, A., & Zheng, Y. (2019). Digital assembly of colloidal particles for nanoscale manufacturing. *Particle & Particle Systems Characterization*, *36*, 1900152. <https://doi.org/10.1002/ppsc.201900152>

Quantum Optomagnetic Plasmonic Nanocircuits



Zahraa Al-Baiaty

Abstract Realization of functional integrated nanophotonic devices depends on the development of scalable and efficient plasmonic nanocircuits comprising quantum emitters. In this context, this work presents an optimized method for the realization of a highly efficient and ultracompact plasmonic circuitry for manipulating the readout of the magnetic resonance of the nitrogen-vacancy (NV) centers in nanodiamonds. We demonstrate that the readout of the electron spins of NV centers can be coupled to plasmonic modes, and propagated along lithographically fabricated nanoplasmonic circuitry-based efficient nanowires. Our optimized method is based on enhancing the plasmon propagation length and improving the coupling efficiency. Our results show a 5 times enhancement in the plasmon propagation length using (3-mercaptopropyl) trimethoxysilane as an adhesion layer and a 5.2 times improvement in the coupling efficiency by introducing grating couplers. The integration of efficient plasmonic circuitry with the excellent spin properties of the NV centers can potentially be leveraged for solid-state quantum technologies and shows a significant step towards the realization of compact on-chip quantum information processing systems.

Keywords Quantum plasmonic circuits · Nitrogen vacancy centers · Optomagnetic circuits · Lithographic plasmonic waveguides · Ultralong propagation length · Grating couplers · Optically detected magnetic resonance · Nanodiamonds · Quantum emitters · Surface plasmon polaritons · Nanoscale magnetometry · Electron beam lithography

Z. Al-Baiaty (✉)

School of Science, RMIT University, Melbourne, VIC, Australia

1 Introduction

The rapidly growing interest in photonic technologies is driven by the eagerness to overcome the fundamental limits in the bandwidth, size, and speed of semiconductor-integrated technologies. To fulfill the large functionality of the future photonic integrated circuits, the optical components have to be miniaturized. However, a natural limitation is the diffraction limit that is dominant when the size of a photonic device is smaller than the wavelength of light in the material. Plasmonics has the potential to control the propagation of light by the use of subwavelength structures. It plays an important role in enhancing the processing speed of future integrated circuits [1, 2]. Manipulating the flow of light at the nanoscale has not only revealed new science but has also driven many important advanced technologies that have had a key impact on society, economy, environment, and photonics community. In other words, plasmonics has the potential to overcome the limitations of photonics and electronics technologies.

The present surge in nanophotonics based on surface plasmon polaritons (SPPs) research is happening at a time where important technological areas such as optical data storage and optical lithography are approaching fundamental limits. The SPPs are free electron density waves that result from an intimate interaction between electromagnetic (EM) waves and metallic surface electrons. EM waves can generally be classified into transverse magnetic (TM) and transverse electric (TE) waves that are polarized in p-polarized and s-polarized electromagnetic modes, respectively. For a propagating wave along with the interface, the electric field must be normal to the interface. By considering SPPs as hybrid EM waves mode incorporate the propagation of both of the transverse waves (in dielectric) and longitudinal waves (plasma oscillations in metals). Since TE waves are purely transverse waves, these waves cannot be coupled to the longitudinal electron oscillations in metal, therefore SPPs mode only exists for a TM (p – polarized) mode [3, 4].

The SPPs can take various forms, ranging from freely propagating electron density waves along metal surfaces to localized electron oscillations on metal nanoparticles. To elucidate the behaviors of the SPPs at a metal/dielectric interface, let us consider a TM wave in a geometry shown in Fig. 1a. Figure 1a consists of a dielectric material with a positive dielectric constant (ϵ_d) and metal with complex frequency-dependent permittivity can be described as $\epsilon_m(\omega) = \epsilon'(\omega) + i\epsilon''(\omega)$ where the imaginary part explains the absorption and scattering losses encountered when materials interact with EM waves. The wave vector ($k_{sp}(\omega)$) of the SPP can be expressed as [5]:

$$k_{sp}(\omega) = \frac{\omega}{c} \sqrt{\frac{\epsilon_m(\omega) \epsilon_d}{\epsilon_m(\omega) + \epsilon_d}} \quad (1)$$

where ω and c are the frequency of the SPP and the light velocity in a vacuum, respectively.

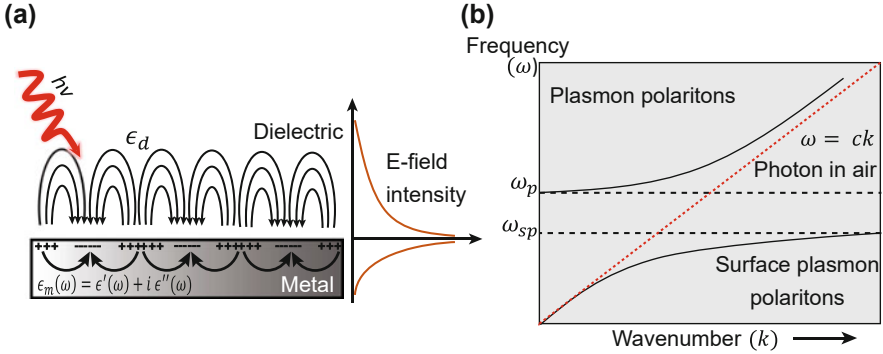


Fig. 1 (a) Schematic diagram of the surface plasmon polaritons (SPPs) generated at the metal/dielectric interface. (b) Dispersion curve of the SPPs on a metal-dielectric interface

Equation (1) can be further modified using the Drude model [6] for huge free electrons, in which the relative permittivity of metal with negligible damping is given by:

$$\epsilon_m(\omega) = 1 - \frac{\omega_p^2}{\omega^2} \tag{2}$$

where ω_p denotes the plasma frequency. Substituting Eq. (2) in Eq. (1), the SPPs dispersion relation can be plotted as in Fig. 1b which shows the dispersion curve of SPPs lies to the right to the dispersion curve of the light line. Equation (1) and Fig. 1b both indicate that the SPPs have a higher wave vector than the light wave of the same frequency. Therefore, SPPs mode cannot be excited directly by the incident light due to its large propagation constant. To overcome the phase mismatch between SPPs and incident light, a phase matching technique such as a grating coupler employing the light diffraction, a prism coupler, and near field excitation with a near field optical microscopy are required to ensure momentum conservation [5, 7]. Further, SPPs have a shorter wavelength, lower in magnitude than that of the ordinary propagating light. This property allows SPPs to be exploited to overcome the optical diffraction limit in super-resolution imaging, hence it can provide a resolution exceeding the limit of an ordinary optical microscope using propagating photons [8].

More recently, plasmonic devices have gained much attention as a key component in miniaturizing the optical components to be comparable with electronic components, and in the integration of photonics circuits with electronics to build integrated nanophotonic circuits that can offer substantial improvements in term of the bandwidth, speed and small physical device size for the next generation of information technologies. Waveguide-based SPPs have the remarkable capability for the ultimate miniaturization of integrated photonic circuitries by offering a unique setting for the manipulation of light “SPPs” via the confinement of

electromagnetic energy beyond the diffraction limit. The development of nanoscale plasmonic circuitries holds great promise to revolutionize quantum information processing protocols, secure communication, and nanoscale bio-sensing.

The dramatic advances in nanofabrication and full-field electromagnetic simulation techniques have enabled the realization of several different plasmonic waveguiding structures including thin metal films [9], chains of metal nanoparticles [10–13], dielectric-loaded surface plasmon polaritons [14, 15], nano-gaps between metallic media [16, 17], metal wedges [18, 19], nano-grooves in metal substrates [20], cylindrical waveguides [21–24], channel plasmon polaritons (CPPs), and hybrid plasmonic polaritons (HPPs) waveguides [25–27]. Although all of these waveguides achieved localization of EM energy in nanoscale regions, in this work we will present only the plasmonic waveguides that can support the long propagation length that is essential for the integration of the plasmonic circuit.

In this chapter, I will demonstrate a novel method for the realization of highly efficient and ultracompact plasmonic nanocircuitry. Recently, for the first time, we have reported that the spin state readouts of the nitrogen vacancy (NV) centers in nanodiamonds (NDs) can be coupled to plasmonic modes of lithographic nanowires (LNWs) and passed through plasmonic elements such as beam splitters [28], which are essential elements needed to form quantum networks. The optimization methods have been well investigated for longer plasmon propagation length (L_p) and higher coupling efficiency (η). The technique I presented adds new potential to both plasmonic waveguides and NV centers in NDs towards the practical realization of nanoscale magnetometry, more complex quantum plasmonic circuits as well as photonic circuits.

2 Background: Towards Functional Plasmonic Nanocircuitry

Nanoscale waveguides-based SPPs are imperative for the ultimate miniaturization of photonic circuitries beyond the diffraction limit. Such circuitries have a wide range of potential applications, in areas such as quantum information and quantum sensing. Consequently, several impressive demonstrations have already been made for the SPPs propagation along various types of plasmonic waveguides. With several promising plasmonic waveguides, CPPs and HPPs geometries have been thoroughly investigated owing to their interesting propagation length and strong mode confinement [20, 29–32]. CPPs based on a V-shaped groove carved in metal have been investigated with plasmonic elements such as beam splitters and Mach-Zehnder interferometers [33]. The energy in these waveguides can be confined in different positions in the groove depending on the modes. Further, the modes and the propagation length can be adjusted through the taper angle [34]. However, the metal V-groove plasmonic waveguides supporting CPPs require advanced fabrication techniques to avoid scattering loss and suppress the field well inside the channel. Furthermore, HPPs can be fabricated using the standard lithography process but

the mode confinement of HPPs is weak if the diameter of a high refractive index nanowire is very small [31].

Many theoretical and experimental studies demonstrate that the low loss SPPs mode can be carried along metallic wires with a subwavelength cross-section [23, 35]. Metallic nanowires (NWs), fabricated with subwavelength diameters and high uniformity, allow the propagation of the electromagnetic field with appreciable propagation length and tight field confinement. These properties make these nanostructures the optimum choice for the miniaturization of optical signal processing devices and for creating miniaturized photonic circuits for optical signal transfer at visible frequencies [5]. The first observation of propagating SPPs in chemically synthesized nanowires (CSNWs) has been reported in [36]. It has been shown that the controlled routing of single plasmons in a plasmonic circuit comprising single-photon sources and silver NWs is possible [35], which may lead to the construction of a complete on-chip quantum plasmonic nanocircuit. Nonetheless, CSNWs are not suitable to be integrated into on-chip circuits as growing such wires in a designed pattern is tedious and time-consuming.

On-chip plasmonic circuitry requires a feasible method for developing plasmonic structures with controllable and optimized geometry. Electron beam lithography (EBL) followed by thermal evaporation of metal is an efficient method to build sub-wavelength plasmonic components as it provides more control over waveguide geometry, allowing the design and manipulation of waveguide modes and their properties. Normally in the lithographic method, plasmonic structures are built by depositing noble metals on a glass substrate. In this approach, a few nanometer adhesion layers, such as chromium (Cr), titanium (Ti), or their oxides forms, have mainly been employed to guarantee a good bonding between the plasmonic structures and the glass surface [37, 38]. However, adding a thin intermediate metallic adhesion layer causes red shifting, damping as well as broadening the plasmon resonance. Further, increasing the thickness of these layers leads to a decrease in the magnitude of the resonance [39–42]. The reason is attributed to the effect of the refractive index of the adhesion material that causes the redshift and decreases in the magnitude of the resonance [42]. Results have shown a 40% increase of the plasmon dephasing time and a decrease in the field enhancement when a single gold nanorod is placed on a 2nm-Ti compared with a single gold nano-rod place on a glass substrate [39]. Besides, optical sensing techniques require a transparent glass substrate but the nanostructures do not stick well on the glass surface [38]. Owing to the limited propagation length in lithographic nanowires, they have not fulfilled their original promise as replacements for CSNWs in integrated nanocircuits.

The challenges of plasmonics come not only from Ohmic losses but also from a lack of efficient coupling to nanoscale emitters that can enable truly sub-diffraction limit optical circuitry. Efficient conversion of external macroscopic incident light to the compressed surface plasmons is challenging yet pivotal. The surface plasmon wave vector is larger than the free space light wave vector as indicated in Eq. (1), therefore the incident photons light on the metal surface cannot excite the SPPs directly unless special techniques for phase matching are employed [5]. Therefore,

for the realization of SPPs based nanophotonic circuits, it is desirable to have an efficient nano coupling capability.

Coupling plasmonic circuits to external bulky sources and detectors limits their practical applications to nanoscale devices. Besides, coupling plasmonic waveguides to nano-lasers remains a challenge that hinders the realization of functional components [34]. Therefore, for a complete demonstration of a plasmonic circuitry, towards employing in integrated nano-photonic circuits, it is essential to utilize coupling to quantum emitters (QEs). Plasmonic nanocircuits integrated with QEs open up new perspectives in the control of light by significantly enhancing QE emission rates and miniaturizing quantum nanophotonic components. Hence, on-chip, bright, and photostable single-photon sources are critical for the realization of solid-state quantum information processing, quantum cryptography, and quantum network [43–45].

Color centers in nanodiamonds have been identified as artificial atoms of choice for their exceptional chemical, biological, structural, mechanical, and optical properties [46]. The most prominent emitter in diamond is the nitrogen vacancy center, in which the negatively charged state forms a spin triplet in the orbital ground state, and allows for optical initialization and readout at room temperature by a technique known as optically detected magnetic resonance (ODMR) [47, 48].

The NV center is a defect formed by one substitutional nitrogen atom and adjacent lattice vacancy in a diamond crystal lattice, as shown in Fig. 2a. An NV center can exist in two charged states, the neutral charge state (NV^0) center, and the negative charge state (NV^-) center. The NV^0 center has five unpaired electrons: four from the neighboring carbon atoms and one from the intrinsic nitrogen atom. For the NV^- center, it is widely accepted to be comprised of six electrons, where the other electron is captured from elsewhere in the crystal lattice. The main features of the NV^- and NV^0 can be identified by their optical zero phonon lines (ZPLs) at 1.945 eV (637 nm) and 2.156 eV (575 nm), respectively, as depicted in Fig. 2b. Even though there are two charged states of the NV center, the focus of this work is the NV^- center for its paramagnetic ground state whose spins can be optically prepared, coherently manipulated hence allowing precision sensing of magnetic fields even at room temperature [49, 50]. In the rest of this work, the NV^- will be denoted simply by an NV center.

The energy level diagram of the NV center can be seen in Fig. 2c. It contains three electronic levels, the ground state 3A_2 , the excited state 3E , and the metastable state 1A . The ground state of the NV center is a spin-triplet with the lowest energy spin sublevel $m_s = 0$ along with $m_s = \pm 1$ spin sublevels. The $m_s = \pm 1$ spin sublevels are degenerate and the crystal field splitting from the $m_s = 0$ is $D = 2.87$ GHz [47]. Further, the NV has a spin-triplet excited state with $m_{sE} = 0$, $m_{sE} = \pm 1$, with zero-field splitting $D_{es} = 1.42$ GHz, and one singlet metastable state. The optical transition between 3A_2 and 3E is radiative, while the transition through 1A is not radiative and is strongly spin selective. An NV center can be pumped from the ground state $m_s = 0$ spin sublevel to the excited state $m_{sE} = 0$ spin sublevels with a 532 nm laser, then decay radiatively towards the ground state $m_s = 0$ with spin-conserving. However, pumping from the ground state $m_s = \pm 1$ spin sublevels to

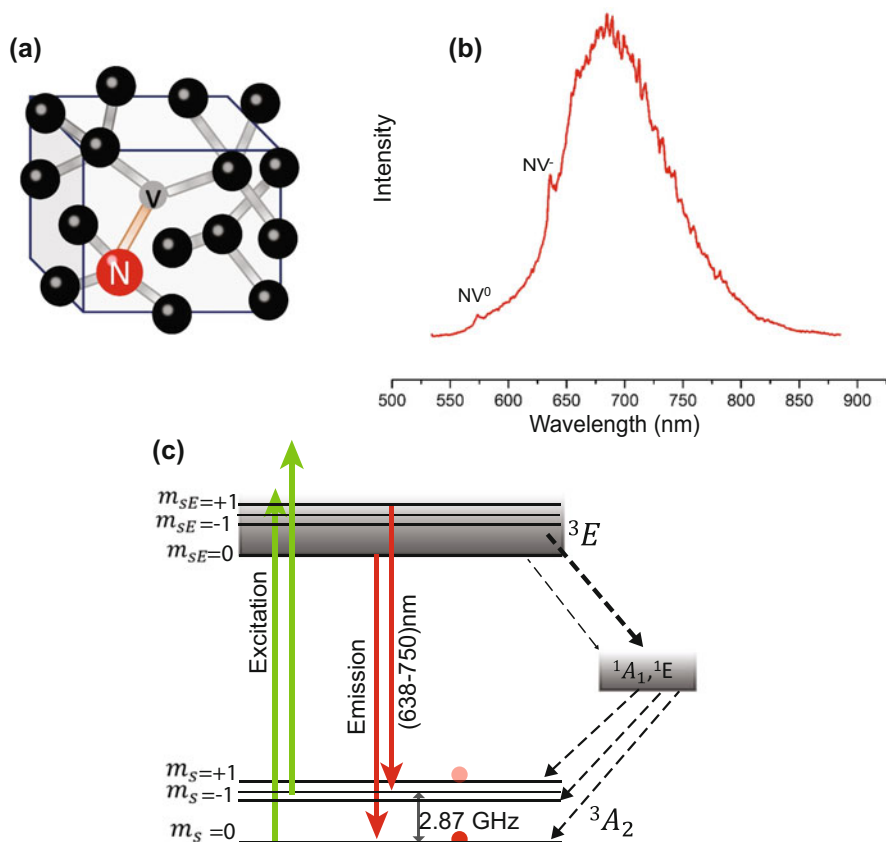


Fig. 2 (a) Schematic of the nitrogen-vacancy center in the diamond lattice. (b) Typical fluorescence emission spectra identifying the ZPLs of the NV⁰ and NV⁻ centers. (c) Electronic levels of the NV center in ND. Solid lines indicate optical and microwave transitions; dashed lines indicate non-radiative transitions

the excited state $m_{sE} = \pm 1$ spin sublevels, there will be a high probability to decay through intersystem transitions to the metastable state, and from there to the $m_s = 0$ with no radiation. The latter is an important feature for practical magnetometry applications.

The spins associated with the NV center defects in diamond have been identified as promising spin qubits for the practical realization of solid-state spin based quantum information processing [48, 51] and nanoscale magnetometry schemes [52–54] at room temperature. In these configurations, the quantum information can be stored in the electron spin states of the NV center while quantum logic can be achieved by modulating the photoluminescence intensity via the ODMR technique [55, 56]. Despite these promising developments, one of the limiting factors of the

ODMR technique is the low collection efficiency of photons emitted by the NV centers in NDs [57–59].

Fortunately, an efficient approach for enhancing the emission from broadband NV center into a narrow band, and improving the overall collection efficiency, can be achieved when NDs are brought close to photonic and plasmonic cavities. The latter is important for the development of solid-state quantum devices with tunable performance [60–62]. While photonic cavities are diffraction-limited, chip-scale broadband plasmonic cavities can be used for channeling and manipulating the emission from the NV centers along plasmonic waveguides.

In particular, coupling the readout of the electron spins of NV centers in NDs to plasmonic modes can be employed for realizing on-chip quantum information processing where the plasmonic waveguides can be used as networks to guide, process, and transfer the spin quantum information along chip-scale devices. Heretofore, experimental investigations on the readout of the ODMR signal in propagating SPPs have only focused on the study of highly crystalline silver NWs [63] which are difficult to form into a circuit, hence their applications are limited. Conversely, LNWs allow controllable circuitry design but show significantly higher losses than CSNWs [64] due to damping by metallic adhesion layer. Even with the recently investigated plasmonic nanocircuits with NDs [29, 65, 66], compact devices with a high coupling efficiency and low propagation loss have so far been elusive.

Certainly, channeling and guiding the emission from the NV centers to highly confined plasmonic modes supported by low loss, scalable, and complex plasmonic nanowaveguides are crucial for the ultimate miniaturization of photonic devices beyond the diffraction limit. Therefore, we have investigated and presented optomagnetic plasmonic nanocircuitry for guiding, routing, and processing the readout of electron spins of NV centers. Figure 3 depicts a schematic for the proposed construction of an on-chip quantum plasmonic splitter coupled to an ND that can be excited with a green continuous-wave (CW) laser. The emitted photons from the NDs are coupled into the plasmonic modes and propagate along the integrated nanostructures. The presented device geometry has been optimized and investigated both theoretically and experimentally, using the experimental setup shown in Fig. 4, toward efficient on-chip ODMR detection of the NV centers spin states. The approach we present enables substantial enhancement in the performance of plasmonic LNWs that can be scaled to more complicated multifunctional circuitries and leveraged for quantum information technology.

3 Optimization of the Lithographic Plasmonic Nanowires

Here, we demonstrate reduced loss and enhanced coupling in lithographic plasmonic silver (Ag) nano waveguides (represented by rectangular-shaped silver nanowires) towards developing efficient plasmonic nanowaveguides viable for scalable on-chip quantum information processing system.

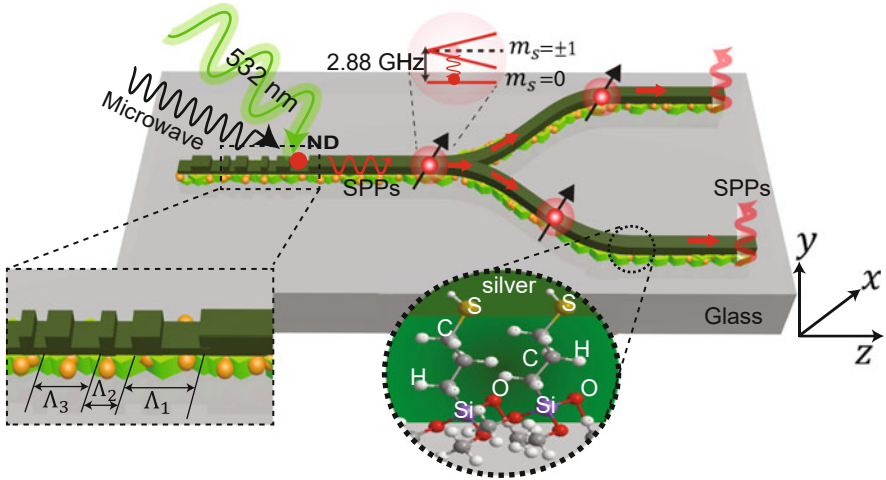


Fig. 3 Schematic illustration of the considered lithographic plasmonic circuitry that can control and process the readout of the electron spins of NV centers in NDs when excited with a 532 nm green laser. The inset (left) shows a close-up of the proposed grating coupler with chirped gratings for high coupling efficiency and directionality of the NV centers broad emission into the plasmonic circuitry, and the inset (right) shows the (3-mercaptopropyl) trimethoxysilane MPTMS adhesion layer

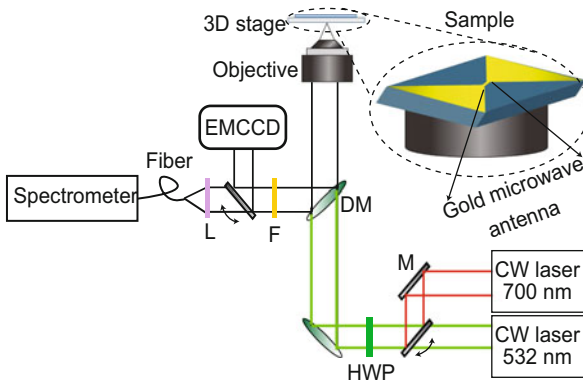


Fig. 4 The optical set-up used for characterization of the ND-plasmonic nanocircuit coupled system. A 532 nm laser is used to excite an ND by an objective lens. The emitted photoluminescence is collected through the same objective and filtered, and directed towards an electron-multiplying charge-coupled device or a spectrometer. *M* mirror, *HWP* half waveplate is used to control the polarization of the laser, *F* fluorescence filters for photon wavelength lies between 647 and 785 nm, *L* focusing lens, and *DM* dichroic mirror. Inset, a close-up illustration of a glass substrate containing a microwave antenna for the ODMR measurements

We enhance the L_p by employing a low-loss efficient fabrication method. Further, we improve the η by optimizing the design of three-dimensional (3D) nanograting

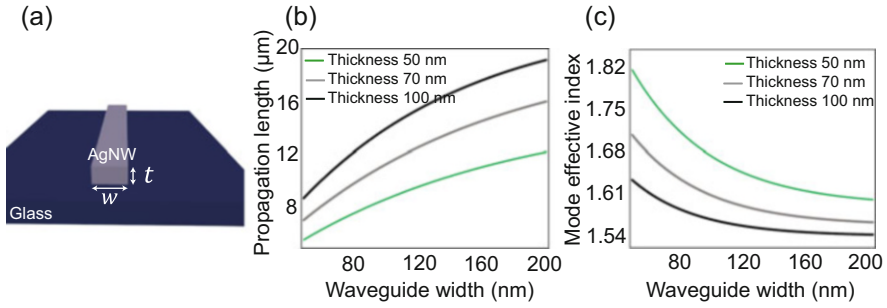


Fig. 5 (a) Schematic diagram of the plasmonic structure under consideration. (b) Plasmon propagation length and (c) Mode effective index plotted as a function of the width of the plasmonic waveguide for different thicknesses

couplers at an air-Ag-SiO₂ interface, which also is suitable for integration with on-chip circuits. Hence, the net coefficient in the nanowire (η_{NW}) can be defined as, $\eta_{NW} = \exp(-1/L_p) z \times \eta$, where z is the local position along the nanowire.

To arrive at a full understanding of these NWs and to find the optimum design parameters, the effective index and propagating length of these plasmonic nanowaveguides were thoroughly studied using the frequency domain finite element (FEM) method implemented in COMSOL. In this simulation, the propagation of the SPPs is along z -direction with an electric field that can be defined as [67]:

$$E = (E_y) \exp i (\omega t - \beta z) \quad (3)$$

where E_y refers to the electric amplitude of traveling plasmon modes at angular frequency ω , and β is the complex propagation constant defined as $\beta = \beta' - i\beta''$ which is related to mode effective index as $n'_{eff} = \beta'/k_0$ (k_0 is the free space wave vector), and propagation length as $L_p = 1/2\beta''$, (L_p is defined as the propagation distance at which the SPP intensity decays by a factor $1/e$ [68]).

We calculated the propagation length and the effective index for the plasmonic waveguide geometry, shown in Fig. 5a, which composes of a rectangular silver nanowaveguide with optical constants being adopted from experimental data by John and Christy [69], and a cross-section of width (w) and thickness (t), placed on a glass substrate with refractive index $n_{glass} = 1.46$, and surrounded by air. Silver is used as the plasmonic material as it shows the lowest loss in the visible spectrum [68, 70].

Figure 5b shows the dependence of the propagation length of the SPPs on the wire dimensions. It is clear that L_p becomes longer when the width of the waveguide increases and its value increases when increasing the waveguide thickness to reach $19.136 \mu\text{m}$ at $t = 100 \text{ nm}$. The width of the waveguide, however, also affects the mode indices. Decreasing the width leads to strong mode confinement, as shown in Fig. 5c. This also implies that higher effective index results in higher losses that can

limit the propagation length of SPPs. The latter indicates the trade-off between the field confinement and the losses in the plasmonic NW.

3.1 Enhancing the Plasmon Propagation Length

To enhance the L_p , the plasmonic structures were fabricated using the EBL method with the (3-mercaptopropyl) trimethoxysilane (MPTMS), which contains functional groups at both terminals of the molecule, as an adhesion layer [38, 71, 72] (see Fig. 3). We numerically investigate silver LNWs of width $w = 100$ nm and thickness $t = 70$ nm in the xy plane that are featuring both reasonably good propagation length and mode confinement (see Fig. 5b, c). The propagation characteristics of the LNWs based on MPTMS adhesion layers are compared with traditional lithographically fabricated NWs which are attached to the glass substrate with Ti adhesion layers. The 3D finite-difference time-domain (FDTD) numerical simulations implemented using Lumerical, with artificial absorbing boundaries surrounding the computational domain, are used to investigate two identical NWs supported with a 2nm-Ti adhesion layer or a 2nm-MPTMS adhesion layer. Simulations for various NW lengths, 2–14 μm , are carried out (see Fig. 6a). The intensity (I_{sp}) of the propagating SPPs signal along the NWs when excited with a 700 nm for both types of samples are measured by placing a set of power monitors (*detectors*) in the transverse xy plane at the far edge of the NWs from the excitation area.

The measured I_{sp} can be explained as the total power of the coupled and propagated SPPs divided by the total power emitted by the excitation source, i.e. $I_{sp}/I_{excitation}$. We placed a set of monitors along the plasmonic wire, in steps of 2 μm . The first monitor was set at $z = 2$ μm from the edge of the waveguide in order to monitor only the waveguided SPPs signal and to eliminate the residual effect of the excitation source. Using a 700 nm excitation source, we excite SPPs at the Ag-SiO₂ interface, to be guided along NWs with varying lengths. The index data of Ti is adapted from [69], and that of the MPTMS is obtained from [71] for incident light at a wavelength of 700 nm. By fitting the results to an exponential decay function as:

$$I(z) = I_0 \times e^{-z/L_p} \quad (4)$$

where I_0 is the initial intensity, an enhancement in the propagation length for NWs supported with MPTMS adhesion layer is observed compared with Ti-based systems.

Our simulation results are shown in Fig. 6a predict a L_p of 8.3 μm for the NW on MPTMS adhesion layer which is a factor of 5 times longer than that of a traditional Ti-based system. Accordingly, we calculate η_l , where $\eta_l = 2\beta''$, results show η_l of 0.12 μm^{-1} and 0.59 μm^{-1} for MPTMS and Ti adhesion layers, respectively. These results demonstrate that adding a thin metallic adhesion layer of Ti limits the L_p of the SPPs, which is attributed to the large value of the imaginary component of the

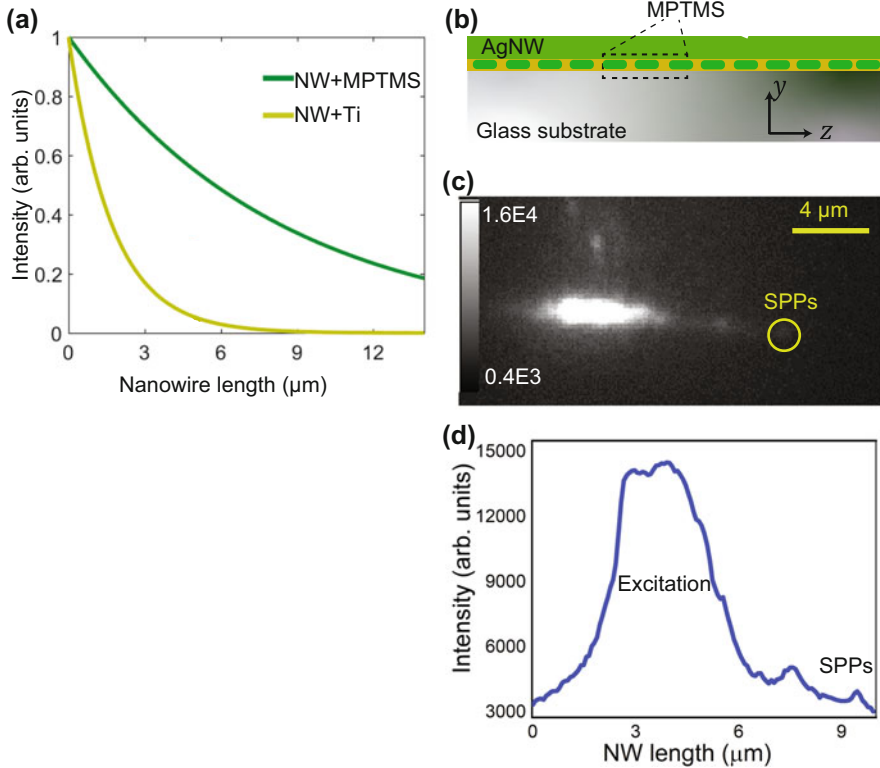


Fig. 6 (a) Simulation of NWs showing the measured I_{sp} as a function of the NW length for LNWs deposited on either a 2nm-Ti adhesion layer or an MPTMS adhesion layer. (b) Schematic illustration of LNW fabricated on the MPTMS pre-treated glass substrate. Experimentally measured SPPs along the presented system in (b) with the respective photon emission map and the intensity profile shown in (c) and (d), respectively

Ti [37]. The losses are worse when Cr is used as an adhesion layer as it is more absorptive than Ti, which increases the rate of plasmon dephasing through charge transfer across the metal-metal interface [39].

In the experiment, LNWs were fabricated using EBL onto either a 2nm-Ti adhesion layer or an MPTMS functionalized glass substrate. The MPTMS forms a thin monolayer [72–74] and has a refractive index comparable with the refractive index of glass substrate [71, 72], thus the precise thickness of the MPTMS does not significantly influence the properties of the plasmonic modes. In the fabrication method, the substrate was cleaned in a Piranha solution to remove metals and organic contaminations. The glass was immersed in a freshly prepared Piranha solution composed of sulphuric acid and hydrogen peroxide (H_2O_2) (3:1) for 30 min at 70 °C. To functionalize the glass with the MPTMS, we optimized the method proposed by Goss et al. [75] to improve the performance of the adhesion layer but for silver nanostructures instead of gold.

In the hydroxylation process, the glass was placed on a hot plate at 100 °C for 10 min to leave –OH groups on the surface of the glass. Meanwhile, a silanization solution was prepared by adding 5 g of MPTMS to a solution of 5 g of H_2O_2 and 200 g of 2-propanol (IPA). After the solution was heated to boiling, the dried glass was immersed for 10 min then rinsed with IPA and dried with nitrogen. The glass was then cured by placing it on a hot plate at 110 °C for 10 min. The procedure of immersing in MPTMS solution, rinsing, and curing was repeated an extra two times to ensure a high probability of covalent Si-O-Si bonds on the glass surface. The functionalized glass was spin-coated with bi-layer poly (methyl methacrylate) (PMMA) for a high-resolution lift-off.

During the EBL process, a beam of electrons with high energy is applied to pattern high-resolution structures. When the resist is exposed with an electron beam, the charges accumulated on the surface especially if the substrate is a glass or a nonconductive material. This causes difficulty in performing the essential alignment procedures of EBL. Moreover, the charging effect can lead to distortion of the designed patterns. To avoid charging effects, it necessary to add a thin layer of conductive material. For this reason, the pre-treated sample was covered with 10 nm of Cr by e-beam evaporation (which will be removed later).

Arrays of LNW patterns were then defined using EBL system (Raith 150) at an acceleration voltage of 10 kV, beam aperture size of 10 μm , working distance of 10 mm and beam current of 0.017 nA. The dose factor in EBL addresses the size and quality of the fabricated patterns. Consequently, the dose was calculated for the area, line, dot, and curved elements according to the exposed resist and considering the values of the beam current, dwell time, and step size for each element. The resolution of the patterns was tested with a range of dose factors from 1 to 4.6 in steps of 0.4. The results show that using dose 1 to dose 1.8 results in well-defined patterns while higher doses cause a collapse of the patterns.

Electron beam evaporation is used to obtain a thin Ag film of a final thickness of 70 nm. The deposition was run at a low-pressure $\approx 2 - 4 \times 10^{-7}$ Torr with 1 Å/sec. deposition rate. The depositing processes were separated by 15 min rest time to allow the sample to cool down and avoid damaging the molecular linker. The lift-off process was carried out by soaking the sample in acetone for 3 h, followed by a sonication bath in acetone for 3–5 min. Finally, the sample was rinsed with IPA and dried with nitrogen.

We experimentally investigated the effect of an MPTMS adhesion layer on propagating SPPs supported by LNWs shown schematically in Fig. 6b. For optical characterization, a confocal and widefield fluorescence microscope system, shown in Fig. 4, was employed. Light from a CW tunable Ti:Sapphire laser with a wavelength of 700 nm is linearly polarized, and adjusted with a half waveplate. This laser is used to excite SPPs along the LNWs, which in turn propagate along the LNWs before being scattered and partially converted into free space photons at the far end of the LNWs. The scattered SPPs signal was collected by the same objective and was optically imaged onto an electron-multiplying charge-coupled device (EMCCD) camera without saturation. To find the optimal coupling location, we adjust the sample in the x , y , and z -directions via a nanopositioning stage in aid of

digital piezo controller and a home built Labview software (National Instruments). The scattered SPPs intensity is identified by the maximum value in the emission site (away from the excitation spot) from the optical image. Consequently, a photon emission map for the LNW is obtained.

We measure the propagation characteristic of the LNWs based on different adhesion layers by using Eq. 4 and by comparing the ratio of the output photons emerging from NW ends to the input excitation intensity along LNWs that are supported either on an MPTMS functionalized glass substrate (Fig. 6b–d) or on a 2nm-Ti adhesion layer (Fig. 11d–f).

Normalized by the total energy input into the SPPs, our results show that using MPTMS as an adhesion layer can lead to an 86% enhancement in the I_{sp} compared with the Ti adhesion layer. Experimental results show η_l of $0.25 \mu\text{m}^{-1}$ and $0.64 \mu\text{m}^{-1}$ for MPTMS and Ti adhesion layers, respectively. These results emphasize that implementing MPMTS as an adhesion layer below Ag LNWs shows a lower propagation loss compared with Ti adhesion layer. These results are in good agreement with the simulation results, indicating that using an MPTMS as an adhesion layer can efficiently link silver waveguides to a glass substrate with no noticeable plasmon damping effect compared with other adhesion layers, verifying the validity of the employed approach used in this work for fabricating of plasmonic silver devices with improved performance.

3.2 Efficient Excitation of the Surface Plasmon Polaritons

Coupling light from and to plasmonic waveguides with large efficiencies is still a relevant challenge. The most common technique for coupling light into plasmonic structures is to use grating couplers. As grating couplers have the advantages of a compact footprint and can enable matching the wave vectors between the free space and the surface plasmons, they are important key components for the realization of high coupling efficiency. Thus, we introduced a chirp into the grating period and groove length. By varying the grating parameters, the strength of the scattered intensity from the grating can be controlled. Figure 7a presents the model under consideration which consists of LNW integrated with grating couplers system supported with a 2nm-Ti adhesion layer placed over a SiO_2 substrate. A Gaussian excitation source with a wavelength of 700 nm is used to excite SPPs at the Ag- SiO_2 interface when the phase-matching condition is achieved.

To study the enhancement in the coupling efficiency of the optimized grating couplers (OGCs), the parameters for the design of the OGCs need to be carefully analyzed. We investigate and optimize the design of a 14 element grating with varying dimensions and parameters. The period of the gratings (Λ) and the groove length (l) for each element are designed in such a way to support propagating SPPs at Ag- SiO_2 . The position and the injection angle of the excitation source are determined such that it excites SPPs propagating vertically up the metal-dielectric interface, i.e. along the z -direction. The coupling efficiency (η) is defined as the ratio

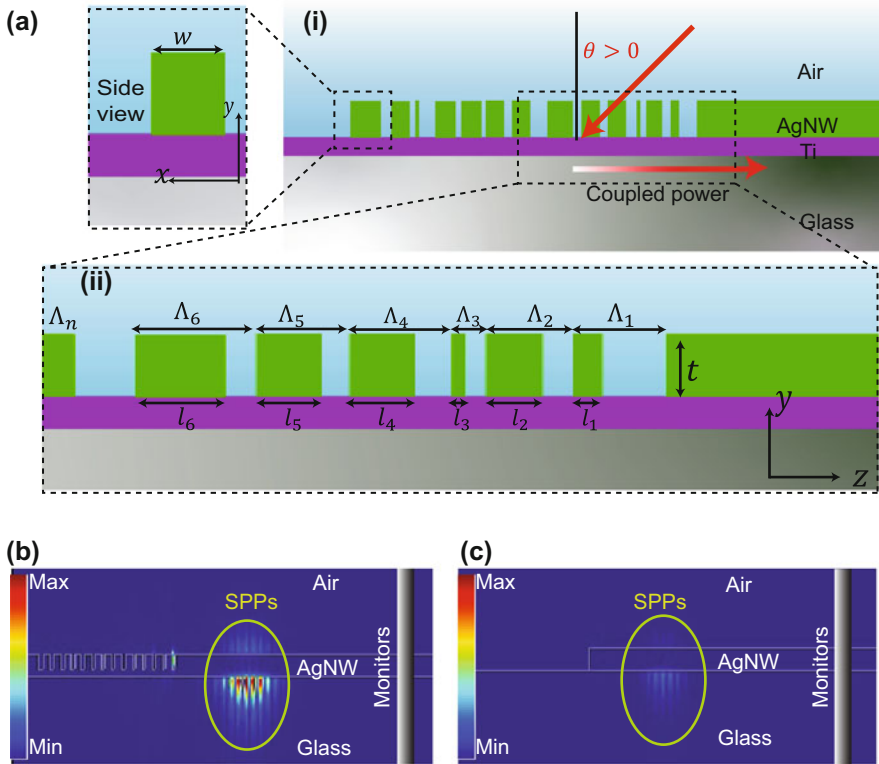
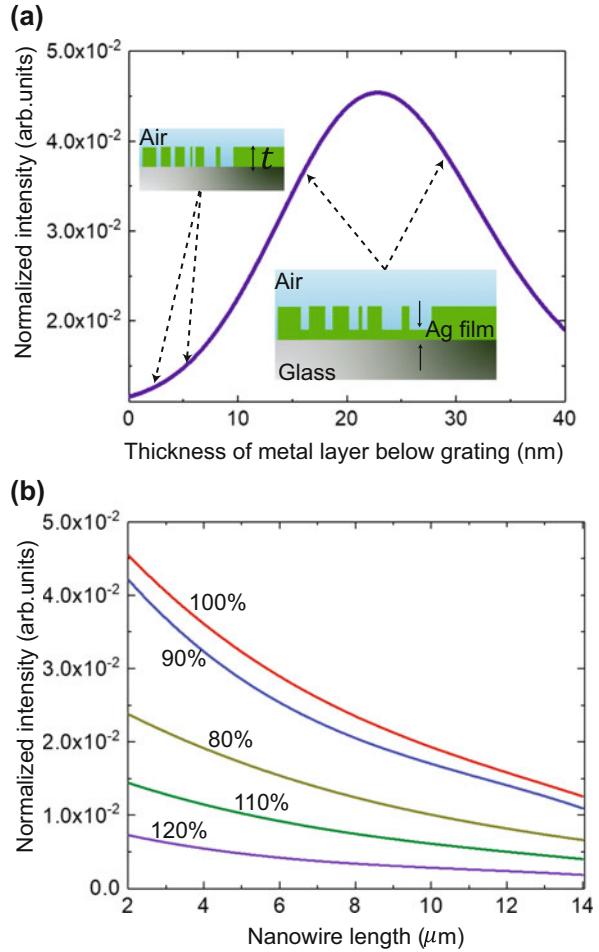


Fig. 7 FDTD simulation of the studied optimized grating couplers (a) Schematic of our optimized gratings design. (i) Illustration of the optimized grating couplers. Inset, close-up of a single groove showing the side view dimensions. (ii) Part of the optimized gratings consists of multiple blocks of varied periodicities and lengths. (b, c) Illustrate the importance of the used grating couplers in enhancing the strength of the coupled SPPs compared with a bare NW

of the total power of the coupled and propagated SPPs divided by the total power of the input excitation beam. The η may reflect the quality of the waveguide and a high η is desired. Figure 7b, c shows FDTD simulation of lithographic nanowires-optimized grating couplers (LNW-OGCs) and NW systems, respectively. It is shown that the guided mode is highly confined to the Ag-SiO₂ interface but extends slightly into the adjacent air region.

We fix the dimensions of the grating in the xy plane, we investigate the effect of varying Λ and l and the corresponding relative I_{sp} of the propagating SPPs. For comparison, we also investigate measuring the I_{sp} of the propagating SPPs along NW only. Figure 7b, c is a video recording (frame capturing) obtained from the FDTD simulation by monitoring the systems in the yz plane, demonstrating the effect of introducing OGCs for the efficient generation of the SPPs compared to bare NW.

Fig. 8 Optimization of the grating couplers for efficient excitation of the SPPs. **(a)** The efficiency of the optimized grating coupler as a function of the thickness of the Ag film. The insets show illustrations when Ag film at the optimum thickness (right), or no silver film (left). **(b)** Normalized intensity measured along the LNWs for the varied percentage change in the grating coupler dimensions to validate the optimized grating coupler design



We probed the dependence of the efficiency on the geometry variations. The coupling efficiency is investigated under the implementation of a thin Ag film between the grating elements. Figure 8a shows a significant enhancement can be achieved when we fill the area between the grooves with a 23 nm thick film of Ag. The latter can be attributed to the reduction in back reflections and to the improvement in the directionality of the grating couplers which is a function of the film thickness i.e. the etch depth of the grating.

To investigate the sensitivity of the OGCs relative to the percentage changes in their geometries, I_{sp} is measured along 14 μm LNW length integrated with the OGCs and by reading the measurements from the power monitors. Figure 8b shows the significance of the optimized grating in generating the efficient propagating SPPs signal even when all the geometries are reduced by 10% from the optimal design (blue curve in Fig. 8b at 90% geometry variations from the optimum design

parameters). These results indicate the capability of the proposed OGCs to produce a high coupling efficiency even when small alterations in the geometries may occur during the nanolithographic fabrication process.

Further, we investigate the dependence of the coupling efficiency on the source position and the incident angle. For maximum coupling efficiency, we place the source in the middle of the LNW-OGCs system, at $x = 0$ (see Fig. 7a). We investigate the detailed coupling mechanisms when the source location is moved along the grating coupling area, i.e. along z -direction. We study five coupling regions, as indicated in the inset of Fig. 9a. Figure 9a shows the sensitivity of the grating to the variations in the source position. We find moving the location of the excitation source by $0.5 \mu\text{m}$ from the optimal location resulted in a reduction in the efficiency by a factor of 1.5. In addition, we test the sensitivity of our optimized grating as a function of the angle of incidence. The results in Fig. 9b show that the angle of the incident beam can be varied by ± 5 degree without significantly reducing the efficiency of our optimized grating couplers. These results confirm the flexibility of the proposed design for the grating couplers.

We compared the performances of LNW-OGCs system and bare NWs. A direct comparison is given in Fig. 10a. The coupling efficiency in the LNW-OGCs system is measured and found to be considerably larger than that of SPPs excited via end coupling (no gratings). The simulation results in Fig. 10a indicate enhancement in η by a factor of 5.2 with respect to that of end coupling measured at $2 \mu\text{m}$ propagation distance away from the excitation source. The big improvement may warrant the validity and the high directivity of our optimized grating.

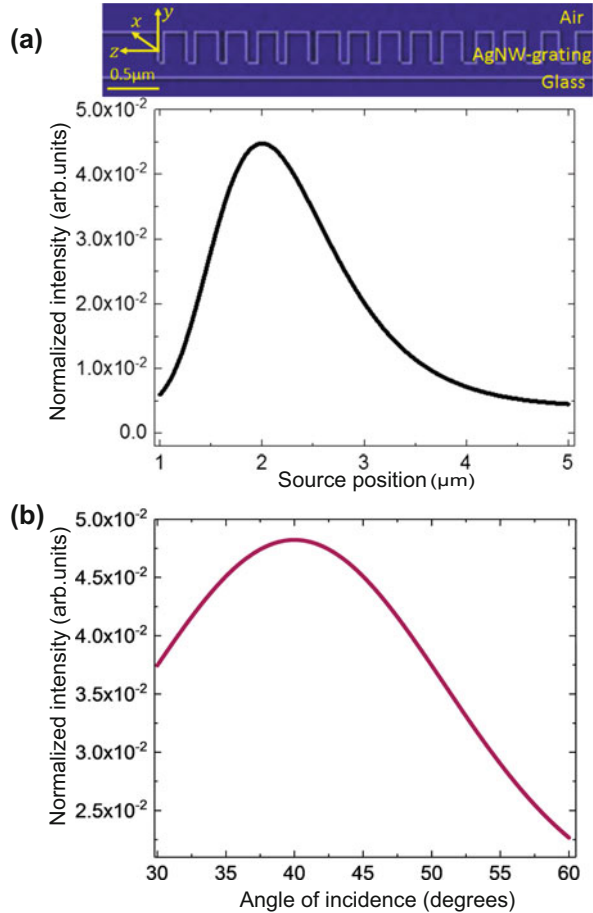
To experimentally determine the coupling efficiency, we measured the SPP excitation on the integrated LNW-OGC systems shown in Fig. 10b and extracted the η from the widefield fluorescence images obtained using the EMCCD camera. We measured the intensity of the decoupled SPPs at the output end of a $5 \mu\text{m}$ length LNW integrated with OGCs (Fig. 10c, d) and bare LNW (Fig. 11d–f) systems that are supported on the surface of glass substrates with 2nm-Ti adhesion layers.

Our experimental results (represented by dots in Fig. 10a) show up to a 4.0 ± 0.5 times enhancement in η when the OGCs are employed in the system compared with end coupling. These results indicating that the LNW-OGC system is a significantly more efficient coupling scheme that allows for more advanced device architectures. It should be pointed out that, to compare coupling efficiencies with and without the grating, we use the same adhesion layer (Ti) in both of the two cases such that any propagation loss cancels out.

4 Highly Efficient Lithographic Plasmonic Nanowires

To illustrate the performance improvement of combined couplers and the MPTMS adhesion layer, we performed experimental characterizations of the LNW-OGC systems when fabricated on MPTMS pre-treated glass substrate (shown schematically in Fig. 11a). The results were compared to lithographic NWs fabricated on a thin Ti

Fig. 9 The coupling efficiency of the optimized gratings as a function of source position in (a) and angle of the incident beam in (b). Results show the sensitivity of our optimized grating couplers to small changes in the coupling position as the coupling efficiency decreases significantly when the excitation source is moved by $0.5 \mu\text{m}$ from the optimal excitation area while there are no significant changes in the coupling efficiency when the angle of the incident beam is varied by ± 5 degree. The inset in (a) shows the studied coupling areas for the respective positions of the excitation source



adhesion layer and excited by end coupling (shown schematically in Fig. 11d). We study the output of the coupling signal and the excitation signal along the nanowire obtained from the optical image. Clearly, an enhancement in the propagating SPP signal has been achieved when both a low loss adhesion layer and an efficient coupling scheme are used together (Fig. 11b, c) compared with a bare NW on a Ti adhesion layer (Fig. 11e, f).

A comparison of the two systems in Fig. 11 indicates a 6 times enhancement in η_{NW} can be obtained experimentally (8 times obtained from numerical simulations) [28]. The latter verifying the validity of the employed approach used in this work for fabricating plasmonic silver devices with improved performance by employing both efficient coupling and low loss fabrication methods.

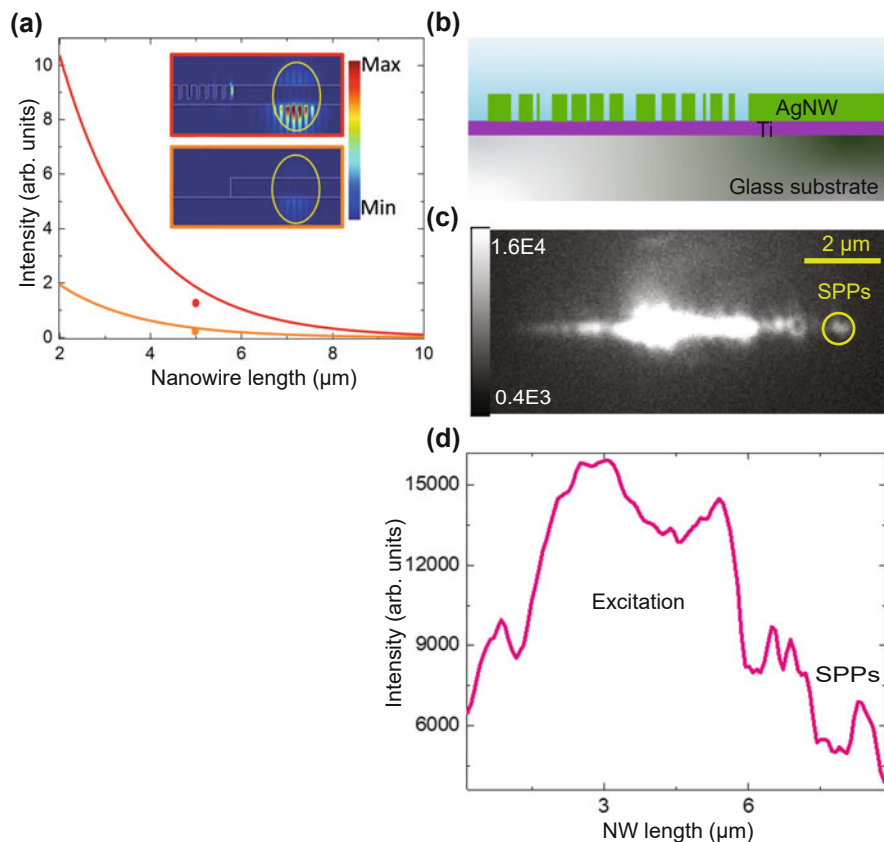


Fig. 10 (a) The coupling efficiency as a function of the LNW length for two different coupling schemes. The dots in (a) present the experimentally obtained results. (b) Schematic illustration of LNW-OGCs system fabricated on a 2nm-Ti adhesion layer. The respective photon emission map and the intensity profile are shown (c) and (d), respectively

5 Effect of Coupling to Nanoemitters

Scalable nanoplasmonic waveguides require efficient on-chip photon sources coupled to integrated plasmonic devices. Combining scalable nanoplasmonic waveguides with on chip photon sources could significantly increase the complexity of the plasmonic nanocircuits. Here, we assess the suitability of the optimized LNW-OGC systems for integrated solid-state quantum systems. To gain an understanding of the physical situation of coupling emitters to LNW and LNW-OGCs, we employ Lumerical solutions FDTD to analyze these systems. For calculation, we represent the NV center by a dipole emitter with an excitation wavelength of $\lambda = 700$ nm and when the dipole is in vacuum [76] and the tabled values of the Ref. [69] was used for the wavelength-dependent dielectric function of silver. The LNW was modeled

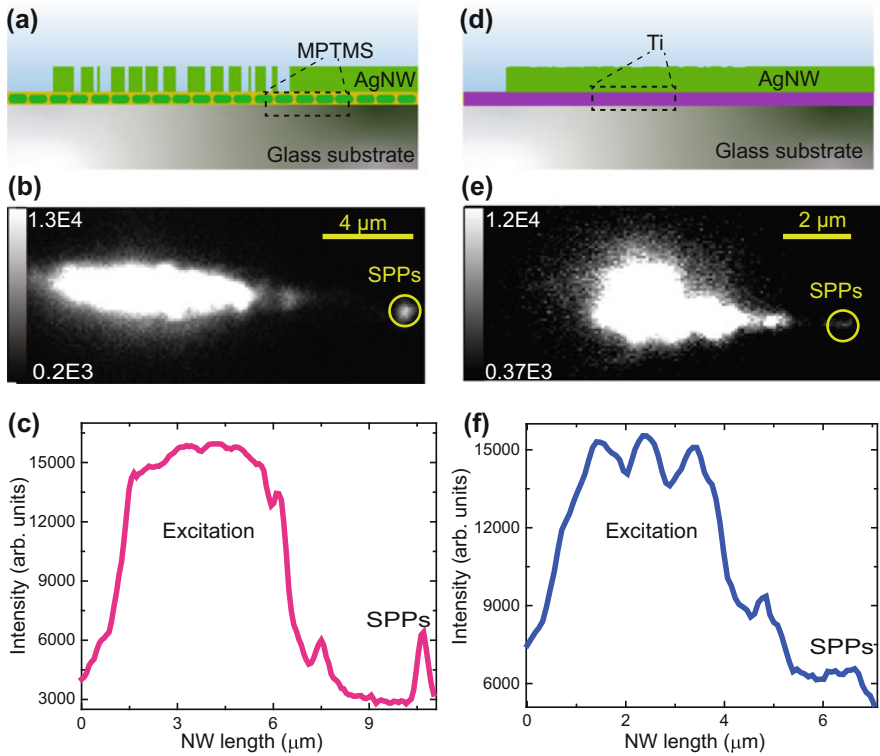


Fig. 11 Optical characterizations of the optimized lithographic nanowires for efficient on-chip plasmonic circuitry. (a) Schematic illustrations for the LNW-OGCs fabricated on the MPTMS pre-treated glass substrate and for the bare NW fabricated on a 2nm-Ti adhesion layer are shown in (a) and (d), respectively. Photon emission maps of the LNW-OGCs in (b) and the bare NW in (e) show the excitation at the left results SPPs at the far end of the NW. The respective intensity profiles are shown in (c) and (f), respectively

as $100 \text{ nm} \times 70 \text{ nm} \times 10 \text{ } \mu\text{m}$ of width, depth, and length, respectively. We defined the emitter position at $0.5 \text{ } \mu\text{m}$ away from the edge of the LNW along z -direction and at the middle of the width ($x = 0$) in such a way to excite SPP modes at the Ag-SiO₂ interface (see Fig. 12), and we measured the resulting I_{sp} .

To validate our optimized grating, we studied the coupling efficiency between dipole emitters and plasmonic waveguides when the OGCs are introduced. Both the LNW (Fig. 12a) and the LNW-OGCs (Fig. 12b) configurations were placed on an MPTMS adhesion layer that functionalized the glass substrates. We defined the enhancement factor when the SPPs are excited with dipole emitter, and when the system comprises grating/no grating couplers as $\eta_{internal}$. The results show the validity of our optimized grating in enhancing the strength of the propagating SPP signal through elevating the coupling mechanism, see Fig. 12a, b. The simulation

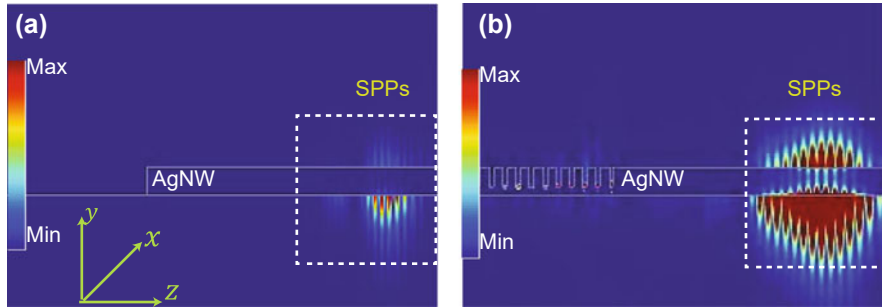


Fig. 12 The time-domain snapshot observed in the two-directional viewer from the FDTD simulations of bound SPP modes propagating at the silver-glass interface showing the effect of coupling the emission of a dipole emitter to propagating SPPs in (a) LNW with end coupling, and (b) LNW-OGCs system. SPPs propagation from left to right along the NW

results show introducing a grating coupler leads to 12.4 times enhancement in $\eta_{internal}$ compared with the case when ND emission coupled to a bare NW only.

To further understand the detailed coupling mechanism of a dipole emitter to the LNW-OGCs system, the effect of spatial variation of the dipole with respect to the plasmonic system is investigated. We probe the coupling efficiency when the position of the emitter is moved with respect to the y & z -axes of each groove in the gratings. We studied the coupling characterizations when the dipole was placed in the first, in the second, or the third grating closer to the edge of the nanowire, as shown in Fig. 13a, and when the dipole was moved vertically upward from the silver.

Figure 13b–d shows the simulation results when the dipole was located at the first grating, second grating, or third grating, respectively. Our results show that by placing the dipole emitter in the first grating and by optimizing the distance from the dipole to the grating, that is along the y -axis, the coupling efficiency from the emitter to the integrated LNW-OGCs system can reach 90% (see Fig. 13b). However, this coupling was reduced drastically when the emitter was placed at the second grating or the third grating away from the LNW edge, as shown in Fig. 13c, d. Furthermore, the influence of the vertical displacement of the emitter on the coupling shows that the highest coupling can be achieved when the emitter is located closer to the metallic surface (red lines in Fig. 13b–d) due to the induced Purcell enhancement in the emission of the nanoemitters [61, 77, 78]. This efficiency was reduced by 50% when we displace the position of the emitter from the optimum position along the y -axis. Accordingly, we designed the first two grating elements such that it can host only one ND of 70 nm in size to be investigated later in the experimental work. Our numerical analyses show that exploiting optimized grating couplers can enable efficient collection of the emitted photons and direct them to the nanocircuits.

To experimentally demonstrate the coupling efficiency of an ND coupled to the optimized LNW-OGCs system shown in Fig. 14a, an aqueous solution of NDs with

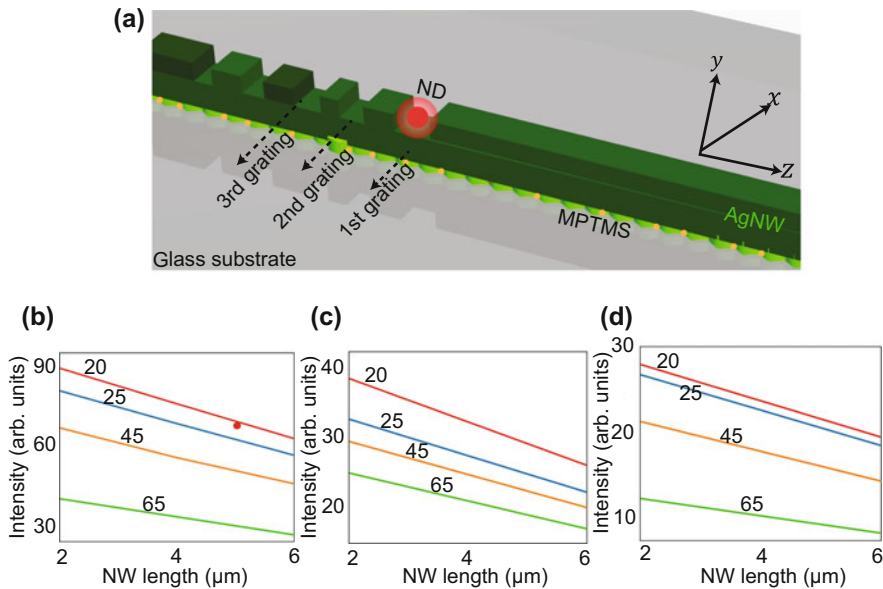


Fig. 13 Characterisation of the coupling between a dipole emitter and the LNW-OGCs system. (a) Schematic of the LNW-OGC system coupled to a dipole source showing a map of the variable displacement of the dipole source. (b–d) Characterization of the coupling between a dipole emitter and the LNW-OGC when the dipole is placed in the first grating, second grating, and third grating, respectively. Distance dependence of the coupling in (b–d), for vertical displacement of 20–65 nm of an emitter away from the metallic surface, shows the coupling of a dipole emitter into the LNW-OGC system can reach 90% when the dipole source is placed at the first grating and 20 nm upwards from the silver surface. The red dot in (b) indicates the experimentally obtained results of coupling the emission of NV center in ND to the LNW-OGC system

an average size of 70 nm was sonicated before being spin-coated, to get large area self-assembled monolayers of NDs, on a glass substrate containing arrays of lithographically fabricated LNW-OGCs. Widefield fluorescence and white light imaging are used to locate an ND located at the first or the second grating close to the edge of the LNW. We used a 532 nm CW green laser to excite a nanodiamond. An EMCCD camera image shows the coupling between an ND and LNW-OGC and subsequent evidence of SPPs emission at the far end of a 5 μm length silver nanowire, see Fig. 14b, c.

By comparing the ratio of the output SPPs intensity to the input excitation intensity (including all the intensities measured at the ND position), based on experimental results, represented by a dot in Fig. 13b, we determine $68.3 \pm 2.50\%$ of the total power being coupled to propagating SPPs supported by the first grating element in the integrated LNW-OGCs system. Furthermore, we performed this experiment on the LNW system (without OGCs). By coupling the emission from an excited ND, located at the end of NW, a scattered SPPs signal at the far end of a 5 μm length LNW was observed. To investigate the effect of the optimized grating on the

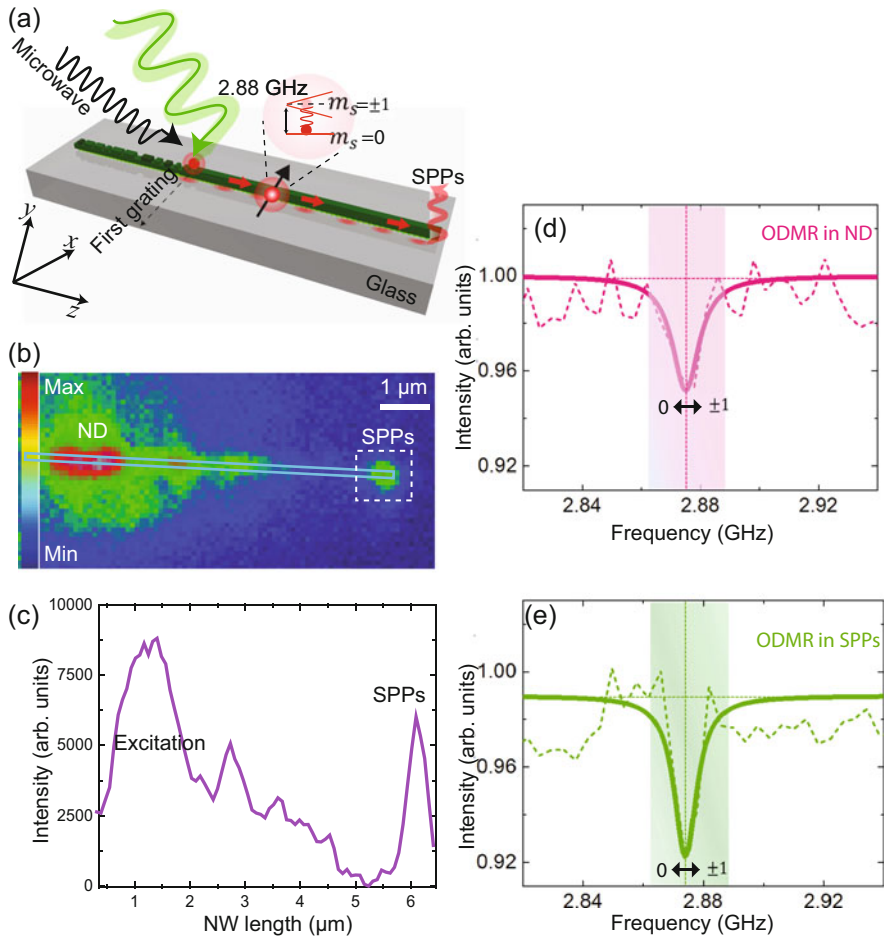


Fig. 14 (a) Schematic of NV center coupled to propagating SPPs along lithographically fabricated LNW-OGCs system based on an MPTMS adhesion layer. The photon emission map and intensity profile for the studied system are shown in (b) and (c), respectively. Measurement of the NV spin-state readout in an ND coupled LNW-OGC system showing a reduction in the photoluminescence intensity in ND emission (d) and a reduction in the SPP scattering strength (e)

coupling efficiency when an internal source (NV center in ND) is implemented for SPPs excitation, we compare $\eta_{internal}$ for both studied systems (i.e. LNW-OGCs and LNW only). Results show enhancement in $\eta_{internal}$ up to a factor of 12.19 ± 0.37 can be obtained. This result is consistent with our simulation result that shows up to 12.4 times enhancement when ND coupled to LNW-OGCs compared to a bare LNW. The LNW-OGCs system we proposed in this work, which utilizes efficient coupling and low loss SPPs, is efficient and significantly smaller than recent demonstrations of plasmonic nanocircuitry with NDs studied in [29, 65]. It also shows the robustness

of our designed grating especially when a quantum emitter is used for excitation instead of a bulky source.

6 Surface Plasmon Detected Magnetic Resonance

The possibility of initialization, manipulation, and readout of the defects' electron spin of the NV center allows its use as a spin qubit or nanoscale magnetometer. The optical readout of the spin states of the NV centers relies on fluorescence intensity measurements. We now assess the integrated LNW-OGCs system when coupled to NV centers, and we investigate the NV center spin states readout after propagating through the plasmonic nanocircuit.

We measure the spin states of the NV centers when coupled and propagated via SPPs along a 5 μm length LNW-OGCs attached MP-TMS pre-treated glass substrates shown schematically in Fig. 14a. We probe the potential of these nanowires to manipulate the NV center magnetic resonance in an integrated device structure by performing the ODMR measurements.

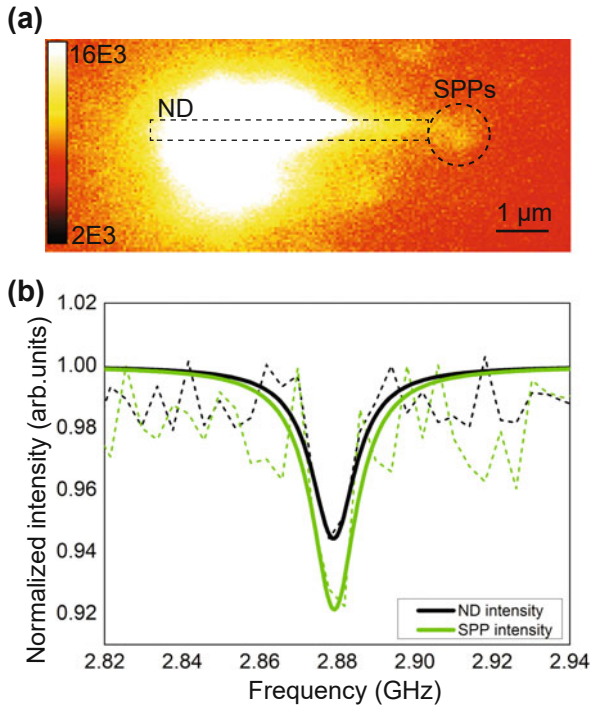
The experiments are performed by combining optical and microwave excitation integrated with optical detection and by using a confocal and a widefield fluorescence microscope system shown in Fig. 4. To excite NV electron spins from the $m_s = 0$ to the $m_s = \pm 1$ states, we used a glass substrate containing a gold microwave antenna in the shape of two triangles that are connected in the middle by a $\approx 20 \mu\text{m}$ gold (Au) microwave antenna (see inset of Fig. 4). This antenna was fabricated at the center of the glass by patterning an Au layer of 75 nm over a Cr layer of 25 nm to allow microwave signals to pass through. The glass substrate is placed onto a programmed circuit board (PCB) sample holder containing two large triangles of copper, with 34.7 μm thickness, to connect the external radio frequency (RF) signal to the gold microwave antenna through silver conductive glue. By connecting two RF coaxial SMA socket panel connectors on both the end side of the PCB, microwave signals from a microwave generator can be passed through the gold antenna from one end to the oscilloscope on the other end. The NDs are continuously excited via a 532 nm CW green laser whilst a microwave frequency around the zero-field resonant transition between the $m_s = 0$ and $m_s = \pm 1$ spin states of the NV center were swept.

We set the microwave signal generator in triggered mode while the microwave signal was amplified by a microwave power amplifier. We synchronized the pulses generated from the microwave generator with the number of the kinetic frames from the EMCCD, as well as the dwell time of each pulse with the exposure time of the EMCCD camera. The acquisition sequence was triggered externally by the signal generator. At each frequency within the sweep, the strength of both the ND emission and the emission from the nanowire ends are monitored. The measurements were repeated 10 times to determine the mean and error of the ODMR contrast, linewidth, and resonant frequency. The ODMR spectra from the ND emission (Fig. 14d) and

the SPPs scattering (Fig. 14e) are fit with the Lorentzian function to determine the quality of the resonance before and after propagating along the LNW-OGCs.

By investigating the measured and best-fit data in Fig. 14d, e, a comparison between the ODMR spectra of the ND emission and that of the scattered SPPs signal in LNW-OGCs system can be obtained. In both cases, we observe a reduction in the SPP scattering intensity at a frequency of ≈ 2.875 GHz similar to the reduction observed in the ND emission. Further, the linewidth of the resonance dip in the SPP spectra matches that in the ODMR spectra with an average value of 10 MHz. Furthermore, the percentage change in the contrast between the SPPs scattering signal and ND emission (R_c) of 62.5% is observed when the ND emission is coupled and propagated along the LNW-OGCs system, where $R_c \% = ((R_{cSPP} - R_{cND})/R_{cND})$, R_{cSPP} and R_{cND} represent the ODMR contrast in SPP and ND signals, respectively. These results reveal that the NV center spin readout can be preserved and propagated along lithographically defined SPPs in a similar trend to what we observed before in CSNWs [63]. Also, we have observed improvement in the spin contrast due to an improvement in the signal to noise ratio in the ODMR signal at the far end of the LNW away from the excitation point (where the luminescence of NV centers and autofluorescence of the glass substrate are overlapped). The contrast in LNW-OGC is higher even when compared to coupling ND emission to LNW with no grating, see Fig. 15, which shows R_c of 39% only. The

Fig. 15 Measurement of the NV spin states readout in an ND-LNW coupled system. (a) The photon emission map of the studied system. (b) The reduction in photoluminescence intensity in ND emission and the SPPs intensity indicates the ability to transfer and detect the ODMR signal through the propagation of the SPPs



enhancement in contrast in SPP signal when ND coupled to LNW-OGCs system can be attributed to both noise filtering and directional effect of the optimized gratings.

7 Optomagnetic Plasmonic Circuitry

Plasmonic circuitries play essential roles in the realization of integrated optical circuits. Nonetheless, exploiting plasmonic circuitry for the quantum optical network is depends on resolving some critical issues, such as the implementation of functional components within the limitations imposed by the SPPs propagation loss, and the efficient coupling between nanoscale waveguides. In addition, to achieve functionalized plasmonic circuitry, it is essential to use a simple and efficient lithographic fabrication method. Even with the recent developments in coupling NDs to plasmonic circuitries [29, 65], yet spin manipulation of the NV centers, which is important in applications from quantum computing to imaging and magnetic field sensing, has not been investigated.

Upon having achieved efficient grating coupling and low loss adhesion layer for Ag plasmonic LNWs, a natural step is to employ them to accomplish a significant increase in the complexity of the plasmonic nanocircuit. We have presented that by employing a low-loss fabrication method and an efficient coupling method, we can extend the propagation length of the lithographic silver NWs up to 5 times higher than that using the standard lithography method. Our demonstrated approach could significantly extend the functionalities of the plasmonic circuitries and enable complex plasmonic devices.

Here, we demonstrate that optomagnetic plasmonic circuitry can be used to guide, split and process the ODMR signal from the NV center into different arms. In particular, we demonstrate propagation through a plasmonic splitter as it is an important component for routing, extracting information, and for the on-chip realization of quantum optical networks. The circuit shown in Fig. 3 is numerically simulated to determine the resulting net coefficient (η_{all}) by reading the strength of the power flow of propagating SPPs intensity along the circuitry. We derive a simple expression for η_{all} as, $\eta_{all} = \exp(-1/L_p) z \times \eta \times \eta_{splitter}$, where $\eta_{splitter}$ is the splitter efficiency defined as the relative SPPs intensities at the end of the splitter ports (I_a & I_b), as indicated in Fig. 16a, expressed as a fraction of the relative SPPs intensity at the beginning of the splitter (I_c), i.e. $\eta_{splitter} = (I_a + I_b)/I_c$.

The design characterization of the plasmonic circuitry as a function of the splitter length and offset distance is shown in Fig. 16b, c. A plasmonic splitter consists of an Ag 1×2 port plasmonic element in which coupling occurs at the terminal edge (along the z -direction) in the middle of the width ($x = 0$) of the input port while two output ports are separated with an offset distance h_s . Each output port is designed with an S-bend connecting two straight waveguides having a length of L_s . To couple light into the splitter, we connect the input port to an Ag waveguide of 2 μm length. To investigate the characteristics of the device, we numerically simulate the plasmonic splitter following the work presented in [79]. The slit medium between

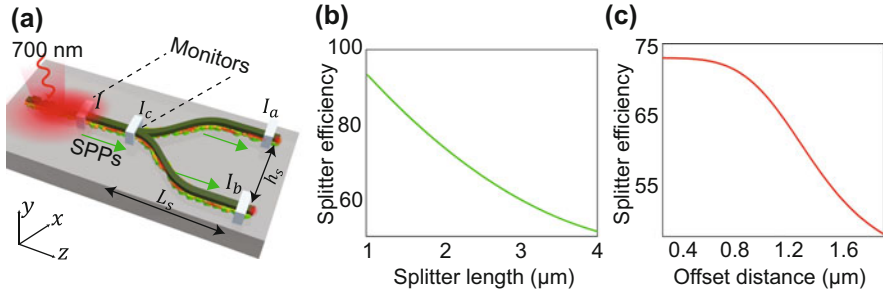


Fig. 16 (a) Schematic of the plasmonic splitter device composed of two mirrored S-bends of $100 \text{ nm} \times 70 \text{ nm}$ of width and thickness, respectively, modeled with FDTD simulations at 700 nm operating wavelength. Monitors are used to reading the power flow along the studied system. (b) Splitter efficiency dependence on the splitter length for a fixed offset distance. (c) Dependence of the Splitter efficiency on the offset distance

the splitter is assumed to be air. Ports with dimensions of 100 nm width and depth of 70 nm are used in our simulations to match the experimental structures. All the results have been calculated for an operating wavelength of 700 nm .

Figure 16b reveals that the $\eta_{splitter}$ may raise up to 94% at splitter length of $1 \mu\text{m}$ however a small L_s cannot assure optical isolation from output ports. Further, it shows that the values of the $\eta_{splitter}$ attenuate rapidly when we increase the splitter length due to the absorption of the metal. The $\eta_{splitter}$ has been investigated by characterizing the beam splitter with a variable offset separation distance between the two output ports. Fig. 16c shows $\eta_{splitter}$ of the plasmonic beam splitter as a function of the offset distance h_s , while L_s is fixed to the optimal value, $L_s = 2 \mu\text{m}$. We observe for a small value of h_s , the splitter shows the best performance. However, gradually increasing h_s beyond $1 \mu\text{m}$ leads to a significant decrease in $\eta_{splitter}$. This is attributed to a significant bend loss that occurs at high values of h_s , which are in good agreement with Ref. [80, 81]. Nonetheless, in our design, we avoid a very small h_s to ensure the optical isolation between the output ports. We perform FDTD simulation to investigate the propagation of the SPPs along the plasmonic splitter when the NV center in ND is used as an internal excitation source. We fixed the orientation of the dipole vertically so it matches the polarization of plasmonic modes supported by the splitter. In order to further investigate the influence of efficient coupling in such a system, we studied the coupled plasmon power when the OGCs are introduced.

Based on our previous results on the optimized design of the grating couplers and fabrication methods, we propose our current system. The propagation of the SPPs before and after being splitted on the plasmonic splitter-optimized grating couplers (PS-OGCs) system is shown in Fig. 17a, b, respectively. Results present enhancement in $\eta_{splitter}$ by a factor of ≈ 5 when the OGCs integrated with the plasmonic splitter compared to the plasmonic splitter with no gratings. Further, numerical analysis reveals that the η_{all} for the demonstrated plasmonic circuitry in Fig. 3 reaches up to 29.5% obtained by integrating the overall efficiency of each component.

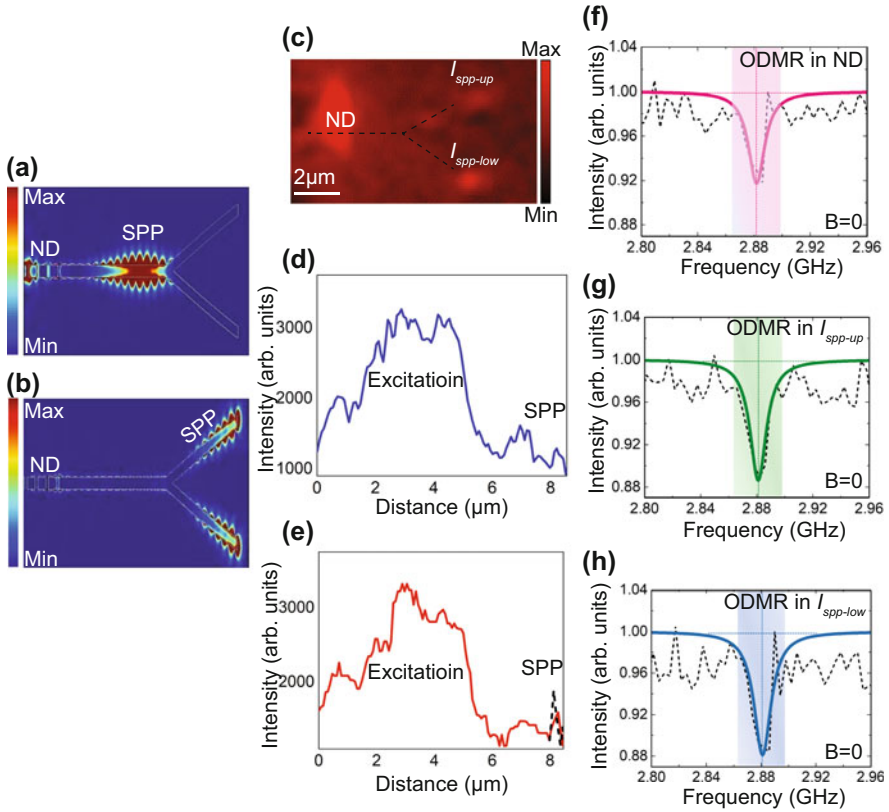


Fig. 17 Plasmonically detected magnetic resonance along an on-chip nanocircuit. **(a, b)** Single frame of the SPP-propagation's video observed in the two-dimensional view from the FDTD simulation of bound SPP modes propagating along the PS-OGCs system showing the SPP power flow before and after being splitted, respectively. **(c)** EMCCD camera image of the plasmonic beam splitter when an ND is excited and the resulting emission at the far end of the splitter ports, confirming the coupling from the NV center to the plasmonic mode. **(d, e)** The intensity profile for the upper and lower ports in the plasmonic splitter-ND coupling system, respectively. The black dashed line in **(e)** indicates the sum of the SPP signal intensity at both ends of the splitter. Measurement of the NV spin-state readout at zero magnetic field ($B = 0$), when coupled to the plasmonic splitter, proves the conservation of the ODMR signal after propagating along the splitter output ports. **(f)** ODMR signal in ND emission, and **(g, h)** Plasmonically detected magnetic resonance signal in the upper and lower output ports of the plasmonic nanosplitter, respectively

The coefficient of the PS-OGC system is experimentally measured. The unsaturated photon emission map (shown in Fig. 17c) and the intensity profile along the splitter ports (I_{spp-up} and $I_{spp-low}$ shown in Fig. 17d, e, respectively) are used to estimate the experimental η_{all} by plotting a line cut of intensity extracted from the widefield fluorescence images starting from the excitation spot. Since in the experiment we can only read the excitation and the out-coupling intensities,

we depend on them for estimating η_{all} . Our experimental results show η_{all} of $27.7 \pm 2.3\%$ can be obtained in the studied PS-OGCs system which is 4 times higher compared to the case when ND coupled to the plasmonic splitter with no gratings.

As a major aim of this work is to develop prototype sensitive yet compact integrated magnetometry systems based on the SPPs, we investigated the ability of the demonstrated plasmonic circuitry to guide and process the NV center spin state readouts when coupled and propagated through the nanocircuit. In the experimental investigation, a 532 nm laser was employed to excited an ND coupled with the integrated PS-OGCs. We performed ODMR measurements and monitored the emission from the ND at the excitation area and the scattered SPPs at the far ends of the splitter. We observed the characteristics of the ODMR spectra in the ND emission (as shown in Fig. 17f) and the SPPs scattering strength (as shown in Fig. 17g and h) with a reduction in the SPPs intensity at an applied microwave frequency of 2.88 GHz, matching that in the photoluminescence spectra of the NV center.

In addition, the line width of the magnetic resonance remains consistent at ≈ 14 MHz for the ND and SPPs at both splitter's ends. We defined the change in the contrast between the SPPs scattering signal at both ends of the splitter and the ND emission as; $((R_{cSPP-up} - R_{cND})/R_{cND})$ and $((R_{cSPP-low} - R_{cND})/R_{cND})$, where $R_{cSPP-up}$ and $R_{cSPP-low}$ represent the ODMR contrast in the SPPs in the upper and the lower ports of the splitter, respectively. Our results show the change in the contrast between the SPP signals and ND emission are improved by a factor of 38% and 40% in the upper and lower splitter ports, respectively. These attributes mark a critical point in utilizing the NV centers for various emergent quantum technologies.

8 Conclusions

Plasmonic nanocircuits play a crucial role in constructing highly integrated nanophotonic circuits beyond the diffraction limit for future quantum information, secure communication, and sensing applications. Nonetheless, developing multifunction plasmonic nano circuitries for such applications is depends on resolving some critical issues, such as the implementation of functional components within the limitations imposed by the SPPs propagation loss, and the efficient coupling between nanoscale elements. One area that depends on a solution to these challenges is the coupling of quantum emitters to plasmonic devices. Such systems can be utilized to extend the applications of quantum emitters such as NDs and yield a great platform for the realization of an on-chip quantum information network.

This chapter reviewed both the theoretical and experimental investigations of the lithographic nanoplasmonic waveguides under differents fabrication and excitation conditions. Following the theoretical investigation, we propose the idea of exploiting MPTMS as an adhesion layer in fabricating multifunction plasmonic circuitry instead of a metallic adhesion layer to increase the propagation length of propagating SPPs by reducing damping losses. We also demonstrate an optimized design for nanograting couplers that has the potential for integration and combination

with other plasmonic components to further improve coupling efficiency. Our experimental results show that using the MPTMS as an adhesion layer can increase the plasmon propagation length by a factor of up to 5 times when the MPTMS adhesion layer is used compared to the Ti-based system. These results demonstrate that adding a thin metallic embedding layer of a Ti limits the propagation length of the SPPs, and showing that MPTMS is the better adhesion layer for lithographic fabrication of plasmonic silver nanowaveguides.

Besides, results demonstrate a 5.2 times improvement in the coupling efficiency by introducing OGCs to the LNW. By solving the challenges of the low loss fabrication method and the efficient coupling scheme, our results show the resulting coefficient in our system can be enhanced up to 8 times compared with the case when SPPs are excited along NW that is fabricated using the traditional lithographic method and excited by end coupling. Further, the lithographic systems have been explored when coupled to NV centers in NDs. Experimental results show that 68.3% of the total power being coupled to propagating SPPs when the emission from an excited ND is coupled to LNW-OGCs system. Furthermore, our results show that we can enhance the coupling efficiency by up to 12.4 times compared to the case when ND is coupled to NW only.

This may lead to the construction of efficient nanoscale devices, allowing the long-distance transfer of energy for an on-chip integrated quantum information processing system.

We demonstrate on-chip optomagnetic plasmonic circuitry based on efficient NWs for directing and processing the spin state readouts of NV centers. The implementation of the plasmonic splitter, comprising an ND as the single-photon source, for reading and routing the spin states signal from the NV center serves as a basis for a more complex system and has been motivated for broadening the application of NDs in versatile sensing applications. Our experimental results show the conservation of the NV center spin state readouts after propagation and splitting through the circuitry. We investigate the ODMR signals along the nanoplasmonic splitter to prove the concept. Nonetheless, our innovative technique is robust, scalable and easy, and moreover, can be applied to various plasmonic waveguides. Our promising simulation results show bound SPP modes propagating along a highly compact Mach-Zehnder interferometer (shown schematically in Fig. 18a with the corresponding scanning electron microscope image in Fig. 18b) when NV center in ND is used as an internal excitation source. FDTD results in Fig. 18c and d show that this method can be utilized to extend the functionality of such plasmonic devices for advanced signal analysis and processing, leading the way to exploring the benefit of NDs in a versatile range of sensing applications and for the practical realization of on-chip quantum networks.

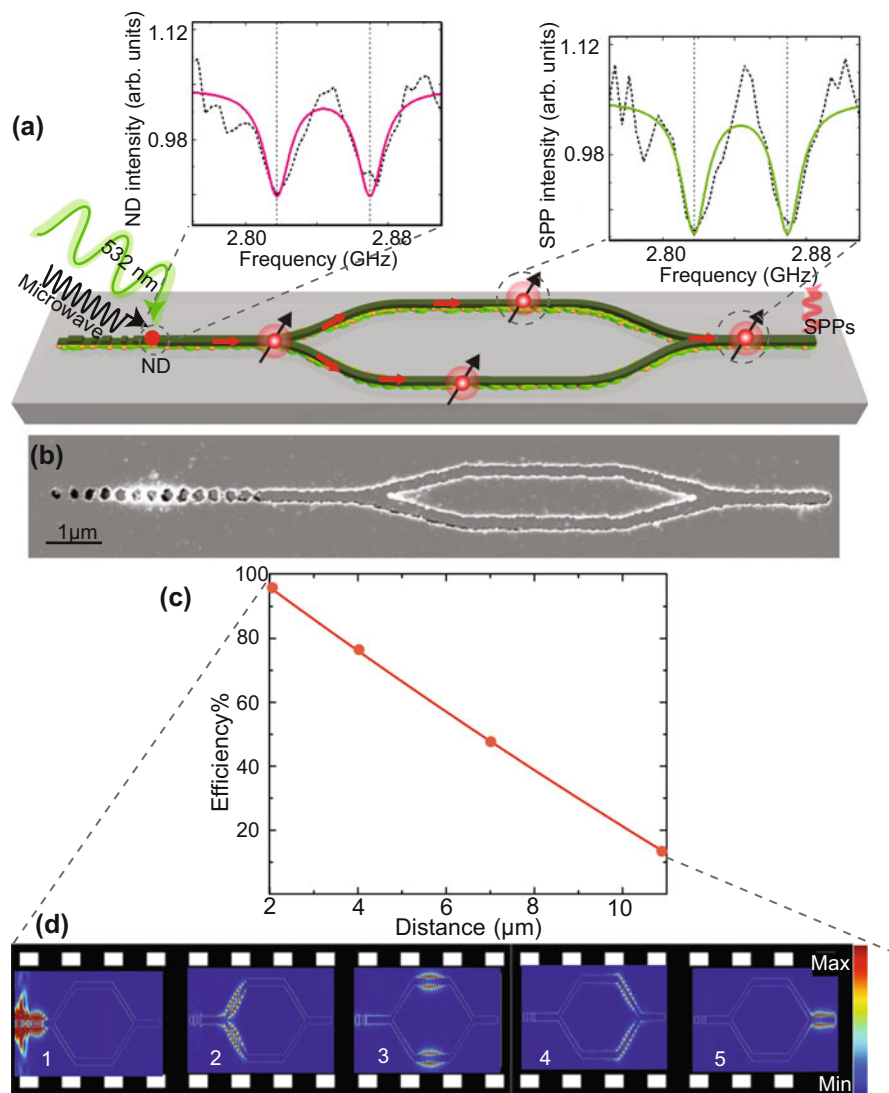


Fig. 18 (a) Schematic illustration of a chip-scale plasmonic Mach Zehnder interferometer integrated with our OGCs and coupled to an ND containing single photon emitter. Inset shows ODMR signals at $B \neq 0$. (b) A scanning electron microscope image of fabricated plasmonic nanocircuit on an MPTMS functionalized glass surface. (c, d) FDTD simulation of bound SPP modes propagating along 11 μm length multifunction plasmonic circuitry showing the SPPs power flow along each part of the circuit. SPPs propagation from left to right along the nanocircuit

Acknowledgments This work is part of the research program funded by the Australian Research Council Centre of Excellence for Ultrahigh Bandwidth Devices for Optical Systems (project number CE110001018).

References

1. Zia, R., Schuller, J. A., Chandran, A., & Brongersma, M. L. (2006). Plasmonics: The next chip-scale technology. *Materials Today*, *9*, 20–27.
2. Anwar, R. S., Ning, H., & Mao, L. (2018). Recent advancements in surface plasmon polaritons-plasmonics in subwavelength structures in microwave and terahertz regimes. *Digital Communications and Networks*, *4*, 244–257.
3. Bozhevolnyi, S. I. (2009). *Plasmonic nanoguides and circuits*. Pan Stanford.
4. Pitarke, J. M., Silkin, V. M., Chulkov, E. V., & Echenique, P. M. (2007). Theory of surface plasmons and surface-plasmon polaritons. *Reports on Progress in Physics*, *70*, 1–87.
5. Maier, S. A. (2007). *Plasmonics: Fundamentals and applications*. Springer.
6. Drude, P. (1900). Zur Elektronentheorie der metalle. *Annalen der Physik*, *306*, 566–613.
7. Huang, C. P., & Zhu, Y. Y. (2007). Plasmonics: Manipulating light at the subwavelength scale. *Active and Passive Electronic Components*, *2007*, 1–13.
8. Inouye, Y., & Kawata, S. (1994). Near-field scanning optical microscope with a metallic probe tip. *Optics Letters*, *19*, 159–161.
9. Economou, E. N. (1969). Surface plasmons in thin films. *Physical Review*, *182*, 539–554.
10. Maier, S. A., Kik, P. G., Atwater, H. A., Meltzer, S., Harel, E., Koel, B. E., et al. (2003). Local detection of electromagnetic energy transport below the diffraction limit in metal nanoparticle plasmon waveguides. *Nature Materials*, *2*, 229–232.
11. Quinten, M., Leitner, A., Krenn, J. R., & Aussenegg, F. R. (1998). Electromagnetic energy transport via linear chains of silver nanoparticles. *Optics Letters*, *23*, 1331–1333.
12. Andrea, A., & Nader, E. (2010). Effect of small random disorders and imperfections on the performance of arrays of plasmonic nanoparticles. *New Journal of Physics*, *12*, 013015.
13. Liu, N., Mukherjee, S., Bao, K., Li, Y., Brown, L. V., Nordlander, P., et al. (2012). Manipulating magnetic plasmon propagation in metallic nanocluster networks. *ACS Nano*, *6*, 5482–5488.
14. Steinberger, B., Hohenau, A., Ditzbacher, H., Aussenegg, F. R., Leitner, A., & Krenn, J. R. (2007). Dielectric stripes on gold as surface plasmon waveguides: Bends and directional couplers. *Applied Physics Letters*, *91*, 081111.
15. Briggs, R. M., Grandidier, J., Burgos, S. P., Feigenbaum, E., & Atwater, H. A. (2010). Efficient coupling between dielectric-loaded plasmonic and silicon photonic waveguides. *Nano Letters*, *10*, 4851–4857.
16. Tanaka, K., Tanaka, M., & Sugiyama, T. (2005). Simulation of practical nanometric optical circuits based on surface plasmon polariton gap waveguides. *Optics Express*, *13*, 256–266.
17. Jung, K. Y., Teixeira, F. L., & Reano, R. M. (2009). Surface plasmon coplanar waveguides: Mode characteristics and mode conversion losses. *IEEE Photonics Technology Letters*, *21*, 630–632.
18. Ming, Y., Zi-jian, W., Hao, W., Fei, X., & Lu, Y.-q. (2012). Surface plasmon interferometer based on wedge metal waveguide and its sensing applications. *IEEE Photonics Journal*, *4*, 291–299.
19. Boardman, A. D., Aers, G. C., & Teshima, R. (1981). Retarded edge modes of a parabolic wedge. *Physical Review B*, *24*, 5703–5712.
20. Bozhevolnyi, S. I., Volkov, V. S., Devaux, E., & Ebbesen, T. W. (2005). Channel plasmon-polariton guiding by subwavelength metal grooves. *Physical Review Letters*, *95*, 046802.
21. Wang, K., & Mittleman, D. M. (2006). Dispersion of surface plasmon polaritons on metal wires in the terahertz frequency range. *Physical Review Letters*, *96*, 157401.
22. Sanders, A. W., Routenberg, D. A., Wiley, B. J., Xia, Y., Dufresne, E. R., & Reed, M. A. (2006). Observation of plasmon propagation, redirection, and fan-out in silver nanowires. *Nano Letters*, *6*, 1822–1826.
23. Ditzbacher, H., Hohenau, A., Wagner, D., Kreibig, U., Rogers, M., Hofer, F., et al. (2005). Silver nanowires as surface plasmon resonators. *Physical Review Letters*, *95*, 257403.
24. Fang, Y., Wei, H., Hao, F., Nordlander, P., & Xu, H. (2009). Remote-excitation surface-enhanced Raman scattering using propagating Ag nanowire plasmons. *Nano Letters*, *9*, 2049–2053.

25. Amirhosseini, A., & Safian, R. (2013). A hybrid plasmonic waveguide for the propagation of surface plasmon polariton at 1.55 μm on SOI substrate. *IEEE Transactions on Nanotechnology*, *12*, 1031–1036.
26. Gramotnev, D. K., & Bozhevolnyi, S. I. (2010). Plasmonics beyond the diffraction limit. *Nature Photonics*, *4*, 83–91.
27. Oulton, R. F., Sorger, V. J., Genov, D. A., Pile, D. F. P., & Zhang, X. (2008). A hybrid plasmonic waveguide for subwavelength confinement and long-range propagation. *Nature Photonics*, *2*, 496–500.
28. Al-Baiaty, Z., Cumming, B. P., Gan, X., & Gu, M. (2019). Optomagnetic plasmonic nanocircuits. *Nanoscale Advances*, *1*, 3131–3138.
29. Bermúdez-Ureña, E., Gonzalez-Ballester, C., Geiselmann, M., Marty, R., Radko, I. P., Holmgaard, T., et al. (2015). Coupling of individual quantum emitters to channel plasmons. *Nature Communications*, *6*, 7883.
30. Smith, C. L. C., Thilsted, A. H., Garcia-Ortiz, C. E., Radko, I. P., Marie, R., Jeppesen, C., et al. (2014). Efficient excitation of channel plasmons in tailored, UV-lithography-defined V-grooves. *Nano Letters*, *14*, 1659–1664.
31. Chen, Z.-x., Wu, Z.-j., Ming, Y., Zhang, X.-j., & Lu, Y.-q. (2014). Hybrid plasmonic waveguide in a metal V-groove. *AIP Advances*, *4*, 017103.
32. Luo, Y., Chamanzar, M., Apuzzo, A., Salas-Montiel, R., Nguyen, K. N., Blaize, S., et al. (2015). On-chip hybrid photonic-plasmonic light concentrator for nanofocusing in an integrated silicon photonics platform. *Nano Letters*, *15*, 849–856.
33. Bozhevolnyi, S. I., Volkov, V. S., Devaux, E., Laluet, J.-Y., & Ebbesen, T. W. (2006). Channel plasmon subwavelength waveguide components including interferometers and ring resonators. *Nature*, *440*, 508–511.
34. Fang, Y., & Sun, M. (2015). Nanoplasmonic waveguides: Towards applications in integrated nanophotonic circuits. *Light: Science & Applications*, *4*, 1–11.
35. Kumar, S., Kristiansen, N. I., Huck, A., & Andersen, U. L. (2014). Generation and controlled routing of single plasmons on a chip. *Nano Letters*, *14*, 663–669.
36. Dickson, R. M., & Lyon, L. A. (2000). Unidirectional plasmon propagation in metallic nanowires. *The Journal of Physical Chemistry B*, *104*, 6095–6098.
37. Desalegn, D., Pijush, G., David, F., & Joseph, H. (2017). Surface plasmon damping effects due to Ti adhesion layer in individual gold nanodisks. *Optical Materials Express*, *7*, 73–84.
38. Shen, H., Guillot, N., Rouxel, J., Lamy de la Chapelle, M., & Toury, T. (2012). Optimized plasmonic nanostructures for improved sensing activities. *Optics Express*, *20*, 21278–21290.
39. Habteyes, T. G., Dhuey, S., Wood, E., Gargas, D., Cabrini, S., Schuck, P. J., et al. (2012). Metallic adhesion layer induced plasmon damping and molecular linker as a nondamping alternative. *ACS Nano*, *6*, 5702–5709.
40. Sukham, J., Takayama, O., Lavrinenko, A. V., & Malureanu, R. (2017). High-quality ultrathin gold layers with an APTMS adhesion for optimal performance of surface plasmon polariton-based devices. *ACS Applied Materials & Interfaces*, *9*, 25049–25056.
41. Jeppesen, C., Mortensen, N. A., & Kristensen, A. (2010). The effect of Ti and ITO adhesion layers on gold split-ring resonators. *Applied Physics Letters*, *97*, 263103.
42. Aouani, H., Wenger, J., Gérard, D., Rigneault, H., Devaux, E., Ebbesen, T. W., et al. (2009). Crucial role of the adhesion layer on the plasmonic fluorescence enhancement. *ACS Nano*, *3*, 2043–2048.
43. Aramesh, M., Cervenka, J., Roberts, A., Djalalian-Assl, A., Rajasekharan, R., Fang, J., et al. (2014). Coupling of a single-photon emitter in nanodiamond to surface plasmons of a nanochannel-enclosed silver nanowire. *Optics Express*, *22*, 15530–15541.
44. Budker, D. (2011). Diamond nanosensors: The sense of colour centres. *Nature Physics*, *7*, 453–454.
45. Roger, J., Jan, L., Michael, M., Daniel, S., Sébastien, P., & Jan, M. (2017). Bright optical centre in diamond with narrow, highly polarised and nearly phonon-free fluorescence at room temperature. *New Journal of Physics*, *19*, 053008.

46. Kaur, R., & Badea, I. (2013). Nanodiamonds as novel nanomaterials for biomedical applications: Drug delivery and imaging systems. *International Journal of Nanomedicine*, *8*, 203–220.
47. Horowitz, V. R., Alemán, B. J., Christle, D. J., Cleland, A. N., & Awschalom, D. D. (2012). Electron spin resonance of nitrogen-vacancy centers in optically trapped nanodiamonds. *Proceedings of the National Academy of Sciences*, *109*, 13493–13497.
48. Jelezko, F., Gaebel, T., Popa, I., Gruber, A., & Wrachtrup, J. (2004). Observation of coherent oscillations in a single electron spin. *Physical review letters*, *92*, 076401.
49. Doherty, M. W., Manson, N. B., Delaney, P., Jelezko, F., Wrachtrup, J., & Hollenberg, L. C. L. (2013). The nitrogen-vacancy colour centre in diamond. *Physics Reports*, *528*, 1–45.
50. Neumann, P., Kolesov, R., Jacques, V., Beck, J., Tisler, J., Batalov, A., et al. (2009). Excited-state spectroscopy of single NV defects in diamond using optically detected magnetic resonance. *New Journal of Physics*, *11*, 013017.
51. Childress, L., Gurudev Dutt, M. V., Taylor, J. M., Zibrov, A. S., Jelezko, F., Wrachtrup, J., et al. (2006). Coherent dynamics of coupled electron and nuclear spin qubits in diamond. *Science*, *314*, 281–285.
52. Degen, C. (2008). Scanning magnetic field microscope with a diamond single-spin sensor. *Applied Physics Letters*, *92*, 243111.
53. Maze, J. R., Stanwix, P. L., Hodges, J. S., Hong, S., Taylor, J. M., Cappellaro, P., et al. (2008). Nanoscale magnetic sensing with an individual electronic spin in diamond. *Nature*, *455*, 644–647.
54. Balasubramanian, G., Chan, I. Y., Kolesov, R., Al-Hmoud, M., Tisler, J., Shin, C., et al. (2008). Nanoscale imaging magnetometry with diamond spins under ambient conditions. *Nature*, *455*, 648–651.
55. Maurer, P. C., Kucsko, G., Latta, C., Jiang, L., Yao, N. Y., Bennett, S. D., et al. (2012). Room-temperature quantum bit memory exceeding one second. *Science*, *336*, 1283–1286.
56. Dutt, M. V., Childress, L., Jiang, L., Togan, E., Maze, J., Jelezko, F., et al. (2007). Quantum register based on individual electronic and nuclear spin qubits in diamond. *Science*, *316*, 1312–1316.
57. Choy, J. T., Hausmann, B. J. M., Babinec, T. M., Bulu, I., Khan, M., Maletinsky, P., et al. (2011). Enhanced single-photon emission from a diamond-silver aperture. *Nature Photonics*, *5*, 738–743.
58. Bourgeois, E., Jarmola, A., Siyushev, P., Gulka, M., Hruby, J., Jelezko, F., et al. (2015). Photoelectric detection of electron spin resonance of nitrogen-vacancy centres in diamond. *Nature Communications*, *6*, 8577.
59. Bray, K., Previdi, R., Gibson, B. C., Shimoni, O., & Aharonovich, I. (2015). Enhanced photoluminescence from single nitrogen-vacancy defects in nanodiamonds coated with phenolic complexes. *Nanoscale*, *7*, 4869–4874.
60. Schietinger, S., Barth, M., Aichele, T., & Benson, O. (2009). Plasmon-enhanced single photon emission from a nanoassembled metal-diamond hybrid structure at room temperature. *Nano Letters*, *9*, 1694–1698.
61. Huck, A., Kumar, S., Shakoor, A., & Andersen, U. L. (2011). Controlled coupling of a single nitrogen-vacancy center to a silver nanowire. *Physical Review Letters*, *106*, 096801.
62. Schell, A. W., Kewes, G., Hanke, T., Leitenstorfer, A., Bratschitsch, R., Benson, O., et al. (2011). Single defect centers in diamond nanocrystals as quantum probes for plasmonic nanostructures. *Optics Express*, *19*, 7914–7920.
63. Al-Baiaty, Z., Cumming, B. P., Gan, X., & Gu, M. (2018). Detection of the ODMR signal of a nitrogen vacancy centre in nanodiamond in propagating surface plasmons. *Journal of Optics*, *20*, 035001.
64. Kusar, P., Gruber, C., Hohenau, A., & Krenn, J. R. (2012). Measurement and reduction of damping in plasmonic nanowires. *Nano Letters*, *12*, 661–665.

65. Siampour, H., Kumar, S., & Bozhevolnyi, S. I. (2017). Nanofabrication of plasmonic circuits containing single photon sources. *ACS Photonics*, *4*, 1879–1884.
66. Siampour, H., Kumar, S., Davydov, V. A., Kulikova, L. F., Agafonov, V. N., & Bozhevolnyi, S. I. (2018). On-chip excitation of single germanium vacancies in nanodiamonds embedded in plasmonic waveguides. *Light: Science & Applications*, *7*, 61.
67. Holmgaard, T., & Bozhevolnyi, S. I. (2007). Theoretical analysis of dielectric-loaded surface plasmon-polariton waveguides. *Physical Review B*, *75*, 245405.
68. Wang, W., Yang, Q., Fan, F., Xu, H., & Wang, Z. L. (2011). Light propagation in curved silver nanowire plasmonic waveguides. *Nano Letters*, *11*, 1603–1608.
69. Johnson, P. B., & Christy, R. W. (1972). Optical constants of the noble metals. *Physical Review B*, *6*, 4370–4379.
70. Pfaff, W., Vos, A., & Hanson, R. (2013). Top-down fabrication of plasmonic nanostructures for deterministic coupling to single quantum emitters. *Journal of Applied Physics*, *113*, 024310.
71. Colas, F., Barchiesi, D., Kessentini, S., Toury, T., & Chapelle, M. L. (2015). Comparison of adhesion layers of gold on silicate glasses for SERS detection. *Journal of Optics*, *17*, 114010.
72. Pushkar, K. G., Dhruv, G., & Venu Gopal, A. (2018). MPTMS self-assembled monolayer deposition for ultra-thin gold films for plasmonics. *Journal of Physics Communications*, *2*, 035005.
73. Mahapatro, A. K., Scott, A., Manning, A., & Janes, D. B. (2006). Gold surface with sub-nm roughness realized by evaporation on a molecular adhesion monolayer. *Applied Physics Letters*, *88*, 151917.
74. Lamy de la Chapelle, M., Shen, H., Guillot, N., Frémaux, B., Guelorget, B., & Toury, T. (2013). New gold nanoparticles adhesion process opening the way of improved and highly sensitive plasmonics technologies. *Plasmonics*, *8*, 411–415.
75. Goss, C. A., Charych, D. H., & Majda, M. (1991). Application of (3-mercaptopropyl)trimethoxysilane as a molecular adhesive in the fabrication of vapor-deposited gold electrodes on glass substrates. *Analytical Chemistry*, *63*, 85–88.
76. Martín-Cano, D., Martín-Moreno, L., García-Vidal, F. J., & Moreno, E. (2010). Resonance energy transfer and superradiance mediated by plasmonic nanowaveguides. *Nano Letters*, *10*, 3129–3134.
77. Akimov, A. V., Mukherjee, A., Yu, C. L., Chang, D. E., Zibrov, A. S., Hemmer, P. R., et al. (2007). Generation of single optical plasmons in metallic nanowires coupled to quantum dots. *Nature*, *450*, 402–406.
78. Barthes, J., Bouhelier, A., Dereux, A., & Francs, G. C. (2013). Coupling of a dipolar emitter into one-dimensional surface plasmon. *Scientific Reports*, *3*, 2734.
79. Kumar, A., & Aditya, S. (1998). Performance of S-bends for integrated-optic waveguides. *Microwave and Optical Technology Letters*, *19*, 289–292.
80. Holmgaard, T., Bozhevolnyi, S. I., Markey, L., & Dereux, A. (2008). Dielectric-loaded surface plasmon-polariton waveguides at telecommunication wavelengths: excitation and characterization. *Applied Physics Letters*, *92*, 011124.
81. Holmgaard, T., Chen, Z., Bozhevolnyi, S. I., Markey, L., Dereux, A., Krasavin, A. V., et al. (2008). Bend- and splitting loss of dielectric-loaded surface plasmon-polariton waveguides. *Optics Express*, *16*, 13585–13592.

Recent Advances and Opportunities of Plasmonic Sensors



B. Bhagat, K. Mehta, T. K. Sinha, P. K. Baruah, and K. Mukherjee

Abstract The Surface Plasmon Resonance (SPR) associated with metallic nanoparticles, noble metals in particular, have revolutionised the field of sensing technology. Plasmonic sensing has made its presence felt in a big way in the areas related to biosensors, chemical sensors, etc. The plasmonic response of a material is strongly dependent on its size, structure, and even the surrounding medium, so that any material with different morphologies can possess varying plasmonic wavelengths ranging from the ultraviolet to the far infra-red. Very recently, there has been an upsurge in the number of applications of plasmonic materials in the domain of various sensing technologies. These developments have brought about rapid advances in applications like plasmon-enhanced fluorescence, surface enhanced Raman spectroscopy, tip-enhanced Raman spectroscopy, photocatalysis, photo-acoustics, solar cells and nonlinear optics, etc. In the present review, we highlight some of the most recent developments in the field of plasmon-based sensors and its applications. The impact of such sensors in the detection of biomolecules as well as in environmental monitoring is also assessed in this review. The chapter ends with a discussion on the possible challenges and based on it an outlook is presented.

Keywords Plasmonic sensor · Surface Plasmon Resonance · Nanoparticles · Noble metals

B. Bhagat · K. Mukherjee (✉)

Department of Chemistry, Pandit Deendayal Energy University, Gandhinagar, Gujarat, India
e-mail: kalisadhan.mukherjee@sot.pdpu.ac.in

K. Mehta · P. K. Baruah (✉)

Department of Physics, Pandit Deendayal Energy University, Gandhinagar, Gujarat, India
e-mail: prahlad.baruah@sot.pdpu.ac.in

T. K. Sinha

Department of Materials Engineering and Convergence Technology, Gyeongsang National University, Jinju, South Korea

1 Preamble on Plasmonic Sensor

The metallic nanostructures, in particular, noble metals like gold and silver are drawing significant research interest in the field of chemistry, physics, biology, material sciences, etc. [1–4]. As per the data (i.e., number of published documents) available at Scopus (dated June 6, 2021) with the keyword “plasmonic”, a testimony in support to the aforementioned immense applicability of the nanostructured plasmonic materials is represented as the documents published per year (Fig. 1a) as well as the documents reported from different countries (Fig. 1b).

The bright prospects of these materials have paved the way for its indispensable role in various sensing applications like metal-enhanced fluorescence (MEF), surface enhanced Raman scattering (SERS), surface plasmon resonance (SPR) based sensors, etc. [5–8]. These materials exhibit excellent electronic, optical and catalytic properties which can be easily tuned by varying the size, shape and the surrounding dielectric medium [9–11].

Apart from the various interesting properties of these noble metal nanostructures, the most notable and important is the surface plasmon resonance (SPR). SPR is a collective oscillation of the surface electrons when an external electromagnetic field (for example, light) is incident on the surface. Materials that possess a negative real and a small positive imaginary dielectric constant can, in principle, support SPR [12–14]. In short, the plasmonic nanomaterials are a special class of nanostructured materials whose electron density in the interface between the particles and dielectric medium can interact with the incident light (electromagnetic radiation) having a wavelength larger than the particle size. The term “plasmon” is the oscillation of free electrons that arises as a consequence of the dipoles formed due to the light-matter interaction. These special features of the plasmonic nanomaterial have been exploited in various applications like sensing, electronics,

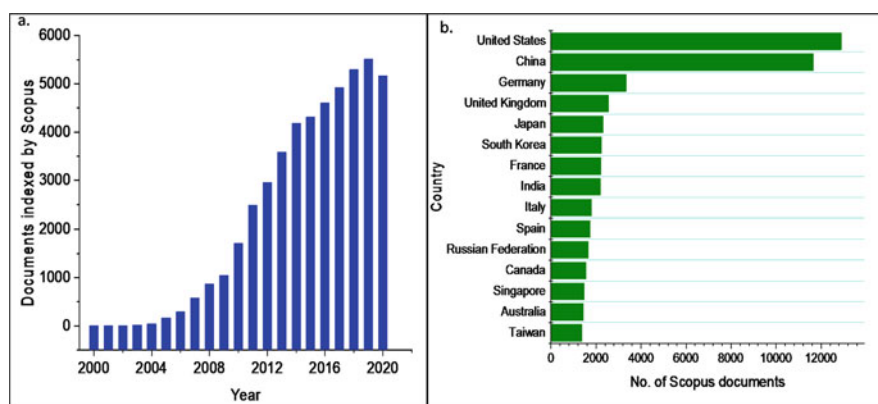


Fig. 1 Number of documents published with the keyword “Plasmonic” (a) Year wise, (b) Country wise. (Source: Scopus)

medicine, etc. The advances in fabrication methodologies in recent times have facilitated the development of new plasmonic materials as well as the manipulation (structural and morphological) of other metallic nanostructures including nanoparticles, nanoprisms, nanocubes, etc. [15–17]. Over the years, with the improvements in the tools and theories to study the electromagnetic coupling in materials, there has also been a drastic improvement in the understanding of the optical properties of plasmonic materials towards fast forwarding their binding and detection efficacy for various targets needed to advance the area of biological and chemical sensing [18, 19].

The plasmons in SPR can be either propagating or localized. In the former case which is commonly termed as surface plasmon polaritons, the propagation of the plasmons occur in the x- and y-directions along the interface of a metal and a dielectric [12, 20]. The plasmons propagate for longer distances upto hundreds of microns and decay in the z-direction. In the latter case, which is known as the localized surface plasmons, the incident electromagnetic fields interacts with nanoparticles having size less than that of the incident wavelength [12, 21, 22]. In this case, there are collective oscillations of the plasmons around the nanoparticle with a frequency which is known as the localized surface plasmon resonance (LSPR). The difference between the propagating SPR and LSPR is schematically represented in Fig. 2a, b [12].

Sensors that are based on propagating SPR usually have higher refractive index sensitivity but have issues like reflection associated with it that may reduce its sensitivity in devices. Similarly, although the refractive index sensitivity of LSPR based sensors is less than that of its propagating counterpart the LSPR based sensors are more sensitive towards molecular binding. Hence, depending on the interest of application, either of propagating or localized SPR is chosen.

The processing of the nanomaterials in desired shape, size and morphology, biocompatibility, cost-effectiveness, and reproducibility have made plasmonic sensors suitable to be applied for the detection of various analytes [23–26]. The metallic nanostructures via its plasmonic resonances can greatly increase the light-matter interactions due to the spatial confinement of optical field in the nano-domain. Following the significant improvements in the area of plasmonic sensors, currently the conventional instruments are being upgraded towards more portable devices using nanomaterials, smartphones, etc. [27, 28] In fact, the development of smartphone-based plasmonic sensor has been a significant landmark in the biosensing technology and lab-on-chip platform [29–31]. This has enabled the plasmonic sensors effective for onsite monitoring of environmental pollutants, pathogenic biomolecules, food quality, etc. For the optimum utilization of plasmonic sensors, there has to be proper integration of the plasmonic materials with the optical components, surface chemistry, detection systems, etc. [32–34].

Viewing the aforementioned applications as well as opportunities of plasmonic sensors it seems important to review the recent advances in this domain. There are numerous reports on various plasmonic sensors in literature. However, one may find these reports scattered and thus may not be concise and comprehensive to beginners in this field. As one lecture note article, the present article starts the description of

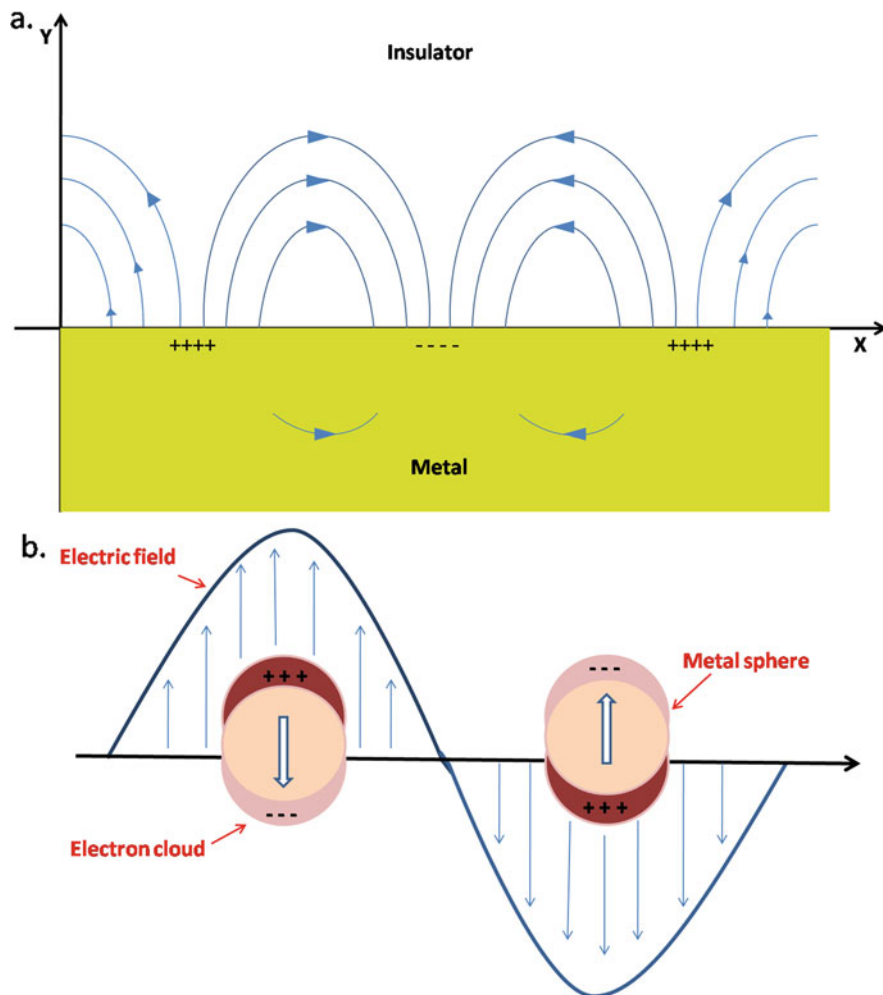


Fig. 2 Surface plasmon resonance (a) Propagating (b) Localized

various conventional as well as hybrid plasmonic materials. Thereafter, the synthesis methodologies of different plasmonic materials followed by the recent advances in the field of plasmonic sensors are described citing relevant research activities.

2 Introduction on Plasmonic Materials

It has already been discussed that nanomaterials which show surface plasmon resonance (SPR) under the exposure of light are collectively known as plasmonic nanomaterials [35]. Noble metals based plasmonic materials are attractive to the

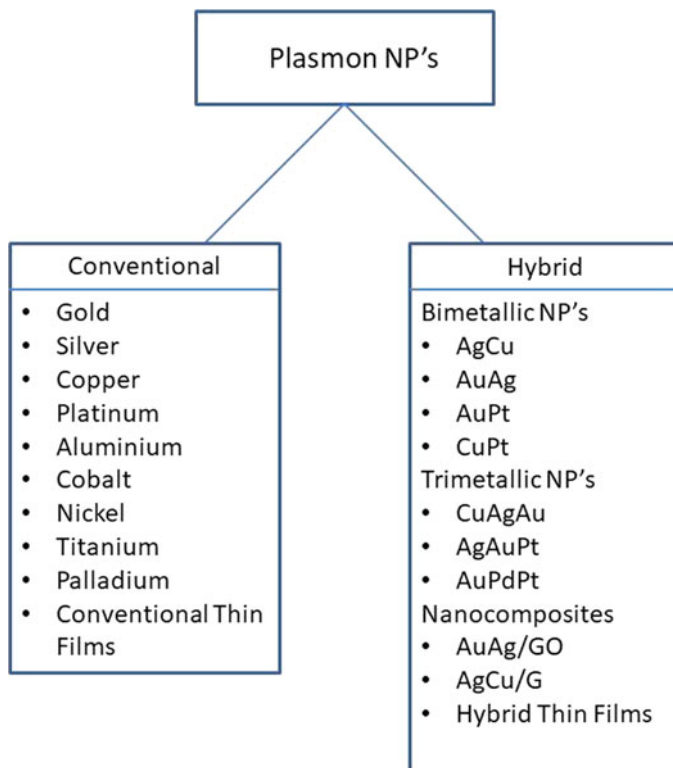


Fig. 3 Different Types of Plasmon NP's with examples

researchers since their plasmon resonance frequency lies within UV-VIS region. The resonant frequency can also be modulated by changing their shape, size or morphology.

Plasmon nanomaterials are broadly divided in two categories, conventional (mainly single metal nanostructures) and hybrid materials (as exemplified in Fig. 3). As envisaged from the figure, single metal nanoparticles can be categorized as conventional whereas blending/composites of more than one metal (for example, bimetallic nanoparticles) are classified as hybrid. Noble metal NPs e.g. Au, Ag etc. are studied extensively by different research groups for their plasmonic properties [36–38]. Au, Ag plasmonic particles are usually effective under the exposure of visible light and the resonant frequency of these metal NPs in infrared region is not frequent [39]. Exploring the plasmonic properties of different metallic as well as composite/blended particles remains interesting to the researchers for different applications and thus enormous numbers of plasmonic materials are known today. In the forthcoming sections we will introduce briefly the relevant properties of a few conventional as well as hybrid plasmonic materials.

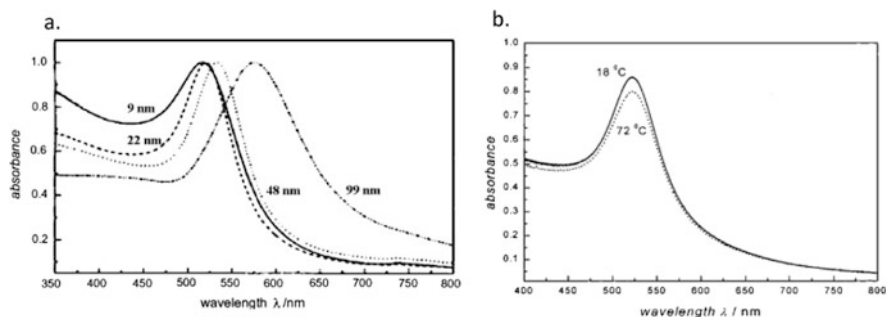


Fig. 4 Visible light absorbance spectra of (a) Au NPs with different sizes (b) of 22 nm Au NP's at 18 °C and 72 °C. These images have been reproduced from Ref. [52]. (a) Shows the visible light absorbance spectra of Au NPs with different sizes. Typically, the SPR wavelengths for Au NPs appear around 520 nm. However, as represented in the figure, the SPR wavelength varies depending on the size of the nanoparticles. The visible light spectrum captured at 18 and 72 °C for Au NPs having same size and shape are shown in (b) Significant deviation in SPR is not observed when the temperature is varied for the same sample

2.1 Conventional Plasmonic Materials

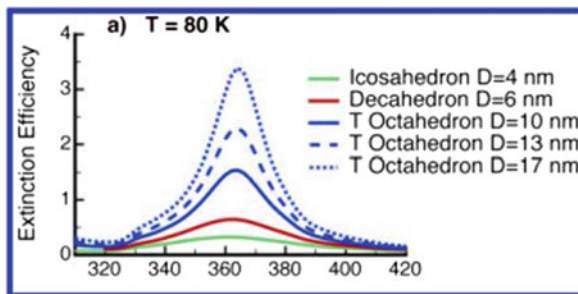
(a) Gold

Gold (Au) NPs as plasmonic materials are much sought-after for a variety of applications which include biomedical use in sensing [13, 40, 41], imaging [13, 42, 43], drug delivery [44], cancer therapy [45, 46] as well as catalysis [47, 48], electronics [49], and optics. There are several underlying reasons which make Au NPs useful for such diverse applications. Au NPs are physically and chemically very stable and they are biocompatible, making it suitable for curative purposes in biomedicine [46, 50, 51]. Au NPs possess large number of polarizable conduction electrons which interact preferentially with electromagnetic fields of incident light and induces coherent collective oscillation of conduction band electrons with respect to the positively charged metallic core [44]. Such bipolar oscillation resonates with the specific frequency of incoming light and depends appreciably on the shape and size of the particles. The influence of temperature is also found negligible on the plasmonic properties of Au since the plasmonic motion of electrons in Au NPs originate due to electron- electron repulsion and not electron-phonon interaction [52].

(b) Silver

Silver (Ag) NPs are known as other low cost but efficient noble metal NPs to show strong plasmonic response [7, 31]. It is well known to us for its antimicrobial properties [53, 54]. It has also found applications in plasmon based sensors [55], photovoltaic devices [53], Surface-Enhance Raman Spectroscopy (SERS) [7] and are even found to contribute in single molecule detection systems [56].

Fig. 5 Extinction efficiency v/s wavelength of Ag NPs of different size such as 4 nm, 6 nm, 10 nm, 13 nm, and 17 nm at Temperature (a) 80 K. (This image has been reproduced from Ref. [57])



Gonzalez et al., have demonstrated computational techniques, to determine the morphology of Ag NPs. They have shown that different morphologies such as icosahedron, decahedron and octahedron have different SPR peak frequency. Figure 5 shows the absorbance spectra or extinction efficiency of Ag NPs of different size such as 4 nm, 6 nm, 10 nm, 13 nm, and 17 nm [57]. Ag NPs show Surface Plasmon Resonance (SPR) peak in near-UV region. Hence, for UV based applications Ag NPs are more suitable than Au NPs.

(c) Copper

Copper (Cu) does not have plasmonic properties at par with gold or silver due to its instability, but it is the best contender or replacement of gold and silver due to its low cost, which is important for commercial viability [11]. Cu NPs can have resonance in the near infrared region making them useful for thermal applications [58]. Yeshchenko et al., have studied the variations of absorbance with temperature for copper nanoparticles. They have reported redshift in the SPR wavelength which is attributed to electron-phonon interaction and thermal expansion of Cu NPs [59].

It is important here to mention that the conventional plasmonic nanomaterials are not restricted to NPs only, but the plasmonic thin films of conventional noble metals are also known. The SPR here depends on thickness of films as well as the nature of the substrate on which film is developed [60]. Plasmonic thin films have applications as SERS substrate [61], biosensors [62], imaging [63], etc.

2.2 Hybrid Plasmonic Nanomaterials

Hybrid plasmonic nanomaterials are developed using two or more materials that are capable of enhancing local electric field by SPR. These materials can be metals, metal oxides, rare earth elements, nanocomposites and also a combination of these. Hybrid plasmonic nanomaterials especially bimetallic nanoparticles (BMNPs), trimetallic nanoparticles (TMNPs) & rare-earth metal nanoparticles (REMNPs) have also drawn significant attention due to their tunability in plasmonic properties [64, 65]. The properties of these materials are determined by the constituting materi-

als and their size. These hybrid materials have the tendency to improve functionality as compared to their constituent metals. The properties of hybrid NPs may differ from that of the constituent elemental particles and exhibits unique size dependent optical, electronic and catalytic effects. Due to the enormous potential, researchers are preparing new hybrid nanomaterials in different forms, such as alloys, multiple shells, aggregates, thin films with metal nano-island, nanocomposites, etc. [66]. In the following section, a brief discussion on the properties and applications of some hybrid plasmonic materials is presented.

(a) **Bimetallic Nanoparticles (BMNPs)**

Bimetallic Nanoparticles (BMNPs) constitute two metals which may be in the form of nano-alloys, core shell structure or random segregation. The properties of such NPs can change depending on their size, morphology and composition of constituent metals [67]. Many BMNPs such as Au-Ag, Ag-Cu, Au-Cu, Au-Pt, etc. are synthesized and studied in terms of their plasmonic properties. Here, the plasmonic properties of AgCu NPs which is in the class of BMNPs are discussed. To study the formation of solid solution under non-equilibrium conditions, Ag-Cu system is often referred as a model system [68]. The nanoalloys of Ag and Cu have also been studied for different applications such as antibacterial, conducting ink, catalyst, sensors, solar cell, thermal transport, etc. because of their high electron conductivity and better adhesion properties [69–77]. In Ag-Cu system, synergies of both metals allow them to retain its unique properties which are not observed in individual Ag NPs or Cu NPs. For instance, oxidation of Cu within Ag-Cu BMNPs can be reduced remarkably. By tuning the size of BMNPs and changing the ratio of Ag and Cu, the SPR wavelength can be tuned very effectively. Figure 6 shows the absorbance spectra of Ag-Cu NPs and the individual Ag NPs and Cu NPs [78]. It is envisaged from the figure that SPR peak at 590 nm appears for Ag-Cu NPs whereas for individual Ag NPs and Cu NPs the peaks are observed at approximately 454 and 650 nm, respectively.

(b) **Trimetallic Nanoparticles (TMNPs)**

Trimetallic nanoparticles (TMNPs) are typically a blend of three metals. However, polymeric/ceramic counterparts are also mixed with the metals. TMNPs with various structures such as nano-alloys, multiple core-shells or nano-onions, nanocrystals are already known. In these materials, the SPR wavelength will depend on the structure, shape, composition of constituent metals and the ambient temperature.

Kunnwar et al., have reported the synthesis of AgAuPt TMNPs using high temperature annealing [79]. Figure 7 shows the absorbance spectra of AgAuPt TMNPs. AgAuPt TMNPs show better SPR with stronger absorbance peaks than AuPt BMNPs in UV, visible and NIR region. It is also observed that there is a blueshift of the SPR peaks with the increase in temperature. Due to strong SPR peak, TMNPs have wide range of applications in catalysis, bio-imaging, various cancer treatments, antimicrobial activity, bio-sensing etc. [80–83]

Fig. 6 Absorbance spectra of AgCuNPs, compared with spectra of Ag and Cu NPs respectively. (This image has been reproduced from Ref. [78])

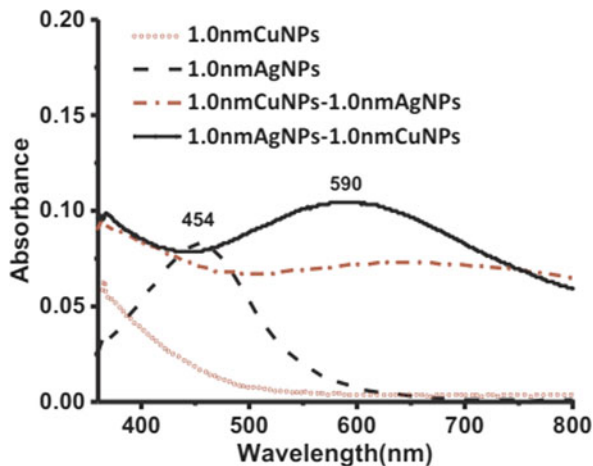
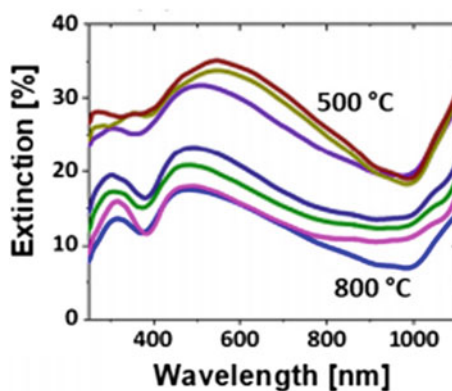


Fig. 7 absorbance spectra of AgAuPt TMNPs at temperatures ranging from 500 °C to 800 °C. (This image has been reproduced from Ref. [80])

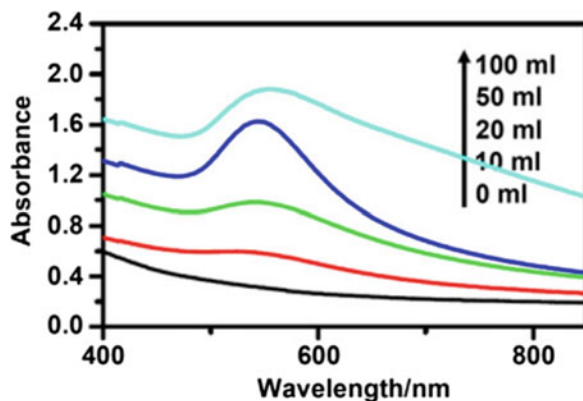


2.3 Nanocomposite Plasmonic Materials

Another class of hybrid materials is nanocomposite based materials which are sometimes functionalized for plasmonic applications. In this class of materials, structures such as monometallic, bimetallic or trimetallic nano-islands, nanosheets are already known. Addition of plasmonic materials to carbon and its derivatives such as carbon nanotubes (CNTs), graphene, etc. have proved to be a boon. These materials show promising plasmonic response along with their stable mechanical and chemical properties.

Graphene based nanocomposites have been reported for anti-microbial activity, therapeutic treatment of cancer, antibiotic film, chemical sensors, etc. [84–88]. For plasmonic application such as SERS, graphene is used as an effective substrate because of its good thermal transport ability, surface functionalization ability, fluorescence quenching and high elasticity [89, 90]. These graphene-based plasmonic nanocomposites have the ability of regulating the oxidation of metals attached to

Fig. 8 Absorbance spectra of GO-IONP-Au by adding different gold growth solution. (This image has been reproduced from Ref. [86])



them, hence increasing their stability. The SPR peaks for such nanocomposites depend on the thickness of nanosheet/thin film, composition of the constituent nanoparticles (monometal, bimetal or trimetal) attached with nanosheet, and ambient temperature. Figure 8 shows the absorbance spectrum of graphene oxide-iron oxide-AuNPs-nanocomposites (GO-IONP-Au). As the amount of gold increases, the SPR peak redshifts from visible towards NIR region. The SPR peak becomes stronger as volume of gold increases and the strongest SPR peak is observed at maximum volume of Au solution (100 ml gold solution in Fig. 8) [86].

3 Synthesis of Plasmonic Materials

Increasing interest in plasmonic materials has led to the development of various synthesis methods. Among these, some methods have certain disadvantages as scaling up of the products is a challenge. As discussed in the preceding sections, plasmonicnanomaterials exhibit SPR, whose resonance peaks depend on its shape, size, surrounding media, etc. So, synthesis methods with size tunability, which gives rise to wide variations of shapes and sizes of nanomaterials are preferred. Synthesis of nanomaterials is, in general, divided into two categories based on their method of synthesis, namely the top-down approach and the bottom-up approach [91]. Top down approach refers to those methods of synthesis in which nanomaterials are synthesized by the decomposition of its bulk counterpart. Bottom up approach, on the other hand, utilizes atoms, molecules and ions to generate nanoparticles [92]. These methods can be further divided into three categories, namely the physical, chemical and biological or green synthesis. The aforementioned conventional and hybrid plasmonic nanoparticles are mostly prepared via the chemical and physical methods but very recently there has been an upsurge in the number of documents reporting the synthesis of plasmonic nanoparticles via biological methods. Figure 9 shows the classification of methods through which plasmonic nanoparticles can

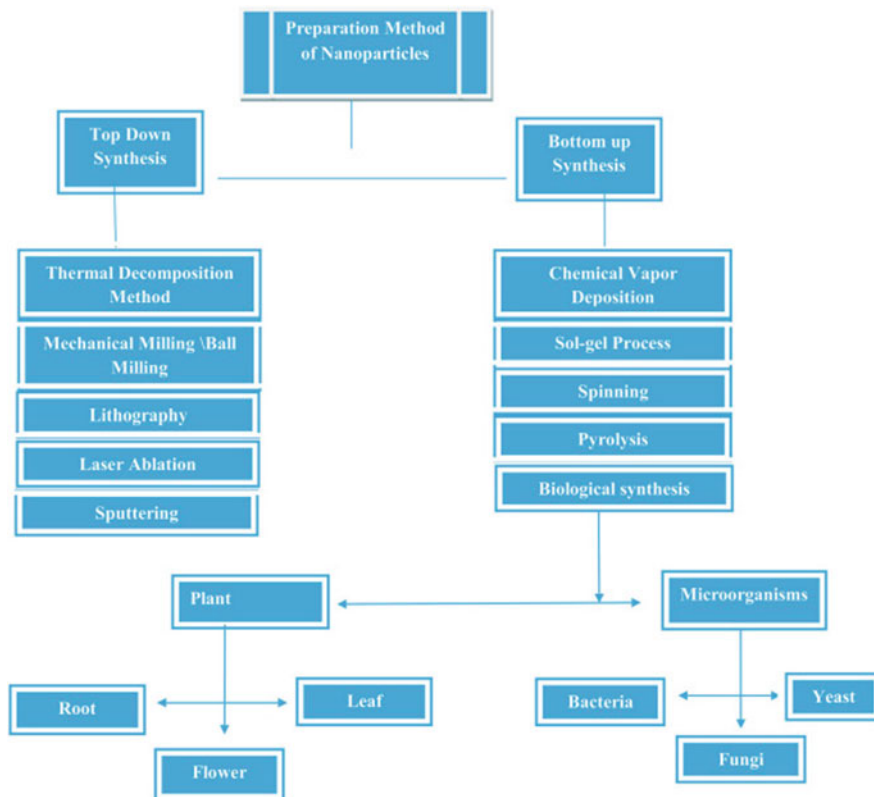


Fig. 9 synthesis methods of nanoparticles. (Reproduced with permission from Ref. [91])

be prepared [91]. In Table 1, a summary of the methodologies for the synthesis of conventional as well as hybrid nanoparticles is depicted.

4 Sensing Performances of Plasmonic Sensors

In this section, the sensing performances of some of the different plasmonic sensors reported in the literature are reviewed. These sensors include gas sensors, biosensors, nanoparticle array based sensors, and some other very recent state-of-the-art works in the domain of plasmonic sensing.

Starting with gas sensors, its role is crucial for environmental monitoring, agricultural and medical applications. Harmful and toxic gases such as H_2S , NH_3 , CO , and volatile organic chemicals (VOCs) released from various industries need to be monitored to avoid health issues. Plasmonic sensors play a vital role in the detection of these gases. Ankun et al., presented a nanofabrication approach

Table 1 Plasmonic nanoparticles and their methods of synthesis

Plasmonic NP	Type of Plasmon NM	Synthesis type	Synthesis method	Nanoparticle size	Nanoparticle morphology	References		
Au	Conventional	Physical	Laser ablation in liquid	4–50 nm	Sphere	[91, 93]		
			Sputtering	3.5 nm	Sphere	[94]		
			Electrochemical	32.6 nm	Cube	[95]		
		Chemical	Seed mediated growth	30–75 nm	Cube, rhombus, cylinder, triangular	[96]		
			Microemulsion	10–50 nm	Sphere	[97]		
		Biosynthesis	Biosynthesis using plants	21.9 nm	Sphere	[98]		
			Biosynthesis using microorganism	15 nm	Hexagonal, triangular	[99]		
			Laser ablation in liquid	2–20	Sphere	[100, 101]		
		Ag		Physical	Ball milling	14, 28 nm	Crystalline	[102]
					Sputtering	5.9, 5.4 and 3.8 nm	Grains	[103]
Pyrolysis	20 nm				Sphere	[104]		
Chemical	Chemical reduction			9, 11, 24 and 30 nm	Sphere	[105–107]		
	Sol Gel method			12–60 nm	Sphere	[108, 109]		
	Microemulsion			<10 nm	Sphere	[110]		
	Biosynthesis using plants			10–50 nm	Sphere	[111, 112]		
Biosynthesis using microorganisms	20–50 nm	Sphere	[113, 114]					

CuO		Physical	Laser ablation in liquid	40–50 nm	Sphere	[11]
Cu		Physical	Laser ablation in liquid	3 nm	Sphere	[115]
		Chemical	Sputtering	9 nm, 2–3 nm	Crystalline	[116, 117]
			Chemical reduction	2–10 nm	Sphere	[118, 119]
			Microemulsion	10–70 nm	Sphere	[120]
		Electrochemical	40–60 nm	Sphere	[121, 122]	
	Biosynthesis	Biosynthesis using plants	50–130 nm	Sphere	[123]	
Au/Ag		Physical	Laser Ablation in liquid	20 nm Ag core, 4 nm Au shell	Core-shell, nano-alloy	[69, 124]
		Chemical	Microemulsion	4–22 nm	Nano-alloy	[125]
			Annealing		Nanorods	[126]
		Biosynthesis	Biosynthesis using plants	12 nm	Core shell & nano-alloy	[127]

(continued)

Table 1 (continued)

Plasmonic NP	Type of Plasmon NM	Synthesis type	Synthesis method	Nanoparticle size	Nanoparticle morphology	References
AgCu	Hybrid-BMNP	Physical	Laser ablation in liquid	Various sized	Core-shell	[68, 69]
			Electrochemical	Various	Nano-alloy	[128]
		Chemical	Chemical reduction	<100 nm	Nano-alloy	[129]
AuPtPd	Hybrid-TMNP	Biosynthesis	Biosynthesis using plants	30–47 nm, 10 nm, 100 nm	Nano-alloy	[130–132]
		Physical	Sputtering	2.3–5.92 nm	Nano-alloy	[133]
		Chemical	Chemical reduction	30.3 nm	Core-shell	[80]
		Chemical	Chemical reduction	10 nm	Nano-alloy	[82]
AgCu/GO	Hybrid-nanocomposites	Chemical	Chemical vapor deposition		GO Nanosheet containing AgCu BMNP	[70]
					Graphenenanosheet containing AgCu BMNP	[87]
GO-IONP-Au			Chemical reduction			[86]

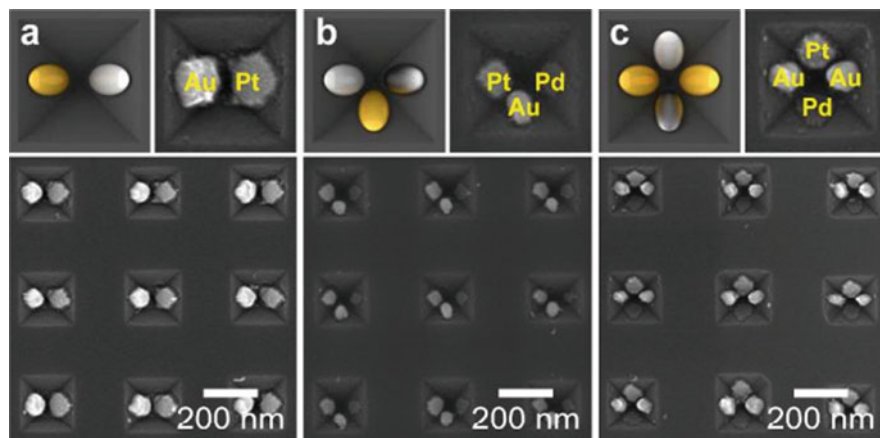


Fig. 10 SEM images of (a) Au-Pt heterodimers, (b) Au-Pd-Pt hetero-trimers and (c) Au-Pd-Pt hetero-tetramers synthesized using reconstructable mask lithography. (Reproduced with permission from Ref. [134])

comprising of reconstructable mask lithography to create large area arrays. They made a tetramer assembly of Au NP oligomers from a monomer unit. The group also studied the coupling between Pd and Au nanoantennas (dimers and trimers) for hydrogen sensing. They reported that the Au-Pd dimer showed small red shifts whereas large blue shifts are observed in Au-Pdtrimers. This shift is dependent on the size of the side gap of the arrays. As compared to template assisted methods, reconstructable mask lithography is better suited because they help in controlling the composition of NP. In their work, Cr slit mask with a width of 100 nm was used to obtain Au and Pt NPs (ca. 80 nm). Au-Pd-Pt hetero-trimers are prepared using the Cr slit mask by rotating the substrate to 180°. For preparing Au-Pd-Pt hetero-tetramer with two Au nanoantennas, two Cr slits are constructed. Au antennas and Pt and Pd are used commonly for sensing and catalysis. The arrangement of NPs can be observed in the SEM images for Au-Pt heterodimers (Fig. 10a), Au-Pd-Pt hetero-trimers (Fig. 10b) and Au-Pd-Pt hetero-tetramers (Fig. 10c) [134].

In another recent work, Yashar et al., proposed a plasmonic gas sensor which can be operated in the infrared (IR) region. A meta-material absorber has been used as thin silicon dioxide layer between gold film and an array of graphene-coated gold nano-disks. It is observed that the gold nano-disks have improved the sensitivity of the sensor. The metamaterial has shown three distinct resonances in visible and infrared regions. As claimed, the metamaterial configuration is relatively easy to fabricate and can be used to monitor low concentrations of various gases in different applications ranging from environmental monitoring to home safety monitoring systems.

Monfared et al., have reported a sensitive D-shaped photonic crystal fiber-based surface plasmon resonance (PCF-SPR) sensor. The group has examined three combinations of materials (silver only, graphite on silver, and graphene on silver)

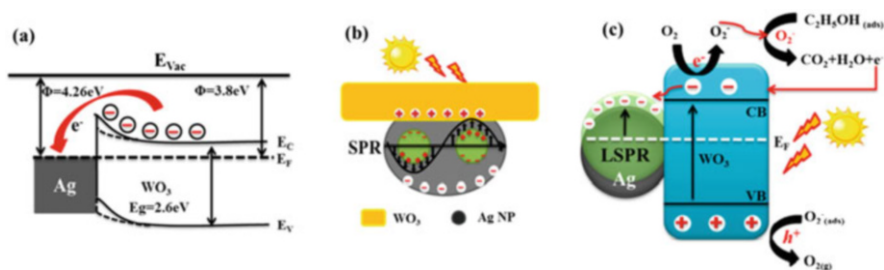


Fig. 11 Schematic illustration (a) of the energy diagram and charge transfer process in the Ag-WO₃ HNSs; (b) for the surface plasmon resonance (SPR) effect of Ag nanoparticle; and (c) Sensing of alcohol vapor by Agx-WO₃ sensor in the presence of visible light. (Reproduced with permission from Ref. [136])

as plasmonic nanofilm for the PCF-SPR. Amongst them graphene-assisted PCF has shown maximum sensitivity and overall merit of the sensor has improved considerably. The group has also proposed two distinct ways of analyte sensing. Either the liquid analytes can be filled internally into the top two air holes of the PCF, or externally into a rectangle channel at the top of the fiber. Authors have claimed that the sensor can act as a promising candidate for biosensing applications [135].

Yao et al., have developed another plasmonic gas sensor by coating Ag nanocrystals on the inner shell surface of WO₃ hollow nanospheres (HNSs). The synthesized nanostructures have achieved high sensitivity towards alcohol vapor. The group has also reported that when the sensor is illuminated with light at 405 and 900 nm, the absorption of Ag NPs and surface oxygen vacancies resonate with the light wavelength. The sensor works on the principle of localized surface plasmon resonance (LSPR) effect as observed in Fig. 11. High surface to volume ratio of Ag-WO₃ HNSs is favoured for gas diffusion and adsorption. The vacancies formed in WO₃ lead to the transfer of electrons from their conduction band as observed in Fig. 11a. They behave as an n-type semiconducting metal oxide and a Schottky junction is formed when electrons transfer from WO₃ to Ag at the interface of Ag-WO₃. A dissociative adsorption phenomenon takes place on the surface of Ag when a reducing gas is injected. The molecule then reacts with the chemisorbed ionic oxygen to produce CO₂ and H₂O as seen in the Fig. 11c. Due to surface plasmonic effect, there is formation of charge-density oscillation when the Ag NPs are simulated with optical energy as seen in Fig. 11b. Thus, it leads to a better sensing response [136].

Prado et al., have developed a hydrogen sulphide (H₂S) gas detector using silica optical fibre and AuNPs. The localized surface plasmon resonance occurs in Au NPs and the strong bonding between Au and sulphur is utilized to develop the colorimetric detector for H₂S gas. Polyvinyl alcohol is used for adhesion between the NPs and the fibre surface [137].

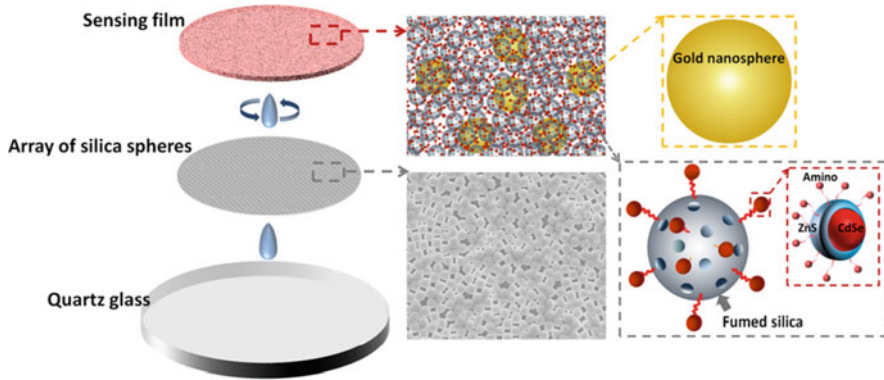


Fig. 12 Schematic representation for the fabrication process of the CdSe@ZnS quantum dots (QDs), fumed silica (FS), and gold nanoparticles (GNs) sensing film. SEM images of silica sphere array and sensing film with GN, FS, and QD nanoparticles. (Reproduced with permission from Ref. [138])

Xue et al., have proposed a reproducible surface plasmon-enhanced optical sensor for the detection of gaseous formaldehyde. In this work, a sensing layer has been prepared layer by layer on a quartz glass substrate as observed in the Fig. 12. On the surface of the glass substrate, uniform silica microsphere solution has been added dropwise to form an array of silica sphere. A sensing layer on the array is prepared using the mixture of CdSe@ZnS quantum dots (QDs), fumed silica (FS), and Au NP solution in the volume ratio 1:1:1. The solution is then spin coated on the silica sphere array to form a uniform layer which is confirmed from SEM image shown in Fig. 12. The proposed method has been claimed to be highly convenient for formaldehyde detection. Enhanced fluorescence quenching is observed on exposing the sensor to formaldehyde molecules. It has also been found that ultralow concentration of gaseous formaldehyde could be detected through this sensor. This work provides a simple and low-cost approach for fabrication of optical sensor for the detection of formaldehyde [138].

Biosensing

In another work, Miranda et al., have proposed a nanocomposite hybrid material where AuNPs are embedded in a hydrogel network. The reason for choosing a hydrogel network in place of a colloidal aqueous solution is the more stability that the hydrogel network provides as an embedding medium. The optical properties and sensitivity of this material could be tuned by varying the mean diameter of particle. Based on these, a 3D plasmonic sensing platform comprised of cysteamine modified AuNPs in PEGDA hydrogel is developed to capture biotin [139].

Alba et al., have developed a plasmonic sensor consists of low-power light-emitting diode, a multimode optical fiber coupler, a miniature spectrometer and multimode optical fibres. The facets of the fibres are coated with Au NPs which made them selective towards the detection of biomolecules, metal ions, etc. This

sensor is capable to monitor the change in the nanospectroscopic absorption of the Au NPs. As claimed by the authors, these sensors can be used for the real time monitoring of environmental studies [140].

Meisam et al., have designed a biosensor based on the plasmonic resonance of graphene. The sensor comprised of nanofluidic delivery channel is fabricated using photolithography techniques. The nanofluidic channel acts here as the sensing layer. The group has developed a method in which the sensitivity of the sensor has increased by placing two graphene sheets over the substrate rather than placing a metallic layer over the substrate. It is observed that on increasing the number of graphene sheets, the absorption through the biosensor is enhanced [141].

In the work reported by Henderson et al., Finite-Difference-Time-Domain (FDTD) simulation method has been implemented in the studies of GaN based structures for sensing applications. These structures are coated with NPs and the optical properties of these structures have shown sharp peaks when the refractive index of layers are changed. The LSPR effect observed in these sensors confirmed that these structures can easily be used in biosensing applications [142].

Shukla et al., have developed a plasmonic device for the detection of bioanalytes. The device can capture changes in the refractive index of the analyte in the optical communication band through modified Attenuated Total Reflection (ATR) configuration. It is found that the sensitivity of the device is increased by addition of silicon-graphene stacked layers. The high dielectric index of the Si layer has led to the better adsorption of bioanalytes. In this work, Rodent urine has been used as an analyte to demonstrate the functionality of proposed sensor. The sensor can detect varying concentration of *Leptospira bacterium* [143].

In another work, a simple hexagonal photonic crystal fiber (PCF) based surface plasmon resonance (SPR) refractive index (RI) sensor has been proposed by Rahman et al., The sensor is comprised of circular air-holes of same radii. On the outer surface of the sensor, indium tin oxide (ITO) layer is applied and the data obtained are analyzed through finite element method (FEM). The sensor is used for the analysis of RI range 1.33–1.40 in the NIR wavelength region. The simple structure and external sensing approach of this sensor make it suitable for detecting various chemical and biological analytes [144].

Samavati et al., have designed an optical sensor for the detection of glycoprotein. In this sensor, Ag nanostructures are deposited through cladding treatment and electrodeless deposition. The optimization of this sensor is carried out by putting the sensing fibre into starch-eliminated ipomoea batatas (sweet potato) solution. The hydrophobicity nature of the sensing layer here increases the sensitivity of the sensor [145].

Plasmonic sensors are also employed to diagnose the disease of human being. Ankitha et al., have reported the development of a biosensor for the detection of chikungunya, an infectious mosquito-borne disease with chronic musculoskeletal pain and acute febrile illness. They have detected the CHIKV antigen using optical transduction method. For developing the sensor, a U bent plasmonic optical fibre based biosensor has been designed. The core and cladding of the sensor is made of polymethyl methacrylate (PMMA) and a fluorinated polymer. A

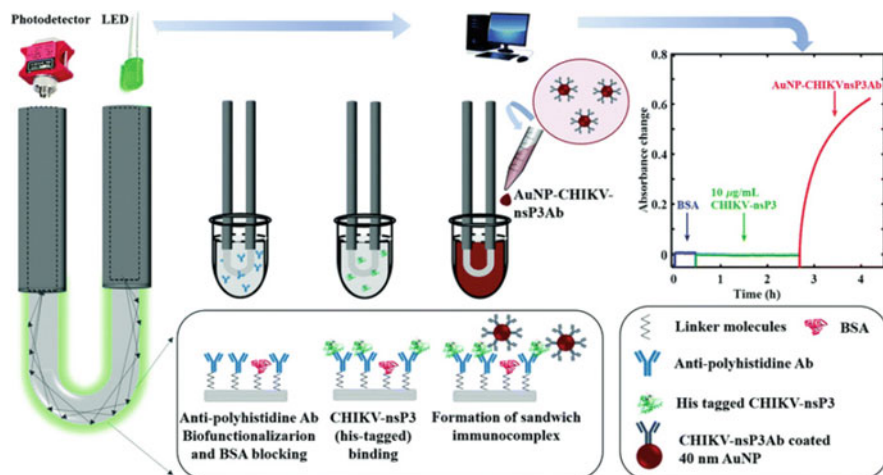


Fig. 13 Design of U bent Plasmonic optical fibre based biosensor for detection of CHIKV-nsP3. (Reproduced with permission from Ref. [146])

sandwich immunoassay is performed where monoclonal anti-polyhistidine antibody is immobilized on the probe surface. As a detection analyte CHIKVnsP3Ab is used as secondary metabolite. Then, the real time absorbance change is monitored when probe surface is exposed to the antibodies. The biofunctionalized surface is then exposed to AuNP@CHIKVnsP3Ab. Varying concentrations of CHIKV-nsP3 analyte has been used to optimize the sensor systems as observed in Fig. 13 [146].

Recently, Arash et al., have designed a sensor that detects SARS-CoV-2 virus protein at femtomolar (fM) level. The group has developed a toroidal plasmonic immuno-sensor based on the fact that toroidal dipole resonant metasurfaces show low radiative losses. The sensor is comprised of a multipixel planar molecule. Functionalized colloidal AuNPs are used here to capture the spike proteins from the samples. As claimed, the sensitivity of the sensor is high and the obtained limit of detection is ~ 4.2 fM. These meta-sensor has the potential to become future technology for the rapid and precise screening of SARS-CoV-2 and other virus carrier infections [147].

Carcinoembryonic antigen (CEA) is detected by Yang et al., using ultrasensitive and selective photo-electrochemical (PEC) biosensor. The sensor is comprised of plasmonic TiO₂@Au nanoparticles/CdS quantum dots (TiO₂@Au NPs//CdS QDs). The TiO₂@Au NPs are fabricated using in situ deposition of Au NPs (prepared through ascorbic acid-reduction method) on TiO₂ surface which is used as photoactive material. The prepared TiO₂@Au NPs have shown a cathodic background signal and the anodic photocurrent generated is dependent on the LSPR effect of Au between TiO₂ and CdS. The limit of detection of the sensor is found ~ 18.9 fg/mL which suggest that it can have potential applications in bioanalysis and diseases diagnosis [148].

Plasmon-enhanced electrochemiluminescence (ECL) nanosensor based on magnetic-plasmonic Fe₃O₄ yolk/Au shell (M@Au) is designed by Zhang et al., for the detection of Kirsten rat sarcoma K-RAS gene. In this mouse sarcoma virus oncogene mutation occurs in the initial phase of malignant tumor transformation. Thus, the detection of K-RAS is meaningful for the diagnosis of early cancer. The research group found that graphite phase carbon nitride quantum dots (g-C₃N₄ QDs) are not suitable for sensing applications due to its low electro-chemiluminescence (ECL) intensity. They then constructed a sandwich-typed sensor with a combination of M@Au and g-C₃N₄ QDs. The inner Fe₃O₄ NPs showed good magnetic property and outer Au shell showed better surfaceplasmon coupling (SPC) effect [149].

Gao et al., have reported an effective approach to tune the plasmonic properties of morphology-invariant NPs by changing their internal structure. To prepare the Ag@(Ag–Au) shell@shell nanocages, the growth of Ag in the inner surface of Ag–Au alloyed nanocages selectively done. The amount of Ag deposited could conveniently and effectively tune the plasmonic properties of Ag@(Ag–Au) nanocages. The prepared nanocages are then employed in colorimetric sensing of human carcinoembryonic antigen (CEA). The concept worked well for low level detection using crafted plasmonic NPs [150].

Surface-enhanced Raman scattering (SERS) is identified by Chen et al., when natural chitin film from the pupa of walnut pest *C. japonica* is coated with thermally evaporated nanoscopic Ag film. The ventral and dorsal side of the developed films contain nanostructured patterns as shown in SEM images (Fig. 14). Micro-capillary surface structure of chitin observed on the dorsal side of the film. The SERS activity is carried out using confocal Raman spectrometer (at 532 nm laser) [151].

In another work, Xiong et al., have constructed a nanoantenna with the configuration of a nanoparticle-on-mirror (NPOM). In this configuration, Au NPs are immobilized onto a gold mirror. It is found that the NPOM configuration is capable to produce strong light scattering as compared to that of isolated Au NPs [152].

Two-dimensional Au plasmonic nanostructure arrays with a periodic one-dimensional plasmonic nanocavity are fabricated by Wang et al. These are fabricated by self-assembly and reactive ion etching technology. Trace detection of multiple harmful chemicals is reported by the developed SERS sensor [153].

Yasli et al. have studied the performances of photonic crystal fiber (PCF) based SPR sensor composed of hexagonally arranged air holes in the cladding region. The PCF structure is prepared using Au or Ag-graphene layer. The prepared sensor is found promising for analysing the blood components (water, cytop, blood plasma, white blood cell (WBC)). It is reported that the change in the structural properties like air hole quantity, placement or shape, etc. of the crystal fibres can lead to distinguishable change in its sensitivity [154].

In another interesting work, mid-infrared active plasmonic sensing is studied by Leonetta et al. They fabricated antennas employing heavily doped Ge films grown epitaxially on Si wafers. The Ge antennas are found to be compatible with silicon CMOS technology. It is found that as compared to bare Si substrate, the Ge antennas grown on Si shows 2 orders of signal enhancement for the detection of target molecules [155].

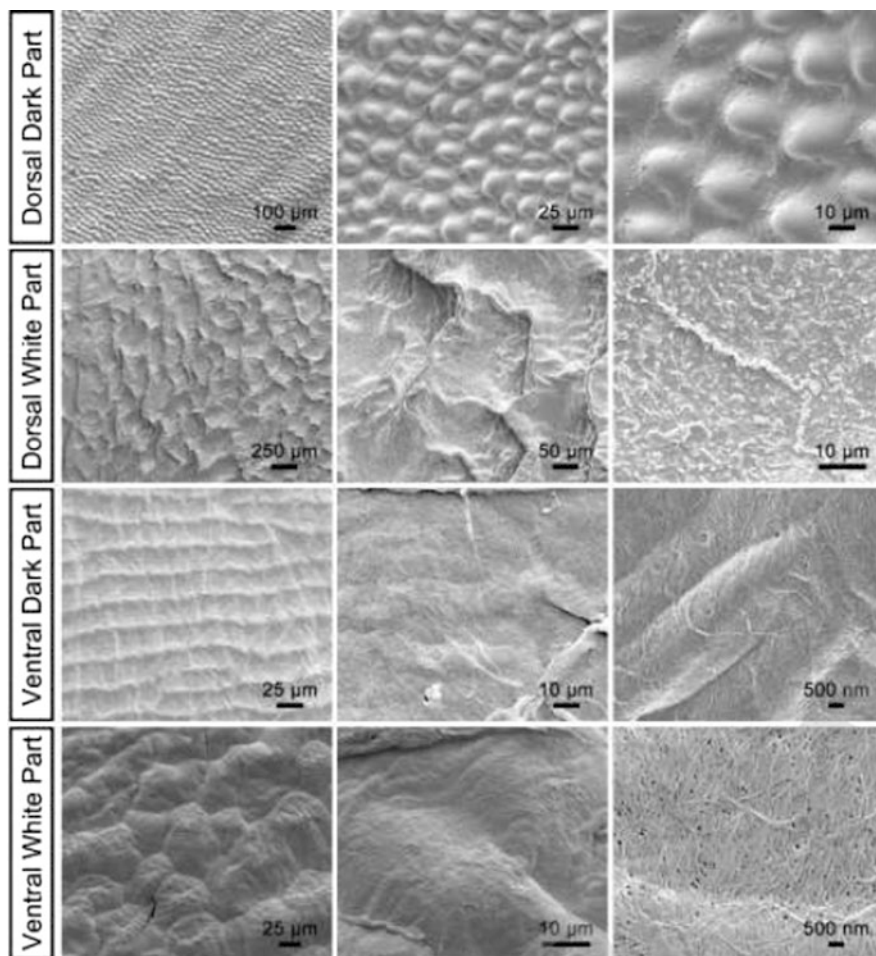
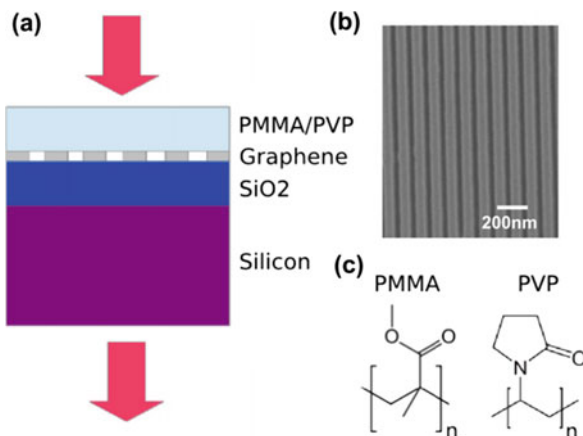


Fig. 14 SEM images of dark and light parts of the dorsal and ventral sides of the chitin film obtained from pupa shells of *C. Japonica*. (Reproduced with permission from Ref. [151])

Li et al. have studied the influence of graphene nanoribbon plasmon excitation on the vibrational spectra of surface absorbed polymers. They have developed graphene nano-ribbon array on Si/SiO₂ substrate using electron beam lithography and chemical vapor deposition (Fig. 15a). Polymethylmethacrylate (PMMA) and polyvinylpyrrolidone (PVP) layers are spin coated on the nanoribbon-covered substrates. The SEM image of graphene layer and the chemical structures of PMMA and PVP are shown in Fig. 15b, c respectively. The nanoribbon like structure of graphene is identified in Fig. 15b. The presence of carbonyl ($-C=O$) groups in PMMA and PVP are found in their chemical structure. From the sensing studies, it is observed that the sensitivity for the detection of ($-C=O$) vibration for the developed

Fig. 15 (a) Composition of sample: a thin layer of PMMA or PVP, a graphenenanoribbon (GNR) array, and thick SiO₂ layer on top of a bulk Si substrate. (b) SEM image of graphenenanoribbons. (c) PMMA and PVP both contain the carbonyl double-bond (C=O). (Reproduced with permission from Ref. [156])



graphene based systems is increased by a factor of about 5 which is identified in the IR attenuation spectra. The group has reported that the modulation of the graphene plasmon attenuation spectrum by the PMMA-PVA polymers is because of near-field electromagnetic coupling [156].

Tang et al. have developed plasmonic Au NP arrays on shape memory polyurethane (SMPU) substrates. AuNP arrays are prepared using di-block copolymer through ultrasonic treatment. The arrays are then transferred from rigid silicon wafers onto flexible SMPU substrates. It is observed that LSPR arising from AuNP arrays is increased by negative bending on SMPU substrates, whereas the LSPR is decreased by positive bending. This approach of incorporating AuNP arrays on SMPU substrates for tuning plasmonic properties has great potential applications in SERS, fluorescence enhancement, and new optoelectronic materials [157].

The plasmonic materials are not only used to develop sensors for detection of toxic gases or biomolecules, but these are also employed as solar light absorbers. Luca et al. and Alberto et al. have developed plasmonic-based solar light absorber which in sub- μm thickness, exhibit complete light absorption. This is obviously an efficient alternative absorber to mm-thick carbon-based materials usually employed for solar-driven steam generation. The ultrathin plasmonic titanium nitride (TiN) nanocavity arrays are the key component of solar absorber. Figure 16a depicts the TiN-based solar absorber (TSA) which is enclosed in polytetrafluoroethylene (PTFE) cell. The PTFE cell acts as thermal insulator and on the top of this unit, a basin works for the collection of water.

Steam generation takes place when the surface of water is simulated with solar light. The TSA consists of three different layers (Fig. 16b). The first layer is a TiN nanocavity array and the second layer is a Ti₂N layer of $\sim 1 \mu\text{m}$ thickness. The Ti₂N layer is formed due to the diffusion of NH₃ through the base layer i.e. Ti plate. The SEM image of the TiN nanocavities is shown in Fig. 16c. The approach to ultrathin plasmonic absorbers can boost the performance of devices

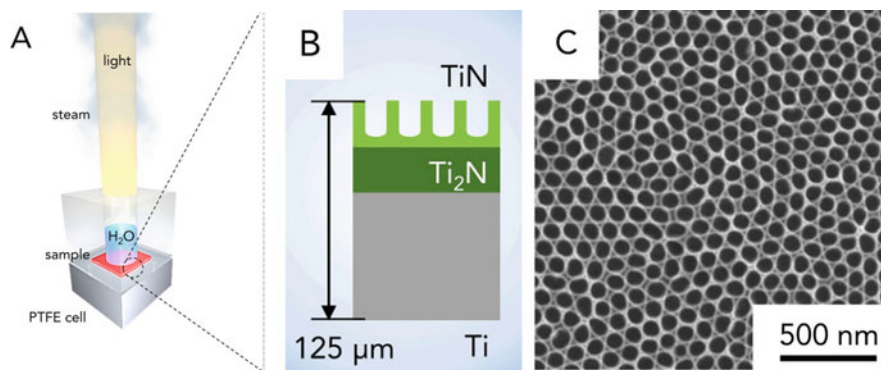


Fig. 16 (a) Schematic representation of TiN-based solar absorber (TSA) enclosed in polytetrafluoroethylene (PTFE) cell. (b) Structure of the TSA: TiN nanocavities (250 nm thickness), Ti₂N thermal layer (~ 1 μm), and rest of the Ti substrate. (c) Top-view SEM image of TiN nanocavities. (Reproduced with permission from Ref. [158])

for evaporation/desalination and holds promise for a broader range of phase separation processes [158].

5 Future Scopes of Plasmonic

Nowadays, the detection of biological and chemical molecules becomes essential for a wide range of applications ranging from medical diagnostic to environmental monitoring. Many conventional sensors are found to be incapable particularly for some specific analytes such as cancer biomarkers in the blood. During the last few decades, with the advancement of nanotechnology, SPR sensors have been used in identifying various molecular interactions and monitoring for various essential or harmful analytes. In this regard, noble metal nanoparticles, for instance, AuNp, because of their easy processing, tunable morphology, biocompatibility, long-term stability, tailorable functionality (e.g., gold-thiol), are well known and commercially available nanomaterials to be used in wide varieties of SPR sensing applications. However, noble metals are cost intensive. The nanostructures of these materials are reactive and prone to be oxidized by the abundant oxygen or sulfur in the surroundings. Thus, as mentioned earlier, the noble metal nanostructures are needed to be stabilized via surface coating. The way of nanostructure synthesis (mainly via reduction of precursor salts using some reducing agent like NaOH), purification (to remove the inorganic impurities via various techniques like dialysis), their stabilization using different polymers or surfactants is also can be considered as tedious or time-consuming, which can also be accounted as an additional disadvantage. In this regard, solvent-mediated reduction or stabilization can be considered advantageous [159–161]. Although various composite nanostructures as mentioned earlier are

being proposed to enhance the SPR sensitivity, environmental stability, and cost reduction, many more scopes are emerging to deal with. Aluminum (Al), being an abundant and low-cost material, attempts are being taken to exploit its plasmonic properties in SPR sensing [162–166]. But it is readily oxidizable. A suitable technique is thus crucial to broaden the area of Al in SPR sensing. It has been observed that mostly all the nanostructure materials reported for plasmonic sensing applications, are either visible light or UV-light responsive. In the broadband solar spectrum, nearly 55% goes to near infrared (NIR), which is nondestructive. Very few reports are available dealing with the NIR-based plasmonic nanostructures [167–171]. Thus, the availability of nanostructures exhibiting plasmonic effect under the NIR light can advance the plasmonic sensing beyond the UV and Visible region in a non-destructive way.

6 Summary

In the present article, we have made attempt to represent a comprehensive survey on the use of plasmonic sensors for the detection of different analytes which include, but not limited to toxic chemicals, biomolecules and important biomarkers. The article starts with the significance and advantages of plasmonic sensors in the multifaceted modern applications followed by the brief introduction on surface plasmon resonance and its utility for plasmonic sensing. It has been reported that the shape, size of the plasmonic materials and the nature of dielectric materials in their vicinity influence significantly the sensing characteristics. In order to provide the beginners in the field an awareness about plasmonic materials, a section has been devoted on the description of various traditional and hybrid plasmonic materials. Some of the popular traditional plasmonic materials are gold, silver, copper etc. whereas hybrid plasmonic materials include either bimetallic/polymetallic alloys or the composites of single metal or multimetals with polymers or carbonaceous materials. The synthesis of both traditional and hybrid plasmonic materials are carried out using topdown and bottom up approaches, few of which are discussed from the available literature in the chapter. In the subsequent section, the sensing performances of various state-of-the-art plasmonic sensors prepared for the detection of gases (e.g. alcohol vapors, formaldehyde, H₂S etc.), biomolecules (e.g. glycoprotein, carcinoembryonic antigen, kirsten rat sarcoma K-RAS gene) are discussed. Plasmonic sensors play an important role in biomedical applications since they can detect low concentrations biomarkers of different diseases effectively at room temperature. For instance, it has been found that the antigen for chikungunya, an infectious mosquito-borne disease has been identified using plasmonic sensor.

Researchers have even detected newly invented SARS-CoV-2 virus protein at femtomolar (fM) level with the help of toroidal plasmonic immunosensor. The different strategies adopted by the researchers for the improvement of plasmonic sensing are discussed concurrently. Apart from the traditional modulation in the shape and size of plasmonic materials, evidence of improving the plasmonic sensing

is also found when plasmonic materials are blended with graphene, polymers or coated on shape memory materials. The modulation of vibrational spectra of functional groups ($-C=O$) for polymers has also been identified employing plasmonic sensors. While discussing the various examples, without limiting to the sensors that are active in the visible light, NIR active plasmonic sensors are also taken into account. The present article thus could provide a useful insight to the researchers working in the field of plasmonic materials.

References

1. Rodrigues, T. S., da Silva, A. G., & Camargo, P. H. (2019). Nanocatalysis by noble metal nanoparticles: Controlled synthesis for the optimization and understanding of activities. *Journal of Materials Chemistry A*, 7, 5857–5874.
2. Sakhno, O., Yezhov, P., Hryn, V., Rudenko, V., & Smirnova, T. (2020). Optical and nonlinear properties of photonic polymer nanocomposites and holographic gratings modified with noble metal nanoparticles. *Polymers*, 12, 480.
3. Paramasivam, G., Kayambu, N., Rabel, A. M., Sundramoorthy, A. K., & Sundaramurthy, A. (2017). Anisotropic noble metal nanoparticles: Synthesis, surface functionalization and applications in biosensing, bioimaging, drug delivery and theranostics. *Acta Biomaterialia*, 49, 45–65.
4. Pareek, V., Bhargava, A., Gupta, R., Jain, N., & Panwar, J. (2017). Synthesis and applications of noble metal nanoparticles: A review. *Advanced Science, Engineering and Medicine*, 9, 527–544.
5. Jeong, Y., Kook, Y.-M., Lee, K., & Koh, W.-G. (2018). Metal enhanced fluorescence (MEF) for biosensors: General approaches and a review of recent developments. *Biosensors and Bioelectronics*, 111, 102–116.
6. Langer, J., Jimenez de Aberasturi, D., Aizpurua, J., Alvarez-Puebla, R. A., Auguie, B., Baumberg, J. J., Bazan, G. C., Bell, S. E., Boisen, A., & Brolo, A. G. (2019). Present and future of surface-enhanced Raman scattering. *ACS Nano*, 14, 28–117.
7. Baruah, P. K., Singh, A., Rangan, L., Sharma, A. K., & Khare, A. (2020). Elucidation of size, structure, surface plasmon resonance, and photoluminescence of Ag nanoparticles synthesized by pulsed laser ablation in distilled water and its viability as SERS substrate. *Applied Physics A: Materials Science & Processing*, 126, 1–14.
8. Amirjani, A., & Haghshenas, D. F. (2018). Ag nanostructures as the surface plasmon resonance (SPR) based sensors: A mechanistic study with an emphasis on heavy metallic ions detection. *Sensors and Actuators B: Chemical*, 273, 1768–1779.
9. Lesyuk, R., Klein, E., Yaremchuk, I., & Klinke, C. (2018). Copper sulfide nanosheets with shape-tunable plasmonic properties in the NIR region. *Nanoscale*, 10, 20640–20651.
10. Ghosh, S., Saha, M., Paul, S., & De, S. (2017). Shape controlled plasmonic Sn doped CdO colloidal nanocrystals: A synthetic route to maximize the figure of merit of transparent conducting oxide. *Small*, 13, 1602469.
11. Baruah, P. K., Sharma, A. K., & Khare, A. (2018). Effective control of particle size, surface plasmon resonance and stoichiometry of Cu@Cu_xO nanoparticles synthesized by laser ablation of Cu in distilled water. *Optics and Laser Technology*, 108, 574–582.
12. Willets, K. A., & Van Duyne, R. P. (2007). Localized surface plasmon resonance spectroscopy and sensing. *Annual Review of Physical Chemistry*, 58, 267–297.
13. Amendola, V., Pilot, R., Frasconi, M., Marago, O. M., & Iati, M. A. (2017). Surface plasmon resonance in gold nanoparticles: A review. *Journal of Physics: Condensed Matter*, 29, 203002.

14. Stewart, M. E., Anderton, C. R., Thompson, L. B., Maria, J., Gray, S. K., Rogers, J. A., & Nuzzo, R. G. (2008). Nanostructured plasmonic sensors. *Chemical Reviews*, *108*, 494–521.
15. De Abajo, F. J. G., Sapienza, R., Noginov, M., Benz, F., Baumberg, J., Maier, S., Graham, D., Aizpurua, J., Ebbesen, T., & Pinchuk, A. (2015). Plasmonic and new plasmonic materials: General discussion. *Faraday Discussions*, *178*, 123–149.
16. Kostyukov, A. S., Ershov, A. E., Gerasimov, V. S., Filimonov, S. A., Rasskazov, I. L., & Karpov, S. V. (2019). Super-efficient laser hyperthermia of malignant cells with core-shell nanoparticles based on alternative plasmonic materials. *Journal of Quantitative Spectroscopy and Radiative Transfer*, *236*, 106599.
17. Shao, L., Zhuo, X., & Wang, J. (2018). Advanced plasmonic materials for dynamic color display. *Advanced Materials*, *30*, 1704338.
18. Patil, P. O., Pandey, G. R., Patil, A. G., Borse, V. B., Deshmukh, P. K., Patil, D. R., Tade, R. S., Nangare, S. N., Khan, Z. G., & Patil, A. M. (2019). Graphene-based nanocomposites for sensitivity enhancement of surface plasmon resonance sensor for biological and chemical sensing: A review. *Biosensors and Bioelectronics*, *139*, 111324.
19. Falahati, M., Attar, F., Sharifi, M., Saboury, A. A., Salihi, A., Aziz, F. M., Kostova, I., Burda, C., Priecl, P., & Lopez-Sanchez, J. A. (2020). Gold nanomaterials as key suppliers in biological and chemical sensing, catalysis, and medicine. *Biochimica et Biophysica Acta (BBA)-General Subjects*, *1864*, 129435.
20. Shrivastav, A. M., Usha, S. P., & Gupta, B. D. (2016). A localized and propagating SPR, and molecular imprinting based fiber-optic ascorbic acid sensor using an in situ polymerized polyaniline–Ag nanocomposite. *Nanotechnology*, *27*, 345501.
21. Sepúlveda, B., Angelomé, P. C., Lechuga, L. M., & Liz-Marzán, L. M. (2009). LSPR-based nanobiosensors. *Nano Today*, *4*, 244–251.
22. Petryayeva, E., & Krull, U. J. (2011). Localized surface plasmon resonance: Nanostructures, bioassays and biosensing—A review. *Analytica Chimica Acta*, *706*, 8–24.
23. Masson, J.-F. (2020). Portable and field-deployed surface plasmon resonance and plasmonic sensors. *Analyst*, *145*, 3776–3800.
24. Yockell-Lelievre, H., Bukar, N., McKeating, K., Arnaud, M., Cosin, P., Guo, Y., Dupret-Carruel, J., Mougin, B., & Masson, J.-F. (2015). Plasmonic sensors for the competitive detection of testosterone. *Analyst*, *140*, 5105–5111.
25. Shankaran, D. R., Gobi, K. V., & Miura, N. (2007). Recent advancements in surface plasmon resonance immunosensors for detection of small molecules of biomedical, food and environmental interest. *Sensors and Actuators B: Chemical*, *121*, 158–177.
26. Hammond, J. L., Bhalla, N., Rafiee, S. D., & Estrela, P. (2014). Localized surface plasmon resonance as a biosensing platform for developing countries. *Biosensors*, *4*, 172–188.
27. Lertvachirapaiboon, C., Baba, A., Shinbo, K., & Kato, K. (2018). A smartphone-based surface plasmon resonance platform. *Analytical Methods*, *10*, 4732–4740.
28. Guner, H., Ozgur, E., Kokturk, G., Celik, M., Esen, E., Topal, A. E., Ayas, S., Uludag, Y., Elbuken, C., & Dana, A. (2017). A smartphone based surface plasmon resonance imaging (SPRi) platform for on-site biodetection. *Sensors and Actuators B: Chemical*, *239*, 571–577.
29. Liu, Y., Liu, Q., Chen, S., Cheng, F., Wang, H., & Peng, W. (2015). Surface plasmon resonance biosensor based on smart phone platforms. *Scientific Reports*, *5*, 1–9.
30. Preechaburana, P., Suska, A., & Filippini, D. (2014). Biosensing with cell phones. *Trends in Biotechnology*, *32*, 351–355.
31. da Silva Freire, C., da Silva Moreira, C., de Souza Filho, C. A., Santa Cruz, R. M., Falqueto, A., Valle, A. L., Goulart Filho, L. R., de Medeiros, E. S., & do Nascimento Ferreira, K. (2019). Application of a smartphone-based SPR platform for glyphosate detection. In *2019 IEEE sensors applications symposium (SAS)* (pp. 1–6). IEEE.
32. Shackelford, J. A., Grote, R., Currie, M., Spanier, J. E., & Nabet, B. (2009). Integrated plasmonic lens photodetector. *Applied Physics Letters*, *94*, 083501.
33. Zhang, P., Wang, T., & Gong, J. (2015). Mechanistic understanding of the plasmonic enhancement for solar water splitting. *Advanced Materials*, *27*, 5328–5342.

34. Maier, S. A. (2006). Plasmonics: The promise of highly integrated optical devices. *IEEE Journal of Selected Topics in Quantum Electronics*, *12*, 1671–1677.
35. Wei, A. (2004). Plasmonic nanomaterials. In V. Rotello (Ed.), *Nanoparticles: Building blocks for nanotechnology* (pp. 173–200). Springer US.
36. Jeong, S. H., Choi, H., Kim, J. Y., Lee, T. W. J. P., & Characterization, P. S. (2015). Silver-based nanoparticles for surface plasmon resonance in organic optoelectronics. *Particle Particle Systems Characterization*, *32*, 164–175.
37. Eustis, S., & El-Sayed, M. A. J. C. S. R. (2006). Why gold nanoparticles are more precious than pretty gold: Noble metal surface plasmon resonance and its enhancement of the radiative and nonradiative properties of nanocrystals of different shapes. *Chemical Society Reviews*, *35*, 209–217.
38. Shao, L. Y., Coyle, J. P., Barry, S. T., & Albert, J. (2011). Anomalous permittivity and plasmon resonances of copper nanoparticle conformal coatings on optical fibers. *Optical Materials Express*, *1*, 128–137.
39. Mattox, T. M., & Urban, J. J. (2018). Tuning the surface plasmon resonance of lanthanum hexaboride to absorb solar heat: A review. *Materials (Basel)*, *11*, 2473.
40. Saha, K., Agasti, S. S., Kim, C., Li, X., & Rotello, V. M. J. C. R. (2012). Gold nanoparticles in chemical and biological sensing. *Chemical Reviews*, *112*, 2739–2779.
41. Di Fabrizio, E., Schlücker, S., Wenger, J., Regmi, R., Rigneault, H., Calafiore, G., West, M., Cabrini, S., Fleischer, M., & Van Hulst, N. F. J. J. O. O. (2016). Roadmap on biosensing and photonics with advanced nano-optical methods. *Journal of Optics*, *18*, 063003.
42. Murphy, C. J., Gole, A. M., Stone, J. W., Sisco, P. N., Alkilany, A. M., Goldsmith, E. C., & Baxter, S. C. (2008). Gold nanoparticles in biology: Beyond toxicity to cellular imaging. *Accounts of Chemical Research*, *41*, 1721–1730.
43. Austin, L. A., Kang, B., & El-Sayed, M. A. (2015). Probing molecular cell event dynamics at the single-cell level with targeted plasmonic gold nanoparticles: A review. *Nano Today*, *10*, 542–558.
44. Ghosh, P., Han, G., De, M., Kim, C. K., & Rotello, V. M. (2008). Gold nanoparticles in delivery applications. *Advanced Drug Delivery Reviews*, *60*, 1307–1315.
45. Al-Bayati, A. M., Munef, R. A., & Al-Haddad, R. M. J. S. R. I. P. (2020). Shape and size effect of surface plasmons on gold nanoparticles. *Systematic Reviews in Pharmacy*, *11*, 507–514.
46. Huang, X. H., & El-Sayed, M. A. (2010). Gold nanoparticles: Optical properties and implementations in cancer diagnosis and photothermal therapy. *Journal of Advanced Research*, *1*, 13–28.
47. Anker, J. N., Hall, W. P., Lyandres, O., Shah, N. C., Zhao, J., Van Duyne, R. P. J. N., & T.A.C.O.R.F.N. Journals. (2010). Biosensing with plasmonic nanosensors. *Nanoscience Technology: A Collection of Reviews from Nature Journals*, 308–319.
48. Chen, X. J., Cabello, G., Wu, D. Y., & Tian, Z. Q. (2014). Surface-enhanced Raman spectroscopy toward application in plasmonic photocatalysis on metal nanostructures. *Journal of Photochemistry and Photobiology C: Photochemistry Reviews*, *21*, 54–80.
49. Cho, E. S., Kim, J., Tejerina, B., Hermans, T. M., Jiang, H., Nakanishi, H., Yu, M., Patashinski, A. Z., Glotzer, S. C., Stellacci, F., & Grzybowski, B. A. (2012). Ultrasensitive detection of toxic cations through changes in the tunnelling current across films of striped nanoparticles. *Nature Materials*, *11*, 978–985.
50. Dreaden, E. C., Alkilany, A. M., Huang, X., Murphy, C. J., & El-Sayed, M. A. (2012). The golden age: Gold nanoparticles for biomedicine. *Chemical Society Reviews*, *41*, 2740–2779.
51. Amendola, V., & Meneghetti, M. (2009). Laser ablation synthesis in solution and size manipulation of noble metal nanoparticles. *Physical Chemistry Chemical Physics*, *11*, 3805–3821.
52. Link, S., & El-Sayed, M. A. (1999). Size and temperature dependence of the plasmon absorption of colloidal gold nanoparticles. *Journal of Physical Chemistry B*, *103*, 4212–4217.
53. Zhang, S., Tang, Y., & Vlahovic, B. (2016). A review on preparation and applications of silver-containing nanofibers. *Nanoscale Research Letters*, *11*, 80.

54. Baruah, P. K., Raman, M. A., Chakrabarty, I., Rangan, L., Sharma, A. K., & Khare, A. (2018). Antibacterial effect of silk treated with silver and copper nanoparticles synthesized by pulsed laser ablation in distilled water. In *AIP conference proceedings* (p. 030064). AIP Publishing LLC.
55. Chen, Y., & Ming, H. (2012). Review of surface Plasmon resonance and localized surface Plasmon resonance sensor. *Photonic Sensors*, 2, 37–49.
56. Xu, H., & Kall, M. (2002). Surface-plasmon-enhanced optical forces in silver nanoaggregates. *Physical Review Letters*, 89, 246802.
57. Gonzalez, A. L., Noguez, C., Beranek, J., & Barnard, A. S. (2014). Size, shape, stability, and color of plasmonic silver nanoparticles. *Journal of Physical Chemistry C*, 118, 9128–9136.
58. Chan, G. H., Zhao, J., Hicks, E. M., Schatz, G. C., & Van Duyne, R. P. J. N. L. (2007). Plasmonic properties of copper nanoparticles fabricated by nanosphere lithography. *Nano Letters*, 7, 1947–1952.
59. Yeshchenko, O. A. (2013). Temperature effects on the surface Plasmon resonance in copper nanoparticles. *Ukrainian Journal of Physics*, 58, 249–259.
60. Meriaudeau, F., Downey, T. R., Passian, A., Wig, A., & Ferrell, T. L. (1998). Environment effects on surface-plasmon spectra in gold-island films potential for sensing applications. *Applied Optics*, 37, 8030–8037.
61. Zhu, S. Q., Zhang, T., Guo, X. L., Wang, Q. L., Liu, X., & Zhang, X. Y. (2012). Gold nanoparticle thin films fabricated by electrophoretic deposition method for highly sensitive SERS application. *Nanoscale Research Letters*, 7, 613.
62. Larsson, E. M., Alegret, J., Kall, M., & Sutherland, D. S. (2007). Sensing characteristics of NIR localized surface plasmon resonances in gold nanorings for application as ultrasensitive biosensors. *Nano Letters*, 7, 1256–1263.
63. Choi, S. H., & Byun, K. M. (2010). Investigation on an application of silver substrates for sensitive surface plasmon resonance imaging detection. *Journal of the Optical Society of America. A, Optics, Image Science, and Vision*, 27, 2229–2236.
64. Sharma, G., Gupta, V. K., Agarwal, S., Kumar, A., Thakur, S., & Pathania, D. J. J. O. M. L. (2016). Fabrication and characterization of Fe@ MoPO nanoparticles: Ion exchange behavior and photocatalytic activity against malachite green. *Journal of Molecular Liquids*, 219, 1137–1143.
65. Sharma, G., Kumar, A., Sharma, S., Naushad, M., Dwivedi, R. P., AL-Othman, Z. A., & Mola, G. T. J. J. O. K. S. U.-S. (2019). Novel development of nanoparticles to bimetallic nanoparticles and their composites: A review. *Journal of King Saud University – Science*, 31, 257–269.
66. Sharma, G., Naushad, M., Kumar, A., Devi, S., & Khan, M. R. (2015). Lanthanum/Cadmium/Polyaniline bimetallic nanocomposite for the photodegradation of organic pollutant. *Iranian Polymer Journal*, 24, 1003–1013.
67. Major, K. J., De, C., & Obare, S. O. (2009). Recent advances in the synthesis of plasmonic bimetallic nanoparticles. *Plasmonics*, 4, 61–78.
68. Malviya, K. D., & Chattopadhyay, K. J. T. J. O. P. C. C. (2014). Synthesis and mechanism of composition and size dependent morphology selection in nanoparticles of Ag–Cu alloys processed by laser ablation under liquid medium. *The Journal of Physical Chemistry C*, 118, 13228–13237.
69. Navas, M. P., & Soni, R. K. (2015). Laser-generated bimetallic Ag–Au and Ag–Cu Core-Shell nanoparticles for refractive index sensing. *Plasmonics*, 10, 681–690.
70. Perdikaki, A., Galeou, A., Pilatos, G., Karatasios, I., Kanellopoulos, N. K., Prombona, A., & Karanikolos, G. N. J. A. A. M. (2016). Interfaces, Ag and Cu monometallic and Ag/Cu bimetallic nanoparticle–graphene composites with enhanced antibacterial performance. *ACS Applied Materials*, 8, 27498–27510.
71. Stelzig, S. H., Menneking, C., Hoffmann, M. S., Eisele, K., Barcikowski, S., Klapper, M., & Mullen, K. (2011). Compatibilization of laser generated antibacterial Ag- and Cu-nanoparticles for perfluorinated implant materials. *European Polymer Journal*, 47, 662–667.

72. Tang, X. F., Yang, Z. G., & Wang, W. J. (2010). A simple way of preparing high-concentration and high-purity nano copper colloid for conductive ink in inkjet printing technology. *Colloids and Surfaces A: Physicochemical and Engineering Aspects*, 360, 99–104.
73. Sharma, A. K., & Mohr, G. J. (2008). On the performance of surface plasmon resonance based fibre optic sensor with different bimetallic nanoparticle alloy combinations. *Journal of Physics D: Applied Physics*, 41, 055106.
74. Shin, K., Kim, D. H., Yeo, S. C., & Lee, H. M. (2012). Structural stability of AgCu bimetallic nanoparticles and their application as a catalyst: A DFT study. *Catalysis Today*, 185, 94–98.
75. Ceylan, A., Jastrzembki, K., & Shah, S. I. (2006). Enhanced solubility Ag-Cu nanoparticles and their thermal transport properties. *Metallurgical and Materials Transactions A: Physical Metallurgy and Materials Science*, 37a, 2033–2038.
76. Hai, H. T., Takamura, H., & Koike, J. J. J. O. A. (2013). Compounds, oxidation behavior of Cu–Ag core–shell particles for solar cell applications. *Journal of Alloys*, 564, 71–77.
77. Jiang, H., Moon, K.-s., & Wong, C. (2005). Synthesis of Ag-Cu alloy nanoparticles for lead-free interconnect materials. In *Proceedings. International symposium on advanced packaging materials: Processes, properties and interfaces*, 2005 (pp. 173–177). IEEE.
78. Hao, H. L., Li, H. H., Wang, S., Cheng, Z. T., & Fang, Y. C. (2020). Epitaxial growth of Ag-Cu bimetallic nanoparticles via thermal evaporation deposition. *Applied Surface Science*, 505, 143871.
79. Kunwar, S., Pandey, P., Pandit, S., Sui, M., & Lee, J. (2020). Tunable localized surface plasmon resonance by self-assembly of trimetallic and bimetallic alloy nanoparticles via Ag sublimation from Ag/Au/Pt tri-layers. *Applied Surface Science*, 504, 144545.
80. Kang, S. W., Lee, Y. W., Park, Y., Choi, B.-S., Hong, J. W., Park, K.-H., & Han, S. W. J. A. N. (2013). One-pot synthesis of trimetallic Au@ PdPt core–shell nanoparticles with high catalytic performance. *ACS Nano*, 7, 7945–7955.
81. Singh, R., & Soni, R. K. (2014). Improved catalytic activity of laser generated bimetallic and trimetallic nanoparticles. *Journal of Nanoscience and Nanotechnology*, 14, 6872–6879.
82. Ye, X. S., He, X. X., Lei, Y. L., Tang, J. L., Yu, Y. R., Shi, H., & Wang, K. M. (2019). One-pot synthesized Cu/Au/Pt trimetallic nanoparticles with enhanced catalytic and plasmonic properties as a universal platform for biosensing and cancer theranostics. *Chemical Communications*, 55, 2321–2324.
83. Ali, S., Sharma, A. S., Ahmad, W., Zareef, M., Hassan, M. M., Viswadevarayalu, A., Jiao, T., Li, H., & Chen, Q. (2020). Noble metals based bimetallic and Trimetallic nanoparticles: Controlled synthesis, antimicrobial and anticancer applications. *Critical Reviews in Analytical Chemistry*, 5, 1–28.
84. Komarneni, S. J. J. O. M. C. (1992). Nanocomposites. *Journal of Materials Chemistry*, 2, 1219–1230.
85. Thostenson, E. T., Li, C. Y., & Chou, T. W. (2005). Nanocomposites in context. *Composites Science and Technology*, 65, 491–516.
86. Shi, X., Gong, H., Li, Y., Wang, C., Cheng, L., & Liu, Z. (2013). Graphene-based magnetic plasmonic nanocomposite for dual bioimaging and photothermal therapy. *Biomaterials*, 34, 4786–4793.
87. Zhang, X., Xu, S., Jiang, S., Wang, J., Wei, J., Xu, S., Gao, S., Liu, H., Qiu, H., & Li, Z. J. A. S. S. (2015). Growth graphene on silver–copper nanoparticles by chemical vapor deposition for high-performance surface-enhanced raman scattering. *Applied Surface Science*, 353, 63–70.
88. Darabdhara, G., Sharma, B., Das, M. R., Boukherroub, R., & Szunerits, S. (2017). Cu-Ag bimetallic nanoparticles on reduced graphene oxide nanosheets as peroxidase mimic for glucose and ascorbic acid detection. *Sensors and Actuators B: Chemical*, 238, 842–851.
89. Jiang, J.-W. J. F. O. P. (2015). Graphene versus MoS 2: A short review. *Frontiers of Physics*, 10, 287–302.
90. Jang, J., Lee, J. M., Oh, S. B., Choi, Y., Jung, H. S., & Choi, J. (2020). Development of Antibiofilm nanocomposites: Ag/Cu bimetallic nanoparticles synthesized on the surface of graphene oxide Nanosheets. *ACS Applied Materials & Interfaces*, 12, 35826–35834.

91. Ijaz, I., Gilani, E., Nazir, A., & Bukhari, A. J. G. C. L. (2020). Reviews, detail review on chemical, physical and green synthesis, classification, characterizations and applications of nanoparticles. *Green Chemistry Letters Reviews*, *13*, 223–245.
92. Dhand, C., Dwivedi, N., Loh, X. J., Ying, A. N. J., Verma, N. K., Beuerman, R. W., Lakshminarayana, R., & Ramakrishna, S. J. R. A. (2015). Methods and strategies for the synthesis of diverse nanoparticles and their applications: A comprehensive overview. *RSC Advances*, *5*, 105003–105037.
93. Wender, H., Andreatza, M. L., Correia, R. R., Teixeira, S. R., & Dupont, J. (2011). Synthesis of gold nanoparticles by laser ablation of an Au foil inside and outside ionic liquids. *Nanoscale*, *3*, 1240–1245.
94. Hu, X., Takai, O., & Saito, N. (2013). Synthesis of gold nanoparticles by solution plasma sputtering in various solvents. In *Journal of physics: Conference series* (p. 012030). IOP Publishing.
95. Huang, C.-J., Wang, Y.-H., Chiu, P.-H., Shih, M.-C., & Meen, T.-H. J. M. L. (2006). Electrochemical synthesis of gold nanocubes. *Materials Letters*, *60*, 1896–1900.
96. Wu, H.-L., Kuo, C.-H., & Huang, M. H. J. L. (2010). Seed-mediated synthesis of gold nanocrystals with systematic shape evolution from cubic to trisoctahedral and rhombic dodecahedral structures. *Langmuir*, *26*, 12307–12313.
97. Malik, M. A., Wani, M. Y., & Hashim, M. A. J. A. J. O. C. (2012). Microemulsion method: A novel route to synthesize organic and inorganic nanomaterials: 1st Nano update. *Arabian Journal of Chemistry*, *5*, 397–417.
98. Ankamwar, B. (2010). Biosynthesis of gold nanoparticles (Green-Gold) using leaf extract of Terminalia Catappa. *E-Journal of Chemistry*, *7*, 1334–1339.
99. Agnihotri, M., Joshi, S., Kumar, A. R., Zinjarde, S., & Kulkarni, S. (2009). Biosynthesis of gold nanoparticles by the tropical marine yeast *Yarrowia lipolytica* NCIM 3589. *Materials Letters*, *63*, 1231–1234.
100. Hajiesmaeilbaigi, F., Mohammadalipour, A., Sabbaghzadeh, J., Hoseinkhani, S., & Fallah, H. J. L. P. L. (2005). Preparation of silver nanoparticles by laser ablation and fragmentation in pure water. *Laser Physics Letters*, *3*, 252.
101. Pyatenko, A., Shimokawa, K., Yamaguchi, M., Nishimura, O., & Suzuki, M. (2004). Synthesis of silver nanoparticles by laser ablation in pure water. *Applied Physics A: Materials Science & Processing*, *79*, 803–806.
102. Khayati, G. R., & Janghorban, K. (2013). Preparation of nanostructure silver powders by mechanical decomposing and mechanochemical reduction of silver oxide. *Transactions of Nonferrous Metals Society of China*, *23*, 1520–1524.
103. Asanithi, P., Chaikyakun, S., & Limsuwan, P. J. J. O. N. (2012). Growth of silver nanoparticles by DC magnetron sputtering. *Journal of Nanomaterials*, *2012*, 1–8.
104. Pingali, K. C., Rockstraw, D. A., & Deng, S. G. (2005). Silver nanoparticles from ultrasonic spray pyrolysis of aqueous silver nitrate. *Aerosol Science and Technology*, *39*, 1010–1014.
105. Guzmán, M. G., Dille, J., & Godet, S. J. I. J. C. B. E. (2009). Synthesis of silver nanoparticles by chemical reduction method and their antibacterial activity. *International Journal of Chemical and Biomolecular Engineering*, *2*, 104–111.
106. Suriati, G., Mariatti, M., & Azizan, A. (2014). Synthesis of silver nanoparticles by chemical reduction method: Effect of reducing agent and surfactant concentration. *International Journal of Automotive and Mechanical Engineering*, *10*, 1920–1927.
107. Gudikandula, K., & Maringanti, S. C. (2016). Synthesis of silver nanoparticles by chemical and biological methods and their antimicrobial properties. *Journal of Experimental Nanoscience*, *11*, 714–721.
108. Lkhagvajav, N., Yasa, I., Celik, E., Koizhaiganova, M., & Sari, O. (2011). Antimicrobial activity of colloidal silver nanoparticles prepared by Sol-Gel method. *Digest Journal of Nanomaterials and Biostructures*, *6*, 149–154.
109. Saraidarov, T., Levchenko, V., & Reinfeld, R. J. P. S. S. C. (2010). Synthesis of silver nanoparticles and their stabilization in different sol-gel matrices: Optical and structural characterization. *Physica Status Solidi C*, *7*, 2648–2651.

110. Zhang, W., Qiao, X., & Chen, J. J. M. S. (2007). Synthesis of silver nanoparticles—Effects of concerned parameters in water/oil microemulsion. *Materials Science Engineering: B*, *142*, 1–15.
111. Prathna, T. C., Chandrasekaran, N., Raichur, A. M., & Mukherjee, A. (2011). Biomimetic synthesis of silver nanoparticles by Citrus limon (lemon) aqueous extract and theoretical prediction of particle size. *Colloids and Surfaces. B, Biointerfaces*, *82*, 152–159.
112. Chandran, S. P., Chaudhary, M., Pasricha, R., Ahmad, A., & Sastry, M. J. B. P. (2006). Synthesis of gold nanotriangles and silver nanoparticles using Aloe vera plant extract. *Biotechnology Progress*, *22*, 577–583.
113. Korbekandi, H., Irvani, S., & Abbasi, S. (2012). Optimization of biological synthesis of silver nanoparticles using *Lactobacillus casei* subsp. *casei*. *Journal of Chemical Technology and Biotechnology*, *87*, 932–937.
114. Sunkar, S., & Nachiyar, C. V. J. A. P. J. O. T. B. (2012). Biogenesis of antibacterial silver nanoparticles using the endophytic bacterium *Bacillus cereus* isolated from *Garcinia xanthochymus*. *Asian Pacific Journal of Tropical Biomedicine*, *2*, 953–959.
115. Tilaki, R. M., Zad, A. I., & Mahdavi, S. M. (2007). Size, composition and optical properties of copper nanoparticles prepared by laser ablation in liquids. *Applied Physics A: Materials Science & Processing*, *88*, 415–419.
116. Jaiswal, J., Chauhan, S., & Chandra, R. J. I. J. S. T. M. (2015). Influence of sputtering parameters on structural, optical and thermal properties of copper nanoparticles synthesized by dc magnetron sputtering. *International Journal Of Science Technology & Management*, *4*, 678–688.
117. Nakagawa, K., Narushima, T., Udagawa, S., & Yonezawa, T. (2013). Preparation of copper nanoparticles in liquid by matrix sputtering process. In *Journal of physics: Conference series* (p. 012038). IOP Publishing.
118. Lisiecki, I., Billoudet, F., & Pileni, M. J. T. J. O. P. C. (1996). Control of the shape and the size of copper metallic particles. *The Journal of Physical Chemistry*, *100*, 4160–4166.
119. Goia, D. V., & Matijević, E. J. N. J. O. C. (1998). Preparation of monodispersed metal particles. *New Journal of Chemistry*, *22*, 1203–1215.
120. Solanki, J. N., Sengupta, R., & Murthy, Z. V. P. (2010). Synthesis of copper sulphide and copper nanoparticles with microemulsion method. *Solid State Sciences*, *12*, 1560–1566.
121. Raja, M., Shuba, J., Ali, F. B., & Ryu, S. H. (2008). Synthesis of copper nanoparticles by electroreduction process. *Materials and Manufacturing Processes*, *23*, 782–785.
122. Allagui, A., Wuthrich, R., & Baranova, E. A. (2008). Copper and nickel nanoparticles: Synthesis by electrochemical discharges. In *2008 1st microsystems and nanoelectronics research conference* (pp. 65–68). IEEE.
123. Sharma, P., Pant, S., Poonia, P., Kumari, S., Dave, V., & Sharma, S. (2018). Green synthesis of colloidal copper nanoparticles capped with *Tinospora cordifolia* and its application in catalytic degradation in textile dye: An ecologically sound approach. *Journal of Inorganic and Organometallic Polymers and Materials*, *28*, 2463–2472.
124. Intartaglia, R., Das, G., Bagga, K., Gopalakrishnan, A., Genovese, A., Povia, M., Di Fabrizio, E., Cingolani, R., Diaspro, A., & Brandi, F. (2013). Laser synthesis of ligand-free bimetallic nanoparticles for plasmonic applications. *Physical Chemistry Chemical Physics*, *15*, 3075–3082.
125. Chen, D.-H., & Chen, C.-J. J. J. O. M. C. (2002). Formation and characterization of Au–Ag bimetallic nanoparticles in water-in-oil microemulsions. *Journal of Materials Chemistry*, *12*, 1557–1562.
126. Ni, Y., Kan, C. X., He, L. B., Zhu, X. Z., Jiang, M. M., & Shi, D. N. (2019). Alloyed Au–Ag nanorods with desired plasmonic properties and stability in harsh environments. *Photonics Research*, *7*, 558–565.
127. Kumari, M. M., Jacob, J., & Philip, D. J. S. A. P. A. M. (2015). B. Spectroscopy, green synthesis and applications of Au–Ag bimetallic nanoparticles. *Spectrochimica Acta Part A: Molecular Biomolecular Spectroscopy*, *137*, 185–192.

128. Salam, A. A., Singaravelan, R., Vasanthi, P., & Alwar, S. B. J. J. O. N. I. C. (2015). Electrochemical fabrication of Ag–Cu nano alloy and its characterization: An investigation. *Journal of Nanostructure in Chemistry*, 5, 383–392.
129. Bernard, V., Zobač, O., Sopoušek, J., & Mornstein, V. J. J. O. C. R. (2014). AgCu bimetallic nanoparticles under effect of low intensity ultrasound: The cell viability study in vitro. *Journal of Cancer Research*, 2014, 1–6.
130. Thakore, S. I., Nagar, P. S., Jadeja, R. N., Thounaojam, M., Devkar, R. V., & Rathore, P. S. (2019). Sapota fruit latex mediated synthesis of Ag, Cu mono and bimetallic nanoparticles and their in vitro toxicity studies. *Arabian Journal of Chemistry*, 12, 694–700.
131. Ashishie, P. B., Anyama, C. A., Ayi, A. A., Oseghale, C. O., Adesuji, E. T., & Labulo, A. H. J. I. J. O. P. S. (2018). Green synthesis of silver monometallic and copper-silver bimetallic nanoparticles using *Kigelia africana* fruit extract and evaluation of their antimicrobial activities. *International Journal of Physical Sciences*, 13, 24–32.
132. Sharma, D., Ledwani, L., Kumar, N., Mehrotra, T., Pervaiz, N., & Kumar, R. J. A. J. F. S. (2020). Engineering, an investigation of physicochemical and biological properties of Rheum emodi-mediated bimetallic Ag–Cu nanoparticles. *Arabian Journal for Science*, 46, 275–285.
133. Mattei, J. G., Grammatikopoulos, P., Zhao, J. L., Singh, V., Vernieres, J., Steinhauer, S., Porkoyich, A., Danielson, E., Nordlund, K., Djurabekova, F., & Sowwan, M. (2019). Gas-phase synthesis of trimetallic nanoparticles. *Chemistry of Materials*, 31, 2151–2163.
134. Yang, A., Huntington, M. D., Cardinal, M. F., Masango, S. S., Van Duyne, R. P., & Odom, T. W. J. A. N. (2014). Hetero-oligomer nanoparticle arrays for plasmon-enhanced hydrogen sensing. *ACS Nano*, 8, 7639–7647.
135. Monfared, Y. E., & Qasymeh, M. J. R. I. P. (2021). Graphene-assisted infrared plasmonic metamaterial absorber for gas detection. *Results in Physics*, 23, 103986.
136. Yao, Y., Ji, F., Yin, M., Ren, X., Ma, Q., Yan, J., & Liu, S. F. J. A. A. M. (2016). Interfaces, Ag nanoparticle-sensitized WO₃ hollow nanosphere for localized surface plasmon enhanced gas sensors. *ACS Applied Materials Interfaces*, 8, 18165–18172.
137. Prado, A. R., Díaz, C. A., Nunes, L. G. L., Oliveira, J. P., Guimarães, M. C., Leal-Junior, A., Ribeiro, M. R., & Pontes, M. J. J. P. (2021). Surface Plasmon resonance-based optical fiber sensors for H₂S In Situ detection. *Plasmonics*, 16, 787–797.
138. Xue, S., Jiang, X.-F., Zhang, G., Wang, H., Li, Z., Hu, X., Chen, M., Wang, T., Luo, A., & Ho, H.-P. J. A. S. (2020). Surface plasmon-enhanced optical formaldehyde sensor based on CdSe@ZnS quantum dots. *ACS Sensors*, 5, 1002–1009.
139. Miranda, B., Moretta, R., De Martino, S., Dardano, P., Rea, I., Forestiere, C., & De Stefano, L. J. J. O. A. P. (2021). A PEGDA hydrogel nanocomposite to improve gold nanoparticles stability for novel plasmonic sensing platforms. *Journal of Applied Physics*, 129, 033101.
140. Calatayud-Sanchez, A., Catalan-Carrio, R., Ortega, Á., Lázaro, J. B., Zubia, J., Lopez, F. B., Villatoro, J., & Basabe, L. (2021). Plasmon resonance energy-transfer-based fiber-optic platform for ultrasensitive sensing. In *Smart photonic and optoelectronic integrated circuits XXIII* (p. 116900G). International Society for Optics and Photonics.
141. Esfandiari, M., Jarchi, S., Nasiri-Shehni, P., & Ghaffari-Miab, M. J. A. O. (2021). Enhancing the sensitivity of a transmissive graphene-based plasmonic biosensor. *Applied Optics*, 60, 1201–1208.
142. Henderson, Z., Borovac, D., Sammarco, C., Liu, X., & Tan, C.-K. (2021). GaN biosensor design with localized surface plasmon resonance. In *Physics and simulation of optoelectronic devices XXIX* (p. 116801E). International Society for Optics and Photonics.
143. Shukla, S., & Arora, P. J. S. (2021). Design and analysis of aluminum-silicon-graphene based Plasmonic device for biosensing applications in the optical communication band. *SILICON*, 13, 3703–3711.
144. Rahman, K. M., Alam, M. S., Ahmed, R., & Islam, M. A. J. R. I. P. (2021). Irregular hexagonal core based surface Plasmon resonance sensor in near-infrared region. *Results in Physics*, 23, 103983.

145. Samavati, Z., Samavati, A., Ismail, A. F., Rahman, M. A., Othman, M. H. D., & Yeganeh, F. N. J. O. F. T. (2021). Optical fiber sensor for glycoprotein detection based on localized surface plasmon resonance of discontinuous Ag-deposited nanostructure. *Optical Fiber Technology*, *62*, 102476.
146. George, A., Amrutha, M., Srivastava, P., Sunil, S., Sai, V., & Srinivasan, R. J. A. (2021). Development of a U-bent plastic optical fiber biosensor with plasmonic labels for the detection of chikungunya non-structural protein 3. *Analyst*, *146*, 244–252.
147. Ahmadivand, A., Gerislioglu, B., Ramezani, Z., Kaushik, A., Manickam, P., & Ghoreishi, S. A. J. B. (2021). Bioelectronics, functionalized terahertz plasmonic metasensors: Femtomolar-level detection of SARS-CoV-2 spike proteins. *Biosensors Bioelectronics*, *177*, 112971.
148. Yang, R., Jiang, G., Liu, J., Wang, Y., Jian, N., He, L., Liu, L. E., Qu, L., & Wu, Y. J. A. C. A. (2021). Plasmonic TiO₂@ Au NPs//CdS QDs photocurrent-direction switching system for ultrasensitive and selective photoelectrochemical biosensing with cathodic background signal. *Analytica Chimica Acta*, *1153*, 338283.
149. Zhang, Q., Liu, Y., Nie, Y., Ma, Q. J. S., & Chemical, A. B. (2020). Magnetic-plasmonic yolk-shell nanostructure-based plasmon-enhanced electrochemiluminescence sensor. *Sensors and Actuators B: Chemical*, *319*, 128245.
150. Gao, Z., Shao, S., Gao, W., Tang, D., Tang, D., Zou, S., Kim, M. J., & Xia, X. J. A. N. (2021). Morphology-invariant metallic nanoparticles with tunable plasmonic properties. *ACS Nano*, *15*, 2428–2438.
151. Chen, Y.-M., Pekdemir, S., Bilican, I., Koc-Bilican, B., Cakmak, B., Ali, A., Zang, L.-S., Onses, M. S., & Kaya, M. J. C. P. (2021). Production of natural chitin film from pupal shell of moth: Fabrication of plasmonic surfaces for SERS-based sensing applications. *Carbohydrate Polymers*, *262*, 117909.
152. Xiong, Y., Fu, T., Zhang, D., Zhang, S., & Xu, H. J. N. (2021). Superradiative plasmonic nanoantenna biosensors enable sensitive immunoassay using the naked eye. *Nanoscale Research Letters*, *13*, 2429–2435.
153. Wang, H., Rao, G., Wang, Y., Du, X., Zhang, M., Wang, X., Hu, A., Hu, Y., Huang, J., & Chu, J. J. T. J. O. P. C. C. (2021). Low field gradient and highly enhanced plasmonic nanocavity array for supersensitive determination of multiple hazardous Chemical residues. *The Journal of Physical Chemistry C*, *125*, 4710–4719.
154. Yasli, A., & Ademgil, H. J. O. (2021). Effect of bending on photonic crystal fiber based surface plasmon resonance biosensor. *Optik*, *241*, 166640.
155. Baldassarre, L., Sakat, E., Frigerio, J., Samarelli, A., Gallacher, K., Calandrini, E., Isella, G., Paul, D. J., Ortolani, M., & Biagioni, P. J. N. I. (2015). Midinfrared plasmon-enhanced spectroscopy with germanium antennas on silicon substrates. *Nano Letters*, *15*, 7225–7231.
156. Li, Y., Yan, H., Farmer, D. B., Meng, X., Zhu, W., Osgood, R. M., Heinz, T. F., & Avouris, P. J. N. I. (2014). Graphene plasmon enhanced vibrational sensing of surface-adsorbed layers. *Nano Letters*, *14*, 1573–1577.
157. Tang, Z., Wu, J., Yu, X., Hong, R., Zu, X., Lin, X., Luo, H., Lin, W., & Yi, G. J. A. A. M. (2021). Interfaces, fabrication of au nanoparticle arrays on flexible substrate for tunable localized surface Plasmon resonance. *ACS Applied Materials Interfaces*, *13*(7), 9281–9288.
158. Mascaretti, L., Schirato, A., Zbořil, R., Kment, Š., Schmuki, P., Alabastri, A., & Naldoni, A. J. N. E. (2021). Solar steam generation on scalable ultrathin thermoplasmonic TiN nanocavity arrays. *Nano Energy*, *83*, 105828.
159. Rishi, M., Sinha, T. K., Bhattacharya, S., Datta, P. K., & Ray, K. (2017). Facile one-pot synthesis of highly stable graphene–Ag₀ hybrid nanostructures with enhanced optical properties. *The Journal of Physical Chemistry C*, *121*(39), 21591–21599.
160. Rishi, M., Sinha, T. K., Mukherjee, S., Adhikari, B., & Ray, S. K. (2016). Enhanced and selective photodetection using graphene-stabilized hybrid plasmonic silver nanoparticles. *Plasmonics*, *11*(5), 1297–1304.
161. Kumar, S. T., Ghosh, S. K., Maiti, R., Jana, S., Adhikari, B., Mandal, D., & Ray, S. K. (2016). Graphene-silver-induced self-polarized PVDF-based flexible plasmonic nanogenerator toward the realization for new class of self powered optical sensor. *ACS Applied Materials & Interfaces*, *8*(24), 14986–14993.

162. Wei, C. C., Raja, S. S., Chang, C., Hang, X., Liu, P., Lee, Y., Shih, C. K., & Gwo, S. (2020). Epitaxial aluminum plasmonics covering full visible spectrum. *Nano*, *10*(1), 627–637.
163. Mark, K., King, N. S., Liu, L., Everitt, H. O., Nordlander, P., & Halas, N. J. (2014). Aluminum for plasmonics. *ACS Nano*, *8*(1), 834–840.
164. Jyoti, K., & Soni, R. K. (2013). Size-and shape-dependent plasmonic properties of aluminum nanoparticles for nanosensing applications. *Journal of Modern Optics*, *60*(20), 1717–1728.
165. Mehrnoosh, S., Mahani, F. F., & Mokhtari, A. (2019). Design of aluminum-based nanoring arrays for realizing efficient plasmonic sensors. *Journal of the Optical Society of America B*, *36*(3), 786–793.
166. Alexander, L., Valiulis, S. N., Malinick, A. S., Tanabe, I., & Cheng, Q. (2020). Plasmonic biosensing with aluminum thin films under the Kretschmann configuration. *Analytical Chemistry*, *92*(13), 8654–8659.
167. Paulo, S., Almeida, J., Santos, I. P., & Coelho, L. (2021). Advances in plasmonic sensing at the NIR—A review. *Sensors*, *21*(6), 2111.
168. Pradeep, B., Verma, S. S., & Sinha, M. M. (2020). Tunable plasmonic properties of elongated bimetallic alloys nanoparticles towards deep UV-NIR absorbance and sensing. *Journal of Quantitative Spectroscopy and Radiative Transfer*, *241*, 106751.
169. Jun, Z., Zhang, C., Braun, P. V., & Giessen, H. (2012). Large-area low-cost Plasmonic nanostructures in the NIR for Fano resonant sensing. *Advanced Materials*, *24*(35), OP247–OP252.
170. Minh, K., Lee, J., & Nam, J. (2019). Plasmonic photothermal nanoparticles for biomedical applications. *Advanced Science*, *6*(17), 1900471.
171. Sujan, K., Curtin, K., & Wu, N. (2019). A review of 2D and 3D plasmonic nanostructure array patterns: Fabrication, light management and sensing applications. *Nano*, *8*(12), 2065–2089.

Index

A

- ab initio* TDDFT, 166
- Absorption and photoluminescence spectroscopy, 222
- Achiral plasma structure, 9
- Active ENZ plasmonic waveguides
 - applications
 - complex frequency excitation, 83
 - counter-propagating plane waves, 80
 - group velocity, 82
 - integrated nanophotonic components, 81
 - nonlinear case, 81
 - nonlinear PT-symmetric photonic systems, 82
 - nonlinear transmission hysteresis, 82
 - perfect directional absorption, 80, 81
 - radiation's wavelength, 82
 - reciprocal symmetric system, 81
 - super scattering, 80
 - third-order nonlinearity, 81
 - transmission and reflection coefficients, 81
 - z -polarized plane wave, 81
 - Active ENZ waveguides, numerical modeling
 - active material dispersion, 72
 - FP resonance response, 73
 - Kramers-Kronig relations, 72
 - Lorentzian dispersion, 73
 - nanochannels, 72
 - passive waveguides, 72
 - plasmonic channels, 72
 - zero-reflection response, 72
 - Active ENZ waveguides, theoretical analysis
 - ABCD parameters, 75
 - active dielectric material, 79
 - amplification and dissipation, 79
 - complex eigenvalues, 78
 - constant impedance, 74
 - Drude permittivity dispersion, 75
 - eigenvalues and eigenvectors, 77
 - EP degeneracy, 78
 - gain coefficients, 79
 - Hermitian system, 77
 - impedance matching conditions, 76
 - input impedance, 76
 - quasi-TE mode, 75
 - radial frequency, 75
 - reflection and transmission coefficients, 76
 - reflection coefficient, 76
 - scattering (lasing) response, 73
 - spectral degeneracy point, 79
 - 3D distribution, 76
 - transfer matrix components, 77
 - transmission and reflection, 79
 - transmission line segment, 73
 - transmission-line theoretical model, 73, 77
 - two-port network, 75
- Adiabatic frequency conversion (AFC), 45–47
- Aerosol science, 227–228
- Ag₆H₂O, 171
- Ag plasmonic LNWs, 286
- Ag-WO₃ hollow nanospheres (HNSs), 312
- Aluminum (Al), 320
- Aluminum-doped Zinc Oxide (AZO), 35
- Anisotropic 2D plano-concave waveguide, 37
- Applications of plasmonic optical trapping, life sciences
 - Acoustic Raman spectra, 196
 - BSA molecule, 193

- Applications of plasmonic optical trapping, life sciences (*cont.*)
- DNH
 - aperture, 194
 - nanoholes, metallic films, 193
 - optical tweezers, 193
 - EAR spectroscopy, 195
 - electrophoretic force, 196
 - energy barrier, 195
 - fluorophore-based methods, 193
 - inverted bowtie plasmonic nanopore optical tweezers, 196
 - microbubbles, 199
 - nano-aperture optical trapping, 193
 - nanopore-based detection platforms, 195
 - optothermal manipulation techniques, 199
 - opto-thermoelectric trapping technique, 198
 - plasmonic nanostructures, 193
 - RMS, 195
- Applications of plasmonic tweezers
- aerosol science, 227–228
 - atoms trapping, 226
 - cell biology
 - adhesion and structure, bacterial Pili, 221
 - cellular adhesion forces, 219–221
 - directed neuronal growth, 221
 - microchemistry
 - liquid droplets, 226
 - vesicle and membrane manipulation, 226
 - vesicle fusion, 227
 - optofluidics and LOC
 - monolithic integration, 225
 - optical sorting, 224
 - spectroscopy
 - absorption and photoluminescence spectroscopy, 222
 - Raman spectroscopy, 223
- Aqueous droplets, 226, 227
- Artificial chiral metamaterials, 8
- Artificially structured materials, 102
- Artificial magnetism, 102
- Asymmetric transmission (AT), 3, 4
- chiral plasmonic nanostructures, 10
 - circularly polarized light, 10
 - connected gammadion-shaped nanostructure, 14
 - conversion transmittance, 10
 - counter-handed transmitted field component, 12
 - G-shaped structures, 11
 - helical plasmonic nanostructures, 10
 - layer-by-layer structure, 11
 - nanoslit-nanorod arrays, 11
 - nanostructure arrays, 13
 - planar structures, 13
 - polarization state, 10
 - spiral/multilayered chiral metamaterials, 11
 - tilted rectangular nanohole, 13
- Atomic layer deposition (ALD) method, 92, 93
- Atoms trapping, 222
- Attenuated Total Reflection (ATR) configuration, 314
- AuNIs, *see* Gold nano-islands (AuNIs)
- Au-Pd dimer, 311
- Au-Pd-Pt hetero-tetramers, 311
- Au-Pd-Pt hetero-trimers, 311
- Au-Pd-Pt hetero-trimersare, 311
- Au-Pd trimers, 311
- Au-Pt heterodimers, 311
- B**
- Bacteria, 221
- Bezier curves for molding nanostructure geometries
 - control points, 139
 - degree n , 139
 - electromagnetic radiation, 140
 - polynomial curves, 139
 - polynomial surfaces manipulation, 139
 - 2D and 3D geometrical designs, 139
- Bi₂Se₃ microribbon arrays, 111
- Bi₂Te₃-involved solar cell, 109
- BIC-based plasmonic resonances, 124
- Bimetallic nanoparticles (BMNPs), 304, 305
- Biosensing
 - ATR configuration, 314
 - Au NPs, 313–314
 - blood components, 316
 - CEA, 315, 316
 - CHIKV antigen, 314
 - CHIKVnsP3Ab, 315
 - development, 314
 - ECL nanosensor, 316
 - FDTD simulation method, 314
 - fluorinated polymer, 314
 - Ge antennas, 316
 - GNR array, 317
 - ITO layer, 314
 - K-RAS, 316
 - LSPR, 314
 - mid-infrared active plasmonic sensing, 316
 - morphology-invariant NPs, 316
 - NPOM, 316
 - optical properties and sensitivity, 313

- optical sensor, 314
- PCF, 314
- PCF based SPR sensor, 316
- plasmonic Au NP arrays, 318
- plasmonic resonance of graphene, 314
- plasmonic sensor, 313
- PMMA, 314
- PMMA/PVP, 317–318
- RI, 314
- SARS-CoV-2, 315
- SERS, 316, 317
- SMPU substrates, 318
- SPC effect, 316
- steam generation, 318
- TiNnanocavities, 318–319
- toxic gases/biomolecules, 318
- TSA, 318, 319
- U bent Plasmonic optical fibre, 314–315
- Blood components, 316
- BMNPs, *see* Bimetallic nanoparticles (BMNPs)
- Boltzmann constant, 185
- Bound states in the continuum (BIC), 118
- Bovine serum albumin (BSA) molecule, 193
- Bowtie nanostructures, 191
- Broadband solar spectrum, 320
- Broadband THz generation, nonlinear metasurfaces
 - arbitrary nonmagnetic material, 120
 - cut-off frequency, 120
 - deficient absorption, 119
 - FDTD algorithm, 120
 - first-principle FDTD calculation, 121
 - first-principle method, 120
 - FWHM, 119
 - high-speed telecommunications range, 123
 - incident Gaussian pulse, 120
 - next-generation computation and communication, 122
 - non-dispersive dielectric materials, 121
 - normal incidence, 121
 - out-of-phase polarization, 122
 - pump pulse intensity, 123
 - second-order nonlinear susceptibility, 119
 - SRRs, 119, 121, 122
 - sum-frequency generation, 121
 - temporal Gaussian envelope, 119
 - THz conversion efficiency, 119, 122
 - THz emission, 119, 123
 - THz radiation, 123
 - THz spectrum, 120
 - vacuum permittivity and permeability, 120
 - wave impedance, 122
- Brownian force, 184
- Brownian motion, 227
- BSA, *see* Bovine serum albumin (BSA) molecule
- BSTS light absorption, 109
- Bulk permittivities, 94
- C**
- Carbon nanotubes (CNTs), 305
- Carcino embryonic antigen (CEA), 315, 316
- Cavity-enhanced Raman scattering (CERS), 226
- CD enhancement factor, 20
- CdSe@ZnS QDs, FS and Au NP, 313
- CEA, *see* Carcino embryonic antigen (CEA)
- Cell biology
 - adhesion and structure, bacterial Pili, 221
 - cellular adhesion forces, 219–221
 - directed neuronal growth, 221
- Cells, 58, 93, 108, 127
- Cellular adhesion forces, 219–221
- Cellular dynamics, 219
- Cellular functions, 219
- CERS, *see* Cavity-enhanced Raman scattering (CERS)
- Channel plasmon polaritons (CPPs), 264
- Chemically synthesized nanowires (CSNWs), 265, 268, 285
- Chemical vapor deposition (CVD), 93
- Chick dorsal root ganglia (DRGs), 221
- CHIKV antigen, 314
- CHIKVnsP3Ab, 315
- Chiral biomolecules, 18, 19
- Chiral conic nanoshell metallic nanostructure (CCNM), 18
- Chiral “hot spot,” 3
- Chirality
 - AT, 4
 - CB and CD, 3
 - common natural phenomenon, 2
 - definition, 2
 - far-field effect, 3
 - limonene, 2
 - living matter characteristics, 3
 - medicine, 2
 - near-field (*see* Optical chirality)
 - objects, 2
 - optical chirality density, 3
 - Pasteur’s experiments, 3
 - plasmonic nanostructures/metasurfaces, 3
 - polarized states, 4
 - role in animal world, 2
- Chiral metal nanostructures, 22
- Chiral molecular sensing, 21

- Chiral objects, 2
- Chiral photonic crystals, 2
- Chiral plasmonic nanostructure, 10
- Chiral plasmonic structure, 3
- Chiral plasmons, 21
- Circular birefringence (CB), 3
- Circular dichroism (CD), 3
- chiral L-shaped nanostructure, 16
 - chiral metamaterial structure, 17
 - colloidal monolayer technology, 16
 - differential absorption/transmission, 14
 - F–P cavity strategy, 17
 - GLAD method, 17
 - helix, 15
 - layer-by-layer structures, 17
 - L-shaped nanostructure, 17
 - MIM structures, 17
 - planar chiral nanostructures, 18
 - planar heptamer gold nanostructures, 18
 - sample–matrix interface, 17
 - SRR, 17
 - 3D AFM measurement, 16
 - 3D nanostructures, 17
 - tilted rectangular nanohole arrays, 15
 - transmittance spectra, 15
 - U-shaped 3D structure, 16
- Circularly polarized light, 5, 10
- Classical dipole nanoantenna (CDN), 138, 151
- Clausius-Mossotti relation, 182
- CNTs, *see* Carbon nanotubes (CNTs)
- Coherent light-matter interactions, 83
- Coherent perfect absorption (CPA)
- definition, 61
 - effect, 61
 - linear plasmonic waveguides (*see* Linear CPA, ENZ)
 - nanostructures, 61
 - nonlinear plasmonic waveguides (*see* Nonlinear tunable CPA, ENZ)
 - PT symmetric photonic systems, 61
 - ZIM, 61
- Colloidal particles, 199, 237
- Complementary metal-oxide-semiconductor (CMOS) technology, 93
- Complementary optimization studies, 150
- Complex frequency modal analysis, 38
- COMSOL, 59, 270
- Continuous-wave (CW) laser, 268, 273, 282, 284
- Conventional optical tweezers, 187
- Conventional plasmonic materials
- Ag NPs, 302–303
 - Au NPs, 302
 - Cu NPs, 303
- “Conventional” scales, 138
- Copper (Cu) NPs, 303
- Counter-propagating laser beams, 177
- Coupled mode theory (CMT), 131, 132
- Coupling efficiency (η)
- characterisation, 281, 282
 - defined, 274–275
 - dipole emitters and plasmonic waveguides, 280, 281
 - and directionality of NV centers, 269
 - EMCCD, 282
 - emitter position, 280
 - LNW, 279–281
 - LNW-OGCs, 277, 279–283
 - NDs, 281
 - OGCs, 274, 290
 - quantum emitter, 284
 - scalable nanoplasmonic waveguides, 279
- CPPs, *see* Channel plasmon polaritons (CPPs)
- Crafted plasmonic NPs, 316
- Cr slit mask, 311
- CSNWs, *see* Chemically synthesized nanowires (CSNWs)
- Cylindrical waveguides, 264
- D**
- Decahedron, 303
- Dentroder, 222
- Density functional theory (DFT), 96
- Dielectric-loaded surface plasmon polaritons, 264
- Digital holography (DH), 104
- Dipole approximation regime, 181–183
- Dipole emitter, 279–282
- Dirac cone-like dispersion, 35
- Dirac plasmons
- Bi₂Se₃ microribbons, 97, 98
 - EBL, 97
 - long wavelength limit, 98
 - microribbon arrays, 98
 - permittivities, 98
 - plasmonic and phonon modes, 98
 - RIE, 97
 - s-SNOM, 98
- Directional quantum dot emission, 37
- DNH, *see* Double nanohole (DNH)
- DNH optical tweezers, 190, 193
- Double-exposure holographic interferometry, 104
- Double field enhancement, 83
- Double nanohole (DNH), 190
- Double-peaked extinction spectra, 162

- Drag force, 184
 DRGs, *see* Chick dorsal root ganglia (DRGs)
 Drude and Tauc-Lorentz dispersion models, 94, 95
 Drude model, 42, 263
- E**
- EAR spectroscopy, *see* Extraordinary acoustic Raman (EAR) spectroscopy
 EBL, *see* Electron beam lithography (EBL)
 Electro-chemiluminescence (ECL) nanosensor, 316
 Electromagnetic (EM) waves, 262
 Electron beam evaporation, 273
 Electron beam lithography (EBL), 3, 265, 271–274, 315
 Electron collision frequency, 94
 Electron-electron interactions, 161
 Electron-electron relaxation, 160
 Electron-electron scattering, 160, 163, 164
 Electron-multiplying charge-coupled device (EMCCD), 273, 277, 282, 284, 288
 Electron-phonon scattering, 44
 Electron-photon rate, 161
 Electron transfer
 direct, 163–165, 167–169, 171
 indirect, 163–166, 171
 Electrothermoplasmonic (ETP) flow, 197
 mechanism, 251–252
 techniques and applications, 252
 EMCCD, *see* Electron-multiplying charge-coupled device (EMCCD)
 Energy-dispersive X-ray spectroscopy (EDS), 93
 Enhanced light harvesting
 Bi₂Te₃ nanoplates, 109
 BSTS nanocones, 108, 109
 current-density-voltage (J - V) properties, 108
 IPCE, 109
 plasmon-induced electric field, 108
 Si/PEDOT:PSS solar cell, 108
 Tamm plasmons, 109
 topological insulator-based plasmonics, 109
 wavelength, 108
 Enhanced photoluminescence (PL) emission
 CdSe/ZnS QD structure, 107
 enhanced UV, 108
 magnetic resonance vanishment, 107
 monolayer MoS₂ response, 106
 Sb₂Te₃ nanogrooves, 106, 107
 solvothermal method-synthesized Bi₂Te₃ nanoplates, 107
 wavelengths, 106
 ENZ cut-off frequency, 57
 ENZ linear optical phenomena
 ENZ mode, 38–40
 optical absorption, 36
 PA, 40–41
 radiation characteristics, 37–38
 ultra-thin ENZ materials, 36
 ENZ media
 field enhancement, 31–33
 temporal and spatial properties, 30
 unconventional optical properties, 30
 wavelength expansion, 30–31
 zero group velocity, 31
 ENZ mode
 field distribution, 38
 field enhancement, 39
 longitudinal component, 38
 optical coupling, 38
 quantum-well intersubband transition, 40
 quasi-static behavior, 38
 resonance frequency, 38
 triple resonance splitting, 39
 zero-crossing wavelength, 39
 ENZ-nanorod system, 37
 ENZ-plasmonic optical phenomena
 AFC, 45–47
 applications, 42
 boosted nonlinearity origins
 field enhancement, 42
 hot electrons, 42–44
 interband transitions, 44
 intensity-dependent refractive, 44–45
 optical wave mixing, 47–49
 plasmonic materials, 42
 ENZ-plasmonic structure, 45, 48, 49
 ENZ-plasmonic systems, 30
 optical phenomena, 28
 theoretical and experimental progress, 28
 ENZ plasmonic waveguide
 applications, 58
 channels, 58
 characterized, 58
 coherent optical effects, 57
 CPA (*see* Coherent perfect absorption (CPA))
 enhanced and homogeneous fields, 60
 EPs (*see* Exceptional points (EPs))
 FP resonances, 60
 lengths, 59
 lowest-order mode, 58

- ENZ plasmonic waveguide (*cont.*)
 nanochannels, 57
 relative permittivity, 58
 SPPs, 58
 transmission and reflection coefficients, 60
 zero transmittance, 59
- ENZ resonance, 59
- Epsilon-near-zero (ENZ) materials
 effects, 28
 media, 30–33
 optical field enhancements, 28
 plasmonics, 28–30
 vanishing electric permittivity, 28
- Escherichia coli*, 221
- ETP, *see* Electrothermoplasmonic (ETP)
- Evolutionary algorithms
 biological analogies, 144
 cross genetic operation, 143
 dipole nanoantenna, 143
 electromagnetic field, 144
 false convergence, 144
 fitness function, 143
 genetic (*see* Genetic algorithm)
 geometric optimization, 140
 mathematical function, 141
 micro and submicrometric geometries, 143
 nanometric dimensions, 142
 optimization of problem solutions, 141
 organism-specific genetic information, 140
 parameters, 140
 self-assembly techniques, 143
 simulated/experimental value, 143
 two-dimensional geometries, 144
- Evolutionary Dipole Nanoantenna (EDN), 151
- Exceptional points (EPs), 57
 branch point singularities, 67
 enhanced electromagnetic mode, 68
 formation, 68
 material permittivity, 68
 non-Hermitian nanophotonic system, 68
 numerical modeling (*see* Active ENZ waveguides, numerical modeling)
 phase-controlled amplification, 69
 PT-symmetric effects, 68
 PT symmetric non-Hermitian photonic systems, 67
 spectral degeneracy, 69
 spectral singularities, 68
 symmetric plasmonic configuration, 69
- Extraordinary acoustic Raman (EAR) spectroscopy, 195
- F**
- Fabrications of topological insulators
 ALD method, 92
 binary sesquichalcogenides, 91
 CVD method, 93
 MSC method, 92
 PLD method, 93
 QL, 91
- Fabry-Pérot (FP) resonances, 60
- False convergence, 144
- Far-field chirality, 3
- Far-field light-matter interactions
 AT (*see* Asymmetric transmission (AT))
 artificial nanostructures, 8
 CB, 9
 CD (*see* Circular dichroism (CD))
- FDTD simulation, *see* Finite-difference time-domain (FDTD) simulation
- FEM, *see* Finite element method (FEM)
- Fermi-Dirac distribution, 163
- Field displacement, 42
- Field intensity enhancement (FIE)
 ENZ material, 31
 fabrication, 32
 isotropic-ENZ cases, 32
 longitudinal-ENZ media, 32
- Figures of merit (FOM), 95
- Finite-difference time-domain (FDTD) simulation, 314
 frame capturing, 275
 GaN, 314
 grating couplers, 274, 275
 LNW-OGCs, 275
 NW systems, 275
 SPP modes, 288, 291
 3d, 271
- Finite element method (FEM), 270, 314
- First-generation plasmonic tweezers, 216–217
- Fluorinated polymer, 314
- Focused ion beam (FIB), 3, 101
- Form of conductivity, 96
- Fourier transform, 170
- Fourier-transform infrared spectroscopy (FTIR), 95
- Four-wave mixing (FWM), 47, 48
- Fruit fly pheromone oil palm, 2
- Full width at half maximum (FWHM), 119
- G**
- Gallium-doped Zinc Oxide (GZO), 35
- Gas sensors, 307, 311

Gaussian excitation source, 274
 Gauss's law, 30, 180
 Ge antennas, 316
 Genetic algorithm
 biological analogies, 144
 COMSOL Multiphysics, 147
 constraint requirement, 146
 electrical conductivity, 146
 electromagnetic wave, 147
 general values, 144
 generic flow diagram, 142
 geometries, 148
 Holland genetic algorithm, 143
 multi-objective, 145, 147, 150
 normalized electric field, 147–150
 numerical simulation, 147
 Seebeck coefficients, 147
 total electric current density, 146
 Genotype, 140
 Geometric optimization, 138
 Giant multilamellar vesicles, 227
 Glancing angle deposition (GLAD), 16
 Glycoprotein, 314
 Gold bowtie plasmonic tweezer, 214
 Gold nano-bowtie LSPRR tweezer, 228
 Gold nano-islands (AuNIs), 236
 Gold (Au) NPs, 302, 311, 313
 Gold optical nanoantennas, 189
 Gradient force, 182, 184, 209, 210
 Graphene, 217, 305–306
 Graphene-assisted PCF, 312
 Graphene nano-ribbon (GNR) array, 317
 Graphene oxide-iron oxide-AuNPs-nanocomposites (GO-IONP-Au), 306
 Graphene plasmonics (GPs)
 nanoscale light control, 90
 3D topological insulators, 91
 Graphene plasmonic tweezers, 217
 Grating couplers, 263, 269, 274–278, 280, 281, 287, 289
 Green's tensor technique, 185
 Group velocity, 82

H

H₂ photosplitting, 166
 H₂ splitting dynamics, 166
 Hamiltonian of plasmonic nonlinear system, 126
 Harmful and toxic gases, 307
 Helical plasmonic nanostructures, 10
 Helix, 6, 15
 Hermitian system, 77

Highly efficient lithographic plasmonic nanowires, 277–280
 High-refractive-index topological insulator, 110
 High-resolution transmission electron microscopy (HRTEM), 93
 Holland genetic algorithm, 143
 Horizontally polarized pump, 49
 Hot-electron-driven catalysis, 157
 direct electron transfer, 167–169
 indirect electron transfer, 166
 mechanisms, 165
 plasmon-mediated hot electrons, 166
 Hot-electron-induced nonlinearity, 157, 169–171
 Hot electrons, 42–44
 catalysis (*see* Hot-electron-driven catalysis)
 generation and relaxation, 159–161
 indirect/direct electron transfer, 157
 LSPR, 157
 phonon modes, metal nanoparticles, 157
 photoemission process, 156
 photoexcitation, 156
 physical and chemical processes, 156
 plasmon, 157
 plasmon decay, 163
 plasmonic nanostructures, 157
 positive/negative energy, 157
 HPPs, *see* Hybrid plasmonic polaritons (HPPs)
 Hybrid electro-thermo-plasmonic nanotweezers, 197
 Hybrid photonic-plasmonic tweezers, 193
 Hybrid plasmonic nanomaterials
 BMNPs, 304, 305
 properties, 304
 REMNPs, 303
 TMNPs, 304–305
 Hybrid plasmonic polaritons (HPPs), 264–265
 Hydrodynamic consideration, 118
 Hydrodynamic model, 120
 Hydrogen sulphide (H₂S) gas detector, 312
 Hydroxylation process, 273

I

Icosahedron, 303
 Incident photon-to-charge carrier efficiency (IPCE), 109
 Indium-doped Cadmium Oxide (ICO), 35
 Indium tin oxide (ITO) layer, 314
 Induced CD signal, 19
 Induced circular dichroism (ICD), 19
 Inscribed graphene dual-rings arrays (IGDAs), 19

- In situ* single-molecule identification technique, 199
- Intensity-dependent refraction, 44
- Intensity-dependent refractive index, 44
- Interband transitions, 44
- Interdigital capacitors, 150
- Interlayer spacing, 6
- J**
- Jones matrix T_{circ} of circular polarization, 4
- K**
- K-RAS, 316
- Kretschmann structure, 99, 100, 104
- L**
- Lab-on-a-chip (LOC) model
monolithic integration, 225
optical sorting, 224
- Langevin equation, 185
- Large intensity enhancement, 45
- Laser beam, 178
- Lateral trapping, 209
- Layer-by-layer nanostructures, 6
- Left circularly polarized (LCP), 3
- Light-matter interaction, 6, 27
- Linear CPA, ENZ
channel's thickness, 62
coherent perfect transmission, 64
counter-propagating beams, 63
counter-propagating plane waves, 64
field distribution, 62, 65
field enhancement, 65
guided wave number, 62
incident radiation energy, 64, 65
light-matter interactions, 65
material permittivity dispersion, 62
normal incident plane wave, 64
normal incident z -polarized plane, 62
reflection amplitude, 64
scattering matrix elements, 64
transfer matrix method, 63
transmission, 64
- Linear light-matter interaction, 118
- Linearly polarized light, 9
- Linear polarization rotation, 9
- Linear Raman effect, 223
- Line optical tweezers, 226
- Lipkin's research, 4
- Liquid droplets, 226
- Lithographic nanowires (LNWs)
Ag plasmonic, 286
characteristics, 271
coupling efficiency, 279
coupling schemes, 279
EBL, 272, 273
fabricated, 272
grating couplers, 274
highly efficient, 277–280
ND emission, 285
optical characterization, 273
optimization
effective index, 270
FEM, 270
highly efficient, 277–280
low-loss efficient fabrication method, 269
mode effective index, 270
propagation length, 270–274
scalable on-chip quantum information processing system, 268
surface plasmon polaritons, 274–277
3D nanograting couplers, 269–270
photon emission map, 274
plasmonic modes, 264
scattered SPPs signal, 273
- Lithographic nanowires-optimized grating couplers (LNW-OGCs)
and bare NWs, 277
characterizations, 277
coupling efficiency, 277
dipole emitter, 281
and dipole emitter, 282
experimental characterizations, 277
FDTD simulation, 275
MPTMS, 280, 284
and NDs, 281–283
photon emission maps, 280
SPPs, 285
- Lithographic plasmonic waveguides, 264
- LNW-OGCs, *see* Lithographic nanowires-optimized grating couplers (LNW-OGCs)
- LNWs, *see* Lithographic nanowires (LNWs)
- LOC, *see* Lab-on-a-chip (LOC) model
- Local density of optical states (LDOSs), 124
- Localized plasmon resonances (LPRs), 90
BSTS nanocone arrays, 100, 101
crystalline-amorphous phase, 102
Dirac plasmons, 102
FDTD simulated field distribution, 101
FIB milling method, 101
LPR wavelength, 101

- Lycurgus glass cup, 100
 - VIS and NIF plasmonic resonances, 102
- Localized surface plasmon resonances (LSPRs), 18, 157, 158, 161, 163, 164, 169, 208, 211–213, 216, 218, 219, 223, 228, 235, 299, 312, 314, 315, 318
- Localized surface plasmons (LSPs), 29, 118, 299
- Loop-wire nanostructures, 6
- Lorentz force, 180, 181
- Lorentz-Mie scattering, 179
- Lowest unoccupied molecular orbital (LUMO), 170, 171
- Low-loss efficient fabrication method, 269
- LSPRs, *see* Localized surface plasmon resonances (LSPRs)
- LUMO, *see* Lowest unoccupied molecular orbital (LUMO)

- M**
- Magnetic Mie resonances, 7
- Magnetic plasmon resonances (MPRs)
 - enhancing light-matter interactions, 102
 - experimental measurements, 104
 - FDTD simulations, 103
 - FIB milling method, 102
 - graphene split rings, 102
 - micro-spectrometer system, 102
 - topological insulator, 102
- Manipulation of nanoparticles, 191, 199, 213, 244
- Marangoni convection
 - mechanism, 248
 - techniques and applications, 249–250
 - trapping, 247
- Material platforms, ENZ media
 - Drude model, 33
 - metals, 34
 - optical metamaterials, 35–36
 - permittivity, 33
 - real and imaginary components, 33
 - TCOs, 34–35
 - transition metal nitrides, 34
 - zero-crossing, 34
- Maxwell's equations, 120, 179
- Maxwell's stress tensor, 180, 214
- MEF, *see* Metal-enhanced fluorescence (MEF)
- Melting and slow-cooling (MSC) method, 92
- 3-Mercaptopropyl trimethoxysilane (MPTMS), 269, 271–274, 277, 280, 283, 284, 289–291
- Metal-based plasmonics, 90
- Metal–dielectric–metal metasurface, 6
- Metal-dielectric structures, 35
- Metal-enhanced fluorescence (MEF), 298
- Metal films, 264
- Metal-insulator-metal waveguide, 35
- Metallic nanocavity, 185
- Metallic nanoparticles, 29
- Metallic nanostructures, 178, 197
- Metallic nanowires (NWs), 265
- Metallic surface electrons, 262
- Metal nanoparticles (NPs), 157, 264
- Metal nanostructures, 5
- Metasurfaces, 29, 90
- Microchemical reaction vessels, 226
- Microchemistry
 - liquid droplets, 226
 - plasmon-enhanced optical tweezing systems
 - vesicle and membrane manipulation, 226
 - vesicle fusion, 227
- Microscopic solid/liquid particles, 227
- Microwave signals, 284
- Mid-infrared (MIF), 90, 316
- Mie resonances, 35
- Molecular beam epitaxy (MBE), 93
- Molecular chirality, 199
- Monolayer MoS₂, 106
- Monolithic integration, 225
- Morphology-invariant NPs, 316
- MPTMS, *see* 3-Mercaptopropyl trimethoxysilane (MPTMS)
- Multi-objective restricted genetic algorithm, 145, 146
- Multi-spiral nanostructure, 6

- N**
- Nano-antennas, 138, 216
- Nano-aperture-based plasmonic tweezers, 199
- Nano-aperture optical trapping, 193
- Nanocomposite plasmonic materials, 305–306
- Nanodiamonds (NDs)
 - application, 290
 - color centers, 266
 - coupling efficiency, 281
 - emission, 284–285, 288
 - and LNW-OGC, 282, 283
 - NV centers in, 264, 267–269, 282, 283, 290
 - plasmonic nanocircuitry, 283
 - PS-OGCs, 289
- Nanoemitters, 279–284
- Nanofabrication and full-field electromagnetic simulation techniques, 264
- Nanofabrication approach, 307

- Nano-gaps, 264
 - Nanometer adhesion layers, 265
 - Nano-optical conveyor belt, 191
 - Nanoparticle-on-mirror (NPOM), 316
 - Nanoparticles, 199
 - BMNPs, 301, 304
 - copper, 303
 - LSPRs (*see* Localized surface plasmon resonances (LSPRs))
 - plasmonic, 306–310
 - single, 301
 - TMNPs, 304
 - trapping, metallic nanocavity, 186
 - Nanophotonic system, 83
 - Nanoscale magnetometry, 264, 267
 - Nanoscale symmetric plasmonic active ENZ configuration, 57, 83
 - Nanoscale torque, 183
 - Nanoscale waveguides-based SPPs, 264
 - Nanoscience, 208
 - Nanostructure processing technologies, 3
 - ND-LNW coupled system, 286
 - NDs, *see* Nanodiamonds (NDs)
 - Near-field chirality enhancement, 8
 - Near-infrared (NIR), 90
 - Negative-energy hot electrons, 157
 - Nitrogen vacancy (NV) centers
 - and autofluorescence, 285
 - in diamond lattice, 266–267
 - dipole emitter, 279
 - electron spins, 268, 269
 - LNW-OGCs system, 284
 - measurement, 285
 - in NDs, 264, 268, 282, 283, 287, 290
 - photoluminescence spectra, 289
 - Noble metal nanoparticles, 319
 - Noble metals, 298, 301–303, 319
 - Nonlinear BIC-based metasurfaces, 125
 - Nonlinear four-wave mixing interaction, 130, 131
 - Nonlinear interaction, 118
 - Nonlinearity, 169–171
 - Nonlinear optical processes, 118
 - Nonlinear plasmonics, 169
 - broadband THz generation (*see* Broadband THz generation, nonlinear metasurfaces)
 - linear plasmonic resonances, 118
 - multiple photon absorption and multiplexing, 133
 - nonlinear Fano resonances, 124–127
 - topological graphene plasmons, 127–132
 - vacuum fluctuation scenarios, 133
 - Nonlinear tunable CPA, ENZ
 - absorption dip, 67
 - amplitude modulators design, 66
 - field confinement and enhancement, 67
 - input intensity, 66
 - Kerr nonlinear effect, 65
 - passive Q-switching, 66
 - relative permittivity, 65
 - third-order Kerr nonlinearity, 66
 - third-order nonlinear susceptibility, 65
 - two z -polarized plane waves, 66
 - Non-parabolic conduction band, 43
 - Nonspherical particle, 183
 - Non-zero imaginary permittivity, 37
 - Non-zero optical chirality, 5
 - NPOM, *see* Nanoparticle-on-mirror (NPOM)
 - Numerical aperture (NA), 178
 - Numerical modeling, active ENZ waveguides
 - approximation, 69
 - electric field enhancement distribution, 71
 - field enhancement, 69
 - free-standing waveguide geometry, 69
 - loss-compensated ENZ response, 71
 - non-Hermitian system, 69, 72
 - ohmic losses, 70
 - optical nonlinearities, 71
 - silver permittivity dispersion values, 69
 - transmittance and reflectance, 70–72
 - z -polarized plane wave, 70
 - NV centers, *see* Nitrogen vacancy (NV) centers
- O**
- OAM, *see* Orbital angular momentum (OAM)
 - Octahedron, 303
 - ODMR, *see* Optically detected magnetic resonance (ODMR)
 - OGCs, *see* Optimized grating couplers (OGCs)
 - On-chip plasmonic circuitry, 265
 - Optical chirality
 - chiral electromagnetic fields, 7
 - chiral molecular signals, 5
 - circularly polarized light, 5
 - electromagnetic field, 4, 5, 8
 - helical plasmonic nanoantenna, 5
 - layer-by-layer nanostructures, 6
 - metal–dielectric–metal metasurface, 6
 - multi-spiral nanostructure, 6
 - optical chirality density, 4, 5
 - pitch values, 7
 - planar gammadion structure, 7
 - planar polymer nanostructure, 6
 - plasmonic nanostructures, 6

- quantity pseudo vector, 4
- refractive index material, 8
- Si nanodisks, 8
- 3D nanostructures, 6
- Optical constants of topological insulators
 - ARPES experiments, 93
 - Cauchy principal, 94
 - DFT, 96
 - Drude and Tauc-Lorentz models, 95
 - electron collision frequency, 94
 - electronic excitations, 96
 - FOM superior, 95
 - FTIR, 95
 - Kramers-Kronig equations, 94
 - permittivities, 93
 - phonon modes, 96
 - surface conductance, 96
 - surface-on-bulk double layer model, 95
 - surface permittivity, 95
 - 3D topological insulators, 96
 - topological insulator film, 96
- Optical data storage, 262
- Optical emission, 222
- Optical forces
 - dipole, 179
 - dipole approximation regime, 181–183
 - Lorentz-Mie scattering, 179–181
 - momentum vector, 208
 - optical manipulation, plasmonic nanostructures (*see* Optical manipulation, plasmonic nanostructures)
 - optical torque, 183–184
 - trapping potential, 185
- Optical frequency conversion, 28
- Optical lattice, 191
- Optical lithography, 262
- Optically detected magnetic resonance (ODMR), 266–269, 284–286, 288–290
- Optical manipulation, plasmonic nanostructures
 - ASR, 193
 - bowtie nanostructures, 189
 - DNH optical tweezers, 190
 - Fano resonance peaks, 192, 193
 - gold optical nanoantennas, 189
 - hybrid photonic-plasmonic tweezers, 193
 - nanoring nano-apertures, 192
 - optical trapping, micro-and nanoparticles, 192
 - oscillating point-like nonlinear optical sources, 189
 - photons, 192
 - plasmonic lattice, 190
 - POTs, 189
 - SIBA optical trapping, 189, 190
- Optical manipulation tools, 226
- Optical metamaterials, 35–36
- Optical peristalsis, 191
- Optical sensing, 265
- Optical sensor, 314
- Optical signal processing, 118
- Optical sorting, 224
- Optical spectroscopy, 222
- Optical torque, 183–184
- Optical trapping, 209
 - atomic scale, 225
 - plasmon resonance shift induced, 185
 - SPPs, 187
 - technique, 178
- Optical tweezers
 - airborne particles, 227
 - biology, 178
 - classical electromagnetic wave theory, 178
 - definition, 208
 - fibroblasts, 220
 - gradient force optical trap, 208
 - metallic nanostructures, 178
 - metal nanostructures, 208
 - optical trapping, 208
 - physics and biophysics, 178
 - trapping and manipulating particles, 210
- Optical wave mixing, 47
- Optimal conditions, 138
- Optimal nanostructures yielding variables, 138
- Optimization
 - lithographic plasmonic nanowires (*see* Lithographic plasmonic nanowires)
- Optimized grating couplers (OGCs)
 - coupling efficiency, 274, 280
 - LNW (*see* Lithographic nanowires-optimized grating couplers (LNW-OGCs))
 - PS, 287–289
- Optofluidics
 - monolithic integration, 225
 - optical sorting, 224
 - synergic combination, microfluidics and optics, 224
- Optomagnetic circuits, *see* Optomagnetic plasmonic circuitry
- Optomagnetic plasmonic circuitry
 - Ag plasmonic LNWs, 286
 - design characterization, 286
 - EMCCD, 288
 - fabrication methods, 287
 - FDTD simulation, 287

- Optomagnetic plasmonic circuitry (*cont.*)
 grating couplers, 287
 ND-LNW coupled system, 285
 ODMR, 286, 289
 OGCs, 287
 plasmonic splitter, 286–287
 PS-OGCs system, 287–289
 quantum optical network, 286
 SPPs, 286, 289
- Optothermal plasmonic optical tweezers,
 197–199
- Opto-thermoelectric manipulation
 cations and anions, 241
 conventional, 242
 CTAC molecules, 244
 mechanism, 242–243
 techniques and applications, 243
 trapping, 244
- Opto-thermoelectric trapping technique, 198
- Opto-thermophoretic manipulation
 Boltzmann constant, 239
 mechanism, 237
 techniques and applications, 238
 thermophobicity and thermophilicity, 237
 trapping of objects, 240, 241
- Orbital angular momentum (OAM), 183, 184
- P**
- PCB, *see* Programmed circuit board (PCB)
- PEDOT:PSS film, 108
- PEGDA hydrogel, 313
- Per-atom occupation probability, 162
- Perfect absorption (PA)
 absorption measurements, 40
 air/ENZ/metal structure, 40
 angle of incidence, 40
 applications, 40
 bandwidth, 41
 ENZ-plasmonic systems, 41
 field distribution, 40
 permittivity, 41
 sub-wavelength thickness, 40
 TM-polarized light, 40
 wavelength, 41
 zero-crossing frequency, 40
- Periodically nanostructured graphene
 monolayer, 118
- Perturbation theory, 185
- Phase-dependent CPA effect, 83
- Phase matching technique, 263
- Photocatalysis, 171
- Photoelectric effect
 Einstein, A., 155
 Hertz, H., 155
- Photoemission process, 156
- Photogenerated hot electron, 157
- Photolithography techniques, 314
- Photoluminescence spectroscopy, 222
- Photonic crystal fiber (PCF), 314
- Photonic crystal fiber-based surface plasmon
 resonance (PCF-SPR) sensor,
 311–312, 316
- Photonic force microscope, 187
- Photons, 192, 207
- Photovoltaic devices, 302
- Physics behind optical tweezers, 178
- Pili, 221
- Planar polymer nanostructure, 6
- Plasma-enhanced CD, 20
- Plasmon, 157
- Plasmon-assisted magnetic resonances, 102
- Plasmon decay, 161–163, 165
- Plasmon driven photocatalysis, 165
- Plasmon-enhanced light-matter interactions
 enhanced light harvesting, 108–109
 enhanced PL emission, 106–108
 refractive index monitoring, 104–106
- Plasmon-enhanced Si/PEDOT:PSS solar cell,
 108
- Plasmonic Au NP arrays, 318
- Plasmonic behaviors, topological insulators
 Dirac plasmons, 97–98
 LPRs, 100–102
 MPRs, 102–104
 SPR, 99–100
- Plasmonic BICs
 AlGaAs nanodisks, 125
 coupling interaction, 125
 Friedrich-Wintgen condition, 124
 Hamiltonian, 126
 light-matter interaction, 125
 localization, 124
 localized electromagnetic field, 124
 non-leaky mode, 124
 nonlinear interactions, 127
 nonlinear optical effects, 125
 optical nonlinearity, 126
 plasmonic nanostructures, 124
 quantum mechanics, 124
 radiative dissipation, 124
 spatiotemporal nonlinear beam shaping and
 control, 127
 suppression phenomenon, 126

- surface-to-volume ratio, 127
- symmetry-protected, 124, 125
- 2PA and 3PA, 125, 126
- Plasmonic catalysis, 166
- Plasmonic chirality, 22, 23
- Plasmonic circuitry, 286–289
- Plasmonic electric field, 90
- Plasmonic energy conversion, 162
- Plasmonic excitations, 118
- Plasmonic heating
 - heat generation, 234
 - mechanism, 234
 - optical tweezers, 234
 - principles and applications, 235
- Plasmonic hotspot, 216
- Plasmonic metasurfaces, 36
- Plasmonic nanoantennas, 29
- Plasmonic nanocircuitry
 - coupling, 266
 - CPPs, 264
 - EBL, 265
 - HPPs, 264–265
 - lithographic, 268, 269
 - LNWs, 268
 - metallic NWs, 265
 - nanometer adhesion layers, 265
 - NDs (*see* Nanodiamonds (NDs))
 - NV centers, 266–268
 - ODMR, 266–268
 - on-chip plasmonic circuitry, 265
 - optical sensing, 265
 - QEs, 266
 - quantum information and sensing, 264
 - SPPs (*see* Surface plasmon polaritons (SPPs))
 - types of, 264
- Plasmonic nanodisk array, 38
- Plasmonic nanomaterials, 298–301
 - conventional, 302–303
 - hybrid, 303–305
 - nanocomposite, 305–306
 - resonant frequency, 301
 - synthesis, 306–310
 - types, 301
- Plasmonic nanoparticle, 22
- Plasmonic nanoring arrays, 191
- Plasmonic nanostructures, 29, 30
- Plasmonic nanowaveguide array system, 59
- Plasmonic non-Hermitian nanophotonic system, 69, 79
- Plasmonic optical trapping-induced crystallisation, 200
- Plasmonic optical tweezers (POTs)
 - Abbe's diffraction, 187
 - DNH aperture, 194
 - experimental implementation, 189
 - fundamental drawback, 187
 - future perspectives, 199–200
 - heating limits, 187
 - heat sink, 188
 - high-power lasers, 187
 - metallic nanostructures, 188
 - optothermal POTs, 197–199
 - photothermal effects, 188
 - plasmonic-induced heating, 189
 - potential energy surface, 188
 - power flow magnitudes, 188
 - SPPs, 187
 - thermal side effects, 189
 - trapping efficiency, 189
 - trapping forces, 187
- Plasmonic photothermal effect
 - AuNIs, 236
 - heat management, 236
 - in-plane Bloch mode, 236
 - LSPR, 235
 - metallic nanostructures, 235, 237
 - nano-sized metallic components, 236
 - polarization, 236
- Plasmonic plane chiral metamaterial (PCM), 18
- Plasmonic resonant energy, 157
- Plasmonics, 262
- Plasmonic sensors
 - Ag-WO₃ hollow nanospheres (HNSs), 312
 - Aluminum (Al), 320
 - applications, 299–300
 - Au NP oligomers, 311
 - Au-Pd dimer, 311
 - Au-Pd-Pt hetero-tetramers, 311
 - Au-Pd-Pt hetero-trimers, 311
 - Au-Pd-Pt hetero-trimersare, 311
 - Au-Pd trimers, 311
 - Au-Pt heterodimers, 311
 - biosensing, 313–319
 - broadband solar spectrum, 320
 - CdSe@ZnS QDs, FS and Au NP, 313
 - Cr slit mask, 311
 - gas sensors, 307, 311
 - graphene-assisted PCF, 312
 - H₂S gas detector, 312
 - harmful and toxic gases, 307
 - LSPR, 312
 - materials, 300–307
 - MEF, 298
 - metallic nanostructures, 299
 - nanofabrication approach, 307
 - nanomaterials, 298–299
 - nanostructured plasmonic materials, 298

- Plasmonic sensors (*cont.*)
 noble metal nanoparticles, 319
 PCF-SPR sensor, 311–312
 SERS, 298
 smart phone-based, 299
 solvent-mediated reduction/stabilization, 319
 SPR (*see* Surface plasmon resonance (SPR))
 tedious/time-consuming, 319
 utilization, 299
- Plasmonic splitter, 286–287
- Plasmonic splitter-optimized grating couplers (PS-OGCs) system, 287–289
- Plasmonic thin films, 303
- Plasmonic tweezer
 applications (*see* Applications of plasmonic tweezers)
 Fröhlich condition, 212
 Gaussian laser beam, 209
 geometrical properties, 213
 gold bowtie, 214
 gradient force, 209, 210
 LSPRRs, 211–213
 manipulation and trapping, 209
 Maxwell stress tensor, 214
 nano-bowtie tweezing system, 214
 optical force, 214
 optical radiation pressure, 209
 optical trapping, 209
 polarizability, 212, 213
 scattering force, 209, 210
 SPPs, 211, 212
 surface plasmon, 210, 213
 3D FDTD simulations, 214
 trapping force, 214–216
 2D and 3D profiles, 214, 215
 types (*see* Types of plasmonic tweezers)
- Plasmonic tweezers electric field gradient, 226
- Plasmon-induced H₂ splitting, Ag atomic chain, 166, 167
- Plasmon-induced hot electrons, metallic nanoparticles
 adsorbed molecule, 163
 atomic-scale distributions, 162
 Au₅₅, MoS₂ monolayer, 163–165
 carrier distribution, 158
 direct and indirect electron transfer, 163–165
 Fermi–Dirac-like distribution, 159
 hot-electron generation and relaxation, 159–161
 LSPR excitation, 157
 nanoscale characterization, 171
 nanostructure
 shape, 161–163
 size, 161–163
 nanotechnology, 171
 non-radiative decay, 158
 plasmon decay, 159
 plasmonic metals, 159
 plasmonic resonant energy, 157
 surface plasmon excitation and decay, 158
- Plasmon-induced transparency (PIT), 90
- Plasmon-induced water splitting, Au nanosphere, 168
- Plasmon-mediated hot electrons, 166
- Plasmon propagation length, 271–274
- PMMA, *see* Polymethyl methacrylate (PMMA)
- Polarizability, 212, 213
- Polymer nanostructures, 7
- Polymethyl methacrylate (PMMA), 273, 314, 317, 318
- Polytetrafluoroethylene (PTFE) cell, 318, 319
- Polyvinyl alcohol, 312
- POTs, *see* Plasmonic optical tweezers (POTs)
- Poynting’s theorem, 236
- Programmed circuit board (PCB), 284
- PT-symmetric photonic systems, 71
- Pulsed laser deposition (PLD) method, 93
- Q**
- QDs, *see* Quantum dots (QDs)
- QEs, *see* Quantum emitters (QEs)
- Quantum cryptography, 266
- Quantum dots (QDs), 107, 189
- Quantum emitters (QEs), 266, 284, 289
- Quantum mechanics, 207
- Quantum network, 266
- Quantum plasmonic circuits
 coupling, 279–284
 lithographic plasmonic nanowires, 268–279
 optomagnetic plasmonic circuitry, 286–289
 plasmonic nanocircuitry, 264–268
 surface plasmon detected magnetic resonance, 284–286
- Quintuple layer (QL), 91
- R**
- Raman shift spectrum, 93
- Raman signal, 223
- Raman spectroscopy, 223, 225
- Raman tweezers, 223
- Rare-earth metal nanoparticles (REMNPs), 303

- Rayleigh scattering, 181, 182, 222
 Refractive index (RI), 104, 314
 REMNPs, *see* Rare-earth metal nanoparticles (REMNPs)
 Resonance pinning effect, 37
 Resonance valley, 20
 RI, *see* Refractive index (RI)
 Right circularly polarized (RCP), 3
 RMS, *see* Root mean squared (RMS)
 Root mean squared (RMS), 195
- S**
- SAM, *see* Spin angular momentum (SAM)
 SARS-CoV-2, 315
 Sb gasification process, 93
 Scalable nanoplasmonic waveguides, 279
 Scanning electron microscope (SEM), 93
 Scattering force, 182, 183, 209, 210
 Scattering-type scanning near-infrared optical microscopy (s-SNOM), 98
 Schottky junction, 312
 Second-generation plasmonic tweezers, 217–219
 Second harmonic generation (SHG), 47
 Seebeck coefficients, 147
 Selected area electron diffraction (SAED), 93
 Self-induced back-action (SIBA), 189, 190
 Semiconductor-integrated technologies, 262
 Sensor
 CCNM, 18
 CD spectra, 20
 chiral biomolecules, 18
 chiral molecular sensing, 21
 chiral plasmons, 21
 ICD, 19
 IGDAs, 19
 LSPRs, 18
 PCM, 18
 surface plasmonic nanostructures, 21
 SERS, *see* Surface-enhanced Raman spectroscopy (SERS)
 SERS optical tweezers, 223
 Shape memory polyurethane (SMPU) substrates, 318
 SIBA, *see* Self-induced back-action (SIBA)
 SIBA optical trapping, 189
 Silver (Ag) NPs, 302–303
 Si nanodisks, 8
 Si nanoparticles, 7
 Single-beam gradient optical tweezers, 177
 Single-objective optimization, 145
 Smart phone-based plasmonic sensor, 299
 Solid-state quantum information processing, 266
 Soret effect, 237
 Spatiotemporal coupling, 30
 Spectral singularities, 67
 (quasi-)spherical membrane, 226
 Spin angular momentum (SAM), 183, 184
 Split-ring resonators (SRRs), 17, 119
 SPPs, *see* Surface plasmon polaritons (SPPs)
 SPR, *see* Surface plasmon resonance (SPR)
 SPR angle sensitivity, 105
 SPR holographic imaging, 104
 Standard CMOS technology, 34
 Standard nanolithography methods, 49
 Steam generation, 318
 “Superchiral” plasmon near-fields, 3
 Super-resolution imaging, 263
 Surface-enhanced Raman scattering (SERS), 298, 316, 317
 Surface-enhanced Raman spectroscopy (SERS), 28, 223, 302
 Surface plasmon, 157, 158, 161, 210, 211, 213
 Surface plasmon coupling (SPC) effect, 316
 Surface plasmon detected magnetic resonance, 284–286
 Surface plasmon effects, 23
 Surface plasmonic nanostructures, 21
 Surface plasmon polaritons (SPPs), 29, 118, 187, 189, 211, 212, 275–279, 299
 at Ag-SiO₂, 274
 CSNWs, 265
 dipole emitter, 280, 281
 dispersion curve, 263
 Drude model, 263
 electric field, 270
 EM waves, 262
 enhancement factor, 280
 intensity decays, 270
 metal/dielectric interface, 262, 263
 nanoscale waveguides-based, 264
 phase matching, 263, 265
 propagation characteristics, 274
 propagation length, 270, 271, 273
 scattered intensity, 274
 scattering strength, 289
 TM (p-polarized) mode, 262
 waveguide-based, 263
 waveguided, 271
 Surface plasmon resonance (SPR)
 angle sensitivity, 105
 DH, 104
 double-exposure holographic interferometry principle, 104

- Surface plasmon resonance (SPR) (*cont.*)
 holographic imaging, 104
 intensity sensitivity, 105
 Kretschmann structure, 100, 104
 and LSPR, 299
 metal nanofilm, 99
p- and *s*-polarized components, 105
 phase sensitivity, 106
p-polarized light, 100
 principle, 298
 propagating/localized, 299, 300
 refractive index, 104
 Sb₂Te₃ film, 99, 100, 104
 sensors, 319
 SNOM measurement, 100
 surface electrons, 298
 topological insulator-based, 100
 traditional gold-based, 105
 WP, 104
- Surface plasmons (SPs), 28, 90
 Surface plasmons decay, 161
 Surface tension, 226
 Symmetry-breaking meta-atoms, 118
 Symmetry-protected BICs, 124, 125
- T**
- TCO-based ENZ materials, 42, 45, 49
 TDDFT, *see* Time-dependent density-functional theory (TDDFT)
 Terahertz (THz), 118
 Thermal effects, 208
 Thermoelectric analysis, 151
 Thermophoresis, 238
 Thermo-plasmonic convection
 mechanism, 245–246
 techniques and applications, 247
 Third harmonic generation (THG), 47
 Third-order optical nonlinear material, 82
 3D metal spiral system, 9
 3D nanograting couplers, 269–270
 3D optical chirality map, 7
 3D topological insulators, 91, 92, 110
 Three photon absorption (3PA), 125
 Ti adhesion layer, 278
 Time-dependent density-functional theory (TDDFT), 164, 169
 TiN-based solar absorber (TSA), 318, 319
 Tin-doped Indium Oxide (ITO), 34
 TiN split ring resonators, 49
 TiO₂
 Ag nanorods, 163
 TM mode, 59
- TMNPs, *see* Trimetallic nanoparticles (TMNPs)
- TM-polarized light, 45
- Topological graphene plasmons
 bandgap, 128
 bulk band diagrams, 129
 CMT, 131
 deep-subwavelength scale, 132
 defect-immune propagation, 131
 external magnetic field, 128
 gap Chern number, 128
 metasurfaces, 127, 129
 near-field distributions, 130
 nonlinear dynamics, 131
 nonlinear edge-waveguide coefficient, 127
 nonlinear FWM interaction, 130
 normalized wave vector mismatch, 131
 numerical calculations, 128
 opportunities, 127
 periodically nanostructured monolayer, 127
 photonic devices development, 127
 plasmonic effects, 129
 relaxation time, 128
 scattering boundary conditions, 131
 surface conductivity tensor, 128
 ultralow-power-consumption, 132
 unidirectional propagation, 131
 visible-light region, 128
- Topological insulator plasmonics (TIPs), 91
- Topological insulators
 conducting edge/surface state, 91
 critical role, 91
 fabrications, 91–93
 intrinsic surface-on-bulk structures, 110
 optical constants, 93–96
 plasmonic behaviors (*see* Plasmonic behaviors, topological insulators)
 quantum spin Hall effect, 110
 topological property, 91
 tunable, 91
 unique band structure, 91
- Torque
 additional forces, dielectric particles, 183–184
 dipole approximation regime, 181–183
 Maxwell's stress tensor, 179–181
 optical, 183–184
- Toxic gases/biomolecules, 318
- Traditional gold-based SPR systems, 105
- Transfer matrix method, 62
- Transformation transmittance, 10
- Transformed transmittance, 10
- Transition metal dichalcogenides (TMDCs), 106

- Transition metal nitrides, 34
- Transmission matrix, 4
- Transparent conducting oxides (TCOs), 34, 90
- Transverse electric (TE) waves, 59, 262
- Transverse magnetic (TM) waves, 28, 31, 262
- Trapping approach, 187
- Trapping force, 214–216
- Trimetallic nanoparticles (TMNPs), 304–305
- Triple-helical nanowire configuration, 9
- TSA, *see* TiN-based solar absorber (TSA)
- 2D (planar) achiral nanostructures, 3
- 2D CdTe/HgTe/CdTe quantum wells, 91
- 2D nanoantenna evolution and comparison, 145
- Two-dimensional (2D) massless Dirac electrons, 90
- Two photon absorption (2PA), 125
- Types of plasmonic tweezers
 - first generation, 216–217
 - second generation, 217–219

- U**
- U bent Plasmonic optical fibre, 314–315
- Ultra-sensitive chiral molecular sensing, 18
- Ultra-thin ENZ films, 42
- Unilamellar vesicles, 227

- U-shaped ENZ channel, 31
- UV-to-MIF range, 95

- V**
- Vesicle and membrane manipulation, 226

- W**
- Waveguide-based SPPs, 263
- Wavelength-multiplexed nonlinear plasmon-MoS₂ hybrid metasurface, 126
- Wollaston prism (WP), 104

- X**
- X-ray diffraction (XRD), 93

- Z**
- Zero-crossing wavelength, 43
- Zero group velocity, 31
- Zero index metamaterials (ZIM), 61
- Zero phonon lines (ZPLs), 266
- Zinc telluride nonlinear crystals, 119
- ZPLs, *see* Zero phonon lines (ZPLs)